

**Quantum simulation and metrology with multilevel
fermions in an optical lattice**

by

Michael A. Perlin

B.S., Oregon State University, 2015

M.S., University of Colorado at Boulder, 2019

A thesis submitted to the
Faculty of the Graduate School of the
University of Colorado in partial fulfillment
of the requirements for the degree of
Doctor of Philosophy
Department of Physics

2021

Committee Members:

Ana Maria Rey, Chair

Rahul Nandkishore

Jun Ye

James Thompson

Sandeep Sharma

Perlin, Michael A. (Ph.D., Physics)

Quantum simulation and metrology with multilevel fermions in an optical lattice

Thesis directed by Prof. Ana Maria Rey

Ultracold atomic systems are exquisite platforms for studying many-body physics and developing quantum technologies. Alkaline-earth(-like) atoms (AEA) in particular offer unique capabilities for pushing the state-of-the-art in quantum simulation and sensing capabilities. These atoms have an ultranarrow electronic transition that is used as the basis for the world's best atomic clocks. Moreover, AEAs can have a rich internal structure owing to nuclear spin degrees of freedom that are largely untapped as a scientific, metrological, and computational resource. In this thesis, we explore some of the possibilities and prospects for exploring many-body quantum phenomena and advancing sensing capabilities with ultracold AEAs.

We begin on the simulation end with a deep dive into the emergence of multi-body interactions between ultracold AEAs. We then present a proposal to harness collisional interactions and inhomogeneities in an AEA-based clock for the preparation of many-body entangled states known as spin-squeezed states, which allow for a quantum enhancement to clock sensitivity. In order to analyze this proposal's prospects and limitations, we develop a numerical technique for simulating collective quantum spin systems, which may find external applications for studying operator growth and quantum chaos. Borrowing ideas from the proposal to improve AEA-based clocks, we examine the possibility of spin squeezing using power-law interactions that can be found in a variety of atomic, molecular, and optical systems. Combining the spirit of our investigation into exotic interactions with the roadmap of our proposal to improve AEA-based clocks, we then propose a way to engineer a multilevel spin model with infinite-range interactions in the nuclear spin degrees of freedom of AEAs. We study the dynamical phases of this system, characterized by order parameters with a simple physical interpretation, and propose ways to measure these order parameters using standard techniques.

Dedication

To my friend, partner, and wife, Eva.

Acknowledgements

Graduate school has been an exciting journey. There is no real hope of enumerating the countless family, friends, colleagues, peers, and mentors that carried me through this journey, but here I make a partial attempt nonetheless. I would first and foremost like to thank my wife, Eva Morgun, who has been an invaluable friend and indispensable partner throughout these years. I would like to thank Eva's father, Andrey Morgun, for playing the role of both father and mentor to me after the death of my own father (Alexander Perlin) in 2013. I am also blessed to have the emotional and psychological support of my mother Natalie Perlin, step-mother Anna Kelbert, siblings Daniel Perlin, Sophie Perlin, and Boris Perlin, mother-in-law Natalia Shulzhenko, and brother-in-law Nikolay Morgun.

No less important than a family, particularly for a young adult finding their own path through life, is a close network of friends. I would like to thank some of my dear friends predating graduate school: John Shin, Paho Lurie-Gregg, Novela Auprey, Aaron Watt, Austin Valeske, MacKenzie Lenz, Rodney Snyder, Cameron Oden, Jackie Liu, Rachel Kim, Theresa Russell, Andrew C. Drake, and Youngjoo Lee. The various happenings of our personal lives, our careers, and a global pandemic have brought us close or carried us apart at different times, but these wonderful people have had a tremendous positive impact on my personal development and well-being throughout the years, and I hope to stay in touch with them for the rest of my life.

The last five years brought more people into my life, who have likewise provided me support and camaraderie throughout our postgraduate careers. From my graduate program in Boulder, these include: "Laser Dan" I. Herman, Eddie G. Nerney, Josh Levin, and Curtis Rau; and from the

Chicago area: Sam Genardi, Mike Brew, Shivani Baisiwala, Wes Peng, Leonie Schroeder, Ruslan Shaydulin, and Claire Textor. I have little doubt that these new friends will continue to feature regularly in my life after graduate school.

Finally, I would like to thank my scientific and career mentors, most notably Ana Maria Rey, Graeme Smith, and David Roundy, as well as Robert J. Lewis-Swan, Arghavan Safavi-Naini, Martin Suchara, and James C. Osborn; my colleagues Aki Goban, Peiru He, Chunlei Qu, Diego Barberena, Mikhail Mamaev, Sean R. Muleady, Asier P. Orioli, Thomas Bilitewski, Bhuvanesh Sundar, Zain H. Saleem, and Teague Tomesh; and my graduate (qualifying and doctoral) committee members Rahul Nandkishore, Jun Ye, James K. Thompson, Sandeep Sharma, Oliver DeWolfe, Matt Glaser, and Leo Radzihovsky. A special thanks to the extraordinary assistants and administrators Jeanne M. Nijhowne, Gwen Dickinson, and Corey Keasling, who are all remarkably helpful, efficient, and a pleasure to work with.

There is much that I wish to say about each person listed above (and more people that are not!), as well as the role that they played in my life through graduate school. But alas, I am writing a doctoral thesis, not a memoir. Suffice to say that each name carries with it a lengthy story and a wealth of gratitude. Going forward in life, I would be delighted to surround myself with people even half as wonderful and supportive as those that I have encountered thus far. Onward!

Contents

Chapter

1	Context and outline	1
2	Introduction and background	3
2.1	Alkaline-earth(-like) atoms	3
2.2	Individual atoms in a trap	6
2.3	Optical lattices and magic wavelengths	7
2.4	Spin-orbit coupling	9
2.5	Nuclear spin decoupling and $SU(n)$ symmetry	13
2.6	Two-body interactions	14
2.7	Spin operators	17
2.8	Collective spins and the Dicke manifold	18
2.9	Spin squeezing	20
3	Effective multi-body $SU(n)$ -symmetric interactions of ultracold fermionic atoms on a 3D lattice	23
3.1	Introduction	24
3.2	Background and overview	27
3.3	Low-energy effective theory	33
3.3.1	Diagrammatic representation of effective Hamiltonians	36
3.3.2	Effective two-body interactions and renormalization	38

3.3.3	Effective three-body interactions at second order	40
3.3.4	Effective three-body interactions at third order	41
3.3.5	Effective four-body interactions at third order	45
3.4	Low-excitation Hamiltonians, eigenstates, and spectra	46
3.4.1	Many-body state spectroscopy	49
3.4.2	Experimental signatures and comparison	50
3.4.3	Orbital-state dynamics of a nuclear spin mixture	56
3.5	Summary and outlook	59
3.A	Derivation of the effective Hamiltonian expansion	61
3.B	Diagram counting and symmetry factors	63
3.C	Effective coupling constants in a lattice	66
3.D	Momentum-dependent s -wave interactions	68
3.E	Bounds on theoretical uncertainties from inter-site effects	70
3.F	Perturbative parameters for the effective theory	72
3.G	Low-excitation M -body Hamiltonian coefficients	73
4	Engineering spin squeezing in a 3D optical lattice with interacting spin-orbit-coupled fermions	76
4.1	Introduction	78
4.2	Spin squeezing with the Fermi-Hubbard model	80
4.2.1	Model validity	84
4.2.2	Two-axis twisting	86
4.3	Experimental implementation and practical considerations	87
4.4	Conclusions	91
4.A	Derivation of the effective one-axis-twisting model	92
4.B	Numerical benchmarking of the OAT model	95
4.C	Two-axis twisting, decoherence, and the residual axial field	98

4.D	Dynamical decoupling in the TAT protocol	100
4.E	Clock interrogation after squeezing	102
4.F	Decoherence in the 3D ^{87}Sr optical lattice clock	106
4.G	Time-series of squeezing via OAT and TAT	106
4.H	Solving Heisenberg equations of motion for collective spin systems	109
4.I	Effect of a harmonic confining trap	112
4.J	Accounting for p -wave inelastic collisions	114
5	Short-time expansion of Heisenberg operators in open collective quantum spin systems	118
5.1	Introduction	119
5.2	Theory	121
5.3	Spin squeezing, benchmarking, and breakdown	126
5.4	Two-time correlation functions and out-of-time-ordered correlators	131
5.5	Conclusions	134
5.A	Basic spin operator identities	134
5.B	Commutation relations between powers of transverse spin operators	136
5.C	Product of arbitrary ordered collective spin operators	141
5.D	Sandwich identities for single-spin decoherence calculations	141
5.E	Uncorrelated, permutationally-symmetric single-spin decoherence	143
5.E.1	Decay-type decoherence	143
5.E.2	Dephasing	144
5.E.3	The general case	144
5.F	Sandwich identities for collective-spin decoherence calculations	146
5.G	Collective spin decoherence	147
5.G.1	Decay-type decoherence and dephasing	147
5.G.2	The general case	148
5.H	Emulating particle loss in a spin model	149

5.I	Initial conditions	151
5.J	Computing correlators with the truncated short-time (TST) expansion	153
5.K	Analytical results for the one-axis twisting model	155
5.L	Diagnosing breakdown of the TST expansion	156
5.M	Spin squeezing with strong decoherence	158
5.N	Heisenberg operators in open quantum systems	160
5.O	Short-time linear response and two-time correlators	163
6	Spin squeezing with short-range spin-exchange interactions	164
6.1	Introduction	165
6.2	Background and theory	166
6.3	Results	169
6.4	Discussion	174
6.5	Experimental applications	175
6.A	Spectral gap of the long-range XXX model	176
6.B	Numerical results in one spatial dimension	177
6.C	Benchmarking DTWA for the power-law XXZ model	179
6.D	Scaling relations for the collective phase in $D = 2$ spatial dimensions	183
6.E	Thermalization and long-range order	186
6.F	Sub-unit filling fractions	189
7	Engineering infinite-range $SU(n)$ interactions with spin-orbit-coupled fermions in an optical lattice	192
7.1	Introduction	193
7.2	From lattice fermions to an $SU(n)$ spin model	195
7.3	External control fields	200
7.4	Spin-orbit coupling	204
7.5	Mean-field theory and dynamical phases	207

7.5.1	Initial spin-polarized state	210
7.5.2	Initial kitten states	213
7.6	Conclusions and future directions	217
7.A	Numerical benchmarking of the spin model	218
7.B	Perturbation theory for $SU(n)$ ferromagnets	219
7.B.1	Generating excitation energy eigenstates	222
7.B.2	Recovering spin-wave theory	224
7.C	Restricting spin operators to the permutationally symmetric manifold	225
7.D	Relaxing assumptions of the three-laser drive	226
7.E	Mean-field theory	227
7.F	Schwinger boson equations of motion for quadratic spin Hamiltonians	228
7.G	Lax vector analysis	229
8	Spin qudit tomography and state reconstruction error	232
8.1	Introduction	233
8.2	Polarization operators	235
8.3	Spin tomography as signal recovery on the sphere	238
8.4	State reconstruction error	240
8.5	Tomography protocol	247
8.A	Rotating polarization operators	250
8.B	An improved reconstruction error bound	252
8.B.1	Errors in the spin-projection basis	253
8.B.2	Errors in the polarization operator basis	254
8.B.3	Revisiting the reconstruction error bound	256
8.C	Exact reconstruction error	257
8.C.1	Comments on a tight reconstruction error bound	260
8.D	Polarization operator product expansion	261

8.E Optimizing the method of Newton and Young	262
9 Summary and conclusions	264
References	266

Tables

Table

- 3.1 Low-excitation eigenvalues of M -body Hamiltonians H_M . Many-body energy eigenstates are labeled by the nuclear spins they occupy (i.e. \mathcal{N} with $N \equiv |\mathcal{N}|$) and whether they are in an orbital ground (0), singly-excited symmetric (+), or singly-excited asymmetric (-) state. The corresponding N -body eigenvalues $E_{NX}^{(M)}$ of H_M are given in terms of the coefficients U_{MX} as appearing in (3.47) (first three rows), in addition to the M -body eigenvalues $E_{MX}^{(M)}$ (last three rows). 48
- 6.1 Scaling exponents ν (with $\xi_{\text{opt}}^2 \sim 1/N^\nu$) for the values of J_z/J_\perp and α shown in Figure 6.9, in $D = 2$ spatial dimensions. Though provided here for the sake of practical interest and transparency (these are essentially the slopes of the dashed lines Figure 6.9), we note that these values are subject to correction in future work, as ruling out effects such as finite sampling errors may require a more extensive numerical analysis. 186
- 7.1 Drive Hamiltonians (left column) that can be implemented with different amplitude-matching conditions (right three columns), some of which are specified by an arbitrary sign $\sigma \in \{+1, -1\}$. The drives shown here are equal to that of Eq. (7.12) up to a possible energy shift of $\hat{s}_x^2 + \hat{s}_y^2 + \hat{s}_z^2 = s(s+1)$, and come in mutually commuting pairs: a drive with $|\Omega_m| = 1$ and $\Omega_n = 0$ for both $n \neq m$ commutes with the drive in which $\Omega_m = 0$ and both $|\Omega_n| = 1$ 202

Figures

Figure

- 2.1 Simplified energy level diagram for the low-lying electronic states of ^{87}Sr , reproduced from Ref. [14]. Dashed and dotted lines respectively show spin-orbit (LS) and hyperfine (HFI) coupling between bare electronic states. Solid lines show optical transitions between electronic eigenstates, with the corresponding wavelengths given in nanometers. Fractions indicate the net spin of the hyperfine manifold (involving nuclear spin) within the associated electronic energy level. 5
- 2.2 Band structure (orbital energy) of atoms in a periodic lattice potential $V_{\text{ext}}(z) = V_0 \cos^2\left(\frac{\pi z}{a}\right)$ with depth $V_0 = 4E_{\text{R}}$, where the lattice recoil energy $E_{\text{R}} = k_{\text{L}}^2/2m$ is defined in terms of the atomic mass m and the wavenumber k_{L} of the lattice light. Color indicates band index n as specified in the legend. 9
- 2.3 Band structure identical to that in Figure 2.2, but after relabeling excited-state quasi-momenta with $\hat{c}_{q_z+k_z,e}^\dagger \rightarrow \hat{c}_{q_z,e}^\dagger$ and $k_z = 2\pi/3$. Solid and dashed lines respectively show kinetic energies for ground- and excited-state atoms. 13
- 2.4 Husimi distributions for $N = 40$ spins in a spin-polarized state (left), as well as the Dicke states $|-10\rangle$ (middle) and $|0\rangle$ (right). A darker color at a point \mathbf{v} on the sphere indicates a larger overlap with the state $|\mathbf{v}\rangle$ maximally polarized along \mathbf{v} . For visibility, the color scale is normalized independently on each sphere. 20

2.5 Representations of the state $|\psi(t)\rangle$ of $N = 40$ spins initially polarized along the equator, and subsequently evolved under the OAT Hamiltonian \hat{H}_{OAT} for a time t up to the optimal OAT squeezing time $t_{\text{opt}}^{\text{OAT}} \sim N^{-2/3}$. Figure reproduced from Ref. [4]. 22

3.1 An example second-order diagram and the corresponding three-body interaction term in $H_{\text{int}}^{(2)}$, with $n > 0$ and $\hat{c}_{\mu s} \equiv \hat{c}_{0,\mu s}$. Diagrams are read from left to right to construct a sequence of operators from right to left. Solid (dashed) lines represent field operators acting on the lowest (arbitrary) motional states. For the sake of presentation, this diagram has colors associated with nuclear spin and orbital states, an arrow on each line to emphasize that they are directed left-to-right, and an explicit coupling constant written next to each vertex; we will generally not include these features, as they are not necessary to uniquely identify the term represented by a diagram. We will also drop explicit appearances of the ground-state projector \mathcal{P}_0 in our expressions, with the understanding that the low-energy effective theory implicitly addresses only non-interacting motional ground states. 37

3.2 Multiplicities of the magnitudes of reduced Rabi frequencies $\omega_{\mathcal{N}X} \equiv \Omega_{\mathcal{N}X}/\Omega_0\sqrt{N}$ in a lattice with a uniform mixture of nuclear spins with $I = 9/2$ and single-site occupation numbers N which are achievable in current ^{87}Sr experiments. 51

- 3.3 Population (in arbitrary units) of the excited 3P_0 orbital state of ^{87}Sr atoms in a uniform mixture of nuclear spins. Atoms are prepared in the ground state of a lattice with depth $\mathcal{U} = 54E_R$, where $E_R \approx 3.5 \times 2\pi$ kHz is the lattice photon recoil energy of the atoms, and interrogated by a laser with Rabi frequency $\Omega_I = 50 \times 2\pi$ Hz for a time $t = \pi/\Omega_I$. **(Left)** Populations predicted by the low-energy effective theory (with s -wave scattering parameters retrieved from Ref. [53]), averaged over all nuclear spin combinations of $N \in \{1, \dots, 5\}$ atoms per lattice site for a fixed total atom number. **(Right)** Experimental measurements of 3P_0 populations retrieved from Ref. [7], with Lorentzian fits to each peak as a visual guide. Resonance peaks are identified by the many-body orbital states which are excited at the peak. 52
- 3.4 Multi-body excitation energies of ultracold ^{87}Sr atoms at various lattice depths. The top plot in each sub-figure with fixed N, X shows the excitation energies $\Delta_{NX} \equiv E_{NX} - E_{N,0}$ measured experimentally in Ref. [7] and those predicted by the low-energy effective theory at different orders in the coupling constants, when applicable both with and without four-body contributions. The bottom plot in each sub-figure shows the relative error $\eta_{NX} \equiv \Delta_{NX}^{\text{theory}}/\Delta_{NX}^{\text{experiment}} - 1$. Error bars represent experimental error or conservatively estimated theoretical uncertainties from nearest-neighbor hopping of virtual states in the low-energy effective theory (see Appendix 3.E). 54
- 3.5 Summary of the many-body excitation spectra in Figure 3.4, retrieved from Ref. [7]. 55
- 3.6 Net population of the N -body orbital excited states $\{|\mathcal{N}\pm\rangle\}$ after interrogation of an initial mixed state $\rho_{N,0} = \mathcal{P}_{N,0}/\text{tr } \mathcal{P}_{N,0}$ for a reduced time $\tau_N \equiv t\Omega_0/\sqrt{N}$ (i.e. with real time t) by a laser with bare Rabi frequency Ω_0 which is resonant with the N -body excitation energy Δ_{NX} . Here \mathcal{P}_{NX} , defined in (3.60), is a projector onto the space of the N -body orbital states $|\mathcal{N}X\rangle$ 58
- 3.7 Dependence of the perturbative parameters KG_X/Δ on the lattice depth \mathcal{U} 73

4.1 **Schematic of the setup for spin squeezing.** (a) We consider N fermionic atoms with two (pseudo-)spin components, represented by red and blue spheres, trapped in the ground band of an optical lattice (shown in 2D for the sake of presentation). Atoms tunnel to neighboring sites at a rate J and experience on-site interactions with strength U . An external laser carrying a position dependent phase $e^{i\mathbf{k}_L \cdot \mathbf{r}}$ couples the spin states of the atoms. (b) After a gauge transformation, different spin states exhibit different dispersion relations with a relative phase $\phi = k_L a$, where a is the lattice spacing. The external laser couples spin states with identical quasi-momenta q in the gauge-transformed frame. (c) If interactions are sufficiently weak, all motional degrees of freedom become frozen in momentum space, with atoms effectively pinned to fixed quasi-momentum modes \mathbf{q} . The dynamics on the frozen \mathbf{q} -space lattice can then be mapped to a spin model in which collisional interactions correspond to a uniform, all-to-all ferromagnetic Heisenberg Hamiltonian with strength U/L , where L is the total number of lattice sites. (d) The spin dependence of the dispersion relation is captured by a mode-dependent axial field B_q that generates inhomogeneous spin precession. This axial field couples exchange-symmetric many-body Dicke states with total spin $S = N/2$ to spin-wave states with $S = N/2 - 1$. The all-to-all interaction opens an energy gap fU (with $f = N/L$ the filling fraction of spatial modes) between the Dicke states and the spin-wave states, which forbids population transfer between them in the weak-field limit. (e) To generate spin squeezing via one-axis twisting, we initialize a product state with all spins polarized in $-z$ (i.e. in $|\downarrow\rangle$), and apply a fast external laser pulse to rotate all spins into x . We then let atoms freely evolve for a variable time t (with a spin-echo pulse), after which the amount of spin squeezing can be determined experimentally from global spin measurements. The spin-squeezed state can be used for a follow-up clock interrogation protocol (see Appendix 4.E). 81

4.2 **Benchmarking the spin and one-axis twisting models.** Comparisons of maximum squeezing (top panels, **a.i** and **b.i**) and optimal squeezing time (lower panels, **a.ii** and **b.ii**) between the Fermi-Hubbard (FH), spin, and one-axis twisting (OAT) models; obtained numerically via the protocol depicted in Figure 4.1(e) in a 1D lattice with $L = 12$ sites. Results are shown for half filling with $N = 12$, $f \equiv N/L = 1$ (left panels, **a.i** and **a.ii**) and filling $f = 5/6$ (right panels, **b.i** and **b.ii**) as a function of U/J and the SOC angle ϕ . In both cases, the system is initialized in the corresponding ground state. Insets for both $f = 1$ and $f = 5/6$ show (in green) regions of the U - ϕ plane in which both the optimal squeezing (in dB) and the corresponding squeezing time of all three models agree to within 20%. At half filling (**a.i** and **a.ii**), mode-changing collisions are suppressed by Pauli blocking, resulting in almost exact agreement between the FH and spin models; both of these models converge onto the OAT model in the gap-protected, weak SOC regime of large U/J and small ϕ . The spin and OAT models show similar behavior away from half filling (**b.i** and **b.ii**), but the presence of mode-changing collisions results in their disagreement with the FH model as interactions begin to dominate at larger U/J . Even below half filling, however, the FH exhibits comparable amounts of squeezing to the spin model across a broad range of U/J and ϕ , albeit at earlier times when $U/J \gtrsim 2$ 85

4.3 **Optimal squeezing** with one- and two-axis twisting in a 2D section of the 3D ^{87}Sr optical lattice clock. **(a)** The maximum amount of squeezing depends only on the atom number $N = \ell^2$, where ℓ is the number of lattice sites along each axis of the lattice. While the time scales for squeezing generally depend on several experimental parameters, the time at which maximal squeezing occurs can be minimized at any given lattice depth V_0 by choosing SOC angles ϕ that saturate $\tilde{B}/U \approx 0.05$, where \tilde{B} is the variance of the SOC-induced axial field and U is the two-atom on-site interaction energy. Panels **(b, c)** show these minimal squeezing times as a function of the depth V_0 and linear size ℓ of the lattice. Lattice depths V_0 are normalized to the atomic lattice recoil energy E_R , and the upper axis on panels **(b, c)** marks values of U/J at fixed lattice depths. In general, TAT achieves more squeezing than OAT for any system size, and achieves optimal squeezing faster for $N \gtrsim 400$ atoms, as denoted by a dotted line in panels **(b, c)**. 89

- 4.4 **Optimal squeezing with decoherence** via one- and two-axis twisting in a 2D section of the 3D ^{87}Sr optical lattice clock (OLC). In practice, decoherence due to light scattering limits the amount of squeezing that is attainable in the the 3D ^{87}Sr OLC. Due to growing squeezing times with increasing system size, the maximal squeezing obtainable via OAT saturates past $\ell \approx 30$ sites along each axis of the lattice, with $N \approx 10^3$ atoms total. The more favorable size-dependence of TAT time scales, however, allow for continued squeezing gains through $\ell = 100$ ($N = 10^4$). While the OAT results in (a) are exact, the TAT results in (b) reflect only a lower bound on the maximum squeezing obtainable, albeit one that is likely close (within a few dB) to the actual value. Optimal squeezing times in the presence of decoherence are generally smaller than the corresponding times shown in Figure 4.3, as decoherence typically degrades squeezing before it reaches the decoherence-free maximum. The decoherence considered in this work also limits maximally achievable squeezing to ~ 20 dB less than the decoherence-free maxima shown in Figure 4.3. Sample plots of squeezing over time for particular choices of lattice size (ℓ) and depth (V_0/E_R) are provided in Appendix 4.G. 90
- 4.5 **Relative error** between maximal squeezing (measured in dB) obtained by the OAT [Eqn. (4.4)] and spin [Eqn. (4.3)] models of the main text in a system of 20 particles. The OAT model correctly captures the maximal squeezing (in dB) of the spin model to within 3% (marked by the horizontal reference line) within the gap-protected regime $\tilde{B}/U < 0.06$ 96

- 4.6 **Comparison between the OAT and the spin model in the presence of decoherence.** (a) The difference between the maximal squeezing (measured in dB) obtained by the OAT [Eqn. (4.4)] and spin [Eqn. (4.3)] models increases with the particle number N and the single-particle spontaneous emission rate γ . This disagreement is attributed in part to the fact that spontaneous emission transfers population of the collective spin state outside of the Dicke manifold, violating an assumption of the OAT model; see panel (b). The rate of population transfer outside of the Dicke manifold increases with both particle number and spontaneous emission rate. (Parameters for simulations in this figure: $U = 1000$ Hz, $J = 200$ Hz, and $\phi = \pi/20$). 97
- 4.7 **Optimal squeezing as a function of π -pulses** applied prior to the optimal TAT squeezing time in a CPMG sequence with (a) $N = 100$ and (b) $N = 1000$ atoms. Results are shown for OAT, TAT, and TAT $_{\pm,z}$, where TAT $_{\pm,z}$ denotes squeezing via the Hamiltonian $\hat{H}_{\text{TAT}}^{(\pm,z)} \equiv \hat{H}_{\text{TAT}}^{(\pm)} - \mathcal{J}_0(\beta_{\pm}) \langle \overline{B} \rangle_f^{\text{rms}} \hat{S}_z$. Details about experimental parameters for these simulations are provided in the text. 101
- 4.8 **Squeezing via OAT and TAT** in a 2D section of the 3D ^{87}Sr optical lattice clock, shown for (a) $\ell = 40$ and (b) $\ell = 100$ sites per axis (with $N = \ell^2$ atoms total), and a lattice depth of $V_0 = 4 E_R$, where E_R is the atomic lattice recoil energy. Atoms are confined along the direction transverse to the 2D layer by a lattice of depth $60 E_R$. Squeezing over time is shown for OAT (blue) and TAT (green), both with (solid lines) and without (dashed lines) decoherence via uncorrelated decay and dephasing of individual spins at rates of 0.1 sec^{-1} (see Appendix 4.F). 108

4.9 Dynamics of non-interacting spin-orbit coupled fermions in a 1D lattice with SOC angle $\phi = \pi/50$, plus a harmonic trap with $\Omega/J = 0.01$. Starting with a spin-polarized cloud in \downarrow ground state, an initial clock laser pulse is applied to rotate spins into x , and the atoms are allowed to evolve during the dark time. We track the dynamics of the \uparrow particle density for the cases of (a) $N = 20$ and (b) $N = 60$ atoms. Panel (c) shows the time-averaged fluctuations of the \uparrow particle density for each site index j from its initial value following the Ramsey pulse; see Eqn. (4.64). For $N = 60$, we have filled all delocalized modes as well as several localized modes, resulting in a large region of no density fluctuations at the trap center. Panel (d) contains the eigenspectrum for a single internal state in the presence of the trap (with the index n labeling the eigenvalues in order of increasing energy), where the critical mode n_c dividing the spatially delocalized and localized modes is indicated by a black dash-dotted line. The highest occupied mode in the \downarrow ground state for $N = 20$ and $N = 60$ is indicated by the green and red solid lines, respectively. . . . 110

- 4.10 Dynamics of interacting spin-orbit coupled fermions in a 1D lattice plus a harmonic trap for $U/J = 1$ (a), 2 (b), and 4 (c). For a 1D lattice with 10 sites and an SOC angle $\phi = \pi/50$, we apply a $\pi/2$ clock laser pulse to the \downarrow ground state and let the system evolve during the dark time. In (a.i)-(c.i) we show the squeezing dynamics of the system for both $N = 10$ (solid lines) and $N = 9$ (dashed lines) for a variety of trapping strengths. In (a.ii)-(c.ii), we plot the time-averaged fluctuations in total particle density, $\overline{\delta n_j}$ (as in Eqn. (4.64) but with $\hat{n}_{j,\uparrow}$ replaced by $\sum_{\alpha} \hat{n}_{j,\alpha}$). In (a.iii)-(c.iii), we plot the growth of the doublon population $N_d(t)$ (see Eqn. (4.65)) as a function of time, noting the absence of squeezing in the presence of a large doublon population. For the chosen trap strengths, the corresponding values of n_c are 28 ($\Omega/J = 0.01$), 14 ($\Omega/J = 0.04$), and 6 ($\Omega/J = 0.2$). In panels where the results for the homogeneous case (orange curves) are not visible, they are nearly identical to the results for $\Omega/J = 0.01$ (green curves). Here, we utilize periodic boundary conditions to minimize finite size effects. 111
- 4.11 ***p*-wave loss rates.** Both the averaged *p*-wave inelastic collision rate γ (orange) and the ratio of this collision rate to the optimal squeezing rate χ_{opt} (blue) are suppressed as the lattice depth increases. χ_{opt} is obtained by choosing SOC angles ϕ that saturate $\tilde{B}/U \approx 0.05$, where \tilde{B} is the variance of the SOC-induced axial field and U is the two-atom on-site interaction energy. 115
- 4.12 **Squeezing via OAT in the presence of inelastic collisions.** (a) For fixed particle number $N = 100$, the optimal squeezing decreases as the inelastic collision rate increases. Panel (b) shows squeezing over time for $\gamma/\chi_{\text{opt}} = 0.04$ (solid lines), which corresponds to $U/J = 6$, and compares it with $\gamma = 0$ (dashed lines) for different particle numbers. Inelastic collisions prevent the growth of optimal squeezing with particle number. For $N = 1000$, the maximum squeezing saturates to ~ 10 dB. . . . 116

- 5.1 Spin squeezing of $N = 10^4$ spins initially in $|X\rangle$ under (a) unitary and (b) non-unitary dynamics, computed using exact methods (solid lines), quantum trajectory simulations (dots), and the TST expansion in Eq. (5.8) with $M = 35$ (dashed lines). Solid circles mark the times at which the TST expansion gives an unphysical result with $\xi^2 < 0$ 127
- 5.2 Spin squeezing of $N = 10^4$ spins initially in $|X\rangle$ with spontaneous decay, excitation, and dephasing of individual spins at rates $\gamma_- = \gamma_+ = \gamma_z = 100\chi$. Computed using the TST expansion in Eq. (5.8) with $M = 35$. Solid circles mark the times at which the TST expansion gives an unphysical result with $\xi^2 < 0$ 130
- 5.3 The two-time connected correlator $C(t)$ and squared commutator $D(t)$, respectively defined in Eqs. (5.13) and (5.14), for $N = 10^4$ spins initially in the polarized state $|X\rangle \propto (|\uparrow\rangle + |\downarrow\rangle)^{\otimes N}$ evolving under the squeezing Hamiltonians in Eqs. (5.9)–(5.11). Results are shown for both unitary dynamics (solid lines) and non-unitary dynamics with $\gamma_- = \gamma_+ = \gamma_z = \gamma_0 = 100\chi$ (dashed lines), computed using the TST expansion in Eq. (5.8) with $M = 20$ 133
- 5.4 Spin squeezing throughout decoherence-free evolution of $N = 100$ spins initially in the state $|X\rangle$, computed using both exact methods (solid lines) and the TST expansion in Eq. (5.8) with $M = 35$ (dashed lines). Solid circles mark the times at which the TST expansion gives an unphysical result with $\xi^2 < 0$ 157
- 5.5 A collective spin correlator in the TAT model with $N = 100$ spins and no decoherence, computed using the TST expansion with $M = 35$. The divergence of correlators of this sort can be used to diagnose the breakdown of the TST expansion. 157
- 5.6 Optimal spin squeezing of $N = 100$ spins undergoing spontaneous decay, excitation, and dephasing at rates $\gamma_- = \gamma_+ = \gamma_z = \gamma_0$, computed using quantum trajectory simulations with 10^3 trajectories per data point. 159

- 6.1 Representations of the state $|\psi(t)\rangle$ of $N = 40$ spins initially polarized along the equator, and evolved under the OAT Hamiltonian for a time t up to the optimal OAT squeezing time $\chi t_{\text{opt}}^{\text{OAT}} \sim 1/N^{2/3}$. Darker colors at a point $\hat{\mathbf{n}}$ on the sphere correspond to a larger overlap $Q_{\psi(t)}(\hat{\mathbf{n}}) \equiv |\langle \hat{\mathbf{n}} | \psi(t) \rangle|^2$, where $|\hat{\mathbf{n}}\rangle$ is a state in which all spins are polarized along $\hat{\mathbf{n}}$ 167
- 6.2 The optimal squeezing ξ_{opt}^2 (top), minimal squared magnetization $\langle \mathbf{S}^2 \rangle_{\text{min}}$ (middle), and optimal squeezing time t_{opt} (bottom) for $N = 4096 = 64^2 = 16^3$ spins in $D = 2$ (left) and $D = 3$ (right) spatial dimensions. Spins are initially polarized along the equator and evolved under the XXZ Hamiltonian in Eq. (6.3). Squeezing ξ_{opt}^2 is shown in decibels, and $\langle \mathbf{S}^2 \rangle_{\text{min}}$ is normalized to its initial value $\langle \mathbf{S}^2 \rangle_0 = \frac{N}{2} \left(\frac{N}{2} + 1 \right)$. Dashed grey lines mark $\alpha = D$, and dotted grey lines track local minima of $\langle \mathbf{S}^2 \rangle_{\text{min}}$, marking the boundary between regions of collective and Ising-limited squeezing dynamics, respectively denoted “S-collective” and “S-Ising”. Other markers in the middle panels indicate vales of $J_z/J_\perp, \alpha, D$ that are currently accessible with neutral atoms [211, 212] (cyan line), Rydberg atoms [201, 202, 213] (red dots), polar molecules [203, 204, 214] (green line), magnetic atoms [205, 206] (pink square), and trapped ions [191] (blue line). DTWA results are averaged over 500 trajectories. . . 170
- 6.3 Squeezing ξ^2 and squared magnetization $\langle \mathbf{S}^2 \rangle$ over time for the power-law XXZ model with $\alpha = 3$ on a 2D lattice of 64×64 spins. Color indicates the value of J_z/J_\perp , and red lines (at $J_z/J_\perp = -2.2$) mark the approximate transition between S-collective and S-Ising phases, when the “collective” squeezing peak at $\tau \equiv t \times |J_z - J_\perp| \sim 6$ drops below the “Ising” peak at $\tau \sim 1$. For the parameters shown, $\langle \mathbf{S}^2 \rangle$ reaches a minimum at $\tau \sim 2$, which means that optimal squeezing at $\tau \sim 1$ is reached before maximal decay of $\langle \mathbf{S}^2 \rangle$ in the S-Ising phase. 172

- 6.4 Optimal squeezing ξ_{opt}^2 as a function of system size for the power-law XXZ model with $\alpha = 3$ on a 2D lattice of $N = L \times L$ spins. Whereas the amount of squeezing generated in the S-Ising phase is insensitive to system size, squeezing in the S-collective phase grows with system size and as $J_z/J_\perp \rightarrow 1$ (from below). Dotted grey line tracks minima of $\langle \mathbf{S}^2 \rangle_{\text{min}}$ as a function of J_z/J_\perp , as in Figure 6.2, marking the approximate dynamical phase boundary. 173
- 6.5 The optimal squeezing ξ_{opt}^2 (top), minimal squared magnetization $\langle \mathbf{S}^2 \rangle_{\text{min}}$ (middle), and optimal squeezing time t_{opt} (bottom) for $N = 4096 = 64^2 = 16^3$ spins in $D = 1, 2, 3$ spatial dimensions. Spins are initially polarized along the equator and evolved under the XXZ Hamiltonian in Eq. (6.3) of the main text. The results for $D = 2$ and 3 shown here are a subset of the results in Figure 6.2, presented in the same format as that for $D = 1$ for comparison. 178
- 6.6 Maximal populations $\langle \mathcal{P}_n \rangle_{\text{max}}$ of the total spin $S = N/2 - n$ manifolds \mathcal{P}_n throughout squeezing dynamics of 7×7 spins, initially polarized along the equator and evolved under the XXZ Hamiltonian in Eq. (6.3) of the main text with a power-law exponent $\alpha = 3$. Computed with TS₄ simulations and periodic boundary conditions. Shaded regions indicate $\langle \mathcal{P}_4 \rangle_{\text{max}} > 0.1$, where TS₄ results cannot be trusted due to the likeliness of population leakage into truncated states. All states in \mathcal{P}_1 break translational invariance, so the initial population $\langle \mathcal{P}_1 \rangle_0 = 0$ is protected by the absence of translational symmetry-breaking terms in the Hamiltonian. The population $\langle \mathcal{P}_3 \rangle$, meanwhile, is small because \mathcal{P}_3 is only coupled to \mathcal{P}_2 and \mathcal{P}_4 by matrix elements that are $O(1/N)$ smaller than the couplings between $\mathcal{P}_0 \leftrightarrow \mathcal{P}_2 \leftrightarrow \mathcal{P}_4$ 180

- 6.7 Optimal squeezing ξ_{opt}^2 (top) and minimal squared magnetization $\langle \mathbf{S}^2 \rangle_{\text{min}}$ throughout squeezing dynamics (bottom) as computed via TS_4 and DTWA in the same setting as Figure 6.6, likewise with shaded regions indicating $\langle \mathcal{P}_4 \rangle_{\text{max}} > 0.1$ in the TS_4 simulations. Here squeezing ξ_{opt}^2 is shown in decibels, and $\langle \mathbf{S}^2 \rangle_{\text{min}}$ is normalized to its initial value $\langle \mathbf{S}^2 \rangle_0 = \frac{N}{2} \left(\frac{N}{2} + 1 \right)$. Dashed and dotted lines respectively mark the exactly solvable limits of uniform (OAT, $\alpha = 0$) and power-law Ising (Ising, $J_{\perp} = 0$) interactions. 180
- 6.8 Optimal squeezing ξ_{opt}^2 (top) and minimal squared magnetization $\langle \mathbf{S}^2 \rangle_{\text{min}}$ throughout squeezing dynamics (bottom) on 2D lattices of 3×3 (left) and 4×4 (right) spins, as computed by exact methods (solid lines) and DTWA (dots). The color of each marker indicates the corresponding value of α , as specified in the legend, and the dashed line marks the OAT limit of $\alpha = 0$ 182
- 6.9 Dependence of the optimal squeezing parameter ξ_{opt}^2 on system size N within the collective dynamical phase of the power-law XXZ model in $D = 2$ spatial dimensions. Color indicates the value of J_z/J_{\perp} , sweeping down from +0.5 (dark purple, top) to -1.5 (yellow, bottom) in increments of -0.5. Circles show results computed with DTWA; dashed lines show a fit to $\xi_{\text{opt}}^2 = a/N^{\nu}$ with free parameters a, ν ; and the dotted red line marks the OAT limit for reference. The DTWA results in panel (a) for $\alpha = 3$ are a subset of those in Figure 6.4 of the main text. 184
- 6.10 Dependence of the critical Ising coupling J_z^{crit} at the collective-to-Ising dynamical phase boundary on system size N for the power-law XXZ model in $D = 2$ spatial dimensions. Circles show results computed with DTWA, and dashed lines show a fit to $J_z^{\text{crit}}/J_{\perp} = -\gamma \ln N + b$ with free parameters γ, b . The DTWA results in panel (a) for $\alpha = 3$ are equivalent to the dashed grey lines in Figure 6.4 of the main text. DTWA simulations were run with values of J_z/J_{\perp} that are integer multiples of 0.1, placing a lower bound on the resolution for $J_z^{\text{crit}}/J_{\perp}$ 185

- 6.11 Squeezing ξ^2 and squared magnetization $\langle \mathbf{S}^2 \rangle$ as a function of time t for $N = 4096 = 64^2 = 16^3$ spins in $D = 2$ and 3 spatial dimensions. Color indicates the value of J_z/J_\perp , and the red line highlights behavior at the value of J_z/J_\perp immediately preceding the transition from the S-collective phase (above the red line) to the S-Ising phase (below the red line). 187
- 6.12 Same results as in Figure 6.11, but for values of J_z/J_\perp that cross the dynamical phase boundary at $J_z/J_\perp = 1$. The red line highlights behavior at $J_z/J_\perp = 1.1$, immediately preceding the transition from the S-Ising phase ($J_z > 1$) to the S-collective phase ($J_z < 1$). 188
- 6.13 Dependence of the optimal squeezing parameter ξ_{opt}^2 on filling fraction f for the XXZ model in Eq. (6.3) of the main text with power-law exponent $\alpha = 3$ in $D = 2$ spatial dimensions with 50×50 lattice sites. Results computed using DTWA, with a random choice of $f \times 50 \times 50$ lattice sites to occupy. The shape and color of each marker indicates the corresponding value of J_z/J_\perp , as specified in the legend, and the dotted line marks the OAT limit for reference. 190
- 7.1 (a) Ultracold atoms on a lattice of L sites tunnel between neighboring lattice sites at a rate J , and locally repel each other with interaction energy U . (b,c) When the interaction energy U is small compared to the single-particle bandwidth $4J$, the frozen-mode approximation enables the interaction Hamiltonian to be written as a spin model consisting of exchange terms $\hat{\mathbf{s}}_p \cdot \hat{\mathbf{s}}_q$, which swap the states of two spins pinned to modes p, q . (d) Interactions open an energy gap $u = U \times N/L$ between the manifold of permutationally symmetric states of N spins, and the orthogonal complement of states that break spin-permutation symmetry. 198

- 7.2 Whereas the state of a two-level spin (qubit) can be represented by a point on (or inside) the Bloch sphere, the state of an n -level spin is more generally represented by a probability distribution on the Bloch sphere. The distribution shown for $n = 10$ corresponds to a Haar-random pure state. 199
- 7.3 Sketch of the three-laser drive used to address nuclear spins on a one-dimensional lattice. Two counter-propagating lasers with right-circular polarization and amplitudes Ω_{\pm} point at an angle θ to the lattice axis. A third, linearly polarized laser with amplitude Ω_0 points in a direction orthogonal to both the lattice and the other driving lasers. Absorbing a photon from the laser with amplitude Ω_m induces a transition $(g, \mu) \rightarrow (e, \mu + m)$ for the (electronic, nuclear spin) state of an atom, where nuclear spin is quantized along the z axis. 200
- 7.4 Spin-orbit coupling for 2-level (**a,c**) and 4-level (**b,d**) spins. Colors indicate different spin projections μ . In the “lab frame” (**a,b**), kinetic energy is insensitive to spin, but a spin transition $\mu \rightarrow \mu + 1$ is accompanied by a momentum kick $q \rightarrow q + \phi$ from the drive. Changing into the “gauge frame” (**c,d**), essentially by shifting the momentum label q for each spin state μ , makes the drive diagonal in the momentum index, but comes at the cost of making kinetic energy spin-dependent. 206
- 7.5 Time-averaged magnetization σ_{MF} and interaction energy $\langle\langle \bar{\mathbf{s}} \cdot \bar{\mathbf{s}} \rangle\rangle_{\text{MF}}$ for different spin dimensions n (indicated in the legend) as determined by mean-field simulations of $N = 100$ spins initially in the x-polarized state $|X\rangle$ for a time $T = 10^5/u$. Insets show same data after rescaling $h \rightarrow h \times (n/2)^{1/3}$, and transforming vertical axes according to Eq. (7.29). 209
- 7.6 The critical value of h_{crit} as determined by mean-field simulations of $N = 100$ spins initially in the x-polarized state $|X\rangle$. A single-parameter fit to $h_{\text{crit}} = (n/2)^{-\alpha}$ finds $\alpha = 0.333(5)$, and $\alpha = 1/3$ is consistent with all mean-field results to within an uncertainty determined by the resolution of h in mean-field simulations. 211

- 7.7 A corollary of Figure 7.5 for the initial state $|XX\rangle$. The inset for interaction energy $\langle\langle \bar{\mathbf{s}} \cdot \bar{\mathbf{s}} \rangle\rangle_{\text{MF}}$ in Figure 7.5 subtracts off the minimal value of $\langle\langle \bar{\mathbf{s}} \cdot \bar{\mathbf{s}} \rangle\rangle_{\text{MF}}$ and rescales to lie on the interval $[0, 1]$, as prescribed in Eq. (7.29). Here the subtracting and rescaling is identical, but with a minimal value of $2\gamma(n)$ rather than $\gamma(n)$ 214
- 7.8 A corollary of Figure 7.5 for the initial state $|XX_i\rangle$. Insets show the same data shifted and rescaled identically to Figure 7.5. 214
- 7.9 Numerical results (analogous to Figures 7.5, 7.7, and 7.8 of the main text) for the time-averaged interaction energy and magnetization (both normalized to a maximal value of 1) in a system of $L = 5$ lattice sites, for both a Fermi-Hubbard model (dots) and spin model (lines) with $n = 4$ internal states per spin. The corresponding initial state (defined in Section 7.5 of the main text) is indicated in each panel, and observables are averaged over a time $tJ = 200$. Color indicates the value of U/J , and the field h corresponds to $2J\phi/u$ in the case of the Fermi-Hubbard model. Simulations are performed in real-space, with spin-orbit coupling (SOC) implemented through a homogeneous drive (with no site or ϕ dependence) and nearest-neighbor tunneling terms that contain factors of $e^{\pm i\mu\phi}$. Results for the initial kitten state $|XX_i\rangle$ are excluded because they are identical to those of $|X\rangle$, and magnetization for the initial state $|XX\rangle$ is always 0. Note that while panels (a) and (b) are representative of infinite-time behavior, the inset in panel (c) shows that the Fermi-Hubbard and spin models exhibit different behaviors on very long time scales, although good agreement is restored by rescaling time in the spin model, indicating the likelihood of a need to renormalize spin model parameters. In any case, such time scales are inaccessible in current experiments and diverge as $N \rightarrow \infty$, so these corrections do not affect the main results of our work. 219
- 7.10 Numerical results identical to Figure 7.9, but with $L = 4$ lattice sites and $n = 6$ internal states per spin. 219

- 8.1 Signal recovery on the sphere is the problem of reconstructing an unknown function f (red distribution) from its values $f(\mathbf{v})$ at specific points $\mathbf{v} \in V$ (blue dots) on the sphere. For almost all choices of V , reconstruction of f is possible if there are at least as many points in V as there are degrees of freedom in f 239
- 8.2 Serial runtime to compute \mathcal{S}_V , ϵ_V , or $\mathcal{E}_V(\rho)$ with $|V| = 2d - 1$ randomly chosen measurement axes and a randomly chosen qudit state ρ . Each point is an average over 10^3 calculations or 5 minutes of runtime, whichever comes first. These results do not count fixed runtimes to pre-compute quantities that can be recycled for every new choice of V and ρ . Dashed lines show fits to a runtime $t = cd^\alpha$ for the 20 largest values of d , finding $\alpha \approx 3.8 \pm 0.1$ 244
- 8.3 Empirical measurement-adjusted error scales $\tilde{\beta}(p)$ with p excess measurement axes, determined by minimizing over 10^3 choices of measurement axes V or 5 minutes of runtime (for each p), whichever comes first. Marker and color indicates the qudit dimension d . The rapid initial drop in $\tilde{\beta}(p)$ implies that using more measurement axes can substantially lower the upper bound on reconstruction error provided in Eq. (8.30), and that these benefits plateau after $p \approx d$. Horizontal reference lines mark the smallest measurement-adjusted error scales $\min_\theta \beta_\theta / \tilde{\beta}(0)$ achievable with the method in Ref. [246], which is parameterized by an arbitrarily chosen angle θ . . . 248
- 8.4 Quantum error scale ϵ_θ as a function of the polar angle θ in the tomography method of Ref. [246] for a few qudit dimensions d 263
- 8.5 Optimum angle θ_{opt} as a function of qudit dimension d for the tomography method of Ref. [246], and a fit to $\theta_{\text{opt}} = \frac{\pi}{2}(1 - \frac{1}{xd})$ finding $x \approx 1.34$ 263

Chapter 1

Context and outline

When quantum mechanics was first developed, it was primarily used as abstract microscopic theory with which to explain the behavior of matter on a larger scale, much the way that statistical mechanics is used to explain thermodynamic phenomena. In this way, one of the crowning scientific achievements of the 20th century led to technological innovations such as the transistor, the laser, and the medical magnetic resonance imaging (MRI) scanner. Today, we are in the midst of a new technological revolution that aims to manipulate matter on the scale of individual quanta. We are also just beginning to understand and exploit subtle quantum phenomena such as entanglement to surpass classical limits on what is considered even possible. This is an exciting time to work on quantum technologies.

One of the leading platforms for quantum technologies is that of cold atoms in optical lattices. Cold atoms' first major claim to fame was an experimental confirmation of a quantum phase transition between superfluid and (Mott) insulating phases of the bosonic Hubbard model (that is, a model of particles hopping around on a lattice, with pair-wise local interactions). This achievement was the first major demonstration of an analog *quantum simulator*, in which a quantum mechanical model of interest is meaningfully studied “by analogy” in an experimental platform. Tabletop cold atom experiments also make up the most precise and accurate clocks to date (with ion-based clocks a close rival), and cold atoms take second place for the most precise scientific instruments ever built (trailing kilometer-scale gravitational wave observatories). In addition to quantum simulation, cold atoms are thereby a major tool for the science of measurement, known as *quantum metrology*.

This thesis explores some of the possibilities and prospects for quantum simulation and metrology with cold atom systems, more specifically with fermionic atoms that have a multilevel internal structure. Chapter 2 provides some technical background and a crash course to the main concepts and tools that appear throughout this thesis. Chapters 3–8 walk through some highlights of my graduate work, with each chapter featuring a paper on which (1) I was a primary (i.e. first or “co-first”) author, and (2) Ana Maria Rey was a principal investigator [1–6]. For the sake of brevity and cohesion, I exclude papers from my graduate work in which I played a secondary role [7, 8]; papers that I wrote with colleagues at Argonne National Laboratory and Super.tech [9, 10]; and papers from projects that I started before entering graduate school [11–13], although I consider some of these papers (particularly Refs. [7, 9, 11]) to be equally important parts of my graduate work. Each of Chapters 3–8 begins with a short prologue that informally introduces and contextualizes the paper that follows.

Chapter 2

Introduction and background

2.1 Alkaline-earth(-like) atoms

Much of the work in this thesis refers to “fermions” or “spins” of some sort, probably on a lattice, usually interacting. This general language isolates the essential features of the objects under consideration, but often at the cost of hiding the true star players of our show: alkaline-earth(-like) atoms (AEA). The electronic structure of these group-II elements, along with similarly-structured Ytterbium, allows the breadth of physics explored in this thesis to be observed in a single experimental platform. Specifically, these atoms have two valence electrons with a 1S_0 electronic ground state, and above that a first-excited 3P_0 state. These are often referred to as the *clock states* due to their central role in an AEA-based atomic clocks. A direct, photon-mediated transition between the clock states is *doubly forbidden*:

- (i) First, a 1S_0 - 3P_0 transition is *dipole-forbidden* because both of these states have a total electronic (intrinsic + orbital) angular momentum of 0, as indicated by the “0” in 1S_0 and 3P_0 . There is no way for a spin-0 system to absorb a spin-1 photon and end up in another spin-0 state, as in a direct $^1S_0 \rightarrow ^3P_0$ transition.
- (ii) Second, a 1S_0 - 3P_0 transition is *spin-forbidden* because it couples a state with net intrinsic spin 0 (1S_0 , with a two-electron spin singlet) to a state with net intrinsic spin 1 (3P_0 , with

a spin triplet)^a. Photons couple primarily to the *orbital* angular momentum of electrons in an atom, and therefore should not change their intrinsic spin directly.

Photon-mediated coupling between the 1S_0 and 3P_0 does occur, of course; we would not be discussing this transition otherwise. 1S_0 - 3P_0 coupling is made possible by the hyperfine (i.e. nuclear-spin-mediated) coupling of the “bare” electronic 3P_0 state to “bare” electronic 1P_1 , 3P_1 , and 3P_2 states (see Figure 2.1) [14]. As a result of this hyperfine coupling, the electronic eigenstate that we label “ 3P_0 ” weakly populates these other states as well. In particular, the bare 1P_1 state couples directly to the 1S_0 state, and thereby virtually mediates 1S_0 - 3P_0 coupling. The result of this long song and dance, and ultimately the point of the entire discussion about AEAs thus far, is that the 3P_0 state of AEAs is *metastable* and long-lived, with a lifetime of roughly two minutes in ^{87}Sr [15]. As a corollary, the 1S_0 - 3P_0 transition has an exceptionally narrow linewidth (e.g. a $\sim 10^{-3}$ Hz linewidth on a $\sim 10^{15}$ Hz transition in ^{87}Sr [15]), making AEAs an excellent tool for precision metrology and fundamental physics.

From the perspective of metrology, measurements of the 1S_0 - 3P_0 transition frequency in AEAs are used in the most precise and accurate clocks to date, rivaled only by ion-based “quantum logic” clocks (which, incidentally, address a 1S_0 - 3P_0 transition engineered in group-III atoms by stripping them of one valence electron) [16]. Precise clocks are important for setting time and frequency standards (e.g. defining the second), which as of 2019 define *all* physical units of measurement in the International System of Units (SI)^b. Any wristwatch, bathroom scale, or oven thermometer built today is calibrated to an atomic clock (albeit one based alkaline Caesium atoms rather than AEAs, for the time being). Moreover, the exquisite precision of atomic clocks admits applications in navigation (such as an advanced global positioning system, GPS) and geodesy (pre-

^a You can tell that 3P_0 has net intrinsic spin 1 because its intrinsic spin must cancel out with orbital spin (which is spin-1, as indicated by the “P” in 3P_0) to result in a total electronic angular momentum of 0.

^b More precisely, the second is the only quantity that must be *measured* to define SI units. All SI units are then defined as the second raised to some power and multiplied by prefactors with numerical values that are fixed by definition.

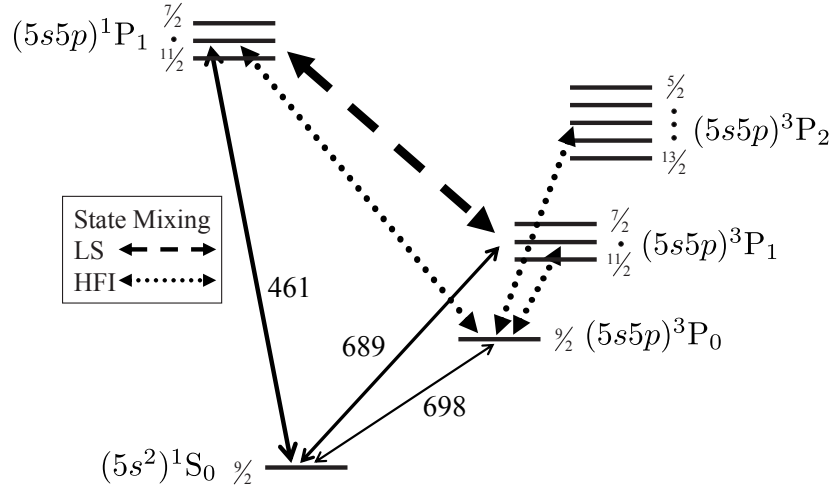


Figure 2.1: Simplified energy level diagram for the low-lying electronic states of ^{87}Sr , reproduced from Ref. [14]. Dashed and dotted lines respectively show spin-orbit (LS) and hyperfine (HFI) coupling between bare electronic states. Solid lines show optical transitions between electronic eigenstates, with the corresponding wavelengths given in nanometers. Fractions indicate the net spin of the hyperfine manifold (involving nuclear spin) within the associated electronic energy level.

cision measurements of the gravitational field, which can be used to determine altitude or geological material density) [17]. From the perspective of fundamental physics, the precision of atomic clocks can be leveraged for applications such as gravitational wave detection, dark matter searches, and searches for the violation of fundamental symmetries (e.g. charge-parity-time reversal symmetry, Lorentz invariance, etc.) [18]. These capabilities are quite remarkable, given the fact that AEA-based experiments are roughly the size of a (meter-scale) optical table, in contrast to the stadium- or kilometer-scale observatories and colliders that are usually necessary for fundamental physics experiments.

Finally, due in part to their metrology-driven technological development, AEA experiments offer an exquisite platform for studying many-body quantum physics. This scientific venture goes hand-in-hand with the practical development of better sensors: improved sensitivity yields a more precise and controllable physics testbed, and a better understanding of relevant physics allows us to mitigate systematic errors and further improve sensitivity. As we will see in Chapters 4 and 6, a deep understanding of the physics underpinning AEA-based atomic clocks can be used to engineer

entangled many-body quantum states that allow us to approach the limits of device performance allowed by physics.

2.2 Individual atoms in a trap

AEAs are typically cooled and trapped in an electromagnetically induced external potential. In the absence of interactions, these atoms can be described by the Hamiltonian ($\hbar = 1$ throughout this thesis)

$$\hat{H}_0 = \int d^3x \sum_{\alpha, \mu} \hat{\psi}_{\alpha\mu}^\dagger(x) \left[-\frac{\nabla^2}{2m} + V_{\text{ext}}^\alpha(x) + E_\alpha \right] \hat{\psi}_{\alpha\mu}(x), \quad (2.1)$$

where α and μ respectively index the electronic and nuclear states of an atom; $\hat{\psi}_{\alpha\mu}$ is the field operator for an atom with internal state α, μ ; $\nabla^2 = \partial_x^2 + \partial_y^2 + \partial_z^2$ is a spatial Laplacian; m is the mass of an atom; V_{ext}^α is an external potential, which may generally depend on the electronic state α ; and E_α is the electronic (internal) energy of state α . The field operator $\hat{\psi}_{\alpha\mu}$ can be expanded in the form

$$\hat{\psi}_{\alpha\mu}(x) = \sum_q w_q^\alpha(x) \hat{c}_{q\alpha\mu}, \quad (2.2)$$

where q indexes an orthonormal basis of spatial wavefunctions w_q^α for atoms in state α , and the operator $\hat{c}_{q\alpha\mu}$ annihilates an atom in mode (q, α, μ) . The operator $\hat{c}_{q\alpha\mu}$ may generally be bosonic or fermionic depending on the species of the atom, but we will primarily consider fermionic atoms in this thesis. Substituting this expansion into (2.1) yields

$$\hat{H}_0 = \sum_{q, q', \alpha, \mu} J_{qq'}^\alpha \hat{c}_{q\alpha\mu}^\dagger \hat{c}_{q'\alpha\mu} + \sum_\alpha E_\alpha \hat{N}_\alpha, \quad (2.3)$$

where $\hat{N}_\alpha = \sum_{q, \mu} \hat{c}_{q\alpha\mu}^\dagger \hat{c}_{q\alpha\mu}$ counts the number of atoms in state α , and

$$J_{qq'}^\alpha = \int d^3x w_q^*(x) \mathcal{H}_{\text{spatial}}^\alpha(x) w_{q'}(x), \quad (2.4)$$

is a tunneling matrix defined in terms of the Hamiltonian density

$$\mathcal{H}_{\text{spatial}}^\alpha(x) = -\frac{\nabla^2}{2m} + V_{\text{ext}}^\alpha(x). \quad (2.5)$$

For a fixed electronic state α , the off-diagonal ($q \neq q'$) components of $J_{qq'}^\alpha$ are essentially the rate at which atoms tunnel between modes q and q' . Choosing the eigenfunctions of $\mathcal{H}_{\text{spatial}}^\alpha$ as the basis of wavefunctions w_q^α yields a tunneling matrix $J_{qq'}^\alpha$ that is diagonal, in which case J_{qq}^α is simply the orbital energy of an α -state atom in mode q (where “orbital” refers to the “orbit” of an α -state atom in the external potential V_{ext}^α). However, the best choice of basis for wavefunctions will generally depend on the particular setting and parameter regime under consideration. If atoms are trapped on a lattice, for example (see below), it might be convenient to use a basis of wavefunctions localized to individual lattice sites, and treat the effect of inter-site tunneling as a dynamical or perturbative process.

2.3 Optical lattices and magic wavelengths

An important class of traps that will play a central role in this thesis are optical lattices. An optical lattice is generated by retroreflected or counter-propagating laser beams that form an electromagnetic standing wave. By off-resonantly coupling different electronic states of atoms in the optical lattice, the lattice light induces AC Stark shifts that are proportional to the electric field intensity of the lasers, as well as the electric polarizability of the atoms. In a two-state model of the AC Stark shift, a laser with frequency ν couples electronic state α with energy E_α to an excited state β with energy $E_\beta = E_\alpha + \omega$. If the detuning $\Delta = \omega - \nu$ is much larger than the coupling strength Ω between these states^c, then the coupling can be treated perturbatively, leading to a second-order shift of the α -state energy by $\sim \Omega^2/\Delta$ [19]. In practice, each state α gets coupled to a large number of excited states, with associated coupling strengths and detunings for every pair of states. Altogether, the electromagnetic potential induced by an optical lattice (standing wave) oriented along the z axis takes the form

$$V_{\text{ext}}^\alpha(z) = V_\alpha \sin^2(kz), \quad (2.6)$$

^c By a coupling Ω between states α and β , we mean some Hamiltonian of the form $\Omega (|\beta\rangle\langle\alpha| + |\alpha\rangle\langle\beta|)$.

where V_α is the *lattice depth* for α -state atoms, k is the wavenumber of the lattice light, and we restrict ourselves to one spatial dimension for simplicity.

Eigenfunctions of the Hamiltonian $\mathcal{H}_{\text{spatial}}^\alpha$ in (2.5) with the sinusoidal potential in (2.6) are known as Mathieu functions, which can be decomposed into Bloch waves as $w_q^\alpha(z) = e^{iq_z z} u_{q_z n}^\alpha(z)$ [20]. Here the mode $q \sim (q_z, n)$ is indexed by a *quasi-momentum* q_z with periodicity $q_z = q_z + 2\pi$ and an integer *band index* $n \geq 0$, and the function $u_{q_z n}^\alpha$ has the same periodicity as the lattice: $u_{q_z n}^\alpha(z) = u_{q_z n}^\alpha(z + a)$, where $a = \pi/k$ is the distance between neighboring lattice sites (i.e. the lattice constant). For theoretical analysis and numerical simulations, it is often convenient to consider lattice of L sites with periodic boundary conditions, in which case the quasi-momentum $q_z = 2\pi/L \times j$ for some integer j . Efficient numerical methods for computing Mathieu functions can be found in Ref. [20].

We now (and for the remainder of this thesis) restrict ourselves to the two lowest-lying electronic states, i.e. the clock states $\alpha \in \{^1S_0 \leftrightarrow g, ^3P_0 \leftrightarrow e\}$. By tuning the lattice light to a so-called “magic wavelength” at which these states have the same electric polarizability, the potential V_{ext}^α can be made independent of the electronic state α , in which case the single-particle Hamiltonian becomes [21, 22]

$$\hat{H}_0 = \sum_{q, \alpha, \mu} E_q \hat{c}_{q\alpha\mu}^\dagger \hat{c}_{q\alpha\mu} + \omega \hat{N}_e, \quad (2.7)$$

where $E_q = J_{qq}$ is the orbital energy of Bloch mode q (see Figure 2.2)^d, and $\omega = E_e - E_g$ is the $|g\rangle \leftrightarrow |e\rangle$ transition frequency. We assume that atoms are trapped in a magic-wavelength lattice for the remainder of this thesis.

As a final point, we note that the same light that forms an optical lattice unavoidably induces dissipation called *light scattering* in AEA. Although the clock states are themselves (meta)stable, the lattice light off-resonantly couples the clock states to excited states that can have fast decay rates. The clock states thereby inherit the loss channels of virtually populated excited states,

^d We will often consider atoms that occupy only the lowest Bloch band ($n = 0$), in which case $E_{q_z} = -2J \cos(q_z a)$, where J is the tunneling rate between neighboring lattice sites.

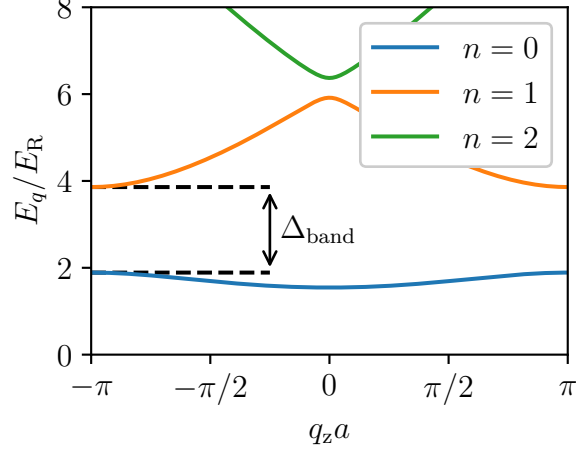


Figure 2.2: Band structure (orbital energy) of atoms in a periodic lattice potential $V_{\text{ext}}(z) = V_0 \cos^2(\frac{\pi z}{a})$ with depth $V_0 = 4E_R$, where the lattice recoil energy $E_R = k_L^2/2m$ is defined in terms of the atomic mass m and the wavenumber k_L of the lattice light. Color indicates band index n as specified in the legend.

albeit only perturbatively^e. For this reason, the coherence time of the clock states of ^{87}Sr atoms in a magic-wavelength optical lattice is typically ~ 10 seconds, rather than the $\sim 10^2$ second lifetime of the $^3\text{P}_0$ state, although it may be possible to mitigate light scattering by the construction of optical lattices with larger lattice constants [23].

2.4 Spin-orbit coupling

As an added ingredient and control knob, we can turn on a linearly-polarized laser with wavenumber k and frequency $\nu \approx \omega$ to induce an electric dipole transition between the $|g\rangle$ and $|e\rangle$ states of AEAs. There are several ways to deduce the corresponding drive Hamiltonian governing the AEAs; here we take a semi-classical, phenomenological approach that avoids digressions into subjects and techniques that are outside the scope of this thesis. We treat driving laser “semi-classically” in the sense that we do not quantize the corresponding electromagnetic field (equivalently, we make the reasonable assumption that the laser light is in a coherent state with

^e If a dissipation-free clock state is coupled with amplitude Ω and detuning Δ to an excited state with dissipation rate Γ , then virtual occupation of the excited state shifts the clock-state energy by $\sim \Omega^2/\Delta$, and causes the clock state to dissipate at a rate $\sim \Gamma \times \Omega^2/\Delta^2$ [19].

a large mean photon number), but we retain the fact that individual photons are spin-1 particles, which means their absorption or emission by an AEA must accompany an appropriate internal spin transition. In the plane-wave approximation, the “bare” drive Hamiltonian for AEAs is then

$$\hat{H}_{\text{drive}}^{\text{bare}} = \int d^3x \sum_{\mu} \Omega_{\mu} e^{i(k \cdot x - \nu t)} \hat{\psi}_{e,\mu}^{\dagger}(x) \hat{\psi}_{g,\mu}(x) + \text{h.c.}, \quad (2.8)$$

where the nuclear spin $\mu \in \{s, s-1, \dots, -s\}$ for a spin- s atom (e.g. $s = 9/2$ for ^{87}Sr) is quantized along an axis in the plane orthogonal to k ; Ω_{μ} is a spin-dependent drive amplitude; and “h.c.” denotes the Hermitian conjugate of preceding terms. The drive amplitude Ω_{μ} has its physical origins in atom-light coupling to an electric dipole transition, and is therefore proportional to both the electric field intensity of the driving laser and the differential electric polarizability of the $|g\rangle$ and $|e\rangle$ states. Moreover, the Hamiltonian in (2.8) describes a spin- s atom absorbing a spin-1 photon with spin projection 0 onto the quantization axis, which implies that $\Omega_{\mu} \propto \langle s\mu; 1, 0 | s\mu \rangle \propto \mu$, where $\langle \ell_1 m_1; \ell_2 m_2 | \ell_3 m_3 \rangle$ is a Clebsch-Gordan coefficient. We consider a more general case of lasers with any polarization and arbitrary orientation relative to the spin quantization axis in Appendix 7.D of Chapter 7.

Our first order of business is to eliminate the time dependence from the drive Hamiltonian in (2.8), which we can do by moving into a rotating frame that takes $e^{-i\nu t} \hat{\psi}_{e,\mu}^{\dagger} \rightarrow \hat{\psi}_{e,\mu}^{\dagger}$. Such a transformation is achieved by subtracting ν off of the energy of $|e\rangle$ -state atoms, in effect replacing the excitation energy ω in (2.7) by the detuning $\Delta = \omega - \nu$ ^f. After making this replacement, the drive Hamiltonian becomes

$$\hat{H}_{\text{drive}} = \sum_{q,q',\mu} \Omega_{\mu} \mathcal{I}_{qq'} \hat{c}_{q,e,\mu}^{\dagger} \hat{c}_{q',g,\mu} + \text{h.c.}, \quad (2.9)$$

^f Mathematically, the transformation $e^{-i\nu t} \hat{\psi}_{e,\mu}^{\dagger} \rightarrow \hat{\psi}_{e,\mu}^{\dagger}$ is implemented by the unitary $U = \exp\left(i\nu t \int d^3x \sum_{\mu} \hat{\psi}_{e,\mu}^{\dagger} \hat{\psi}_{e,\mu}\right)$. If we rotate states $|\phi\rangle \rightarrow |\tilde{\phi}\rangle = U|\phi\rangle$, the accompanying transformation of the overall Hamiltonian $H \rightarrow \tilde{H}$ (which can be derived by enforcing the Schrödinger equation $\tilde{H}|\tilde{\phi}\rangle = i\partial_t|\tilde{\phi}\rangle$) is given by $\tilde{H} = UHU^{\dagger} + i\partial_t UU^{\dagger}$. This transformation removes the time dependence from the bare drive Hamiltonian in (2.8), and subtracts ν off the energy of $|e\rangle$ -state atoms by the addition of $i\partial_t UU^{\dagger} = -\nu \int d^3x \sum_{\mu} \hat{\psi}_{e,\mu}^{\dagger} \hat{\psi}_{e,\mu}$.

where the overlap integral

$$\mathcal{I}_{qq'} = \int d^3x e^{ik \cdot x} w_q^*(x) w_{q'}(x). \quad (2.10)$$

We now assume that our atoms are trapped on a three-dimensional cubic lattice oriented along the (x, y, z) axes, and with strong confinement in the x - y plane, such that atoms' spatial degrees of freedom are frozen within this plane. This assumption is straightforward to relax when necessary, but doing so complicates the analysis in this section without added benefit. The effect of this assumption is essentially to replace the three-dimensional integral in (2.10) by a one-dimensional integral along the z axis:

$$\mathcal{I}_{qq'} \rightarrow \int dz e^{ik_z z} w_q^*(z) w_{q'}(z), \quad (2.11)$$

where k_z is the projection of k onto the z axis, and the spatial integral over the x - y plane in (2.10) can be absorbed into the definition of the drive amplitude Ω_μ in (2.9).

The spatial modes $q \sim (q_z, n)$ are indexed by a quasi-momentum q_z and band index n (see Section 2.3). When atoms are *ultracold*, it may be reasonable to assume that their temperature is small compared to the energy gap Δ_{band} between the two lowest bands (see Figure 2.2). If atoms are furthermore initialized in the lowest band $n = 0$, as long as $|\Omega_\mu| \ll \Delta_{\text{band}}$ (which prevents drive-induced coupling to higher bands) we can neglect the band index n , unambiguously identify $q \sim q_z$, and substitute the Bloch-wave decomposition $w_q(z) = e^{iqz} u_q(z)$ into the overlap integral in (2.11) to get

$$\mathcal{I}_{qq'} = \int dz e^{i(k_z + q' - q)z} u_q^*(z) u_{q'}(z). \quad (2.12)$$

We now make the final assumption that k_z is commensurate with the lattice, which is to say that k_z is an allowed quasi-momentum along the z axis (i.e. an integer multiple of $2\pi/La$). The assumptions of periodic boundary conditions and drive commensurability can be more cumbersome to relax than that of tight transverse confinement, particularly when considering the limit $k_z a \ll 1$ (which features in Chapters 4 and 7), or when considering length scales over which the plane-wave

approximation for the lattice laser breaks down. We defer a careful scrutiny of these assumptions and their breakdown to another time (see, for example, Ref. [24] and Appendix 4.I of Chapter 4).

If k_z, q, q' are all integer multiples of $2\pi/La$, we can split the position z into an integer multiple of a and a remainder, $z = aj + r$ with $j = \lfloor z/a \rfloor$ and $r = z \bmod a$; here j essentially indexes a lattice site, and r is a position within that site. The periodicity of $u_q(z)$ then implies that the overlap integral in (2.12) can then be written in the form

$$\mathcal{I}_{qq'} = \sum_{j=1}^L e^{i(k_z+q'-q)aj} \int_0^a dr e^{i(k_z+q'-q)r} u_q^*(r) u_{q'}(r). \quad (2.13)$$

Here $(k_z+q'-q)a$ is an integer multiple of $2\pi/L$, so the sum over j vanishes unless $k_z+q'-q = 0$. We thus find that the overlap integral $\mathcal{I}_{qq'} = 0$ unless $q = q' + k_z$, so altogether the drive Hamiltonian in (2.9) becomes

$$\hat{H}_{\text{drive}} = \sum_{q,\mu} \Omega_{q\mu} \hat{c}_{q+k_z,e,\mu}^\dagger \hat{c}_{q,g,\mu} + \text{h.c.}, \quad (2.14)$$

where $\Omega_{q\mu} = \Omega_\mu \times \mathcal{I}_{q+k_z,q}$ is typically independent of q to a good approximation[§].

A few notes concerning the drive Hamiltonian in (2.14). First, the result of the long journey from (2.8) to (2.14) can be summarized by conservation of quasi-momentum: an atom that transitions from $|g\rangle$ to $|e\rangle$ by absorbing a photon must also absorb the quasi-momentum of that photon. Second, drive Hamiltonian in (2.14) exhibits *spin-orbit coupling*, which is to say that it changes electronic (“pseudo-spin”) and spatial (“orbital”) degrees of freedom in a correlated fashion. To further simplify this drive, we can relabel quasi-momenta for the excited electronic state, taking $\hat{c}_{q+k_z,e}^\dagger \rightarrow \hat{c}_{q,e}^\dagger$, which takes

$$\hat{H}_{\text{drive}} \rightarrow \sum_{q,\mu} \Omega_{q\mu} \hat{c}_{q,e,\mu}^\dagger \hat{c}_{q,g,\mu} + \text{h.c.}. \quad (2.15)$$

This relabeling comes at the cost of making kinetic energy electronic-state-dependent (see Figure 2.3), but can simplify the theoretical treatment of AEAs, which is most clear when atoms are

[§] This approximation breaks down in very shallow lattices, in which the inter-site tunneling rate J exceeds the lattice recoil energy $E_R = k_L^2/2m$ (defined in terms of the atomic mass m and the wavenumber k_L of the lattice laser).

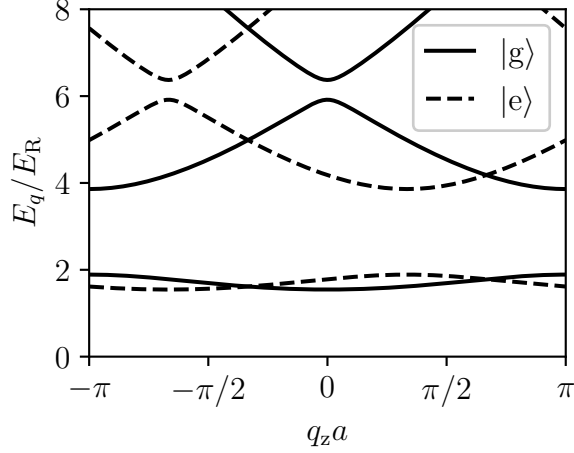


Figure 2.3: Band structure identical to that in Figure 2.2, but after relabeling excited-state quasi-momenta with $\hat{c}_{q_z+k_z,e}^\dagger \rightarrow \hat{c}_{q_z,e}^\dagger$ and $k_z = 2\pi/3$. Solid and dashed lines respectively show kinetic energies for ground- and excited-state atoms.

nuclear-spin-polarized and the dependence of $\Omega_{q\mu}$ on q is negligible, which allows us to write $\hat{H}_{\text{drive}} = \Omega \sum_q \hat{c}_{q,e}^\dagger \hat{c}_{q,g} + \text{h.c.}$ (where we suppress a fixed nuclear spin index). We elaborate on this point in our discussion of spin operators in Section 2.7.

On one hand, spin-orbit coupling is a complication that limits the capabilities of atomic clocks by exacerbating the deleterious effect of inhomogeneities on inter-atomic coherence at low lattice depths (which are desirable to reduce atomic losses from scattering off of high-intensity lattice light). On the other hand, spin-orbit coupling gives us access to a variety of exotic phenomena, such as topological phases of matter and the possibility to prepare metrologically useful quantum states [2, 25–27]. Getting a handle on these phenomena is a promising route to push the limits of current atomic clocks.

2.5 Nuclear spin decoupling and $SU(n)$ symmetry

An important consequence of the fact that the both 1S_0 and 3P_0 states have a total electronic (intrinsic + orbital) angular momentum of 0 is the near perfect decoupling of AEAs’ electronic and nuclear spin degrees of freedom. Mathematically, the (first-quantized) Hilbert space of AEAs occupying 1S_0 and 3P_0 states neatly factorizes into a tensor product of uncoupled [electronic-

state] \otimes [nuclear-spin] Hilbert spaces. This decoupling implies that, in the absence of an external magnetic field, freely evolving atoms that interact only through collisions (which are dominated by electric forces, and thereby electronic-state parameters) exhibit an $SU(n)$ symmetry, where $n = 2s + 1$ is the number of nuclear spin levels in a spin- s atom (e.g. $n = 10$ for ^{87}Sr with nuclear spin $s = 9/2$) [28]. Specifically, the dynamics of such AEAs are invariant under arbitrary global unitary transformations of atoms' nuclear spin states. As a consequence, interaction parameters such as s -wave scattering lengths and p -wave scattering volumes should be (approximately) independent of spin.

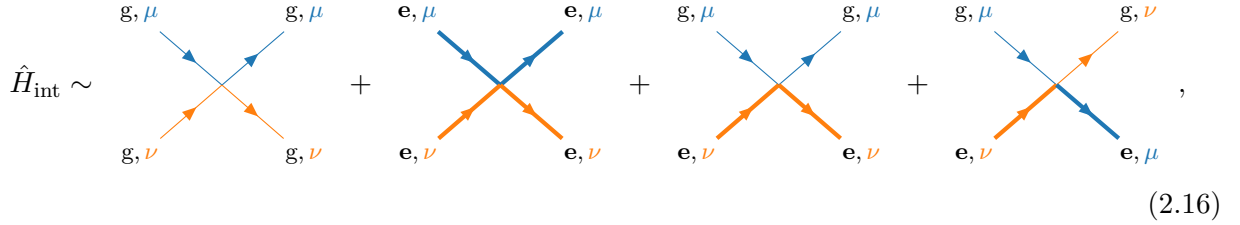
However, the same hyperfine interactions that enable photon-mediated $^1\text{S}_0$ - $^3\text{P}_0$ coupling also violate the $SU(n)$ symmetry that results from the decoupling of atoms' electronic and nuclear states. The dominant violations of $SU(n)$ symmetry occur due to hyperfine coupling of the $^K\text{P}_J$ states (i.e. $^1\text{P}_1$, $^3\text{P}_0$, $^3\text{P}_1$, and $^3\text{P}_2$). Violation of $SU(n)$ symmetry in the $^1\text{S}_0$ state is in turn mediated by virtual occupation of symmetry-breaking $^K\text{P}_J$ states during collision. By estimating the effect of these virtual occupations on the two-body collisional phase shift Φ , $SU(n)$ symmetry-breaking corrections $\delta\Phi$ have been estimated to be $\delta\Phi \sim 10^{-3}$ for $^3\text{P}_0$ -state atoms, and $\delta\Phi \sim 10^{-9}$ for $^1\text{S}_0$ [29]^h. We will consider such corrections negligible in the remainder of this thesis.

2.6 Two-body interactions

Collisional interactions are primarily governed by electronic-state parameters, which almost perfectly decouple from atoms' nuclear spin states. As a result, a pair of atoms occupying nuclear spin states (μ, ν) must occupy the same nuclear spin states after collision, since there is no mechanism by which to change nuclear spin state occupations. Moreover, interaction energy scales are typically much smaller than the electronic excitation energy ($U_{\text{int}} \sim 10^3$ Hz vs. $\omega \sim 10^{15}$ Hz in ^{87}Sr), so we can ignore processes in which interactions change the number of $|e\rangle$ -state atoms.

^h The s -wave scattering length $a \sim \Phi\Delta t$, where Φ is a collisional phase shift and Δt is the time that a pair of atoms spend in the short-range part of their intermolecular potential during collision ($\Delta t \approx 1$ picosecond for ^{87}Sr [29]). A correction $\delta\Phi \sim \eta$ implies that scattering lengths a acquire $SU(n)$ symmetry-breaking corrections δa with $\delta a/a \sim \eta$.

Once both nuclear and electronic state occupation numbers are fixed, there are only four possible interaction channels: one each for a pair of $|g\rangle$ - or $|e\rangle$ -state atoms that scatter off of each other, one “direct” channel in which a pair of atoms in distinct electronic states interact *without* changing their respective nuclear spin states, and one “exchange” channel in which a pair of atoms in distinct electronic states swap their nuclear spin states. Schematically, the interaction Hamiltonian must have the form



$$\hat{H}_{\text{int}} \sim \text{[Diagram 1]} + \text{[Diagram 2]} + \text{[Diagram 3]} + \text{[Diagram 4]}, \quad (2.16)$$

where we indicate excited-state atoms by a thicker line, and use color to indicate nuclear spin. At low temperatures, the most general low-energy (s -wave) interaction Hamiltonian consistent with these constraints is^{ij}:

$$\hat{H}_{\text{int}} = \int d^3x \sum_{\mu, \nu} \left[\sum_{\alpha \in \{g, e\}} \frac{1}{2} G_{\alpha\alpha} \hat{\rho}_{\alpha\mu} \hat{\rho}_{\alpha\nu} + G_+ \hat{\rho}_{e, \mu} \hat{\rho}_{g, \nu} + G_- \hat{\psi}_{e, \mu}^\dagger \hat{\psi}_{g, \nu}^\dagger \hat{\psi}_{e, \nu} \hat{\psi}_{g, \mu} \right], \quad (2.17)$$

where G_X are two-body coupling constants, $\hat{\rho}_{\alpha\mu} = \hat{\psi}_{\alpha\mu}^\dagger \hat{\psi}_{\alpha\mu}$ is an atomic density field operator, and we suppress the implicit dependence of $\hat{\rho}_{\alpha\mu}$ and $\hat{\psi}_{\alpha\mu}$ on the position x . Eigenstates of \hat{H}_{int} are strictly symmetric or anti-symmetric under the pairwise exchange of atoms' electronic states. For example, two-body eigenstates of \hat{H}_{int} have electronic states of the form $|\alpha\alpha\rangle$ or $|ge\rangle \pm |eg\rangle$, with corresponding interaction energies of the form $E_{\alpha\alpha} = G_{\alpha\alpha} \mathcal{I}$ or $E_{eg\pm} = (G_+ \pm G_-) \mathcal{I}$, where \mathcal{I} is a spatial overlap integral. Matching these interaction energies to s -wave scattering lengths as

ⁱ Technically speaking, there are two ways to arrive at the Hamiltonian in (2.17): (i) approximating the intermolecular potential of two atoms by a delta function (formally an *unregularized, energy-independent pseudopotential*), or (ii) the phenomenological approach of *effective field theory*, which considers all possible types of (local) interactions and keeps only those that are dominant in the low-energy (small momentum) limit.

^j The factor of 1/2 in the first term of (2.17) corrects for the fact that a sum over all μ, ν double-counts the interaction between a pair of atoms with identical electronic states $\alpha \in \{g, e\}$.

$E_X = \frac{4\pi}{m} a_X \mathcal{I}$, we thus find that

$$G_{\alpha\alpha=\text{gg,ee}} = \frac{4\pi}{m} a_{\alpha\alpha}, \quad G_{\pm} = \frac{4\pi}{m} \frac{a_{\text{eg}+} \pm a_{\text{eg}-}}{2}. \quad (2.18)$$

If atoms occupy only the lowest band on a three-dimensional lattice, then we can invoke the *tight-binding* approximation and neglect interactions between atoms on different lattice sites, because these interactions will be proportional to inter-site overlap integrals that are much smaller than on-site overlap integrals. If further assume that all AEAs occupy the same nuclear spin state (for example, if they are nuclear-spin-polarized with $\mu = \nu = 9/2$), then the electronic state of any pair of interacting atoms must be anti-symmetric under exchange in order to obey fermionic statistics. Suppressing irrelevant (fixed) nuclear spin indices, the only non-vanishing terms in (2.17) are then

$$\hat{H}_{\text{int}}^{\text{NSP}} = G_{\text{eg}-} K \sum_j \hat{c}_{j,e}^{\dagger} \hat{c}_{j,e} \hat{c}_{j,g}^{\dagger} \hat{c}_{j,g} = G_{\text{eg}-} K \sum_j \frac{1}{2} \hat{N}_j (\hat{N}_j - 1), \quad (2.19)$$

where $G_{\text{eg}-} = G_+ - G_- = \frac{4\pi}{m} \times a_{\text{eg}-}$, the overlap integral

$$K = \int d^3x |w_{\text{loc}}(x)|^4 \quad (2.20)$$

is defined in terms of the (Wannier) wavefunction w_{loc} of an atom localized to a single lattice site^k [24], $\hat{c}_{j\alpha}$ destroys an atom on lattice site j with electronic state α , and \hat{N}_j is the number of atoms on lattice site j .

Rather than fixing atoms' nuclear spin states and letting their electronic states evolve, we can fix all atoms in their electronic ground state $|g\rangle$ and let their nuclear spin states evolve. In this case all terms in (2.17) aside from $\sim G_{\text{gg}}$ vanish, and the interaction Hamiltonian becomes

$$\hat{H}_{\text{int}}^{\text{gg}} = G_{\text{gg}} K \sum_{\substack{j \\ \mu < \nu}} \hat{c}_{j\mu}^{\dagger} \hat{c}_{j\mu} \hat{c}_{j\nu}^{\dagger} \hat{c}_{j\nu} = G_{\text{gg}} K \sum_j \frac{1}{2} \hat{N}_j (\hat{N}_j - 1), \quad (2.21)$$

^k In the plane-wave approximation for the light forming an optical lattice, the overlap integral in (2.20) is independent of the choice of lattice site on which to localize w_{loc} .

where we have suppressed the irrelevant (fixed) electronic-state index g . In both cases of (2.19) and (2.21), after appropriately fixing nuclear or electronic degrees of freedom the interaction Hamiltonian can be written in terms of number operators \hat{N}_j that are insensitive to atoms' internal states. These Hamiltonians simply assign an energetic penalty to all pairs of atoms occupying the same lattice site, which are counted by the binomial coefficient $\frac{1}{2}\hat{N}_j(\hat{N}_j - 1) = \binom{\hat{N}_j}{2}$. We investigate some of the physics accessible with these interactions, which manifest due to an underlying $SU(n)$ symmetry, in Chapters 3 and 7.

2.7 Spin operators

Fermions are notoriously difficult to study with a pen and paper (and even computer). One simplifying technique for modeling fermionic AEAs is thus to map them onto a more tractable *spin model*, which may be possible when atoms' spatial degrees of freedom play no role in their dynamics. Leaving the details, discussion, and benchmarking of some such mappings to Chapters 4 and 7, the basic idea is to define the spin operators

$$\hat{s}_{x,j} \equiv \frac{1}{2}\hat{c}_{je}^\dagger\hat{c}_{j,g} + \text{h.c.}, \quad \hat{s}_{y,j} \equiv -\frac{i}{2}\hat{c}_{je}^\dagger\hat{c}_{j,g} + \text{h.c.}, \quad \hat{s}_{z,j} \equiv \frac{1}{2}\left(\hat{c}_{j,e}^\dagger\hat{c}_{j,e} - \hat{c}_{j,g}^\dagger\hat{c}_{j,g}\right), \quad (2.22)$$

where we tentatively assume that atoms are nuclear-spin-polarized for simplicity (allowing us to suppress the nuclear spin indices), and j indexes a spatial mode (such as a lattice site or quasi-momentum). These spin operators obey standard $SU(2)$ commutation relations: $[\hat{s}_{\alpha j}, \hat{s}_{\beta j}] = i\hat{s}_{\gamma j}$ for any (α, β, γ) that is a cyclic permutation of (x, y, z) . This is simply a fancy way of saying that the operators defined in (2.22) behave, for example, like the standard spin-1/2 operators for the intrinsic spin of an electron. We can think of each atom as a two-level “spin”, identifying $|g\rangle \leftrightarrow |\downarrow\rangle$ with “spin-down” and $|e\rangle \leftrightarrow |\uparrow\rangle$ with “spin-up”. The electronic state of a single atom can then be visualized as a point on the Bloch sphere, and exponentiating the spin operators $s_{\alpha j}$ generates rotations of this state. Specifically, defining the spin vector $\hat{\mathbf{s}}_j = (\hat{s}_{x,j}, \hat{s}_{y,j}, \hat{s}_{z,j})$ and spatial axis $\mathbf{v} = (v_x, v_y, v_z)$ with $\mathbf{v} \cdot \mathbf{v} = 1$, the unitary $e^{-i\theta \mathbf{v} \cdot \hat{\mathbf{s}}_j}$ rotates the state of spin j about axis \mathbf{v} by an angle θ .

Summing over the mode index j yields the *collective* spin operators

$$\hat{S}_\alpha \equiv \sum_j \hat{s}_{\alpha,j}, \quad (2.23)$$

which obey the same commutation relations as the on-site operators $\hat{s}_{\alpha,j}$. In terms of a collective spin vector $\hat{\mathbf{S}} = (\hat{S}_x, \hat{S}_y, \hat{S}_z)$, the unitary $e^{-i\theta \mathbf{v} \cdot \hat{\mathbf{S}}} = \prod_j e^{-i\theta \mathbf{v} \cdot \hat{s}_j}$ now rotates all spins identically. The use of collective spin operators can greatly simplify the theoretical treatment of AEAs. If atoms' spatial degrees of freedom are frozen (e.g. due to trapping in a deep lattice), an external drive detuned by Δ from atoms' $|g\rangle \leftrightarrow |e\rangle$ transition (as in Section 2.4) induces the Hamiltonian

$$\hat{H}_{\text{drive}} = \Omega \hat{S}_x + \Delta \hat{S}_z, \quad (2.24)$$

where we include the energy splitting Δ between $|g\rangle$ and $|e\rangle$ in the rotating frame of the drive. This driving Hamiltonian simply rotates all spins about the axis $(\Omega, 0, \Delta)$.

If all atoms are prepared (and kept) in the electronic ground state, it can be similarly useful to define nuclear spin operators and their collective versions:

$$\hat{s}_{\mu\nu j} \equiv \hat{c}_{j,g,\mu}^\dagger \hat{c}_{j,g,\nu}, \quad \hat{S}_{\mu\nu} \equiv \sum_j \hat{s}_{\mu\nu,j}. \quad (2.25)$$

The on-site spin operators $\hat{s}_{\mu\nu j}$ destroy an atom in state ν and create one in state μ , and can thus be represented as $\hat{s}_{\mu\nu j} := |\mu\rangle\langle\nu|_j$. These operators obey the commutation relations of an $\text{SU}(n)$ algebra: $[\hat{s}_{\mu\nu j}, \hat{s}_{\rho\sigma j}] = \delta_{\nu\rho} \hat{s}_{\mu\sigma j} - \delta_{\sigma\mu} \hat{s}_{\rho\nu j}$, where $\delta_{\alpha\beta} = 1$ if $\alpha = \beta$ and 0 otherwise. As we discuss in Chapter 7, multi-laser driving schemes addressing the excited state $|e\rangle$ far off resonance can induce effective Hamiltonians that are expressed neatly in terms of the spin operators $\hat{s}_{\mu\nu j}$ and $\hat{S}_{\mu\nu}$. We explore some of the physics accessible with nuclear spin driving and $\text{SU}(n)$ -symmetric interactions in Chapter 7.

2.8 Collective spins and the Dicke manifold

Spin systems have a tensor product structure that typically makes them simpler to analyze than comparably-sized fermion systems. Even so, the Hilbert space of a spin system is still too

large to simulate more than a handful of spins exactly: the Hilbert space of N two-level spins has dimension 2^N , which is to say that we need 2^N complex numbers to represent an arbitrary (pure) state of N two-level spins. However, symmetries can cleave this Hilbert space into independent subspaces (known as “superselection sectors”) that scale more favorably with system size. One such symmetry that makes frequent appearances in this thesis and related work is that of *permutation symmetry*, in which the dynamics of a spin system are invariant under arbitrary permutations of its constituent spins.

Regardless of the origin, a spin system that is initially prepared in a PS state (such as a spin-polarized state) and evolves under a PS Hamiltonian remains in the PS manifold. The PS manifold of N two-level spins is known as the *Dicke manifold* [30] with spin $S = N/2$, which is spanned by the set of spin-polarized states¹. However, the set of spin-polarized states is an overcomplete (not to mention non-orthogonal and uncountably large) basis for the PS manifold; a minimal basis is provided by the *Dicke states* $|m\rangle$, which can be classified by their spin projection onto a spin quantization axis: $\hat{S}_z |m\rangle = m |m\rangle$, with $m \in \{N/2, N/2 - 1, \dots, -N/2\}$. The Dicke state $|m\rangle$ is a uniform superposition of all states in which exactly $N/2 + m \in \{0, 1, \dots, N\}$ spins point up along the spin quantization axis:

$$|m\rangle = \binom{N}{N/2 + m}^{-1/2} \sum_{\substack{\text{distinct} \\ \text{permutations} \\ P \text{ of } |\tilde{m}\rangle}} P |\tilde{m}\rangle, \quad |\tilde{m}\rangle = \underbrace{|\uparrow\uparrow \cdots \uparrow\rangle}_{N/2+m \text{ times}} \underbrace{|\downarrow\downarrow \cdots \downarrow\rangle}_{N/2-m \text{ times}}, \quad (2.26)$$

where $\binom{N}{N/2+m} = \frac{N!}{(N+m/2)!(N/2-m)!}$ is a binomial coefficient that is equal to the number of terms in the sum above. Altogether, the dimension of the PS manifold (namely, $N + 1$) grows only linearly with system size N , which makes it amenable to numerical simulations.

The PS manifold is also amenable to visualization and geometric reasoning. A state $|\psi\rangle$ within the PS manifold can be uniquely represented up to global phase by a probability distribution^m Q_ψ on the sphere, sometimes called the “Husimi distribution” or “Husimi- Q function”, with the value

¹ By a *spin-polarized state* we mean any state in which all spins are polarized along the same axis.

^m For convenience, the “probability distribution” Q_ψ is normalized to a geometric factor that is determined by N .



Figure 2.4: Husimi distributions for $N = 40$ spins in a spin-polarized state (left), as well as the Dicke states $|-10\rangle$ (middle) and $|0\rangle$ (right). A darker color at a point \mathbf{v} on the sphere indicates a larger overlap with the state $|\mathbf{v}\rangle$ maximally polarized along \mathbf{v} . For visibility, the color scale is normalized independently on each sphere.

$Q_\psi(\mathbf{v})$ at a point $\mathbf{v} = (v_x, v_y, v_z)$ on the sphere equal to the overlap of $|\psi\rangle$ with a state $|\mathbf{v}\rangle$ that is maximally polarized in the direction of \mathbf{v} : $Q_\psi(\mathbf{v}) = |\langle \mathbf{v} | \psi \rangle|^{2n}$. A spin-polarized state, for example, corresponds to a Gaussian-like distribution on the sphere, while Dicke states $|m\rangle$ correspond to rings at a fixed height along the quantization axis (see Figure 2.4).

2.9 Spin squeezing

A central goal in the field of quantum metrology is the realization of a quantum advantage, in which a sensor makes use of uniquely quantum effects such as entanglement to push the state-of-the-art in sensing capabilities. Averaging over N independent measurements of a physical parameter θ (for example by using one system to identically measure N times, or by measuring once using N independent systems) results in an uncertainty $\Delta\theta \propto 1/\sqrt{N}$. This scaling of uncertainty with measurement number N is commonly referred to as the standard quantum limit (SQL), although the term can be misleading: the SQL is the limit for *classical* averaging over N independent samples of θ . As has been known for 15 years now (and suspected for decades prior), the actual limit imposed by quantum mechanics on measurement precision, known as the Heisenberg limit, is in fact $\Delta\theta \propto 1/N$ [31]. On a high level, beating the SQL is made possible by quantum correlations that conspire to reduce the uncertainty in θ : if one system over-estimates the value of θ , another correlated system is (conditionally) more likely to under-estimate it.

ⁿ The Husimi distribution for a mixed state $\hat{\rho}$ is $Q_{\hat{\rho}}(\mathbf{v}) = \langle \mathbf{v} | \hat{\rho} | \mathbf{v} \rangle$.

One of the most promising strategies for surpassing classical limits on measurement precision is known as *spin squeezing* [32–35]. The paradigmatic setting for spin squeezing is the one-axis twisting (OAT) model, in which N two-level spins evolve under the Hamiltonian

$$\hat{H}_{\text{OAT}} = \chi \hat{S}_z^2, \quad (2.27)$$

where χ is the squeezing strength and \hat{S}_z is a collective spin- z operator. Recall that \hat{S}_z generates rotations about the z axis, and has the expansion $\hat{S}_z = \sum_m m |m\rangle\langle m|$ into Dicke states $|m\rangle$ that are labeled by a total projection of spin onto the z axis (namely, m). The OAT Hamiltonian $\hat{H}_{\text{OAT}} = \sum_m \chi m \hat{S}_z |m\rangle\langle m|$ can thus be interpreted as generating rotations about the z axis (by \hat{S}_z) at a rate that is proportional to the projection of spin onto the z axis (namely, χm). Living up to its name, the net effect of \hat{H}_{OAT} is thereby to *twist* a state about the z axis (see Figure 2.5).

Given an initial state polarized along the equator, represented by a Gaussian-like distribution on the sphere, the effect of the OAT Hamiltonian is to shear this distribution, resulting in a *squeezed state* that has a reduced variance $(\Delta\theta)^2$ along some axis. Here θ is the projection of spin onto an axis orthogonal to the mean spin direction $\langle \hat{\mathbf{S}} \rangle = (\langle \hat{S}_x \rangle, \langle \hat{S}_y \rangle, \langle \hat{S}_z \rangle)$. The reduced variance $(\Delta\theta)^2$ allows for an enhanced sensitivity to rotations of the collective spin state along the squeezed axis. The amount of squeezing can be quantified by the maximal gain in the resolution $\Delta\theta$ over that achieved by a spin-polarized state [34, 35]:

$$\xi^2 \equiv \frac{(\Delta\theta_{\min})^2}{(\Delta\theta_{\text{polarized}})^2} = \min_{\substack{\mathbf{v} \perp \langle \hat{\mathbf{S}} \rangle \\ \mathbf{v} \cdot \mathbf{v} = 1}} \text{var}(\hat{\mathbf{S}} \cdot \mathbf{v}) \times \frac{N}{|\langle \hat{\mathbf{S}} \rangle|^2}, \quad (2.28)$$

where the minimization is performed over unit vectors $\mathbf{v} = (v_x, v_y, v_z)$ in the plane orthogonal to the mean spin vector $\langle \hat{\mathbf{S}} \rangle$, and $\text{var}(\hat{X}) \equiv \langle \hat{X}^2 \rangle - \langle \hat{X} \rangle^2$ is the variance of \hat{X} . A spin squeezing parameter $\xi^2 < 1$ implies the presence of many-body entanglement that enables a sensitivity to rotations beyond that which is allowed by classical limits on measurement precision (i.e. the standard quantum limit) [35]. The OAT model can prepare squeezed states with $\xi^2 \sim 1/N^{2/3}$. Other models, such as the *two-axis twisting* model $\hat{H}_{\text{TAT}} = \chi (\hat{S}_z^2 - \hat{S}_y^2)$, can prepare squeezed states that saturate the ultimate limit on measurement precision that is allowed by quantum mechanics (i.e. the Heisenberg

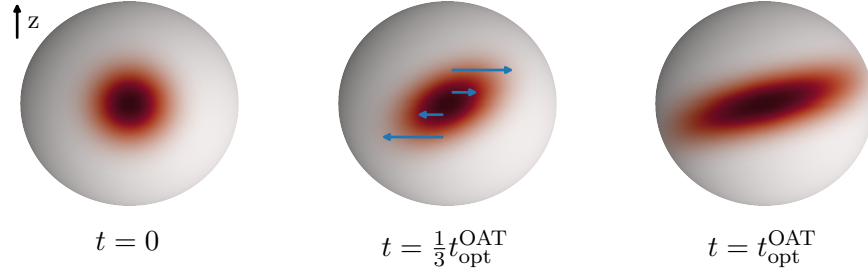


Figure 2.5: Representations of the state $|\psi(t)\rangle$ of $N = 40$ spins initially polarized along the equator, and subsequently evolved under the OAT Hamiltonian \hat{H}_{OAT} for a time t up to the optimal OAT squeezing time $t_{\text{opt}}^{\text{OAT}} \sim N^{-2/3}$. Figure reproduced from Ref. [4].

limit), namely $\xi^2 \sim 1/N$ [35]. Note that collective interactions are not necessary for spin squeezing, and that a spin-squeezed state need not lie within the PS manifold. We consider some of the prospects for spin squeezing with power-law interactions in Chapter 6.

Chapter 3

Effective multi-body $SU(n)$ -symmetric interactions of ultracold fermionic atoms on a 3D lattice

Prologue

One of the exciting aspects of working with cold atomic, molecular, and optical systems is the capability to study how many-body effects emerge from single- and few-body physics. Understanding the mechanics of this emergence can illuminate universal and non-universal aspects of observed phenomena, and can help engineer systems of external interest. In this chapter, we take a deep dive into the theory behind emergent multi-body interactions between ultracold fermions on an optical lattice. These multi-body interactions exhibit an $SU(n)$ symmetry that makes them interesting from the standpoint of fundamental physics. The experimental observation of these interactions is made possible by the exquisite precision of the 3D ^{87}Sr optical lattice clock, which thereby serves not only as a cutting-edge timekeeping device, but also as a powerful quantum simulation platform. The bulk of this chapter is taken from Ref. [1], which is a theory paper accompanying the experimental work of Ref. [7].

Abstract

Rapid advancements in the experimental capabilities with ultracold alkaline-earth-like atoms (AEAs) bring to a surprisingly near term the prospect of performing quantum simulations of spin

models and lattice field theories exhibiting $SU(N)$ symmetry^a. Motivated in particular by recent experiments preparing high density samples of strongly interacting ^{87}Sr atoms in a three-dimensional optical lattice, we develop a low-energy effective theory of fermionic AEAs which exhibits emergent multi-body $SU(N)$ -symmetric interactions, where N is the number of atomic nuclear spin levels. Our theory is limited to the experimental regime of (i) a deep lattice, with (ii) at most one atom occupying each nuclear spin state on any lattice site. The latter restriction is a consequence of initial ground-state preparation. We fully characterize the low-lying excitations in our effective theory, and compare predictions of many-body interaction energies with direct measurements of many-body excitation spectra in an optical lattice clock. Our work makes the first step in enabling a controlled, bottom-up experimental investigation of multi-body $SU(N)$ physics.

3.1 Introduction

Fermionic alkaline-earth atoms (AEAs), in addition to other atoms such as ytterbium (Yb) sharing similar electronic structure, are currently the building blocks of the most precise atomic clocks in the world [17, 36, 37]. These atoms have a unique, ultra-narrow optical transition between metastable 1S_0 and 3P_0 electronic orbital states, i.e. the “clock states”, that allows for coherence times which can exceed 100 seconds [38, 39]. Furthermore, AEAs can be trapped in fully controllable optical lattice potentials and interrogated with ultra-stable lasers that can resolve and probe their rich hyperfine spectra, consisting of N different nuclear spin levels with N as large as 10 in strontium (^{87}Sr) and 6 in ytterbium (^{173}Yb).

In 2015 the ^{87}Sr optical lattice clock (OLC) at JILA, operated in a one-dimensional (1-D) lattice at microkelvin temperatures, achieved a total fractional uncertainty of 2×10^{-18} [40, 41]. More recently (2017), a new generation of OLCs became operational at JILA, interrogating a Fermi degenerate gas of ^{87}Sr atoms in a 3-D lattice at nanokelvin temperatures [42]. All of these atoms’ degrees of freedom, including the electronic orbital, nuclear spin, and motional states, can be fully

^a To minimize notational collisions and complications, in the bulk of this chapter we denote the number of nuclear spin states by the capital letter N , rather than the lower-case letter n (as in the rest of this thesis).

controlled with high fidelity in a 3-D lattice [43–46]. With frequency measurements reaching the 10^{-19} fractional uncertainty level, the new OLCs are thus enabling an exciting opportunity to probe, for the first time, quantum dynamics with sub-millihertz spectral resolution [42].

A wonderful consequence of the efforts to build better clocks is the development of highly controllable quantum simulators of many-body systems in the strongly-interacting regime, where inter-particle interactions set the largest energy scale relevant for system dynamics [42, 47, 48]. The marriage between precision clock spectroscopy and quantum many-body physics [49–54] has an enormous potential to enable novel explorations of physics for the same reason that makes AEAs such remarkable time-keepers. Specifically, due to the lack of electronic orbital angular momentum in the 1S_0 and 3P_0 states, AEAs exhibit decoupled orbital and nuclear spin degrees of freedom. For atoms with N nuclear spin levels, this decoupling leads to nuclear-spin-conserving $SU(N)$ -symmetric interactions governed entirely by orbital-state parameters [49, 53, 55].

The presence of this exotic $SU(N)$ symmetry in a highly controllable experimental platform opens the door to experimental studies of e.g. the $SU(N)$ Heisenberg model, whose phase diagram is believed to exhibit features such as a chiral spin liquid (CSL) phase with topological order and fractional statistics [56–58]. In addition to illuminating open questions in our understanding of the fractional quantum Hall effect and unconventional superconductivity [59–61], the CSL can support non-Abelian excitations which allow for universal topological quantum computation [57, 62]. Harnessing the $SU(N)$ -symmetric interactions of AEAs might also enable the simulation of various lattice gauge theories [63, 64], some of which share important qualitative features with quantum chromodynamics such as few-body bound states and confinement [65, 66]. These direct, quantum simulations have an extraordinary potential to provide novel insights by circumventing e.g. severe sign problems which plague classical simulations of strongly interacting fermionic systems [63, 67].

In this work, we investigate the first experimental capabilities with ultracold fermionic AEAs to prepare high-density samples in a 3-D lattice with multiple occupation of individual lattice sites [7]. Specifically, we consider ground-state preparation of isolated few-body systems in the

deep-lattice limit, and carry out a bottom-up investigation of emergent multi-body interactions on multiply-occupied lattice sites. These multi-body interactions appear in a low-energy effective theory of the atoms, and inherit the $SU(N)$ symmetry of their bare, pair-wise interactions, thereby enabling experimental studies of multi-body $SU(N)$ physics through the exquisite capabilities with OLCs. Our theory is limited to the experimental regime of at most one atom occupying each nuclear spin state on any lattice site, which is a consequence of the experimental protocol which starts with all atoms in the ground state.

Though effective multi-body interactions have previously been studied in the context of harmonically [68, 69] and lattice-confined [70] neutral bosons prepared in a single hyperfine state, our work deals for the first time with fermions that have internal degrees of freedom and multiple collisional parameters. Some past work has detected experimental signatures of multi-body interactions in the form of quantum phase revivals [71]. We instead compare the many-body interaction energies predicted by our low-energy effective theory to the experimental measurements of the density-dependent orbital excitation spectra performed in Ref. [7], similarly to the measurements with bosons performed in Ref. [72]. To facilitate this comparison of excitation spectra and to characterize the low-lying excitations in our effective theory, we consider a restriction of our theory to states with at most one orbital excitation per lattice site. In this case, we find that the $SU(N)$ symmetry of atomic collisions allow the effective multi-body interactions to take a remarkably simple form.

The remainder of this paper is structured as follows. In Section 3.2 we summarize the experimental procedures relevant to our work, provide an overview of the one- and two-body physics of ultracold atoms in a deep lattice, and preview our main technical results. In Section 3.3 we discuss our method for deriving a low-energy effective theory, provide a perturbative expansion for the net effective Hamiltonian, and compute all M -body Hamiltonians through third order in the low-energy effective theory. We then analyze the low-lying excitations of the effective theory in Section 3.4, comparing spectral predictions with experimental measurements, and study the orbital-state dynamics of nuclear spin mixtures interrogated via Rabi spectroscopy. Finally, we summarize

and conclude our findings in Section 3.5, and provide some discussion of future outlooks.

3.2 Background and overview

The work in this paper is closely tied to the experimental work reported in Ref. [7]; we begin with a short summary of the relevant experimental procedures therein. The experiment begins by preparing a degenerate gas of 10^4 - 10^5 (fermionic) ^{87}Sr atoms in a uniform mixture of their ten nuclear spin states and at ~ 0.1 of their fermi temperature (~ 10 nanokelvin) [42, 73]. This gas is loaded into a primitive cubic optical lattice at the “magic wavelength” for which both ground (1S_0) and first-excited (3P_0) electronic orbital states of the atoms experience the same lattice potential [22]. Lattice depths along the principal axes of the lattice are roughly equal in magnitude, with a geometric mean that can be varied from 30 to 80 E_R , where $E_R \approx 3.5 \times 2\pi$ kHz is the lattice photon recoil energy of the atoms (with the reduced Planck constant $\hbar = 1$ throughout this paper). These lattice depths are sufficiently large as to neglect tunneling on the time scales relevant to the experiment. The temperature of the atoms is also low enough to neglect thermal occupation of motional states outside the ground-state manifold.

Once loaded into an optical lattice, atoms are addressed by an external (“clock”) interrogation laser with an ultranarrow (26 mHz) linewidth, detuned by Δ from the single-atom $^1S_0 - ^3P_0$ transition frequency ω_0 . After a fixed interrogation time, the experiment turns off the interrogation laser, removes all ground-state (1S_0) atoms from the lattice, and uses absorption imaging to count the remaining excited-state (3P_0) atoms. Non-interacting atoms in singly-occupied lattice sites feature the typical single particle lineshape peaked at $\Delta = 0$. The lineshapes of multiply-occupied lattice sites, meanwhile, are shifted by inter-atomic interactions, which results in spectroscopic peaks (i.e. local maxima in excited-state atom counts) away from $\Delta = 0$. A sweep across different detunings Δ (on the scale of inter-atomic interaction energies) thus constitutes a measurement of the many-body orbital excitation spectrum. We note that this spectroscopic protocol addresses only singly-excited orbital states of lattice sites. Doubly-excited states are off resonant due to (i) the interaction-induced non-linearity (\sim kHz) of the orbital excitation energies, and (ii) the ultranarrow

linewidth (\sim mHz) of the interrogation laser.

Although an external trapping potential will generally break discrete translational symmetry of the lattice, any background inhomogeneity can be made negligible by spectroscopically addressing a sufficiently small region of the lattice [7]. Throughout this paper, we work strictly in the deep-lattice regime with negligible tunneling between lattice sites. We also neglect any lattice inhomogeneities and assume that both atomic orbital states (i.e. 1S_0 and 3P_0) experience identical lattice potentials. The single-particle Hamiltonian of the atoms can then be written in the form

$$H_0 = \sum_{i,n,\mu,s} E_n \hat{c}_{in\mu s}^\dagger \hat{c}_{in\mu s}, \quad (3.1)$$

where $\hat{c}_{in\mu s}$ is a fermionic operator which annihilates a single atom on lattice site $i \in \mathbb{Z}^3$ in motional state $n \in \mathbb{N}_0^3$ with nuclear spin $\mu \in \{-I, -I+1, \dots, I\}$ (i.e. projected onto a quantization axis) and orbital state $s \in \{g, e\}$; and E_n is the energy of a single atom in motional state n . In a harmonic trap approximation we would have $E_n = (3/2 + n_x + n_y + n_z)\omega$ for an on-site angular trap frequency ω , but in general the anharmonicity of the lattice potential will cause a non-negligible shift in motional state energies.

In the absence of hyperfine coupling, as when addressing the spinless 1S_0 (g) and 3P_0 (e) orbital states of AEAs, interactions between any two atoms are governed by their orbital states alone, and are therefore characterized by four scattering lengths a_X with $X \in \{gg, eg^-, eg^+, ee\}$, where the $+$ ($-$) superscript denotes symmetrization (anti-symmetrization) of a two-body orbital state under particle exchange. In the low-energy limit, we can write the bare two-body interaction Hamiltonian in the form [29]

$$H_{\text{int}} = \sum_{\substack{\mu < \nu \\ s}} G_s \int d^3x \hat{\rho}_{\mu s} \hat{\rho}_{\nu s} + G_+ \sum_{\mu, \nu} \int d^3x \hat{\rho}_{\mu, e} \hat{\rho}_{\nu, g} + G_- \sum_{\mu, \nu} \int d^3x \hat{\psi}_{\mu, e}^\dagger \hat{\psi}_{\nu, g}^\dagger \hat{\psi}_{\nu, e} \hat{\psi}_{\mu, g}, \quad (3.2)$$

where $\hat{\psi}_{\mu s}$ is a fermionic field operator for atoms with nuclear spin μ and orbital state s ; $\hat{\rho}_{\mu s} \equiv \hat{\psi}_{\mu s}^\dagger \hat{\psi}_{\mu s}$ is an atomic density field operator; and the coupling constants G_X are defined in terms of the scattering lengths a_Y by

$$G_{s=g,e} \equiv \frac{4\pi}{m_A} a_{ss}, \quad G_{\pm} \equiv \frac{2\pi}{m_A} (a_{eg^+} \pm a_{eg^-}), \quad (3.3)$$

where m_A is the mass of a single atom. Defining for brevity

$$G_{st}^{qr} \equiv \begin{cases} G_q & q = r = s = t \\ G_+ & q \neq r \text{ and } (q, r) = (s, t) \\ G_- & q \neq r \text{ and } (q, r) = (t, s) \\ 0 & \text{otherwise} \end{cases}, \quad (3.4)$$

where $q, r, s, t \in \{g, e\}$ are orbital state indices, we can alternately write the bare two-body interaction Hamiltonian in the more compact form

$$H_{\text{int}} = \frac{1}{2} \sum_{\substack{q,r,s,t \\ \mu,\nu}} G_{st}^{qr} \int d^3x \hat{\psi}_{\mu s}^\dagger \hat{\psi}_{\nu t}^\dagger \hat{\psi}_{\nu r} \hat{\psi}_{\mu q}. \quad (3.5)$$

For nuclear spins μ, ν , the symbol G_{st}^{qr} gives the coupling constant between the two-atom states $(\mu, q) + (\nu, r) \leftrightarrow (\mu, s) + (\nu, t)$.

Note that the Hamiltonian in (3.5) is not the true microscopic interaction Hamiltonian of AEAs, but rather a generic form for a low-energy effective field theoretic description of two-body interactions [29, 51, 55, 68–70, 74, 75]. There are therefore two important points to keep in mind concerning our use of (3.5) to describe two-body interactions. First, the use of effective field theory generically gives rise to divergences that must be dealt with either through regularization, e.g. of the zero-range interaction potential implicitly assumed in the expression of (3.5) [76], or through renormalization of the coupling constants in the theory. We chose the latter approach, as we will in any case find it convenient to renormalize the coupling constants in the effective theory developed in Section 3.3. The choice of method to regulate divergences has no effect on the underlying physics.

Second, (3.5) is only the first term in a low-energy expansion of two-body interactions in effective field theory, which generally includes additional terms containing derivatives of field operators. Derivative terms correspond to the dependence of two-body scattering on the relative momentum k of particles involved, with $k \rightarrow 0$ in the zero-energy limit. In the present case of s -wave scattering, the leading dependence of the two-body interaction Hamiltonian on the relative momentum k can be captured by use of an energy-dependent pseudo-potential, which amounts to using a k -dependent

effective scattering length [77]. This effective scattering length can be determined by expanding the s -wave collisional phase shift in powers of the relative momentum k [76, 78]. Details of this expansion will depend on the characteristic length scale of finite-range interactions. In our work, these corrections to (3.5) will be relevant only for the calculation of two-body interaction energies, appearing at third order in the coupling constants G_X . As we are primarily interested in M -body interactions for $M \geq 3$, we defer this calculation to Appendix 3.D. We note that our approach of using an unregularized contact potential, renormalizing coupling constants, and separately accounting for momentum-dependent scattering is essentially the same as the approach used for similar calculations in Refs. [68–70]. While this approach does not provide insight into the microscopic structure of inter-atomic interactions, it is suitable for the phenomenological description of these interactions, and in particular for our eventual development of a low-energy effective theory.

We now expand the field operators $\hat{\psi}_{\mu s}$ in the Wannier basis for a 3-D lattice, such that $\hat{\psi}_{\mu s}(x) = \sum_{i,n} \phi_{in}(x) \hat{c}_{in\mu s}$ with spatial wavefunctions ϕ_{in} and fermionic annihilation operators $\hat{c}_{in\mu s}$ indexed by lattice sites i and motional states n . Invoking the tight-binding approximation, we assume that the spatial overlap integral in (3.5) is negligible unless all wavefunctions are localized at the same lattice site; we discuss the breakdown of this approximation and its consequences for our low-energy effective theory in Appendix 3.E. The relevant spatial overlap integral is then

$$K_{mn}^{k\ell} \equiv \int d^3x \phi_{im}^* \phi_{in}^* \phi_{i\ell} \phi_{ik}, \quad (3.6)$$

which for a lattice with discrete translational invariance is independent of the lattice site i . The two-body interaction Hamiltonian can be written in terms of this overlap integral as

$$H_{\text{int}} = \frac{1}{2} \sum_{\substack{i,k,\ell,m,n \\ q,r,s,t \\ \mu,\nu}} K_{mn}^{k\ell} G_{st}^{qr} \hat{c}_{im\mu s}^\dagger \hat{c}_{in\nu t}^\dagger \hat{c}_{i\ell\nu r} \hat{c}_{ik\mu q} \equiv \frac{1}{2} \sum K_{mn}^{k\ell} G_{st}^{qr} \hat{c}_{m\mu s}^\dagger \hat{c}_{n\nu t}^\dagger \hat{c}_{\ell\nu r} \hat{c}_{k\mu q}, \quad (3.7)$$

where for brevity we will henceforth suppress the identical site index (i) on all operators, and implicitly sum over all free indices in a summand (i.e. indices which do not have a fixed value). We may also at times suppress motional state indices on the overlap integral $K_{mn}^{k\ell}$, in which case the

suppressed indices are implicitly zero (corresponding to a motional ground state); i.e.

$$K_n^{\ell m} \equiv K_{n,0}^{\ell m}, \quad K_n^m \equiv K_{n,0}^{m,0}, \quad K_{mn} \equiv K_{mn}^{0,0}, \quad K_n \equiv K_{n,0}^{0,0}, \quad K \equiv K_{0,0}^{0,0}. \quad (3.8)$$

For simplicity, we will also generally work in a gauge for which all two-body overlap integrals are real, such that $K_{mn}^{k\ell} = K_{mn}^{k\ell *} = K_{k\ell}^{mn}$. The existence of such a gauge is guaranteed by the analytic properties of the Wannier wavefunctions ϕ_{in} [79].

Current experiments with ^{87}Sr can prepare up to five atoms in the same (ground) orbital state on a single lattice site, and coherently address states with a single orbital excitation per lattice site [7]. At ultracold temperatures well below the non-interacting motional excitation energies $\Delta_n \equiv E_n - E_0$ for $n > 0$, atoms only occupy their motional ground state in the lattice. For this reason, it is common to map the description of these atoms onto a single-band Hubbard model that captures all dynamics within the subspace of motional ground states of non-interacting atoms, i.e. with wavefunctions $\phi_{i,0}$. Interactions, however, modify atoms' motional ground-state wavefunctions. The true motional ground state of a collection of interacting atoms is then an admixture of the non-interacting motional eigenstates, and a naive Hubbard model that assumes atomic wavefunctions $\phi_{i,0}$ will fail to reproduce the interacting atoms' orbital excitation spectrum. Formally, corrections to the spectrum of interacting atoms can be accounted for by a perturbative treatment of far-off-resonant terms in the interaction Hamiltonian of (3.7) that create atoms in excited motional states, e.g. $\sim \hat{c}_{n\mu s}^\dagger \hat{c}_{0,\nu t}^\dagger \hat{c}_{0,\nu r} \hat{c}_{0,\mu q}$ with $n > 0$. These corrections can be understood through interaction-induced *virtual* occupation of higher bands (i.e. excited motional states), which becomes relevant as more atoms occupy the same lattice site, such that their interaction energy becomes non-negligible compared to the motional excitation energies Δ_n .

In order to recast interaction-induced modifications to orbital excitation spectra as corrections to the simple Hubbard model (i.e. computed using the non-interacting ground-state wavefunctions $\phi_{i,0}$), we develop a low-energy effective theory of interacting AEAs in a deep lattice. To simplify our theory, we assume that any N atoms on a single lattice site occupy distinct nuclear spin states. This assumption applies for any experimental protocol in which all atoms are initially prepared

in their orbital and motional ground states (as e.g. in Ref. [7]). In this case, multiple occupation of a single nuclear spin state on any given lattice site is initially forbidden by fermionic statistics. Subsequent violation of this condition cannot occur in the absence of inter-site effects or hyperfine coupling between nuclear spin states, as is the case of the experiment in Ref. [7].

Our low-energy effective theory exhibits $SU(N)$ -symmetric multi-body interactions, such that the effective interaction Hamiltonian can be written in the form

$$H_{\text{int}}^{\text{eff}} = \sum_{M=2}^{2I+1} \sum_{p \geq 1} H_M^{(p)}, \quad (3.9)$$

where $H_M^{(p)}$ is an M -body Hamiltonian of order p in the coupling constants G_X , and I is the total nuclear spin of each atom (e.g. $I = 9/2$ for ^{87}Sr). The sum terminates at $2I + 1$ because this is the largest number of atoms which may initially occupy a single lattice site. We explicitly compute all M -body Hamiltonians $H_M \equiv \sum_p H_M^{(p)}$ through order $p = 3$, yielding effective two-, three-, and four-body interactions. To (i) facilitate a comparison with the experimental measurements of many-body orbital excitation spectra performed in Ref. [7] and (ii) characterize the low-lying excitations in our effective theory, we additionally restrict the multi-body Hamiltonians H_M to states with at most one orbital excitation per lattice site. Under this restriction, we find that the $SU(N)$ symmetry of atomic collisions allows us to express all multi-body Hamiltonians in the simple form

$$H_M = \sum_{|\{\mu_j\}|=M} H_2^{(\mu_1, \mu_2)} \prod_{\alpha=3}^M \hat{n}_{\mu_\alpha, g}, \quad (3.10)$$

where $H_2^{(\mu_1, \mu_2)}$ is a two-body Hamiltonian addressing atoms with nuclear spin μ_1, μ_2 ; and $\hat{n}_{\mu s} = \hat{c}_{\mu s}^\dagger \hat{c}_{\mu s}$ is a number operator for atoms with nuclear state μ and orbital state s . The sum in (3.10) is performed over all choices of nuclear spins μ_j with $j = 1, 2, \dots, M$ for which all μ_j are distinct, or equivalently all choices of μ_j for which the set $\{\mu_j\}$ contains M elements, for a total of $\binom{2I+1}{M} \times (M!)$ nuclear spin combinations. The key feature of the M -body interactions in (3.10) is that they ultimately take the same form as two-body interactions, but with the addition of $M - 2$

spectator atoms. This form is a direct consequence of the $SU(N)$ symmetry of underlying two-body interactions.

3.3 Low-energy effective theory

The net Hamiltonian $H = H_0 + H_{\text{int}}$ for interacting AEAs on a lattice is not diagonal with respect to single-particle motional state indices (e.g. $n \in \mathbb{N}_0^3$). The problem of determining interacting atoms' orbital excitation spectrum therefore nominally involves all atomic motional degrees of freedom. At zero temperature, however, each orbital state of a collection of interacting atoms is associated with a single motional ground state. In order to compute an orbital excitation spectrum at zero temperature, in principle we need to identify this motional ground state. We can then ignore all excited motional states, which will be neither thermally occupied nor externally interrogated. Such a procedure would drastically reduce the dimensionality of the Hilbert space necessary to describe the atoms, thereby greatly simplifying any description of the atoms' orbital spectrum and internal (i.e. nuclear and orbital) dynamics. In practice, however, identifying the motional ground states of interacting atoms and writing down a Hamiltonian restricted to this subspace is a very difficult process to carry out analytically.

We denote the motional ground-state subspace of the non-interacting Hamiltonian H_0 by $\mathcal{H}_{\text{ground}}^{\text{single}}$, and the motional ground-state subspace of the interacting Hamiltonian $H = H_0 + H_{\text{int}}$ by $\mathcal{H}_{\text{ground}}^{\text{multi}}$. That is, all atomic wavefunctions for states within $\mathcal{H}_{\text{ground}}^{\text{single}}$ are described by $\phi_{i,0}$, while the atomic wavefunctions for states within $\mathcal{H}_{\text{ground}}^{\text{multi}}$ are generally unknown, and are in principle determined by minimizing the energy of a state with respect to its motional degrees of freedom. Both $\mathcal{H}_{\text{ground}}^{\text{single}}$ and $\mathcal{H}_{\text{ground}}^{\text{multi}}$ are subspaces of the full Hilbert space $\mathcal{H}_{\text{full}}$. When interactions are sufficiently weak compared to the spectral gap Δ between $\mathcal{H}_{\text{ground}}^{\text{single}}$ and its orthogonal complement $\mathcal{H}_{\text{full}} \setminus \mathcal{H}_{\text{ground}}^{\text{single}}$, one can identify a particular unitary operator U (acting on the full Hilbert space $\mathcal{H}_{\text{full}}$) which rotates $\mathcal{H}_{\text{ground}}^{\text{multi}}$ into $\mathcal{H}_{\text{ground}}^{\text{single}}$ [80]. This unitary U can be used to construct an *effective Hamiltonian* $H_{\text{eff}} = UH_0U^\dagger$ with two key properties: (i) H_{eff} is diagonal in the same (known) basis as the non-interacting Hamiltonian H_0 , and (ii) the spectrum of H_{eff} on $\mathcal{H}_{\text{ground}}^{\text{single}}$ is identical

to that of the interacting Hamiltonian H on $\mathcal{H}_{\text{ground}}^{\text{multi}}$. The use of an effective Hamiltonian H_{eff} thus overcomes the need to identify $\mathcal{H}_{\text{ground}}^{\text{multi}}$ in order to compute the orbital spectrum of H at zero temperature. This method for constructing an effective theory is commonly known as the Schrieffer-Wolff transformation, named after the authors of its celebrated application in relating the Anderson and Kondo models of magnetic impurities in metals [81].

Using the machinery developed in Ref. [80] for performing a rotation between low-energy subspaces of a perturbed (i.e. interacting) and unperturbed (i.e. non-interacting) Hamiltonian, we derive an expansion for an effective interaction Hamiltonian $H_{\text{int}}^{\text{eff}}$ in terms two-body interaction Hamiltonian H_{int} (see Appendix 3.A). This expansion takes the form

$$H_{\text{int}}^{\text{eff}} = \sum_{p \geq 1} H_{\text{int}}^{(p)}, \quad (3.11)$$

where $H_{\text{int}}^{(p)}$ is order p in H_{int} . Letting $\mathcal{E}_0 \equiv \mathcal{H}_{\text{full}} \setminus \mathcal{H}_{\text{ground}}^{\text{single}}$ denote the orthogonal complement of $\mathcal{H}_{\text{ground}}^{\text{single}}$ (i.e. \mathcal{E}_0 is the space of all states with at least one atom in an excited motional state), $\mathcal{B}_0(\mathcal{E}_0)$ denote an eigenbasis of \mathcal{E}_0 with respect to the single-particle Hamiltonian H_0 , and E_α denote the motional energy (with respect to H_0) of a state $|\alpha\rangle \in \mathcal{E}_0$ relative to the corresponding motional ground-state energy, we define the operator

$$\mathcal{I} \equiv \sum_{|\alpha\rangle \in \mathcal{B}_0(\mathcal{E}_0)} \frac{|\alpha\rangle\langle\alpha|}{E_\alpha}, \quad (3.12)$$

which sums over projections onto excited states with corresponding energetic suppression factors. The operator \mathcal{I} together with the projector \mathcal{P}_0 onto $\mathcal{H}_{\text{ground}}^{\text{single}}$ allows us concisely write the first few terms in (3.11) as

$$H_{\text{int}}^{(1)} = \mathcal{P}_0 H_{\text{int}} \mathcal{P}_0, \quad H_{\text{int}}^{(2)} = -\mathcal{P}_0 H_{\text{int}} \mathcal{I} H_{\text{int}} \mathcal{P}_0, \quad (3.13)$$

$$H_{\text{int}}^{(3)} = \mathcal{P}_0 H_{\text{int}} \mathcal{I} H_{\text{int}} \mathcal{I} H_{\text{int}} \mathcal{P}_0 - \frac{1}{2} \left[\mathcal{P}_0 H_{\text{int}} \mathcal{P}_0, \mathcal{P}_0 H_{\text{int}} \mathcal{I}^2 H_{\text{int}} \mathcal{P}_0 \right]_+, \quad (3.14)$$

where $[X, Y]_+ \equiv XY + YX$. Writing down a single-band Hubbard model that simply neglects excited atomic motional states and uses H_{int} directly to describe the orbital spectrum of interacting

atoms is thus equivalent to truncating our expansion for $H_{\text{int}}^{\text{eff}}$ at first order. In addition to this first order term, the expansion involves *effective corrections* to the action of H_{int} on the non-interacting motional ground states (i.e. on $\mathcal{H}_{\text{ground}}^{\text{single}}$) in the form of higher-order terms with *intermediate* or *virtual occupation* of excited states, manifest in \mathcal{I} .

Substituting the definition of \mathcal{I} into (3.13)-(3.14) yields expressions that are highly reminiscent of standard non-degenerate perturbation theory in quantum mechanics, but which nonetheless exhibit crucial differences. The first, and most obvious difference is that these expressions are operator equations, and that the sums over virtual states are performed over a basis for the orthogonal complement of the subspace $\mathcal{H}_{\text{ground}}^{\text{single}}$, rather than a basis for the orthogonal complement of a single state, as in non-degenerate perturbation theory. Second, the non-degeneracy condition in standard perturbation theory is here elevated to a restriction on the magnitude of the perturbation H_{int} relative to the spectral gap Δ of the non-interacting Hamiltonian H_0 between $\mathcal{H}_{\text{ground}}^{\text{single}}$ and the excited subspace \mathcal{E}_0 . Specifically, the validity of (3.13)-(3.14) is conditional only on $\|H_{\text{int}}\| \leq \Delta/2$, where $\|X\| \equiv \max_{|\psi\rangle \in \mathcal{H}} \sqrt{\langle \psi | X^\dagger X | \psi \rangle}$ is the operator norm, with no restrictions on spectral gaps or degeneracies within $\mathcal{H}_{\text{ground}}^{\text{single}}$ [80, 82]. Finally, the effective theory involves no corrections to the non-interacting many-body energy eigenstates; the purpose of constructing the effective Hamiltonian $H_{\text{eff}} = H_0 + H_{\text{int}}^{\text{eff}}$ is to reproduce, on the known eigenstates of the non-interacting Hamiltonian H_0 within $\mathcal{H}_{\text{ground}}^{\text{single}}$, the spectrum of the interacting Hamiltonian $H = H_0 + H_{\text{int}}$ on $\mathcal{H}_{\text{ground}}^{\text{multi}}$. “Correcting” the eigenstates of the non-interacting Hamiltonian H_0 on $\mathcal{H}_{\text{ground}}^{\text{single}}$ thus invalidates the effective theory.

As a last comment, we note that our chosen method for constructing an effective Hamiltonian is distinct from adiabatic elimination methods which are commonly used in the atomic physics and quantum optics communities to develop effective theories for e.g. the low-lying levels of a Lambda system [83–86]. Unlike the perturbative, but exact Schieffer-Wolff transformation, adiabatic elimination methods use approximations which rely on the fast dynamics of excited states. While generally reasonable, these approximations must be made carefully to avoid potential problems with self-consistency (see Section 3 of Ref. [83]), and yield no obvious or straightforward means

to compute effective corrections beyond second order in the couplings between low- and high-energy sectors of a Hilbert space [84–86]. While at least one attempt at systematically computing higher-order corrections in the framework of adiabatic elimination has recently been made [86], the resulting expressions do not lend themselves as nicely to analytical treatment, and were in any case found by the authors to be equivalent to a Schrieffer-Wolff transformation.

3.3.1 Diagrammatic representation of effective Hamiltonians

The form of the bare two-body interaction Hamiltonian H_{int} in (3.7) motivates a diagrammatic representation of terms in the effective Hamiltonian H_{eff} in (3.11), similarly to the diagrams used to represent elements of the scattering matrix in standard quantum field theory. Effective M -body interaction terms at order p in H_{int} can be represented by directed graphs containing p vertices with degree greater than one, which we call *internal vertices*. Each internal vertex and its associated edges correspond respectively to a coupling constant and the associated field operators in H_{int} . An example 2-vertex diagram representing an effective 3-body interaction term is provided in Figure 3.1. All diagrams are read from left to right to construct a sequence of operators from right to left; the internal vertices of a diagram are thus strictly ordered, with the n -th internal vertex from the left corresponding to the n -th interaction Hamiltonian H_{int} from the right in (3.13) or (3.14). Solid (dashed) lines represent field operators acting on the lowest (arbitrary) motional states. Spatial overlap factors at each vertex are determined by the motional states of the edges which connect to (i.e. field operators associated with) that vertex. While it is possible to construct explicit rules for determining the energetic suppression factors (i.e. from \mathcal{I}) of the term represented by a diagram, these factors are most easily determined by examination of the effective Hamiltonians in (3.13) and (3.14).

The diagram in Figure 3.1 explicitly labels all edges with indices of the corresponding field operators, but in general we may suppress these indices, in which case the diagram includes a sum over the suppressed indices. These sums are performed over all allowed values of the suppressed indices, with the restriction that virtual states (i.e. vertical slices of the diagram between internal

$$\begin{aligned}
&= \mathcal{P}_0 \left(\frac{1}{2} K_n G_{ge}^{eg} \hat{c}_{\nu, g}^\dagger \hat{c}_{\rho, e}^\dagger \hat{c}_{\rho, g} \hat{c}_{\nu, e} \right) \frac{1}{E_n} \left(\frac{1}{2} K_n G_{ge}^{ge} \hat{c}_{\mu, g}^\dagger \hat{c}_{\nu, e}^\dagger \hat{c}_{\nu, e} \hat{c}_{\mu, g} \right) \mathcal{P}_0 \\
&= \frac{1}{4} \frac{K_n^2}{E_n} G_{ge}^{ge} G_{ge}^{eg} \mathcal{P}_0 \hat{c}_{\mu, g}^\dagger \hat{c}_{\nu, g}^\dagger \hat{c}_{\rho, e}^\dagger \hat{c}_{\rho, g} \hat{c}_{\nu, e} \hat{c}_{\mu, g} \mathcal{P}_0
\end{aligned}$$

Figure 3.1: An example second-order diagram and the corresponding three-body interaction term in $H_{\text{int}}^{(2)}$, with $n > 0$ and $\hat{c}_{\mu s} \equiv \hat{c}_{0, \mu s}$. Diagrams are read from left to right to construct a sequence of operators from right to left. Solid (dashed) lines represent field operators acting on the lowest (arbitrary) motional states. For the sake of presentation, this diagram has colors associated with nuclear spin and orbital states, an arrow on each line to emphasize that they are directed left-to-right, and an explicit coupling constant written next to each vertex; we will generally not include these features, as they are not necessary to uniquely identify the term represented by a diagram. We will also drop explicit appearances of the ground-state projector \mathcal{P}_0 in our expressions, with the understanding that the low-energy effective theory implicitly addresses only non-interacting motional ground states.

vertices) represented with dashed lines must have at least one motional excitation. While we include factors of $1/2$ from H_{int} as expressed in (3.7) in the definition of a diagram, in all but the two-body case these factors of $1/2$ will be cancelled out by corresponding symmetry factors, i.e. the appearance of duplicate diagrams which are equal up to a relabeling of indices (see Appendix 3.B). The explicit signs and factor of $1/2$ which appear in the effective Hamiltonians in (3.13) and (3.14) are not included in the definition of a diagram, and must be kept track of manually.

3.3.2 Effective two-body interactions and renormalization

The effective two-body Hamiltonian in (3.11) has contributions at all orders in the coupling constants, and can be expanded in the form

$$H_2 = \text{diagram 1} - \text{diagram 2} + \text{diagram 3} + \dots \equiv \text{diagram 4}, \quad (3.15)$$

where the blob on the right schematically represents the net effective two-body interaction. On physical grounds, the net two-body interaction must clearly be finite, but individual sums over excited states in the loop diagrams of (3.15) may generally diverge [68]. These divergences ultimately appear due to our use of effective field theory to describe inter-atomic interactions in (3.2), (3.5), and (3.7), rather than a detailed microscopic description of two-atom scattering. Divergences of this sort are a generic feature of field theories, and can be dealt with using standard techniques such as renormalization. We therefore renormalize our coupling constants by introducing counter-terms \tilde{G}_X into the interaction Hamiltonian.

The introduction of counter-terms is merely a formal decomposition of the “bare” coupling constants G_X^{bare} that are used in (3.15) as $G_X^{\text{bare}} = G_X + \tilde{G}_X$. In performing such a decomposition, we are free to choose the values of G_X , which in turn fixes the values of $\tilde{G}_X \equiv G_X^{\text{bare}} - G_X$. For convenience, we can choose the values of G_X to be those of the net effective coupling constants on the right-hand side of (3.15). Representing the new coupling constants G_X by regular vertices and

the counter-terms \tilde{G}_X by a crossed dot (i.e. \otimes), this choice leads to the *renormalization condition*

$$\begin{array}{c} \diagup \quad \diagdown \\ \diagdown \quad \diagup \\ \mathcal{O}(G) \end{array} + \begin{array}{c} \diagup \quad \diagdown \\ \diagdown \quad \diagup \\ \otimes \\ \mathcal{O}(\tilde{G}) \end{array} - \begin{array}{c} \diagup \quad \diagdown \\ \diagdown \quad \diagup \\ \circ \\ \mathcal{O}(G^2) \end{array} + \dots = \begin{array}{c} \diagup \quad \diagdown \\ \diagdown \quad \diagup \\ \cdot \\ \mathcal{O}(G) \end{array}. \quad (3.16)$$

This renormalization condition has the benefit of allowing us to express effective two-body interactions simply in terms of net effective two-body coupling constants, rather than in terms of long sums at all order of the bare coupling constants. By construction, the counter-terms we have introduced exactly cancel all terms beyond leading order in (3.15), which implies that the effective two-body interaction Hamiltonian is simply

$$H_2 = \begin{array}{c} \diagup \quad \diagdown \\ \diagdown \quad \diagup \\ \cdot \\ \mathcal{O}(G) \end{array} = \frac{1}{2} \alpha_2^{(1)} \sum_{|\{\mu, \nu\}|=2} G_{st}^{qr} \hat{c}_{\mu s}^\dagger \hat{c}_{\nu t}^\dagger \hat{c}_{\nu r} \hat{c}_{\mu q}, \quad (3.17)$$

where for consistency with existing literature [68] we define $\alpha_2^{(1)} \equiv K$ as the overlap integral between two atoms occupying non-interacting motional ground states.

Before moving on to consider effective three-body interactions, there are a few comments we must make concerning renormalization and the result in (3.17). First, the effective two-body interaction H_2 in (3.17) takes the same form as the bare two-body interaction H_{int} in (3.7), but without excited motional states, and with renormalized coupling constants. Our choice of renormalization scheme, while convenient for the analytical development of a low-energy effective theory, no longer allows us to use the coupling constants G_X as defined by the free-space scattering lengths a_X in (3.3) to compute interaction energies. The renormalization condition in (3.16) explicitly fixes G_X to the net effective coupling constants in any given setting. Instead of using free-space coupling constants to compute interaction energies in a lattice, we must therefore first compute the effective coupling constants $G_X^{\text{lattice}}(\mathcal{U})$, which now depend on the lattice depth \mathcal{U} , and in turn use these effective coupling constants to compute interaction energies. We discuss the calculation of effective coupling constants in Appendix 3.C.

Second, the renormalization condition in (3.16) implies that the counter terms \tilde{G}_X are second order in the coupling constants G_X , i.e. $\tilde{G}_X \sim G_X^2$. Although the effective Hamiltonian expansions in (3.13) and (3.14) are organized in powers of the interaction Hamiltonian H_{int} , the couplings G_X

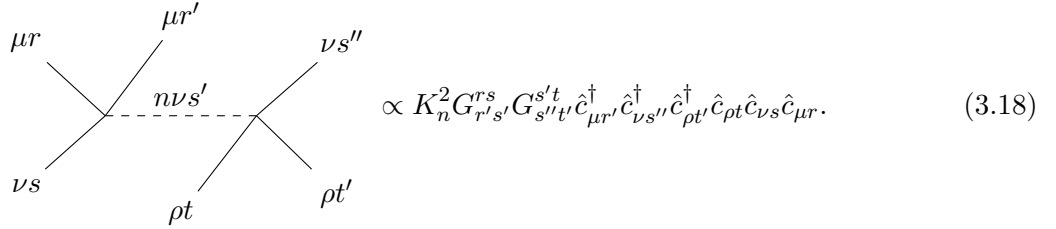
are the “small” parameters in which we can formally organize a perturbation theory; more specifically, the formally small quantities organizing our perturbation theory are two-body ground-state interaction energies (proportional to the couplings G_X) divided by the spectral gap of the single-atom Hamiltonian H_0 (see Appendix 3.F). If M atoms can only couple through terms represented by a p -vertex diagrams for $p \geq p_M^{\min}$, then the leading order contribution to M -body interactions is order p_M^{\min} in the couplings G_X . If the same p_M^{\min} -vertex diagrams involve any counter-terms, however, then these diagrams are at least order $p_M^{\min} + 1$ in the couplings G_X . Counter-terms therefore only appear at next-to-leading order (NLO) in the calculation of effective M -body interactions.

Finally, our result in (3.17) neglects the effect of momentum-dependent two-body scattering. When the effective range of interactions is comparable to the scattering lengths a_X , as is the case for ultracold ^{87}Sr , these momentum-dependent effects are third order in the coupling constants G_X . Just as the $\mathcal{O}(G^2)$ counter-terms do not affect M -body interactions until next-to-leading order (NLO), the $\mathcal{O}(G^3)$ momentum-dependent terms do not come into play until next-next-leading order (NNLO). Given that we develop our low-energy effective theory through third order in the coupling constants, these interactions will not appear in any of our three- and four-body calculations, but they do need to be considered in the calculation of pair-wise interaction energies. The primary interest of our work, however, concerns effective M -body interactions for $M \geq 3$; we therefore defer the calculation of momentum-dependent two-body interactions to Appendix 3.D.

3.3.3 Effective three-body interactions at second order

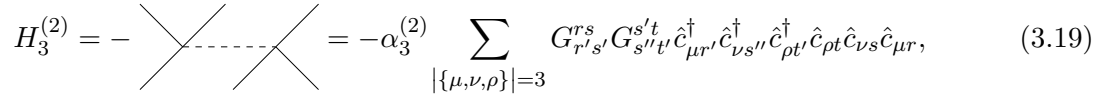
Our theory of effective multi-body interactions assumes no non-universal contribution to the three-body interaction energy, which is to say that we assume the absence of real (as opposed to effective), bare three-body interactions. Consequently, three-body interactions do not appear until second order in the coupling constants of the effective theory, in the expansion of $H_{\text{int}}^{(2)}$ in (3.13). The virtual state of three-body terms in $H_{\text{int}}^{(2)}$ cannot have two atoms in excited motional states, as otherwise the second application of H_{int} in $H_{\text{int}}^{(2)}$ would have to address both of these atoms to bring them back down to the ground state, resulting in a two-body process as in the second

diagram of (3.15). All second-order three-body terms must therefore have only one excited atom in the virtual state, and take the form



$$\propto K_n^2 G_{r's'}^{rs} G_{s''t'}^{s't} \hat{c}_{\mu r'}^\dagger \hat{c}_{\nu s''}^\dagger \hat{c}_{\rho t'}^\dagger \hat{c}_{\rho t} \hat{c}_{\nu s} \hat{c}_{\mu r}. \quad (3.18)$$

Unlike for the two-body diagram in (3.17), the explicit factors of 1/2 which appear in the bare two-body Hamiltonian H_{int} in (3.7) are now cancelled out by symmetry factors which account for duplicate diagrams; this cancellation will generally occur for all connected M -body diagrams with $M > 2$ (see Appendix 3.B). The net effective three-body interaction Hamiltonian at second order is then given by the sum over all diagrams of the form in (3.18), i.e.



$$H_3^{(2)} = - \sum_{|\{\mu, \nu, \rho\}|=3} \alpha_3^{(2)} G_{r's'}^{rs} G_{s''t'}^{s't} \hat{c}_{\mu r'}^\dagger \hat{c}_{\nu s''}^\dagger \hat{c}_{\rho t'}^\dagger \hat{c}_{\rho t} \hat{c}_{\nu s} \hat{c}_{\mu r}, \quad (3.19)$$

where $\alpha_3^{(2)} \equiv \sum_{n>0} K_n^2/E_n$, and the preceding minus sign is as prescribed by $H_{\text{int}}^{(2)}$ in (3.13).

3.3.4 Effective three-body interactions at third order

The third-order effective interaction Hamiltonian $H_{\text{int}}^{(3)}$ in (3.14) contains both three- and four-body terms. To compactly enumerate and evaluate all three-body diagrams at third order, we introduce an expanded coupling symbol

$$G_{\rho s; \sigma t}^{\mu q; \nu r} \equiv \begin{cases} G_{st}^{qr} & (\mu, \nu) = (\rho, \sigma) \\ -G_{ts}^{qr} & (\mu, \nu) = (\sigma, \rho) \\ 0 & \text{otherwise} \end{cases} \quad (3.20)$$

for more general $(\mu, q) + (\nu, r) \leftrightarrow (\rho, s) + (\sigma, t)$ coupling induced by terms proportional to $\hat{c}_{\rho s}^\dagger \hat{c}_{\sigma t}^\dagger \hat{c}_{\nu r} \hat{c}_{\mu q}$.

The minus sign in (3.20) accounts for fermionic statistics: if $(\mu, \nu) = (\sigma, \rho)$, then we are considering a term of the form

$$G_{\nu s; \mu t}^{\mu q; \nu r} \hat{c}_{\nu s}^\dagger \hat{c}_{\mu t}^\dagger \hat{c}_{\nu r} \hat{c}_{\mu q} = -G_{ts}^{qr} \hat{c}_{\nu s}^\dagger \hat{c}_{\mu t}^\dagger \hat{c}_{\nu r} \hat{c}_{\mu q} = G_{ts}^{qr} \hat{c}_{\mu t}^\dagger \hat{c}_{\nu s}^\dagger \hat{c}_{\nu r} \hat{c}_{\mu q}. \quad (3.21)$$

At the cost of introducing an additional sum over new nuclear spin indices, the expanded coupling symbol allows us to collect together diagrams which have the same graph topology, but represent different matrix elements of the effective Hamiltonian due to the exchange of nuclear spins at a vertex. The third order three-body diagrams in $H_{\text{int}}^{(3)}$ are then

$$\propto K_{\ell m} K_n^m K_{\ell n} G_{r's'}^{rs} G_{\nu's'''}^{\nu s'; \rho t} G_{r''s'''}^{r's''} \hat{c}_{\mu r'}^\dagger \hat{c}_{\nu s'''}^\dagger \hat{c}_{\rho t'}^\dagger \hat{c}_{\rho t} \hat{c}_{\nu s} \hat{c}_{\mu r}, \quad (3.22)$$

$$\propto K_{\ell m} K_n^{\ell m} K_n G_{r's'}^{rs} G_{r''s'''}^{r's''} G_{s''t'}^{s''t} \hat{c}_{\mu r'}^\dagger \hat{c}_{\nu s'''}^\dagger \hat{c}_{\rho t'}^\dagger \hat{c}_{\rho t} \hat{c}_{\nu s} \hat{c}_{\mu r}, \quad (3.23)$$

and the mirror image of (3.23). As prescribed by $H_{\text{int}}^{(3)}$ in (3.14), these diagrams have an associated minus sign if they contain only one excited virtual state, and a factor of 1/2 if they contain a virtual ground state. Remembering that counter-terms are $\mathcal{O}(G^2)$, there are additionally two third-order three-body diagrams in $H_{\text{int}}^{(2)}$, namely

$$\propto K_n^2 \tilde{G}_{r's'}^{rs} G_{s''t'}^{s''t} \hat{c}_{\mu r'}^\dagger \hat{c}_{\nu s''}^\dagger \hat{c}_{\rho t'}^\dagger \hat{c}_{\rho t} \hat{c}_{\nu s} \hat{c}_{\mu r} \quad (3.24)$$

and its mirror image, where \tilde{G}_{st}^{qr} is equal to the counter-term associated with G_{st}^{qr} .

The net contribution to the third-order three-body interaction Hamiltonian from three-particle-loop diagrams of the form in (3.22) is

$$= \left(\alpha_{3,1}^{(3)} - \alpha_5^{(3)} \right) \mathcal{H}_{3,1}^{(3)}, \quad (3.25)$$

where

$$\alpha_{3,1}^{(3)} \equiv \sum_{\substack{\ell+m>0 \\ \ell+n>0}} \frac{K_{\ell m} K_n^m K_{\ell n}}{E_{\ell m} E_{\ell n}}, \quad \alpha_5^{(3)} \equiv K \sum_{n>0} \frac{K_n^2}{E_n^2}, \quad (3.26)$$

and

$$\mathcal{H}_{3,1}^{(3)} \equiv \sum_{|\{\mu,\nu,\rho\}|=3} G_{r's'}^{rs} G_{\nu's''\rho't'}^{\nu s' \rho t} G_{r''s''}^{r' s''} \hat{c}_{\mu r''}^\dagger \hat{c}_{\nu' s''}^\dagger \hat{c}_{\rho' t'}^\dagger \hat{c}_{\rho t} \hat{c}_{\nu s} \hat{c}_{\mu r}. \quad (3.27)$$

Even though this contribution comes from loop diagrams, the factors $\alpha_{3,1}^{(3)}$ and $\alpha_5^{(3)}$ in (3.26) are finite. At large motional state indices n , atoms become free particles for which n essentially indexes discrete momentum states. These atoms thus have an energy which asymptotically scales as $E_n \sim n^2 \equiv n_x^2 + n_y^2 + n_z^2$. Furthermore, the oscillatory behavior of atomic wavefunctions with increasing motional state indices ℓ, m implies that the overlap integral $K_{\ell m}$ becomes sharply peaked at $\ell \approx m$ as ℓ and m get large. The asymptotic behavior of $\alpha_{3,1}^{(3)}$ at large ℓ, m, n is therefore

$$\alpha_{3,1}^{(3)} \sim \int \frac{d^3 \ell \, d^3 m \, d^3 n}{(\ell^2 + m^2)(\ell^2 + n^2)} \delta(\ell - m) \delta(\ell - n) \sim \int \frac{d^3 \ell}{\ell^4} \sim \int_{\ell_{\min}}^{\infty} \frac{d\ell}{\ell^2} \sim \frac{1}{\ell_{\min}}, \quad (3.28)$$

where in the last integral we changed to spherical coordinates, and ℓ_{\min}^2 is the minimum value of ℓ^2 for which (i) the energy $E_\ell \sim \ell^2$, and (ii) the integral expression in (3.28) is a good approximation to the corresponding sum in (3.26). Note that the introduction of ℓ_{\min} amounts to neglecting a finite number of terms in the sum over ℓ, m, n in (3.26), whose contribution to the value of $\alpha_{3,1}^{(3)}$ is finite. Convergence of $\alpha_5^{(3)}$ is similarly guaranteed by the fact that the overlap integral K_n does not asymptotically grow with increasing n , such that $\alpha_5^{(3)}$ asymptotically behaves as

$$\alpha_5^{(3)} \sim \int \frac{d^3 n}{n^4} \sim \int_{n_{\min}}^{\infty} \frac{dn}{n^2} \sim \frac{1}{n_{\min}}, \quad (3.29)$$

where again n_{\min} is defined similarly to ℓ_{\min} .

The sum over loop diagrams in (3.23), meanwhile, contains a divergence that must be cancelled out by the counter-terms in (3.24). To leading order in the coupling constants, the renormalization condition in (3.16) implies that

$$\text{Diagram 1} = \text{Diagram 2}, \quad (3.30)$$

which can be expanded to find

$$K\tilde{G}_{r''s''}^{rs} = \sum_{\ell,m,r',s'} \frac{K_{\ell m}^2}{E_{\ell m}} G_{r's'}^{rs} G_{r''s''}^{r's'}. \quad (3.31)$$

In terms of ordinary coupling constants, the counter-term diagram in (3.24) is therefore

$$\begin{array}{c} \mu r \\ \diagdown \\ \otimes \\ \diagup \\ \nu s \end{array} \begin{array}{c} \mu r'' \\ \diagdown \\ \text{---} \\ \diagup \\ \rho t \end{array} \begin{array}{c} \nu s''' \\ \diagdown \\ \text{---} \\ \diagup \\ \rho t' \end{array} = \sum_{\ell,m,r',s'} \frac{K_{\ell m}^2 K_n^2}{K E_{\ell m} E_n} G_{r's'}^{rs} G_{r''s''}^{r's'} G_{s'''t}^{s''t} \hat{c}_{\mu r''}^\dagger \hat{c}_{\nu s'''}^\dagger \hat{c}_{\rho t'}^\dagger \hat{c}_{\rho t} \hat{c}_{\nu s} \hat{c}_{\mu r}. \quad (3.32)$$

Altogether, the contribution to the third-order three-body interaction Hamiltonian from loop diagrams of the form in (3.23) and counter-term diagrams of the form in (3.24) is

$$\begin{array}{c} \text{---} \\ \diagdown \\ \text{---} \\ \diagup \\ \text{---} \end{array} \begin{array}{c} \text{---} \\ \diagdown \\ \text{---} \\ \diagup \\ \text{---} \end{array} - \begin{array}{c} \text{---} \\ \diagdown \\ \otimes \\ \diagup \\ \text{---} \end{array} \begin{array}{c} \text{---} \\ \diagdown \\ \text{---} \\ \diagup \\ \text{---} \end{array} - \frac{1}{2} \begin{array}{c} \text{---} \\ \diagdown \\ \text{---} \\ \diagup \\ \text{---} \end{array} \begin{array}{c} \text{---} \\ \diagdown \\ \text{---} \\ \diagup \\ \text{---} \end{array} - \frac{1}{2} \begin{array}{c} \text{---} \\ \diagdown \\ \text{---} \\ \diagup \\ \text{---} \end{array} \begin{array}{c} \text{---} \\ \diagdown \\ \text{---} \\ \diagup \\ \text{---} \end{array} \\ = \left(\alpha_{3,2}^{(3)} - \frac{1}{2} \alpha_{4,3}^{(3)} - \frac{1}{2} \alpha_5^{(3)} \right) \mathcal{H}_{3,2}^{(3)}, \quad (3.33)$$

where

$$\alpha_{3,2}^{(3)} \equiv \sum_{\substack{\ell+m>0 \\ n>0}} \frac{K_{\ell m} K_n}{E_{\ell m} E_n} \left(K_n^{\ell m} - \frac{K_{\ell m} K_n}{K} \right), \quad \alpha_{4,3}^{(3)} \equiv K \sum_{m+n>0} \frac{K_{mn}^2}{E_{mn}^2}, \quad (3.34)$$

and

$$\mathcal{H}_{3,2}^{(3)} \equiv \sum_{|\{\mu,\nu,\rho\}|=3} G_{r's'}^{rs} G_{r''s''}^{r's'} G_{s'''t}^{s''t} \hat{c}_{\mu r''}^\dagger \hat{c}_{\nu s'''}^\dagger \hat{c}_{\rho t'}^\dagger \hat{c}_{\rho t} \hat{c}_{\nu s} \hat{c}_{\mu r}. \quad (3.35)$$

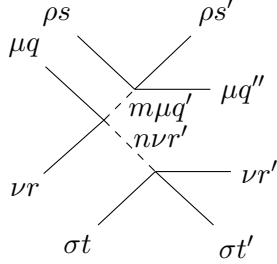
An equal contribution comes from the mirror images of these diagrams, such that the net third-order three-body interaction Hamiltonian is

$$H_3^{(3)} = \left(\alpha_{3,1}^{(3)} - \alpha_5^{(3)} \right) \mathcal{H}_{3,1}^{(3)} + \left(2\alpha_{3,2}^{(3)} - \alpha_{4,3}^{(3)} - \alpha_5^{(3)} \right) \mathcal{H}_{3,2}^{(3)}. \quad (3.36)$$

Note that the aforementioned divergence and its cancellation are buried in $\alpha_{3,2}^{(3)}$. Formally, this factor is calculated by imposing an ultraviolet cutoff Λ for the maximum values of motional state indices ℓ, m, n , and then taking the limit $\Lambda \rightarrow \infty$. This procedure ensures that there are no divergences in $\alpha_{3,2}^{(3)}$.

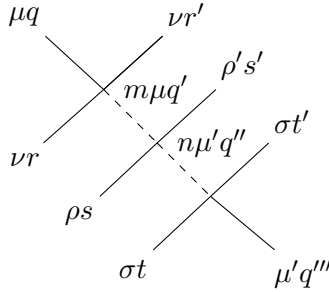
3.3.5 Effective four-body interactions at third order

At third order in the coupling constants, we have four-body terms of the form



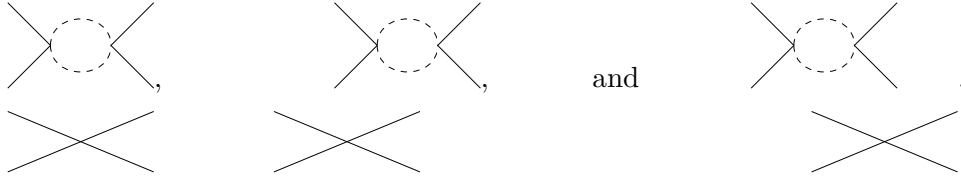
$$\propto K_{mn} K_m K_n G_{q'r'}^{qr} G_{q''s'}^{q's} G_{r''t'}^{r't} \hat{c}_{\mu q''}^\dagger \hat{c}_{\nu r''}^\dagger \hat{c}_{\rho s'}^\dagger \hat{c}_{\sigma t'}^\dagger \hat{c}_{\sigma t} \hat{c}_{\rho s} \hat{c}_{\nu r} \hat{c}_{\mu q} \quad (3.37)$$

and its mirror image, as well as



$$\propto K_m K_n^m K_n G_{q'r'}^{qr} G_{\mu'q''\rho's'}^{\mu q' \rho s} G_{q''t'}^{q''t} \hat{c}_{\mu'q''}^\dagger \hat{c}_{\nu r'}^\dagger \hat{c}_{\rho's'}^\dagger \hat{c}_{\sigma t'}^\dagger \hat{c}_{\sigma t} \hat{c}_{\rho s} \hat{c}_{\nu r} \hat{c}_{\mu q}. \quad (3.38)$$

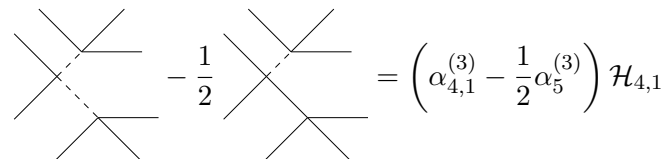
As we are computing the leading-order contribution to effective four-body interactions, there are no counter-terms contributions. In principle, there is now also the possibility to make the disconnected diagrams of the form



$$\quad \quad \quad \text{and} \quad \quad \quad . \quad (3.39)$$

As prescribed by $H_{\text{int}}^{(3)}$ in (3.14), however, the second and third of these diagrams pick up a factor of $-1/2$, so the sum over disconnected diagrams vanishes.

The contribution to the third-order four-body interaction Hamiltonian from diagrams of the form in (3.37) is



$$= \left(\alpha_{4,1}^{(3)} - \frac{1}{2} \alpha_5^{(3)} \right) \mathcal{H}_{4,1}, \quad (3.40)$$

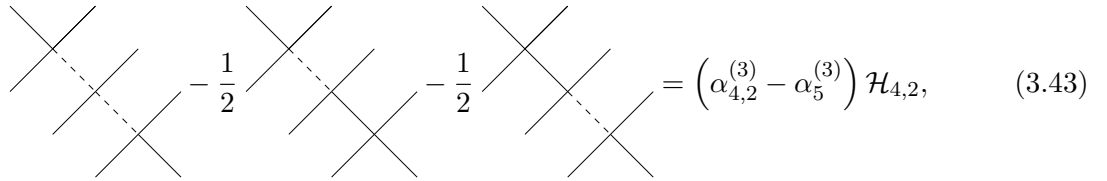
where

$$\alpha_{4,1}^{(3)} \equiv \sum_{\substack{m \geq 0 \\ n > 0}} \frac{K_{mn} K_m K_n}{E_{mn} E_n}, \quad (3.41)$$

and

$$\mathcal{H}_{4,1}^{(3)} \equiv \sum_{|\{\mu, \nu, \rho, \sigma\}|=4} G_{q'r'}^{qr} G_{q''s'}^{q's} G_{r''t'}^{r't} \hat{c}_{\mu q''}^\dagger \hat{c}_{\nu r''}^\dagger \hat{c}_{\rho s'}^\dagger \hat{c}_{\sigma t'}^\dagger \hat{c}_{\sigma t} \hat{c}_{\rho s} \hat{c}_{\nu r} \hat{c}_{\mu q}. \quad (3.42)$$

An equal contribution comes from the mirror images of these diagrams. The contribution from diagrams of the form in (3.38), meanwhile, is



$$-\frac{1}{2} \text{diag}_1 - \frac{1}{2} \text{diag}_2 - \frac{1}{2} \text{diag}_3 = \left(\alpha_{4,2}^{(3)} - \alpha_5^{(3)} \right) \mathcal{H}_{4,2}, \quad (3.43)$$

where

$$\alpha_{4,2}^{(3)} \equiv \sum_{m,n > 0} \frac{K_m K_n^m K_n}{E_m E_n}, \quad (3.44)$$

and

$$\mathcal{H}_{4,2}^{(3)} \equiv \sum_{|\{\mu, \nu, \rho, \sigma\}|=4} G_{q'r'}^{qr} G_{\mu'q''\rho's'}^{\mu q' \rho s} G_{q'''t'}^{q''t} \hat{c}_{\mu'q''}^\dagger \hat{c}_{\nu r'}^\dagger \hat{c}_{\rho's'}^\dagger \hat{c}_{\sigma t'}^\dagger \hat{c}_{\sigma t} \hat{c}_{\rho s} \hat{c}_{\nu r} \hat{c}_{\mu q}. \quad (3.45)$$

The net third-order four-body interaction Hamiltonian is therefore

$$H_4^{(3)} = \left(2\alpha_{4,1}^{(3)} - \alpha_5^{(3)} \right) \mathcal{H}_{4,1}^{(3)} + \left(\alpha_{4,2}^{(3)} - \alpha_5^{(3)} \right) \mathcal{H}_{4,2}^{(3)}. \quad (3.46)$$

3.4 Low-excitation Hamiltonians, eigenstates, and spectra

Current experiments with ultracold ^{87}Sr on a lattice can coherently address ground states and single orbital excitations of up to five atoms per lattice site [7]. Due to the $\text{SU}(N)$ symmetry of inter-atomic interactions, manifest in the fact that all coupling constants are independent of nuclear spin, a restriction of the M -body Hamiltonians $H_M = \sum_p H_M^{(p)}$ to the subspace of experimentally addressed states takes the form

$$H_M = \sum_{|\{\mu_j\}|=M} \left(U_{M,g} \hat{n}_{\mu_1,g} \hat{n}_{\mu_2,g} + U_{M,+} \hat{n}_{\mu_1,e} \hat{n}_{\mu_2,g} + U_{M,-} \hat{c}_{\mu_1,g}^\dagger \hat{c}_{\mu_2,e}^\dagger \hat{c}_{\mu_2,g} \hat{c}_{\mu_1,e} \right) \prod_{\alpha=3}^M \hat{n}_{\mu_\alpha,g}, \quad (3.47)$$

where $\hat{n}_{\mu s} \equiv \hat{c}_{\mu s}^\dagger \hat{c}_{\mu s}$ is a number operator, and the coefficients U_X can be determined from the coupling constants G_Y and prefactors $\alpha_Z^{(p)}$ of the effective M -body Hamiltonians derived in Section 3.3 (see Appendix 3.G). For a lattice with $N \geq M$ atoms occupying nuclear spins $\mathcal{N} = \{\mu_j\}$ for $j = 1, 2, \dots, N$, the M -body Hamiltonian H_M has a single ground state $|\mathcal{N}, 0\rangle$, and a singly-excited state $|\mathcal{N}, +\rangle$ which is fully symmetric in the orbital degrees of freedom; these states are

$$|\mathcal{N}, 0\rangle \equiv \left(\prod_{\mu \in \mathcal{N}} \hat{c}_{\mu, g}^\dagger \right) |\text{vacuum}\rangle, \quad |\mathcal{N}, +\rangle \equiv \frac{1}{\sqrt{N}} \sum_{\mu \in \mathcal{N}} \hat{c}_{\mu, e}^\dagger \hat{c}_{\mu, g} |\mathcal{N}, 0\rangle. \quad (3.48)$$

As these states are fully symmetric in their orbital degrees of freedom, they are anti-symmetric in their nuclear spin degrees of freedom, forming an $SU(N)$ singlet. Furthermore, the symmetric state is particularly interesting as its orbital degrees of freedom form an N -body entangled W state, which belongs to a special class of multi-partite entangled states that are robust against disposal or loss of particles. This state thus constitutes an important resource for many quantum information processing and quantum communication tasks [87].

In addition to the states in (3.48), the multi-body Hamiltonian H_M in (3.47) has an $(N - 1)$ -fold degenerate excited-state eigenspace which is asymmetric in the orbital degrees of freedom, spanned by the states

$$|\mathcal{N}, -, j\rangle \equiv \frac{1}{\sqrt{2}} \left(\hat{c}_{\mu_1, e}^\dagger \hat{c}_{\mu_1, g} - \hat{c}_{\mu_j, e}^\dagger \hat{c}_{\mu_j, g} \right) |\mathcal{N}, 0\rangle \quad (3.49)$$

for $j = 2, \dots, N$. If $N > 2$, the asymmetric states are not separable in their orbital and nuclear spin degrees of freedom. An important feature of the excited states in (3.48) and (3.49) is that they are entirely independent of M , which implies that the effect of multi-body interactions is simply to modify the many-body atomic energy spectra without affecting the energy eigenstates. The eigenvalues $E_{NX}^{(M)} = \langle \mathcal{N}X | H_M | \mathcal{N}X \rangle$ of H_M associated with each of the eigenstates in (3.48) and (3.49) are provided in table 3.1, both in terms of the coefficients U_{MX} of H_M as expressed in (3.47) and the M -body eigenvalues $E_{MX}^{(M)}$. Due to the $SU(N)$ symmetry of the multi-body Hamiltonian H_M , the eigenvalues $E_{NX}^{(M)}$ depend on the number of nuclear spins on a lattice site, N , but not on the actual nuclear spins $\mu \in \mathcal{N}$ which are occupied. The total N -body interaction energies E_{NX} are given in terms of the M -body eigenvalues $E_{NX}^{(M)}$ by $E_{NX} = \sum_M E_{NX}^{(M)}$.

Table 3.1: Low-excitation eigenvalues of M -body Hamiltonians H_M . Many-body energy eigenstates are labeled by the nuclear spins they occupy (i.e. \mathcal{N} with $N \equiv |\mathcal{N}|$) and whether they are in an orbital ground (0), singly-excited symmetric (+), or singly-excited asymmetric (-) state. The corresponding N -body eigenvalues $E_{NX}^{(M)}$ of H_M are given in terms of the coefficients U_{MX} as appearing in (3.47) (first three rows), in addition to the M -body eigenvalues $E_{MX}^{(M)}$ (last three rows).

Eigenstate	H_M eigenvalue ($M \leq N$)
$ \mathcal{N}, 0\rangle$	$M! \binom{N}{M} U_{M,g}$
$ \mathcal{N}, +\rangle$	$M! \binom{N-1}{M} U_{M,g} + (M-1)! \binom{N-1}{M-1} (U_{M,+} + U_{M,-})$
$ \mathcal{N}, -\rangle$	$M! \binom{N-1}{M} U_{M,g} + (M-1)! \binom{N-1}{M-1} U_{M,+} - (M-2)! \binom{N-2}{M-2} U_{M,-}$
$ \mathcal{N}, 0\rangle$	$\binom{N}{M} E_{M,0}^{(M)}$
$ \mathcal{N}, +\rangle$	$\binom{N-1}{M} E_{M,0}^{(M)} + \binom{N-1}{M-1} E_{M,+}^{(M)}$
$ \mathcal{N}, -\rangle$	$\binom{N-1}{M} E_{M,0}^{(M)} + M^{-1} \left[\binom{N-1}{M-1} - \binom{N-2}{M-2} \right] E_{M,+}^{(M)} + \left[(1 - M^{-1}) \binom{N-1}{M-1} + M^{-1} \binom{N-2}{M-2} \right] E_{M,-}^{(M)}$

3.4.1 Many-body state spectroscopy

Spectroscopic interrogation is a powerful means to probe the internal structure and dynamics of a system under examination. Consequently, we consider Rabi spectroscopy of the low-lying energy eigenstates in multiply-occupied lattice sites. If we interrogate a lattice site by a laser red-detuned by Δ from the single-atom orbital state excitation energy, we realize the Hamiltonian

$$H_{\text{Rabi}} = \sum_X E_X \mathcal{P}_X + \sum_\mu \left(\Delta T_\mu^z + \Omega_\mu T_\mu^x \right), \quad (3.50)$$

where E_X is an eigenvalue of the effective interaction Hamiltonian $H_{\text{int}}^{\text{eff}}$, \mathcal{P}_X is a projector onto the corresponding eigenspace, and

$$T_\mu^z \equiv \frac{1}{2} \left(\hat{c}_{\mu,e}^\dagger \hat{c}_{\mu,e} - \hat{c}_{\mu,g}^\dagger \hat{c}_{\mu,g} \right), \quad T_\mu^x \equiv \frac{1}{2} \left(\hat{c}_{\mu,e}^\dagger \hat{c}_{\mu,g} + \hat{c}_{\mu,g}^\dagger \hat{c}_{\mu,e} \right), \quad (3.51)$$

are single-atom pseudospin operators. The Rabi frequency Ω_μ is proportional to the Clebsch-Gordan coefficient $\langle I, \mu; 1, 0 | I, \mu \rangle \propto \mu$ for a photon-induced nuclear-spin-conserving orbital state transition of an atom with nuclear spin μ . We therefore define the ‘‘bare’’ Rabi frequency $\Omega_0 \equiv \Omega_\mu / \mu$ to explicitly factor out dependence on nuclear spins μ .

Consider now a single lattice site in the orbital ground state $|\mathcal{N}, 0\rangle$ with nuclear spins $\mathcal{N} \equiv \{\mu_j\}$ for $j = 1, 2, \dots, N$. If we red-detune the interrogation laser by δ from a many-body orbital state excitation energy, i.e. set $\Delta = \Delta_{NX} - \delta$ for $\Delta_{NX} \equiv E_{NX} - E_{N,0}$ and $X \in \{+, -\}$, then in the subspace of the target states $\{|\mathcal{N}, 0\rangle, |\mathcal{N}X\rangle\}$ the Hamiltonian in (3.50) becomes

$$H_{NX} = \delta S_{NX}^z + \Omega_{NX} S_{NX}^x, \quad (3.52)$$

where

$$S_{NX}^z \equiv \frac{1}{2} (|\mathcal{N}X\rangle\langle\mathcal{N}X| - |\mathcal{N}, 0\rangle\langle\mathcal{N}, 0|), \quad (3.53)$$

$$S_{NX}^x \equiv \frac{1}{2} (|\mathcal{N}X\rangle\langle\mathcal{N}, 0| + |\mathcal{N}, 0\rangle\langle\mathcal{N}X|), \quad (3.54)$$

are many-body pseudospin operators, and the Rabi frequencies Ω_{NX} are determined by

$$H_{\text{Rabi}} |\mathcal{N}, 0\rangle = \frac{1}{2} \Omega_0 \sum_\mu \mu \hat{c}_{\mu,e}^\dagger \hat{c}_{\mu,g} |\mathcal{N}, 0\rangle = \frac{1}{2} \Omega_{\mathcal{N},+} |\mathcal{N}, +\rangle + \frac{1}{2} \Omega_{\mathcal{N},-} |\mathcal{N}, -\rangle. \quad (3.55)$$

While the symmetric excited state $|\mathcal{N}, +\rangle$ is given in (3.48), at this point we have not explicitly solved for the asymmetric excited state $|\mathcal{N}, -\rangle$. The asymmetric state is implicitly defined by (3.55), and lies somewhere in the span of the $N - 1$ asymmetric states given in (3.49). Determining the symmetric-state Rabi frequency $\Omega_{\mathcal{N},+}$ is simply a matter of projecting the expression in (3.55) onto $|\mathcal{N}, +\rangle$, which yields

$$\Omega_{\mathcal{N},+} = \langle \mathcal{N}, + | \Omega_0 \sum_{\mu} \mu \hat{c}_{\mu,e}^{\dagger} \hat{c}_{\mu,g} | \mathcal{N}, 0 \rangle = \Omega_0 \sum_{\mu \in \mathcal{N}} \frac{\mu}{\sqrt{N}} = \Omega_0 \sqrt{N} \bar{\mu}_{\mathcal{N}}, \quad (3.56)$$

where $\bar{\mu}_{\mathcal{N}} \equiv \sum_{\mu \in \mathcal{N}} \mu / N$ is the average nuclear spin $\mu \in \mathcal{N}$. In order to determine the asymmetric-state Rabi frequency $\Omega_{\mathcal{N},-}$, we rearrange (3.55) to find

$$\Omega_{\mathcal{N},-} |\mathcal{N}, -\rangle = \Omega_0 \sum_{\mu} \mu \hat{c}_{\mu,e}^{\dagger} \hat{c}_{\mu,g} | \mathcal{N}, 0 \rangle - \Omega_{\mathcal{N},+} |\mathcal{N}, +\rangle = \Omega_0 \sum_{\mu \in \mathcal{N}} (\mu - \bar{\mu}_{\mathcal{N}}) \hat{c}_{\mu,e}^{\dagger} \hat{c}_{\mu,g} | \mathcal{N}, 0 \rangle. \quad (3.57)$$

Denoting the standard deviation of nuclear spins $\mu \in \mathcal{N}$ by $\sigma_{\mathcal{N}}$, normalization of $|\mathcal{N}, -\rangle$ thus determines the asymmetric-state Rabi frequency

$$\Omega_{\mathcal{N},-} = \Omega_0 \left[\sum_{\mu \in \mathcal{N}} (\mu - \bar{\mu}_{\mathcal{N}})^2 \right]^{1/2} = \Omega_0 \sqrt{N} \sigma_{\mathcal{N}}, \quad (3.58)$$

which in turn implies that the asymmetric excited state $|\mathcal{N}, -\rangle$ is

$$|\mathcal{N}, -\rangle = \frac{1}{\sqrt{N}} \sum_{\mu \in \mathcal{N}} \left(\frac{\mu - \bar{\mu}_{\mathcal{N}}}{\sigma_{\mathcal{N}}} \right) \hat{c}_{\mu,e}^{\dagger} \hat{c}_{\mu,g} | \mathcal{N}, 0 \rangle. \quad (3.59)$$

Figure 3.2 shows multiplicities of the magnitudes of reduced Rabi frequencies $\omega_{\mathcal{N}X} \equiv \Omega_{\mathcal{N}X} / \Omega_0 \sqrt{N}$ in a lattice with a uniform mixture of nuclear spins with $I = 9/2$ for single-site occupation numbers N which are achievable in current ^{87}Sr experiments [7]. On average, asymmetric-state Rabi frequencies are greater in magnitude, which becomes more pronounced for larger single-site occupation numbers.

3.4.2 Experimental signatures and comparison

We now consider samples of ^{87}Sr atoms in a uniform mixture of nuclear spins $\mu \in \{-I, -I + 1, \dots, I\}$ prepared in motional ground states of a rectangular lattice with depths $\mathcal{U} = (\mathcal{U}_x, \mathcal{U}_y, \mathcal{U}_z) =$

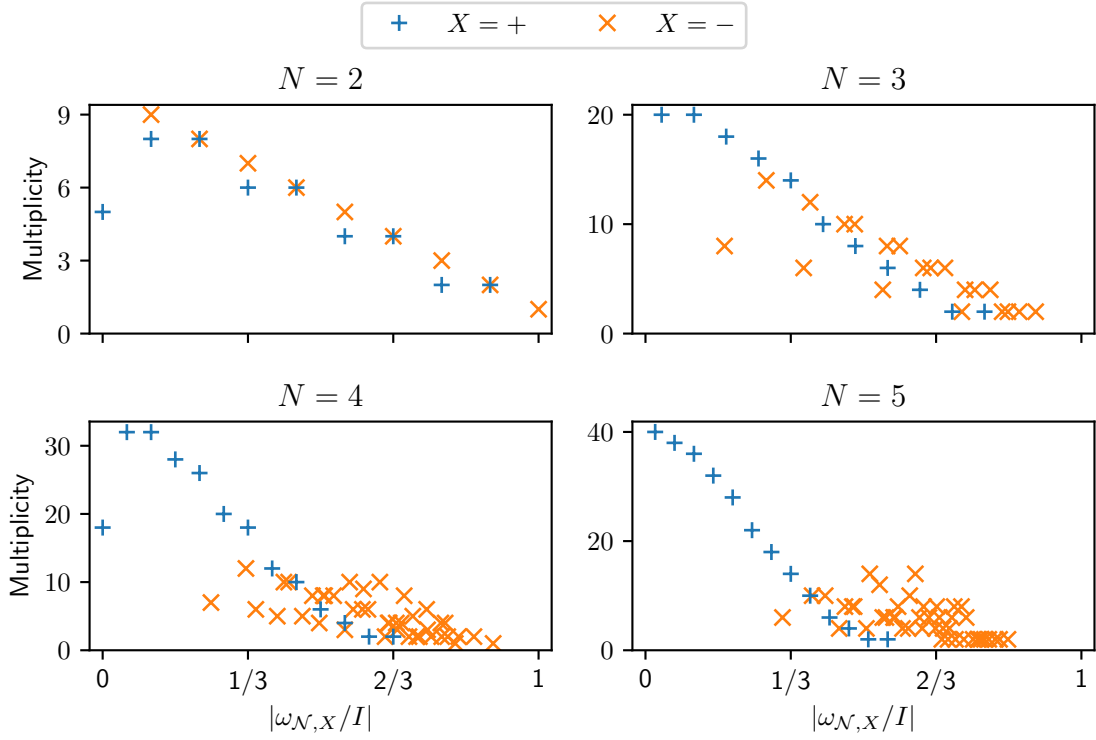


Figure 3.2: Multiplicities of the magnitudes of reduced Rabi frequencies $\omega_{\mathcal{N}X} \equiv \Omega_{\mathcal{N}X}/\Omega_0\sqrt{N}$ in a lattice with a uniform mixture of nuclear spins with $I = 9/2$ and single-site occupation numbers N which are achievable in current ^{87}Sr experiments.

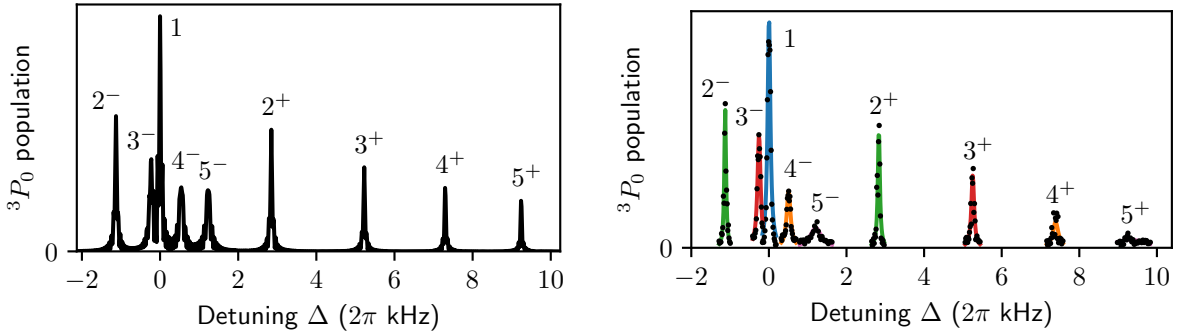


Figure 3.3: Population (in arbitrary units) of the excited 3P_0 orbital state of ${}^{87}\text{Sr}$ atoms in a uniform mixture of nuclear spins. Atoms are prepared in the ground state of a lattice with depth $\mathcal{U} = 54E_R$, where $E_R \approx 3.5 \times 2\pi$ kHz is the lattice photon recoil energy of the atoms, and interrogated by a laser with Rabi frequency $\Omega_I = 50 \times 2\pi$ Hz for a time $t = \pi/\Omega_I$. **(Left)** Populations predicted by the low-energy effective theory (with s -wave scattering parameters retrieved from Ref. [53]), averaged over all nuclear spin combinations of $N \in \{1, \dots, 5\}$ atoms per lattice site for a fixed total atom number. **(Right)** Experimental measurements of 3P_0 populations retrieved from Ref. [7], with Lorentzian fits to each peak as a visual guide. Resonance peaks are identified by the many-body orbital states which are excited at the peak.

$(41, 55, 69) E_R$, where $E_R \approx 3.5 \times 2\pi$ kHz is the lattice photon recoil energy of the atoms. Such samples can be prepared in experiments which can vary the single-site occupation number N , and which can control for the total number of atoms that are addressed by an external interrogation laser. Figure 3.3 shows the population of the excited 3P_0 orbital state when these atoms are interrogated for a time $t = \pi/\Omega_I$ by a laser with Rabi frequency $\Omega_I = 50 \times 2\pi$ Hz (i.e. for individual atoms with nuclear spin $\mu = I$) and detuning Δ from the single-atom $^1S_0 \rightarrow ^3P_0$ orbital excitation energy. The 3P_0 population peaks when the laser detuning Δ is equal to the many-body excitation energy $\Delta_{NX} \equiv E_{NX} - E_{N,0}$ for $X \in \{+, -\}$, as this is precisely when the on-resonance condition $\delta = 0$ is satisfied in the many-body Rabi Hamiltonian H_{NX} in (3.52). Due to experimental uncertainties which vary with single-site occupation number N , the heights of experimental peaks in Figure 3.3 are not well-calibrated between different values of N . Nonetheless, Figure 3.3 exhibits signatures of larger asymmetric-state Rabi frequencies than symmetric-state ones in the form of higher asymmetric-state peaks for fixed N .

Identifying peaks in excitation spectra such as in Figure 3.3 constitutes a measurement of many-body excitation energies, which was performed in Ref. [7] to detect signatures of effective multi-body interactions. Figure 3.4 shows a comparison between (i) experimental measurements of the many-body excitation energies Δ_{NX} for all $(N, X) \in \{3, 4, 5\} \times \{+, -\}$ at various mean lattice depths \mathcal{U} , and (ii) the corresponding values of Δ_{NX} predicted by the low-energy effective theory at different orders in the coupling constants. A known source of error in our effective theory comes from neglecting the inter-site matrix elements of all Hamiltonians. This error is discussed in Appendix 3.E, and leads to theoretical uncertainties represented by error bars on the $\mathcal{O}(G^3)$ theory in Figure 3.4. A summary of Figure 3.4 is provided in Figure 3.5. We note that many-body interaction energy shifts are smaller for asymmetric ($-$) states than symmetric ($+$) ones due to the competition between contributions of opposite sign in the asymmetric case (see rows 2 and 3 of table 3.1, where as a consequence of positive scattering lengths in the case of ^{87}Sr , all U_{MX} for fixed M have the same sign). This competition is a many-body analogue of the two-body case with a competition between direct and exchange terms in the interaction energies of singly-excited states.

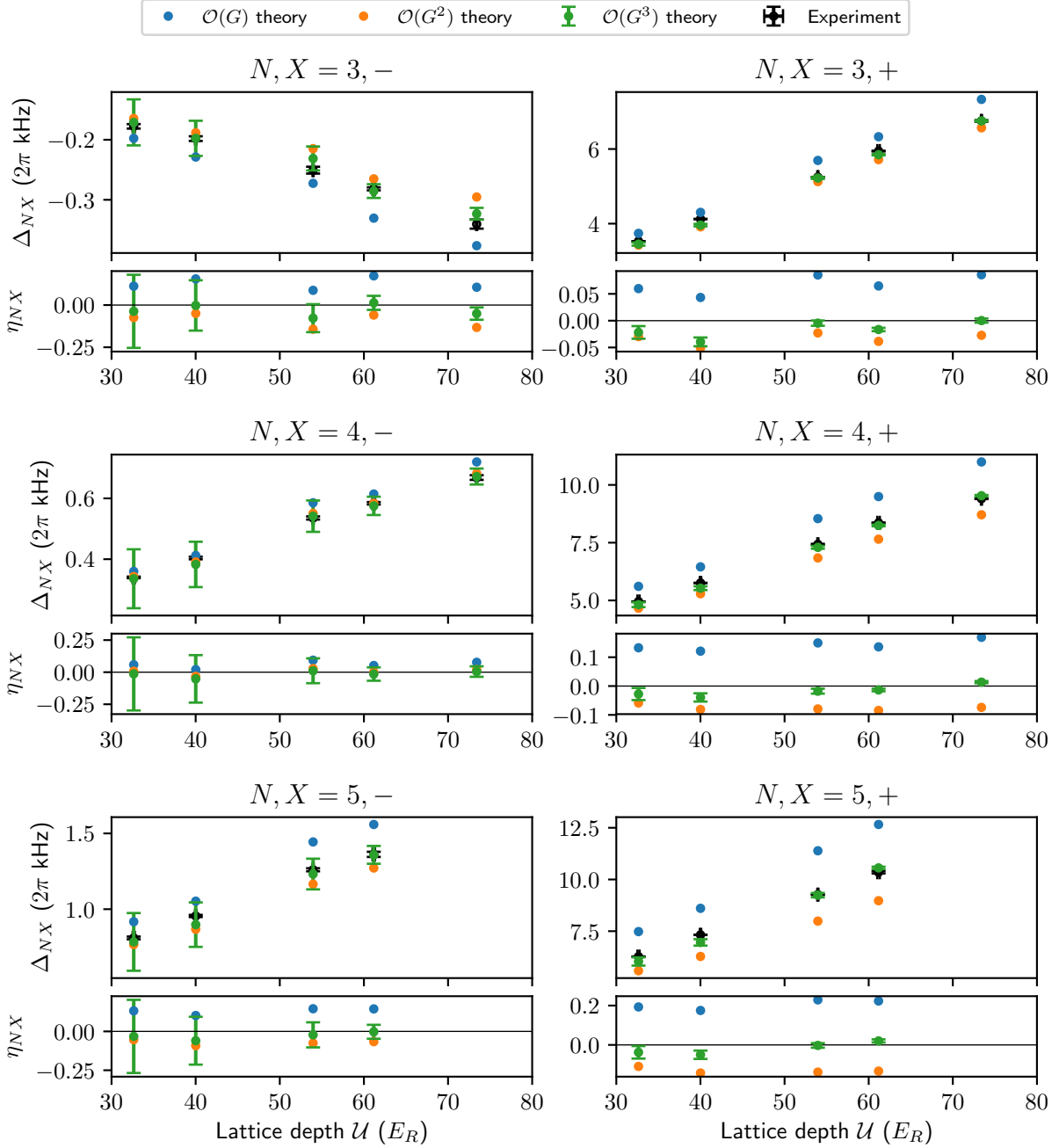


Figure 3.4: Multi-body excitation energies of ultracold ^{87}Sr atoms at various lattice depths. The top plot in each sub-figure with fixed N, X shows the excitation energies $\Delta_{NX} \equiv E_{NX} - E_{N,0}$ measured experimentally in Ref. [7] and those predicted by the low-energy effective theory at different orders in the coupling constants, when applicable both with and without four-body contributions. The bottom plot in each sub-figure shows the relative error $\eta_{NX} \equiv \Delta_{NX}^{\text{theory}} / \Delta_{NX}^{\text{experiment}} - 1$. Error bars represent experimental error or conservatively estimated theoretical uncertainties from nearest-neighbor hopping of virtual states in the low-energy effective theory (see Appendix 3.E).

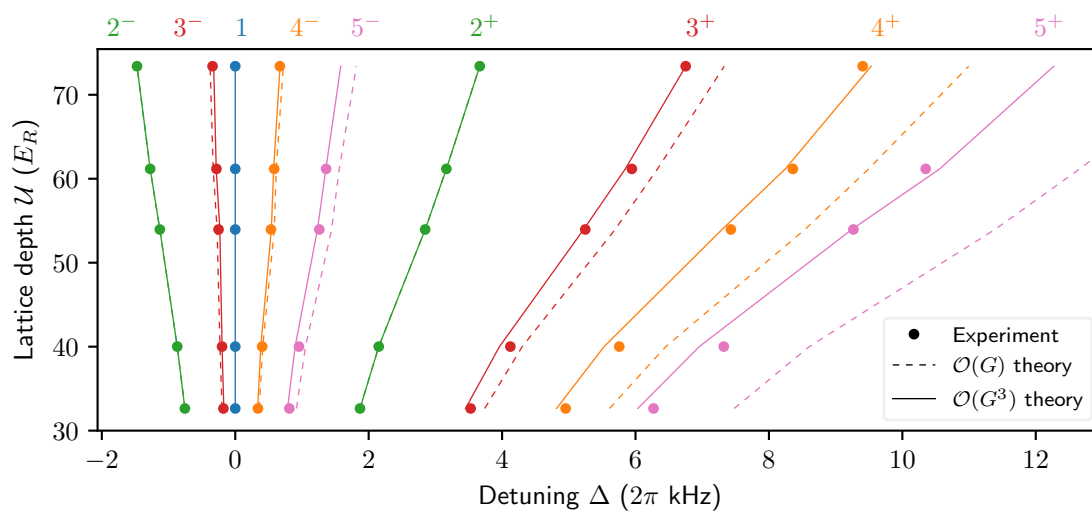


Figure 3.5: Summary of the many-body excitation spectra in Figure 3.4, retrieved from Ref. [7].

The results in Figures 3.4 and 3.5 highlight a few important points about ultracold, high-density ^{87}Sr experiments and our low-energy effective theory. First, these experiments exhibit clear signatures of multi-body interactions, as evidenced by a stark disagreement between the observed many-body excitation energies Δ_{NX} and those that are predicted by the two-body $\mathcal{O}(G)$ theory. Multi-body interactions are thus crucial for understanding these high-density experiments in the context of a single-band Hubbard model, which naturally arises in the zero-temperature limit when all atoms occupy their motional ground state. Second, the inter-atomic interactions in these experiments are strong enough to require going beyond leading order for the description of multi-body interactions in the low-energy effective theory. The formally small quantities organizing our perturbation theory are two-body ground-state interaction energies (proportional to the couplings G_X) divided by the spectral gap of the single-atom Hamiltonian H_0 . These reduced (dimensionless) interaction energies vary from $\sim 0.05 - 0.15$ in the parameter regimes of the ^{87}Sr experiments considered here (see Appendix 3.F). As experiments begin to operate at higher atom densities with amplified interaction effects, reliably predicting interaction energies may require going to yet higher orders in perturbation theory. Due to a combinatorial explosion of the number of diagrams which appear at increasing orders in the effective theory, however, we need more systematic methods to compute effective multi-body Hamiltonians at fourth order. In any case, we are agnostic as to whether such a calculation would provide better agreement between experiment and theory without first performing a detailed analysis of systematic errors.

3.4.3 Orbital-state dynamics of a nuclear spin mixture

In addition to spectral measurements of many-body interaction energies, we consider the dynamics of multiply-occupied lattice sites during spectroscopic interrogation. While these dynamics do not provide information about the nature or origin of effective multi-body interactions, they provide tools and intuition for addressing the low-lying orbital excitations which are readily accessible in an experimental setting. If we initialize all atoms in the N -body ground state with an incoherent

mixture of all nuclear spins, then we prepare the mixed state $\rho_{N,0} = \mathcal{P}_{N,0}/\text{tr } \mathcal{P}_{N,0}$, where

$$\mathcal{P}_{NX} \equiv \sum_{|\mathcal{N}|=N} |\mathcal{N}X\rangle\langle\mathcal{N}X| \quad (3.60)$$

is a projector onto the space of the N -body orbital states $|\mathcal{N}X\rangle$. Interrogating the atoms for a time t by a laser resonant with the excitation energy $\Delta_{N\pm}$ then gives us the state

$$\rho_N^{(\pm)}(t) = \frac{1}{\text{tr } \mathcal{P}_{N,0}} \sum_{|\mathcal{N}|=N} \exp(-it\Omega_{\mathcal{N}\pm} S_{\mathcal{N}\pm}^x) |\mathcal{N}, 0\rangle\langle\mathcal{N}, 0| \exp(it\Omega_{\mathcal{N}\pm} S_{\mathcal{N}\pm}^x), \quad (3.61)$$

where the Rabi frequencies $\Omega_{\mathcal{N},+}, \Omega_{\mathcal{N},-}$ and pseudo-spin operators $S_{\mathcal{N}\pm}^x$ are respectively given in (3.56), (3.58), and (3.54). Denoting the eigenstates of $S_{\mathcal{N}\pm}^x$ by

$$|\mathcal{N}, \mathcal{S}_{\pm}\rangle \equiv \frac{1}{\sqrt{2}} (|\mathcal{N}, 0\rangle + |\mathcal{N}\pm\rangle), \quad |\mathcal{N}, \mathcal{A}_{\pm}\rangle \equiv \frac{1}{\sqrt{2}} (|\mathcal{N}, 0\rangle - |\mathcal{N}\pm\rangle), \quad (3.62)$$

and defining the identity operator projected to the relevant subspace,

$$\mathbb{1}_{\mathcal{N}\pm} \equiv |\mathcal{N}, 0\rangle\langle\mathcal{N}, 0| + |\mathcal{N}\pm\rangle\langle\mathcal{N}\pm| = |\mathcal{N}, \mathcal{S}_{\pm}\rangle\langle\mathcal{N}, \mathcal{S}_{\pm}| + |\mathcal{N}, \mathcal{A}_{\pm}\rangle\langle\mathcal{N}, \mathcal{A}_{\pm}|, \quad (3.63)$$

we can write the state $\rho_N^{(\pm)}(t)$ and excited-state projectors $\mathcal{P}_{N\pm}$ in the form

$$\rho_N^{(\pm)}(t) = \frac{1}{\text{tr } \mathcal{P}_{N,0}} \sum_{|\mathcal{N}|=N} \frac{1}{2} \left[\mathbb{1}_{\mathcal{N}\pm} + e^{i2t\Omega_{\mathcal{N}\pm}} |\mathcal{N}, \mathcal{S}_{\pm}\rangle\langle\mathcal{N}, \mathcal{A}_{\pm}| + e^{-i2t\Omega_{\mathcal{N}\pm}} |\mathcal{N}, \mathcal{A}_{\pm}\rangle\langle\mathcal{N}, \mathcal{S}_{\pm}| \right], \quad (3.64)$$

and

$$\mathcal{P}_{N\pm} = \sum_{|\mathcal{N}|=N} \frac{1}{2} \left[\mathbb{1}_{\mathcal{N}\pm} - |\mathcal{N}, \mathcal{S}_{\pm}\rangle\langle\mathcal{N}, \mathcal{A}_{\pm}| - |\mathcal{N}, \mathcal{A}_{\pm}\rangle\langle\mathcal{N}, \mathcal{S}_{\pm}| \right], \quad (3.65)$$

from which it follows that the net excited-state population at time t is

$$\langle \mathcal{P}_{N\pm}(t) \rangle \equiv \text{tr} \left[\rho_N^{(\pm)}(t) \mathcal{P}_{N\pm} \right] = \frac{1}{2} - \frac{1}{2} \langle \cos(2t\Omega_{\mathcal{N}\pm}) \rangle_{|\mathcal{N}|=N}, \quad (3.66)$$

where $\langle X \rangle_{|\mathcal{N}|=N} \equiv \sum_{|\mathcal{N}|=N} X / \text{tr } \mathcal{P}_{N,0}$ is an average of X over all choices of N distinct nuclear spins.

Figure 3.6 shows the excited-state population $\langle \mathcal{P}_{N\pm}(t) \rangle$ for several occupation numbers N . With the exception of $N = 2$, the asymmetric-state populations generally have an initial short period of growth before falling back to $\langle \mathcal{P}_{N,-} \rangle \approx 1/2$. This behavior can be understood by the fact that for fixed $N > 2$, any pair of Rabi frequencies $\Omega_{\mathcal{N}_1,-}, \Omega_{\mathcal{N}_2,-}$ with $\Omega_{\mathcal{N}_1,-} \neq \Omega_{\mathcal{N}_2,-}$ are

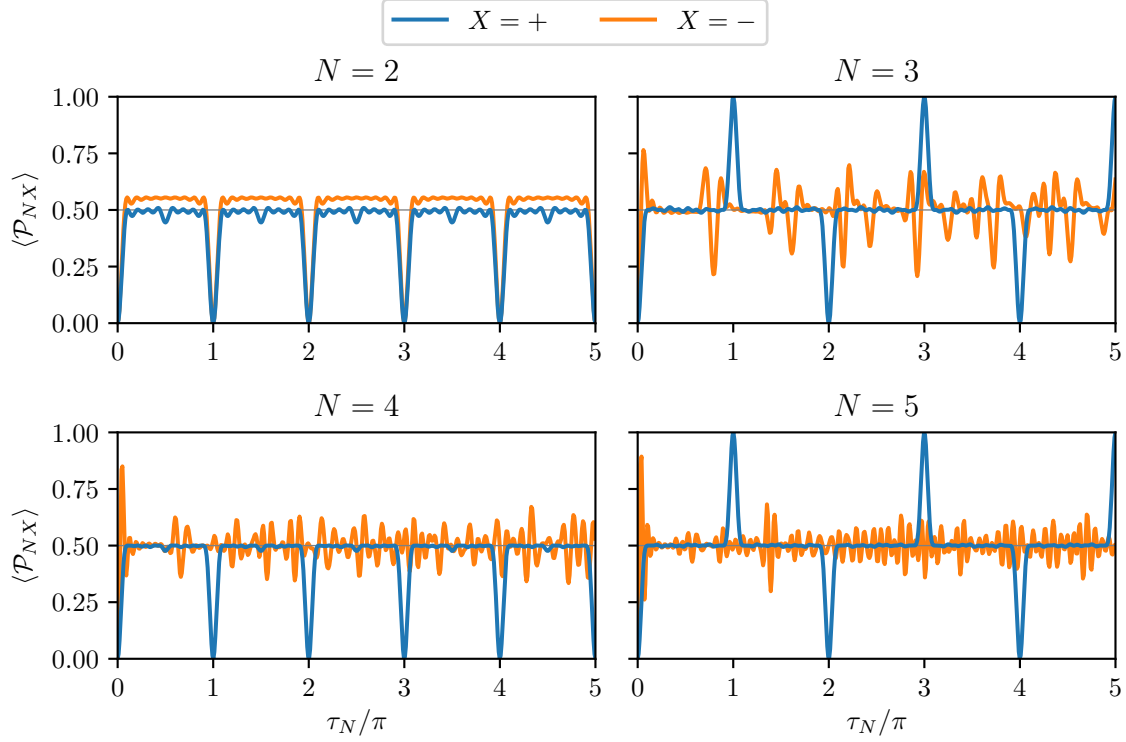


Figure 3.6: Net population of the N -body orbital excited states $\{|\mathcal{N}\pm\rangle\}$ after interrogation of an initial mixed state $\rho_{N,0} = \mathcal{P}_{N,0}/\text{tr } \mathcal{P}_{N,0}$ for a reduced time $\tau_N \equiv t\Omega_0/\sqrt{N}$ (i.e. with real time t) by a laser with bare Rabi frequency Ω_0 which is resonant with the N -body excitation energy Δ_{NX} . Here \mathcal{P}_{NX} , defined in (3.60), is a projector onto the space of the N -body orbital states $|\mathcal{N}X\rangle$.

mutually incommensurate, which implies that at times t with $\min_{|\mathcal{N}|=N} \{2t\Omega_{\mathcal{N},-}\} \gtrsim 1$ the averaging in (3.66) effectively becomes a pseudo-random sampling average of $\cos x$ over values of x , so $\langle \cos(2t\Omega_{\mathcal{N},-}) \rangle_{|\mathcal{N}|=N} \approx 0$. When $N = 2$, the asymmetric-state Rabi frequencies essentially take on the same values as the symmetric-state ones (see Figure 3.2); the behavior of asymmetric-state population dynamics for $N = 2$ can therefore be understood by the following discussion of symmetric-state population dynamics.

To understand the periodic collapse and revival of symmetric-state populations in Figure 3.6, we observe from (3.56) that the symmetric-state phases in (3.64) and (3.66) take the form

$$2t\Omega_{\mathcal{N},+} = \tau_N \sum_{\mu \in \mathcal{N}} 2\mu \quad \text{with} \quad \tau_N \equiv \frac{t\Omega_0}{\sqrt{N}}, \quad (3.67)$$

where for fermionic atoms with half-integer nuclear spin, 2μ is always an odd integer, which implies that the sum in (3.67) is an integer with the same parity (i.e. even/odd) as the occupation number N (i.e. the number of elements in \mathcal{N}). At reduced times $\tau_N = n\pi$ with integer n , therefore, if the occupation number N is even then all phases $2t\Omega_{\mathcal{N},+}$ are integer multiples of 2π , which leads to a collapse of the excited-state populations as $\rho_N^{(\pm)}(t) \Big|_{\tau_N=n\pi} = \rho_N^{(\pm)}(0) = \rho_{N,0}$. If the occupation N is odd, meanwhile, then the phases $2t\Omega_{\mathcal{N},+}$ are all odd (even) integer multiples of π for odd (even) n . This alignment of phases implies a complete population transfer to the excited state $\rho_{N,-} \equiv \mathcal{P}_{N,-} / \text{tr} \mathcal{P}_{N,-}$ for odd n , and a collapse back to the orbital ground state $\rho_{N,0}$ for even n , precisely as observed in Figure 3.6.

3.5 Summary and outlook

Current 3-D optical lattice experiments with fermionic AEAs are capable of operating in the low-temperature, high-density, strongly-interacting limit where inter-atomic interactions set the dominant energy scale governing system dynamics. For AEAs with total nuclear spin I and $N = 2I + 1$ nuclear spin states, these interactions exhibit an exotic $SU(N)$ symmetry which is of great interest for near-term quantum simulations of $SU(N)$ spin models and lattice field theories. Working in the deep-lattice limit and the experimental regime of at most one atom occupying

each nuclear spin state on any lattice site, we have derived a low-energy effective theory of these atoms. Our theory exhibits emergent multi-body interactions that inherit the $SU(N)$ symmetry of the bare two-body interactions. Considering a restriction of our theory to the subspace of at most one orbital excitation per lattice site, we found that the $SU(N)$ symmetry of all M -body Hamiltonians allowed us to express them in a simple form, and to fully characterize their eigenstates and spectra. Capitalizing on the extreme precision of state-of-the-art clock spectroscopy, we have tested spectral predictions of our theory against direct experimental measurements of the many-body ^{87}Sr excitation spectrum. This comparison shows good agreement between theory and experiment, clearly demonstrating the need to consider multi-body effects for understanding the low-energy physics of high density AEA samples on a 3-D lattice. Finally, we analyzed the many-body orbital-state dynamics of multiply-occupied lattice sites prepared in a nuclear spin mixture and interrogated via Rabi spectroscopy. This analysis is useful for future experimental probes of many-body state structures, as well as for the preparation of long-lived states with multipartite entanglement (i.e. $|\mathcal{N}\pm\rangle$) which may be used as a resource to perform quantum information processing tasks.

Despite the nominal success of our low-energy effective theory in reproducing experimental observations, there remains room for improvement in the form of controlled, systematic treatment of higher-order and tunneling processes. Nonetheless, our work makes a major step towards the experimental investigation of multi-body $SU(N)$ physics, providing the necessary framework for future studies going beyond the deep-lattice limit to realize multi-body super-exchange dynamics and orbital $SU(N)$ quantum magnetism with AEAs.

Acknowledgements

We acknowledge helpful discussions with R. B. Hutson, G. E. Marti, S. L. Campbell, J. Ye, P. Julienne, J. P. D’Incao, C. Kennedy, and L. Radzihovsky; and in particular close correspondence and technical contributions from A. Goban. This work is supported by the Air Force Office of Scientific Research (AFOSR) grant FA9550-18-1-0319; the AFOSR Multidisciplinary University

Research Initiative (MURI) grant; the Defense Advanced Research Projects Agency (DARPA) and Army Research Office (ARO) grant W911NF-16-1-0576; the National Science Foundation (NSF) grant PHY-1820885; JILA-NSF grant PFC-173400; and the National Institute of Standards and Technology (NIST).

3.A Derivation of the effective Hamiltonian expansion

Suppose we have a Hamiltonian H_0 on a Hilbert space $\mathcal{H} = \mathcal{G}_0 \oplus \mathcal{E}_0$ for a zero-energy manifold \mathcal{G}_0 decoupled from a positive-energy manifold \mathcal{E}_0 , and that we perturb H_0 by an operator V which weakly couples \mathcal{G}_0 and \mathcal{E}_0 . For all $|\psi_g\rangle \in \mathcal{G}_0$ and $|\phi_e\rangle, |\chi_e\rangle \in \mathcal{E}_0$, we have $\langle\psi_g|H_0|\psi_g\rangle = 0$, $\langle\phi_e|H_0|\psi_g\rangle = 0$, and $|\langle\phi_e|V|\psi_g\rangle| \ll \langle\chi_e|H_0|\chi_e\rangle$. The net Hamiltonian $H = H_0 + V$ will naturally admit a decomposition of the Hilbert space as $\mathcal{H} = \mathcal{G} \oplus \mathcal{E}$ for a subspace \mathcal{G} which is spanned by the low-energy eigenstates of H and has the same dimension as \mathcal{G}_0 , i.e. $|\mathcal{G}| = |\mathcal{G}_0|$.

We can perform a canonical transformation between \mathcal{G} and \mathcal{G}_0 which yields an *effective Hamiltonian* H_{eff} on \mathcal{G}_0 that reproduces the spectrum of H on \mathcal{G} [80]. Given an eigenbasis $\{|\alpha_0\rangle\}$ for H_0 on \mathcal{G}_0 and $\{|\alpha\rangle\}$ for H on \mathcal{G} , this transformation is implemented by a unitary U for which $|\alpha_0\rangle = U|\alpha\rangle$ and $U \rightarrow \mathbb{1}$ as $\|V\| \rightarrow 0$. The effective Hamiltonian is then simply

$$H_{\text{eff}} = U H U^\dagger. \quad (3.68)$$

The prescription in (3.68) for constructing an effective Hamiltonian is commonly known as a Schieffer-Wolff transformation [81]. Unitaries U which follow this prescription are not unique, and different choices of U amount to different realizations of the Schieffer-Wolff transformation. In Ref. [80], the authors construct the unique operator S which generates a *direct* or *minimal* rotation $U_{\text{min}} = e^S$ between \mathcal{G} and \mathcal{G}_0 , and use this construction to expand (3.68) as a perturbative series in V . The rotation U_{min} is minimal in the sense that it minimizes the distance of candidate unitaries U from the identity $\mathbb{1}$ with respect to the Euclidian operator norm^b $\|X\|_{\text{E}} \equiv \sqrt{\text{tr}(X^\dagger X)}$. This rotation is determined uniquely by enforcing (i) that the generator S is strictly block-off-diagonal

^b The Euclidean operator norm is also known as the $L_{2,2}$, Hilbert-Schmidt, or Frobenius norm.

with respect to \mathcal{G}_0 and \mathcal{E}_0 , (ii) that the norm $\|S\|_{\mathcal{E}} < \pi/2$, and (iii) that the block-off-diagonal parts of (3.68) are zero.

To summarize the solution in Ref. [80], the effective Hamiltonian H_{eff} induced by a direct rotation can be expanded as

$$H_{\text{eff}} = \sum_{p \geq 0} H_{\text{eff}}^{(p)}, \quad (3.69)$$

where $H_{\text{eff}}^{(p)}$ is order p in V . Letting \mathcal{P}_0 denote the projector onto \mathcal{G}_0 , $\mathcal{Q}_0 \equiv \mathbf{1} - \mathcal{P}_0$ denote the projector onto \mathcal{E}_0 , and X denote any operator on \mathcal{H} , we define the superoperators

$$\mathcal{D}X \equiv \mathcal{P}_0 X \mathcal{P}_0 + \mathcal{Q}_0 X \mathcal{Q}_0, \quad \mathcal{O}X \equiv \mathcal{P}_0 X \mathcal{Q}_0 + \mathcal{Q}_0 X \mathcal{P}_0, \quad (3.70)$$

which select out the diagonal (\mathcal{D}) and off-diagonal (\mathcal{O}) parts of X with respect to \mathcal{G}_0 and \mathcal{E}_0 , and

$$\mathcal{L}X \equiv \sum_{\alpha, \beta} \frac{|\alpha\rangle\langle\alpha| \mathcal{O}X |\beta\rangle\langle\beta|}{E_\alpha - E_\beta} \quad \text{where} \quad H_0 = \sum_{\alpha} E_\alpha |\alpha\rangle\langle\alpha|. \quad (3.71)$$

The first few terms of the expansion in (3.69) are then, as derived in Ref. [80],

$$H_{\text{eff}}^{(0)} = \mathcal{P}_0 H_0 \mathcal{P}_0, \quad H_{\text{eff}}^{(1)} = \mathcal{P}_0 V \mathcal{P}_0, \quad (3.72)$$

$$H_{\text{eff}}^{(2)} = -\frac{1}{2} \mathcal{P}_0 [\mathcal{O}V, \mathcal{L}V] \mathcal{P}_0, \quad H_{\text{eff}}^{(3)} = \frac{1}{2} \mathcal{P}_0 [\mathcal{O}V, \mathcal{L}[\mathcal{D}V, \mathcal{L}V]] \mathcal{P}_0. \quad (3.73)$$

Exploiting the fact that in our case $\langle\psi|H_0|\psi\rangle = 0$ for all $|\psi\rangle \in \mathcal{G}_0$, we let $\mathcal{B}_0(\mathcal{E}_0)$ denote an eigenbasis of H_0 for \mathcal{E}_0 and define the operator

$$\mathcal{I} \equiv \sum_{|\alpha\rangle \in \mathcal{B}_0(\mathcal{E}_0)} \frac{|\alpha\rangle\langle\alpha|}{E_\alpha}, \quad (3.74)$$

which sums over projections onto excited states with corresponding energetic suppression factors.

We then expand

$$\mathcal{L}X = \mathcal{O}(\mathcal{L}X) = \mathcal{Q}_0 \mathcal{L}X \mathcal{P}_0 + \mathcal{P}_0 \mathcal{L}X \mathcal{Q}_0 = \mathcal{I}X \mathcal{P}_0 - \mathcal{P}_0 X \mathcal{I}, \quad (3.75)$$

which simplifies the expression for $H_{\text{eff}}^{(2)}$ as

$$H_{\text{eff}}^{(2)} = -\frac{1}{2} \mathcal{P}_0 ([\mathcal{O}V, \mathcal{I}V \mathcal{P}_0] - [\mathcal{O}V, \mathcal{P}_0 V \mathcal{I}]) \mathcal{P}_0 = -\mathcal{P}_0 V \mathcal{I} V \mathcal{P}_0. \quad (3.76)$$

Working toward a similar expansion for $H_{\text{eff}}^{(3)}$, we compute

$$[\mathcal{D}V, \mathcal{L}V] = [\mathcal{D}V, \mathcal{I}V\mathcal{P}_0] - [\mathcal{D}V, \mathcal{P}_0V\mathcal{I}] = \mathcal{O}(V\mathcal{I}V) - \mathcal{I}V\mathcal{P}_0V\mathcal{P}_0 - \mathcal{P}_0V\mathcal{P}_0V\mathcal{I}, \quad (3.77)$$

and in turn

$$H_{\text{eff}}^{(3)} = \frac{1}{2}\mathcal{P}_0 \left([\mathcal{O}V, \mathcal{I}[\mathcal{D}V, \mathcal{L}V]\mathcal{P}_0] - [\mathcal{O}V, \mathcal{P}_0[\mathcal{D}V, \mathcal{L}V]\mathcal{I}] \right) \mathcal{P}_0 \quad (3.78)$$

$$= \frac{1}{2}\mathcal{P}_0 (V\mathcal{I}[\mathcal{D}V, \mathcal{L}V] + [\mathcal{D}V, \mathcal{L}V]\mathcal{I}V) \mathcal{P}_0 \quad (3.79)$$

$$= \mathcal{P}_0V\mathcal{I}V\mathcal{I}V\mathcal{P}_0 - \frac{1}{2}\mathcal{P}_0V\mathcal{I}^2V\mathcal{P}_0V\mathcal{P}_0 - \frac{1}{2}\mathcal{P}_0V\mathcal{P}_0V\mathcal{I}^2V\mathcal{P}_0 \quad (3.80)$$

$$= \mathcal{P}_0V\mathcal{I}V\mathcal{I}V\mathcal{P}_0 - \frac{1}{2} \left[\mathcal{P}_0V\mathcal{P}_0, \mathcal{P}_0V\mathcal{I}^2V\mathcal{P}_0 \right]_+, \quad (3.81)$$

where $[X, Y]_+ \equiv XY + YX$. The expressions in (3.72), (3.76), and (3.81) complete the derivation for our expansion of the effective interaction Hamiltonian $H_{\text{int}}^{\text{eff}}$ in (3.11) through third order. In the case of ultracold atoms on a lattice, the motional ground-state subspace \mathcal{G}_0 actually contains many internal atomic states with different energies. Nonetheless, the total Hilbert space is completely separable into uncoupled subspaces associated with each symmetrized many-body internal atomic state. One can therefore diagonalize the interaction Hamiltonian with respect to these internal states and derive an effective theory within each of the corresponding subspaces, in each case setting the appropriate ground-state energy to zero. This procedure is equivalent to simultaneously calculating the effective Hamiltonian $H_{\text{int}}^{\text{eff}}$ for all internal states via the prescriptions we have provided, but letting E_α denote only the motional excitation energy of states $|\alpha_0\rangle \in \mathcal{B}_0(\mathcal{E}_0)$.

3.B Diagram counting and symmetry factors

The fact that we include factors of $1/2$ from the bare two-body interaction Hamiltonian H_{int} in the definition of diagrams implies that p -vertex diagrams acquire a factor of $1/2^p$. In practice, however, these factors are exactly cancelled out by corresponding symmetry factors in all M -body diagrams with $M > 2$. As an illustrative example, consider the second-order effective Hamiltonian

$H_{\text{int}}^{(2)}$ in (3.13), which expanded in full reads

$$H_{\text{int}}^{(2)} = - \sum_{m+n>0} \mathcal{P}_0 \left(\frac{1}{2} K_{mn} G_{s't'}^{st} \hat{c}_{\rho s'}^\dagger \hat{c}_{\sigma t'}^\dagger \hat{c}_{n\sigma t} \hat{c}_{m\rho s} \right) \frac{1}{E_{mn}} \left(\frac{1}{2} K_{mn} G_{q'r'}^{qr} \hat{c}_{m\mu q'}^\dagger \hat{c}_{n\nu r'}^\dagger \hat{c}_{\nu r} \hat{c}_{\mu q} \right) \mathcal{P}_0. \quad (3.82)$$

The three-body terms in this Hamiltonian have $|\{\mu, \nu, \rho, \sigma\}| = 3$ and only one virtually excited atom. The non-vanishing three-body terms must therefore either have $\rho \in \{\mu, \nu\}$ and contain a factor of the form $\hat{c}_X^\dagger \hat{c}_{\sigma t'}^\dagger \hat{c}_{\sigma t} \hat{c}_Y$, or have $\sigma \in \{\mu, \nu\}$ with a factor of the form $\hat{c}_{\rho s'}^\dagger \hat{c}_X^\dagger \hat{c}_Y \hat{c}_{\rho s}$, where the labels X, Y both address whichever nuclear spin (i.e. μ or ν) was excited in the corresponding term. Diagrammatically, we have terms of the form

$$\begin{array}{ccc} \begin{array}{c} \mu q \\ \nu r \end{array} & \begin{array}{c} Z \\ Y \\ X \end{array} & \begin{array}{c} \sigma t \\ \sigma t' \end{array} & \text{and} & \begin{array}{c} \mu q \\ \nu r \end{array} & \begin{array}{c} Z \\ Y \\ X \end{array} & \begin{array}{c} \rho s \\ \rho s' \end{array} & . & (3.83) \end{array}$$

Observing that $\hat{c}_{\rho s'}^\dagger \hat{c}_X^\dagger \hat{c}_Y \hat{c}_{\rho s} = \hat{c}_X^\dagger \hat{c}_{\rho s'}^\dagger \hat{c}_{\rho s} \hat{c}_Y$, however, it is clear that both of the terms represented in (3.83) are equal up to the re-indexing $(\sigma, t, t') \leftrightarrow (\rho, s, s')$. There is therefore a symmetry factor of 2 associated with the second vertex of the diagrams in (3.83), which cancels out with the explicit factor of 1/2 at that vertex, i.e. the first factor of 1/2 in (3.82). A symmetry factor of essentially identical origin appears at every vertex with an “incoming” virtual state, as in e.g. the second and third vertices of

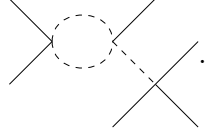
$$\begin{array}{ccc} \begin{array}{c} \mu q \\ \nu r \end{array} & \begin{array}{c} Z \\ Y \\ X \end{array} & \begin{array}{c} \sigma t \\ \sigma t' \end{array} & \text{and} & \begin{array}{c} \mu q \\ \nu r \end{array} & \begin{array}{c} Z \\ Y \\ X \end{array} & \begin{array}{c} \rho s \\ \rho s' \end{array} & . & (3.84) \end{array}$$

or the last vertex of

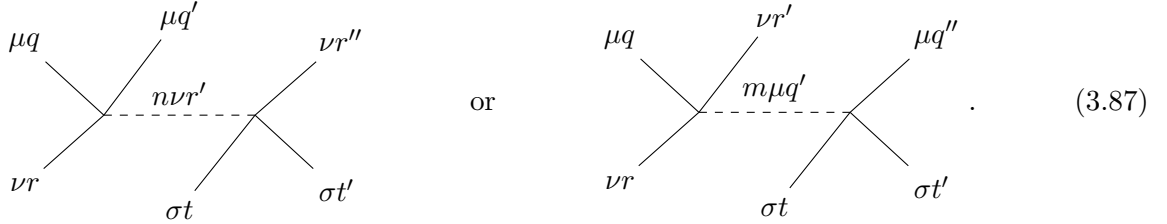
$$\begin{array}{ccc} \begin{array}{c} \mu q \\ \nu r \end{array} & \begin{array}{c} Z \\ Y \\ X \end{array} & \begin{array}{c} \sigma t \\ \sigma t' \end{array} & . & (3.85) \end{array}$$

We can thus account for cancellations of 1/2 at all vertices except those which address two “initial” ground-state atoms, as in the first vertex of the diagrams in (3.83) and (3.84), or the first two vertices of the diagram in (3.85). For such vertices, there are two possibilities: either

- (i) both edges leaving the vertex in question (i.e. leaving to the right) terminate at different vertices, as in the examples above, or
- (ii) both edges leaving the vertex in question terminate at the same vertex, as in for example the first vertex of


(3.86)

In the former case, (i), the vertex in question has an associated symmetry factor of 2 to account for the possibility of a nuclear spin exchange at that vertex. Considering again our example of the second-order effective Hamiltonian $H_{\text{int}}^{(2)}$ in (3.82), the non-vanishing three-body terms must either have $m = 0$ and contain the factor $\hat{c}_{\mu q'}^\dagger \hat{c}_{n\nu r'}^\dagger \hat{c}_{\nu r} \hat{c}_{\mu q}$, or have $n = 0$ with the factor $\hat{c}_{m\mu q'}^\dagger \hat{c}_{\nu r'}^\dagger \hat{c}_{\nu r} \hat{c}_{\mu q}$, which diagrammatically translates to


(3.87)

These terms are equal up to the re-indexing $(\nu, r, r', r'', n) \leftrightarrow (\mu, q, q', q'', m)$, which implies that there is a symmetry factor of 2 associated with the first vertex of the diagrams in (3.87). A symmetry factor of identical origin is associated with the first vertex of the diagrams in (3.84), and the first two vertices of the diagram in (3.85).

The final case we must consider is (ii), which occurs in the first vertex of (3.86). In this case, the symmetry factor of 2 which appears in case (i) to account for the possibility of a nuclear spin exchange simply gets “pushed forward” to the vertex at which the two nuclear spins in question

part ways, e.g. to account for the two possibilities

and

$$(3.88)$$

which are equal up to the re-indexing $(\nu, s, s', s'', s''', m) \leftrightarrow (\mu, r, r', r'', r''', \ell)$. The arguments for a symmetry factor in cases (i) and (ii) fail only if the two nuclear spins in question take identical paths through the internal vertices of a diagram, such that there is no meaningful sense in which two diagrams can be said to differ by a nuclear spin exchange, as in (3.87) and (3.88). If two atoms take identical paths through the internal vertices of a diagram, however, then they have only participated in a two-body process, as in

$$(3.89)$$

After summing over all free indices, therefore, all two-body diagrams have a remaining factor of $1/2$ from the first vertex. In all connected M -body diagrams with $M > 2$, meanwhile, every factor of $1/2$ can be identified one-to-one with a corresponding symmetry factor of 2.

3.C Effective coupling constants in a lattice

Due to our choice of renormalization scheme in Section 3.3.2, the interaction energies prescribed by our low-energy effective theory for multiply-occupied lattice sites are not given directly by the coupling constants G_X defined by the free-space scattering lengths a_X in (3.3). Instead, we must first compute effective coupling constants $G_X^{\text{lattice}}(\mathcal{U})$ in a lattice with depth \mathcal{U} , and in turn use the effective coupling constants to compute interaction energies. As the renormalization procedure $G_X \rightarrow G_X^{\text{lattice}}$ is identical for all coupling constants, we henceforth drop the subscript $X \in \{\text{gg}, \text{eg}^-, \text{eg}^+, \text{ee}\}$ on coupling constants G_X in the remainder of this Appendix. To further simplify notation, we will also neglect the explicit dependence of parameters on the lattice depth \mathcal{U} , which we generally keep fixed.

Proper calculations of the interaction energy of two ultracold fermions in an optical lattice were performed in Refs. [74] and [88] using a two-channel model of a Feshbach resonance, yielding prescriptions for computing effective coupling constants in a lattice from free-space interaction parameters. These calculations, however, are both analytically and numerically involved. We therefore instead opt to use a modified version of the considerably simpler single-channel calculation in Ref. [75] of the interaction energy of two ultracold atoms in a harmonic trap. Our approach is equivalent to the calculation of Hubbard parameters performed in Ref. [89], and has been demonstrated to reproduce correct results in the limit of a deep lattice (compared to the lattice photon recoil energy) and small positive scattering lengths (compared to the effective harmonic oscillator length) [88].

The exact result in Eq. 16 of Ref. [75] for the interaction energy of two ultracold atoms in a harmonic oscillator with angular trap frequency ω can be written in the form

$$(G_{\text{free}}K_{\text{HO}}/\omega)^{-1} = \frac{\sqrt{\pi} \Gamma(-G_{\text{HO}}K_{\text{HO}}/2\omega)}{\Gamma(-G_{\text{HO}}K_{\text{HO}}/2\omega - 1/2)}, \quad K_{\text{HO}} \equiv \int d^3x \left| \phi_0^{\text{HO}} \right|^4, \quad (3.90)$$

where G_{HO} is an effective coupling constant in the harmonic trap, $\phi_0^{\text{HO}}(x)$ is the corresponding non-interacting ground-state wavefunction, and Γ is the gamma function. The expression in (3.90) can be solved numerically as is, or expanded about $G_{\text{HO}}K_{\text{HO}}/\omega = 0$ to get

$$G_{\text{free}}^{-1} = G_{\text{HO}}^{-1} \sum_{n=0}^{\infty} c_n (G_{\text{HO}}K_{\text{HO}}/\omega)^n, \quad (3.91)$$

where the first few coefficients are

$$c_0 = 1, \quad c_1 = 1 - \ln 2, \quad c_2 = -\frac{\pi^2}{24} - \ln 2 + \frac{1}{2} (\ln 2)^2. \quad (3.92)$$

The series in (3.91) can in turn be inverted to solve for G_{HO} with an expansion of the form

$$G_{\text{HO}} = G_{\text{free}} \sum_{n=0}^{\infty} \tilde{c}_n (G_{\text{free}}K_{\text{HO}}/\omega)^n, \quad (3.93)$$

where if we truncate the series in (3.91) at $n = 2$, the first few coefficients of (3.93) are

$$\tilde{c}_0 = 1, \quad \tilde{c}_1 = 1 - \ln 2, \quad \tilde{c}_2 = -\frac{\pi^2}{24} - \ln 2 + \frac{1}{2} (\ln 2)^2 + (1 - \ln 2)^2. \quad (3.94)$$

The coefficients \tilde{c}_n thus found are consistent with the coefficients $c_2^{(n+1)}$ reported in table 1 of Ref. [68], in which the authors compute the first few terms of the two-body Hamiltonian H_2 directly as expressed in (3.15) by using a renormalization scheme which subtracts off divergences term by term.

All of the above results are exact for two atoms in a harmonic oscillator interacting via s -wave scattering. In order to adapt these results for a lattice, we expand the lattice potential about a lattice site centered at $x = (0, 0, 0)$ as

$$\mathcal{U} \sin^2(k_L \cdot x) \approx \mathcal{U} \left[(k_L^x k_L^y k_L^z)^{1/3} x \right]^2 = \frac{1}{2} m_A \omega_{\text{eff}}^2 x^2, \quad \omega_{\text{eff}} \equiv \sqrt{2 \mathcal{U} k_L^2 / m_A}, \quad (3.95)$$

where $k_L = (k_L^x, k_L^y, k_L^z)$ is the lattice wavenumber, m_A is the atomic mass, and ω_{eff} is an effective angular harmonic trap frequency. We then use ω_{eff} in place of ω in (3.90), and use an overlap integral K computed with the ground-state wavefunctions ϕ_0 in a lattice rather than those in a harmonic oscillator. We retrieve free-space s -wave scattering lengths a_{free} for ^{87}Sr from Ref. [53] to determine the free-space coupling constants $G_{\text{free}} \equiv (4\pi/m_A) a_{\text{free}}$. This procedure yields an effective coupling constant G_{lattice} given by

$$(G_{\text{free}} K / \omega_{\text{eff}})^{-1} = \frac{\sqrt{\pi} \Gamma(-G_{\text{lattice}} K / 2\omega_{\text{eff}})}{\Gamma(-G_{\text{lattice}} K / 2\omega_{\text{eff}} - 1/2)}, \quad (3.96)$$

with a solution

$$G_{\text{lattice}} = G_{\text{free}} \sum_{n=0}^{\infty} \tilde{c}_n (G_{\text{free}} K / \omega_{\text{eff}})^n, \quad (3.97)$$

where the first few coefficients are provided in (3.94).

3.D Momentum-dependent s -wave interactions

In addition to the renormalization of coupling constants discussed in Appendix 3.C, computing two-body interaction energies $E_{NX}^{(2)}$ at third order in the low-energy effective theory requires accounting for the contribution of momentum-dependent s -wave interactions. At next-to-leading order in the relative momentum k between two atoms, the effective momentum-dependent scatter-

ing length a_{eff} is given in terms of the zero-momentum scattering length a by [76–78]

$$\frac{1}{a_{\text{eff}}} = \frac{1}{a} - \frac{1}{2}r_{\text{eff}}k^2 = \frac{1}{a} \left(1 - \frac{1}{2}r_{\text{eff}}ak^2 \right), \quad (3.98)$$

which for $r_{\text{eff}}ak^2 \ll 1$, implies that

$$a_{\text{eff}} \approx a \left(1 + \frac{1}{2}r_{\text{eff}}ak^2 \right) = a + \frac{1}{2}r_{\text{eff}}a^2k^2. \quad (3.99)$$

Here r_{eff} is an effective range of $\mathcal{O}(k^2)$ interactions, determined in atomic units by the scattering length a and van der Waals C_6 coefficient by [78]

$$r_{\text{eff}} = \frac{1}{3}\xi^{-2}\chi \left(1 - 2\chi + 2\chi^2 \right) a, \quad \text{where} \quad \xi \equiv \frac{\Gamma(3/4)}{\Gamma(1/4)}, \quad \chi \equiv \sqrt{2} \xi \frac{(m_{\text{A}}C_6)^{1/4}}{a}, \quad (3.100)$$

and Γ is the gamma function. As $\chi \sim 1$ for ^{87}Sr , the momentum-dependent correction to the effective scattering length a_{eff} is $\mathcal{O}(a^3)$ without an additional separation of scales (i.e. which could have occurred if we had $\chi \ll 1$ or $\chi \gg 1$). The momentum-independent $\mathcal{O}(k^0)$ contribution to a_{eff} in (3.99) gives rise to the bare two-body interactions in (3.7) by use of an unregularized contact (i.e. δ -function) potential, while the momentum-dependent $\mathcal{O}(k^2)$ term gives rise to the interaction Hamiltonian [68, 77]

$$H'_{\text{int}} \equiv \frac{1}{2} \sum G'^{qr}_{st} \int d^3x d^3y \delta(z) \left[\hat{\psi}_{\mu q}^\dagger(x) \hat{\psi}_{\nu r}^\dagger(y) \right] \hat{k}_z^2 \left[\hat{\psi}_{\nu t}(y) \hat{\psi}_{\mu s}(x) \right], \quad (3.101)$$

where

$$z \equiv x - y, \quad \hat{k}_z^2 \equiv -\frac{1}{2} \left(\vec{\nabla}_z^2 + \overleftarrow{\nabla}_z^2 \right), \quad (3.102)$$

and the primed couplings G'^{qr}_{st} are defined similarly to unprimed couplings G^{qr}_{st} in (3.3) and (3.4), but with scattering lengths $a \rightarrow r_{\text{eff}}a^2/2$ and the effective range r_{eff} defined by (3.100) for each scattering length with an appropriate C_6 coefficient. We retrieve C_6 coefficients for ^{87}Sr from the supplementary material of Ref. [53]. The squared relative momentum operator \hat{k}_z^2 is represented by symmetrized left- and right-acting derivative operators in order to preserve manifest Hermiticity of H'_{int} . At third order in the low-energy effective theory developed in Section 3.3, the bare momentum-dependent interactions in (3.17) yield only the effective two-body Hamiltonian

$$H'_2 \equiv \frac{1}{2} K' \sum G'^{qr}_{st} \hat{c}_{\mu s}^\dagger \hat{c}_{\nu t}^\dagger \hat{c}_{\nu r} \hat{c}_{\mu q}, \quad (3.103)$$

where, letting $\text{Re}[X]$ denote the real part of X ,

$$K' \equiv \frac{1}{2} \int d^3x \text{Re} \left[(\phi_0^*)^2 \left(\vec{\nabla} \phi_0 \cdot \vec{\nabla} \phi_0 - \phi_0 \vec{\nabla}^2 \phi_0 \right) \right]. \quad (3.104)$$

3.E Bounds on theoretical uncertainties from inter-site effects

In our overview of the relevant one- and two-particle physics of ultracold atoms on a lattice (Section 3.2), we made two approximations which introduce error into the low-energy effective theory. Both approximations concern the on-site locality of the single- and two-body Hamiltonians: we assumed that (i) tunneling between lattice sites and (ii) inter-site interactions are negligible. These approximations are justified for single-particle motional ground states of atoms in a deep lattice, but generally break down when considering virtual states occupying highly excited motional levels, whose spatial wavefunctions can span multiple lattice sites. Nonetheless, we can place upper bounds on the magnitude of inter-site corrections to the effective on-site interaction Hamiltonians by treating tunneling and inter-site interactions of virtual excited states perturbatively and assuming no energetic penalty for nearest-neighbor hopping. These bounds can be used to diagnose the breakdown of the on-site effective theory, and signal when a more careful consideration of inter-site effects is necessary to make precise predictions about many-body spectra and dynamics.

If we still assume negligible overlap between single-particle ground-state wavefunctions in different lattice sites but consider nearest-neighbor wavefunction overlaps of states with motional excitations, our one-body and bare two-body Hamiltonians become

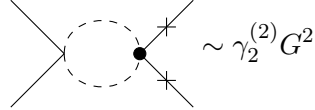
$$H_0 = \sum E_n \hat{c}_{in\mu s}^\dagger \hat{c}_{in\mu s} - \sum_{\substack{\langle i,j \rangle \\ m,n>0}} \left(t_{mn} \hat{c}_{jn\mu s}^\dagger \hat{c}_{im\mu s} + \text{h.c.} \right), \quad (3.105)$$

and

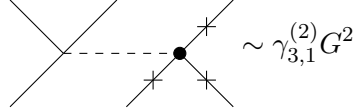
$$\begin{aligned} H_{\text{int}} = & \frac{1}{2} \sum K_{mn}^{k\ell} G_{st}^{qr} \hat{c}_{im\mu s}^\dagger \hat{c}_{in\nu t}^\dagger \hat{c}_{i\ell\nu r} \hat{c}_{ik\mu q} + \frac{1}{2} \sum_{\substack{\langle i,j \rangle \\ n>0}} G_{\rho s; \sigma t}^{\mu q; \nu r} \left(\mathcal{K}_n \hat{c}_{j,0,\rho s}^\dagger \hat{c}_{j,0,\sigma t}^\dagger \hat{c}_{j,0,\nu r} \hat{c}_{im\mu q} + \text{h.c.} \right) \\ & + \frac{1}{2} \sum_{\substack{\langle i,j \rangle \\ m,n>0}} G_{\rho s; \sigma t}^{\mu q; \nu r} \left(\mathcal{K}_{mn} \hat{c}_{j,0,\rho s}^\dagger \hat{c}_{j,0,\sigma t}^\dagger \hat{c}_{in\nu r} \hat{c}_{im\mu q} + \tilde{\mathcal{K}}_{mn} \hat{c}_{in\rho s}^\dagger \hat{c}_{j,0,\sigma t}^\dagger \hat{c}_{j,0,\nu r} \hat{c}_{im\mu q} + \text{h.c.} \right), \quad (3.106) \end{aligned}$$

where t_{mn} is a tunneling rate; $\mathcal{K}_n, \mathcal{K}_{mn}, \tilde{\mathcal{K}}_{mn}$ are inter-site spatial overlap integrals; h.c. denotes a Hermitian conjugate, i.e. $(X + \text{h.c.}) \equiv (X + X^\dagger)$; and $\langle i, j \rangle$ denotes the set of all lattice sites i together with their adjacent sites j . Note that we have neglected terms in (3.106) which involve more than two field operators addressing states with motional excitations, as these terms will not appear in the leading-order corrections to the effective on-site interaction Hamiltonians. We also still neglect terms which involve products of atomic wavefunctions for motional ground states in different lattice sites.

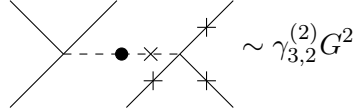
Diagrammatically representing matrix elements of H_0 and H_{int} which are off-diagonal in lattice site by a dot (i.e. \bullet) and marking lines which represent field operators addressing neighboring lattice sites by a cross (i.e. $+$ or \times , depending on the line orientation), the dominant terms in the effective theory which we previously neglected by assuming on-site locality are



$$\sim \gamma_2^{(2)} G^2, \quad \gamma_2^{(2)} \equiv \sum_{n+m>0} \frac{K_{mn} \mathcal{K}_{mn}}{E_{mn}}, \quad (3.107)$$



$$\sim \gamma_{3,1}^{(2)} G^2, \quad \gamma_{3,1}^{(2)} \equiv \sum_{n>0} \frac{K_n \mathcal{K}_n}{E_n}, \quad (3.108)$$



$$\sim \gamma_{3,2}^{(2)} G^2, \quad \gamma_{3,2}^{(2)} \equiv \sum_{n,m>0} \frac{K_m t_{mn} K_n}{E_m E_n}, \quad (3.109)$$

where we have identified, up to an assignment of coupling constants G , the magnitude of all nonzero matrix elements of the diagrams with respect to an eigenbasis of the on-site single-particle Hamiltonian H_0 in (3.1).

The terms in (3.107)-(3.109) can be used to estimate an upper bound on the magnitude of dominant corrections to the spectrum of the low-energy theory from off-diagonal (i.e. in lattice site) matrix elements of the Hamiltonians in (3.105) and (3.106). Conservatively assuming no energetic penalty and no Pauli blocking for any inter-site process, the dominant correction δE_N to the interaction energy of a lattice site with N atoms and b neighboring sites (e.g. $b = 6$ in a

primitive cubic lattice) is roughly bounded as

$$|\delta E_N| \lesssim b \binom{N}{2} \max \left\{ \left| \gamma_2^{(2)} \right|, (N-1) \left| \gamma_{3,1}^{(2)} + \gamma_{3,2}^{(2)} \right| \right\} G^2, \quad (3.110)$$

where the factor of b accounts for the multiplicity of neighboring sites; the factor of $\binom{N}{2}$ accounts for the number of on-site pairs of atoms which are addressed by the diagrams in (3.107)-(3.109); and the factor of $N-1$ on $\gamma_{3,X}^{(2)}$ accounts for the number of atoms in a neighboring site which are addressed by the corresponding processes. These factors count the number of matrix elements in the Hamiltonian with magnitude $\sim \gamma_X^{(2)} G^2$. The maximization in (3.110) is performed because the relevant two- and three-body processes are mutually exclusive, requiring a different number of atoms on neighboring lattice sites. For a conservative bound of $|\delta E_N|$, the coupling factor G^2 in (3.110) can simply be maximized over its allowed values for a given state of atoms on a lattice site, e.g. G_g^2 for a state with no orbital excitations, or $\max \{ G_g^2, G_+^2, G_-^2 \}$ for a state with one net orbital excitation (in both cases, assuming no orbital excitations in neighboring sites). In the latter case, the bound in (3.110) can also be reduced by observing that to conserve energy, it must be the excited atom which moves to a neighboring site, which reduces the factor of $\binom{N}{2}$ in down to $N-1$. We emphasize that the bound in (3.110) is by no means an exact measure of error, and is merely intended to provide a conservative range of energies and corresponding time scales for which inter-site effects could become relevant despite negligible single-particle ground-state tunneling rates.

3.F Perturbative parameters for the effective theory

The perturbative effective theory developed in Section 3.3 is organized in powers of the coupling constants G_X . The formally small, dimensionless quantities for this perturbation theory are the two-body interaction energies KG_X divided by the spectral gap Δ of the non-interacting Hamiltonian H_0 . Here K is a ground-state two-body overlap integral and G_X is a coupling constant. The quantities K , G_X , and Δ all depend on the lattice depth \mathcal{U} . Figure 3.7 shows these parameters for the case of ^{87}Sr atoms with $X \in \{\text{gg}, \text{eg}_-, \text{eg}_+, \text{ee}\}$ at lattice depths $\mathcal{U} \in [30, 80] E_R$, where $E_R \approx 3.5 \times 2\pi$ kHz is the lattice photon recoil energy of the atoms. The fact that these perturbative

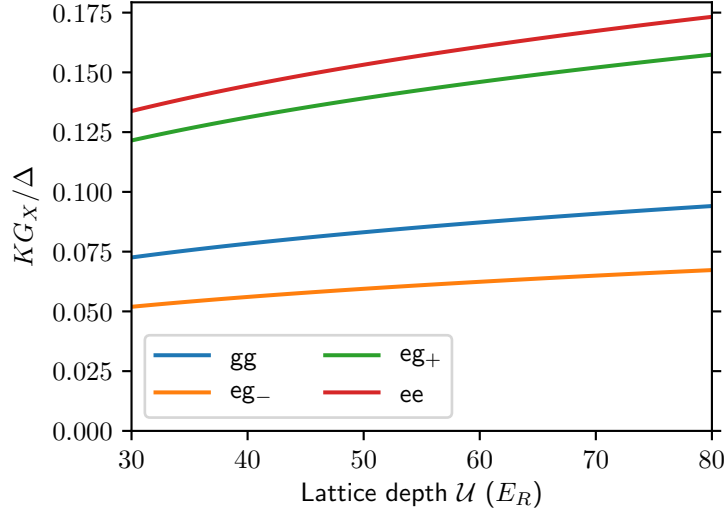


Figure 3.7: Dependence of the perturbative parameters KG_X/Δ on the lattice depth \mathcal{U} .

parameters grow with increasing lattice depth \mathcal{U} is a consequence of the fact that the overlap integral K grows faster with \mathcal{U} than the spectral gap Δ . In the case of a harmonic trap with angular frequency ω , for example, by dimensional analysis these parameters would be

$$\frac{K_{\text{HO}}G_X}{\omega} = \frac{G_X}{\omega} \int d^3x |\phi_{\text{HO}}|^4 = \frac{G_X}{\omega} \left[\int dx \left| \left(\frac{m_\Lambda \omega}{\pi} \right)^{1/4} e^{-m_\Lambda \omega x^2/2} \right|^4 \right]^3 \propto \sqrt{\omega}, \quad (3.111)$$

where we assumed that the coupling constants G_X vary weakly with ω . While this result may seem to suggest that the low-energy effective theory should become better at smaller lattice depths, smaller lattice depths also result in increased theoretical uncertainties from the growing relevance of the inter-site effects discussed in Appendix 3.E.

3.G Low-excitation M -body Hamiltonian coefficients

When restricted to the subspace of at most one orbital excitation per lattice site, the M -body Hamiltonians of the low-energy effective theory developed in Section 3.3 can be written in the form

$$H_M = \sum_{|\{\mu_j\}|=M} \left(U_{M,g} \hat{n}_{\mu_1,g} \hat{n}_{\mu_2,g} + U_{M,+} \hat{n}_{\mu_1,e} \hat{n}_{\mu_2,g} + U_{M,-} \hat{c}_{\mu_1,g}^\dagger \hat{c}_{\mu_2,e}^\dagger \hat{c}_{\mu_2,g} \hat{c}_{\mu_1,e} \right) \prod_{\alpha=3}^M \hat{n}_{\mu_\alpha,g}, \quad (3.112)$$

where the coefficients can be expanded as $U_{MX} = \sum_p U_{MX}^{(p)}$ with terms $U_{MX}^{(p)}$ at order p in the coupling constants G_Y . The terms $U_{MX}^{(p)}$ can be determined from the M -body p -order Hamiltonians $H_M^{(p)}$ derived in Section 3.3, i.e. in (3.17), (3.19), (3.36), and (3.46). For the effective 2-, 3-, and 4-body Hamiltonians through third order in the coupling constants, the coefficients are

$$U_{2,g} = \frac{1}{2}\alpha_2^{(1)}G_g, \quad U_{2,+} = \alpha_2^{(1)}G_+, \quad U_{2,-} = \alpha_2^{(1)}G_-, \quad (3.113)$$

$$U_{3,g}^{(2)} = -\alpha_3^{(2)}G_g^2, \quad U_{3,+}^{(2)} = -\alpha_3^{(2)}G_+(G_+ + 2G_g), \quad (3.114)$$

$$U_{3,-}^{(2)} = -\alpha_3^{(2)}G_-(2G_+ + G_- + 2G_g), \quad (3.115)$$

$$U_{3,g}^{(3)} = \left(\alpha_{3,1}^{(3)} - \alpha_5^{(3)}\right) 2G_g^3 + \left(2\alpha_{3,2}^{(3)} - \alpha_{4,3}^{(3)} - \alpha_5^{(3)}\right) G_g^3, \quad (3.116)$$

$$U_{3,+}^{(3)} = \left(\alpha_{3,1}^{(3)} - \alpha_5^{(3)}\right) \left(G_+^3 + 4G_+^2G_g + G_+G_-^2 + G_+G_g^2 + G_-^3 + G_-^2G_g\right) \\ + \left(2\alpha_{3,2}^{(3)} - \alpha_{4,3}^{(3)} - \alpha_5^{(3)}\right) \left(G_+^3 + G_+^2G_g + G_+G_-^2 + G_+G_g^2 + G_-^2G_g\right), \quad (3.117)$$

$$U_{3,-}^{(3)} = \left(\alpha_{3,1}^{(3)} - \alpha_5^{(3)}\right) G_- \left(3G_+^2 + 2G_+G_- + 8G_+G_g + 3G_-G_g + G_g^2\right) \\ + \left(2\alpha_{3,2}^{(3)} - \alpha_{4,3}^{(3)} - \alpha_5^{(3)}\right) G_- \left(3G_+^2 + 2G_+G_- + 2G_+G_g + G_-^2 + G_g^2\right), \quad (3.118)$$

$$U_{4,g}^{(3)} = \left(2\alpha_{4,1}^{(3)} - \alpha_5^{(3)}\right) G_g^3 + \left(\alpha_{4,2}^{(3)} - \alpha_5^{(3)}\right) 2G_g^3, \quad (3.119)$$

$$U_{4,+}^{(3)} = \left(2\alpha_{4,1}^{(3)} - \alpha_5^{(3)}\right) 2G_+G_g(G_+ + G_g) + \left(\alpha_{4,2}^{(3)} - \alpha_5^{(3)}\right) G_+ \left(G_+^2 + 2G_+G_g + 5G_g^2\right), \quad (3.120)$$

$$U_{4,-}^{(3)} = \left(2\alpha_{4,1}^{(3)} - \alpha_5^{(3)}\right) 2G_-G_g(2G_+ + G_- + G_g) \\ + \left(\alpha_{4,2}^{(3)} - \alpha_5^{(3)}\right) G_- \left(3G_+^2 + 3G_+G_- + 4G_+G_g + G_-^2 + 2G_-G_g + 5G_g^2\right), \quad (3.121)$$

In terms of the spatial overlap integrals defined in (3.6) and (3.8), the prefactors $\alpha_X^{(p)}$ on the coefficients $U_X^{(p)}$ are

$$\alpha_2^{(1)} \equiv K, \quad \alpha_3^{(2)} \equiv \sum_{n>0} \frac{K_n^2}{E_n}, \quad \alpha_5^{(3)} \equiv K \sum_{n>0} \frac{K_n^2}{E_n^2}, \quad (3.122)$$

$$\alpha_{3,1}^{(3)} \equiv \sum_{\substack{\ell+m>0 \\ \ell+n>0}} \frac{K_{\ell m} K_n^m K_{\ell n}}{E_{\ell m} E_{\ell n}}, \quad \alpha_{3,2}^{(3)} \equiv \sum_{\substack{\ell+m>0 \\ n>0}} \frac{K_{\ell m} K_n}{E_{\ell m} E_n} \left(K_n^{\ell m} - \frac{K_{\ell m} K_n}{K} \right), \quad (3.123)$$

$$\alpha_{4,1}^{(3)} \equiv \sum_{\substack{m \geq 0 \\ n > 0}} \frac{K_{mn} K_m K_n}{E_{mn} E_n}, \quad \alpha_{4,2}^{(3)} \equiv \sum_{m,n>0} \frac{K_m K_n^m K_n}{E_m E_n}, \quad \alpha_{4,3}^{(3)} \equiv K \sum_{m+n>0} \frac{K_{mn}^2}{E_{mn}^2}. \quad (3.124)$$

Chapter 4

Engineering spin squeezing in a 3D optical lattice with interacting spin-orbit-coupled fermions

Prologue

The 3D ^{87}Sr optical lattice clock (OLC) is one of the most precise and accurate scientific instruments ever created, rivaled only by other atomic clocks and large-scale gravitational wave detectors. In principle, this clock (or rather, a series of these clocks) could measure the age of the universe (~ 14 billion years) to within an error measured in milliseconds. However, the 3D ^{87}Sr OLC still operates in the “single-particle” regime, deriving its precision primarily from (i) the narrow (millihertz) linewidth of an electronic transition in individual atoms, together with (ii) signal averaging over a large number of independent atoms^a that are addressed simultaneously in the clock. Averaging over N atoms improves clock precision by a factor of $\sim 1/\sqrt{N}$, which can be traced back to the reconstruction of a classical distribution from N independent samples (one sample per atom). A major untapped resource for further improving the 3D ^{87}Sr OLC is the possibility of preparing entangled clock states in which quantum correlations between atoms conspire to reduce sampling error. In theory, this strategy can reduce the “classical” factor of $1/\sqrt{N}$ to a “quantum” factor to $1/N$, which would improve the precision of a 3D clock with $100 \times 100 \times 100$ lattice sites by a factor of 10^3 (at unit filling).

^a The 3D ^{87}Sr OLC operates in a Fermi-degenerate Mott insulating regime, so atoms’ *external* (spatial) degrees of freedom are highly correlated. However, the clock signal is encoded in atoms’ *internal* (electronic) degrees of freedom, which are essentially independent.

In this chapter, we present a concrete protocol for preparing spin-squeezed states of many atoms, whose quantum correlations can be leveraged to improve clock performance. The essential ingredients for the protocol are $SU(2)$ -symmetric inter-atomic interactions, together with a symmetry-breaking inhomogeneous single-particle field. The bulk of this chapter is taken from Ref. [2]. In addition to myself and Ana Maria Rey, this work featured major contributions from Peiru He, Sean R. Muleady, Robert J. Lewis-Swan, Ross B. Hudson, and Jun Ye.

Abstract

One of the most important tasks in modern quantum science is to coherently control and entangle many-body systems, and to subsequently use these systems to realize powerful quantum technologies such as quantum-enhanced sensors. However, many-body entangled states are difficult to prepare and preserve since internal dynamics and external noise rapidly degrade any useful entanglement. Here, we introduce a protocol that counterintuitively exploits inhomogeneities, a typical source of dephasing in a many-body system, in combination with interactions to generate metrologically useful and robust many-body entangled states. Motivated by current limitations in state-of-the-art three-dimensional (3D) optical lattice clocks (OLCs) operating at quantum degeneracy, we use local interactions in a Hubbard model with spin-orbit coupling to achieve a spin-locking effect. In addition to prolonging inter-particle spin coherence, spin-locking transforms the dephasing effect of spin-orbit coupling into a collective spin-squeezing process that can be further enhanced by applying a modulated drive. Our protocol is fully compatible with state-of-the-art 3D OLC interrogation schemes and may be used to improve their sensitivity, which is currently limited by the intrinsic quantum noise of independent atoms. We demonstrate that even with realistic experimental imperfections, our protocol may generate ~ 10 – 14 dB of spin squeezing in ~ 1 second with $\sim 10^2$ – 10^4 atoms. This capability allows OLCs to enter a new era of quantum enhanced sensing using correlated quantum states of driven non-equilibrium systems.

4.1 Introduction

A major frontier of contemporary physics is the understanding of non-equilibrium behaviors of many-body quantum systems, and the application of these behaviors toward the development of novel quantum technologies with untapped capabilities [90]. To this end, ultracold atomic, molecular, and optical systems are ideal platforms for studying unexplored regimes of many-body physics due to their clean preparation and readout, high controllability, and long coherence times [91, 92]. The exquisite capabilities of these systems have pushed the frontiers of metrology, quantum simulation, and quantum information science.

Optical lattice clocks in particular have seen some of the most impressive developments in recent years, reaching record levels of precision ($\sim 3 \times 10^{-19}$) [42, 73] and accuracy ($\sim 1 \times 10^{-18}$) [40, 93]. These advancements required important breakthroughs, including the capability to cool and trap fermionic alkaline-earth atoms in spin-insensitive potentials [22, 94, 95]; the development of ultracoherent lasers [96–98] to fully exploit an ultranarrow clock transition [17]; the detailed characterization of inter-atomic interactions [51–53]; and, more recently, the preparation of a quantum degenerate gas in a three-dimensional (3D) optical lattice [7, 42, 73]. Nonetheless, all improvements in sensing capabilities to date have been based on single-particle control of internal atomic degrees of freedom. Such strategies will eventually have diminishing returns due to practical difficulties in (i) suppressing decoherence from external (motional) degrees of freedom, and (ii) interrogating more particles without additional systematic errors from interactions [17, 50, 73].

Pushing beyond the current independent-particle paradigm requires leveraging many-body quantum correlations. Entangled states such as spin-squeezed states [32, 33, 35] can enhance measurement sensitivity, i.e. the uncertainty $\Delta\theta$ in the estimation of a parameter θ , below the standard quantum limit $\Delta\theta \sim 1/\sqrt{N}$ for N uncorrelated particles [99, 100]. The major challenge for progress in this direction is that generating entanglement requires interactions, which are generally undesirable because they degrade atomic coherence, thereby limiting clock performance [17, 47, 48, 50, 54, 101]. In fact, the most precise and accurate optical lattice clocks were designed to operate

with fermionic atoms in identical nuclear and electronic states to suppress collisional decoherence [42, 47, 102], as identical fermions cannot interact via the otherwise dominant (*s*-wave) collisions at ultracold temperatures. However, an initially spin-polarized Fermi gas still exhibits interactions at later times due to spin-orbit coupling (SOC) that is induced by the laser that drives the clock transition (i.e. the “clock laser”) [25, 26, 103, 104]. Specifically, the momentum kick imparted by this laser imprints a position-dependent phase that induces inhomogeneous spin precession and generates spin dephasing, thereby making atoms distinguishable and vulnerable to collisions. While a deep lattice can suppress SOC, it also intensifies the light scattering which currently limits the coherence time of the clock [7, 23, 105].

In this work, we describe a scheme that can lead to metrological advances in state-of-the-art optical lattice clocks through direct use of quantum entanglement by harnessing the interplay between nominally undesirable collisions and SOC. This scheme is made possible in the weak SOC regime by the formation of an interaction-energy gap that suppresses the SOC-induced population transfer from the exchange-symmetric Dicke manifold (spanned by spin-polarized, and thus non-interacting states) to the remainder of Hilbert space. Interactions thereby prolong inter-particle spin coherence through a spin-locking effect, which additionally transforms the dephasing effect of SOC into a collective spin squeezing process. To generate spin squeezing, our protocol only requires the capability to fix (i) the orientation of the clock laser and (ii) the optical lattice depth. These controls are straightforward to incorporate into current 3D clock interrogation sequences without sacrificing atom numbers or coherence times. Additionally, we show that by applying a modulated drive from the clock laser, one can further prepare states that saturate the Heisenberg limit $\Delta\theta \sim 1/N$ for phase sensitivity [33, 35, 100]. This capability mirrors efforts in other settings, such as nitrogen-vacancy centers in diamond [106, 107] and trapped ions [108], to enhance quantum metrology through the use of driven non-equilibrium phenomena.

Despite an abundance of proof-of-principle experiments with entangled states [100, 109], so far only the remarkable example of LIGO [110, 111] has demonstrated a quantum advantage in a state-of-the-art quantum sensing or measurement system. The new generation of 3D optical

lattice systems have fully quantized motional degrees of freedom [42], allowing for precise control of collisional interactions. We demonstrate how these interactions can naturally give rise to metrologically useful correlated many-body fermionic states, opening a path to not only generate entanglement, but also harness it to achieve a quantum advantage in a world-class sensor. Such an advance will ultimately deliver gains to real-world applications including timekeeping, navigation, telecommunication, and our understanding of the fundamental laws of nature [18].

4.2 Spin squeezing with the Fermi-Hubbard model

We consider N fermionic atoms with two spin states (labeled \uparrow and \downarrow) trapped in a 3D optical lattice. In this discussion, these spin states are associated with the two electronic states of a nuclear-spin-polarized gas. At sufficiently low temperatures, atoms occupy the lowest Bloch band of the lattice and interact only through s -wave collisions. A schematic of this system is provided in Figure 4.1(a), where tight confinement prevents motion along the vertical direction (z), effectively forming a stack of independent 2D lattices. For simplicity and without loss of generality, however, we first consider the case when tunneling can only occur along one direction, x , and thus model the system as living in one dimension.

An external laser with Rabi frequency Ω and wavenumber k_L along the tunneling axis resonantly couples atoms' internal states through the Hamiltonian $\hat{H}_{\text{laser}}/\hbar = \sum_j \Omega e^{ik_L x_j} \hat{c}_{j,\uparrow}^\dagger \hat{c}_{j,\downarrow} + \text{h.c.}$, where $\hat{c}_{j\alpha}$ is a fermionic annihilation operator for an atom on site j with internal state $\alpha \in \{\uparrow, \downarrow\}$ and x_j is the position of site j . This laser imprints a position-dependent phase that equates to a momentum kick k_L when an atom changes internal states by absorbing or emitting a photon, thereby generating spin-orbit coupling [26, 103]. After absorbing the position dependence of the laser Hamiltonian into fermionic operators through the gauge transformation $\hat{c}_{j,\uparrow} \rightarrow e^{ik_L x_j} \hat{c}_{j,\uparrow}$, which makes \hat{H}_{laser} spatially homogeneous, the atoms are well-described in the tight-binding limit by the Fermi-Hubbard Hamiltonian [112]

$$\hat{H}_{\text{FH}}^{(\phi)}/\hbar = -J \sum_j \left(e^{i\phi} \hat{c}_{j,\uparrow}^\dagger \hat{c}_{j+1,\uparrow} + \hat{c}_{j,\downarrow}^\dagger \hat{c}_{j+1,\downarrow} + \text{h.c.} \right) + U \sum_j \hat{n}_{j,\uparrow} \hat{n}_{j,\downarrow}, \quad (4.1)$$

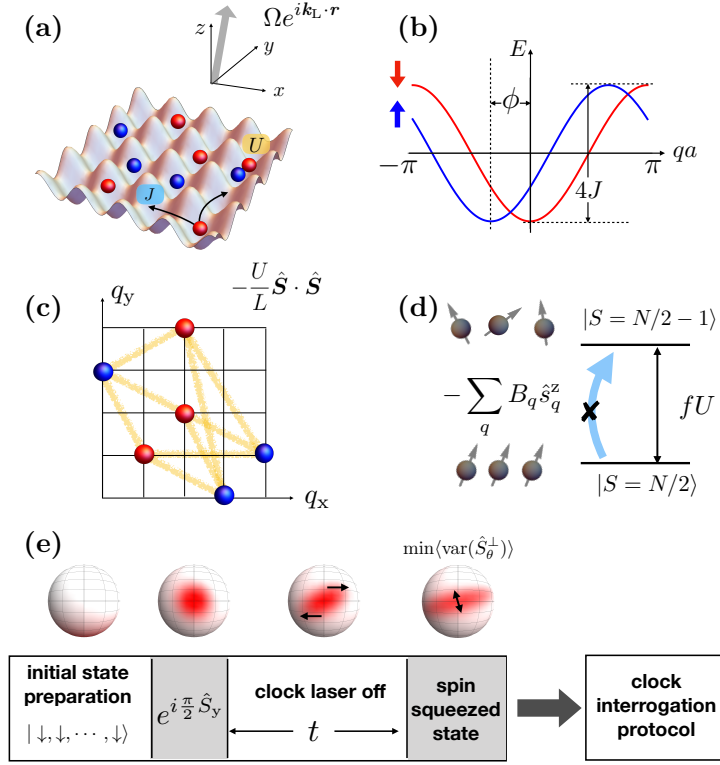


Figure 4.1: **Schematic of the setup for spin squeezing.** (a) We consider N fermionic atoms with two (pseudo-)spin components, represented by red and blue spheres, trapped in the ground band of an optical lattice (shown in 2D for the sake of presentation). Atoms tunnel to neighboring sites at a rate J and experience on-site interactions with strength U . An external laser carrying a position dependent phase $e^{ik_L \cdot r}$ couples the spin states of the atoms. (b) After a gauge transformation, different spin states exhibit different dispersion relations with a relative phase $\phi = k_L a$, where a is the lattice spacing. The external laser couples spin states with identical quasi-momenta q in the gauge-transformed frame. (c) If interactions are sufficiently weak, all motional degrees of freedom become frozen in momentum space, with atoms effectively pinned to fixed quasi-momentum modes \mathbf{q} . The dynamics on the frozen \mathbf{q} -space lattice can then be mapped to a spin model in which collisional interactions correspond to a uniform, all-to-all ferromagnetic Heisenberg Hamiltonian with strength U/L , where L is the total number of lattice sites. (d) The spin dependence of the dispersion relation is captured by a mode-dependent axial field B_q that generates inhomogeneous spin precession. This axial field couples exchange-symmetric many-body Dicke states with total spin $S = N/2$ to spin-wave states with $S = N/2 - 1$. The all-to-all interaction opens an energy gap fU (with $f = N/L$ the filling fraction of spatial modes) between the Dicke states and the spin-wave states, which forbids population transfer between them in the weak-field limit. (e) To generate spin squeezing via one-axis twisting, we initialize a product state with all spins polarized in $-z$ (i.e. in $|\downarrow\rangle$), and apply a fast external laser pulse to rotate all spins into x . We then let atoms freely evolve for a variable time t (with a spin-echo pulse), after which the amount of spin squeezing can be determined experimentally from global spin measurements. The spin-squeezed state can be used for a follow-up clock interrogation protocol (see Appendix 4.E).

where J is the nearest-neighbor tunneling rate; the SOC angle $\phi \equiv k_L a$ determines the phase gained by spin-up atoms upon tunneling from site j to site $j + 1$ (in the gauge-transformed frame) with lattice spacing $a = x_{j+1} - x_j$; U is the on-site interaction energy of two atoms; and $\hat{n}_{j\alpha} \equiv \hat{c}_{j\alpha}^\dagger \hat{c}_{j\alpha}$ is a number operator.

The Fermi-Hubbard Hamiltonian can be re-written in the quasi-momentum basis with annihilation operators $\hat{c}_{q\alpha} \equiv L^{-1/2} \sum_j e^{-iqx_j} \hat{c}_{j\alpha}$, where q is a quasi-momentum and L is the total number of lattice sites. In this basis, the single-particle Hamiltonian exhibits shifted dispersion relations that signify spin-orbit coupling [see Figure 4.1(b)]:

$$\hat{H}_{\text{FH,single}}^{(\phi)}/\hbar = -2J \sum_q [\cos(qa + \phi) \hat{n}_{q,\uparrow} + \cos(qa) \hat{n}_{q,\downarrow}]. \quad (4.2)$$

When $U \lesssim J$, interaction energies are too weak for collisions to change the occupancies of single-particle quasi-momentum modes. Atoms are then pinned to these modes, which form a lattice in quasi-momentum space [see Figure 4.1(c)] [104]. In this strong-tunneling limit, the Fermi-Hubbard Hamiltonian [Eqn. (4.2)] can be mapped to a spin-1/2 system with a collective ferromagnetic Heisenberg interaction and an inhomogeneous axial field, given by [50, 54, 104]

$$\hat{H}_{\text{spin}}/\hbar = -\frac{U}{L} \hat{\mathbf{S}} \cdot \hat{\mathbf{S}} - \sum_q B_q \hat{s}_q^z, \quad (4.3)$$

where $\hat{\mathbf{S}} = \sum_q \hat{\mathbf{s}}_q$ is a collective spin operator; $\hat{\mathbf{s}}_q$ is a spin-1/2 operator for mode q with components $\hat{s}_q^{j=x,y,z} \equiv \frac{1}{2} \sum_{\alpha,\beta} \hat{c}_{q\alpha}^\dagger \sigma_{\alpha\beta}^j \hat{c}_{q\beta}$ defined in terms of the Pauli matrices $\sigma^{j=x,y,z}$; the sums over q run over all occupied quasi-momentum modes; and $B_q \equiv -4J \sin(qa + \phi/2) \sin(\phi/2)$ is the SOC-induced axial field.

On its own, the collective Heisenberg term ($\sim \hat{\mathbf{S}} \cdot \hat{\mathbf{S}}$) in Eqn. (4.3) opens an energy gap fU , with $f \equiv N/L$ the filling fraction of spatial modes, between the collective Dicke states $|S = N/2, M_S\rangle$ and the remainder of Hilbert space [50, 113–115] with $S < N/2$. Here S and M_S respectively label the eigenvalues of the collective spin operators $\hat{\mathbf{S}} \cdot \hat{\mathbf{S}}$ and \hat{S}_z , with eigenvalues $S(S+1)$ for non-negative $S \in \{N/2, N/2 - 1, \dots\}$ and $M_S \in \{-S, -S + 1, \dots, S\}$. The axial field B_q generally couples states within the Dicke manifold to states outside it. In the weak SOC limit

(i.e. $B_q \ll fU$), however, the interaction energy gap suppresses population transfer between states with different total spin S [see Figure 4.1(d)]. In this regime, the virtual occupation of states outside the Dicke manifold can be accounted for perturbatively. The symmetries of SOC as expressed in Eqn. (4.3) dictate that this treatment should yield powers of \hat{S}_z when projected onto the collective Dicke manifold at higher orders in perturbation theory. At second order in perturbation theory (see Appendix 4.A), we thus find that SOC effectively yields a one-axis twisting (OAT) model widely known to generate squeezing dynamics [33, 35]:

$$\hat{H}_{\text{eff}}/\hbar = -\frac{U}{L} \hat{\mathbf{S}} \cdot \hat{\mathbf{S}} - \bar{B} \hat{S}_z + \chi \hat{S}_z^2, \quad \chi \equiv \frac{\tilde{B}^2}{(N-1)fU}, \quad (4.4)$$

where $\bar{B} \equiv \sum_q B_q/N$ is the mean and $\tilde{B}^2 \equiv \sum_q (B_q - \bar{B})^2 / N$ the variance of the axial field. The effect of the $\sim \hat{\mathbf{S}} \cdot \hat{\mathbf{S}}$ term is to generate a relative phase between states with different total spin S and thus has no effect on dynamics restricted to a fixed S . Note also that the collective spin rotation from $\bar{B} \hat{S}_z$ can be eliminated by going into a rotating frame or by using a spin echo.

The entire protocol for preparing a squeezed state via OAT, sketched out in Figure 4.1(e), reduces to a standard Ramsey protocol with a spin echo: after initially preparing a spin-down (i.e. $-\hat{z}$) polarized sample of ultracold atoms populating the lowest Bloch band of a lattice, a fast $\pi/2$ pulse is applied with the clock laser to rotate all spin vectors into $+\hat{x}$. The atoms then freely evolve for a variable time t (possibly with spin-echo π -pulses), after which the amount of metrologically useful spin squeezing, measured by the Ramsey squeezing parameter

$$\xi^2 \equiv \min_{\theta} \langle \text{var}(\hat{S}_{\theta}^{\perp}) \rangle \times N / \left| \langle \hat{\mathbf{S}} \rangle \right|^2, \quad (4.5)$$

can be determined experimentally from global spin measurements. Here $\langle \hat{\mathbf{S}} \rangle$ is the mean collective spin vector and $\langle \text{var}(\hat{S}_{\theta}^{\perp}) \rangle$ is the variance of spin measurements along an axis orthogonal to $\langle \hat{\mathbf{S}} \rangle$, parameterized by the angle $\theta \in [0, 2\pi)$.

The above protocol concerns only the preparation of a spin-squeezed state, which would then be used as an input state for a follow-up clock interrogation protocol without SOC. While increasing the lattice depth to turn off SOC during clock interrogation is the simplest approach, this will limit

the interrogation time due to light scattering (see discussion below). Alternatively, it is possible to keep the same lattice depth used for the spin squeezing generation by adding a specific pulse sequence to suppress SOC. See details in Appendix 4.E.

4.2.1 Model validity

The validity of the OAT model in Eqn. (4.4) relies on two key conditions concerning experimental parameter regimes. First, the on-site interaction energy U should not be much larger in magnitude than the tunneling rate J (clarified below); otherwise, one cannot assume frozen motional degrees of freedom (i.e. with atoms pinned to fixed quasi-momentum modes) and map the Fermi-Hubbard model to a spin model. Second, the SOC-induced fields $B_q \sim J \sin(\phi/2)$ should be considerably smaller in magnitude than the interaction energy gap fU , as otherwise one cannot perturbatively transform SOC into OAT. These two conditions can be satisfied by appropriate choices of U/J and the SOC angle ϕ , which are respectively controlled by tuning the lattice depth and changing the angle between the clock laser and the lattice axes [see Figure 4.1(a)].

We demonstrate the importance of these conditions in Figure 4.2, where we show numerical results from exact simulations of a 1D system with $L = 12$ sites. Therein, optimal squeezing achievable under unitary dynamics is provided in dB, i.e. $-10 \log_{10}(\xi_{\text{opt}}^2)$, while the time at which this squeezing occurs is provided in units of the nearest-neighbor tunneling time $2\pi/J$. At $f = 1$ atom per lattice site, i.e. half filling of all atomic states in the lowest Bloch band, the spin model [Eqn. (4.3)] agrees almost exactly with the Fermi-Hubbard (FH) model [Eqn. (4.2)] up through (and exceeding) $U/J = 8$. The agreement at half filling ($f = 1$) is assisted by Pauli blocking of mode-changing collisions. Below half filling ($f = 5/6$), these two (FH and spin) models show good agreement at $U/J \lesssim 2$, while at $U/J \gtrsim 2$ mode-changing collisions start to become relevant and invalidate the frozen-mode assumption of the spin model. Note that we chose filling $f = 5/6$ to demonstrate that our protocol should work, albeit sub-optimally, even in this highly hole-doped case; in practice, optimized experiments are capable of achieving fillings closer to the optimal $f = 1$ [116]. Interestingly, even with mode-changing collisions the Fermi-Hubbard model exhibits

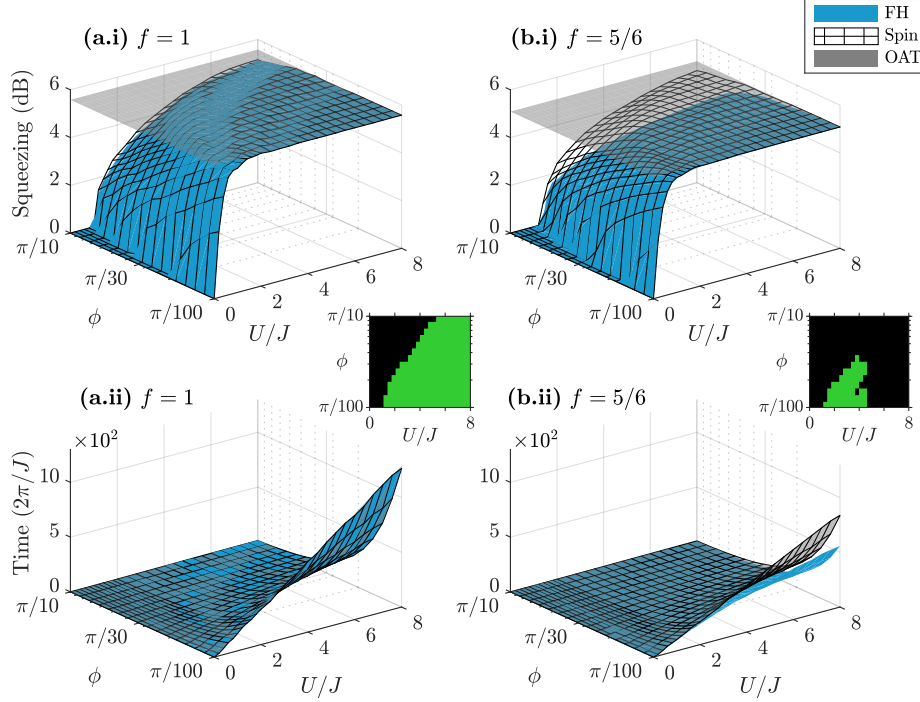


Figure 4.2: Benchmarking the spin and one-axis twisting models. Comparisons of maximum squeezing (top panels, **a.i** and **b.i**) and optimal squeezing time (lower panels, **a.ii** and **b.ii**) between the Fermi-Hubbard (FH), spin, and one-axis twisting (OAT) models; obtained numerically via the protocol depicted in Figure 4.1(e) in a 1D lattice with $L = 12$ sites. Results are shown for half filling with $N = 12$, $f \equiv N/L = 1$ (left panels, **a.i** and **a.ii**) and filling $f = 5/6$ (right panels, **b.i** and **b.ii**) as a function of U/J and the SOC angle ϕ . In both cases, the system is initialized in the corresponding ground state. Insets for both $f = 1$ and $f = 5/6$ show (in green) regions of the U - ϕ plane in which both the optimal squeezing (in dB) and the corresponding squeezing time of all three models agree to within 20%. At half filling (**a.i** and **a.ii**), mode-changing collisions are suppressed by Pauli blocking, resulting in almost exact agreement between the FH and spin models; both of these models converge onto the OAT model in the gap-protected, weak SOC regime of large U/J and small ϕ . The spin and OAT models show similar behavior away from half filling (**b.i** and **b.ii**), but the presence of mode-changing collisions results in their disagreement with the FH model as interactions begin to dominate at larger U/J . Even below half filling, however, the FH exhibits comparable amounts of squeezing to the spin model across a broad range of U/J and ϕ , albeit at earlier times when $U/J \gtrsim 2$.

comparable amounts of squeezing to the spin model, and achieves this squeezing in less time. The spin and OAT models agree in the regime of weak SOC with $\tilde{B} \sim J \sin(\phi/2) \ll fU$, and exhibit different squeezing behaviors outside this regime as single-particle spin dephasing can no longer be treated as a weak perturbation to the spin-locking interactions.

In realistic implementations, the Gaussian profile of the laser beams always introduces an additional effective harmonic potential that modifies the translational invariance assumed so far. We present a detailed discussion of the role of the harmonic trap in Appendix 4.I, where we demonstrate that the addition of harmonic confinement barely modifies the achievable spin squeezing with currently accessible trapping frequencies. We find that the existence of single-particle localized modes in the lattice with harmonic confinement [24, 117] helps to protect spin squeezing and shifts the optimal parameter window to $U/J \gtrsim 2$.

4.2.2 Two-axis twisting

The above scheme for OAT achieves optimal spin squeezing that scales as $\xi_{\text{opt}}^2 \sim N^{-2/3}$ with minimal intervention, i.e. a standard Ramsey protocol. Further improvements upon this scheme can be made by introducing a time-dependent driving field that transforms the OAT Hamiltonian into a two-axis twisting (TAT) one. While the OAT model initially generates squeezing faster than the TAT model, the squeezing generation rate of OAT (measured in dB per second) falls off with time, while the squeezing generation rate for TAT remains approximately constant until reaching Heisenberg-limited amount of spin squeezing with $\xi_{\text{opt}}^2 \sim N^{-1}$ [33].

There are two general strategies for converting OAT into TAT: by use of either a pulsed [118] or continuous [119] drive protocol. For simplicity, we consider the latter in this work, although the pulsed protocol could provide additional advantages, as explained at the end of Appendix 4.E. Following the prescription in Ref. [119], we use the clock laser to apply an amplitude-modulated drive $\hat{H}_{\text{drive}}(t)/\hbar = \Omega_0 \cos(\omega t) \hat{S}_x$. If the modulation frequency ω satisfies $\omega \gg N\chi$ and $\mathcal{J}_0(2\Omega_0/\omega) = \pm 1/3$, where χ is the OAT squeezing strength in Eqn. (4.4) and \mathcal{J}_0 is the zero-order Bessel function of the first kind, then up to (i) an $\sim \hat{\mathbf{S}} \cdot \hat{\mathbf{S}}$ term that contributes only overall phase

factors, and (ii) an $\sim \hat{S}_z$ term that can be eliminated with a simple dynamical decoupling pulse sequence (see Appendix 4.D), the effective Hamiltonian becomes $\hat{H}_{\text{TAT}}^{(+)}/\hbar = (\chi/3)(\hat{S}_z^2 - \hat{S}_x^2)$ or $\hat{H}_{\text{TAT}}^{(-)}/\hbar = (\chi/3)(\hat{S}_y^2 - \hat{S}_x^2)$ (see Appendix 4.C), which squeezes an initial state polarized along the y or z axis, respectively.

4.3 Experimental implementation and practical considerations

Thus far, we have largely considered the general preparation of spin-squeezed states with the Fermi-Hubbard model. Here, we discuss the specific implementation of the above protocols in the state-of-the-art 3D ^{87}Sr optical lattice clock (OLC). If successful, such an implementation would (to our knowledge) for the first time break through the proof-of-principle stage of spin squeezing efforts, and achieve a genuine metrological enhancement of a world-class quantum sensor.

As required for our protocol, 3D ^{87}Sr OLC has demonstrated the capability to load a quantum degenerate gas into a 3D lattice at the “magic wavelength” ($\lambda_{\text{lattice}} = 2a \approx 813$ nm) for which both the ground ($^1S_0, \downarrow$) and first excited ($^3P_0, \uparrow$) electronic states (i.e. the “clock states”) of the atoms experience the same optical potential [42]. Furthermore, the 3D ^{87}Sr OLC currently operates at sufficiently low temperatures to ensure vanishing population above the lowest Bloch band, such that its dynamics are governed by the Fermi-Hubbard Hamiltonian [Eqn. (4.2)] [112].

An external clock laser with wavelength $\lambda_L \approx 698$ nm resonantly interrogates the 1S_0 and 3P_0 states of the atoms and generates spin-orbit coupling (SOC) [103]. While the relative wavelengths of the lattice and clock lasers do not allow for weak SOC along all three lattice axes, weak SOC along two axes can be implemented by, for example, (i) fixing a large lattice depth along the z axis, effectively freezing atomic motion along z , and then (ii) making the clock laser nearly collinear with the z axis, with only a small projection of its wavenumber \mathbf{k}_L onto the x - y plane [see Figure 4.1(a)]. The entire 3D OLC then factorizes into an array of independent 2D systems with $N = f\ell^2$ atoms each, where ℓ is the number of lattice sites along each axis of the lattice. As in the 1D case, atoms within the 2D system experience all-to-all interactions, as well as spin-orbit coupling along two directions characterized by SOC angles $\phi_{x,y} = k_L^{x,y}a$. Generally speaking, higher-dimensional

systems (e.g. 2D vs. 1D) are more desirable because they allow packing more interacting atoms into a fixed system volume, thereby increasing the maximally attainable amount of spin squeezing.

Figure 4.3 shows, for both OAT and TAT protocols, the maximally attainable amount of spin squeezing and the shortest time at which it occurs as a function of the lattice depth V_0 and linear lattice size ℓ in a single half-filled 2D layer (i.e. $f = 1, N = \ell^2$) of the 3D OLC. Atoms are confined along the direction transverse to the 2D layer by a lattice of depth $60 E_R$, where E_R is the atomic lattice recoil energy. The maximally attainable amount of spin squeezing by each protocol in Figure 4.3 depends only on the atom number N , while the shortest attainable time is determined by choosing the largest SOC angles $\phi_x = \phi_y \equiv \phi$ which saturate $\tilde{B}/U \approx 0.05$. We impose this constraint on \tilde{B}/U to ensure validity of the OAT Hamiltonian perturbatively derived in Appendix 4.A (see also Appendix 4.B).

Currently, light scattering from the lattice beams induces decoherence of the clock on a time scale of ~ 10 seconds [7, 23], which is much shorter than the natural 3P_0 lifetime of ~ 160 seconds (see Appendix 4.F). This limitation imposes significant constraints on achievable spin squeezing, as shown in Figure 4.4 where the maximal squeezing with spin decay in the OAT case was determined using exact expressions for spin correlators derived in Ref. [120], while in the TAT case these correlators were determined by solving Heisenberg equations of motion for collective spin operators [3] (see Appendix 4.H). Due to the fast growth of Heisenberg operators in systems with all-to-all interactions, the latter method is not always capable of simulating up to the optimal squeezing time, and thus only provides a lower bound on the maximal squeezing theoretically obtainable via TAT.

The results in Figure 4.4 show that squeezing via OAT saturates with system size around $N \approx 10^3$ ($\ell \approx 30$), while TAT allows for continued squeezing gains through $N = 10^4$ ($\ell = 100$). Even with decoherence, our protocol may realistically generate ~ 10 – 14 dB of spin squeezing in ~ 1 second with $\sim 10^2$ – 10^4 atoms in a 2D section of the lattice, which is compatible with the atom numbers and interrogation times of state-of-the-art optical lattice clocks [42, 73]. This amount of spin squeezing exceeds those reported in the ground-state nuclear spin sublevels of a state-of-the-art

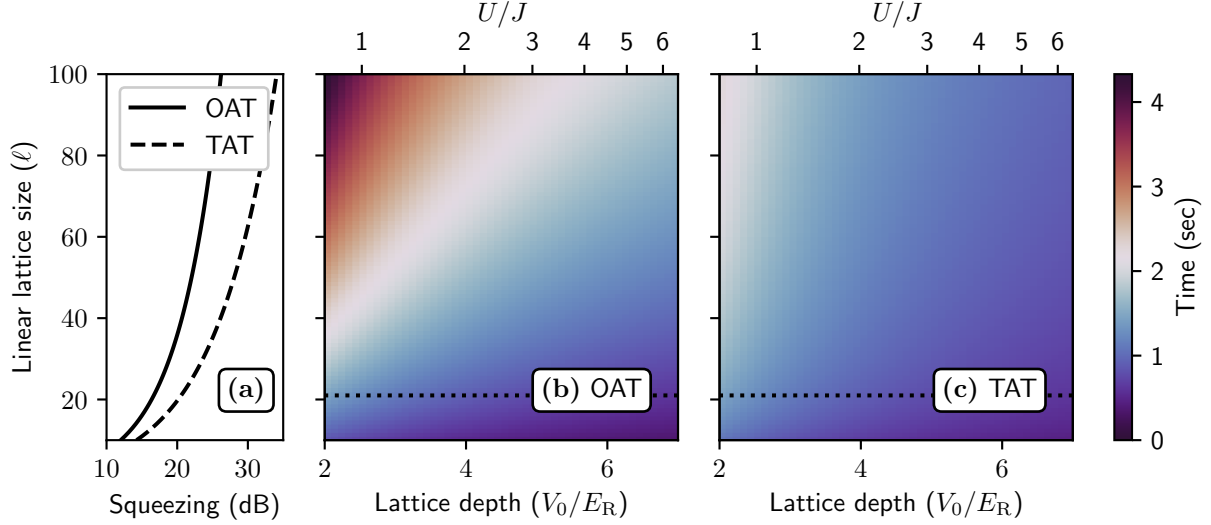


Figure 4.3: **Optimal squeezing** with one- and two-axis twisting in a 2D section of the 3D ^{87}Sr optical lattice clock. (a) The maximum amount of squeezing depends only on the atom number $N = \ell^2$, where ℓ is the number of lattice sites along each axis of the lattice. While the time scales for squeezing generally depend on several experimental parameters, the time at which maximal squeezing occurs can be minimized at any given lattice depth V_0 by choosing SOC angles ϕ that saturate $\tilde{B}/U \approx 0.05$, where \tilde{B} is the variance of the SOC-induced axial field and U is the two-atom on-site interaction energy. Panels (b, c) show these minimal squeezing times as a function of the depth V_0 and linear size ℓ of the lattice. Lattice depths V_0 are normalized to the atomic lattice recoil energy E_R , and the upper axis on panels (b, c) marks values of U/J at fixed lattice depths. In general, TAT achieves more squeezing than OAT for any system size, and achieves optimal squeezing faster for $N \gtrsim 400$ atoms, as denoted by a dotted line in panels (b, c).

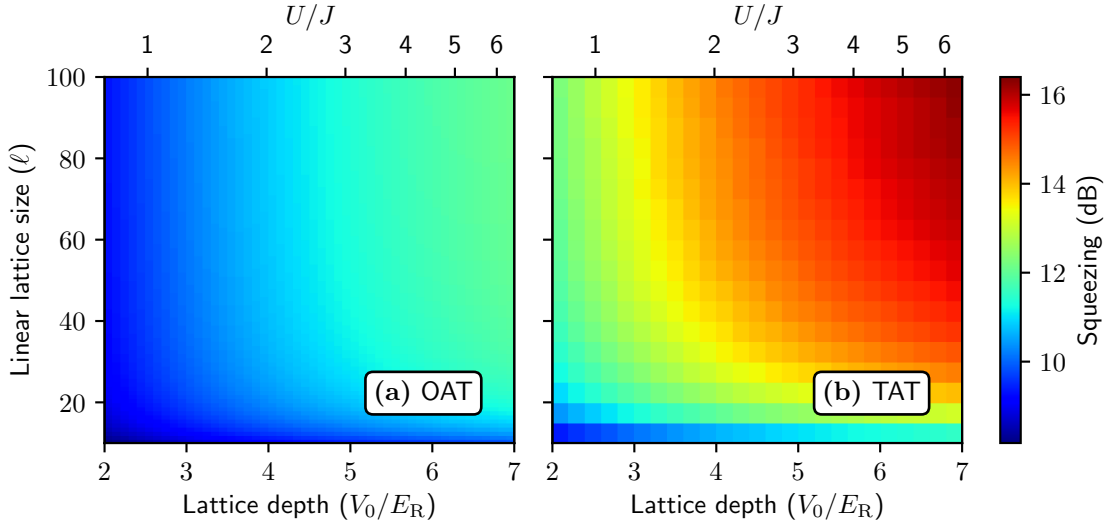


Figure 4.4: **Optimal squeezing with decoherence** via one- and two-axis twisting in a 2D section of the 3D ^{87}Sr optical lattice clock (OLC). In practice, decoherence due to light scattering limits the amount of squeezing that is attainable in the the 3D ^{87}Sr OLC. Due to growing squeezing times with increasing system size, the maximal squeezing obtainable via OAT saturates past $\ell \approx 30$ sites along each axis of the lattice, with $N \approx 10^3$ atoms total. The more favorable size-dependence of TAT time scales, however, allow for continued squeezing gains through $\ell = 100$ ($N = 10^4$). While the OAT results in (a) are exact, the TAT results in (b) reflect only a lower bound on the maximum squeezing obtainable, albeit one that is likely close (within a few dB) to the actual value. Optimal squeezing times in the presence of decoherence are generally smaller than the corresponding times shown in Figure 4.3, as decoherence typically degrades squeezing before it reaches the decoherence-free maximum. The decoherence considered in this work also limits maximally achievable squeezing to ~ 20 dB less than the decoherence-free maxima shown in Figure 4.3. Sample plots of squeezing over time for particular choices of lattice size (ℓ) and depth (V_0/E_R) are provided in Appendix 4.G.

^{171}Yb OLC (~ 6.5 dB) [121]. While the latter protocol might be used to transfer spin squeezing to the electronic clock state, to date there has been no demonstration of spin squeezing in an optical clock transition.

In addition to light scattering, p -wave losses from inelastic 3P_0 collisions [50, 53, 122] can also degrade the maximum achievable spin squeezing, which becomes more pronounced for shallower lattices. More details on p -wave losses are discussed in Appendix 4.J, where we show that operating at lattice depths $V_0 \gtrsim 7E_R$ may be necessary to suppress the impact of inelastic collisions on spin squeezing, at the cost of slightly increasing light scattering.

The sources of decoherence considered above are not fundamental, and can be avoided by, for instance, using two nuclear spin levels as spin-1/2 degrees of freedom that are interrogated by far-detuned Raman transitions instead of a direct optical transition [123]. The strength of SOC for Raman transitions is tunable and, moreover, the lifetimes of ground nuclear spin levels are longer than 100 seconds in the lattice [7]. In this case, our protocol for preparing a squeezed state would additionally end with a coherent state transfer from nuclear to electronic degrees of freedom to retain metrological utility for the atomic clock. If, for example, the $-9/2$ and $-7/2$ nuclear spin states are used for the preparation of a squeezed state, then the collective-spin entanglement of atoms can be transferred to electronic states at the end of the spin squeezing protocol with a σ^- polarized π pulse. Such a pulse can transfer $|g, -7/2\rangle$ to $|e, -9/2\rangle$ without affecting $|g, -9/2\rangle$, where g and e respectively denote the ground and excited (electronic) clock states.

4.4 Conclusions

We have proposed a new protocol to generate spin squeezing in a fermionic 3D optical lattice clock by combining nominally undesirable atomic collisions with spin-orbit coupling. To our knowledge, this is the first proposal to use quantum correlations in a many-body fermionic system to push state-of-the-art quantum sensors beyond the independent-particle regime, thereby achieving a genuine quantum advantage. Such capability could allow for major improvements in clock sensitivity and bandwidth, enhancing not only traditional timekeeping applications such as measurement

standards, navigation (GPS), and telecommunications, but also geodesy and gravitational wave detection, precision tests of fundamental physics, and the search for new physics beyond the standard model [18].

Acknowledgments

We acknowledge helpful discussions with M. Norcia, C. Sanner, and M. Mamaev. This work is supported by the Air Force Office of Scientific Research (AFOSR) grant FA9550-18-1-0319; the AFOSR Multidisciplinary University Research Initiative (MURI) grant; the Defense Advanced Research Projects Agency (DARPA) and Army Research Office (ARO) grant W911NF-16-1-0576; the National Science Foundation (NSF) grant PHY-1820885; JILA-NSF grant PFC-1734006; and the National Institute of Standards and Technology (NIST).

4.A Derivation of the effective one-axis-twisting model

Suppose we have a Hamiltonian of the form ($\hbar = 1$)

$$H = H_0 + V, \quad (4.6)$$

with

$$H_0 = -\frac{U}{L} \mathbf{S} \cdot \mathbf{S}, \quad V = -\sum_n B_n s_z^{(n)} + \Omega S_x, \quad (4.7)$$

and we consider N -particle states initially in the ground-state manifold \mathcal{G}_0 of H_0 , which have total spin $S = N/2$. If the largest eigenvalue of V is smaller in magnitude than half of the collective spin gap $NU/L = fU$, i.e. the energy gap under H_0 between \mathcal{G}_0 and its orthogonal complement \mathcal{E}_0 , then we can formally develop a perturbative treatment for the action of V on \mathcal{G}_0 . Such a treatment yields an effective Hamiltonian on \mathcal{G}_0 of the form $H_{\text{eff}} = \sum_p H_{\text{eff}}^{(p)}$, where $H_{\text{eff}}^{(p)}$ is order p in V . Letting \mathcal{P}_0 (\mathcal{Q}_0) be a projector onto \mathcal{G}_0 (\mathcal{E}_0), we define the super-operators \mathcal{O} and \mathcal{L} by

$$\mathcal{O}V \equiv \mathcal{P}_0 V \mathcal{Q}_0 + \mathcal{Q}_0 V \mathcal{P}_0, \quad \mathcal{L}V \equiv \sum_{\alpha, \beta} \frac{|\alpha\rangle\langle\alpha| \mathcal{O}V |\beta\rangle\langle\beta|}{E_\alpha - E_\beta}, \quad (4.8)$$

where $H_0 = \sum_\alpha E_\alpha |\alpha\rangle\langle\alpha|$. The first few terms in the expansion of the effective Hamiltonian H_{eff} are then, as derived in Ref. [80],

$$H_{\text{eff}}^{(0)} = \mathcal{P}_0 H_0 \mathcal{P}_0, \quad H_{\text{eff}}^{(1)} = \mathcal{P}_0 V \mathcal{P}_0, \quad (4.9)$$

and

$$H_{\text{eff}}^{(2)} = -\frac{1}{2} \mathcal{P}_0 [\mathcal{O}V, \mathcal{L}V]_- \mathcal{P}_0, \quad (4.10)$$

with $[X, Y]_- \equiv XY - YX$. The zero-order effective Hamiltonian $H_{\text{eff}}^{(0)} = H_0$ within the ground-state manifold. To calculate $H_{\text{eff}}^{(1)}$, we note that the ground-state manifold \mathcal{G}_0 is spanned by the Dicke states

$$|m\rangle \propto S_+^{N/2+m} |\downarrow\rangle^{\otimes n}, \quad S_+ \equiv \sum_n s_+^{(n)}, \quad (4.11)$$

in terms of which we can expand the collective spin-z operator as $S_z = \sum_m m |m\rangle\langle m|$. We can likewise expand the collective spin-x operator S_x in terms of x -oriented Dicke states $|m_x\rangle$ as $S_x = \sum_m m |m_x\rangle\langle m_x|$. The ground-state projector \mathcal{P}_0 onto \mathcal{G}_0 can be expanded in either basis as $\mathcal{P}_0 = \sum_m |m\rangle\langle m| = \sum_m |m_x\rangle\langle m_x|$. Defining the mean and residual fields

$$\bar{B} \equiv \frac{1}{N} \sum_n B_n, \quad b_n \equiv B_n - \bar{B}, \quad (4.12)$$

we can then write

$$V = - \sum_n (b_n + \bar{B}) s_z^{(n)} + \Omega S_x = - \sum_n b_n s_z^{(n)} - \bar{B} S_z + \Omega S_x, \quad (4.13)$$

and in turn

$$H_{\text{eff}}^{(1)} = \mathcal{P}_0 \left(- \sum_n b_n s_z^{(n)} - \bar{B} S_z + \Omega S_x \right) \mathcal{P}_0 = - \sum_n b_n \mathcal{P}_0 s_z^{(n)} \mathcal{P}_0 - \bar{B} S_z + \Omega S_x, \quad (4.14)$$

where we used the fact that $\mathcal{P}_0 S_{j=z,x} \mathcal{P}_0 = S_j$ within the ground-state manifold. By construction, the residual fields are mean-zero, i.e. $\sum_n b_n = 0$. Using the particle-exchange symmetry of the Dicke states, we can therefore expand

$$\sum_n b_n \mathcal{P}_0 s_z^{(n)} \mathcal{P}_0 = \sum_{n,m,m'} b_n |m\rangle\langle m| s_z^{(n)} |m'\rangle\langle m'| = \sum_n b_n \sum_{m,m'} |m\rangle\langle m| s_z^{(1)} |m'\rangle\langle m'| = 0, \quad (4.15)$$

which implies

$$H_{\text{eff}}^{(1)} = -\bar{B}S_z + \Omega S_x. \quad (4.16)$$

To calculate the second-order effective Hamiltonian $H_{\text{eff}}^{(2)}$, we let $\mathcal{B}_0(\mathcal{E}_0)$ denote an eigenbasis of H_0 for the excited subspace \mathcal{E}_0 , and set the ground-state energy to 0. We then define the operator

$$\mathcal{I} \equiv \sum_{|\alpha\rangle \in \mathcal{B}_0(\mathcal{E}_0)} \frac{|\alpha\rangle\langle\alpha|}{E_\alpha}, \quad (4.17)$$

which sums over projections onto excited states with corresponding energetic suppression factors, in terms of which we can write

$$H_{\text{eff}}^{(2)} = -\mathcal{P}_0 V \mathcal{I} V \mathcal{P}_0, \quad (4.18)$$

which is simply an operator-level version of the textbook expression for second-order perturbation theory. The only part of V which is off-diagonal with respect to the ground- and excited-state manifolds \mathcal{G}_0 and \mathcal{E}_0 is $-\sum_n b_n s_z^{(n)}$, and the individual spin operators in this remainder can only change the total spin S by at most 1. It is therefore sufficient to expand \mathcal{I} in a basis for states which span the image of \mathcal{G}_0 under all $s_z^{(n)}$ within the $S = N/2 - 1$ manifold. Such a basis is provided by the spin-wave states

$$|mk\rangle \propto \sum_{n=1}^N e^{2\pi i kn/N} s_+^{(n)} |m-1\rangle, \quad (4.19)$$

for $k = 1, 2, \dots, N-1$ [47]. Using the fact that all spin- z operators preserve the projection of total spin onto the z axis, we then have that

$$H_{\text{eff}}^{(2)} = -\frac{1}{fU} \sum_{m,k,n,n'} b_n b_{n'} |m\rangle\langle m| s_z^{(n)} |mk\rangle\langle mk| s_z^{(n')} |m\rangle\langle m|, \quad (4.20)$$

where the relevant matrix elements between the Dicke states and the spin-wave states are [47]

$$\langle m | s_z^{(n)} | mk \rangle = e^{2\pi i kn/N} \sqrt{\frac{(N/2)^2 - m^2}{N^2(N-1)}}, \quad (4.21)$$

which implies

$$H_{\text{eff}}^{(2)} = -\frac{1}{fU} \sum_m \frac{(N/2)^2 - m^2}{N^2(N-1)} |m\rangle\langle m| \times \sum_{k,n,n'} b_n b_{n'} e^{2\pi i k(n-n')/N}. \quad (4.22)$$

Using the fact that $\sum_n b_n = 0$, we can expand

$$\sum_{k,n,n'} b_n b_{n'} e^{2\pi i k(n-n')/N} = \sum_{n,n'} b_n b_{n'} \sum_{k=1}^{N-1} e^{2\pi i k(n-n')/N} = \sum_{n,n'} b_n b_{n'} \sum_{k=0}^{N-1} e^{2\pi i k(n-n')/N}, \quad (4.23)$$

where the sum over k vanishes for $n \neq n'$ and equals N when $n = n'$, so

$$\sum_{k,n,n'} b_n b_{n'} e^{2\pi i k(n-n')/N} = N^2 \tilde{B}^2, \quad (4.24)$$

where

$$\tilde{B}^2 \equiv \frac{1}{N} \sum_n b_n^2 = \frac{1}{N} \sum_n (B_n - \bar{B})^2. \quad (4.25)$$

We therefore have that

$$H_{\text{eff}}^{(2)} = - \sum_m \frac{(N/2)^2 - m^2}{(N-1) fU} \tilde{B}^2 |m\rangle\langle m|, \quad (4.26)$$

where the $(N/2)^2$ term contributes a global energy shift which we can neglect, while the m^2 term is proportional to $m^2 |m\rangle\langle m| = S_z^2$. In total, the effective Hamiltonian through second order in perturbation theory is thus

$$H_{\text{eff}} = -\frac{U}{L} \mathbf{S} \cdot \mathbf{S} - \bar{B} S_z + \Omega S_x + \chi S_z^2, \quad (4.27)$$

with

$$\chi \equiv \frac{\tilde{B}^2}{(N-1) fU}. \quad (4.28)$$

We benchmark the validity of this effective Hamiltonian via exact simulations of the spin [Eqn. (4.3)] and OAT [Eqn. (4.4)] Hamiltonians in a system of 20 spins, finding that the relative error in maximal squeezing (in dB) of the OAT model is less than 3% when $\tilde{B}/U < 0.06$ (see Appendix 4.B).

4.B Numerical benchmarking of the OAT model

Here we provide additional information about our benchmarking of the one-axis twisting model against the spin model. This benchmarking was performed via exact simulations of a 20-spin system. Figure 4.5 shows the relative error in maximal squeezing of the OAT model (measured

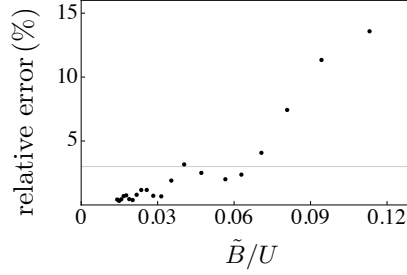


Figure 4.5: **Relative error** between maximal squeezing (measured in dB) obtained by the OAT [Eqn. (4.4)] and spin [Eqn. (4.3)] models of the main text in a system of 20 particles. The OAT model correctly captures the maximal squeezing (in dB) of the spin model to within 3% (marked by the horizontal reference line) within the gap-protected regime $\tilde{B}/U < 0.06$.

against the spin model) as a function of the reduced field variance \tilde{B}/U . Here squeezing is measured in decibels (dB) by $-10 \log_{10} \xi^2$ for the squeezing parameter ξ^2 define in Eqn. (4.5). The relative error in maximal squeezing (in dB) by the OAT model is less than 3% when $\tilde{B}/U < 0.06$.

In principle, spin-changing decoherence compromises the validity of the OAT model, as its perturbative derivation in Appendix 4.A relies on spin population remaining primarily within the Dicke manifold. This assumption breaks down in the presence of, for example, spontaneous emission, which transfers population outside of the Dicke manifold. Nonetheless, we find decent agreement between the OAT and spin models when decoherence is sufficiently weak (see Figure 4.6).

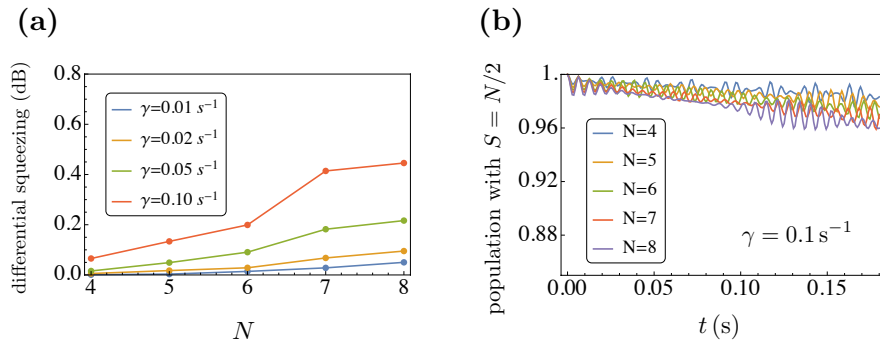


Figure 4.6: **Comparison between the OAT and the spin model in the presence of decoherence.** (a) The difference between the maximal squeezing (measured in dB) obtained by the OAT [Eqn. (4.4)] and spin [Eqn. (4.3)] models increases with the particle number N and the single-particle spontaneous emission rate γ . This disagreement is attributed in part to the fact that spontaneous emission transfers population of the collective spin state outside of the Dicke manifold, violating an assumption of the OAT model; see panel (b). The rate of population transfer outside of the Dicke manifold increases with both particle number and spontaneous emission rate. (Parameters for simulations in this figure: $U = 1000$ Hz, $J = 200$ Hz, and $\phi = \pi/20$).

4.C Two-axis twisting, decoherence, and the residual axial field

The protocol we use to transform one-axis twisting (OAT) into two-axis twisting (TAT) is as previously proposed in Ref. [119]; we provide a summary of this protocol here, in addition to some brief discussion of its implications for decoherence and the residual $\sim \mathbf{S} \cdot \mathbf{S}$ and $\sim S_z$ terms of our OAT protocol. The TAT protocol begins with the OAT Hamiltonian with a time-dependent transverse field,

$$H = \chi S_z^2 + \Omega(t) S_x, \quad \Omega(t) = \beta\omega \cos(\omega t), \quad (4.29)$$

where β is the modulation index of the driving field and the drive frequency $\omega \gg N\chi$, with N the total number of spins. Moving into the rotating frame of $\Omega(t) S_x$ subtracts this term from the Hamiltonian, and transforms operators \mathcal{O} as

$$\mathcal{O} \rightarrow U(t)^\dagger \mathcal{O} U(t), \quad (4.30)$$

where

$$U(t) \equiv \exp \left[-i \int_0^t d\tau \Omega(\tau) S_x \right] = \exp \left[-i\beta \sin(\omega t) S_x \right]. \quad (4.31)$$

In particular, the operators $\tilde{S}_\pm \equiv -S_z \pm iS_y$ (i.e. the raising and lowering operators in the x basis) transform simply as

$$\tilde{S}_\pm \rightarrow U^\dagger \tilde{S}_\pm U = e^{\pm i\beta \sin(\omega t)} \tilde{S}_\pm. \quad (4.32)$$

For any operator \mathcal{O} and drive frequency $\omega \gg \|\mathcal{O}\|$, where $\|\mathcal{O}\| \equiv \max_\psi \sqrt{\langle \psi | \mathcal{O}^\dagger \mathcal{O} | \psi \rangle}$ is the operator norm of \mathcal{O} (i.e. the magnitude of the largest eigenvalue of \mathcal{O}), we can generally make a secular approximation to say

$$e^{\pm im\beta \sin(\omega t)} \mathcal{O} = \sum_{n=-\infty}^{\infty} \mathcal{J}_n(\pm m\beta) e^{in\omega t} \mathcal{O} \approx \mathcal{J}_0(\pm m\beta) \mathcal{O} = \mathcal{J}_0(m\beta) \mathcal{O}, \quad (4.33)$$

where \mathcal{J}_n is the n -th order Bessel function of the first kind. Expanding $S_z^2 = \frac{1}{4} (\tilde{S}_+ + \tilde{S}_-)^2$, one can thus work out that the effective Hamiltonian in the rotating frame of the drive is

$$H_{\text{eff}} \approx \frac{\chi}{2} \left([1 + \mathcal{J}_0(2\beta)] S_z^2 + [1 - \mathcal{J}_0(2\beta)] S_y^2 \right). \quad (4.34)$$

Driving with a modulation index β for which $J_0(2\beta) = \pm 1/3$ then gives us the effective two-axis twisting Hamiltonians

$$H_{\text{eff}}^{(+)} = \frac{\chi}{3} (2S_z^2 + S_y^2) \simeq \frac{\chi}{3} (S_z^2 - S_x^2), \quad (4.35)$$

$$H_{\text{eff}}^{(-)} = \frac{\chi}{3} (S_z^2 + 2S_y^2) \simeq \frac{\chi}{3} (S_y^2 - S_x^2), \quad (4.36)$$

where \simeq denotes equality up to the addition of a term proportional to $\mathbf{S}^2 = S_z^2 + S_x^2 + S_y^2$, which is irrelevant in the absence of coherent coupling between states with different net spin. In a similar spirit, one can work out that single-spin operators transverse to the x -axis transform as

$$\tilde{s}_{\pm} \equiv \frac{1}{2} (-s_z \pm i s_y) \rightarrow U^\dagger \tilde{s}_{\pm} U = e^{\pm i\beta \sin(\omega t)} \tilde{s}_{\pm} \approx \mathcal{J}_0(\beta) \tilde{s}_{\pm}, \quad (4.37)$$

which implies that shifting into the rotating frame of the time-dependent drive takes

$$s_x \rightarrow s_x, \quad s_{y,z} \rightarrow \mathcal{J}_0(\beta) s_{y,z}, \quad (4.38)$$

and

$$s_{\pm} \rightarrow \frac{1}{2} [1 \pm \mathcal{J}_0(\beta)] s_+ + \frac{1}{2} [1 \mp \mathcal{J}_0(\beta)] s_-. \quad (4.39)$$

As the TAT Hamiltonians $H_{\text{eff}}^{(\pm)}$ are realized in a rotating frame, to properly account for decoherence throughout the TAT protocol one must transform jump operators according to Eqns. (4.38)-(4.39).

In practice, our protocols realize the OAT Hamiltonian in Eqn. (4.29) with additional $\sim \mathbf{S} \cdot \mathbf{S}$ and $\sim S_z$ terms [see Eqn. (4.27)]. The effect of the $\sim \mathbf{S} \cdot \mathbf{S}$ term is to generate a relative phase between states with different total spin S (with e.g. $S = N/2$ within the Dicke manifold). In the absence of coherent coupling between states with different total spin, therefore, the $\sim \mathbf{S} \cdot \mathbf{S}$ term has no effect on system dynamics. The $\sim S_z$ term, meanwhile, is important; the magnitude of this term (as measured by the operator norm) is generally comparable to that of the squeezing term χS_z^2 . Unlike in the case of OAT, S_z does not commute with the TAT Hamiltonians, so its effects cannot be eliminated by a single spin-echo π -pulse $\exp(-i\pi S_x)$ half way through the squeezing protocol. Nonetheless, we find that for $N = 10^2$ (10^3) atoms, ~ 5 (10) π -pulses in a CPMG

(Carr-Purcell-Meiboom-Gill) sequence [124, 125] suffice to mitigate the effects of the S_z term in the TAT protocol (see Appendix 4.D). Phase control over these pulses, specifically choices of whether to apply $\exp(\pm i\pi S_x)$ or $\exp(\pm i\pi S_y)$ in any given π -pulse, can be used to construct XY- n pulse sequences [126, 127] that are robust to pulse errors.

4.D Dynamical decoupling in the TAT protocol

The effective Hamiltonian resulting from a perturbative treatment of SOC is (see Appendix 4.A)

$$H_{\text{eff}} = -\frac{U}{L} \mathbf{S} \cdot \mathbf{S} - \bar{B} S_z + \Omega S_x + \chi S_z^2, \quad (4.40)$$

where U is a two-atom on-site interaction strength; L is the number of lattice sites; $\bar{B} \equiv \sum_n B_n/N$ is a residual axial field determined by the occupied quasi-momentum modes $\{n\}$ (with $|\{n\}| = N$ atoms total); Ω is the magnitude of a driving field; and χ is an effective OAT squeezing strength. The effect of the $\sim \mathbf{S} \cdot \mathbf{S}$ term is to generate a relative phase between states with different total spin S (where $S = N/2$ within the Dicke manifold). In the absence of coherent coupling between states with different total spin, therefore, the $\sim \mathbf{S} \cdot \mathbf{S}$ term has no effect on system dynamics, and we are safe to neglect it entirely.

In the parameter regimes relevant to our discussions in the main text, the operator norms of $\bar{B}\hat{S}_z$ and $\chi\hat{S}_z^2$ in Eqn. (4.40) will typically be comparable in magnitude. The OAT protocol sets $\Omega = 0$, and eliminates the effect of $\bar{B}\hat{S}_z$ with a spin-echo π -pulse $\exp(-i\pi\hat{S}_x)$ applied half way through the squeezing protocol. The TAT protocol, meanwhile, effectively takes $\chi\hat{S}_z^2 + \Omega\hat{S}_x \rightarrow \hat{H}_{\text{TAT}}^{(\pm)}$ (as defined in Appendix 4.C) and $\bar{B}\hat{S}_z \rightarrow \mathcal{J}_0(\beta_{\pm})\bar{B}\hat{S}_z$, where \mathcal{J}_0 is the zero-order Bessel function of the first kind and β_{\pm} is the modulation index of the amplitude-modulated driving field Ω , satisfying $\mathcal{J}_0(2\beta_{\pm}) = \pm 1/3$. Unlike in the case of OAT, \hat{S}_z does not commute with the TAT Hamiltonian, so its effect cannot be eliminated with a spin-echo. Nonetheless, this term can be eliminated with a dynamical decoupling pulse sequence that periodically inverts the sign of \hat{S}_z while preserving $\hat{H}_{\text{TAT}}^{(\pm)}$.

Figure 4.7 shows the maximal squeezing generated by $N = 10^2$ and 10^3 atoms via OAT, TAT,

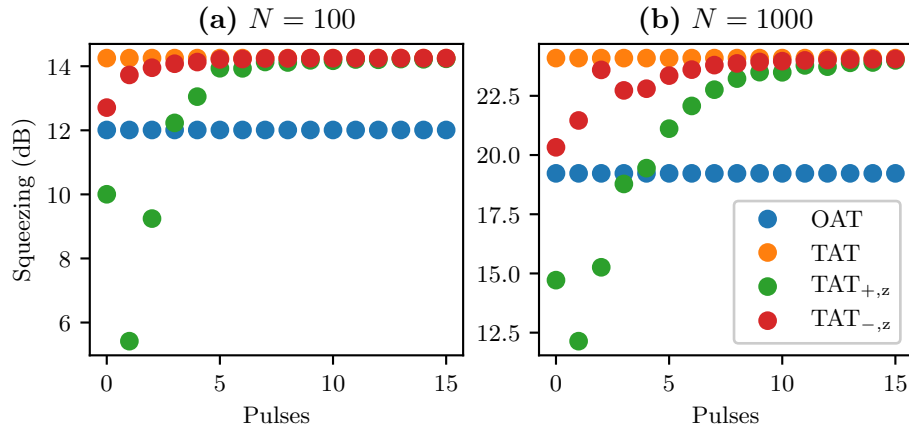


Figure 4.7: **Optimal squeezing as a function of π -pulses** applied prior to the optimal TAT squeezing time in a CPMG sequence with **(a)** $N = 100$ and **(b)** $N = 1000$ atoms. Results are shown for OAT, TAT, and $\text{TAT}_{\pm,z}$, where $\text{TAT}_{\pm,z}$ denotes squeezing via the Hamiltonian $\hat{H}_{\text{TAT}}^{(\pm,z)} \equiv \hat{H}_{\text{TAT}}^{(\pm)} - \mathcal{J}_0(\beta_{\pm}) \langle \bar{B} \rangle_f^{\text{rms}} \hat{S}_z$. Details about experimental parameters for these simulations are provided in the text.

and TAT in the presence of the mean field $\mathcal{J}_0(\beta_{\pm})\overline{B}\hat{S}_z$ as a function of the number of π -pulses performed prior to the optimal TAT squeezing time. These pulses are applied in a CPMG sequence $(\tau_n/2 - \pi_x - \tau_n/2)^n$, where $\tau_n/2$ denotes Hamiltonian evolution for a time $\tau_n/2$, π_x denotes the application of an instantaneous π -pulse $\exp(-i\pi\hat{S}_x)$, and n is the number of pulses, such that the optimal TAT squeezing time is $t_{\text{opt}}^{\text{TAT}} = (\tau_n)^n$. The label TAT $_{\pm,z}$ in Figure 4.7 denotes squeezing through the Hamiltonian $\hat{H}_{\text{TAT}}^{(\pm,z)} \equiv \hat{H}_{\text{TAT}}^{(\pm)} - \mathcal{J}_0(\beta_{\pm})\langle\overline{B}\rangle_f^{\text{rms}}\hat{S}_z$, where $\langle\overline{B}\rangle_f^{\text{rms}}$ is the root-mean-square average of \overline{B} over choices of occupied spacial modes $\{n\}$ at fixed filling f of all spatial modes in the lowest Bloch band of a periodic 2D lattice. While the modulation index β_+ is uniquely defined by $\mathcal{J}_0(2\beta_+) = 1/3$, there are two choices of β_- for which $\mathcal{J}_0(2\beta_-) = -1/3$; we use that which minimizes $|\mathcal{J}_0(\beta_-)|$. Figure 4.7 assumes an SOC angle $\phi = \pi/50$ (although results are independent of ϕ for $\phi \ll 1$), a reduced field variance $\tilde{B}/U = 0.05$, and a filling $f = 5/6$. Note that as the filling $f \rightarrow 1$, the residual axial field vanishes ($\overline{B} \rightarrow 0$), so TAT $_{\pm,z} \rightarrow$ TAT.

4.E Clock interrogation after squeezing

The protocols in our work concern the preparation of spin-squeezed states in an optical lattice clock. Here, we discuss the use of these states in a follow-up clock interrogation protocol. For simplicity, we restrict our discussion to the case of squeezing in 1D, as in Section 4.2 of the main text, with the understanding that a generalization of this discussion to higher dimensions is straightforward.

A spin-squeezed state is generated by interactions and SOC that are generally undesirable during the clock interrogation protocol. In the parameter regimes considered in our work, interactions alone have no effect on clock interrogation: absent of coherence between states with different net spin S , collective $\mathbf{S} \cdot \mathbf{S}$ interactions only generate unobservable global phases within each fixed- S sector of Hilbert space. Therefore, the remaining task to allow clock interrogation after spin squeezing is to turn off SOC, which inhomogeneously detunes atomic transition frequencies by an amount B_q that depends on the quasi-momentum q of an atom. The SOC-induced axial fields $B_q \sim J \sin(\phi/2)$ depend on two tunable parameters: the tunneling rate J and the SOC angle ϕ .

The simplest way to turn off SOC is thus to increase the lattice depth prior to clock interrogation, taking $J \sim B_q \rightarrow 0$. Increasing the lattice depth to turn off SOC is compatible with the current clock interrogation sequence, but is incompatible with ongoing efforts to mitigate light scattering from the lattice beams (currently the primary source of decoherence in the clock; see Appendix 4.F) by using shallower lattices [23]. We thus devote the rest of this section to discussing strategies for turning off SOC that are compatible with using the same lattice depth for clock interrogation as the spin squeezing generation.

If we cannot take the tunneling rate $J \rightarrow 0$, our remaining control parameter for turning off SOC is the SOC angle $\phi = k_L a$, where k_L is the projection of the clock laser wavenumber onto the lattice axis and a is the lattice spacing. The squeezing protocol needs a clock laser with a small but nonzero SOC angle $\phi \ll 1$, while the clock interrogation protocol requires a clock laser with $\phi = 0$. Simply using one clock laser with $\phi \neq 0$ for the squeezing protocol and another clock laser with $\phi = 0$ for the clock interrogation protocol, however, does not resolve this discrepancy, because a state that is squeezed with respect to spin operators that are homogeneous (i.e. of the form S_x, S_y, S_z) in a particular gauge is not necessarily squeezed with respect to spin operators that are homogeneous in a different gauge. In this appendix, we will work explicitly in the “lab gauge” of the clock interrogation protocol, in which the Fermi-Hubbard Hamiltonian is SOC-free and the $\phi = 0$ clock laser is homogeneous. To resolve the fact that our squeezing protocol prepares a state that is squeezed in the “wrong gauge”, we will construct a simple pulse sequence that transforms the inhomogeneous spin operators accessible by the $\phi \neq 0$ laser into a homogeneous form in our lab gauge.

Starting with a spin-down-polarized initial state

$$|-Z\rangle \equiv \left(\prod_j c_{j,\downarrow}^\dagger \right) |\text{vacuum}\rangle, \quad (4.41)$$

our OAT protocol prepares the state

$$|\xi_{\text{OAT}}^{(\theta)}\rangle = e^{-iH_{\text{FH}}^{(0)}t} e^{-i(\pi/2)S_x^{(\theta)}} |-Z\rangle, \quad (4.42)$$

where $H_{\text{FH}}^{(0)}$ is the Fermi-Hubbard Hamiltonian in Eqn. (4.2) without SOC; t is some free evolution time; and $S_x^{(\theta)}$ is the “rotated” spin- x -like generator induced by a clock laser with SOC angle $\phi = \theta$, namely

$$S_x^{(\theta)} = \frac{1}{2} \sum_j e^{i\theta j} c_{j,\uparrow}^\dagger c_{j,\downarrow} + \text{h.c.} \quad (4.43)$$

Defining on-site spin operators (in the lab gauge)

$$s_z^{(j)} \equiv \frac{1}{2} \left(c_{j,\uparrow}^\dagger c_{j,\uparrow} - c_{j,\downarrow}^\dagger c_{j,\downarrow} \right) \quad (4.44)$$

$$s_x^{(j)} \equiv \frac{1}{2} \left(c_{j,\uparrow}^\dagger c_{j,\downarrow} + c_{j,\downarrow}^\dagger c_{j,\uparrow} \right) \quad (4.45)$$

$$s_y^{(j)} \equiv \frac{i}{2} \left(c_{j,\downarrow}^\dagger c_{j,\uparrow} - c_{j,\uparrow}^\dagger c_{j,\downarrow} \right), \quad (4.46)$$

we can identify the rotated collective spin operators

$$S_x^{(\theta)} \equiv \sum_j \left(\cos(\theta j) s_x^{(j)} + \sin(\theta j) s_y^{(j)} \right), \quad (4.47)$$

$$S_y^{(\theta)} \equiv \sum_j \left(\cos(\theta j) s_y^{(j)} - \sin(\theta j) s_x^{(j)} \right). \quad (4.48)$$

The state $|\xi_{\text{OAT}}^{(\theta)}\rangle$ is squeezed with respect to components of the rotated collective spin vector $\mathbf{S}_\theta \equiv (S_x^{(\theta)}, S_y^{(\theta)}, S_z)$. Therefore, to take advantage of the squeezing in $|\xi_{\text{OAT}}^{(\theta)}\rangle$, the clock interrogation protocol effectively needs to rotate this state by some unitary $\exp(-i\boldsymbol{\eta} \cdot \mathbf{S}_\theta)$, and then extract information about the rotation vector $\boldsymbol{\eta}$ from collective spin observables of the form

$$\langle \mathcal{O}_\theta \rangle_{\text{OAT}}^\boldsymbol{\eta} \equiv \left\langle \xi_{\text{OAT}}^{(\theta)} \left| e^{i\boldsymbol{\eta} \cdot \mathbf{S}_\theta} \mathcal{O}_\theta e^{-i\boldsymbol{\eta} \cdot \mathbf{S}_\theta} \right| \xi_{\text{OAT}}^{(\theta)} \right\rangle, \quad (4.49)$$

where \mathcal{O}_θ is some product of the rotated collective spin operators in \mathbf{S}_θ , e.g. $S_x^{(\theta)}$ or $S_x^{(\theta)} S_y^{(\theta)}$. In order to turn off SOC during clock interrogation, however, we are restricted to performing rotations of the form $\exp(-i\boldsymbol{\eta} \cdot \mathbf{S}_0)$ and measuring homogeneous operators \mathcal{O}_0 . We thus seek a “gauge-switching” operation G_θ that maps homogeneous operators \mathcal{O}_0 onto rotated operators \mathcal{O}_θ via $G_\theta^\dagger \mathcal{O}_0 G_\theta = \mathcal{O}_\theta$. Equipped with G_θ , we could decompose

$$\langle \mathcal{O}_\theta \rangle_{\text{OAT}}^\boldsymbol{\eta} = \left\langle \xi_{\text{OAT}}^{(\theta)} \left| G_\theta^\dagger e^{i\boldsymbol{\eta} \cdot \mathbf{S}_0} \mathcal{O}_0 e^{-i\boldsymbol{\eta} \cdot \mathbf{S}_0} G_\theta \right| \xi_{\text{OAT}}^{(\theta)} \right\rangle = \left\langle \tilde{\xi}_{\text{OAT}}^{(\theta)} \left| e^{i\boldsymbol{\eta} \cdot \mathbf{S}_0} \mathcal{O}_0 e^{-i\boldsymbol{\eta} \cdot \mathbf{S}_0} \right| \tilde{\xi}_{\text{OAT}}^{(\theta)} \right\rangle \quad (4.50)$$

for a transformed state

$$\left| \tilde{\xi}_{\text{OAT}}^{(\theta)} \right\rangle \equiv G_\theta \left| \xi_{\text{OAT}}^{(\theta)} \right\rangle \quad (4.51)$$

that is now squeezed with respect to the homogeneous collective spin operators in \mathbf{S}_0 , accessible with the SOC-free ($\phi = 0$) clock laser used during clock interrogation.

Given the definitions of the rotated spin operators $S_x^{(\theta)}, S_x^{(\theta)}$ in Eqns. (4.47), (4.48), a suitable candidate for the gauge-switching operator G_θ is the site-dependent rotation

$$G_\theta = \prod_j \exp\left(i\theta j s_z^{(j)}\right). \quad (4.52)$$

To implement G_θ with “global” (i.e. non-site-selective) experimental controls, we decompose each local rotation into a product of two reflections:

$$\exp\left(i2\alpha s_z^{(j)}\right) \simeq \exp\left(i\pi s_x^{(j)}\right) \exp\left(i\pi s_\alpha^{(j)}\right) \quad (4.53)$$

where \simeq denotes equality up to an overall phase, and $s_\alpha^{(j)} \equiv \cos \alpha s_x^{(j)} + \sin \alpha s_y^{(j)}$. This decomposition implies

$$G_\theta \simeq \exp\left(i\pi S_x^{(0)}\right) \exp\left(i\pi S_x^{(\theta/2)}\right), \quad (4.54)$$

which can be implemented using one SOC-free ($\phi = 0$) clock laser, and one clock laser with SOC angle $\phi = \theta/2$. Appending the two π -pulses given by Eqn. (4.54) to our squeezing protocol thus prepares a state $\left| \tilde{\xi}_{\text{OAT}}^{(\theta)} \right\rangle$ that is squeezed with respect to the homogeneous collective spin operators S_x, S_y, S_z accessible to the SOC-free ($\phi = 0$) clock laser used during clock interrogation.

As presented, the combined squeezing and clock interrogation protocols require three clock lasers in total: one without SOC ($\phi = 0$), and one each for SOC angles $\phi \in \{\theta/2, \theta\}$. We can use G_θ , however, to decompose any pulse $\exp(-i\boldsymbol{\beta} \cdot \mathbf{S}_\theta)$ into composite pulses that use only \mathbf{S}_0 and $\mathbf{S}_{\theta/2}$:

$$\exp(-i\boldsymbol{\beta} \cdot \mathbf{S}_\theta) = G_\theta^\dagger \exp(-i\boldsymbol{\beta} \cdot \mathbf{S}_0) G_\theta. \quad (4.55)$$

The state prepared by the OAT squeezing protocol, for example, can be equivalently prepared via

$$\left| \xi_{\text{OAT}}^{(\theta)} \right\rangle = e^{-iH_{\text{FH}}^{(0)}t} G_{\theta}^{\dagger} e^{-i(\pi/2)S_x^{(0)}} G_{\theta} | -Z \rangle \simeq e^{-iH_{\text{FH}}^{(0)}t} e^{-i\pi S_x^{(\theta/2)}} e^{i(\pi/2)S_x^{(0)}} | -Z \rangle. \quad (4.56)$$

Spin-echo pulses applied throughout OAT can likewise be decomposed according to (4.55), eliminating the need for a clock laser with SOC angle $\phi = \theta$. Applying a continuous drive during a squeezing protocol, however, still requires all three clock lasers. If carefully tuning the relative orientations of three clock lasers proves to be too difficult in practice, converting OAT into TAT would therefore need to be done with a pulsed drive protocol, as in Ref. [118].

4.F Decoherence in the 3D ^{87}Sr optical lattice clock

Currently, light scattering from lattice beams in the 3D ^{87}Sr optical lattice clock induces decoherence on a time scale of ~ 10 seconds [7, 23]. This decoherence acts identically on all atoms in an uncorrelated manner, and can be understood by considering the density operator ρ for a single atom, with effective spin states \downarrow and \uparrow respectively corresponding to the $^1\text{S}_0$ and $^3\text{P}_0$ electronic states. Empirically, the effect of decoherence after a time t within the $\{\downarrow, \uparrow\}$ subspace of a single atom is to take $\rho \rightarrow \rho(t)$ with $\rho(0) \equiv \rho$ and

$$\rho(t) := \begin{pmatrix} \rho_{\uparrow\uparrow} e^{-\Gamma_{\uparrow\uparrow}t} & \rho_{\uparrow\downarrow} e^{-\Gamma_{\uparrow\downarrow}t} \\ \rho_{\uparrow\downarrow}^* e^{-\Gamma_{\uparrow\downarrow}t} & \rho_{\downarrow\downarrow} + (1 - e^{-\Gamma_{\uparrow\uparrow}t}) \rho_{\uparrow\uparrow} \end{pmatrix}, \quad (4.57)$$

where $\Gamma_{\uparrow\uparrow} \approx \Gamma_{\uparrow\downarrow} \approx \Gamma = 0.1 \text{ sec}^{-1}$ are respectively decay rates for $\rho_{\uparrow\uparrow}$ and $\rho_{\uparrow\downarrow}$. This form of decoherence can be effectively modeled by decay and dephasing of individual spins (respectively denoted Γ_{ud} and Γ_{el} in Ref. [120]) at rates Γ . In the language of the section that follows, we would say that this decoherence is captured by the sets of jump operators $\mathcal{J}_- \equiv \{s_-^{(j)}\}$ and $\mathcal{J}_z \equiv \{s_z^{(j)}\}$ with corresponding decoherence rates $\gamma_- = \gamma_z = \Gamma$.

4.G Time-series of squeezing via OAT and TAT

Figure 4.8 shows an example of squeezing over time via OAT and TAT, both with and without decoherence via decay and dephasing of individual spins. The OAT model initially generates

squeezing faster than the TAT model, but the squeezing generation rate of OAT (measured in dB per second) falls off with time. The squeezing generation rate for TAT, meanwhile, remains approximately constant (in the absence of decoherence) until squeezing via TAT surpasses that of OAT. In the absence of decoherence, OAT achieves a maximal amount of squeezing that scales as $\xi^2 \sim N^{-2/3}$, while TAT achieves Heisenberg-limited squeezing with $\xi^2 \sim N^{-1}$. Note that our method for computing squeezing via TAT in the presence of decoherence (described in Appendix 4.H) is not capable of computing squeezing for the full range of times shown in Figure 4.8; the corresponding time-series data in this figure is therefore shown up to the point at which this method breaks down.

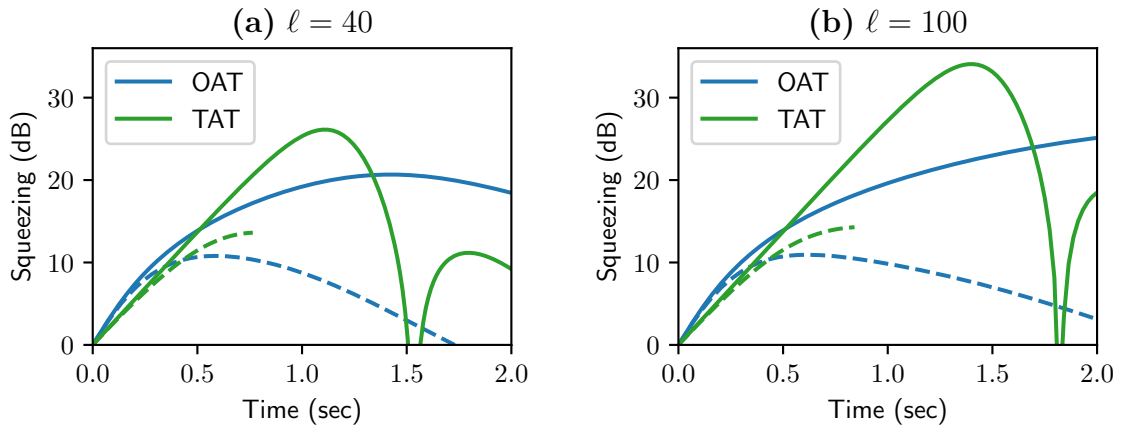


Figure 4.8: **Squeezing via OAT and TAT** in a 2D section of the 3D ^{87}Sr optical lattice clock, shown for (a) $\ell = 40$ and (b) $\ell = 100$ sites per axis (with $N = \ell^2$ atoms total), and a lattice depth of $V_0 = 4 E_R$, where E_R is the atomic lattice recoil energy. Atoms are confined along the direction transverse to the 2D layer by a lattice of depth $60 E_R$. Squeezing over time is shown for OAT (blue) and TAT (green), both with (solid lines) and without (dashed lines) decoherence via uncorrelated decay and dephasing of individual spins at rates of 0.1 sec^{-1} (see Appendix 4.F).

4.H Solving Heisenberg equations of motion for collective spin systems

In order to compute squeezing of a collective spin system, we need to compute expectation values of (homogeneous) collective spin operators. We compute these expectation values using a method recently developed in Ref. [3], and provide a short overview of the method here. Choosing the basis $\{\mathcal{S}_m\}$ for all collective spin operators, where $\mathcal{S}_m \equiv S_+^{m_+} S_z^{m_z} S_-^{m_-}$ with $\mathbf{m} \equiv (m_+, m_z, m_-) \in \mathbb{N}_0^3$, we can expand all collective spin Hamiltonians in the form

$$H = \sum_{\mathbf{m}} h_{\mathbf{m}} \mathcal{S}_m. \quad (4.58)$$

The evolution of a general correlator $\langle \mathcal{S}_n \rangle$ under a Hamiltonian of the form in Eqn. (4.58) is then given by

$$\frac{d}{dt} \langle \mathcal{S}_n \rangle = i \sum_{\mathbf{m}} h_{\mathbf{m}} \langle [\mathcal{S}_m, \mathcal{S}_n]_- \rangle + \sum_{\mathcal{J}} \gamma_{\mathcal{J}} \langle \mathcal{D}(\mathcal{J}; \mathcal{S}_n) \rangle \equiv \sum_{\mathbf{m}} \langle \mathcal{S}_m \rangle T_{mn}, \quad (4.59)$$

where $[X, Y]_{\pm} \equiv XY \pm YX$; \mathcal{J} is a set of jump operators with corresponding decoherence rate $\gamma_{\mathcal{J}}$; the decoherence operator \mathcal{D} is defined by

$$\mathcal{D}(\mathcal{J}; \mathcal{O}) \equiv \sum_{J \in \mathcal{J}} \left(J^\dagger \mathcal{O} J - \frac{1}{2} [J^\dagger J, \mathcal{O}]_+ \right); \quad (4.60)$$

and T_{mn} is a matrix element of the time derivative operator $T \equiv d/dt$. These matrix elements can be calculated analytically using product and commutation rules for collective spin operators. We can then expand correlators in a Taylor series about $t = 0$ to write

$$\langle \mathcal{S}_n \rangle = \sum_{k \geq 0} \frac{t^k}{k!} \left\langle \frac{d^k}{dt^k} \mathcal{S}_n \right\rangle_{t=0} = \sum_{k \geq 0} \frac{t^k}{k!} \sum_{\mathbf{m}} T_{mn;k} \langle \mathcal{S}_m \rangle_{t=0}, \quad (4.61)$$

where $T_{mn;k} \equiv [T^k]_{mn}$ are matrix elements of the k -th time derivative. Expectation values of collective spin operators can thus be computed via the expansion in Eqn. (4.61), which at short times can be truncated at some finite order beyond which all terms have negligible contribution to $\langle \mathcal{S}_n \rangle$.

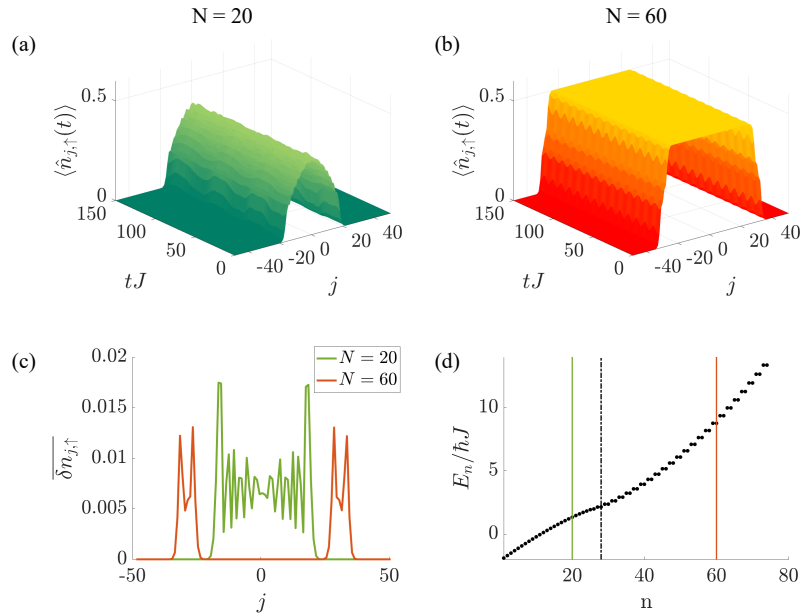


Figure 4.9: Dynamics of non-interacting spin-orbit coupled fermions in a 1D lattice with SOC angle $\phi = \pi/50$, plus a harmonic trap with $\Omega/J = 0.01$. Starting with a spin-polarized cloud in \downarrow ground state, an initial clock laser pulse is applied to rotate spins into x , and the atoms are allowed to evolve during the dark time. We track the dynamics of the \uparrow particle density for the cases of (a) $N = 20$ and (b) $N = 60$ atoms. Panel (c) shows the time-averaged fluctuations of the \uparrow particle density for each site index j from its initial value following the Ramsey pulse; see Eqn. (4.64). For $N = 60$, we have filled all delocalized modes as well as several localized modes, resulting in a large region of no density fluctuations at the trap center. Panel (d) contains the eigenspectrum for a single internal state in the presence of the trap (with the index n labeling the eigenvalues in order of increasing energy), where the critical mode n_c dividing the spatially delocalized and localized modes is indicated by a black dash-dotted line. The highest occupied mode in the \downarrow ground state for $N = 20$ and $N = 60$ is indicated by the green and red solid lines, respectively.

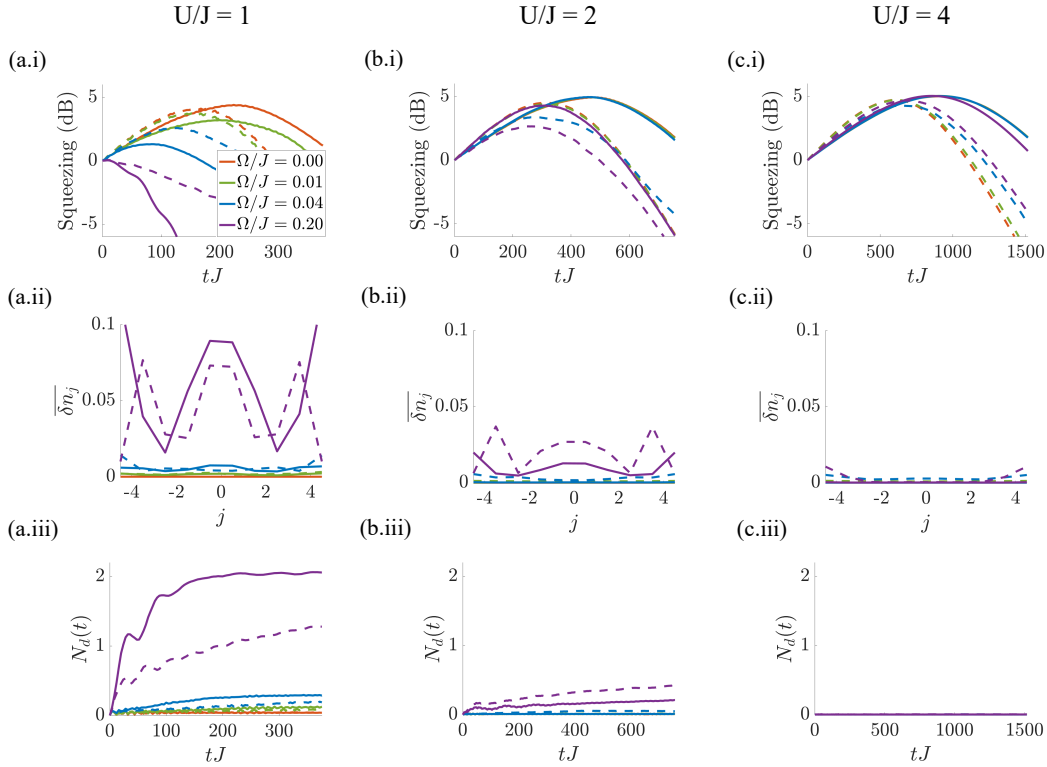


Figure 4.10: Dynamics of interacting spin-orbit coupled fermions in a 1D lattice plus a harmonic trap for $U/J = 1$ (a), 2 (b), and 4 (c). For a 1D lattice with 10 sites and an SOC angle $\phi = \pi/50$, we apply a $\pi/2$ clock laser pulse to the \downarrow ground state and let the system evolve during the dark time. In (a.i)-(c.i) we show the squeezing dynamics of the system for both $N = 10$ (solid lines) and $N = 9$ (dashed lines) for a variety of trapping strengths. In (a.ii)-(c.ii), we plot the time-averaged fluctuations in total particle density, δn_j (as in Eqn. (4.64) but with $\hat{n}_{j,\uparrow}$ replaced by $\sum_{\alpha} \hat{n}_{j,\alpha}$). In (a.iii)-(c.iii), we plot the growth of the doublon population $N_d(t)$ (see Eqn. (4.65)) as a function of time, noting the absence of squeezing in the presence of a large doublon population. For the chosen trap strengths, the corresponding values of n_c are 28 ($\Omega/J = 0.01$), 14 ($\Omega/J = 0.04$), and 6 ($\Omega/J = 0.2$). In panels where the results for the homogeneous case (orange curves) are not visible, they are nearly identical to the results for $\Omega/J = 0.01$ (green curves). Here, we utilize periodic boundary conditions to minimize finite size effects.

4.I Effect of a harmonic confining trap

Current 3D optical lattice implementations involve a harmonic confining potential, which significantly alters the underlying single-particle eigenstructure and can potentially degrade accessible squeezing within our protocol. In this appendix, we examine the effect of a harmonic trap on our protocol and discuss strategies to mitigate undesired effects. We model the trap by the addition of the term

$$\hat{H}_\Omega = \hbar\Omega \sum_{j,\alpha} (j - j_0)^2 \hat{n}_{j,\alpha} \quad (4.62)$$

to our Fermi-Hubbard model (Eqn. (4.2)), where j_0 denotes the trap center and $\Omega = m(\omega a)^2/2\hbar$ characterizes the trap strength for atom mass m , trap frequency ω , and lattice spacing a . In current state-of-the-art 3D ^{87}Sr OLC implementations, values of $\omega \approx 56 \times 2\pi \text{ sec}^{-1}$ can be achieved within each 2D layer of weak SOC by utilizing in-plane lattice depths of $5E_R$ and a lattice depth of $60E_R$ in the axial direction, resulting in a value of $\Omega/J \approx 0.01$. We restrict our discussion to 1D, although for a separable 3D lattice our arguments should extend in a straightforward manner.

We briefly review the structure of the single-particle eigenstates of the system, before discussing the effects on squeezing. In the quasi-momentum basis, the eigenfunctions $\psi_{n,\alpha}(q) = \langle q|n,\alpha \rangle$ are given by the π -periodic Mathieu functions, with the corresponding energies described by the Mathieu characteristic values [24]. In the presence of SOC, using the gauge transformation described in the main text, we obtain the relation

$$\psi_{n,\uparrow}(q) = \psi_{n,\downarrow}(q - \phi/a). \quad (4.63)$$

In contrast to the case of a pure harmonic potential, which generically has spatially delocalized single-particle eigenstates, the addition of a tight-binding lattice causes eigenmodes with quantum number n (index n labels the eigenvalues in order of increasing energy) larger than $n_c \approx 2\sqrt{2J/\Omega}$ to become localized at corresponding lattice sites. Therefore the sites at a distance $n_c/2$ from the trap center with potential energy $2\hbar J$ define the boundary between the delocalized modes at the trap center and the high-energy localized trap edges. Tunneling in the region of localized modes

is typically suppressed by large potential energy differences even in the presence of SOC. These modes are thus largely decoupled and do not contribute to the trap center dynamics. On the other hand the delocalized modes may be approximated by those of a quantum harmonic oscillator with effective mass $m^* = \hbar/(2Ja^2)$ and frequency $\omega^* = \sqrt{4J\Omega}$.

As emphasized in the main text, the key requirements for our protocol are 1) the validity of the spin model, which depends on the pinning of particles in their initial single particle modes, and 2) the gap protection against SOC dephasing, which arises from collective spin interactions. Concerning the latter point, it is desirable to maintain a weak trap so as to enable a large number of delocalized modes in the trap center, which are the only type capable of contributing to the generation of squeezing. Though the interactions between these modes are not strictly all-to-all, they remain long-ranged, and can thus still lead to a spin-locking effect and a protective gap [54, 115]. For $\Omega/J = 0.01$ we have $n_c = 28$, enabling $\sim 10^3$ contributing modes in each 2D layer of our system. Concerning the validity of the spin model, from a single-particle perspective the eigenmodes of our \uparrow states will be initially displaced in quasi-momentum space from equilibrium by ϕ/a as per Eqn. (4.63), and will generally undergo dipole oscillations and not remain strictly pinned to their initial modes. However, as long as we ensure the displacement is small enough to guarantee a constant density distribution across the trap center, the spin model will remain valid. The localized modes at the trap edges can actually help to satisfy this condition, since they can serve as a barrier against motion. This is demonstrated in Figure 4.9 where we show that filling all delocalized modes guarantees that the trap center maintains a constant density; we characterize this by the time-averaged fluctuations of the \uparrow density at each site j about its initial value following the Ramsey pulse,

$$\overline{\delta n_{j,\uparrow}} \equiv \sqrt{\lim_{t \rightarrow \infty} \frac{1}{t} \int_0^t d\tau \left(\langle \hat{n}_{j,\uparrow}(\tau) \rangle - \langle \hat{n}_{j,\uparrow}(0) \rangle \right)^2}, \quad (4.64)$$

choosing sufficiently large evolution times to ensure convergence.

In the presence of interactions, an additional point of concern is that the interplay between the trap and interactions may induce resonances that enable the formation of a significant doublon

population,

$$N_d(t) = \sum_j \langle \hat{n}_{j,\uparrow}(t) \hat{n}_{j,\downarrow}(t) \rangle, \quad (4.65)$$

which in turn may alter the density distribution and invalidate the spin model. Since doublon formation in the localized edges will not have consequences for our squeezing protocol, we must only ensure that doublons are not formed in the trap center, which requires $U > \Omega(n_c/2)^2 = 2J$ [117]. In Figure 4.10, we perform exact simulations to assess the effect of the trap on our system. Though restricted to small system sizes, the results demonstrate that for $U/J \lesssim 2$, the trap will always lead to a decrease of squeezing due to the formation of doublons in the trap center, while for $U/J \gtrsim 2$, we are protected from this process even for trap strengths much stronger than the experimentally relevant ones.

4.J Accounting for p -wave inelastic collisions

Inelastic 3P_0 (electronic state e or \uparrow) collisions are detrimental for optical lattice clocks. For the nuclear-spin-polarized gas discussed in this work, ee losses are only possible via the p -wave scattering channel since s -wave collisions are suppressed by Fermi statistics. The big advantage here compared to prior experiments done in a 1D lattice at μK temperature [50] is that in a Fermi degenerate gas loaded in a 3D optical lattice, p -wave losses are further suppressed by the centrifugal barrier and Pauli blocking, and only happen through a wave-function overlap between atoms at different lattice sites. In this appendix, we quantify the effect of p -wave interactions on squeezing. To account for p -wave losses, we describe the dynamics using a master equation for the system's density matrix $\hat{\rho}$:

$$\frac{d\hat{\rho}}{dt} = -\frac{i}{\hbar} [\hat{H}_{\text{eff}}, \hat{\rho}] + \mathcal{L}\hat{\rho}, \quad (4.66)$$

where $\hat{H}_{\text{eff}} = \chi \hat{S}_z^2$ is the effective one-axis twisting Hamiltonian obtained from the original Fermi-Hubbard Hamiltonian with spin-orbit coupling, and \mathcal{L} is the Lindblad superoperator that accounts for p -wave ee inelastic collisions. This latter term can be written using a pseudo-potential approx-

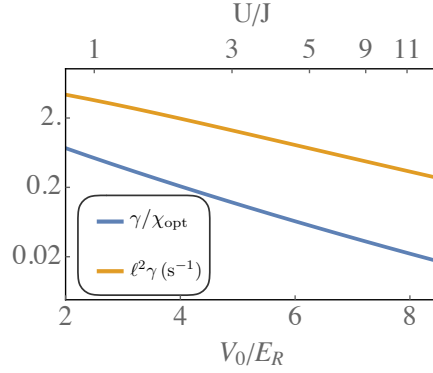


Figure 4.11: ***p*-wave loss rates.** Both the averaged *p*-wave inelastic collision rate γ (orange) and the ratio of this collision rate to the optimal squeezing rate χ_{opt} (blue) are suppressed as the lattice depth increases. χ_{opt} is obtained by choosing SOC angles ϕ that saturate $\tilde{B}/U \approx 0.05$, where \tilde{B} is the variance of the SOC-induced axial field and U is the two-atom on-site interaction energy.

imation as [54]:

$$\mathcal{L}\hat{\rho} = \sum_{\mathbf{k}\mathbf{k}'} \Gamma_{\mathbf{k}\mathbf{k}'} \left[\hat{A}_{\mathbf{k}\mathbf{k}'} \hat{\rho} \hat{A}_{\mathbf{k}\mathbf{k}'}^\dagger - \frac{1}{2} \left(\hat{A}_{\mathbf{k}\mathbf{k}'}^\dagger \hat{A}_{\mathbf{k}\mathbf{k}'} \hat{\rho} + \hat{\rho} \hat{A}_{\mathbf{k}\mathbf{k}'}^\dagger \hat{A}_{\mathbf{k}\mathbf{k}'} \right) \right], \quad (4.67)$$

where the jump operators are $\hat{A}_{\mathbf{k}\mathbf{k}'} = \hat{c}_{\mathbf{k},\uparrow} \hat{c}_{\mathbf{k}',\uparrow}$, and \mathbf{k}, \mathbf{k}' sum over all the populated quasi-momentum modes. The decay matrix elements $\Gamma_{\mathbf{k}\mathbf{k}'}$ are given by:

$$\Gamma_{\mathbf{k}\mathbf{k}'} = \frac{3\pi\hbar b_{\text{im}}^3}{m} \left(\int d\mathbf{r}^3 W[\phi_{\mathbf{k}}(\mathbf{r}), \phi_{\mathbf{k}'}(\mathbf{r})] \right), \quad (4.68)$$

where $b_{\text{im}} = 121a_0$ [7, 53] is the *p*-wave inelastic scattering length (with $a_0 = 5.29 \times 10^{-11}$ m the Bohr radius), $\phi_{\mathbf{k}}(\mathbf{r})$ is the Bloch function with quasi-momentum \mathbf{k} , and

$$W[\phi_{\mathbf{k}}(\mathbf{r}), \phi_{\mathbf{k}'}(\mathbf{r})] \equiv \left[(\nabla \phi_{\mathbf{k}}^*(\mathbf{r})) \phi_{\mathbf{k}'}^*(\mathbf{r}) - \phi_{\mathbf{k}}^*(\mathbf{r}) (\nabla \phi_{\mathbf{k}'}^*(\mathbf{r})) \right] \cdot \left[(\nabla \phi_{\mathbf{k}}(\mathbf{r})) \phi_{\mathbf{k}'}(\mathbf{r}) - \phi_{\mathbf{k}}(\mathbf{r}) (\nabla \phi_{\mathbf{k}'}(\mathbf{r})) \right] \quad (4.69)$$

In Figure 4.11, we show the averaged decay rate $\gamma \equiv \sum_{\mathbf{k}\mathbf{k}'} \Gamma_{\mathbf{k}\mathbf{k}'} / \ell^2$, where ℓ is the number of lattice sites along the *x* and *y* axes, as a function of the lattice depth V_0 along these axes. Here, we assume the same lattice depth in the *z* direction used in the main text, $V = 60E_R$. The decay rate γ is suppressed exponentially with increasing lattice depth V_0 . To quantify the effect of these losses on the spin squeezing generation process, we follow a similar methodology to the one described in detail

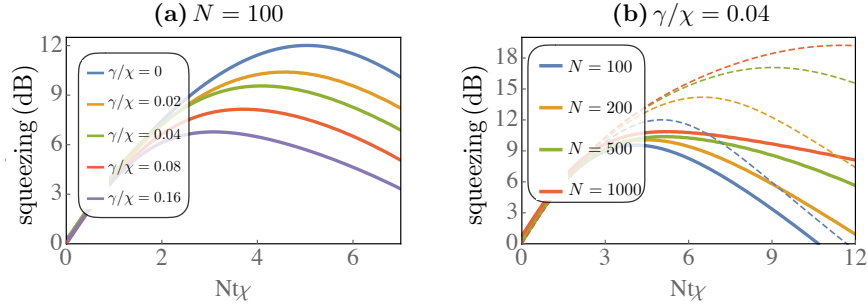


Figure 4.12: **Squeezing via OAT in the presence of inelastic collisions.** (a) For fixed particle number $N = 100$, the optimal squeezing decreases as the inelastic collision rate increases. Panel (b) shows squeezing over time for $\gamma/\chi_{\text{opt}} = 0.04$ (solid lines), which corresponds to $U/J = 6$, and compares it with $\gamma = 0$ (dashed lines) for different particle numbers. Inelastic collisions prevent the growth of optimal squeezing with particle number. For $N = 1000$, the maximum squeezing saturates to ~ 10 dB.

in Ref. [54]. The basic idea is to take advantage of the so-called Truncated-Wigner Approximation (TWA) [128, 129], which allows us to capture the development of spin squeezing using semi-classical phase-space methods. In the TWA the quantum dynamics are accounted for by solving mean field equations of motion supplemented by noise. The mean field equations are derived by assuming that the many-body density matrix of the system can be factorized as $\hat{\rho} = \bigotimes_i \hat{\rho}(i)$, where $\hat{\rho}(i)$ is the reduced density matrix of the particle in quasi-momentum mode \mathbf{q}_i [see Eqn. (4.57)]. Under this assumption, the non-linear mean field equations are given by

$$\frac{d\rho_{\uparrow\uparrow}(j)}{dt} = - \sum_{j'} \Gamma_{\mathbf{k}_j \mathbf{k}_{j'}} \rho_{\uparrow\uparrow}(j) \rho_{\uparrow\uparrow}(j'), \quad \frac{d\rho_{\downarrow\downarrow}(j)}{dt} = 0 \quad (4.70)$$

and

$$\frac{d\rho_{\uparrow\downarrow}(j)}{dt} = \rho_{\uparrow\downarrow}(j) \sum_{j'} \left[i\chi(\rho_{\uparrow\uparrow}(j') - \rho_{\downarrow\downarrow}(j')) - \frac{1}{2} \Gamma_{\mathbf{k}_j \mathbf{k}_{j'}} \rho_{\uparrow\uparrow}(j') \right], \quad (4.71)$$

where $\rho_{\sigma\sigma'} \equiv \langle \hat{\rho}_{\sigma\sigma'} \rangle$. Since we are interested in the collective behavior, one can define $\rho_{\sigma\sigma'}^T = \sum_j \rho_{\sigma\sigma'}(j)$. For these observables the equations of motion simplify to

$$\frac{d\rho_{\uparrow\uparrow}^T}{dt} = -f\gamma(\rho_{\uparrow\uparrow}^T)^2, \quad \frac{d\rho_{\downarrow\downarrow}^T}{dt} = 0 \quad (4.72)$$

and

$$\frac{d\rho_{\uparrow\downarrow}^T}{dt} = \rho_{\uparrow\downarrow}^T \left[i\chi(\rho_{\uparrow\uparrow}^T - \rho_{\downarrow\downarrow}^T) - \frac{1}{2}f\gamma\rho_{\uparrow\uparrow}^T \right], \quad (4.73)$$

where $f \equiv N/\ell^2$ is the filling fraction.

Under the TWA, one accounts for quantum fluctuations during the dynamics by averaging over different mean field trajectories generated by sampling over different initial conditions chosen to reconstruct the Wigner function of the initial coherent spin state at $t = 0$ [54]. This method has proven to be successful in simulating quantum spin dynamics. Using this approach, Figure 4.12 shows numerical simulation results of squeezing over time in the presence of inelastic collisions. For shallow lattices ($V_0 \lesssim 7E_R$), the effect of inelastic collisions can limit the spin squeezing to ~ 10 dB. Thus, in this regime, losses are as relevant as light scattering. The role of inelastic interactions could be mitigated by either operating at deeper lattices as shown in Figure 4.12, or by using nuclear spin states to generate the squeezing instead of the clock states directly.

Chapter 5

Short-time expansion of Heisenberg operators in open collective quantum spin systems

Prologue

Collective spin systems, which are invariant under permutations of their constituent spins, make frequent appearances as idealized models in atomic, molecular, and optical platforms (see, for example, Chapters 4, 6, and 7). The high degree of symmetry in these systems can make them numerically tractable in the mesoscopic regime of $10^2 - 10^5$ particles, which is typically inaccessible for exact simulations of quantum systems. These features make collective spins systems attractive models for theoretical and numerical studies of phenomena such as dynamical phase transitions and spin squeezing (i.e. quantum-enhanced metrology). The results shown in Figure 4.3, for example, were obtained via exact numerical simulations of collective spin systems. However, realistic systems in the laboratory typically break permutational symmetry, for example through incoherent decay and dephasing processes that kick the system out of the space of permutationally-symmetric states. In some cases, such as the Ising model, even these sorts of decoherence processes are analytically tractable, which enabled the calculation of exact numerical results in Figure 4.4(a). In other cases, one must resort to suitable approximation schemes or specialized techniques, where available. This chapter is about one such technique, which was essentially developed to calculate the results in Figure 4.4(b). The bulk of this chapter is taken from Ref. [3].

Abstract

We present an efficient method to compute short-time expectation values in large collective spin systems with typical forms of Markovian decoherence. Our method is based on a Taylor expansion of a formal solution to the equations of motion for Heisenberg operators. This expansion can be truncated at finite order to obtain virtually exact results at short times that are relevant for metrological applications such as spin squeezing. In order to evaluate the expansion for Heisenberg operators, we compute the relevant structure constants of a collective spin operator algebra. We demonstrate the utility of our method by computing spin squeezing, two-time correlation functions, and out-of-time-ordered correlators for 10^4 spins in strong-decoherence regimes that are otherwise inaccessible via existing numerical methods. Our method can be straightforwardly generalized to the case of a collective spin coupled to bosonic modes, relevant for trapped ion and cavity QED experiments, and may be used to investigate short-time signatures of quantum chaos and information scrambling.

5.1 Introduction

Collective spin systems are a versatile resource in quantum science for a range of applications including quantum-enhanced metrology and quantum simulation. The study of such systems dates back to the mid-twentieth century with the introduction of the Dicke model [30] that describes atoms cooperatively interacting with a single mode of a radiation field, and the Lipkin-Meshkov-Glick (LMG) model, a toy model for testing many-body approximation methods in contemporary nuclear physics [130–132]. On the experimental side, the development of advanced trapping, cooling, and control techniques in atomic, molecular, and optical (AMO) systems have enabled the realization of collective spin models in a broad range of platforms, including cold atomic gasses [133, 134], Bose-Einstein condensates [135–138], ultracold Fermi gasses [50, 104, 115], trapped ions [139], and optical cavities [114, 140–148], among others. These implementations compliment innumerable theoretical studies in a variety of rich subjects, including quantum phase transitions and criticality [149–152],

non-equilibrium phenomena [153–160], and precision metrology [2, 32, 33, 35, 119, 161–167].

One of the primary motivations for studying collective spin systems is their application to quantum-enhanced metrology. Quantum projection noise limits the error $\Delta\phi$ in the measurement of a phase angle ϕ with N independent spins to $\Delta\phi \sim 1/\sqrt{N}$ [32, 99]. Collective spin systems provide a means to break through this limit via the preparation of many-body entangled states such as spin-cat states [164, 168, 169] and most notably spin-squeezed states [32, 33, 35] that allow for measurement errors $\Delta\phi \sim 1/N^\varepsilon$ with $1/2 < \varepsilon \leq 1$, where $\varepsilon = 1$ saturates the Heisenberg limit [170]. Such entangled states can be prepared either via heralded methods such as quantum nondemolition measurements [133, 134, 140, 141], or via deterministic methods that require nonlinear dynamics, typically realized with phonon-mediated [139], photon-mediated [114, 135, 142–148] or collisional [50, 104, 115, 136–138] interactions. Although a truly collective spin model requires uniform, all-to-all interactions, as long as measurements do not distinguish between constituent particles, even non-uniform systems may be effectively described by a uniform model with renormalized parameters [171].

In the absence of decoherence, permutation symmetry and total spin conservation divide the total Hilbert space of a collective spin system into superselection sectors that grow only linearly with system size N , thereby admitting efficient classical simulation of its dynamics. Decoherence generally violates total spin conservation and requires the use of density operators, increasing the dimension of accessible state space to $O(N^3)$ [172, 173]. In this case, exact simulations can be carried out for $N \lesssim 100$ particles. If decoherence is sufficiently weak, dynamics can be numerically solvable for $N \lesssim 10^5$ particles via “quantum trajectory” Monte Carlo methods [174, 175] (also known as “quantum jump” or “Monte Carlo wavefunction” methods) that can reproduce all expectation values of interest. When decoherence is strong, however, these Monte Carlo methods can take a prohibitively long time to converge, as simulations become dominated by incoherent jumps that generate large numbers of distinct quantum trajectories that need to be averaged in order to accurately compute expectation values. Even with strong decoherence, dynamics are sometimes solvable through the cumulant expansion [176] that neglects all n -body connected correlators for

$n > 2$. The growth of genuinely multi-body correlations, however, eventually causes the cumulant expansion to yield incorrect results with no clear signature of failure. In the absence of other means to compute correlators, it can therefore be difficult to identify the point at which correlators computed via the cumulant expansion can no longer be trusted.

In this work, we present an efficient method to compute short-time dynamics of collective spin systems with typical forms of Markovian decoherence. The only restriction on decoherence (beyond Markovianity) is that, like the coherent collective dynamics, it must act identically on all constituent particles. Our method is based on a formal solution to the equations of motion for Heisenberg operators, thereby bearing some resemblance to the Mori formalism [177] and related work [178]. Specifically, we expand a formal solution for a Heisenberg operator into a Taylor series whose truncation can yield negligible error at sufficiently short times. Evaluating the resulting expansion requires knowing the structure constants of a collective spin operator algebra; the calculation of these structure constants (in Appendices 5.A–5.C) is one of the main technical results of this work, which we hope will empower both analytical and numerical studies of collective spin systems in the future. We benchmark our method against exact results from both analytical calculations and quantum trajectory Monte Carlo computations of spin squeezing in accessible parameter regimes, highlighting both advantages and limitations of the short-time expansion. Finally, we showcase applications of our method by computing quantities that are inaccessible to other numerical methods.

5.2 Theory

In this section we provide the basic theory for our method to compute expectation values of collective spin operators, deferring lengthy derivations to the appendices. We consider a system of N distinct spin-1/2 particles. Defining individual spin-1/2 operators $\hat{s}_{\alpha=x,y,z} \equiv \hat{\sigma}_\alpha/2$ and $\hat{s}_\pm \equiv \hat{s}_x \pm i\hat{s}_y = \hat{\sigma}_\pm$ with Pauli operators $\hat{\sigma}_\alpha$, we denote an operator that acts with \hat{s}_α on the spin indexed by j and trivially (i.e. with the identity $\hat{\mathbb{1}}$) on all other spins by $\hat{s}_\alpha^{(j)}$. We then define the collective spin operators $\hat{S}_\alpha \equiv \sum_{j=1}^N \hat{s}_\alpha^{(j)}$ for $\alpha \in \{x, y, z, +, -\}$. Identifying the set $\{\hat{\mathcal{S}}_m\}$ as a basis for all

collective spin operators, with $\mathbf{m} \equiv (m_+, m_z, m_-) \in \mathbb{N}_0^3$ and $\hat{\mathcal{S}}_{\mathbf{m}} \equiv \hat{S}_+^{m_+} \hat{S}_z^{m_z} \hat{S}_-^{m_-}$, we can expand any collective spin operator $\hat{\mathcal{O}}$ in the form

$$\hat{\mathcal{O}} = \sum_{\mathbf{m}} \mathcal{O}_{\mathbf{m}} \hat{\mathcal{S}}_{\mathbf{m}} \quad (5.1)$$

with scalar coefficients $\mathcal{O}_{\mathbf{m}} \in \mathbb{C}$. If $\hat{\mathcal{O}}$ is self-adjoint, for example, then $\mathcal{O}_{\mathbf{m}^*} = \mathcal{O}_{\mathbf{m}}$ with $\mathbf{m}^* \equiv (m_-, m_z, m_+)$. The corresponding Heisenberg operator is then $\hat{\mathcal{O}}(t) = \sum_{\mathbf{m}} \mathcal{O}_{\mathbf{m}}(t) \hat{\mathcal{S}}_{\mathbf{m}} + \hat{\mathcal{E}}_{\mathcal{O}}(t)$, with time-dependent coefficients $\mathcal{O}_{\mathbf{m}}(t)$ for time-independent Schrödinger operators $\hat{\mathcal{S}}_{\mathbf{m}}$, and mean-zero “noise” operators $\hat{\mathcal{E}}_{\mathcal{O}}(t)$ that result from interactions between the spin system and its environment, initially $\hat{\mathcal{E}}_{\mathcal{O}}(0) = 0$. These noise operators will essentially play no role in the present work, but are necessary to include for a consistent formalism of Heisenberg operators in an open quantum system; see Appendix 5.N for further discussion. The expectation values of Heisenberg operators evolve according to

$$\frac{d}{dt} \langle \hat{\mathcal{O}}(t) \rangle = \langle \check{T} \hat{\mathcal{O}}(t) \rangle = \sum_{\mathbf{m}, \mathbf{n}} \langle \hat{\mathcal{S}}_{\mathbf{m}} \rangle T_{\mathbf{m}\mathbf{n}} \mathcal{O}_{\mathbf{n}}(t) \quad (5.2)$$

with a Heisenberg-picture time derivative operator $\check{T} = d/dt$ whose matrix elements $T_{\mathbf{m}\mathbf{n}} \in \mathbb{C}$ are defined by

$$\check{T} \hat{\mathcal{S}}_{\mathbf{n}} \equiv i \left[\hat{H}, \hat{\mathcal{S}}_{\mathbf{n}} \right]_- + \sum_{\mathcal{J}} \gamma_{\mathcal{J}} \check{\mathcal{D}}(\mathcal{J}) \hat{\mathcal{S}}_{\mathbf{n}} = \sum_{\mathbf{m}} \hat{\mathcal{S}}_{\mathbf{m}} T_{\mathbf{m}\mathbf{n}}, \quad (5.3)$$

where $[X, Y]_{\pm} \equiv XY \pm YX$; \hat{H} is the collective spin Hamiltonian; \mathcal{J} is a set of jump operators with a corresponding decoherence rate $\gamma_{\mathcal{J}}$; and $\check{\mathcal{D}}$ is a Heisenberg-picture dissipator, or Lindblad superoperator, defined by

$$\check{\mathcal{D}}(\mathcal{J}) \hat{\mathcal{O}} \equiv \sum_{\hat{J} \in \mathcal{J}} \left(\hat{J}^\dagger \hat{\mathcal{O}} \hat{J} - \frac{1}{2} \left[\hat{J}^\dagger \hat{J}, \hat{\mathcal{O}} \right]_+ \right). \quad (5.4)$$

Decoherence via uncorrelated decay of individual spins, for example, would be described by the set of jump operators $\mathcal{J}_- \equiv \left\{ \hat{s}_-^{(j)} : j = 1, 2, \dots, N \right\}$. The commutator in Eq. (5.3) can be computed by expanding the product $\hat{\mathcal{S}}_{\ell} \hat{\mathcal{S}}_{\mathbf{m}} = \sum_{\mathbf{n}} f_{\ell\mathbf{m}\mathbf{n}} \hat{\mathcal{S}}_{\mathbf{n}}$ with structure constants $f_{\ell\mathbf{m}\mathbf{n}} \in \mathbb{R}$ that we work out in Appendices 5.A–5.C, and the effects of decoherence from jump operators (i.e. elements of

\mathcal{J}) of the form $\hat{g}^{(j)} = \sum_{\alpha} g_{\alpha} \hat{s}_{\alpha}^{(j)}$ and $\hat{G} = \sum_{\alpha} G_{\alpha} \hat{S}_{\alpha}$ are worked out in Appendices 5.D–5.G. We consider these calculations to be some of the main technical contributions of this work, with potential applications beyond the short-time simulation method presented here. These ingredients are sufficient to compute matrix elements T_{mn} of the time derivative operator \check{T} in Eq. (5.3) in most cases of practical interest.

We note that particle loss is an important decoherence mechanism in many experimental realizations of collective spin models [35]. In principle, a spin model has no notion of the particle annihilation operators that generate particle loss, and therefore cannot capture this effect directly. Nonetheless, for a system initially composed of N particles, the effect of particle loss can be emulated with $O(1/N)$ error by the dissipator \check{D}_{loss} defined by $\check{D}_{\text{loss}} \hat{S}_{\mathbf{m}} = -|\mathbf{m}| \hat{S}_{\mathbf{m}}$, where $|\mathbf{m}| \equiv \sum_{\alpha} m_{\alpha}$ (see Appendix 5.H). Furthermore, the effect particle loss can be accounted for exactly by (i) introducing an additional index on spin operators, $\hat{S}_{\mathbf{m}} \rightarrow \hat{S}_{N\mathbf{m}}$, to keep track of different sectors of fixed particle number within a multi-particle Fock space, and (ii) constructing jump operators that appropriately couple spin operators within different particle-number sectors. We defer a detailed exact accounting of particle loss to future work.

The time derivative operator \check{T} will generally couple spin operators $\hat{S}_{\mathbf{n}}$ to spin operators $\hat{S}_{\mathbf{m}}$ with higher “weight”, i.e. with $|\mathbf{m}| > |\mathbf{n}|$. The growth of operator weight signifies the growth of many-body correlations. Keeping track of this growth eventually becomes intractable, requiring us to truncate our equations of motion somehow. The simplest truncation strategy would be to take

$$\frac{d}{dt} \langle \hat{O}(t) \rangle \rightarrow \sum_{w(\mathbf{m}) < W} \langle \hat{S}_{\mathbf{m}} \rangle \sum_{\mathbf{n}} T_{mn} \mathcal{O}_{\mathbf{n}}(t) \quad (5.5)$$

for some weight measure w , e.g. $w(\mathbf{m}) = |\mathbf{m}|$, and a high-weight cutoff W . The truncation in Eq. (5.5) closes the system of differential equations defined by Eq. (5.2), and allows us to solve it using standard numerical methods. Some initial conditions for this system of differential equations, namely expectation values of collective spin operators with respect to spin-polarized (Gaussian) states that are generally simple to prepare experimentally, are provided in Appendix 5.I.

The truncation strategy in Eq. (5.5) has a few limitations: (i) simulating a system of differ-

ential equations for a large number of operators can be time-consuming, (ii) the weight measure w may need to be chosen carefully, as the optimal measure is generally system-dependent, and (iii) simulation results can only be trusted up to the time at which the initial values of operators $\hat{\mathcal{S}}_{\mathbf{m}}$ with weight $w(\mathbf{m}) \geq W$ have a non-negligible contribution to expectation values of interest. The last limitation in particular unavoidably applies in some form to any method tracking only a subset of all relevant operators. We therefore devise an alternate truncation strategy built around limitation (iii).

We can formally expand Heisenberg operators $\hat{\mathcal{O}}(t)$ in a Taylor series about the time $t = 0$ to write

$$\langle \hat{\mathcal{O}}(t) \rangle = \langle e^{t\tilde{T}} \hat{\mathcal{O}}(0) \rangle = \sum_{k \geq 0} \frac{t^k}{k!} \sum_{\mathbf{m}, \mathbf{n}} \langle \hat{\mathcal{S}}_{\mathbf{m}} \rangle T_{\mathbf{m}\mathbf{n}}^k \mathcal{O}_{\mathbf{n}}(0), \quad (5.6)$$

where the matrix elements $T_{\mathbf{m}\mathbf{n}}^k$ of the k -th time derivative operator \tilde{T}^k are

$$T_{\mathbf{m}\mathbf{n}}^0 \equiv \delta_{\mathbf{m}\mathbf{n}}, \quad T_{\mathbf{m}\mathbf{n}}^1 \equiv T_{\mathbf{m}\mathbf{n}}, \quad T_{\mathbf{m}\mathbf{n}}^{k > 1} \equiv \sum_{\mathbf{p}_1, \mathbf{p}_2, \dots, \mathbf{p}_{k-1}} T_{\mathbf{m}\mathbf{p}_{k-1}} \cdots T_{\mathbf{p}_3 \mathbf{p}_2} T_{\mathbf{p}_2 \mathbf{p}_1} T_{\mathbf{p}_1 \mathbf{n}}, \quad (5.7)$$

with $\delta_{\mathbf{m}\mathbf{n}} = 1$ if $\mathbf{m} = \mathbf{n}$ and zero otherwise. For sufficiently short times, we can truncate the series in Eq. (5.6) by taking

$$\langle \hat{\mathcal{O}}(t) \rangle \rightarrow \sum_{k=0}^M \frac{t^k}{k!} \sum_{\mathbf{m}, \mathbf{n}} \langle \hat{\mathcal{S}}_{\mathbf{m}} \rangle T_{\mathbf{m}\mathbf{n}}^k \mathcal{O}_{\mathbf{n}}(0). \quad (5.8)$$

We refer to Eq. (5.8) as the truncated short-time (TST) expansion of Heisenberg operators. Note that when computing an expectation value $\langle \hat{\mathcal{O}}(t) \rangle$, the relation $\hat{\mathcal{S}}_{\mathbf{m}}^\dagger = \hat{\mathcal{S}}_{\mathbf{m}^*}$, which by Hermitian conjugation of Eq. (5.2) also implies that $T_{\mathbf{m}^* \mathbf{n}^*} = T_{\mathbf{m}\mathbf{n}}^*$, cuts both the number of initial-time expectation values $\langle \hat{\mathcal{S}}_{\mathbf{m}} \rangle$ and the number of matrix elements $T_{\mathbf{m}\mathbf{n}}$ that we may need to explicitly compute roughly in half.

Unlike the weight-based truncation in Eq. (5.5), the nonzero matrix elements $T_{\mathbf{m}\mathbf{n}}^k$ for $k = 0, 1, \dots, M$ in Eq. (5.8) tell us which operators $\hat{\mathcal{S}}_{\mathbf{m}}$ are relevant for computing the expectation value $\langle \hat{\mathcal{O}}(t) \rangle$ to a fixed order M . The TST expansion thereby avoids the introduction of a weight measure w that chooses which operators to keep track of, and trades the cost of solving a system of

differential equations for the cost of computing expectation values $\langle \hat{S}_{\mathbf{m}} \rangle$ and matrix elements T_{mn}^k . In all cases considered in this work, we find that the TST expansion is both faster to evaluate and provides accurate correlators $\langle \hat{O}(t) \rangle$ until later times t than the weight-based expansion in (5.5) with weight measure $w(\mathbf{m}) = |\mathbf{m}|$ and cutoff $W \approx M$. We therefore restrict the remainder of our discussions to the TST expansion in Eq. (5.8), and provide a pedagogical tutorial for computing correlators using the TST expansion in Appendix 5.J.

Three primary considerations limit the maximum time t to which we can accurately compute a correlator $\langle \hat{S}_{\mathbf{n}}(t) \rangle$ using the TST expansion. First, maintaining accuracy at larger times t requires going to higher orders M in the TST expansion. An order- M TST expansion of the correlator $\langle \hat{S}_{\mathbf{n}}(t) \rangle$ can involve a significant fraction of operators $\hat{S}_{\mathbf{m}}$ with weight $|\mathbf{m}| \lesssim M$, which implies the need to compute $O(M^3)$ initial-time expectation values $\langle \hat{S}_{\mathbf{m}} \rangle$ and $O(M^4)$ matrix elements T_{mn}^k . In practice, with a straightforward implementation of the TST expansion we find that these requirements generally restrict $M \lesssim 50 - 70$ with 8 – 50 gigabytes of random access memory (RAM). Second, individual terms at high orders of the TST expansion in Eq. (5.8) can grow excessively large, greatly amplifying any numerical errors and thereby spoiling cancellations that are necessary to arrive at a physical value of a correlator, i.e. with $|\langle \hat{S}_{\mathbf{n}}(t) \rangle| \lesssim S^{|\mathbf{n}|}$ (where $S \equiv N/2$). Finally, the TST expansion is essentially perturbative in the time t , which implies that its validity as a formal expansion eventually breaks down. Precisely characterizing the implications of these last two considerations for the TST expansion requires additional analysis that we defer to future work. An investigation of connections between the TST expansion and past work related to the Mori formalism [177, 178], for example, might answer questions about the breakdown and convergence of the TST expansion. As we show from benchmarks of the TST expansion in Section 5.3, however, a detailed understanding of breakdown is not necessary to diagnose the breakdown time $t_{\text{break}}^{(M)}$ beyond which the TST expansion yields inaccurate results. Empirically, we find that going beyond order $M \approx 35$ yields no significant gains in all cases considered in this work.

5.3 Spin squeezing, benchmarking, and breakdown

To benchmark our method for computing collective spin correlators, we consider three collective spin models known to generate spin-squeezed states: the one-axis twisting (OAT), two-axis twisting (TAT), and twist-and-turn (TNT) models described by the collective spin Hamiltonians [35]

$$H_{\text{OAT}} = \chi \hat{S}_z^2, \quad (5.9)$$

$$H_{\text{TAT}} = \frac{\chi}{3} \left(\hat{S}_z^2 - \hat{S}_y^2 \right), \quad (5.10)$$

$$H_{\text{TNT}} = \chi \hat{S}_z^2 + \Omega \hat{S}_x, \quad (5.11)$$

where we include a factor of 1/3 in the TAT Hamiltonian because it naturally appears in realistic proposals to experimentally implement TAT [118, 119]. For simplicity, we further fix $\Omega = \chi S$ (with $S \equiv N/2$ throughout this work) to the critical value known to maximize the entanglement generation rate of TNT in the large- N limit [179, 180].

Note that the OAT model is a special case of the zero-field Ising model, whose quantum dynamics admits an exact analytic solution even in the presence of decoherence [120]. The approximate and numerics-oriented TST expansion is therefore an inappropriate tool for studying the OAT model, which will merely serve as an exactly solvable benchmark of our methods. Wherever applicable, we will provide exact results for the OAT model (see Appendix 5.K, as well as the Supplementary Material of Ref. [139]).

The Hamiltonians in Eqs. (5.9)–(5.11) squeeze the initial product state $|X\rangle \propto (|\uparrow\rangle + |\downarrow\rangle)^{\otimes N}$ with $\hat{S}_x |X\rangle = S |X\rangle$. Our measure of spin squeezing is the directionally-unbiased Ramsey squeezing parameter determined by the maximal gain in resolution $\Delta\phi$ of a phase angle ϕ over that achieved by any spin-polarized product state (e.g. $|X\rangle$) [32, 35],

$$\xi^2 \equiv \frac{(\Delta\phi_{\min})^2}{(\Delta\phi_{\text{polarized}})^2} = \frac{N}{|\langle \hat{\mathbf{S}} \rangle|^2} \min_{\substack{\mathbf{v} \perp \langle \hat{\mathbf{S}} \rangle \\ \mathbf{v} \cdot \mathbf{v} = 1}} \left\langle \left(\hat{\mathbf{S}} \cdot \mathbf{v} \right)^2 \right\rangle, \quad (5.12)$$

where $\hat{\mathbf{S}} \equiv (\hat{S}_x, \hat{S}_y, \hat{S}_z)$ is a collective spin operator-valued vector, the minimization is performed over all unit vectors \mathbf{v} orthogonal to the mean spin vector $\langle \hat{\mathbf{S}} \rangle$, and for brevity we have suppressed

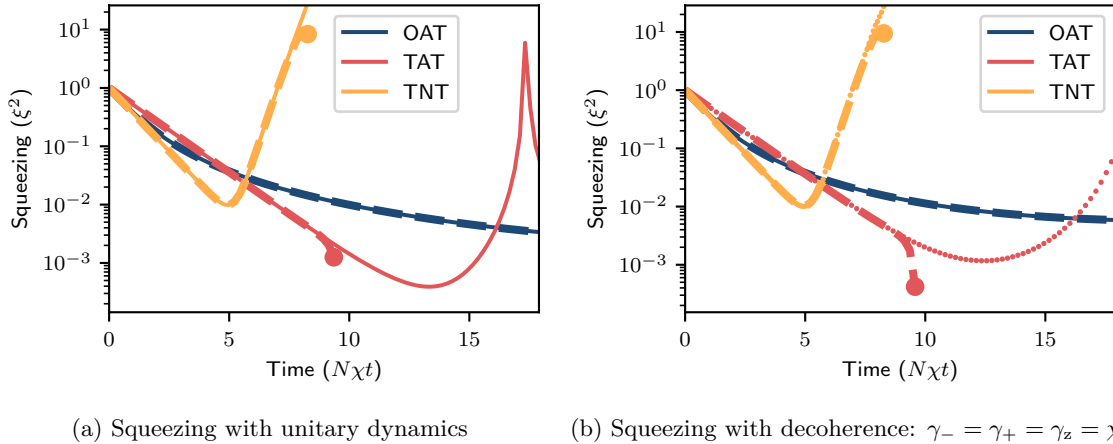


Figure 5.1: Spin squeezing of $N = 10^4$ spins initially in $|X\rangle$ under (a) unitary and (b) non-unitary dynamics, computed using exact methods (solid lines), quantum trajectory simulations (dots), and the TST expansion in Eq. (5.8) with $M = 35$ (dashed lines). Solid circles mark the times at which the TST expansion gives an unphysical result with $\xi^2 < 0$.

the explicit time dependence of operators in Eq. (5.12). This squeezing parameter is entirely determined by one- and two-spin correlators of the form $\langle \hat{S}_\alpha \rangle$ and $\langle \hat{S}_\alpha \hat{S}_\beta \rangle$. For the unitary dynamics discussed in this work, these correlators are obtainable via exact simulations of quantum dynamics in the $(N + 1)$ -dimensional Dicke manifold of states $\{|S, m\rangle\}$ with net spin S and spin projection m onto the z axis, i.e. with $\langle S, m | \hat{S}^2 | S, m \rangle = S(S + 1)$ and $\langle S, m | \hat{S}_z | S, m \rangle = m$ for $m \in \{-S, -S + 1, \dots, S\}$. In the presence of single-spin or collective decoherence, meanwhile, these correlators are obtainable with the collective-spin quantum trajectory Monte Carlo method developed in Ref. [175]. In this work, these exact and quantum trajectory simulations will be used to benchmark the TST expansion in Eq. (5.8).

Figure 5.1 compares the squeezing parameter ξ^2 for $N = 10^4$ spins initially in the state $|X\rangle$ evolved under the Hamiltonians in Eqs. (5.9)–(5.11), as computed via both benchmarking simulations and the TST expansion in Eq. (5.8) with $M = 35$. Squeezing is shown for both unitary dynamics (Figure 5.1a), as well as non-unitary dynamics in the presence of spontaneous decay, excitation, and dephasing of individual spins at rates χ (Figure 5.1b), respectively described by the sets of jump operators $\mathcal{J}_\alpha \equiv \{\hat{s}_\alpha^{(j)}\}$ with corresponding decoherence rates $\gamma_\alpha = \chi$ for $\alpha \in \{-, +, z\}$.

The results shown in Figure 5.1 were computed in a rotated basis with $(\hat{s}_z, \hat{s}_x) \rightarrow (\hat{s}_x, -\hat{s}_z)$ and $|X\rangle \rightarrow |-Z\rangle \equiv |\downarrow\rangle^{\otimes N}$, as well as appropriate transformations of the Hamiltonian and jump operators. The only effects of this rotation on the results presented in Figure 5.1 are to (i) reduce the time it takes to compute correlators $\langle \hat{O}(t) \rangle$ with the TST expansion, and (ii) prolong the time for which the TST expansion of TNT results agree with benchmarking simulations. The speedup in a different basis occurs because for the initial state $|-Z\rangle$, all initial-time correlators $\langle \hat{S}_m \rangle$ are zero unless $m_+ = m_- = 0$, and all non-zero correlators take $O(1)$ (i.e. constant in N) time to compute, rather than $O(N)$ time (see Appendix 5.I). In total, the use of a rotated basis reduces the computation time of initial-time correlators from $O(M^3N)$ to $O(M)$. The reason for prolonged agreement of TNT results in a rotated basis is not entirely understood, and provides a clue into the precise mechanism by which the TST expansion breaks down (discussed below). We defer a detailed study of this breakdown to future work.

The main lesson from Figure 5.1 is that the TST expansion yields essentially exact results right up until a sudden and drastic departure that can be diagnosed by inspection. The breakdown of the TST expansion in Figure 5.1 induces an unphysical squeezing parameter $\xi^2 < 0$. In general, however, there is no fundamental relationship between the breakdown of the TST expansion and the conditions for a physical squeezing parameter ξ^2 . A proper diagnosis of breakdown therefore requires inspection of the correlators $\langle \hat{S}_n(t) \rangle$ used to compute the squeezing parameter ξ^2 , which upon breakdown will rapidly take unphysical values with $|\langle \hat{S}_n(t) \rangle| \gtrsim S^{|n|}$ (see Appendix 5.L for an example). The sudden and drastic departure from virtually exact results is consistent with the limitations of the TST expansion discussed at the end of Section 5.2. Specifically, we identify three possible mechanisms for breakdown: (i) a rapid growth in the order M necessary for the TST expansion to converge, (ii) the growth of numerical errors in excessively large terms of the TST expansion, and (iii) the formal breakdown of the perturbative expansion in the time t . In all of these cases, a detailed cancellation eventually ceases to occur between large terms at high orders in the TST expansion. These large terms grow with the time t raised to some large power (as high as M), and therefore rapidly yield wildly unphysical results. In contrast to other approximate methods

such as the cumulant expansion [176], the TST expansion can thus diagnose its own breakdown, which is an important feature when working in parameter regimes that are inaccessible via other means to compute correlators. Note that, due to the breakdown mechanisms of the TST expansion, going up through order $M = 70$ does not significantly increase the breakdown time $t_{\text{break}}^{(M)}$ in Figure 5.1, and in some cases even shortens $t_{\text{break}}^{(M)}$.

Although the TST expansion breaks down at short times, it has two key advantages over the quantum trajectory Monte Carlo method to compute correlators in the presence of decoherence. First, computing spin correlators with the TST expansion is generally faster and requires fewer computing resources. The TST expansion results in Figure 5.1b, for example, take ~ 10 seconds to compute with a single CPU on modern computing hardware. The quantum trajectory Monte Carlo results in the same figure, meanwhile, take $\sim 10^4$ CPU hours to compute on similar hardware; the bulk of this time is spent performing sparse matrix-vector multiplication, leaving little room to further optimize serial runtime. Parallelization can reduce actual runtime of the Monte Carlo simulations to ~ 10 hours by running all trajectories at once, but at the cost of greatly increasing computing resource requirements. Though it may be possible to further speed up quantum trajectory Monte Carlo simulations by introducing new truncation schemes, any modifications (i) should be made carefully to ensure that simulations still yield correct results, and (ii) are unlikely to bridge the orders of magnitude in computing resource requirements.

The second advantage of the TST expansion is the capability to compute spin correlators in strong-decoherence regimes of large systems that are entirely inaccessible to other methods. As an example, Figure 5.2 shows squeezing of $N = 10^4$ spins initially in $|X\rangle$, undergoing spontaneous decay, excitation, and dephasing of individual spins at rates $\gamma_- = \gamma_+ = \gamma_z = 100\chi$. The system size in these simulations is too large for straightforward application of exact methods for open quantum systems. Quantum trajectory Monte Carlo simulations, meanwhile, take a prohibitively long time to converge with such strong decoherence due to the multiplicity of quantum trajectories that require averaging.

The results in Figure 5.2 show that the TNT model can generate more squeezing than the

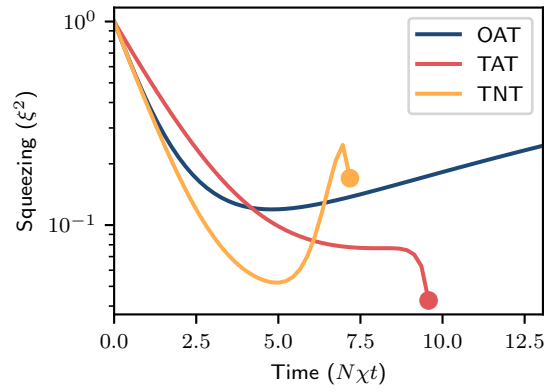


Figure 5.2: Spin squeezing of $N = 10^4$ spins initially in $|X\rangle$ with spontaneous decay, excitation, and dephasing of individual spins at rates $\gamma_- = \gamma_+ = \gamma_z = 100\chi$. Computed using the TST expansion in Eq. (5.8) with $M = 35$. Solid circles mark the times at which the TST expansion gives an unphysical result with $\xi^2 < 0$.

OAT or TAT models in the presence of strong decoherence. The better performance of TNT is in part a consequence of the fact that TNT initially generates squeezing at a faster rate than OAT or TAT, thereby allowing it to produce more squeezing before the degrading effects of decoherence kick in. We corroborate this finding with quantum trajectory simulations of a smaller system in Appendix 5.M. Strong-decoherence computations of the sort used for Figure 5.2 put lower bounds on theoretically achievable spin squeezing via TAT with decoherence in Ref. [2], exemplifying a concrete and practical application of the TST expansion and the collective-spin structure constants calculated in this work.

5.4 Two-time correlation functions and out-of-time-ordered correlators

As a final example of collective-spin physics that is numerically accessible via the TST expansion of Heisenberg operators, we consider the calculation of two-time correlation functions and out-of-time-ordered correlators (OTOCs). In particular, we consider the effect of decoherence on short-time behavior of the two-time connected correlator

$$C(t) \equiv \frac{1}{S} \left(\langle \hat{S}_+(t) \hat{S}_-(0) \rangle - \langle \hat{S}_+(t) \rangle \langle \hat{S}_-(0) \rangle \right), \quad (5.13)$$

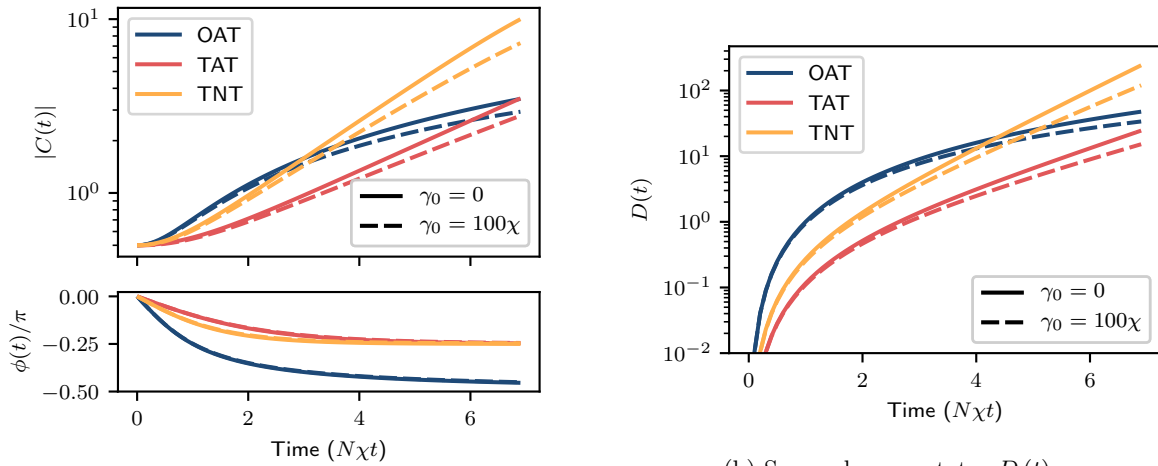
and the expectation value of a squared commutator,

$$D(t) \equiv \frac{1}{S^2} \left\langle \left[\hat{S}_+(t), \hat{S}_-(0) \right]_-^\dagger \left[\hat{S}_+(t), \hat{S}_-(0) \right]_- \right\rangle_{\text{nn}}, \quad (5.14)$$

in the context of the squeezing models in Section 5.3. The subscript on $\langle \cdot \rangle_{\text{nn}}$ in Eq. (5.14) stands for “no noise”, and denotes a correlator computed without the noise contributions $\hat{\mathcal{E}}_{\mathcal{O}}(t)$ to Heisenberg operators $\hat{\mathcal{O}}(t)$. While linear contributions from noise operators as e.g. in Eq. (5.13) always vanish under Markovian decoherence (see Appendix 5.N), quadratic contributions that would otherwise appear in Eq. (5.14) generally do not [181]. Determining the effect of these noise terms generally requires making additional assumptions about the environment, which would be a digression for the purposes of the present work. We therefore exclude these noise terms in (5.14) in order to keep our discussion simple and general; see Ref. [181] for more detailed discussions of noise terms and the quantum regression theorem underlying the calculation of multi-time correlators.

In an equilibrium setting, correlation functions similar to that in Eq. (5.13) contain information about the linear response of Heisenberg operators to perturbations of a system; in a non-equilibrium setting, they contribute to short-time linear response (see Appendix 5.O). Similar correlators have made appearances as order parameters for diagnosing time-crystalline phases of matter [182]. Squared commutators such as that in Eq. (5.14), meanwhile, are commonly examined for signatures of quantum chaos and information scrambling [183–185]. In typical scenarios, such squared commutators initially vanish by construction through a choice of spatially separated operators. Collective spin systems, however, have no intrinsic notion of locality or spatial separation. In our case, therefore, with the choice of initial state $|X\rangle \propto (|\uparrow\rangle + |\downarrow\rangle)^{\otimes N}$ we merely have $D(0) \sim 1/N$.

Figure 5.3 shows the behavior of $C(t)$ and $D(t)$ for $N = 10^4$ spins, initially in the state $|X\rangle$, evolving under the squeezing Hamiltonians in Eqs. (5.9)–(5.11) both with and without spontaneous decay, excitation, and dephasing of individual spins at rates $\gamma_- = \gamma_+ = \gamma_z = 100\chi$. In the case of unitary evolution under OAT, we find that to an excellent approximation $|C(t)|$ takes the functional form $f(t) = f(0) + aN\chi t + (bN\chi t)^2$ with $a \sim b \sim 1$, and with a virtually perfect fit $D(t) = D(0) + ([N + 1]\chi t)^2$. For unitary evolution under TAT and TNT, we find that to an excellent approximation both $|C(t)|$ and $D(t)$ take the functional form $f(t) = f(0) + a[\exp(bN\chi t) - 1]$ with $a \sim b \sim 1$. As may be expected, the growth of $C(t)$ and $D(t)$ is generally suppressed by decoherence. Figure 5.3 serves as an example for the type of behavior that is accessible at short times with the TST expansion. These examples are straightforward to extend to equilibrium settings and spin-boson systems.



(a) Two-time correlator $C(t) \equiv |C(t)| \exp[i\phi(t)]$.

(b) Squared commutator $D(t)$.

Figure 5.3: The two-time connected correlator $C(t)$ and squared commutator $D(t)$, respectively defined in Eqs. (5.13) and (5.14), for $N = 10^4$ spins initially in the polarized state $|X\rangle \propto (|\uparrow\rangle + |\downarrow\rangle)^{\otimes N}$ evolving under the squeezing Hamiltonians in Eqs. (5.9)–(5.11). Results are shown for both unitary dynamics (solid lines) and non-unitary dynamics with $\gamma_- = \gamma_+ = \gamma_z = \gamma_0 = 100\chi$ (dashed lines), computed using the TST expansion in Eq. (5.8) with $M = 20$.

5.5 Conclusions

We have presented an efficient method for computing correlators at short times in collective spin systems. This method is based on truncating a short-time expansion of Heisenberg operators, and can access correlators on time scales that are relevant to metrological applications such as spin squeezing. In order to evaluate the truncated short-time (TST) expansion of Heisenberg operators, we have computed the structure constants of a collective spin operator algebra, which we hope will empower future analytical and numerical studies of collective spin systems. Even though we considered only non-equilibrium spin-squeezing processes in this work, our method can be applied directly in an equilibrium setting, and is straightforward to generalize to systems such as trapped ions and optical cavities with collective spin-boson interactions. In such contexts, our method may be used to benchmark the short-time effects of decoherence, or study the onset of quantum chaos and information scrambling.

Acknowledgments

We acknowledge helpful discussions with Robert Lewis-Swan, Kris Tucker, and Colin Kennedy; as well as some technical contributions from Diego Barberena. This work is supported by the Air Force Office of Scientific Research (AFOSR) grant FA9550-18-1-0319; the Defense Advanced Research Projects Agency (DARPA) and Army Research Office (ARO) grant W911NF-16-1-0576 and W911NF-19-1-0210; the National Science Foundation (NSF) grant PHY-1820885; JILA-NSF grant PFC-1734006; and the National Institute of Standards and Technology (NIST).

5.A Basic spin operator identities

The appendices in this work make ubiquitous use of various spin operator identities; we collect and derive some basic identities here for reference. Note that despite the working definition of collective spin operators from $S_\alpha = \sum_j s_\alpha^{(j)}$, the identities we will derive involving only collective spin operators apply just as well to large-spin operators that cannot be expressed as the sum of

individual spin-1/2 operators. The elementary commutation relations between spin operators are, with $\bar{\mu} \equiv -\mu \in \{+1, -1\}$ for brevity,

$$\left[s_z^{(j)}, s_\mu^{(k)} \right]_- = \delta_{jk} \mu s_\mu^{(j)}, \quad \left[S_z, s_\mu^{(j)} \right]_- = \left[s_z^{(j)}, S_\mu \right]_- = \mu s_\mu^{(j)}, \quad \left[S_z, S_\mu \right]_- = \mu S_\mu, \quad (5.15)$$

$$\left[s_\mu^{(j)}, s_{\bar{\mu}}^{(k)} \right]_- = \delta_{jk} 2\mu s_z^{(j)}, \quad \left[S_\mu, s_{\bar{\mu}}^{(j)} \right]_- = \left[s_\mu^{(j)}, S_{\bar{\mu}} \right]_- = 2\mu s_z^{(j)}, \quad \left[S_\mu, S_{\bar{\mu}} \right]_- = 2\mu S_z. \quad (5.16)$$

These relations can be used to inductively compute identities involving powers of collective spin operators. By pushing through one spin operator at a time, we can find

$$(\mu S_z)^m s_\mu^{(j)} = (\mu S_z)^{m-1} s_\mu^{(j)} (1 + \mu S_z) = (\mu S_z)^{m-2} s_\mu^{(j)} (1 + \mu S_z)^2 = \cdots = s_\mu^{(j)} (1 + \mu S_z)^m, \quad (5.17)$$

and

$$\mu s_z^{(j)} S_\mu^m = S_\mu \mu s_z^{(j)} S_\mu^{m-1} + s_\mu^{(j)} S_\mu^{m-1} = \cdots = S_\mu^m \mu s_z^{(j)} + m s_\mu^{(j)} S_\mu^{m-1}, \quad (5.18)$$

where we will generally find it nicer to express results in terms of $\mu s_z^{(j)}$ and μS_z rather than $s_z^{(j)}$ and S_z . Summing over the single-spin index j in both of the cases above gives us the purely collective-spin versions of these identities:

$$(\mu S_z)^m S_\mu = S_\mu (1 + \mu S_z)^m, \quad \mu S_z S_\mu^m = S_\mu^m (m + \mu S_z), \quad (5.19)$$

where we can repeat the process of pushing through individual S_z operators ℓ times to get

$$(\mu S_z)^\ell S_\mu^m = (\mu S_z)^{\ell-1} S_\mu^m (m + \mu S_z) = (\mu S_z)^{\ell-2} S_\mu^m (m + \mu S_z)^2 = \cdots = S_\mu^m (m + \mu S_z)^\ell. \quad (5.20)$$

Multiplying (5.20) through by $(\mu\nu)^\ell$ (for $\nu \in \{+1, -1\}$) and taking its Hermitian conjugate, we can say that more generally

$$(\nu S_z)^\ell S_\mu^m = S_\mu^m (\mu\nu m + \nu S_z)^\ell, \quad S_\mu^m (\nu S_z)^\ell = (-\mu\nu m + \nu S_z)^\ell S_\mu^m. \quad (5.21)$$

Finding commutation relations between powers of transverse spin operators, i.e. S_μ and $S_{\bar{\mu}}$, turns out to be considerably more difficult than the cases we have worked out thus far. We therefore save this work for Appendix 5.B.

5.B Commutation relations between powers of transverse spin operators

To find commutation relations between powers of transverse collective spin operators, we first compute

$$S_\mu^m s_{\bar{\mu}}^{(j)} = S_\mu^{m-1} s_{\bar{\mu}}^{(j)} S_\mu + S_\mu^{m-1} 2\mu s_z^{(j)} \quad (5.22)$$

$$= S_\mu^{m-2} s_{\bar{\mu}}^{(j)} S_\mu^2 + S_\mu^{m-2} 2\mu s_z^{(j)} S_\mu + S_\mu^{m-1} 2\mu s_z^{(j)} \quad (5.23)$$

$$= s_{\bar{\mu}}^{(j)} S_\mu^m + \sum_{k=0}^{m-1} S_\mu^k 2\mu s_z^{(j)} S_\mu^{m-k-1}. \quad (5.24)$$

While (5.24) gives us the commutator $[S_\mu^m, s_{\bar{\mu}}^{(j)}]_-$, we would like to enforce an ordering on products of spin operators, which will ensure that we only keep track of operators that are linearly independent. We choose (for now) to impose an ordering with all $s_{\bar{\mu}}^{(j)}$ operators on the left, and all $s_z^{(j)}$ operators on the right. Such an ordering will prove convenient for the calculations in this section^a.

This choice of ordering compels us to expand

$$\sum_{k=0}^{m-1} S_\mu^k 2\mu s_z^{(j)} S_\mu^{m-k-1} = \sum_{k=0}^{m-1} S_\mu^k \left[2(m-k-1) s_{\bar{\mu}}^{(j)} S_\mu^{m-k-2} + S_\mu^{m-k-1} 2\mu s_z^{(j)} \right] \quad (5.25)$$

$$= m(m-1) s_{\bar{\mu}}^{(j)} S_\mu^{m-2} + m S_\mu^{m-1} 2\mu s_z^{(j)}, \quad (5.26)$$

which implies

$$S_\mu^m s_{\bar{\mu}}^{(j)} = s_{\bar{\mu}}^{(j)} S_\mu^m + m(m-1) s_{\bar{\mu}}^{(j)} S_\mu^{m-2} + m S_\mu^{m-1} 2\mu s_z^{(j)}, \quad (5.27)$$

and in turn

$$S_\mu^m S_{\bar{\mu}} = S_{\bar{\mu}} S_\mu^m + m S_\mu^{m-1} (m-1 + 2\mu S_z). \quad (5.28)$$

^a In retrospect, it may have been nicer to push all $s_{\bar{\mu}}^{(j)}$ operators to the right throughout these calculations, due to the enhanced symmetry that expressions would have with respect to Hermitian conjugation. In any case, we provide the final result of this section in both ordering conventions, and therefore feel no need to reproduce these calculations with a different ordering of spin operators.

As the next logical step, we take on the task of computing

$$S_\mu^m S_{\bar{\mu}}^n = S_\mu^{m-1} S_{\bar{\mu}}^n S_\mu + n \left[S_\mu^{m-1} S_{\bar{\mu}}^{n-1} (1 - n + 2\mu S_z) \right] = S_{\bar{\mu}}^n S_\mu^m + n \sum_{k=0}^{m-1} S_\mu^{m-k-1} S_{\bar{\mu}}^{n-1} (1 - n + 2\mu S_z) S_\mu^k, \quad (5.29)$$

which implies

$$\left[S_\mu^m, S_{\bar{\mu}}^n \right]_- = C_{mn;\mu} \equiv n \sum_{k=0}^{m-1} S_\mu^{m-k-1} S_{\bar{\mu}}^{n-1} (1 - n + 2\mu S_z) S_\mu^k. \quad (5.30)$$

We now need to rearrange the operators in $C_{mn;\mu}$ into a standard order, which means pushing all S_z operators to the right and, for the purposes of this calculation, all $S_{\bar{\mu}}$ operators to the left. We begin by pushing S_μ^k to the left of S_z , which takes $2\mu S_z \rightarrow 2\mu S_z + 2k$, and then push S_μ^{m-k-1} to the right of $S_{\bar{\mu}}^{n-1}$, giving us

$$C_{mn;\mu} = n \sum_{k=0}^{m-1} \left(S_{\bar{\mu}}^{n-1} S_\mu^{m-k-1} + C_{m-k-1, n-1; \mu} \right) S_\mu^k (2k + 1 - n + 2\mu S_z) \quad (5.31)$$

$$= D_{mn;\mu} + n \sum_{k=0}^{m-2} C_{m-k-1, n-1; \mu} S_\mu^k (2k + 1 - n + 2\mu S_z), \quad (5.32)$$

where we have dropped the last ($k = m - 1$) term in the remaining sum because $C_{m-k-1, n-1; \mu} = 0$ if $k = m - 1$, and

$$D_{mn;\mu} \equiv mn S_{\bar{\mu}}^{n-1} S_\mu^{m-1} (m - n + 2\mu S_z). \quad (5.33)$$

To our despair, we have arrived in (5.32) at a *recursive* formula for $C_{mn;\mu}$. Furthermore, we have not even managed to order all spin operators, as $C_{m-k-1, n-1; \mu}$ contains S_z operators that are to the left of S_μ^k . To sort all spin operators once and for all, we define

$$C_{mn;\mu}^{(k)} \equiv C_{m-k, n; \mu} S_\mu^k, \quad D_{mn;\mu}^{(k)} \equiv D_{m-k, n; \mu} S_\mu^k, \quad (5.34)$$

which we can expand as

$$D_{mn;\mu}^{(k)} = (m - k) n S_{\bar{\mu}}^{n-1} S_\mu^{m-k-1} (m - k - n + 2\mu S_z) S_\mu^k \quad (5.35)$$

$$= (m - k) n S_{\bar{\mu}}^{n-1} S_\mu^{m-1} (k + m - n + 2\mu S_z), \quad (5.36)$$

and

$$C_{mn;\mu}^{(k)} = D_{m-k,n;\mu} S_\mu^k + n \sum_{j=0}^{m-k-2} C_{m-k-j-1,n-1;\mu} S_\mu^j (2j+1-n+2\mu S_z) S_\mu^k \quad (5.37)$$

$$= D_{mn;\mu}^{(k)} + n \sum_{j=0}^{m-k-2} C_{m-k-j-1,n-1;\mu} S_\mu^{j+k} (2j+2k+1-n+2\mu S_z) \quad (5.38)$$

$$= D_{mn;\mu}^{(k)} + n \sum_{j=0}^{m-k-2} C_{m-1,n-1;\mu}^{(k+j)} (2[j+k]+1-n+2\mu S_z) \quad (5.39)$$

$$= D_{mn;\mu}^{(k)} + n \sum_{j=k}^{m-2} C_{m-1,n-1;\mu}^{(j)} (2j+1-n+2\mu S_z). \quad (5.40)$$

While the resulting expression in (5.40) strongly resembles that in (5.32), there is one crucial difference: all spin operators in (5.40) have been sorted into a standard order. We can now repeatedly substitute $C_{mn;\mu}^{(k)}$ into itself, each time decreasing m and n by 1, until one of m or n reaches zero. Such repeated substitution yields the expansion

$$C_{mn;\mu} = C_{mn;\mu}^{(0)} = D_{mn;\mu} + \sum_{p=1}^{\min\{m,n\}-1} E_{mn;\mu}^{(p)}, \quad (5.41)$$

where the first two terms in the sum over p are

$$E_{mn;\mu}^{(1)} = n \sum_{k=0}^{m-2} D_{m-1,n-1;\mu}^{(k)} (2k+1-n+2\mu S_z), \quad (5.42)$$

$$E_{mn;\mu}^{(2)} = n \sum_{k_1=0}^{m-2} (n-1) \sum_{k_2=k_1}^{m-3} D_{m-2,n-2;\mu}^{(k_2)} (2k_2+2-n+2\mu S_z) (2k_1+1-n+2\mu S_z), \quad (5.43)$$

and more generally for $p > 1$,

$$E_{mn;\mu}^{(p)} = \frac{n!}{(n-p)!} \sum_{k_1=0}^{m-2} \sum_{k_2=k_1}^{m-3} \cdots \sum_{k_p=k_{p-1}}^{m-p-1} D_{m-p,n-p;\mu}^{(k_p)} \prod_{j=1}^p (2k_j + j - n + 2\mu S_z). \quad (5.44)$$

In principle, the expressions in (5.33), (5.36), (5.41), and (5.44) suffice to evaluate the commutator $\left[S_\mu^m, S_\mu^n \right]_- = C_{mn;\mu}$, but this result is – put lightly – quite a mess: the expression for $E_{mn;\mu}^{(p)}$ in (5.44) involves a sum over p mutually dependent intermediate variables, each term of which additionally contains a product of p factors. We therefore devote the rest of this section to simplifying our result for the commutator $\left[S_\mu^m, S_\mu^n \right]_-$.

Observing that in (5.44) we always have $0 \leq k_1 \leq k_2 \leq \dots \leq k_p \leq m-p-1$, we can rearrange the order of the sums and relabel $k_p \rightarrow \ell$ to get

$$E_{mn;\mu}^{(p)} = \frac{n!}{(n-p)!} \sum_{\ell=0}^{m-p-1} D_{m-p,n-p;\mu}^{(\ell)} (2\ell + F_{np;\mu}) \sum_{(\mathbf{k}, p-1, \ell)} \prod_{j=1}^{p-1} (2k_{p-j} - j + F_{np;\mu}), \quad (5.45)$$

where for shorthand we define

$$F_{np;\mu} \equiv p - n + 2\mu S_Z, \quad \sum_{(\mathbf{k}, q, \ell)} X \equiv \sum_{k_1=0}^{\ell} \sum_{k_2=k_1}^{\ell} \dots \sum_{k_q=k_{q-1}}^{\ell} X. \quad (5.46)$$

We now further define

$$f_{np\ell;\mu}(k, q) \equiv (\ell - k + q) (\ell + k - q + F_{np;\mu}), \quad (5.47)$$

and evaluate sums successively over $k_{p-1}, k_{p-2}, \dots, k_1$, finding

$$\sum_{(\mathbf{k}, p-1, \ell)} \prod_{j=1}^{p-1} (2k_{p-j} - j + F_{np;\mu}) = \sum_{(\mathbf{k}, p-2, \ell)} \prod_{j=2}^{p-1} (2k_{p-j} - j + F_{np;\mu}) f_{np\ell;\mu}(k_{p-2}, 1) \quad (5.48)$$

$$= \frac{1}{(r-1)!} \sum_{(\mathbf{k}, p-r, \ell)} \prod_{j=r}^{p-1} (2k_{p-j} - j + F_{np;\mu}) \prod_{q=1}^{r-1} f_{np\ell;\mu}(k_{p-r}, q) \quad (5.49)$$

$$= \frac{1}{(p-1)!} \prod_{q=1}^{p-1} f_{np\ell;\mu}(0, q) \quad (5.50)$$

$$= \binom{\ell + p - 1}{p - 1} \prod_{q=1}^{p-1} (\ell - q + F_{np;\mu}). \quad (5.51)$$

Substitution of this result together with $D_{m-p,n-p;\mu}^{(\ell)}$ using (5.36) into (5.45) then gives us

$$E_{mn;\mu}^{(p)} = \frac{n!}{(n-p-1)!} S_{\bar{\mu}}^{n-p-1} S_{\mu}^{m-p-1} G_{mnp;\mu} \quad (5.52)$$

with

$$G_{mnp;\mu} \equiv \sum_{\ell=0}^{m-p-1} \binom{\ell + p - 1}{p - 1} (m - p - \ell) (\ell + m - p + F_{np;\mu}) (2\ell + F_{np;\mu}) \prod_{q=1}^{p-1} (\ell - q + F_{np;\mu}) \quad (5.53)$$

$$= \binom{m}{p+1} \prod_{q=0}^p (m - p - q + F_{np;\mu}). \quad (5.54)$$

We can further simplify

$$\prod_{q=0}^p (m - p - q + F_{np;\mu}) = \prod_{q=0}^p (m - n - q + 2\mu S_z) = \sum_{q=0}^{p+1} (-1)^{p+1-q} \begin{bmatrix} p+1 \\ q \end{bmatrix} (m - n + 2\mu S_z)^q, \quad (5.55)$$

where $\begin{bmatrix} p \\ q \end{bmatrix}$ is an unsigned Stirling number of the first kind, and finally

$$\sum_{q=0}^p (-1)^{p-q} \begin{bmatrix} p \\ q \end{bmatrix} (m - n + 2\mu S_z)^q = \sum_{q=0}^p (-1)^{p-q} \begin{bmatrix} p \\ q \end{bmatrix} \sum_{\ell=0}^q \binom{q}{\ell} (m - n)^{q-\ell} (2\mu S_z)^\ell \quad (5.56)$$

$$= \sum_{\ell=0}^p 2^\ell \sum_{q=\ell}^p (-1)^{p-q} \begin{bmatrix} p \\ q \end{bmatrix} \binom{q}{\ell} (m - n)^{q-\ell} (\mu S_z)^\ell. \quad (5.57)$$

Putting everything together, we finally have

$$E_{mn;\mu}^{(p-1)} = p! \binom{m}{p} \binom{n}{p} S_{\bar{\mu}}^{n-p} S_{\mu}^{m-p} \sum_{\ell=0}^p \epsilon_{mn}^{p\ell} (\mu S_z)^\ell, \quad (5.58)$$

with

$$\epsilon_{mn}^{p\ell} \equiv 2^\ell \sum_{q=\ell}^p (-1)^{p-q} \begin{bmatrix} p \\ q \end{bmatrix} \binom{q}{\ell} (m - n)^{q-\ell}, \quad (5.59)$$

where in this final form $E_{mn;\mu}^{(0)} = D_{mn;\mu}$, which together with the expansion for $C_{mn;\mu}$ in (5.41)

implies that

$$\left[S_{\mu}^m, S_{\bar{\mu}}^n \right]_- = \sum_{p=1}^{\min\{m,n\}} p! \binom{m}{p} \binom{n}{p} S_{\bar{\mu}}^{n-p} S_{\mu}^{m-p} \sum_{\ell=0}^p \epsilon_{mn}^{p\ell} (\mu S_z)^\ell, \quad (5.60)$$

and

$$S_{\mu}^m S_{\bar{\mu}}^n = \sum_{p=0}^{\min\{m,n\}} p! \binom{m}{p} \binom{n}{p} S_{\bar{\mu}}^{n-p} S_{\mu}^{m-p} \sum_{\ell=0}^p \epsilon_{mn}^{p\ell} (\mu S_z)^\ell. \quad (5.61)$$

If we wish to order products of collective spin operators with S_z in between $S_{\bar{\mu}}$ and S_{μ} , then

$$S_{\mu}^m S_{\bar{\mu}}^n = \sum_{p=0}^{\min\{m,n\}} p! \binom{m}{p} \binom{n}{p} S_{\bar{\mu}}^{n-p} Z_{mn;\bar{\mu}}^{(p)} S_{\mu}^{m-p}, \quad (5.62)$$

where

$$Z_{mn;\bar{\mu}}^{(p)} \equiv \sum_{\ell=0}^p \epsilon_{mn}^{p\ell} (-[m-p] + \mu S_z)^\ell = \sum_{q=0}^p \zeta_{mn}^{pq} (\bar{\mu} S_z)^q, \quad (5.63)$$

with

$$\zeta_{mn}^{pq} \equiv \sum_{\ell=q}^p \epsilon_{mn}^{p\ell} \binom{\ell}{q} (-1)^\ell (m-p)^{\ell-q} = (-1)^p 2^q \sum_{s=q}^p \begin{bmatrix} p \\ s \end{bmatrix} \binom{s}{q} (m+n-2p)^{s-q}. \quad (5.64)$$

Here $\begin{bmatrix} p \\ s \end{bmatrix}$ is an unsigned Stirling number of the first kind.

5.C Product of arbitrary ordered collective spin operators

The most general product of collective spin operators that we need to compute is

$$\mathcal{S}_{\ell mn;\mu}^{pqr} = S_{\mu}^p (\mu S_z)^q S_{\bar{\mu}}^r S_{\mu}^{\ell} (\mu S_z)^m S_{\bar{\mu}}^n = \sum_{k=0}^{\min\{r,\ell\}} k! \binom{r}{k} \binom{\ell}{k} S_{\mu}^{p+\ell-k} \tilde{Z}_{qr\ell m;\mu}^{(k)} S_{\bar{\mu}}^{r+n-k}, \quad (5.65)$$

where

$$\tilde{Z}_{qr\ell m;\mu}^{(k)} \equiv (\ell - k + \mu S_z)^q Z_{r\ell;\mu}^{(k)} (r - k + \mu S_z)^m \quad (5.66)$$

$$= \sum_{a=0}^k \zeta_{r\ell}^{ka} \sum_{b=0}^q (\ell - k)^{q-b} \binom{q}{b} \sum_{c=0}^m (r - k)^{m-c} \binom{m}{c} (\mu S_z)^{a+b+c}, \quad (5.67)$$

is defined in terms of $Z_{r\ell;\mu}^{(k)}$ and $\zeta_{r\ell}^{ka}$ as respectively given in (5.63) and (5.64). The (anti-)commutator of two ordered products of collective spin operators is then simply

$$\left[S_{\mu}^p (\mu S_z)^q S_{\bar{\mu}}^r, S_{\mu}^{\ell} (\mu S_z)^m S_{\bar{\mu}}^n \right]_{\pm} = \mathcal{S}_{\ell mn;\mu}^{pqr} \pm \mathcal{S}_{pqr;\mu}^{\ell mn}. \quad (5.68)$$

5.D Sandwich identities for single-spin decoherence calculations

In this section we derive several identities that will be necessary for computing the effects of single-spin decoherence on ordered products of collective spin operators, i.e. on operators of the form $S_{\mu}^{\ell} (\mu S_z)^m S_{\bar{\mu}}^n$. These identities all involve sandwiching a collective spin operator between operators that act on individual spins only, and summing over all individual spin indices. Our general strategy will be to use commutation relations to push single-spin operators together, and then evaluate the sum to arrive at an expression involving only collective spin operators.

We first compute sums of single-spin operators sandwiching $(\mu S_z)^m$, when necessary making use of the identity in (5.17). The unique cases up to Hermitian conjugation are, for $S \equiv N/2$ and

$\mu, \nu \in \{+1, -1\}$,

$$\sum_j s_z^{(j)} (\mu S_z)^m s_z^{(j)} = \sum_j s_z^{(j)} s_z^{(j)} (\mu S_z)^m = \frac{1}{4} \sum_j \mathbb{1}_j (\mu S_z)^m = \frac{1}{2} S (\mu S_z)^m, \quad (5.69)$$

$$\sum_j s_z^{(j)} (\mu S_z)^m s_\nu^{(j)} = (\mu S_z)^m \sum_j s_z^{(j)} s_\nu^{(j)} = \frac{1}{2} (\mu S_z)^m \nu S_\nu = \frac{1}{2} \nu S_\nu (\mu\nu + \mu S_z)^m, \quad (5.70)$$

$$\sum_j s_\nu^{(j)} (\mu S_z)^m s_\nu^{(j)} = \sum_j s_\nu^{(j)} s_\nu^{(j)} (\mu\nu + \mu S_z)^m = 0, \quad (5.71)$$

$$\sum_j s_{\bar{\nu}}^{(j)} (\mu S_z)^m s_\nu^{(j)} = \sum_j s_{\bar{\nu}}^{(j)} s_\nu^{(j)} (\mu\nu + \mu S_z)^m = (S - \nu S_z) (\mu\nu + \mu S_z)^m. \quad (5.72)$$

We are now equipped to derive similar identities for more general collective spin operators. Making heavy use of identities (5.18) and (5.27) to push single-spin operators through transverse collective-spin operators, we again work through all combinations that are unique up to Hermitian conjugation, finding

$$\sum_j s_z^{(j)} S_\mu^\ell (\mu S_z)^m S_{\bar{\mu}}^n s_z^{(j)} = \frac{1}{2} (S - \ell - n) S_\mu^\ell (\mu S_z)^m S_{\bar{\mu}}^n + \ell n S_\mu^{\ell-1} (S + \mu S_z) (-1 + \mu S_z)^m S_{\bar{\mu}}^{n-1}, \quad (5.73)$$

$$\begin{aligned} \sum_j s_z^{(j)} S_\mu^\ell (\mu S_z)^m S_{\bar{\mu}}^n s_\mu^{(j)} &= \frac{1}{2} \mu S_\mu^{\ell+1} (1 + \mu S_z)^m S_{\bar{\mu}}^n - \mu n \left(S - \ell - \frac{1}{2} [n - 1] \right) S_\mu^\ell (\mu S_z)^m S_{\bar{\mu}}^{n-1} \\ &\quad - \mu \ell n (n - 1) S_\mu^{\ell-1} (S + \mu S_z) (-1 + \mu S_z)^m S_{\bar{\mu}}^{n-2}, \end{aligned} \quad (5.74)$$

$$\sum_j s_z^{(j)} S_\mu^\ell (\mu S_z)^m S_{\bar{\mu}}^n s_{\bar{\mu}}^{(j)} = -\frac{1}{2} \mu S_\mu^\ell (\mu S_z)^m S_{\bar{\mu}}^{n+1} + \mu \ell S_\mu^{\ell-1} (S + \mu S_z) (-1 + \mu S_z)^m S_{\bar{\mu}}^n, \quad (5.75)$$

$$\sum_j s_\mu^{(j)} S_\mu^\ell (\mu S_z)^m S_{\bar{\mu}}^n s_\mu^{(j)} = n S_\mu^{\ell+1} (\mu S_z)^m S_{\bar{\mu}}^{n-1} - n (n - 1) S_\mu^\ell (S + \mu S_z) (-1 + \mu S_z)^m S_{\bar{\mu}}^{n-2}, \quad (5.76)$$

$$\sum_j s_\mu^{(j)} S_\mu^\ell (\mu S_z)^m S_{\bar{\mu}}^n s_{\bar{\mu}}^{(j)} = S_\mu^\ell (S + \mu S_z) (-1 + \mu S_z)^m S_{\bar{\mu}}^n, \quad (5.77)$$

$$\begin{aligned} \sum_j s_{\bar{\mu}}^{(j)} S_\mu^\ell (\mu S_z)^m S_{\bar{\mu}}^n s_\mu^{(j)} &= S_\mu^\ell (S - \ell - n - \mu S_z) (1 + \mu S_z)^m S_{\bar{\mu}}^n + \ell n (2S - \ell - n + 2) S_\mu^{\ell-1} (\mu S_z)^m S_{\bar{\mu}}^{n-1} \\ &\quad + \ell n (\ell - 1) (n - 1) S_\mu^{\ell-2} (S + \mu S_z) (-1 + \mu S_z)^m S_{\bar{\mu}}^{n-2}. \end{aligned} \quad (5.78)$$

5.E Uncorrelated, permutationally-symmetric single-spin decoherence

In this section we work out the effects of permutationally-symmetric decoherence of individual spins on collective spin operators of the form $S_\mu^\ell (\mu S_z)^m S_\mu^n$. For compactness, we define

$$\mathcal{D}(g)\mathcal{O} \equiv \mathcal{D}\left(\left\{g^{(j)} : j = 1, 2, \dots, N\right\}\right)\mathcal{O} = \sum_j \left(g^{(j)\dagger}\mathcal{O}g^{(j)} - \frac{1}{2}\left[g^{(j)\dagger}g^{(j)}, \mathcal{O}\right]_+\right), \quad (5.79)$$

where g is an operator that acts on a single spin, $g^{(j)}$ is an operator that acts with g on spin j and trivially on all other spins, and N is the total number of spins.

5.E.1 Decay-type decoherence

The effect of decoherence via uncorrelated decay ($\mu = -1$) or excitation ($\mu = 1$) of individual spins is described by

$$\mathcal{D}(s_\mu)\mathcal{O} = \sum_j \left(s_\mu^{(j)}\mathcal{O}s_\mu^{(j)} - \frac{1}{2}\left[s_\mu^{(j)}s_\mu^{(j)}, \mathcal{O}\right]_+\right) = \sum_j s_\mu^{(j)}\mathcal{O}s_\mu^{(j)} - S\mathcal{O} + \frac{\mu}{2}[S_z, \mathcal{O}]_+. \quad (5.80)$$

In order to determine the effect of this decoherence on general collective spin operators, we expand the anti-commutator

$$\left[S_z, S_\mu^\ell (\mu S_z)^m S_\mu^n\right]_+ = S_z S_\mu^\ell (\mu S_z)^m S_\mu^n + S_\mu^\ell (\mu S_z)^m S_\mu^n S_z = \mu S_\mu^\ell (\ell + n + 2\mu S_z) (\mu S_z)^m S_\mu^n, \quad (5.81)$$

which implies, using (5.77),

$$\mathcal{D}(s_\mu)\left(S_\mu^\ell (\mu S_z)^m S_\mu^n\right) = S_\mu^\ell (S + \mu S_z) (-1 + \mu S_z)^m S_\mu^n - S_\mu^\ell \left[S + \frac{1}{2}(\ell + n) + \mu S_z\right] (\mu S_z)^m S_\mu^n, \quad (5.82)$$

and, using (5.78),

$$\begin{aligned} \mathcal{D}(s_\mu)\left(S_\mu^\ell (\mu S_z)^m S_\mu^n\right) &= S_\mu^\ell (S - \ell - n - \mu S_z) (1 + \mu S_z)^m S_\mu^n - S_\mu^\ell \left[S - \frac{1}{2}(\ell + n) - \mu S_z\right] (\mu S_z)^m S_\mu^n \\ &\quad + \ell n (2S - \ell - n + 2) S_\mu^{\ell-1} (\mu S_z)^m S_\mu^{n-1} \\ &\quad + \ell n (\ell - 1) (n - 1) S_\mu^{\ell-2} (S + \mu S_z) (-1 + \mu S_z)^m S_\mu^{n-2}. \end{aligned} \quad (5.83)$$

Decoherence via jump operators $s_{\bar{\mu}}^{(j)}$ only couples operators $S_{\mu}^{\ell} (\mu S_z)^m S_{\bar{\mu}}^n$ to operators $S_{\mu}^{\ell} (\mu S_z)^{m'} S_{\bar{\mu}}^n$ with $m' \leq m$. Decoherence via jump operators $s_{\mu}^{(j)}$, meanwhile, makes operators $S_{\mu}^{\ell} (\mu S_z)^m S_{\bar{\mu}}^n$ “grow” in m through the last term in (5.83), although the sum $\ell + m + n$ does not grow.

5.E.2 Dephasing

The effect of decoherence via single-spin dephasing is described by

$$\mathcal{D}(s_z) \mathcal{O} = \sum_j \left(s_z^{(j)} \mathcal{O} s_z^{(j)} - \frac{1}{2} \left[s_z^{(j)} s_z^{(j)}, \mathcal{O} \right]_+ \right) = \sum_j s_z^{(j)} \mathcal{O} s_z^{(j)} - \frac{1}{2} S \mathcal{O}. \quad (5.84)$$

From (5.73), we then have

$$\mathcal{D}(s_z) \left(S_{\mu}^{\ell} (\mu S_z)^m S_{\bar{\mu}}^n \right) = -\frac{1}{2} (\ell + n) S_{\mu}^{\ell} (\mu S_z)^m S_{\bar{\mu}}^n + \ell n S_{\mu}^{\ell-1} (S + \mu S_z) (-1 + \mu S_z)^m S_{\bar{\mu}}^{n-1}. \quad (5.85)$$

Decoherence via single-spin dephasing makes operators $S_{\mu}^{\ell} (\mu S_z)^m S_{\bar{\mu}}^n$ “grow” in m , although the sum $\ell + m + n$ does not grow.

5.E.3 The general case

The most general type of single-spin decoherence is described by

$$\mathcal{D}(g) \mathcal{O} = \sum_j \left(g^{(j)\dagger} \mathcal{O} g^{(j)} - \frac{1}{2} \left[g^{(j)\dagger} g^{(j)}, \mathcal{O} \right]_+ \right), \quad g \equiv g_z s_z + g_+ s_+ + g_- s_-. \quad (5.86)$$

To simplify (5.86), we expand

$$g^{\dagger} \mathcal{O} g = |g_z|^2 s_z \mathcal{O} s_z + \sum_{\mu} \left(|g_{\mu}|^2 s_{\bar{\mu}} \mathcal{O} s_{\mu} + g_{\bar{\mu}}^* g_{\mu} s_{\mu} \mathcal{O} s_{\mu} + g_z^* g_{\mu} s_z \mathcal{O} s_{\mu} + g_{\bar{\mu}}^* g_z s_{\mu} \mathcal{O} s_z \right), \quad (5.87)$$

and

$$g^{\dagger} g = \frac{1}{4} |g_z|^2 + \frac{1}{2} \sum_{\mu} \left[|g_{\mu}|^2 (1 - 2\mu s_z) + \mu \left(g_z^* g_{\mu} - g_{\bar{\mu}}^* g_z \right) s_{\mu} \right], \quad (5.88)$$

which implies

$$\begin{aligned} \mathcal{D}(g) \mathcal{O} = & \sum_{X \in \{z, +, -\}} |g_X|^2 \mathcal{D}(s_X) \mathcal{O} + \sum_{\mu, j} \left(g_{\bar{\mu}}^* g_{\mu} s_{\mu}^{(j)} \mathcal{O} s_{\mu}^{(j)} + g_z^* g_{\mu} s_z^{(j)} \mathcal{O} s_{\mu}^{(j)} + g_{\bar{\mu}}^* g_z s_{\mu}^{(j)} \mathcal{O} s_z^{(j)} \right) \\ & - \frac{1}{4} \sum_{\mu} \mu \left(g_z^* g_{\mu} - g_{\bar{\mu}}^* g_z \right) [S_{\mu}, \mathcal{O}]_+. \end{aligned} \quad (5.89)$$

In order to compute the effect of this decoherence on general collective spin operators, we expand the anti-commutator

$$\left[S_\mu, S_\mu^\ell (\mu S_z)^m S_\mu^n \right]_+ = S_\mu^{\ell+1} [(\mu S_z)^m + (1 + \mu S_z)^m] S_\mu^n - n S_\mu^\ell (n - 1 + 2\mu S_z) (\mu S_z)^m S_\mu^{n-1}. \quad (5.90)$$

Recognizing a resemblance between terms in (5.90) and (5.74), we collect terms to simplify

$$\sum_j s_z^{(j)} S_\mu^\ell (\mu S_z)^m S_\mu^n s_\mu^{(j)} - \frac{1}{4} \mu \left[S_\mu, S_\mu^\ell (\mu S_z)^m S_\mu^n \right]_+ = K_{\ell mn; \mu} + L_{\ell mn; \mu} \quad (5.91)$$

and likewise

$$\sum_j s_\mu^{(j)} S_\mu^\ell (\mu S_z)^m S_\mu^n s_z^{(j)} + \frac{1}{4} \mu \left[S_\mu, S_\mu^\ell (\mu S_z)^m S_\mu^n \right]_+ = K_{\ell mn; \mu} + M_{\ell mn; \mu} \quad (5.92)$$

with

$$K_{\ell mn; \mu} \equiv \frac{1}{4} \mu S_\mu^{\ell+1} [(1 + \mu S_z)^m - (\mu S_z)^m] S_\mu^n, \quad (5.93)$$

$$L_{\ell mn; \mu} \equiv -\mu n S_\mu^\ell \left[S - \ell - \frac{3}{4} (n - 1) - \frac{1}{2} \mu S_z \right] (\mu S_z)^m S_\mu^{n-1} - \mu \ell n (n - 1) S_\mu^{\ell-1} (S + \mu S_z) (-1 + \mu S_z)^m S_\mu^{n-2}, \quad (5.94)$$

$$M_{\ell mn; \mu} \equiv \mu n S_\mu^\ell \left[(S + \mu S_z) (-1 + \mu S_z)^m - \frac{1}{2} \left(\frac{1}{2} [n - 1] + \mu S_z \right) (\mu S_z)^m \right] S_\mu^{n-1}. \quad (5.95)$$

Defining for completion

$$P_{\ell mn; \mu} \equiv \sum_j s_\mu^{(j)} S_\mu^\ell (\mu S_z)^m S_\mu^n s_\mu^{(j)} = n S_\mu^{\ell+1} (\mu S_z)^m S_\mu^{n-1} - n (n - 1) S_\mu^\ell (S + \mu S_z) (-1 + \mu S_z)^m S_\mu^{n-2}, \quad (5.96)$$

and

$$Q_{\ell mn; \mu}^{(g)} \equiv g_\mu^* g_\mu P_{\ell mn; \mu} + \left(g_z^* g_\mu + g_\mu^* g_z \right) K_{\ell mn; \mu} + g_z^* g_\mu L_{\ell mn; \mu} + g_\mu^* g_z M_{\ell mn; \mu}, \quad (5.97)$$

we finally have

$$\mathcal{D}(g) \left(S_\mu^\ell (\mu S_z)^m S_\mu^n \right) = \sum_{X \in \{z, +, -\}} |g_X|^2 \mathcal{D}(s_X) \left(S_\mu^\ell (\mu S_z)^m S_\mu^n \right) + Q_{\ell mn; \mu}^{(g)} + \left[Q_{nm\ell; \mu}^{(g)} \right]^\dagger. \quad (5.98)$$

Note that the sum $\ell + m + n$ for operators $S_\mu^\ell (\mu S_z)^m S_\mu^n$ does not grow under this type of decoherence.

5.F Sandwich identities for collective-spin decoherence calculations

In analogy with the work in Appendix 5.D, in this section we work out sandwich identities necessary for collective-spin decoherence calculations. The simplest cases are

$$S_\mu S_\mu^\ell (\mu S_z)^m S_{\bar{\mu}}^n S_{\bar{\mu}} = S_\mu^{\ell+1} (\mu S_z)^m S_{\bar{\mu}}^{n+1}, \quad (5.99)$$

$$S_\mu S_\mu^\ell (\mu S_z)^m S_{\bar{\mu}}^n S_z = \mu S_\mu^{\ell+1} (n + \mu S_z) (\mu S_z)^m S_{\bar{\mu}}^n, \quad (5.100)$$

$$S_z S_\mu^\ell (\mu S_z)^m S_{\bar{\mu}}^n S_z = S_\mu^\ell \left[\ell n + (\ell + n) \mu S_z + (\mu S_z)^2 \right] (\mu S_z)^m S_{\bar{\mu}}^n. \quad (5.101)$$

With a bit more work, we can also find

$$S_\mu^\ell (\mu S_z)^m S_{\bar{\mu}}^n S_\mu = S_\mu^{\ell+1} (1 + \mu S_z)^m S_{\bar{\mu}}^n - n S_\mu^\ell (n - 1 + 2\mu S_z) (\mu S_z)^m S_{\bar{\mu}}^{n-1}, \quad (5.102)$$

which implies

$$S_\mu S_\mu^\ell (\mu S_z)^m S_{\bar{\mu}}^n S_\mu = S_\mu^{\ell+2} (1 + \mu S_z)^m S_{\bar{\mu}}^n - n S_\mu^{\ell+1} (n - 1 + 2\mu S_z) (\mu S_z)^m S_{\bar{\mu}}^{n-1}, \quad (5.103)$$

$$\begin{aligned} S_z S_\mu^\ell (\mu S_z)^m S_{\bar{\mu}}^n S_\mu &= \mu S_\mu^{\ell+1} (\ell + 1 + \mu S_z) (1 + \mu S_z)^m S_{\bar{\mu}}^n \\ &\quad - \mu n S_\mu^\ell \left[\ell (n - 1) + (2\ell + n - 1) \mu S_z + 2 (\mu S_z)^2 \right] (\mu S_z)^m S_{\bar{\mu}}^{n-1}. \end{aligned} \quad (5.104)$$

Finally, we compute

$$\begin{aligned} S_{\bar{\mu}} S_\mu^\ell (\mu S_z)^m S_{\bar{\mu}}^n S_\mu &= \left[S_\mu^\ell S_{\bar{\mu}} - \ell S_\mu^{\ell-1} (\ell - 1 + 2\mu S_z) \right] (\mu S_z)^m \left[S_\mu S_{\bar{\mu}}^n - n (n - 1 + 2\mu S_z) S_{\bar{\mu}}^{n-1} \right] \\ &= S_\mu^\ell S_{\bar{\mu}} (\mu S_z)^m S_\mu S_{\bar{\mu}}^n \\ &\quad - S_\mu^\ell \left[\ell (\ell + 1) + n (n + 1) + 2 (\ell + n) \mu S_z \right] (1 + \mu S_z)^m S_{\bar{\mu}}^n \\ &\quad + \ell n S_\mu^{\ell-1} \left[(\ell - 1) (n - 1) + 2 (\ell + n - 2) \mu S_z + 4 (\mu S_z)^2 \right] (\mu S_z)^m S_{\bar{\mu}}^{n-1}, \end{aligned} \quad (5.105)$$

where

$$S_{\bar{\mu}} (\mu S_z)^m S_\mu = S_{\bar{\mu}} S_\mu (1 + \mu S_z)^m = (S_\mu S_{\bar{\mu}} - 2\mu S_z) (1 + \mu S_z)^m = S_\mu (2 + \mu S_z)^m S_{\bar{\mu}} - 2\mu S_z (1 + \mu S_z)^m, \quad (5.106)$$

so

$$\begin{aligned}
S_{\bar{\mu}} S_{\mu}^{\ell} (\mu S_z)^m S_{\bar{\mu}}^n S_{\mu} &= S_{\mu}^{\ell+1} (2 + \mu S_z)^m S_{\bar{\mu}}^{n+1} \\
&\quad - S_{\mu}^{\ell} [\ell(\ell+1) + n(n+1) + 2(\ell+n+1)\mu S_z] (1 + \mu S_z)^m S_{\bar{\mu}}^n \\
&\quad + \ell n S_{\mu}^{\ell-1} [(\ell-1)(n-1) + 2(\ell+n-2)\mu S_z + 4(\mu S_z)^2] (\mu S_z)^m S_{\bar{\mu}}^{n-1}.
\end{aligned} \tag{5.107}$$

5.G Collective spin decoherence

In this section we work out the effects of collective decoherence on general collective spin operators. For shorthand, we define

$$\mathcal{D}(G) \mathcal{O} \equiv \mathcal{D}(\{G\}) \mathcal{O} = G^{\dagger} \mathcal{O} G - \frac{1}{2} [G^{\dagger} G, \mathcal{O}]_+, \tag{5.108}$$

where G is a collective spin jump operator.

5.G.1 Decay-type decoherence and dephasing

Making use of the results in Appendix 5.F, we find that the effects of collective decay-type decoherence on general collective spin operators are given by

$$\begin{aligned}
\mathcal{D}(S_{\bar{\mu}}) \left(S_{\mu}^{\ell} (\mu S_z)^m S_{\bar{\mu}}^n \right) &= -S_{\mu}^{\ell+1} [(1 + \mu S_z)^m - (\mu S_z)^m] S_{\bar{\mu}}^{n+1} \\
&\quad + \frac{1}{2} S_{\mu}^{\ell} [\ell(\ell-1) + n(n-1) + 2(\ell+n)\mu S_z] (\mu S_z)^m S_{\bar{\mu}}^n,
\end{aligned} \tag{5.109}$$

and

$$\begin{aligned}
\mathcal{D}(S_{\mu}) \left(S_{\mu}^{\ell} (\mu S_z)^m S_{\bar{\mu}}^n \right) &= S_{\mu}^{\ell+1} [(2 + \mu S_z)^m - (1 + \mu S_z)^m] S_{\bar{\mu}}^{n+1} \\
&\quad - S_{\mu}^{\ell} [\ell(\ell+1) + n(n+1) + 2(\ell+n+1)\mu S_z] (1 + \mu S_z)^m S_{\bar{\mu}}^n \\
&\quad + \frac{1}{2} S_{\mu}^{\ell} [\ell(\ell+1) + n(n+1) + 2(\ell+n+2)\mu S_z] (\mu S_z)^m S_{\bar{\mu}}^n \\
&\quad + \ell n S_{\mu}^{\ell-1} [(\ell-1)(n-1) + 2(\ell+n-2)\mu S_z + 4(\mu S_z)^2] (\mu S_z)^m S_{\bar{\mu}}^{n-1}.
\end{aligned} \tag{5.110}$$

Similarly, the effect of collective dephasing is given by

$$\mathcal{D}(S_z) \left(S_{\mu}^{\ell} (\mu S_z)^m S_{\bar{\mu}}^n \right) = -\frac{1}{2} (\ell-n)^2 S_{\mu}^{\ell} (\mu S_z)^m S_{\bar{\mu}}^n. \tag{5.111}$$

5.G.2 The general case

More generally, we consider jump operators of the form

$$G \equiv G_z S_z + G_+ S_+ + G_- S_-, \quad (5.112)$$

whose decoherence effects are determined by

$$G^\dagger \mathcal{O} G = |G_z|^2 S_z \mathcal{O} S_z + \sum_{\mu} \left(|G_{\mu}|^2 S_{\bar{\mu}} \mathcal{O} S_{\mu} + G_{\bar{\mu}}^* G_{\mu} S_{\mu} \mathcal{O} S_{\mu} + G_z^* G_{\mu} S_z \mathcal{O} S_{\mu} + G_{\bar{\mu}}^* G_z S_{\mu} \mathcal{O} S_z \right), \quad (5.113)$$

and

$$G^\dagger G = |G_z|^2 S_z^2 + \sum_{\mu} \left(|G_{\mu}|^2 S_{\bar{\mu}} S_{\mu} + G_z^* G_{\mu} S_z S_{\mu} + G_{\bar{\mu}}^* G_z S_{\mu} S_z + G_{\bar{\mu}}^* G_{\mu} S_{\mu}^2 \right), \quad (5.114)$$

which implies

$$\begin{aligned} \mathcal{D}(G) \mathcal{O} &= \sum_{X \in \{z, +, -\}} |G_X|^2 \mathcal{D}(S_X) \mathcal{O} + \sum_{\mu} \left(G_{\bar{\mu}}^* G_{\mu} S_{\mu} \mathcal{O} S_{\mu} + G_z^* G_{\mu} S_z \mathcal{O} S_{\mu} + G_{\bar{\mu}}^* G_z S_{\mu} \mathcal{O} S_z \right) \\ &\quad - \frac{1}{2} \sum_{\mu} \left(G_{\bar{\mu}}^* G_{\mu} [S_{\mu}^2, \mathcal{O}]_+ + G_z^* G_{\mu} [S_z S_{\mu}, \mathcal{O}]_+ + G_{\bar{\mu}}^* G_z [S_{\mu} S_z, \mathcal{O}]_+ \right). \end{aligned} \quad (5.115)$$

In order to compute the effect of this decoherence on general collective spin operators, we expand the anti-commutators

$$\begin{aligned} [S_{\mu}^2, S_{\mu}^{\ell} (\mu S_z)^m S_{\bar{\mu}}^n]_+ &= S_{\mu}^{\ell+2} [(2 + \mu S_z)^m + (\mu S_z)^m] S_{\bar{\mu}}^n - 2n S_{\mu}^{\ell+1} (n + 2\mu S_z) (1 + \mu S_z)^m S_{\bar{\mu}}^{n-1} \\ &\quad + n(n-1) S_{\mu}^{\ell} \left[(n-1)(n-2) + 2(2n-3)\mu S_z + 4(\mu S_z)^2 \right] (\mu S_z)^m S_{\bar{\mu}}^{n-2}, \end{aligned} \quad (5.116)$$

$$\begin{aligned} [S_z S_{\mu}, S_{\mu}^{\ell} (\mu S_z)^m S_{\bar{\mu}}^n]_+ &= \mu S_{\mu}^{\ell+1} [(\ell+1 + \mu S_z) (\mu S_z)^m + (n+1 + \mu S_z) (1 + \mu S_z)^m] S_{\bar{\mu}}^n \\ &\quad - \mu n S_{\mu}^{\ell} \left[n(n-1) + (3n-1)\mu S_z + 2(\mu S_z)^2 \right] (\mu S_z)^m S_{\bar{\mu}}^{n-1}, \end{aligned} \quad (5.117)$$

$$\begin{aligned} [S_{\mu} S_z, S_{\mu}^{\ell} (\mu S_z)^m S_{\bar{\mu}}^n]_+ &= \mu S_{\mu}^{\ell+1} [(\ell + \mu S_z) (\mu S_z)^m + (n + \mu S_z) (1 + \mu S_z)^m] S_{\bar{\mu}}^n \\ &\quad - \mu n S_{\mu}^{\ell} \left[(n-1)^2 + 3(n-1)\mu S_z + 2(\mu S_z)^2 \right] (\mu S_z)^m S_{\bar{\mu}}^{n-1}. \end{aligned} \quad (5.118)$$

Collecting terms and defining

$$G_{z,\mu}^{(\pm)} \equiv \frac{1}{2} \left(G_z^* G_{\mu} \pm G_{\bar{\mu}}^* G_z \right), \quad (5.119)$$

$$\begin{aligned}
\tilde{L}_{\ell mn;\mu}^{(G)} &\equiv \mu \left[\left(\ell - n + \frac{1}{2} \right) G_{z,\mu}^{(+)} + \left(\ell + \frac{1}{2} \right) G_{z,\mu}^{(-)} \right] S_{\mu}^{\ell+1} (1 + \mu S_z)^m S_{\bar{\mu}}^n \\
&\quad - \mu \left[\left(\ell - n + \frac{1}{2} \right) G_{z,\mu}^{(+)} + \left(n + \frac{1}{2} \right) G_{z,\mu}^{(-)} \right] S_{\mu}^{\ell+1} (\mu S_z)^m S_{\bar{\mu}}^n \\
&\quad + \mu G_{z,\mu}^{(-)} S_{\mu}^{\ell+1} \mu S_z [(1 + \mu S_z)^m - (\mu S_z)^m] S_{\bar{\mu}}^n, \tag{5.120}
\end{aligned}$$

$$\begin{aligned}
\tilde{M}_{\ell mn;\mu}^{(G)} &= -\mu n (n-1) \left[\left(\ell - n + \frac{1}{2} \right) G_{z,\mu}^{(+)} + \left(\ell - \frac{1}{2} \right) G_{z,\mu}^{(-)} \right] S_{\mu}^{\ell} (\mu S_z)^m S_{\bar{\mu}}^{n-1} \\
&\quad - 2\mu n \left[\left(\ell - n + \frac{1}{2} \right) G_{z,\mu}^{(+)} + \left(\ell + \frac{1}{2} n - 1 \right) G_{z,\mu}^{(-)} \right] S_{\mu}^{\ell} (\mu S_z)^{m+1} S_{\bar{\mu}}^{n-1} \\
&\quad - 2\mu n G_{z,\mu}^{(-)} S_{\mu}^{\ell} (\mu S_z)^{m+2} S_{\bar{\mu}}^{n-1}, \tag{5.121}
\end{aligned}$$

$$\begin{aligned}
\tilde{P}_{\ell mn;\mu} &\equiv -\frac{1}{2} S_{\mu}^{\ell+2} [(2 + \mu S_z)^m - 2(1 + \mu S_z)^m + (\mu S_z)^m] S_{\bar{\mu}}^n \\
&\quad + n S_{\mu}^{\ell+1} [(n + 2\mu S_z)(1 + \mu S_z)^m - (n-1 + 2\mu S_z)(\mu S_z)^m] S_{\bar{\mu}}^{n-1} \\
&\quad - n(n-1) S_{\mu}^{\ell} \left[\frac{1}{2} (n-1)(n-2) + (2n-3)\mu S_z + 2(\mu S_z)^2 \right] (\mu S_z)^m S_{\bar{\mu}}^{n-2}, \tag{5.122}
\end{aligned}$$

$$\tilde{Q}_{\ell mn;\mu}^{(G)} \equiv G_{\bar{\mu}}^* G_{\mu} \tilde{P}_{\ell mn;\mu} + \tilde{L}_{\ell mn;\mu}^{(G)} + \tilde{M}_{\ell mn;\mu}^{(G)}, \tag{5.123}$$

we then have

$$\mathcal{D}(G) \left(S_{\mu}^{\ell} (\mu S_z)^m S_{\bar{\mu}}^n \right) = \sum_{X \in \{z,+, -\}} |G_X|^2 \mathcal{D}(S_X) \left(S_{\mu}^{\ell} (\mu S_z)^m S_{\bar{\mu}}^n \right) + \tilde{Q}_{\ell mn;\mu}^{(G)} + \left[\tilde{Q}_{nm\ell;\mu}^{(G)} \right]^{\dagger}. \tag{5.124}$$

Note that the sum $\ell + m + n$ for operators $S_{\mu}^{\ell} (\mu S_z)^m S_{\bar{\mu}}^n$ grows by one if $G_{\mu} \neq 0$ or $G_{\bar{\mu}} \neq 0$, and does not grow otherwise.

5.H Emulating particle loss in a spin model

Here we discuss the details of emulating particle loss with $O(1/N)$ error, where N is the initial number of particles in a system that we wish to describe with a spin model. Starting with the full algebra of creation and annihilation operators (whether bosonic or fermionic) in a system, spin models are typically implemented by identifying a subalgebra of relevant ‘‘spin’’ operators that satisfy appropriate commutation relations. Two-state particles on a lattice, for example, are described by annihilation operators c_{j_s} indexed by a lattice site $j \in \mathbb{Z}$ and an internal state index

$s \in \{\uparrow, \downarrow\}$, enabling the straightforward construction of spin operators

$$\sigma_x^{(j)} \equiv c_{j,\uparrow}^\dagger c_{j,\downarrow} + \text{h.c.}, \quad \sigma_y^{(j)} \equiv -i c_{j,\uparrow}^\dagger c_{j,\downarrow} + \text{h.c.}, \quad \sigma_z^{(j)} \equiv c_{j,\uparrow}^\dagger c_{j,\uparrow} - c_{j,\downarrow}^\dagger c_{j,\downarrow}, \quad \mathbb{1}^{(j)} \equiv c_{j,\uparrow}^\dagger c_{j,\uparrow} + c_{j,\downarrow}^\dagger c_{j,\downarrow}, \quad (5.125)$$

which satisfy the same commutation relations as the standard Pauli operators. These spin operators can be more compactly defined in the form

$$\sigma_\alpha^{(j)} \equiv \sum_{r,s \in \{\uparrow, \downarrow\}} c_{jr}^\dagger \langle r | \sigma_\alpha | s \rangle c_{js}, \quad (5.126)$$

where σ_α for $\alpha \in \{x, y, z, \mathbb{1}\}$ is a Pauli operator, with $\sigma_\mathbb{1} \equiv \mathbb{1}$; and $\langle r | \sigma_\alpha | s \rangle$ denotes a matrix element of σ_α . This construction exemplifies how the set of jump operators $\mathcal{J}_{\text{loss}}^{\text{bare}} \equiv \{c_{js}\}$ that generate particle loss cannot be constructed from spin operators, which are generally bilinear in particle creation or annihilation operators. When working on the level of a spin model, therefore, we can at best only *emulate* the effect of particle loss by some indirect means.

To understand the effect of particle loss on collective spin operators, we first define a single multi-body spin operator addressing sites $\mathbf{j} = \{j_1, j_2, \dots, j_{|\mathbf{j}|}\}$,

$$\sigma_{\mathbf{j}\alpha} \equiv \prod_{j \in \mathbf{j}} \sigma_{\alpha_j}^{(j)}, \quad (5.127)$$

and expand

$$\mathcal{D} \left(\mathcal{J}_{\text{loss}}^{\text{bare}} \right) \sigma_{\mathbf{j}\alpha} = \sum_{k,s} \left(c_{ks}^\dagger \sigma_{\mathbf{j}\alpha} c_{ks} - \frac{1}{2} \left[c_{ks}^\dagger c_{ks}, \sigma_{\mathbf{j}\alpha} \right]_+ \right) \quad (5.128)$$

$$= \sum_{k \in \mathbf{j}} \sum_s c_{ks}^\dagger \sigma_{\alpha_k}^{(k)} c_{ks} \prod_{\substack{j \in \mathbf{j} \\ j \neq k}} \sigma_{\alpha_j}^{(j)} + \sum_{k \notin \mathbf{j}} \sum_s c_{ks}^\dagger c_{ks} \sigma_{\mathbf{j}\alpha} - \frac{1}{2} \sum_k \left[\mathbb{1}^{(k)}, \sigma_{\mathbf{j}\alpha} \right]_+ \quad (5.129)$$

$$= \sum_{k \in \mathbf{j}} \sum_{q,r,s} \langle q | \sigma_{\alpha_k} | r \rangle c_{ks}^\dagger c_{kq}^\dagger c_{kr} c_{ks} \prod_{\substack{j \in \mathbf{j} \\ j \neq k}} \sigma_{\alpha_j}^{(j)} - |\mathbf{j}| \sigma_{\mathbf{j}\alpha}. \quad (5.130)$$

In order to have an actual spin model, fermionic statistics or energetic considerations must forbid multiple occupation of individual lattice sites. In that case, the on-site four-point product $c_{ks}^\dagger c_{kq}^\dagger c_{kr} c_{ks} = 0$ vanishes, and

$$\mathcal{D} \left(\mathcal{J}_{\text{loss}}^{\text{bare}} \right) \sigma_{\mathbf{j}\alpha} = -|\mathbf{j}| \sigma_{\mathbf{j}\alpha}. \quad (5.131)$$

Up to $O(1/N)$ corrections, a collective spin operator $\mathcal{S}_{\mathbf{m}}$ essentially consists of $|\mathbf{m}|$ -body operators of the form $\sigma_{j\alpha}$ with $|j| = |\mathbf{m}|$, which implies that the dissipator $\mathcal{D}_{\text{loss}}$ defined by $\mathcal{D}_{\text{loss}}\mathcal{S}_{\mathbf{m}} = -|\mathbf{m}|\mathcal{S}_{\mathbf{m}}$ describes particle loss with $O(1/N)$ error. We note that the dissipator $\mathcal{D}_{\text{loss}}$ is essentially the depolarizing channel, i.e. $\mathcal{D}_{\text{loss}} = \mathcal{D}(\mathcal{J}_{\text{loss}})$ for $\mathcal{J}_{\text{loss}} = \{s_{\alpha}^{(j)}\}$ with $\alpha \in \{x, y, z\}$ and $j \in \{1, 2, \dots, N\}$. A direct implementation of $\mathcal{D}_{\text{loss}}$ with $\mathcal{D}_{\text{loss}}\mathcal{S}_{\mathbf{m}} = -|\mathbf{m}|\mathcal{S}_{\mathbf{m}}$, however, is much more efficient than evaluating the depolarizing channel $\mathcal{D}(\mathcal{J}_{\text{loss}})$ with the ingredients in Appendices 5.D and 5.E.

5.I Initial conditions

Here we compute the expectation values of collective spin operators with respect to spin-polarized (also Gaussian, or spin-coherent) states. These states are parameterized by polar and azimuthal angles $\theta \in [0, \pi)$, $\phi \in [0, 2\pi)$, and lie within the Dicke manifold spanned by states $|k\rangle \propto S_+^{S+k} |\downarrow\rangle^{\otimes N}$ with $S \equiv N/2$ and $S_z |k\rangle = k |k\rangle$:

$$|\theta, \phi\rangle \equiv \left[\cos(\theta/2) e^{-i\phi/2} |\uparrow\rangle + \sin(\theta/2) e^{i\phi/2} |\downarrow\rangle \right]^{\otimes N} = \sum_{k=-S}^S \binom{N}{S+k}^{1/2} \cos(\theta/2)^{S+k} \sin(\theta/2)^{S-k} e^{-ik\phi} |k\rangle. \quad (5.132)$$

We can likewise expand, within the Dicke manifold,

$$S_z = \sum_{k=-S}^S k |k\rangle\langle k|, \quad S_{\mu} = \sum_{k=-S+\delta_{\mu,-1}}^{S-\delta_{\mu,1}} g_{\mu}(k) |k+\mu\rangle\langle k| = \sum_{k=-S+\delta_{\bar{\mu},-1}}^{S-\delta_{\bar{\mu},1}} g_{\bar{\mu}}(k) |k\rangle\langle k+\bar{\mu}|, \quad (5.133)$$

where $\bar{\mu} \equiv -\mu \in \{+1, -1\}$ and

$$g_{\mu}(k) \equiv \sqrt{(S - \mu k)(S + \mu k + 1)}, \quad (5.134)$$

which implies

$$S_\mu^\ell (\mu S_z^m) S_\mu^n = \sum_{k=-S+\delta_{\mu,-1} \max\{\ell,n\}}^{S-\delta_{\mu,1} \max\{\ell,n\}} (\mu k)^m \left[\prod_{p=0}^{\ell-1} g_\mu(k+\mu p) \right] \left[\prod_{q=0}^{n-1} g_\mu(k+\mu q) \right] |k+\mu\ell\rangle\langle k+\mu n| \quad (5.135)$$

$$= \sum_{\mu k=-\mu S-\delta_{\mu,-1} \max\{\ell,n\}}^{\mu S-\delta_{\mu,1} \max\{\ell,n\}} (\mu k)^m \frac{(S-\mu k)!}{(S+\mu k)!} \left[\frac{(S+\mu k+\ell)! (S+\mu k+n)!}{(S-\mu k-\ell)! (S-\mu k-n)!} \right]^{1/2} |k+\mu\ell\rangle\langle k+\mu n| \quad (5.136)$$

$$= \sum_{k=-S}^{S-\max\{\ell,n\}} k^m \frac{(S-k)!}{(S+k)!} \left[\frac{(S+k+\ell)! (S+k+n)!}{(S-k-\ell)! (S-k-n)!} \right]^{1/2} |\mu(k+\ell)\rangle\langle\mu(k+n)|. \quad (5.137)$$

This expansion allows us to compute the expectation value

$$\langle\theta, \phi| S_\mu^\ell (\mu S_z^m) S_\mu^n |\theta, \phi\rangle = e^{i\phi\mu(\ell-n)} N! \sum_{k=-S}^{S-\max\{\ell,n\}} \frac{k^m (S-k)! f_{\mu\ell n}(k, \theta)}{(S+k)! (S-k-\ell)! (S-k-n)!} \quad (5.138)$$

$$= e^{i\phi\mu(\ell-n)} (-1)^m N! \sum_{k=0}^{N-\max\{\ell,n\}} \frac{(S-k)^m (N-k)! \tilde{f}_{\mu\ell n}(k, \theta)}{k! (N-k-\ell)! (N-k-n)!} \quad (5.139)$$

where

$$f_{\mu\ell n}(k, \theta) \equiv \cos(\theta/2)^{N+\mu(2k+\ell+n)} \sin(\theta/2)^{N-\mu(2k+\ell+n)}, \quad (5.140)$$

$$\tilde{f}_{\mu\ell n}(k, \theta) \equiv f_{\mu\ell n}(k-S, \theta) = \cos(\theta/2)^{2N\delta_{\mu,-1}+\mu(2k+\ell+n)} \sin(\theta/2)^{2N\delta_{\mu,1}-\mu(2k+\ell+n)}. \quad (5.141)$$

Defining the states

$$|+Z\rangle \equiv |0, 0\rangle = |\uparrow\rangle^{\otimes N}, \quad |-Z\rangle \equiv |\pi, 0\rangle = |\downarrow\rangle^{\otimes N}, \quad |X\rangle \equiv |\pi/2, 0\rangle = \left(\frac{|\uparrow\rangle + |\downarrow\rangle}{\sqrt{2}} \right)^{\otimes N}, \quad (5.142)$$

some particular expectation values of interest are

$$\langle\nu Z| S_\mu^\ell (\mu S_z^m) S_\mu^n |\nu Z\rangle = \delta_{\ell n} \times \begin{cases} (S-n)^m \frac{N!n!}{(N-n)!} & \mu = \nu, \\ \delta_{n,0} (-S)^m & \mu \neq \nu, \end{cases} \quad (5.143)$$

and

$$\langle X| S_\mu^\ell (\mu S_z^m) S_\mu^n |X\rangle = (-1)^m \frac{N!}{2^N} \sum_{k=0}^{N-\max\{\ell,n\}} \frac{(S-k)^m (N-k)!}{k! (N-k-\ell)! (N-k-n)!}. \quad (5.144)$$

5.J Computing correlators with the truncated short-time (TST) expansion

Here we provide a pedagogical tutorial for computing correlators using the truncated short-time TST expansion. For concreteness, we nominally consider N spins evolving under the one-axis twisting (OAT) Hamiltonian

$$H_{\text{OAT}} = \chi S_z^2, \quad (5.145)$$

additionally subject to spontaneous single-spin decay at rate γ_- , with jump operators $\mathcal{J}_- = \{s_-^{(j)} : j = 1, 2, \dots, N\}$. The equation of motion for a Heisenberg operator $(S_+^\ell S_z^m S_-^n)(t)$ is

$$\frac{d}{dt} \langle S_+^\ell S_z^m S_-^n \rangle = i\chi \left\langle [S_z^2, S_+^\ell S_z^m S_-^n]_- \right\rangle + \gamma_- \left\langle \mathcal{D}(\mathcal{J}_-)(S_+^\ell S_z^m S_-^n) \right\rangle, \quad (5.146)$$

where we have suppressed the explicit time dependence of operators for brevity. Using the results in appendices 5.C and 5.E.1 respectively to evaluate the commutator $[S_z^2, S_+^\ell S_z^m S_-^n]_-$ and dissipator $\mathcal{D}(\mathcal{J}_-)(S_+^\ell S_z^m S_-^n)$ in (5.146), we can expand

$$\begin{aligned} & \frac{d}{dt} \langle S_+^\ell S_z^m S_-^n \rangle \\ &= i\chi \langle (\ell - n) S_+^\ell (\ell + n + 2S_z) S_z^m S_-^n \rangle + \gamma_- \left\langle S_+^\ell \left[(S + S_z) (-1 + S_z)^m - \left(S + \frac{\ell + n}{2} + S_z \right) S_z^m \right] S_-^n \right\rangle. \end{aligned} \quad (5.147)$$

In practice, we do not want to keep track of such an expansion by hand, especially in the case of e.g. the two-axis twisting (TAT) and twist-and-turn (TNT) models with more general types of decoherence, for which the analogue of (5.147) may take several lines just to write out in full. Defining the operators $\mathcal{S}_m \equiv S_+^{m_+} S_z^{m_z} S_-^{m_-}$ with $\mathbf{m} \equiv (m_+, m_z, m_-)$ for shorthand, we note that the vector space spanned by $\{\mathcal{S}_m\}$ is closed under time evolution. We therefore expand

$$\frac{d}{dt} \langle \mathcal{S}_n \rangle = \langle T \mathcal{S}_n \rangle = \sum_{\mathbf{m}} \langle \mathcal{S}_m \rangle T_{m\mathbf{n}}, \quad (5.148)$$

where T is a superoperator that generates time evolution for Heisenberg operators. In the present example, the matrix elements $T_{m\mathbf{n}} \in \mathbb{C}$ of T are defined by (5.147) and (5.148). For any Hamiltonian

H with decoherence characterized by sets of jump operators \mathcal{J} and decoherence rates $\gamma_{\mathcal{J}}$, the matrix elements T_{mn} are more generally defined by

$$T\mathcal{S}_n = i[H, \mathcal{S}_n]_- + \sum_{\mathcal{J}} \gamma_{\mathcal{J}} \mathcal{D}(\mathcal{J}) \mathcal{S}_n = \sum_{\mathbf{m}} \mathcal{S}_{\mathbf{m}} T_{mn}. \quad (5.149)$$

The results in Appendices 5.C, 5.E, and 5.G can be used to write model-agnostic codes that compute matrix elements T_{mn} , taking a particular Hamiltonian H and decoherence processes $\{(\mathcal{J}, \gamma_{\mathcal{J}})\}$ as inputs.

In order to compute a quantity such as spin squeezing, we need to compute correlators of the form $\langle \mathcal{S}_n(t) \rangle$, where for clarity we will re-introduce the explicit time dependence of Heisenberg operators $\mathcal{S}_n(t)$. The order- M truncated short-time (TST) expansion takes

$$\langle \mathcal{S}_n(t) \rangle = \langle e^{tT} \mathcal{S}_n(0) \rangle = \sum_{k \geq 0} \frac{t^k}{k!} \langle T^k \mathcal{S}_n(0) \rangle = \sum_{k \geq 0} \frac{t^k}{k!} \sum_{\mathbf{m}} \langle \mathcal{S}_{\mathbf{m}}(0) \rangle T_{mn}^k \rightarrow \sum_{k=0}^M \frac{t^k}{k!} \sum_{\mathbf{m}} \langle \mathcal{S}_{\mathbf{m}}(0) \rangle T_{mn}^k, \quad (5.150)$$

where T_{mn}^k are matrix elements of the k -th time derivative operator T^k , given by

$$T_{mn}^0 \equiv \begin{cases} 1 & \mathbf{m} = \mathbf{n}, \\ 0 & \text{otherwise} \end{cases}, \quad T_{mn}^1 \equiv T_{mn}, \quad T_{mn}^{k>1} \equiv \sum_{\mathbf{p}_1, \mathbf{p}_2, \dots, \mathbf{p}_{k-1}} T_{m\mathbf{p}_{k-1}} \cdots T_{\mathbf{p}_3\mathbf{p}_2} T_{\mathbf{p}_2\mathbf{p}_1} T_{\mathbf{p}_1\mathbf{n}}. \quad (5.151)$$

Matrix elements T_{mn}^k and initial-time expectation values $\langle \mathcal{S}_{\mathbf{m}}(0) \rangle$ are thus computed as needed for any particular correlator $\langle \mathcal{S}_n(t) \rangle$ of interest, and combined according to (5.150). Note that initial-time expectation values $\langle \mathcal{S}_{\mathbf{m}}(0) \rangle$ are an *input* to the TST expansion, and need to be computed separately for any initial state of interest; expectation values with respect to spin-polarized (Gaussian) states are provided in Appendix 5.I. In practice, we further collect terms in (5.150) to write

$$\langle \mathcal{S}_n(t) \rangle \rightarrow \sum_{k=0}^M c_{nk} t^k, \quad c_{nk} \equiv \frac{1}{k!} \sum_{\mathbf{m}} \langle \mathcal{S}_{\mathbf{m}}(0) \rangle T_{mn}^k, \quad (5.152)$$

where c_{nk} are time-independent coefficients for the expansion of $\langle \mathcal{S}_n(t) \rangle$. After computing the coefficients c_{nk} , there is only negligible computational overhead to compute the correlator $\langle \mathcal{S}_n(t) \rangle$ for any time t .

5.K Analytical results for the one-axis twisting model

The one-axis twisting (OAT) Hamiltonian for N spin-1/2 particles takes the form

$$H_{\text{OAT}} = \chi S_z^2 = \frac{1}{2}\chi \sum_{j < k} \sigma_z^{(j)} \sigma_z^{(k)} + \frac{1}{4}N\chi, \quad (5.153)$$

where $\sigma_z^{(j)}$ represents a Pauli- z operator acting on spin j . This model is a special case of the zero-field Ising Hamiltonian previously solved in Ref. [120] via exact, analytical treatment of the quantum trajectory Monte Carlo method for computing expectation values. The solution therein accounts for coherent evolution in addition to decoherence via uncorrelated single-spin decay, excitation, and dephasing respectively at rates γ_- , γ_+ , and γ_z (denoted by Γ_{ud} , Γ_{du} , and Γ_{el} in Ref. [120]). Letting $S \equiv N/2$ and $\mu, \nu \in \{+1, -1\}$, we adapt expectation values computed in Ref. [120] for the initial state $|X\rangle \propto (|\uparrow\rangle + |\downarrow\rangle)^{\otimes N}$ with $S_x |X\rangle = S |X\rangle$ evolving under H_{OAT} , finding

$$\langle S_+(t) \rangle = S e^{-\kappa t} \Phi(\chi, t)^{N-1}, \quad (5.154)$$

$$\langle (S_\mu S_z)(t) \rangle = -\frac{\mu}{2} \langle S_\mu(t) \rangle + S \left(S - \frac{1}{2} \right) e^{-\kappa t} \Psi(\mu\chi, t) \Phi(\chi, t)^{N-2}, \quad (5.155)$$

$$\langle (S_\mu S_\nu)(t) \rangle = (1 - \delta_{\mu\nu}) (S + \mu \langle S_z(t) \rangle) + S \left(S - \frac{1}{2} \right) e^{-2\kappa t} \Phi([\mu + \nu]\chi, t)^{N-2}, \quad (5.156)$$

where

$$\Phi(X, t) \equiv e^{-\lambda t} \left[\cos(\omega_X t) + \frac{\lambda}{\omega_X} \sin(\omega_X t) \right], \quad \Psi(X, t) \equiv e^{-\lambda t} \left(\frac{\Delta + iX}{\omega_X} \right) \sin(\omega_X t), \quad (5.157)$$

for

$$\kappa \equiv \frac{1}{2}(\gamma_+ + \gamma_- + \gamma_z), \quad \lambda \equiv \frac{1}{2}(\gamma_+ + \gamma_-), \quad \Delta \equiv \gamma_+ - \gamma_-, \quad \omega_X \equiv \sqrt{X^2 - \lambda^2 - iX\Delta}. \quad (5.158)$$

In order to compute spin squeezing as measured by the Ramsey squeezing parameter ξ^2 defined in (5.12), we additionally need analytical expressions for $\langle S_z(t) \rangle$ and $\langle S_z^2(t) \rangle$. As these operators commute with both the OAT Hamiltonian and the single-spin operators $\sigma_z^{(j)}$, their evolution is governed entirely by decay-type decoherence (see Appendix 5.E.1), which means

$$\frac{d}{dt} \langle S_z(t) \rangle = S(\gamma_+ - \gamma_-) - (\gamma_+ + \gamma_-) \langle S_z(t) \rangle, \quad (5.159)$$

$$\frac{d}{dt} \langle S_z^2(t) \rangle = S(\gamma_+ + \gamma_-) + 2 \left(S - \frac{1}{2} \right) (\gamma_+ - \gamma_-) \langle S_z(t) \rangle - 2(\gamma_+ + \gamma_-) \langle S_z^2(t) \rangle. \quad (5.160)$$

The initial conditions $\langle S_z(0) \rangle = 0$ and $\langle S_z^2(0) \rangle = S/2$ then imply

$$\langle S_z(t) \rangle = S \left(\frac{\gamma_+ - \gamma_-}{\gamma_+ + \gamma_-} \right) \left(1 - e^{-(\gamma_+ + \gamma_-)t} \right), \quad \langle S_z^2(t) \rangle = \frac{1}{2}S + S \left(S - \frac{1}{2} \right) \left(\frac{\langle S_z(t) \rangle}{S} \right)^2. \quad (5.161)$$

With appropriate assumptions about the relevant sources of decoherence, the expectation values in (5.154)–(5.156) and (5.161) are sufficient to compute the spin squeezing parameter ξ^2 in (5.12) at any time throughout evolution of the initial state $|X\rangle$ under H_{OAT} .

5.L Diagnosing breakdown of the TST expansion

In Figure 5.1 of the main text, the TST expansion provided nearly exact results for squeezing until a sudden departure that quickly resulted in an unphysical squeezing parameter, $\xi^2 < 0$. In general, however, there is no fundamental relationship between the breakdown of the TST expansion and the conditions for a physical squeezing parameter ξ^2 . A proper diagnosis of breakdown therefore requires inspection of the correlators $\langle \mathcal{S}_n(t) \rangle$ used to compute the squeezing parameter ξ^2 , which upon breakdown will rapidly take unphysical values with $|\langle \mathcal{S}_n(t) \rangle| \gtrsim S^{|n|}$. As an example, Figure 5.4 shows the squeezing parameter ξ^2 throughout decoherence-free evolution of $N = 100$ spins initially in the state $|X\rangle$. In this example, the squeezing computed by the TST expansion for the TAT model diverges from the exact answer without an immediate and obvious signature of breakdown. Nonetheless, breakdown can still be diagnosed by inspection of individual correlators, as shown in Figure 5.5, where we plot $\text{Im} \langle S_+^2 \rangle$ as a function of time for $N = 100$ spins evolving under the TAT without decoherence. Figure 5.5 shows that breakdown clearly occurs around $N\chi t \lesssim 7$, when the correlator $\langle S_+^2 \rangle$ begins to diverge to values $\gtrsim S^2 = (N/2)^2 = 2500$ in magnitude. A joint inspection of figures 5.4 and 5.5 suffice to trace the anomalous behavior of ξ^2 from $N\chi t \approx 7$ back to $N\chi t \approx 6$, when it first took a sudden turn before becoming unphysical at $N\chi t \approx 8$.

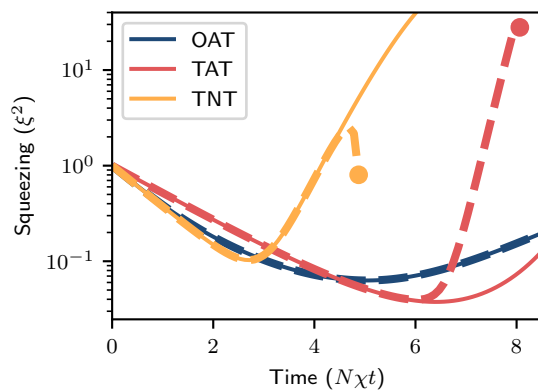


Figure 5.4: Spin squeezing throughout decoherence-free evolution of $N = 100$ spins initially in the state $|X\rangle$, computed using both exact methods (solid lines) and the TST expansion in Eq. (5.8) with $M = 35$ (dashed lines). Solid circles mark the times at which the TST expansion gives an unphysical result with $\xi^2 < 0$.

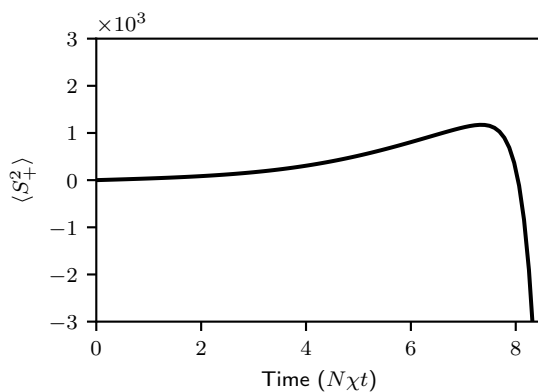


Figure 5.5: A collective spin correlator in the TAT model with $N = 100$ spins and no decoherence, computed using the TST expansion with $M = 35$. The divergence of correlators of this sort can be used to diagnose the breakdown of the TST expansion.

5.M Spin squeezing with strong decoherence

Here we provide supplementary evidence of our finding in Section 5.3 that the TNT model can produce more squeezing than the OAT or TAT models in the presence of strong decoherence. To this end, Figure 5.6 shows the minimal squeezing parameter ξ_{\min}^2 achievable with $N = 100$ spins through the OAT, TAT, and TNT models as a function of the rate γ_0 at which individual spins undergo spontaneous decay, excitation, and dephasing. These results were computed with quantum trajectory simulations, with 10^3 trajectories per data point. While the OAT and TAT models produce more squeezing than the TNT model with weak decoherence, this squeezing falls off faster with an increasing decoherence rate γ_0 . The relative robustness of TNT is in part a consequence of the fact that TNT initially generates squeezing at a faster rate than OAT or TAT, thereby allowing it to produce more squeezing before the degrading effects of decoherence kick in.

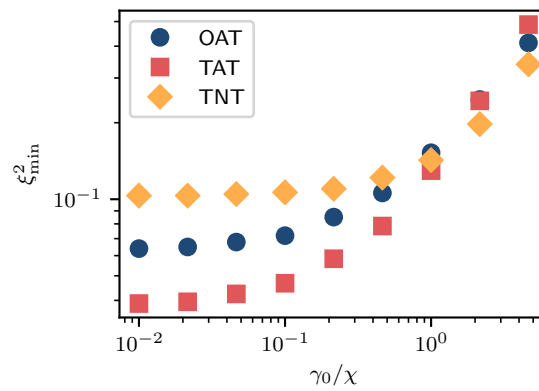


Figure 5.6: Optimal spin squeezing of $N = 100$ spins undergoing spontaneous decay, excitation, and dephasing at rates $\gamma_- = \gamma_+ = \gamma_z = \gamma_0$, computed using quantum trajectory simulations with 10^3 trajectories per data point.

5.N Heisenberg operators in open quantum systems

Here we explain the origin and character of the mean-zero “noise” operators $\mathcal{E}_{\mathcal{O}}(t)$ that appear in the expansion of a Heisenberg operator $\mathcal{O}(t) = \sum_{\mathbf{m}} \mathcal{O}_{\mathbf{m}}(t) \mathcal{S}_{\mathbf{m}} + \mathcal{E}_{\mathcal{O}}(t)$ with time-dependent coefficients $\mathcal{O}_{\mathbf{m}}(t)$ for time-independent Schrödinger operators $\mathcal{S}_{\mathbf{m}}$. Our discussion should clarify why noise operators play no role in our calculation of expectation values of the form $\langle \mathcal{O}(t) \rangle$ and $\langle \mathcal{O} \mathcal{Q}(t) \rangle$, despite the fact that noise operators generally *do* need to be considered in the calculation of more general multi-time correlators in open quantum systems[181].

In any closed quantum system with initial state ρ and propagator $U(t)$, such that the state at time t is $\rho(t) \equiv U(t) \rho U^\dagger(t)$, time-dependent Heisenberg operators $\mathcal{O}(t)$ are uniquely defined from time-independent Schrödinger operators \mathcal{O} by

$$\langle \mathcal{O}(t) \rangle \equiv \text{tr} [\rho(t) \mathcal{O}] = \text{tr} [\rho \mathcal{O}(t)]. \quad (5.162)$$

Enforcing (5.162) for *arbitrary* initial states ρ forces $\mathcal{O}(t) = U^\dagger(t) \mathcal{O} U(t)$. In an open quantum system, however, the definition of a Heisenberg operator is not so straightforward. Open systems can often be understood as subsystems of a larger closed system. Consider therefore an open system S with environment E , a joint initial state ρ_{SE} , and propagator $U_{SE}(t)$. The reduced state $\rho_S(t)$ of S at time t is

$$\rho_S(t) \equiv \text{tr}_E [\rho_{SE}(t)] = \text{tr}_E [U_{SE}(t) \rho_{SE} U_{SE}^\dagger(t)] \equiv \mathcal{U}_{\underline{S}}(t) \rho_S, \quad (5.163)$$

where $\rho_S \equiv \rho_S(0)$ is a time-independent state of S in the Heisenberg picture, \underline{S} denotes the space of operators on S , and the quantum channel $\mathcal{U}_{\underline{S}}(t)$ has the decomposition[186]

$$\mathcal{U}_{\underline{S}}(t) \rho_S = \sum_j \mathcal{U}_S^{(j)}(t) \rho_S \mathcal{U}_S^{(j)\dagger}(t) \quad (5.164)$$

with ordinary operators $\mathcal{U}_S^{(j)}(t)$ on S . We can therefore expand

$$\langle \mathcal{O}_S(t) \rangle = \text{tr} [\rho_S(t) \mathcal{O}_S] = \text{tr} [\mathcal{U}_{\underline{S}}(t) \rho_S \mathcal{O}_S] = \text{tr} [\rho_S \mathcal{U}_{\underline{S}}^\dagger(t) \mathcal{O}_S] = \text{tr} [\rho_S \underline{\mathcal{O}}_S(t)] = \langle \underline{\mathcal{O}}_S(t) \rangle, \quad (5.165)$$

where $\mathcal{U}_{\underline{S}}^\dagger(t)$ is the adjoint map of $\mathcal{U}_{\underline{S}}(t)$ (with respect to a trace inner product between operators on S), and we define the time-dependent operator

$$\underline{\mathcal{O}}_S(t) \equiv \mathcal{U}_{\underline{S}}^\dagger(t) \mathcal{O}_S = \sum_j \mathcal{U}_S^{(j)\dagger}(t) \mathcal{O}_S \mathcal{U}_S^{(j)}(t). \quad (5.166)$$

We thus find that substituting $\underline{\mathcal{O}}_S(t)$ in place of $\mathcal{O}_S(t)$ suffices for the calculation of correlators $\langle \mathcal{O}_S(t) \rangle$, thereby accounting for the validity of the equation of motion in (5.2). As we show below, this substitution also suffices for the calculation of two-time correlators of the form $\langle \mathcal{O}_S \mathcal{Q}_S(t) \rangle$ when the environment E is Markovian.

The problem with *defining* Heisenberg operators $\mathcal{O}_S(t)$ by $\underline{\mathcal{O}}_S(t)$ only becomes evident when considering products of Heisenberg operators. One would like for the product of two Heisenberg operators $\mathcal{O}_S(t)$ and $\mathcal{Q}_S(t)$ to satisfy $\mathcal{O}_S(t) \mathcal{Q}_S(t) = (\mathcal{O}_S \mathcal{Q}_S)(t)$. This intuition can be formalized by observing that

$$\langle \mathcal{O}_S(t) \rangle = \text{tr} [\rho_{SE}(t) (\mathcal{O}_S \otimes \mathbb{1}_E)] = \text{tr} [\rho_{SE} (\mathcal{O}_S \otimes \mathbb{1}_E)(t)] = \langle (\mathcal{O}_S \otimes \mathbb{1}_E)(t) \rangle, \quad (5.167)$$

where $\mathbb{1}_E$ is the identity operator on E , expectation values of Heisenberg operators on system $A \in \{S, E, SE\}$ are taken with respect to the state ρ_A , and

$$(\mathcal{O}_S \otimes \mathbb{1}_E)(t) \equiv U_{SE}^\dagger(t) (\mathcal{O}_S \otimes \mathbb{1}_E) U_{SE}(t). \quad (5.168)$$

By expanding Heisenberg operators similarly to (5.167) and (5.168), we then find

$$\langle \mathcal{O}_S(t) \mathcal{Q}_S(t) \rangle = \langle (\mathcal{O}_S \otimes \mathbb{1}_E)(t) (\mathcal{Q}_S \otimes \mathbb{1}_E)(t) \rangle = \langle (\mathcal{O}_S \mathcal{Q}_S \otimes \mathbb{1}_E)(t) \rangle = \langle (\mathcal{O}_S \mathcal{Q}_S)(t) \rangle. \quad (5.169)$$

The expression in (5.166), however, makes it clear that generally $\underline{\mathcal{O}}_S(t) \underline{\mathcal{Q}}_S(t) \neq (\underline{\mathcal{O}}_S \underline{\mathcal{Q}}_S)(t)$. To correct for this discrepancy, we define

$$\mathcal{O}_S(t) \equiv \underline{\mathcal{O}}_S(t) + \mathcal{E}_{\mathcal{O}_S}(t) \quad (5.170)$$

in terms of new “noise” operators $\mathcal{E}_{\mathcal{O}_S}(t)$ that are essentially defined to enforce the consistency of operator products such as $\mathcal{O}_S(t) \mathcal{Q}_S(t) = (\mathcal{O}_S \mathcal{Q}_S)(t)$. Self-consistency forces noise operators to be mean-zero, as

$$\langle \mathcal{E}_{\mathcal{O}_S}(t) \rangle = \langle \mathcal{O}_S(t) \rangle - \langle \underline{\mathcal{O}}_S(t) \rangle = 0. \quad (5.171)$$

Furthermore, if the environment E is Markovian, then noise operators are also uncorrelated with initial-time observables, i.e. $\langle \mathcal{O}_S \mathcal{E}_{\mathcal{Q}_S}(t) \rangle = 0$, which means that noise operators can be neglected in the calculation of two-time correlators of the form $\langle \mathcal{O}_S \mathcal{Q}_S(t) \rangle$. To see why, we observe that a Markovian environment is essentially defined to satisfy

$$\rho_{SE}(t) = U_{SE}(t) \rho_{SE} U_{SE}^\dagger(t) \approx \rho_S(t) \otimes \rho_E = \mathcal{U}_S(t) \rho_S \otimes \rho_E, \quad (5.172)$$

with ρ_E a time-independent steady state of the environment. If we enforce (5.172) for all states ρ_S , e.g. the maximally mixed state $\rho_S^{(1)} \propto \mathbb{1}_S$ and $\rho_S^{(2)} \equiv \rho_S^{(1)} + \mathcal{O}_S$ with \mathcal{O}_S any traceless operator on S with operator norm $\|\mathcal{O}_S\| \leq 1/\text{tr} \mathbb{1}_S$ (i.e. such that $\rho_S^{(2)}$ remains positive semi-definite, or a valid quantum state), then by linearity we find that

$$U_{SE}(t) (\mathbb{1}_S \otimes \rho_E) U_{SE}^\dagger(t) \approx \mathcal{U}_S(t) \mathbb{1}_S \otimes \rho_E, \quad U_{SE}(t) (\mathcal{O}_S \otimes \rho_E) U_{SE}^\dagger(t) \approx \mathcal{U}_S(t) \mathcal{O}_S \otimes \rho_E, \quad (5.173)$$

which implies that the Markov approximation (5.172) holds even if we replace ρ_S by any operator on S , and in particular

$$U_{SE}(t) \rho_{SE} (\mathcal{O}_S \otimes \mathbb{1}_E) U_{SE}^\dagger(t) = U_{SE}(t) (\rho_S \mathcal{O}_S \otimes \rho_E) U_{SE}^\dagger(t) \approx \mathcal{U}_S(t) (\rho_S \mathcal{O}_S) \otimes \rho_E. \quad (5.174)$$

We can therefore expand

$$\langle \mathcal{O}_S \mathcal{Q}_S(t) \rangle = \text{tr} \left[\rho_{SE} (\mathcal{O}_S \otimes \mathbb{1}_E) U_{SE}^\dagger(t) (\mathcal{Q}_S \otimes \mathbb{1}_E) U_{SE}(t) \right] \quad (5.175)$$

$$= \text{tr} \left[U_{SE}(t) \rho_{SE} (\mathcal{O}_S \otimes \mathbb{1}_E) U_{SE}^\dagger(t) (\mathcal{Q}_S \otimes \mathbb{1}_E) \right], \quad (5.176)$$

and invoke the Markov approximation in (5.174) to find that

$$\langle \mathcal{O}_S \mathcal{Q}_S(t) \rangle \approx \text{tr} \left[\mathcal{U}_S(t) (\rho_S \mathcal{O}_S) \mathcal{Q}_S \right] = \text{tr} \left[\rho_S \mathcal{O}_S \mathcal{U}_S^\dagger(t) \mathcal{Q}_S \right] = \langle \mathcal{O}_S \underline{\mathcal{Q}}_S(t) \rangle, \quad (5.177)$$

which implies

$$\langle \mathcal{O}_S \mathcal{E}_{\mathcal{Q}_S}(t) \rangle = \langle \mathcal{O}_S \mathcal{Q}_S(t) \rangle - \langle \mathcal{O}_S \underline{\mathcal{Q}}_S(t) \rangle \approx 0. \quad (5.178)$$

Noise operators thus play no role in the calculation of correlators such as $C(t)$ in (5.13). In contrast, noise operators generally *do* play a role in the calculation of multi-time correlators of the

form $\langle \prod_j \mathcal{O}_S^{(j)}(t_j) \rangle$ [181]. Furthermore, these calculations generally require additional assumptions about the environment. To keep our discussion simple and general, we therefore exclude the effects of noise terms in Section 5.4.

5.O Short-time linear response and two-time correlators

Here we discuss the appearance of two-time correlation functions in the short-time linear response of correlators to perturbations of a Hamiltonian. Consider an initial Hamiltonian H perturbed by an operator V with $\|V\| \ll \|H\|$, where $\|\mathcal{O}\|$ denotes the operator norm of \mathcal{O} , such that the net Hamiltonian is $\tilde{H} = H + V$. We denote the generator of Heisenberg time evolution under the perturbed (unperturbed) Hamiltonian by \tilde{T} (T). These generators are related by

$$\tilde{T} = T + i\underline{V} \quad (5.179)$$

where \underline{V} is a superoperator whose action on operators \mathcal{O} is defined by

$$\underline{V}\mathcal{O} \equiv [V, \mathcal{O}]_- . \quad (5.180)$$

Through quadratic order in the time t and linear order in the perturbation \underline{V} , we can say that

$$e^{t\tilde{T}} \approx \frac{1}{2} \left[e^{tT}, e^{it\underline{V}} \right]_+ \approx e^{tT} + \frac{1}{2}it \left[e^{tT}, \underline{V} \right]_+ . \quad (5.181)$$

Defining perturbed and unperturbed Heisenberg operators $\tilde{\mathcal{O}}(t)$ and $\mathcal{O}(t)$ that respectively satisfy $\langle \tilde{\mathcal{O}}(t) \rangle = \langle e^{t\tilde{T}} \mathcal{O} \rangle$ and $\langle \mathcal{O}(t) \rangle = \langle e^{tT} \mathcal{O} \rangle$, we thus find that for sufficiently small times t and weak perturbations V ,

$$\langle \tilde{\mathcal{O}}(t) - \mathcal{O}(t) \rangle = \left\langle \left(e^{t\tilde{T}} - e^{tT} \right) \mathcal{O} \right\rangle \approx \frac{1}{2}it \left(\langle [V, \mathcal{O}]_-(t) \rangle + \langle [V, \mathcal{O}(t)]_- \rangle \right) . \quad (5.182)$$

Two-time correlators $\langle V\mathcal{O}(t) \rangle$ and $\langle \mathcal{O}(t)V \rangle$, in addition to the expectation values $\langle (V\mathcal{O})(t) \rangle$ and $\langle (\mathcal{O}V)(t) \rangle$, thus determine the short-time linear response of correlators $\langle \mathcal{O}(t) \rangle$ to perturbations V of a Hamiltonian.

Chapter 6

Spin squeezing with short-range spin-exchange interactions

Prologue

Chapter 4 featured a proposal to generate spin-squeezed states using uniform spin-spin interactions with an $SU(2)$ symmetry that is broken down to $U(1)$ by a single-particle field. The same sort of symmetry breaking can occur by modifying the interactions directly. Instead of adding a single-body axial field, we can add two-body axial (Ising) interactions, which results in a so-called XXZ model. A major advantage to this strategy is that it requires little to no novelty on the experimental front: the XXZ model has already been implemented in a variety of atomic, molecular, and optical platforms. However, most implementations of the XXZ model have interactions that are not uniform, but rather fall off with distance as a power-law. These observations naturally lead to questions about the spin-squeezing properties of the power-law XXZ model, which is the focus of this chapter. The bulk of this chapter is taken from Ref. [4]. In addition to myself and Ana Maria Rey, this work featured major contributions from Chunlei Qu.

Abstract

We investigate many-body spin squeezing dynamics in an XXZ model with interactions that fall off with distance r as $1/r^\alpha$ in $D = 2$ and 3 spatial dimensions. In stark contrast to the Ising model, we find a broad parameter regime where spin squeezing comparable to the infinite-range $\alpha = 0$ limit is achievable even when interactions are short-ranged, $\alpha > D$. A region of “collective” behavior in which optimal squeezing grows with system size extends all the way to the $\alpha \rightarrow \infty$

limit of nearest-neighbor interactions. Our predictions, made using the discrete truncated Wigner approximation (DTWA), are testable in a variety of experimental cold atomic, molecular, and optical platforms.

6.1 Introduction

Quantum technologies receive an enormous amount of attention for their potential to push beyond classical limits on physically achievable tasks. In order to be useful, however, these technologies must demonstrate a practical advantage over their classical counterparts. While most public attention has focused on a quantum advantage in the realm of computing, the quantum metrology community has made tremendous progress in developing strategies and platforms for surpassing classical limits on measurement precision [31, 109, 187–189]. A key element in these strategies is the use of entanglement to enhance the capabilities of individual, uncorrelated quantum systems. Spin squeezing is one of the most promising strategies for using entanglement to achieve a quantum advantage in practical sensing applications [32, 35].

The paradigmatic setting for spin squeezing is the *one-axis twisting* (OAT) model [33, 35], which generates spin-squeezed states by use of uniform, infinite-range Ising interactions that do not distinguish between the constituent spins. These uniform interactions can be implemented directly via collisional interactions between delocalized atoms [2, 50, 190], as well as indirectly through coupling to collective phonon modes [139, 191, 192] or cavity photons [114, 142, 148, 193, 194]. Despite numerous proof-of-principle demonstrations, however, no spin squeezing experiment to date has achieved a practical metrological advantage, and current platforms relying on infinite-range interactions face a host of technical and fundamental difficulties that will require new breakthroughs to overcome.

The Ising model with power-law interactions that fall off with distance r as $1/r^\alpha$ generates squeezing that scales with system size when $\alpha < D$ in D spatial dimensions [195], which is highly desirable for metrological applications. Conversely, the power-law Ising model generates only a constant amount of squeezing that is independent of system size when $\alpha > D$. In practice, only

a limited number of platforms can achieve long-range spin interactions ($\alpha < D$), making it highly desirable to shed light on the possibilities for scalable spin squeezing with short-range interactions ($\alpha > D$), which encompasses e.g. super-exchange, dipolar, Van der Waals, and far-detuned phonon-mediated interactions.

Motivated by the intuition (echoed in Refs. [2, 113, 196–199]) that adding spin-exchange interactions to the Ising model should energetically protect collective behavior reminiscent of the OAT model, in this work we investigate the spin squeezing properties of the power-law XXZ model, whose ground-state physics was studied in Ref. [200]. Remarkably, we find a broad range of parameters for which the power-law XXZ model nearly saturates the amount of squeezing generated in the infinite-range ($\alpha = 0$) limit. Even when interactions are short-ranged ($\alpha > D$), we observe a large region of collective squeezing behavior in which the amount of achievable spin squeezing grows with system size. This region extends through to the $\alpha \rightarrow \infty$ limit of nearest-neighbor interactions. Our work opens up a new prospect of spin squeezing in variety of cold atomic, molecular, and optical (AMO) systems, including ultracold neutral atoms [28, 92], Rydberg atoms [201, 202], electric and magnetic dipolar quantum gasses [203–206], and trapped ions [191, 207].

6.2 Background and theory

We begin with a brief review of spin squeezing and the OAT model, described by the Ising Hamiltonian

$$H_{\text{OAT}} = \chi \sum_{i,j=1}^N s_{z,i} s_{z,j} = \chi S_z^2, \quad (6.1)$$

where χ is the OAT squeezing strength; the spin- z operator $s_{z,i} \equiv \sigma_{z,i}/2$ is defined in terms of the Pauli- z operator $\sigma_{z,i}$ on spin i ; and $S_z \equiv \sum_{i=1}^N s_{z,i}$ is a collective spin- z operator. Eigenstates of H_{OAT} can be classified by a (nonnegative) total spin $S \in \{N/2, N/2 - 1, \dots\}$, and a projection $m_z \in \{S, S - 1, \dots, -S\}$ of spin onto the z axis. The manifold of all states with maximal total spin $S = N/2$ (e.g. spin-polarized states) is known as the *Dicke manifold* [35]. Equivalently, the Dicke manifold consists of all *permutationally symmetric* states that do not distinguish between underlying

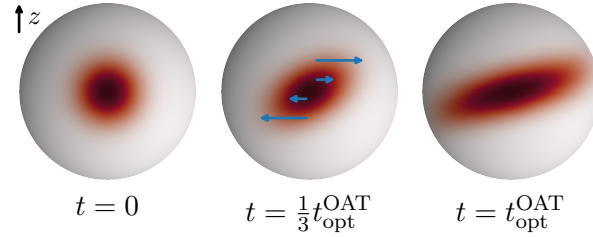


Figure 6.1: Representations of the state $|\psi(t)\rangle$ of $N = 40$ spins initially polarized along the equator, and evolved under the OAT Hamiltonian for a time t up to the optimal OAT squeezing time $\chi t_{\text{opt}}^{\text{OAT}} \sim 1/N^{2/3}$. Darker colors at a point $\hat{\mathbf{n}}$ on the sphere correspond to a larger overlap $Q_{\psi(t)}(\hat{\mathbf{n}}) \equiv |\langle \hat{\mathbf{n}} | \psi(t) \rangle|^2$, where $|\hat{\mathbf{n}}\rangle$ is a state in which all spins are polarized along $\hat{\mathbf{n}}$.

spins. States in the Dicke manifold can be represented by distributions on a sphere, whose variances along different axes must satisfy an appropriate set of quantum (Heisenberg) uncertainty relations (see Figure 6.1). In the case of a single (two-level) spin, this distribution has a fixed, Gaussian-like shape that is uniquely characterized by its orientation. Identifying the peak of this distribution recovers the representation of a qubit state by a point on the Bloch sphere. For $N > 1$ spins, meanwhile, this distribution can acquire additional structure with metrological utility.

Given an initial state of N spins polarized along the equator, represented by a Gaussian-like distribution on a sphere, the net effect of the OAT Hamiltonian is to shear this distribution, resulting in a *squeezed* state with a reduced variance $(\Delta\phi)^2$ along some axis. This reduced variance allows for an enhanced measurement sensitivity to rotations of the collective spin state along the squeezed axis, at the expense of a reduced sensitivity to rotations along an orthogonal axis. Spin squeezing can be quantified by the maximal gain in angular resolution $\Delta\phi$ over that achieved by a spin-polarized state [35],

$$\xi^2 \equiv \frac{(\Delta\phi_{\text{min}})^2}{(\Delta\phi_{\text{polarized}})^2} = \min_{\phi} \text{var}(S_{\phi}^{\perp}) \times \frac{N}{|\langle \mathbf{S} \rangle|^2}, \quad (6.2)$$

where $\mathbf{S} \equiv (S_x, S_y, S_z)$ is a vector of collective spin operators; the operator $S_{\phi}^{\perp} \equiv \mathbf{S} \cdot \hat{\mathbf{n}}_{\phi}^{\perp}$ is the projection of \mathbf{S} onto an axis $\hat{\mathbf{n}}_{\phi}^{\perp}$ parameterized by an angle ϕ in the plane orthogonal to the mean spin vector $\langle \mathbf{S} \rangle$; and $\text{var}(\mathcal{O}) \equiv \langle \mathcal{O}^2 \rangle - \langle \mathcal{O} \rangle^2$ denotes the variance of \mathcal{O} . A spin squeezing parameter $\xi^2 < 1$ implies the presence of many-body entanglement [208] that enables a sensitivity to rotations beyond that set by classical limits on measurement precision [31]. The OAT model can prepare

squeezed states with $\xi^2 \sim 1/N^{2/3}$, whereas the fundamental (Heisenberg) limit imposed by quantum mechanics is $\xi^2 \sim 1/N$ [31].

To accommodate for the fact that physical interactions are typically local, the OAT Hamiltonian in Eq. (6.1) can be modified by the introduction of coefficients $1/|\mathbf{r}_i - \mathbf{r}_j|^\alpha$ in the coupling between spins i, j at positions $\mathbf{r}_i, \mathbf{r}_j$, resulting in the power-law Ising model. The introduction of non-uniform couplings means that the power-law Ising model breaks permutational symmetry, coupling the Dicke manifold of permutationally symmetric states with total spin $S = N/2$ to asymmetric states with $S < N/2$, and thereby invalidating the representation of squeezing dynamics shown in Figure 6.1. The leakage of population outside the manifold of permutationally symmetric states can be energetically suppressed by the additional introduction of spin-aligning $\mathbf{s}_i \cdot \mathbf{s}_j$ interactions, where $\mathbf{s}_i \equiv (s_{x,i}, s_{y,i}, s_{z,i})$ is the spin vector for spin i . In total, we thus arrive at an XXZ model described by the Hamiltonian

$$H_{\text{XXZ}} = \sum_{i \neq j} \frac{J_\perp \mathbf{s}_i \cdot \mathbf{s}_j + (J_z - J_\perp) s_{z,i} s_{z,j}}{|\mathbf{r}_i - \mathbf{r}_j|^\alpha}. \quad (6.3)$$

When interactions are uniform, $\alpha = 0$, the $\sum_{i \neq j} \mathbf{s}_i \cdot \mathbf{s}_j \sim \mathbf{S}^2 = S(S+1)$ term in Eq. (6.3) is a constant of motion within manifolds of definite total spin S , resulting in an OAT model with $\chi = J_z - J_\perp$.

When $J_z - J_\perp = 0$, the XXZ model contains only the spin-aligning $\mathbf{s}_i \cdot \mathbf{s}_j$ terms, and if interactions are long-ranged, $\alpha \leq D$, then the Dicke manifold is gapped away from all orthogonal states by a non-vanishing energy difference $\Delta_{\text{gap}} \gtrsim |J_\perp|$ (see Appendix 6.A). As a consequence, for any finite N and $\alpha \leq D$ there exists a non-vanishing range of coupling strengths $J_z \approx J_\perp$ for which a perturbative treatment of the anisotropic Ising terms in Eq. (6.3) is valid. In this case, the XXZ model becomes precisely the OAT model at first order in perturbation theory, with a squeezing strength $\chi_{\text{eff}} = h_\alpha (J_z - J_\perp)$, where h_α is the average of $1/|\mathbf{r}_i - \mathbf{r}_j|^\alpha$ over all $i \neq j$. If interactions are short-ranged with $\alpha > D$, then generally $\Delta_{\text{gap}} \rightarrow 0$ as $N \rightarrow \infty$, formally invalidating perturbation theory for any J_z at sufficiently large N . Nonetheless, the spin-aligning terms of the XXZ model can still enable a non-perturbative emergence of “collective” behavior

resembling perturbative, gap-protected OAT. We numerically explore the prospect of spin squeezing with short-ranged interactions in the following section, finding that squeezing comparable to OAT may be possible with a wide range of α and J_z , including the $\alpha \rightarrow \infty$ limit of nearest-neighbor interactions.

6.3 Results

Whereas the quantum Ising model is exactly solvable [120, 209], the XXZ model in Eq. (6.3) is not. We therefore investigate the spin squeezing properties of the XXZ model using the discrete truncated Wigner approximation (DTWA) [129] for $N = 4096 = 64^2 = 16^3$ spins, focusing on the case of two ($D = 2$) and three ($D = 3$) spatial dimensions (see Appendix 6.B for $D = 1$, where our main results are less striking but still hold). DTWA has been shown to accurately capture the behavior of collective spin observables in a variety of settings [129, 210], and we provide additional benchmarking of DTWA for the XXZ model on lattices of up to 7×7 spins in Appendix 6.C, although it will ultimately be up to experiments to verify our findings. Our main results are summarized in Figure 6.2, in which we explore the squeezing behavior of XXZ model in Eq. (6.3) around the isotropic (Heisenberg) point at $J_z = J_\perp$ by varying both J_z/J_\perp and the power-law exponent α . Specifically, we examine (i) the optimal squeezing parameter $\xi_{\text{opt}}^2 \equiv \min_t \xi^2(t) = \xi^2(t_{\text{opt}})$, (ii) the minimal squared magnetization throughout squeezing dynamics, $\langle \mathbf{S}^2 \rangle_{\text{min}} \equiv \min_{t \leq t_{\text{opt}}} \langle \mathbf{S}^2 \rangle(t)$, and (iii) the optimal squeezing time t_{opt} .

First and foremost, Figure 6.2 confirms the theoretical argument that OAT-limited squeezing should be achievable with any power-law exponent $\alpha \leq D$ for some non-vanishing range of Ising couplings, $J_z \approx J_\perp$. Moreover, when $\alpha \leq D$ we observe that this capability persists well beyond the perturbative window with $|J_z - J_\perp| \ll |J_\perp|$, covering all $J_z/J_\perp < 1$ shown in Figure 6.2 and an increasing range of $J_z/J_\perp > 1$ as $\alpha \rightarrow 0$. Even more strikingly than the behavior at $\alpha \leq D$, Figure 6.2 shows that squeezing well beyond the Ising limit can still be achievable for a wide range of Ising couplings $J_z/J_\perp < 1$ when interactions are short-ranged, $\alpha > D$. In a nearest-neighbor XXZ model ($\alpha \rightarrow \infty$), the region $|J_z| < |J_\perp|$ corresponds to the equilibrium XY phase, whereas $J_z/J_\perp < -1$

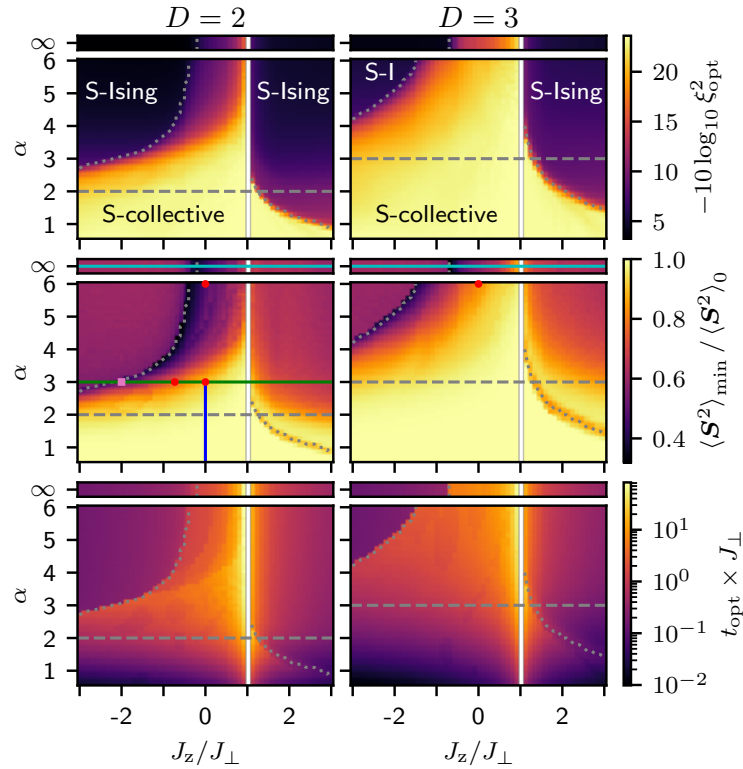


Figure 6.2: The optimal squeezing ξ_{opt}^2 (top), minimal squared magnetization $\langle \mathbf{S}^2 \rangle_{\text{min}}$ (middle), and optimal squeezing time t_{opt} (bottom) for $N = 4096 = 64^2 = 16^3$ spins in $D = 2$ (left) and $D = 3$ (right) spatial dimensions. Spins are initially polarized along the equator and evolved under the XXZ Hamiltonian in Eq. (6.3). Squeezing ξ_{opt}^2 is shown in decibels, and $\langle \mathbf{S}^2 \rangle_{\text{min}}$ is normalized to its initial value $\langle \mathbf{S}^2 \rangle_0 = \frac{N}{2} \left(\frac{N}{2} + 1 \right)$. Dashed grey lines mark $\alpha = D$, and dotted grey lines track local minima of $\langle \mathbf{S}^2 \rangle_{\text{min}}$, marking the boundary between regions of collective and Ising-limited squeezing dynamics, respectively denoted “S-collective” and “S-Ising”. Other markers in the middle panels indicate vales of J_z/J_{\perp} , α , D that are currently accessible with neutral atoms [211, 212] (cyan line), Rydberg atoms [201, 202, 213] (red dots), polar molecules [203, 204, 214] (green line), magnetic atoms [205, 206] (pink square), and trapped ions [191] (blue line). DTWA results are averaged over 500 trajectories.

and $J_z/J_\perp > +1$ correspond to the equilibrium Ising ferromagnet and anti-ferromagnet phases (depending on the sign of J_\perp) [200, 215]. The asymmetry about $J_z = J_\perp$ in Figure 6.2 thus hints at an interesting connection between equilibrium physics [200] and far-from-equilibrium dynamical behavior of the XXZ model (discussed further in the next section)^a.

Though the attainable amount of squeezing generally decreases with shorter range (increasing α) and stronger anisotropy (decreasing $J_z/J_\perp < 1$), a region of “collective” squeezing behavior connected to the OAT limit persists through to the $\alpha \rightarrow \infty$ limit of nearest-neighbor interactions. This region is reminiscent of the $\frac{2}{3}D \leq \alpha < D$ region of the power-law Ising model ($J_\perp = 0$), in which squeezing falls short of the OAT limit, but still grows with system size [195].

In fact, the transition between collective and Ising-limited squeezing regions, which we respectively denote “S-collective” and “S-Ising” (with an “S-” prefix to emphasize the role of squeezing in their characterization), is marked by a discontinuous change in both the minimal squared magnetization $\langle \mathcal{S}^2 \rangle_{\min}$ and the optimal squeezing time t_{opt} , signifying the presence of a dynamical phase transition. The dynamical phases in question can be characterized by the behavior of optimal squeezing ξ_{opt}^2 , which either scales with system size or saturates to a constant value. We discuss and clarify these points below.

The discontinuity in optimal squeezing time t_{opt} at the dynamical phase boundary in Figure 6.2 is the result of a competition between local optima in squeezing over time, shown in Figure 6.3. Large amounts of spin squeezing are generated in the S-collective phase near the isotropic point at $J_z = J_\perp$. The amount of squeezing generated by collective dynamics falls off away from the isotropic point, until it finally drops below an “Ising” squeezing peak that is generated at much short times, resulting in a discontinuous change in the time at which squeezing is optimal. The discontinuous change in the optimal squeezing time is in turn responsible for the sudden change in the minimal squared magnetization $\langle \mathcal{S}^2 \rangle_{\min}$, which has less time to decay in the Ising-limited (S-Ising) regime.

^a In fact, when $J_\perp < 0$ the S-collective region at $J_z/J_\perp < 1$ is contained *within* the ground-state XY phase of the power-law XXZ model [200].

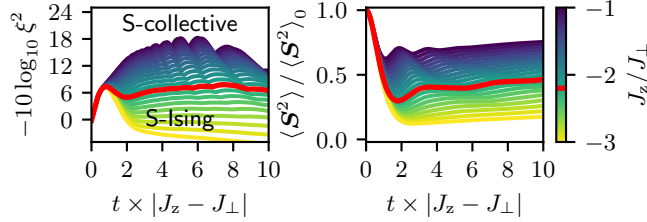


Figure 6.3: Squeezing ξ^2 and squared magnetization $\langle \mathbf{S}^2 \rangle$ over time for the power-law XXZ model with $\alpha = 3$ on a 2D lattice of 64×64 spins. Color indicates the value of J_z/J_\perp , and red lines (at $J_z/J_\perp = -2.2$) mark the approximate transition between S-collective and S-Ising phases, when the “collective” squeezing peak at $\tau \equiv t \times |J_z - J_\perp| \sim 6$ drops below the “Ising” peak at $\tau \sim 1$. For the parameters shown, $\langle \mathbf{S}^2 \rangle$ reaches a minimum at $\tau \sim 2$, which means that optimal squeezing at $\tau \sim 1$ is reached before maximal decay of $\langle \mathbf{S}^2 \rangle$ in the S-Ising phase.

It is no surprise that quantities such as t_{opt} and $\langle \mathbf{S}^2 \rangle_{\text{min}}$ that are defined via minimization exhibit discontinuous behavior, and these discontinuities do not by themselves indicate a transition between different phases of matter. We can formally distinguish the S-collective and S-Ising phases by examining the nature of squeezing that is generated in these regions. Specifically, the S-Ising phase generates an amount of squeezing that is insensitive to system size, whereas the S-collective phase generates an amount of squeezing that scales with system size as $\xi_{\text{opt}}^2 \sim 1/N^\nu$, where the exponent ν generally depends on the values of α and J_z/J_\perp (see Appendix 6.D). Numerically, we find that the S-collective phase spans all $J_z/J_\perp < 1$ when $\alpha \lesssim D$, whereas the transition between S-collective and S-Ising phases occurs at a critical Ising coupling J_z^{crit} that either diverges logarithmically with system size ($J_z^{\text{crit}} \sim -\log N$) or stays constant when $\alpha \gtrsim D$ (see Figure 6.4, where we focus on $D = 2$ and $\alpha = 3$ due to its experimental relevance, and Appendix 6.D). We note that small oscillations in squeezing over time (see Figure 6.3) add minor corrections to the behavior of ξ_{opt}^2 and J_z^{crit} . These oscillations are responsible for the discontinuous behavior of t_{opt} and $\langle \mathbf{S}^2 \rangle_{\text{min}}$ seen in Figure 6.2 within the S-collective phase.

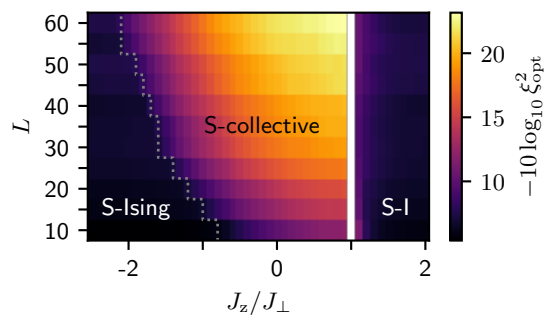


Figure 6.4: Optimal squeezing ξ_{opt}^2 as a function of system size for the power-law XXZ model with $\alpha = 3$ on a 2D lattice of $N = L \times L$ spins. Whereas the amount of squeezing generated in the S-Ising phase is insensitive to system size, squeezing in the S-collective phase grows with system size and as $J_z/J_\perp \rightarrow 1$ (from below). Dotted grey line tracks minima of $\langle \mathbf{S}^2 \rangle_{\text{min}}$ as a function of J_z/J_\perp , as in Figure 6.2, marking the approximate dynamical phase boundary.

6.4 Discussion

The mechanism behind the collective dynamics featured by the XXZ model far from the isotropic point at $J_z = J_\perp$ is not obvious, and lies in a parameter regime beyond the reach of exact treatment with current theoretical capabilities. While an in-depth understanding of collective dynamics will most likely require experimental investigations in the spirit of quantum simulation, we discuss possible phenomenological explanations below.

Collective squeezing behavior when $\alpha < D$ is the least surprising, as the XXZ model essentially interpolates between perturbative, gap-protected OAT (near $J_z = J_\perp$) and the long-range power-law Ising model (at $J_z \rightarrow \pm\infty$), both of which generate collective spin squeezing. When $\alpha > D$, as long as $D > 2$ or $\alpha < 2D$ (i.e. all $\alpha > 3$ when $D = 3$, and $2 < \alpha < 4$ when $D = 2$) a generalized version of the Mermin-Wagner theorem [216] allows for the existence of long-range order in the thermodynamic limit, below a critical temperature [197, 198]. Our observations may therefore be indicative of thermalization to a long-range-ordered steady state in an equilibrium XY phase^a, with significant amounts of collective spin squeezing present in the transient dynamics. This explanation is supported by the fact that the squared magnetization $\langle \mathbf{S}^2 \rangle$ approaches a non-vanishing steady-state value in Figure 6.3 (see also Appendix 6.E). Nevertheless, the persistence of long-range order is a necessary but insufficient condition to characterize the types of dynamical phases considered in this work. Instead, these phases are defined operationally by whether attainable spin squeezing scales with system size, and are thus sensitive to transient effects.

For even shorter range interactions ($\alpha \geq 2D$) when $D \leq 2$, long-range order is forbidden in the steady state. Even so, a spin-polarized initial state can still take an appreciable amount of time to thermalize to a disordered steady state. Squeezing beyond the Ising limit can therefore occur as a transient phenomenon, before long-range order is disrupted (see Appendix 6.E).

6.5 Experimental applications

As indicated in Figure 6.2, our results are readily applicable to the generation of spin squeezed states in a variety of experimental platforms that have been shown to implement the power-law XXZ model, including neutral atoms ($\alpha \rightarrow \infty$) [211, 212], Rydberg atoms ($\alpha = 3, 6$) [201, 202, 213], polar molecules ($\alpha = 3$) [203, 204, 214], and magnetic atoms ($\alpha = 3$) [205, 206]. Note that one may additionally have to consider the effects of a sub-unit filling fraction on the realization of a spin model. In principle, sub-unit filling introduces effective disorder into the XXZ spin couplings [198, 217]. Nonetheless, the precise form of these interactions is not essential to the existence of an S-collective phase in the XXZ model, as evidenced by the fact that this phase persists through to the $\alpha \rightarrow \infty$ limit of nearest-neighbor interactions (see Appendix 6.F).

Finally, we discuss the application of our results to Ising systems without 3D spin-aligning $\mathbf{s}_i \cdot \mathbf{s}_j$ interactions, as in the case of some Rydberg atom ($\alpha = 3, 6$) [201, 202] and trapped ion ($0 \leq \alpha < 3$) [191] experiments. In this case, 2D spin-aligning interactions within the y - z plane can still be engineered by the application of a strong transverse driving field ΩS_x . If the drive strength $|\Omega| \gg \frac{1}{2} N h_\alpha |J_z|$, with h_α the mean of $1/|\mathbf{r}_i - \mathbf{r}_j|^\alpha$ over all $i \neq j$, then moving into the rotating frame of the drive and eliminating fast-oscillating terms results in an XX model described by the Hamiltonian

$$H_{\text{XX}} = \frac{J_z}{2} \sum_{i \neq j} \frac{s_{y,i} s_{y,j} + s_{z,i} s_{z,j}}{|\mathbf{r}_i - \mathbf{r}_j|^\alpha}, \quad (6.4)$$

which is a special case of the XXZ model in Eq. (6.3), with $(J_\perp, J_z) \rightarrow (J_z/2, 0)$. Ising systems with a strong transverse field can thus access a vertical cut along $J_z/J_\perp = 0$ in Figure 6.2. In a similar fashion, dynamic Hamiltonian engineering protocols [218, 219] can transform the Ising model into an XXZ model with any $J_z/J_\perp \geq 0$, albeit at the cost of added complexity.

Acknowledgments

We thank Andrew Lucas, Thomas Bilitewski, Sean R. Muleady, and Jeremy T. Young for helpful technical discussions. This work is supported by the DARPA DRINQs grant, the ARO single

investigator award W911NF-19-1-0210, NSF grant PHY-1820885, AFOSR grant FA9550-19-1-0275, NSF grant PHY-1734006 (JILA-PFC), and by NIST.

6.A Spectral gap of the long-range XXX model

Here we show that the isotropic ($J_z = J_\perp$) XXZ model in Eq. (6.3) of the main text has a spectral gap when $\alpha \leq D$, which implies the existence of a finite range of Ising couplings $J_z \approx J_\perp$ for which the XXZ model formally recovers the OAT model at first order in perturbation theory. For definiteness, we consider an isotropic XXZ model on a cubic lattice with periodic boundary conditions in D dimensions. The translational and $SU(2)$ symmetries of the isotropic XXZ model on such a lattice imply that its lowest-lying excitations can be written as spin waves of the form

$$|m_z, k\rangle \propto \sum_{n \in \mathbb{Z}_L^D} e^{ik \cdot n} s_{z,n} |m_z\rangle, \quad (6.5)$$

where $|m_z\rangle$ is a permutationally-symmetric Dicke state with spin projection m_z onto the z axis, $n = (n_1, n_2, \dots, n_D)$ indexes an individual site on the lattice of $N = L^D$ spins, and $k \in \mathbb{Z}_L^D \times 2\pi/L$ is a wavenumber. The energy of the state $|m_z, k\rangle$ with respect to the isotropic XXZ Hamiltonian is

$$E_k = -J_\perp \sum_{\substack{n \in \mathbb{Z}_L^D \\ |n| \neq 0}} \frac{1 - \cos(k \cdot n)}{|n|^\alpha}, \quad (6.6)$$

where for simplicity we work in units for which the lattice spacing is 1. The energy E_k is minimized (in magnitude) by a wavenumber that underdoes one oscillation across one axis of the lattice, e.g. $k = (2\pi/L, 0, 0, \dots)$, which implies a spectral gap

$$\Delta_{\text{gap}} = |J_\perp| \sum_{\substack{n \in \mathbb{Z}_L^D \\ |n| \neq 0}} \frac{1 - \cos(2\pi n_1/L)}{|n|^\alpha}. \quad (6.7)$$

Letting $\epsilon \equiv 2/L$, we define a rescaled domain $\mathbb{S}_\epsilon = \mathbb{Z}_L/\epsilon \subset [-1, 1]$, and substitute $x = \epsilon n$ to get

$$\Delta_{\text{gap}} = |J_\perp| \epsilon^{\alpha-D} \sum_{\substack{x \in \mathbb{S}_\epsilon^D \\ |x| \geq \epsilon}} \epsilon^D \frac{1 - \cos(\pi x_1)}{|x|^\alpha}, \quad (6.8)$$

which in the thermodynamic limit $\epsilon \rightarrow 0$ is well approximated by an integral that avoids an infinitesimal region at the origin,

$$\Delta_{\text{gap}} \rightarrow |J_{\perp}| \epsilon^{\alpha-D} \mathcal{I}_D(\epsilon), \quad \mathcal{I}_D(\epsilon) \equiv \int_{\mathbb{T}_1^D \setminus \mathbb{T}_\epsilon^D} d^D x \frac{1 - \cos(\pi x_1)}{|x|^\alpha}, \quad (6.9)$$

where $\mathbb{T}_a \equiv (-a, a)$ is a symmetric interval about 0. The integrand of $\mathcal{I}_D(\epsilon)$ is strictly positive and well-behaved on the entirety of its domain except for the origin, where depending on the value of α the integrand may vanish or diverge as $|x| \rightarrow 0$. Together, these facts mean that

$$\mathcal{I}_D(\epsilon) \stackrel{\epsilon \rightarrow 0}{\sim} \epsilon^{-\gamma}, \quad \Delta_{\text{gap}} \stackrel{\epsilon \rightarrow 0}{\sim} \epsilon^{\alpha-(D+\gamma)}, \quad (6.10)$$

for some $\gamma \geq 0$, which implies that $\Delta_{\text{gap}} > 0$ when $\alpha \leq D$.

6.B Numerical results in one spatial dimension

Here we provide additional DTWA simulation results for the squeezing behavior of the power-law XXZ model in $D = 1$ spatial dimension. Figure 6.5 shows results analogous to those in Figure 6.2 of the main text, for $D = 1, 2, 3$ spatial dimensions and integer values of the power-law exponent α (as well as the $\alpha \rightarrow \infty$ limit of nearest-neighbor interactions). The existence of an S-collective dynamical phase persists in one spatial dimension, but for a much narrower range of parameters than in the case of $D = 2$ and 3. The achievable squeezing in the S-collective phase also scales less favorably with system size in the case of $D = 1$. Nonetheless, squeezing beyond the Ising limit is still achievable in $D = 1$ with e.g. $J_z = 0$ and $\alpha > 1$, which is relevant for trapped ion experiments.

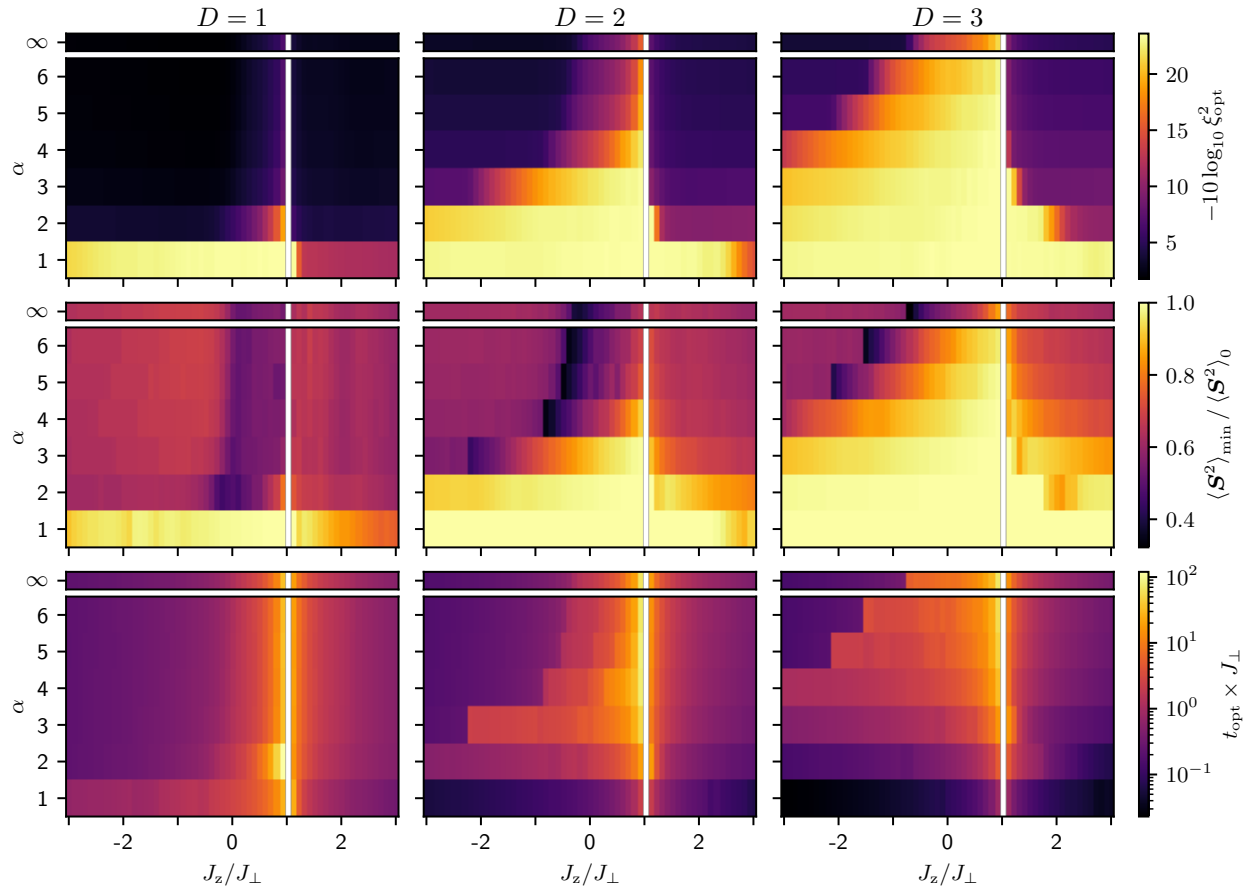


Figure 6.5: The optimal squeezing ξ_{opt}^2 (top), minimal squared magnetization $\langle \mathbf{S}^2 \rangle_{\text{min}}$ (middle), and optimal squeezing time t_{opt} (bottom) for $N = 4096 = 64^2 = 16^3$ spins in $D = 1, 2, 3$ spatial dimensions. Spins are initially polarized along the equator and evolved under the XXZ Hamiltonian in Eq. (6.3) of the main text. The results for $D = 2$ and 3 shown here are a subset of the results in Figure 6.2, presented in the same format as that for $D = 1$ for comparison.

6.C Benchmarking DTWA for the power-law XXZ model

In order to gauge the reliability of DTWA for the XXZ model in this work, we benchmark against *truncated shell* (TS₄) simulations of a 7×7 spin lattice whose dynamics are restricted to the subspace of $\sim N^5$ states with definite total spin $S \geq N/2 - 4$. These simulations are motivated by the idea that spin-aligning $\mathbf{s}_i \cdot \mathbf{s}_j$ interactions energetically suppress the decay of total spin S from its initial value of $N/2$ in a spin-polarized state. As long as the total spin decay is small, TS₄ simulations should faithfully capture the dynamical behavior of a system. The restriction to small total spin decay implies that TS₄ simulations are only reliable near the isotropic point of the XXZ model at $J_z = J_\perp$, and the $O(N^5)$ memory footprint of TS₄ means that it can only be used to simulate moderately-sized systems. Nonetheless, TS₄ has the advantage over DTWA of being “self-benchmarking,” in the sense that its breakdown can be diagnosed by a large population of the $S = N/2 - 4$ manifold, which indicates further population leakage into truncated states with $S < N/2 - 4$ (see Figure 6.6).

We benchmark DTWA simulations against TS₄ in Figure 6.7 by comparing two observables of interest: (i) the optimal spin squeezing parameter $\xi_{\text{opt}}^2 \equiv \min_t \xi^2(t) = \xi^2(t_{\text{opt}})$, and the minimal value of $\langle \mathbf{S}^2 \rangle$ throughout squeezing dynamics, $\langle \mathbf{S}^2 \rangle_{\text{min}} \equiv \min_{t \leq t_{\text{opt}}} \langle \mathbf{S}^2 \rangle(t)$. For reference, Figure 6.7 also shows the values of ξ_{opt}^2 and $\langle \mathbf{S}^2 \rangle_{\text{min}}$ in the exactly solvable limits of uniform (OAT, $\alpha = 0$) and power-law Ising ($J_\perp = 0$) interactions. For initially spin-polarized states, these limits have only one relevant energy scale, $J_z - J_\perp$, so the only effect of changing J_z is to change dynamical time scales.

The results in Figure 6.7 show that DTWA agrees almost exactly with TS₄ in the regimes that TS₄ can be trusted, suggesting that DTWA is a reliable method for studying the spin squeezing behavior of the XXZ model. Values of squeezing $-10 \log_{10} \xi^2 > 0$ are highly sensitive to errors in collective spin observables, so when comparing DTWA and TS₄ one should expect more pronounced (albeit minor) disagreements in spin squeezing $-10 \log_{10} \xi^2$ than in squared magnetization $\langle \mathbf{S}^2 \rangle$. Also, for clarity we used a simple heuristic to identify regimes of validity for TS₄ in Figures 6.6 and

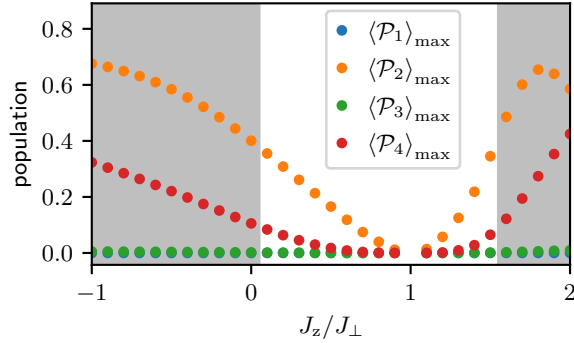


Figure 6.6: Maximal populations $\langle \mathcal{P}_n \rangle_{\max}$ of the total spin $S = N/2 - n$ manifolds \mathcal{P}_n throughout squeezing dynamics of 7×7 spins, initially polarized along the equator and evolved under the XXZ Hamiltonian in Eq. (6.3) of the main text with a power-law exponent $\alpha = 3$. Computed with TS₄ simulations and periodic boundary conditions. Shaded regions indicate $\langle \mathcal{P}_4 \rangle_{\max} > 0.1$, where TS₄ results cannot be trusted due to the likeliness of population leakage into truncated states. All states in \mathcal{P}_1 break translational invariance, so the initial population $\langle \mathcal{P}_1 \rangle_0 = 0$ is protected by the absence of translational symmetry-breaking terms in the Hamiltonian. The population $\langle \mathcal{P}_3 \rangle$, meanwhile, is small because \mathcal{P}_3 is only coupled to \mathcal{P}_2 and \mathcal{P}_4 by matrix elements that are $O(1/N)$ smaller than the couplings between $\mathcal{P}_0 \leftrightarrow \mathcal{P}_2 \leftrightarrow \mathcal{P}_4$.

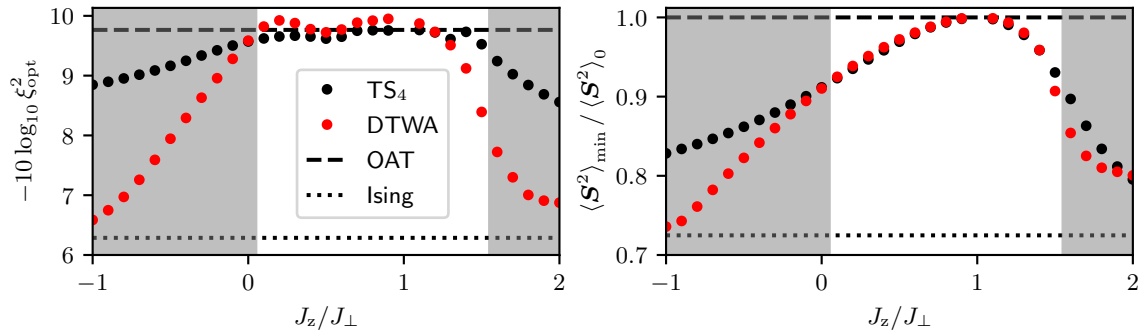


Figure 6.7: Optimal squeezing ξ_{opt}^2 (top) and minimal squared magnetization $\langle \mathcal{S}^2 \rangle_{\min}$ throughout squeezing dynamics (bottom) as computed via TS₄ and DTWA in the same setting as Figure 6.6, likewise with shaded regions indicating $\langle \mathcal{P}_4 \rangle_{\max} > 0.1$ in the TS₄ simulations. Here squeezing ξ_{opt}^2 is shown in decibels, and $\langle \mathcal{S}^2 \rangle_{\min}$ is normalized to its initial value $\langle \mathcal{S}^2 \rangle_0 = \frac{N}{2} \left(\frac{N}{2} + 1 \right)$. Dashed and dotted lines respectively mark the exactly solvable limits of uniform (OAT, $\alpha = 0$) and power-law Ising (Ising, $J_{\perp} = 0$) interactions.

6.7. This heuristic is not intended to be a precise indicator of quantitative accuracy for TS_4 , so it is no surprise that it does not identify the precise values of J_z at which DTWA and TS_4 diverge.

Finally, Figure 6.8 shows comparisons of DTWA with exact simulations in 2D lattices of 3×3 and 4×4 spins. Though the optimal squeezing parameter ξ_{opt}^2 and minimal squared magnetization $\langle \mathbf{S}^2 \rangle_{\text{min}}$ saturate to finite-size values fairly quickly away from the isotropic point at $J_z = J_\perp$, exact simulations clearly show a collective region with OAT-limited behavior when $J_z \approx J_\perp$. Even on small lattices, DTWA does a reasonably good job of estimating ξ_{opt}^2 and $\langle \mathbf{S}^2 \rangle_{\text{min}}$. Notably, DTWA performs better with increasing system size, as can be seen by comparing benchmarks of DTWA in 3×3 , 4×4 , and 7×7 systems, shown in Figures 6.7 and 6.8. This finding is consistent with an ongoing study to benchmark DTWA against state-of-the-art simulations of matrix product states (MPS) using the time-dependent variational principle (TDVP) [220].

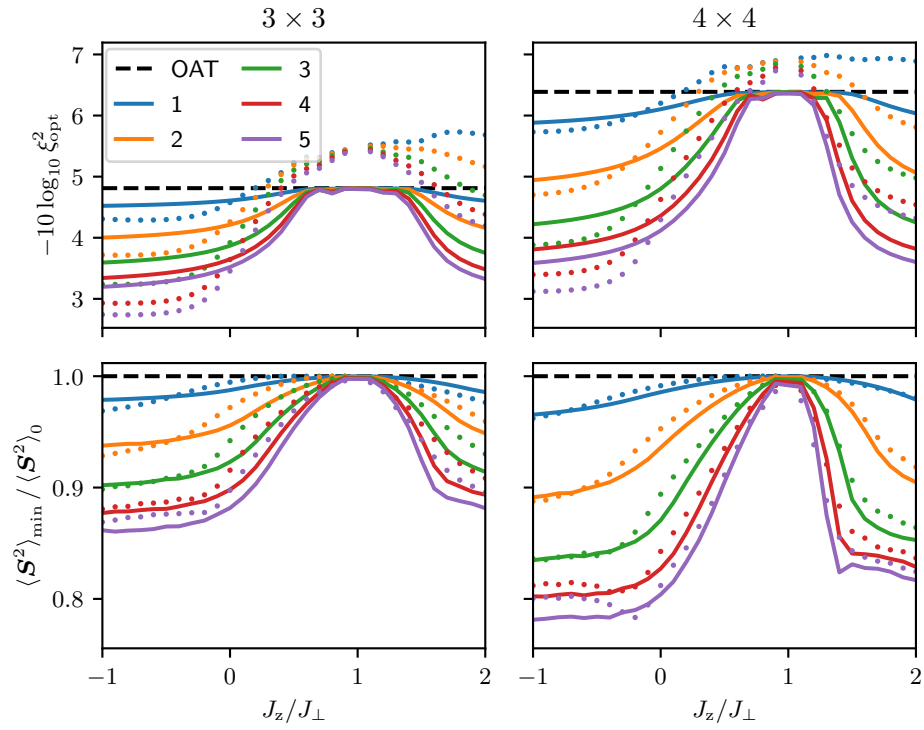


Figure 6.8: Optimal squeezing ξ_{opt}^2 (top) and minimal squared magnetization $\langle \mathbf{S}^2 \rangle_{\text{min}}$ throughout squeezing dynamics (bottom) on 2D lattices of 3×3 (left) and 4×4 (right) spins, as computed by exact methods (solid lines) and DTWA (dots). The color of each marker indicates the corresponding value of α , as specified in the legend, and the dashed line marks the OAT limit of $\alpha = 0$.

6.D Scaling relations for the collective phase in $D = 2$ spatial dimensions

Here we inspect the results in Figure 6.4 of the main text, as well as similar results for different exponents α of the power-law XXZ model, to show that

- (i) optimal squeezing scales as $\xi_{\text{opt}}^2 \sim 1/N^\nu$ in the S-collective dynamical phase (Figure 6.9 and Table 6.1), and
- (ii) the critical Ising coupling J_z^{crit} at the boundary between S-collective and S-Ising phases either diverges logarithmically with system size ($J_z^{\text{crit}} \sim -\log N$), or remains essentially constant when $\alpha \gtrsim D$ (Figure 6.10).

The exponent ν governing the behavior of ξ_{opt}^2 will generally depend on the values of J_z/J_\perp and α . Similarly, the precise dependence of J_z^{crit} on N will depend on the value of α . Note that all DTWA simulations of N -spin systems throughout this work average over $500 \times 64^2/N$ trajectories, i.e. with 500 trajectories (samples of the initial state) for the largest system size, and $\sim 1/N$ scaling to account for the fact that DTWA results converge more slowly in smaller systems. We find that changing these trajectory numbers does not affect our overall results and conclusions. Nonetheless, precise quantitative predictions, such as the exact value of ν as a function of system size, may be beyond our current computational capabilities, since they might require a more extensive numerical analysis to rule out finite sampling errors, or corrections from quantum correlations that are not captured by DTWA.

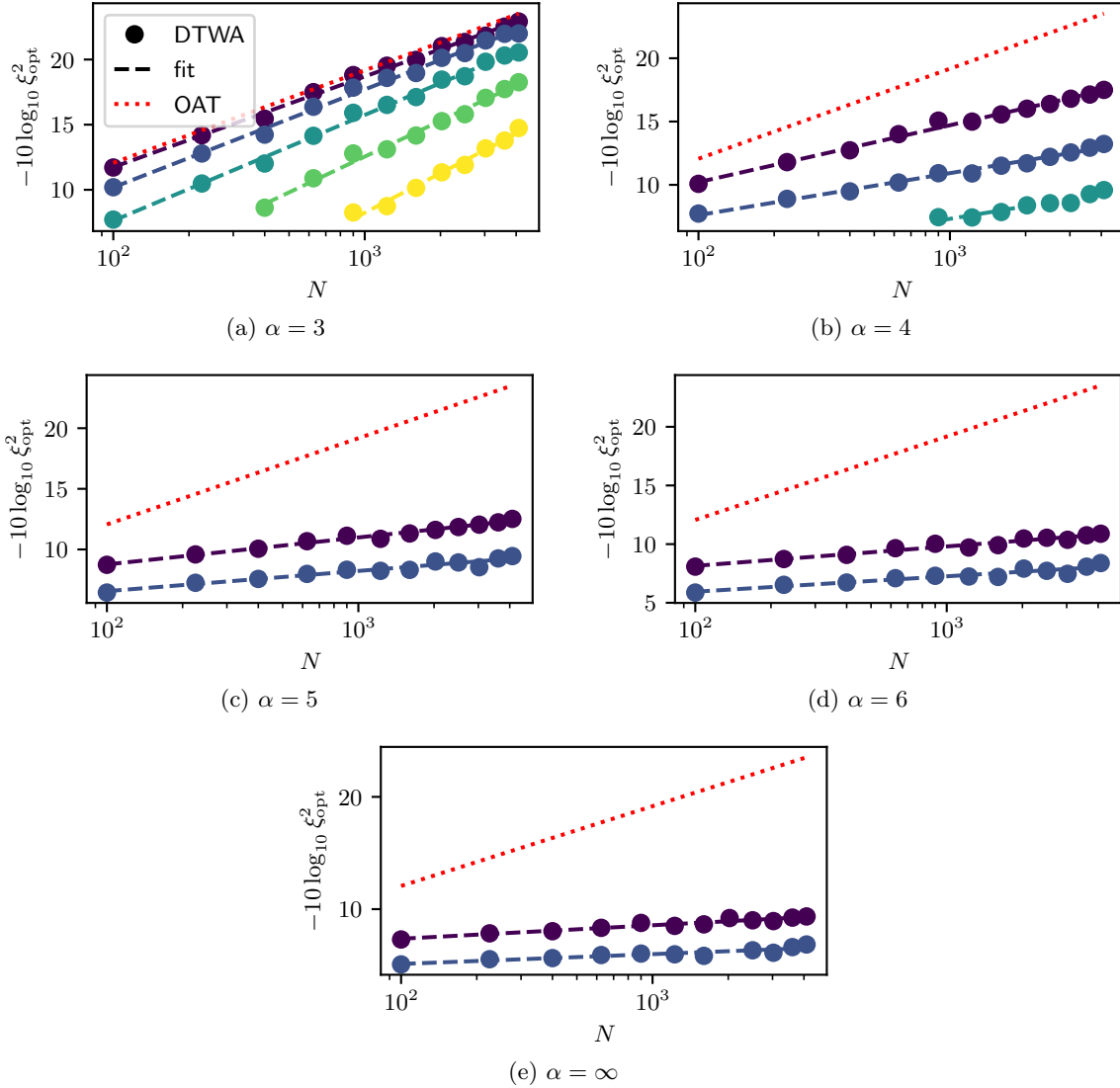


Figure 6.9: Dependence of the optimal squeezing parameter ξ_{opt}^2 on system size N within the collective dynamical phase of the power-law XXZ model in $D = 2$ spatial dimensions. Color indicates the value of J_z/J_{\perp} , sweeping down from +0.5 (dark purple, top) to -1.5 (yellow, bottom) in increments of -0.5. Circles show results computed with DTWA; dashed lines show a fit to $\xi_{\text{opt}}^2 = a/N^{\nu}$ with free parameters a, ν ; and the dotted red line marks the OAT limit for reference. The DTWA results in panel (a) for $\alpha = 3$ are a subset of those in Figure 6.4 of the main text.

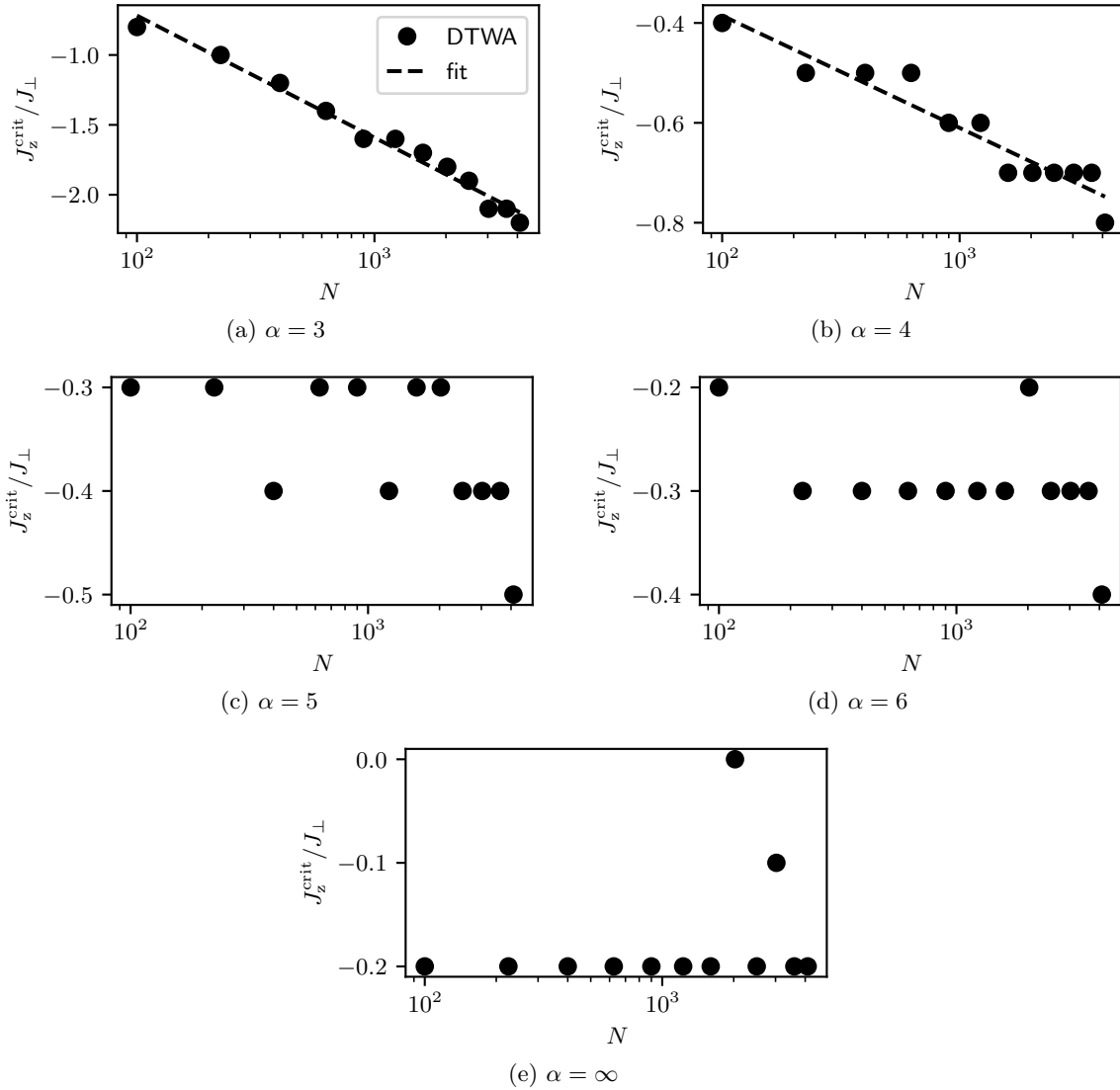


Figure 6.10: Dependence of the critical Ising coupling J_z^{crit} at the collective-to-Ising dynamical phase boundary on system size N for the power-law XXZ model in $D = 2$ spatial dimensions. Circles show results computed with DTWA, and dashed lines show a fit to $J_z^{\text{crit}}/J_{\perp} = -\gamma \ln N + b$ with free parameters γ, b . The DTWA results in panel (a) for $\alpha = 3$ are equivalent to the dashed grey lines in Figure 6.4 of the main text. DTWA simulations were run with values of J_z/J_{\perp} that are integer multiples of 0.1, placing a lower bound on the resolution for $J_z^{\text{crit}}/J_{\perp}$.

		J_z/J_\perp				
		-1.5	-1.0	-0.5	+0.0	+0.5
α	3	1.0	0.9	0.8	0.8	0.7
	4	–	–	0.3	0.3	0.4
	5	–	–	–	0.2	0.2
	6	–	–	–	0.2	0.1
	∞	–	–	–	0.1	0.1

Table 6.1: Scaling exponents ν (with $\xi_{\text{opt}}^2 \sim 1/N^\nu$) for the values of J_z/J_\perp and α shown in Figure 6.9, in $D = 2$ spatial dimensions. Though provided here for the sake of practical interest and transparency (these are essentially the slopes of the dashed lines Figure 6.9), we note that these values are subject to correction in future work, as ruling out effects such as finite sampling errors may require a more extensive numerical analysis.

6.E Thermalization and long-range order

Here we provide time-series DTWA results, similar to those of Figure 6.3 of the main text, to show that the S-collective phase is compatible with thermalization to a long-range-ordered state of the power-law XXZ model when $D > 2$ or $\alpha < 2D$. To this end, Figures 6.11 and 6.12 show both squeezing ξ^2 and the squared magnetization $\langle \mathbf{S}^2 \rangle$ as a function of time for $N = 4096 = 64^2 = 16^3$ spins in $D = 2$ spatial dimensions with $\alpha \in \{2D - 1, 2D, 2D + 1\} = \{3, 4, 5\}$, as well as $D = 3$ spatial dimensions with $\alpha \in \{2D - 1, 2D, \infty\} = \{5, 6, \infty\}$. Figure 6.11 shows simulations with values of J_z/J_\perp that sweep from 0 (in the S-collective phase) to -3 (in the S-Ising phase), while Figure 6.12 shows simulations with values of J_z/J_\perp that sweep from 2 (in the S-Ising phase) to 0 (in the S-collective phase). As long as $D > 2$ or $\alpha < 2D$, the squared magnetization $\langle \mathbf{S}^2 \rangle$ approaches a nonzero steady-state value when $J_z/J_\perp < 1$, indicating thermalization to a steady state with long-range order.

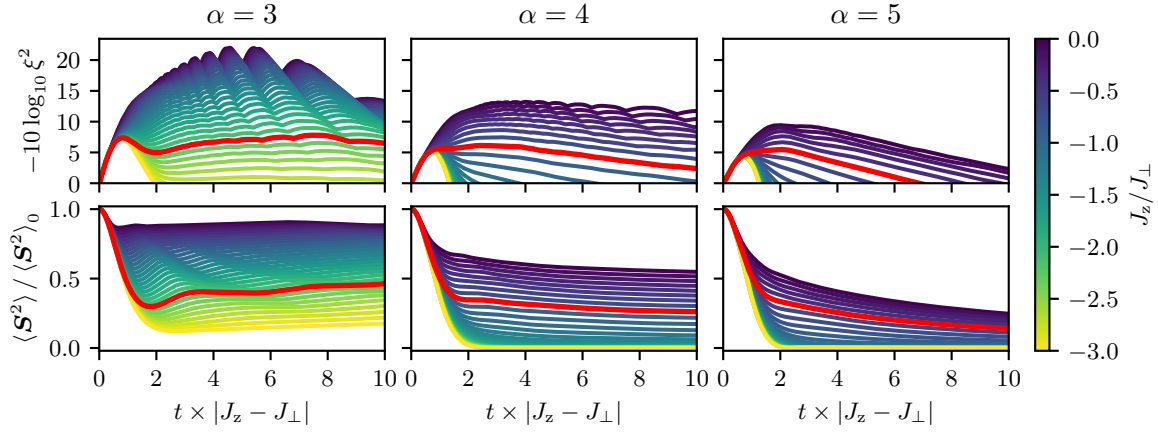
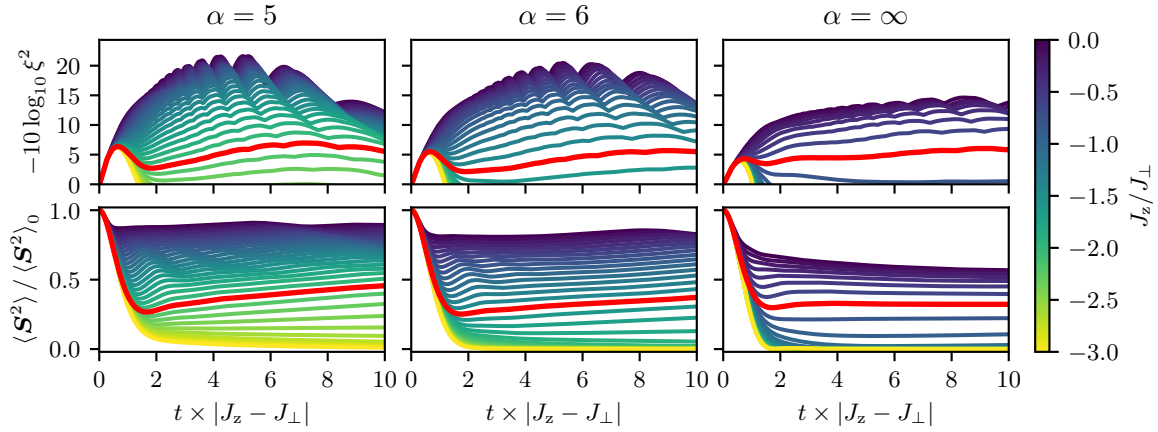
(a) $D = 2$ spatial dimensions(b) $D = 3$ spatial dimensions

Figure 6.11: Squeezing ξ^2 and squared magnetization $\langle \mathbf{S}^2 \rangle$ as a function of time t for $N = 4096 = 64^2 = 16^3$ spins in $D = 2$ and 3 spatial dimensions. Color indicates the value of J_z/J_\perp , and the red line highlights behavior at the value of J_z/J_\perp immediately preceding the transition from the S-collective phase (above the red line) to the S-Ising phase (below the red line).

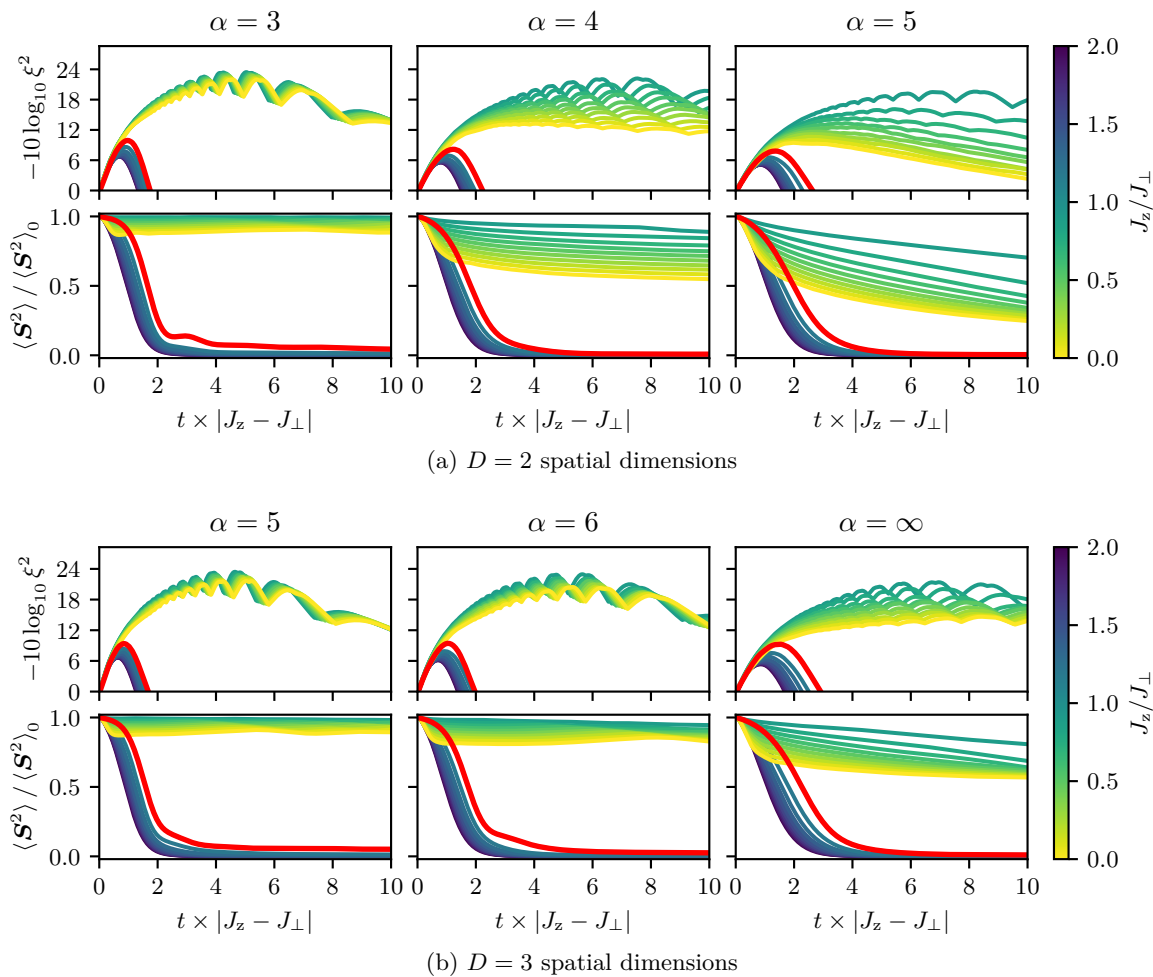


Figure 6.12: Same results as in Figure 6.11, but for values of J_z/J_\perp that cross the dynamical phase boundary at $J_z/J_\perp = 1$. The red line highlights behavior at $J_z/J_\perp = 1.1$, immediately preceding the transition from the S-Ising phase ($J_z > 1$) to the S-collective phase ($J_z < 1$).

6.F Sub-unit filling fractions

Though we do not study the effect of variable filling fractions in detail, here we show that the S-collective phase is stable to filling fractions $f < 1$. To this end, in Figure 6.13 we show the dependence of the optimal squeezing parameter ξ_{opt}^2 on filling fraction f on a 50×50 lattice in $D = 2$ two spatial dimensions with power-law exponent $\alpha = 3$ (as in the case of polar molecules, for which unit filling is difficult to obtain experimentally). Optimal squeezing generally decreases with filling fraction, which is in part attributable to a changing particle number. Nonetheless, squeezing well in excess of the Ising limit is clearly achievable even for small filling fractions, $f \sim 0.1$, as long as the XXZ model is tuned sufficiently close to the isotropic point at $J_z = J_{\perp}$.

On a high level, decreasing the filling fraction f to a value less than 1 can be seen as a two-step process: (i) rescaling all distances as $r \rightarrow r/f^{1/D}$, and (ii) adding positional disorder to spin-spin couplings, in effect transforming the XXZ Hamiltonian as

$$H_{\text{XXZ}} = \sum_{\substack{i \neq j \\ \mu}} \frac{J_{\mu} s_{\mu,i} s_{\mu,j}}{|\mathbf{r}_{ij}|^{\alpha}} \rightarrow \sum_{\substack{i \neq j \\ \mu}} \frac{J_{\mu} s_{\mu,i} s_{\mu,j}}{|\mathbf{r}_{ij}|^{\alpha}} \times f^{\alpha/D} \left(1 + \epsilon_{ij}^f\right), \quad (6.11)$$

where the index $\mu \in \{x, y, z\}$ with $J_x = J_y = J_{\perp}$, and ϵ_{ij}^f are random variables that vanish ($\epsilon_{ij}^f \rightarrow 0$) as $f \rightarrow 1$. The factor $f^{\alpha/D}$ merely changes time scales, so any deviation from squeezing behavior at $f = 1$ is determined by the random variables ϵ_{ij}^f . The general physics of the XXZ model at unit filling is maintained as long as these random variables are small enough to preserve the structure (connectivity) of $1/r^{\alpha}$ couplings. When f gets too small, however, the XXZ model is dominated by random variables, and the values of collective observables are essentially governed by the dynamics of small spin clusters with weak inter-cluster interactions. The question remains: what filling fraction f is “too small”?

In fact, this sort of physics was studied more closely the prior work of Ref. [198], which examined the XX model ($J_z = 0$) with $1/r^3$ interactions ($\alpha = 3$) and variable filling fractions that were treated as positional disorder. By mapping this system onto one of hard-core bosons, using both mean field and numerical techniques the authors found that interactions stabilize the $1/r^3$

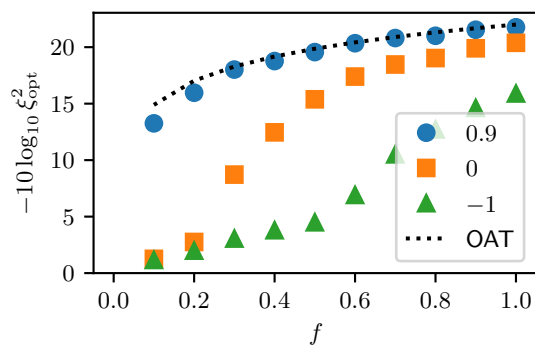


Figure 6.13: Dependence of the optimal squeezing parameter ξ_{opt}^2 on filling fraction f for the XXZ model in Eq. (6.3) of the main text with power-law exponent $\alpha = 3$ in $D = 2$ spatial dimensions with 50×50 lattice sites. Results computed using DTWA, with a random choice of $f \times 50 \times 50$ lattice sites to occupy. The shape and color of each marker indicates the corresponding value of J_z/J_{\perp} , as specified in the legend, and the dotted line marks the OAT limit for reference.

XX model against disorder, such that a transition from order- and disorder-dominated dynamical phases occurs at a critical filling fraction of $f_{\text{crit}} \approx 0.15$. Our results for the generic power-law XXZ model are consistent with previous results, although the role of $J_z \neq 0$ and different α remains an open question. We suspect, for example, that the resilience to low filling fractions to worsen with increasing α , and severely so when $D \leq 2$ and $\alpha \geq 2D$, as a strengthened version of the Mermin-Wagner theorem [216] only allows for long-range order when $D > 2$ or $\alpha < 2D$. Either way, we defer a thorough analysis of this question to future work, for now merely highlighting the robustness of our main results to sub-unit filling fractions.

Chapter 7

Engineering infinite-range $SU(n)$ interactions with spin-orbit-coupled fermions in an optical lattice

Prologue

We began the main technical work of this thesis in Chapter 3 by considering an exotic $SU(n)$ symmetry that naturally occurs between ultracold fermions on a lattice. Subsequent chapters mainly focused on the special and relatively well-understood case of $SU(2)$ -symmetric interactions, in particular considering their potential applications for quantum-enhanced metrology. The prospect of similarly exploiting $SU(n)$ -symmetric interactions (with $n > 2$) to address scientific questions or develop practical technologies remains largely unexplored. This chapter combines the spirit of Chapter 3 with the roadmap of Chapter 4, exploring some of the physics accessible with $SU(n)$ interactions between multilevel fermions with spin-orbit coupling.

One of the major difficulties of dealing with $SU(n)$ symmetries is the lack of tools and structure for taming the vast realm of possibilities with high-dimensional quantum systems. To this end, this chapter brings an optimistic message, showing that $SU(n)$ can share similarities with $SU(2)$ that enable the use of a common language (e.g. expressions that are agnostic to the value of n), and can lead to qualitatively similar dynamical behaviors. The bulk of this chapter is taken from Ref. [5]. In addition to myself and Ana Maria Rey, this work featured major contributions from Diego Barberena, Mikhail Mamaev, Bhuvanesh Sundar, and Robert J. Lewis-Swan.

Abstract

We study multilevel fermions in an optical lattice described by the Hubbard model with on-site $SU(n)$ -symmetric interactions. We show that in an appropriate parameter regime this system can be mapped onto a spin model with all-to-all $SU(n)$ -symmetric couplings. Raman pulses that address internal spin states modify the atomic dispersion relation and induce spin-orbit coupling, which can act as a synthetic inhomogeneous magnetic field that competes with the $SU(n)$ exchange interactions. We investigate the mean-field dynamical phase diagram of the resulting model as a function of n and different initial configurations that are accessible with Raman pulses. Consistent with previous studies for $n = 2$, we find that for some initial states the spin model exhibits two distinct dynamical phases that obey simple scaling relations with n . Moreover, for $n > 2$ we find that dynamical behavior can be highly sensitive to initial intra-spin coherences. Our predictions are readily testable in current experiments with ultracold alkaline-earth(-like) atoms.

7.1 Introduction

$SU(n)$ symmetries play an important role in physics. Underpinning much of high energy physics, the $SU(n)$ gauge theory known as Yang-Mills theory is central to our understanding of the electroweak and strong forces. Extensions of Yang-Mills and $SU(n)$ symmetry feature in the most well-studied examples of holographic duality [221] and the connection between entanglement and gravity [222] through the anti-de Sitter/conformal field theory (AdS/CFT) correspondence. In a condensed matter setting, $SU(2)$ appears ubiquitously as a symmetry of the Hubbard model, with important consequences for the study of quantum magnetism and high temperature superconductivity [59]. The extension of $SU(2)$ Hubbard and spin models to $SU(n)$ has led to predictions of exotic phases of matter such as valence bond solids [57, 223–225] and chiral spin liquids [56–58, 226], as well as the potential to perform universal topological quantum computation [62, 227] and other phenomena [228, 229]. Furthermore, disordered $SU(n)$ spin models have opened analytically tractable avenues for studying quantum chaos and information scrambling [230].

The tremendous theoretical significance of $SU(n)$ symmetries makes it all the more exciting that they appear naturally in experimental atomic, molecular, and optical (AMO) platforms with exquisite degrees of microscopic control. This symmetry arises through the independence of atomic orbital and interaction parameters on the n nuclear spin states of alkaline-earth(-like) atoms, with e.g. $n = 10$ for ^{87}Sr [28, 29, 55, 67]. As a result, AMO experiments can directly probe the role of $SU(n)$ interactions in controllable settings. Recent progress includes studies of the thermodynamic properties of $SU(n)$ fermionic gases [231–238], $SU(n)$ Hubbard phases and phase transitions [49, 239, 240], single- [241] and two-orbital [51–53, 242] $SU(n)$ magnetism, and multi-body $SU(n)$ -symmetric interactions [1, 7].

In the spirit of quantum simulation, further investigations in controlled settings will play an important role in understanding the consequence of $SU(n)$ symmetries for fundamental questions in physics, as well as their practical use in technological applications. For example, $SU(2)$ -symmetric spin interactions can be harnessed to develop quantum sensors that surpass classical limits on measurement precision [2, 4]. The prospect of similarly exploiting more general $SU(n)$ symmetries to achieve a technological advantage is still an unexplored avenue of research with untapped potential.

In this work, we consider an experimentally relevant and theoretically tractable regime of the $SU(n)$ Hubbard model, highlighting differences and similarities with the more familiar case of $SU(2)$. Working at ultracold temperatures and unit spatial filling (one atom per lattice site), we begin by mapping the $SU(n)$ Hubbard model onto a multilevel spin model with all-to-all $SU(n)$ -symmetric interactions in Section 7.2. In Section 7.3 we consider the use of control fields to address nuclear spins, finding a simple three-laser driving scheme that allows for the preparation of interesting states with nontrivial intra-spin correlations when $n > 2$. We consider the effect of spin-orbit coupling (SOC) induced by control fields in Section 7.4, finding in particular that the weak-SOC limit generally gives rise to a (synthetic) inhomogeneous magnetic field, extending previously known results to $n > 2$ [2, 25, 26, 103, 104, 123]. Finally, we combine these ingredients to examine mean-field dynamical behaviors of the $SU(n)$ spin model in Section 7.5, finding that: (i) long-time-averaged observables obey simple scaling relations with the spin dimension n , exhibiting (for spin-

polarized initial states) dynamical ferromagnetic and dynamical paramagnetic phases, as previously seen for the case of $n = 2$ [115, 243], and (ii) for $n > 2$ the long-time dynamics can be highly sensitive to the intra-spin coherences of the initial state. We conclude and discuss future directions in Section 7.6.

7.2 From lattice fermions to an $SU(n)$ spin model

Here we derive a collective $SU(n)$ spin model for a system of ultracold alkaline-earth(-like) atoms trapped in an optical lattice. Without external driving fields, the evolution of such atoms in their electronic ground state is governed by the single-body kinetic and two-body interaction Hamiltonians

$$\hat{H}_{\text{kin}} = -J \sum_{\langle j, j' \rangle, \mu} \hat{c}_{j\mu}^\dagger \hat{c}_{j'\mu} + \text{h.c.}, \quad (7.1)$$

$$\hat{H}_{\text{int}} = \frac{U}{2} \sum_{j, \mu, \nu} \hat{c}_{j\mu}^\dagger \hat{c}_{j\mu} \hat{c}_{j\nu}^\dagger \hat{c}_{j\nu}, \quad (7.2)$$

where $\langle j, j' \rangle$ denotes neighboring lattice sites j and j' ; $\mu, \nu \in \{s, s-1, \dots, -s\}$ index orthogonal spin states of a spin- s nucleus, with $s = \frac{n-1}{2}$ (e.g. $s = \frac{9}{2}$ in the case of ^{87}Sr with 10 nuclear spin states); $\hat{c}_{j\mu}$ is a fermionic annihilation operator, J is a tunneling amplitude (for simplicity assumed to be the same in all directions); and U is a two-body on-site interaction energy. In the present work, we neglect inter-site interactions and interaction-assisted hopping, which is a good approximation for a sufficiently deep lattice, namely when $J \lesssim E_{\text{R}}$, where E_{R} is the atom recoil energy. For simplicity, we now assume a one-dimensional periodic lattice of L sites, and expand the on-site fermionic operators in terms of operators addressing (quasi-)momentum modes q (in units with lattice spacing $a = 1$), $\hat{c}_{j\mu} = \frac{1}{\sqrt{L}} \sum_q e^{-iq \cdot j} \hat{c}_{q\mu}$, finding that

$$\hat{H}_{\text{kin}} = -2J \sum_{q, \mu} \cos(q) \hat{c}_{q\mu}^\dagger \hat{c}_{q\mu}, \quad (7.3)$$

$$\hat{H}_{\text{int}} = \frac{u}{2N} \sum_{k, \ell, p, q, \mu, \nu} \hat{c}_{k\mu}^\dagger \hat{c}_{\ell\mu} \hat{c}_{p\nu}^\dagger \hat{c}_{q\nu} \times \delta_{k+p, \ell+q}, \quad (7.4)$$

where N is the total number of atoms on the lattice, we define $u \equiv U \times N/L$ for convenience, $\delta_{k+p, \ell+q} = 1$ if $k + p = \ell + q$ and zero otherwise (enforcing conservation of momentum).

If the interaction energy U is small compared to the single-particle bandwidth $4J$, then the mode-changing collisions in \hat{H}_{int} become off-resonant, motivating the frozen-mode approximation $\{k, p\} = \{\ell, q\}$ (i.e. either $k = \ell$ and $p = q$, or $k = q$ and $p = \ell$)^a. The terms with $k = \ell$ and $p = q$ are $\frac{u}{2N} \sum \hat{c}_{k\mu}^\dagger \hat{c}_{k\mu} \hat{c}_{p\nu}^\dagger \hat{c}_{p\nu} = \frac{1}{2}Nu$, which is a constant energy shift that we can freely neglect. Defining the spin operators $\hat{s}_{\mu\nu q} \equiv \hat{c}_{q\mu}^\dagger \hat{c}_{q\nu}$, the remaining terms of the kinetic and interaction Hamiltonians are

$$\hat{H}_{\text{kin}} = -2J \sum_{q,\mu} \cos(q) \hat{s}_{\mu\mu q}, \quad (7.5)$$

$$\hat{H}_{\text{int}} = -\frac{u}{2N} \sum_{p,q,\mu,\nu} \hat{s}_{\mu\nu p} \hat{s}_{\nu\mu q}. \quad (7.6)$$

Throughout this work, we will assume that atomic modes are singly-occupied, e.g. due to the initialization of a spin-polarized state with one atom per lattice site, in which multiple occupation of an atomic mode is forbidden by fermionic statistics (Pauli exclusion). In this case we can simply treat our system as N distinguishable n -level quantum spins at “lattice sites” p, q . Note that the “kinetic” terms of this spin model (\hat{H}_{kin}) are proportional to the identity operator, contributing an overall shift in energy that we can neglect at this point. Nevertheless, these kinetic terms will become important in the presence of an external drive, which we discuss in Section 7.4. The validity of approximating the Hubbard model in Eqs. (7.1)–(7.2) by the spin model in Eqs. (7.5)–(7.6) has been previously benchmarked for SU(2)-symmetric interactions [2, 115], and we provide additional benchmarking for SU(4) and SU(6) in Appendix 7.A.

To further simplify the interaction Hamiltonian \hat{H}_{int} and write it in a form reminiscent of more familiar SU(2) spin models, we now construct the operator-valued spin matrix

$$\hat{\mathbf{s}}_q \equiv \sum_{\mu,\nu} \hat{s}_{\mu\nu q} |\mu\rangle\langle\nu|, \quad (7.7)$$

^a Note that the frozen-mode approximation neglects correlated momentum-hopping terms of the form $\hat{c}_{\pi-p,\mu}^\dagger \hat{c}_{\pi-q,\mu} \hat{c}_{p\nu}^\dagger \hat{c}_{q\nu}$, which conserve both momentum and energy. We defer a careful treatment of these terms to future work, noting only that they vanish on the manifold of permutationally symmetric spin states with one atom per lattice site, and that the frozen-mode approximation is benchmarked in Refs. [2, 115] and Appendix 7.A.

and for any pair of such operator-valued matrices $\hat{\mathbf{A}}, \hat{\mathbf{B}}$, we define the inner product

$$\hat{\mathbf{A}} \cdot \hat{\mathbf{B}} \equiv \sum_{\mu, \nu} \hat{A}_{\mu\nu}^\dagger \hat{B}_{\mu\nu}. \quad (7.8)$$

These definitions allow us to write the spin Hamiltonian in Eq. (7.6) as

$$\hat{H}_{\text{int}} = -\frac{u}{2N} \sum_{p,q} \hat{\mathbf{s}}_p \cdot \hat{\mathbf{s}}_q = -\frac{u}{2N} \hat{\mathbf{S}} \cdot \hat{\mathbf{S}}, \quad (7.9)$$

where $\hat{\mathbf{S}} \equiv \sum_q \hat{\mathbf{s}}_q$ is a collective spin matrix, analogous to the collective spin vector $\vec{S} = (\hat{S}_x, \hat{S}_y, \hat{S}_z)$ in the case of SU(2) [2], with $\frac{1}{2} \hat{\mathbf{S}} \cdot \hat{\mathbf{S}} \simeq \vec{S} \cdot \vec{S} = \hat{S}_x^2 + \hat{S}_y^2 + \hat{S}_z^2$ when $n = 2$ (here \simeq denotes equality up to identity terms).

We now discuss the spin Hamiltonian \hat{H}_{int} in Eq. (7.9). The operator $\hat{\mathbf{s}}_p \cdot \hat{\mathbf{s}}_q$ simply swaps the nuclear spin states of two atoms pinned to modes p, q . The term $-\hat{\mathbf{s}}_p \cdot \hat{\mathbf{s}}_q$ thereby assigns a definite energy of -1 ($+1$) to a pair of spins that are symmetric (anti-symmetric) under exchange. In this sense, $\hat{\mathbf{s}}_p \cdot \hat{\mathbf{s}}_q$ is analogous to the enforcement of SU(2) spin alignment by ferromagnetic interactions, which similarly assigns different energies to the anti-symmetric spin-0 singlet $|\uparrow\downarrow\rangle - |\downarrow\uparrow\rangle$ and the symmetric spin-1 triplets $\{|\uparrow\uparrow\rangle, |\downarrow\downarrow\rangle, |\uparrow\downarrow\rangle + |\downarrow\uparrow\rangle\}$. By summing over all pair-wise exchange terms $\hat{\mathbf{s}}_p \cdot \hat{\mathbf{s}}_q$, the interaction Hamiltonian \hat{H}_{int} energetically enforces a permutational symmetry among all spins, opening an energy gap u between the manifold of all permutationally symmetric (PS) states and the orthogonal complement of excited (e.g. spin-wave) states that break permutational symmetry. See Figure 7.1 for a summary of this section thus far.

In the case of SU(2), the PS manifold is precisely the Dicke manifold of collective states $|m_z\rangle$ with total spin $S = \frac{N}{2}$ and definite spin projection $m_z \in \{S, S-1, \dots, -S\}$ onto a fixed quantization axis. Equivalently, Dicke states $|m_z\rangle = |m_\uparrow, m_\downarrow\rangle$ can be labeled by a definite number of spins $m_\uparrow = S + m_z$ ($m_\downarrow = S - m_z$) pointing up (down) along the spin quantization axis, with $m_\uparrow + m_\downarrow = N$. In the general case of SU(n), the PS manifold is similarly spanned by states $|m_s, m_{s-1}, \dots, m_{-s}\rangle$ with a definite number m_μ of spins in state μ , and $\sum_\mu m_\mu = N$. The dimension of the PS manifold is equal to the number of ways of assigning N identical spins to n distinct internal states, or $\binom{N+n-1}{n-1} \sim N^{n-1}$.

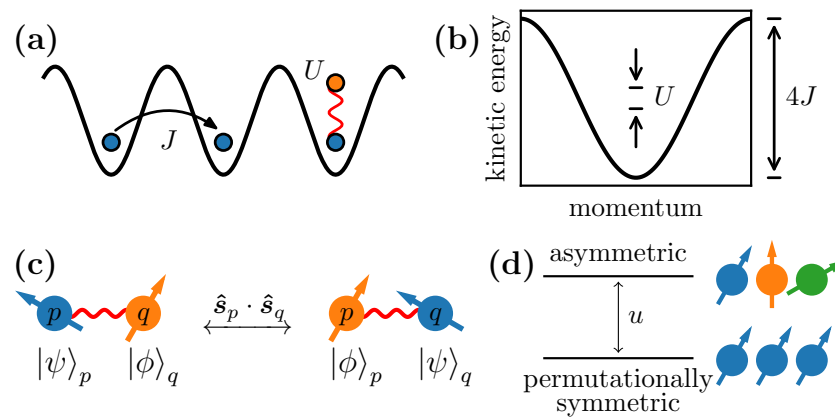


Figure 7.1: (a) Ultracold atoms on a lattice of L sites tunnel between neighboring lattice sites at a rate J , and locally repel each other with interaction energy U . (b,c) When the interaction energy U is small compared to the single-particle bandwidth $4J$, the frozen-mode approximation enables the interaction Hamiltonian to be written as a spin model consisting of exchange terms $\hat{\mathbf{s}}_p \cdot \hat{\mathbf{s}}_q$, which swap the states of two spins pinned to modes p, q . (d) Interactions open an energy gap $u = U \times N/L$ between the manifold of permutationally symmetric states of N spins, and the orthogonal complement of states that break spin-permutation symmetry.

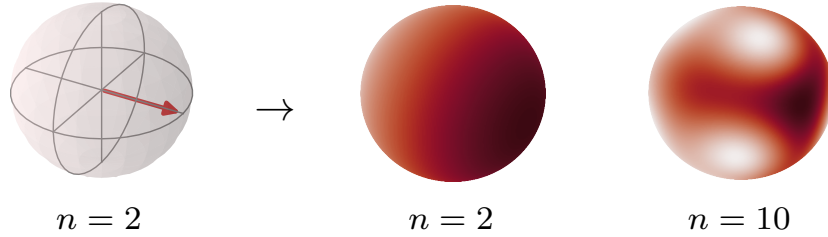


Figure 7.2: Whereas the state of a two-level spin (qubit) can be represented by a point on (or inside) the Bloch sphere, the state of an n -level spin is more generally represented by a probability distribution on the Bloch sphere. The distribution shown for $n = 10$ corresponds to a Haar-random pure state.

External fields or additional interactions that respect permutational symmetry can induce nontrivial dynamics within the PS manifold. Moreover, additional terms that explicitly break permutational symmetry can nevertheless lead to interesting dynamics that can be captured within the PS manifold perturbatively, as long as the coupling to non-PS states is weak compared u (see Appendix 7.B) [80]. This perturbative regime is thereby efficiently simulable, as the PS manifold has dimension $\sim N^{n-1}$ (as compared to n^N for the entire spin Hilbert space). Simulating dynamics within the PS manifold requires calculating matrix elements $\langle \ell | \hat{O} | m \rangle$ of spin operators \hat{O} with respect to PS states $|\ell\rangle, |m\rangle$; we discuss this calculation in Appendix 7.C.

Finally, we take a moment to discuss individual n -level spins. The state of a two-level spin, or a qubit, is commonly represented by a point on (or within) the Bloch sphere. More generally, the state $|\psi\rangle$ of an n -level spin can be represented by a quasi-probability distribution Q_ψ on the Bloch sphere (commonly known as the Husimi- Q function, e.g. in the spin-squeezing community [35]). The value $Q_\psi(\mathbf{v})$ at a point \mathbf{v} on the sphere is equal to the overlap of $|\psi\rangle$ with a pure state $|\mathbf{v}\rangle$ that is maximally polarized in the direction of \mathbf{v} : $Q_\psi(\mathbf{v}) \equiv |\langle \mathbf{v} | \psi \rangle|^2$ (see Figure 7.2). In the case of a mixed state $\hat{\rho}$, this distribution is defined by $Q_{\hat{\rho}}(\mathbf{v}) \equiv \langle \mathbf{v} | \hat{\rho} | \mathbf{v} \rangle$. Closely related spherical representations of multilevel spin states and operators are discussed in Refs. [244, 245]. In practice, it is conceptually useful to identify the Hilbert space of a single n -level spin with the Dicke manifold of $n - 1$ spin- $\frac{1}{2}$ particles.

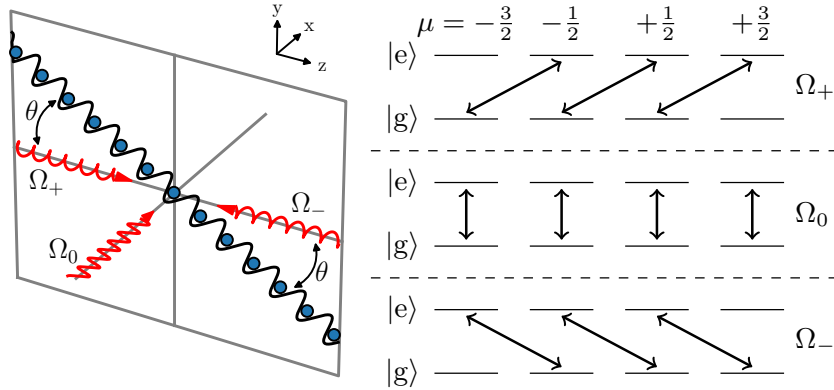


Figure 7.3: Sketch of the three-laser drive used to address nuclear spins on a one-dimensional lattice. Two counter-propagating lasers with right-circular polarization and amplitudes Ω_{\pm} point at an angle θ to the lattice axis. A third, linearly polarized laser with amplitude Ω_0 points in a direction orthogonal to both the lattice and the other driving lasers. Absorbing a photon from the laser with amplitude Ω_m induces a transition $(g, \mu) \rightarrow (e, \mu + m)$ for the (electronic, nuclear spin) state of an atom, where nuclear spin is quantized along the z axis.

7.3 External control fields

We now consider the addition of external control fields to address atoms' internal spin states, which will determine the observables we can access and initial states we can prepare. Specifically, we consider off-resonantly addressing an electronic $|g\rangle \rightarrow |e\rangle$ transition of the atoms, and then perturbatively eliminating electronic $|e\rangle$ excitations to arrive at an effective ground-state Hamiltonian addressing nuclear spins. For simplicity, we will assume that the total spin s of the ground- and excited-state (hyperfine) manifolds are the same, as e.g. with the $^1S_0 \rightarrow ^3P_0$ transition of alkaline-earth-like atoms (AEAs). However, the results of this section (namely the general form of effective nuclear spin Hamiltonians, as well as the corresponding set of accessible observables and initial states) are the same for transitions that take $s \rightarrow s \pm 1$, so in practice one is free to address the hyperfine manifolds of the $^1S_0 \rightarrow ^3P_1$ transition of AEAs.

We consider a specific three-laser driving scheme with a geometry sketched in Figure 7.3. Here the lattice lies in the y - z plane at an angle θ to the z axis, oriented along $\ell = (0, \sin \theta, \cos \theta)$. We set the spin quantization axis along z . The laser setup consists of (i) two counter-propagating right-circularly polarized lasers with drive amplitudes Ω_{\pm} and wavevectors $\kappa \mathbf{v}_{\pm}$, propagating in

opposite directions along the z axis, $\mathbf{v}_\pm = (0, 0, \pm 1)$, and (ii) a third laser linearly polarized along z , with drive amplitude Ω_0 and wavevector $\kappa\mathbf{v}_0$, propagating along the x axis $\mathbf{v}_0 = (1, 0, 0)$. All driving lasers are detuned by Δ below an electronic transition. The full Hamiltonian for this three-laser drive can be written as

$$\hat{H}_{3\text{LD}}^{\text{full}} = \sum_{j,m} \Omega_m \left(e^{-im\phi_j} \hat{s}_{mj} \otimes |e\rangle\langle g|_j + \text{h.c.} \right) + \Delta \hat{N}_e, \quad (7.10)$$

where $m \in \{+1, 0, -1\}$ indexes the laser pointing along \mathbf{v}_m ; the SOC angle $\phi \equiv \kappa\mathbf{v}_+ \cdot \boldsymbol{\ell} = \kappa \cos \theta$ (in units with lattice spacing $a = 1$); $\hat{s}_{z,j}, \hat{s}_{+,j}, \hat{s}_{-,j}$ are standard axial, spin-raising, and spin-lowering operators for the spin at lattice site j ; $\hat{s}_{0,j} \equiv \hat{s}_{z,j}$ for shorthand; $|g\rangle_j$ and $|e\rangle_j$ respectively denote the ground and excited electronic states of atom j ; and $\hat{N}_e = \mathbb{1} \otimes \sum_j |e\rangle\langle e|_j$ counts the number of excited atoms (with $\mathbb{1}$ the identity operator on all spin degrees of freedom).

In the far-detuned limit $|\Delta| \gg |\Omega_m|$, a second-order perturbative treatment of electronic excitations ($|e\rangle$) yields an effective drive Hamiltonian that only addresses ground-state nuclear spins. After additionally making the gauge transformation $\hat{s}_{mj} \rightarrow e^{im\phi_j} \hat{s}_{mj}$ (equivalently $\hat{c}_{j\mu}^\dagger \rightarrow e^{i\phi\mu j} \hat{c}_{j\mu}^\dagger$), the drive Hamiltonian then becomes

$$\hat{H}_{3\text{LD}} = \sum_j \hat{H}_{3\text{LD},j}^{\text{single}}, \quad (7.11)$$

where $\hat{H}_{3\text{LD},j}^{\text{single}}$ denotes the action of $\hat{H}_{3\text{LD}}^{\text{single}}$ on spin j :

$$\hat{H}_{3\text{LD}}^{\text{single}} = \tilde{\Omega}_+ \tilde{\Omega}_- \hat{s}_z + \tilde{\Omega}_0 \tilde{\Omega}_- \hat{s}_x + \tilde{\Omega}_0 \tilde{\Omega}_+ (\hat{s}_z \hat{s}_x + \hat{s}_x \hat{s}_z) - \tilde{\Omega}_0^2 \hat{s}_z^2 - \tilde{\Omega}_+^2 \hat{s}_x^2 - \tilde{\Omega}_-^2 \hat{s}_y^2, \quad (7.12)$$

with

$$\tilde{\Omega}_0 \equiv -\frac{\Omega_0}{\sqrt{\Delta}}, \quad \tilde{\Omega}_\pm \equiv \frac{\Omega_+ \pm \Omega_-}{\sqrt{\Delta}}, \quad (7.13)$$

where we have made the simplifying assumption that all drive amplitudes are real to arrive at the form of $\hat{H}_{3\text{LD}}^{\text{single}}$ in Eq. (7.12). We relax the assumption of real drive amplitudes in Appendix 7.D.

There are three important observations to make about Eqs. (7.11) and (7.12). First, the fact that $\hat{H}_{3\text{LD}}$ acts identically on all spins means we can freely replace the site index j with a

Table 7.1: Drive Hamiltonians (left column) that can be implemented with different amplitude-matching conditions (right three columns), some of which are specified by an arbitrary sign $\sigma \in \{+1, -1\}$. The drives shown here are equal to that of Eq. (7.12) up to a possible energy shift of $\hat{s}_x^2 + \hat{s}_y^2 + \hat{s}_z^2 = s(s+1)$, and come in mutually commuting pairs: a drive with $|\Omega_m| = 1$ and $\Omega_n = 0$ for both $n \neq m$ commutes with the drive in which $\Omega_m = 0$ and both $|\Omega_n| = 1$.

$\hat{H}_{\text{drive}}^{\text{single}}$	$\tilde{\Omega}_0$	$\tilde{\Omega}_+$	$\tilde{\Omega}_-$
$-\hat{s}_z^2$	1	0	0
$-\hat{s}_x^2$	0	1	0
$-\hat{s}_y^2$	0	0	1
$\sigma \hat{s}_z + \hat{s}_z^2$	0	1	σ
$\sigma \hat{s}_x + \hat{s}_x^2$	1	0	σ
$\sigma (\hat{s}_z \hat{s}_x + \hat{s}_x \hat{s}_z) + \hat{s}_y^2$	1	σ	0
$\pm \hat{s}_z \pm \sigma \hat{s}_x + \sigma (\hat{s}_z \hat{s}_x + \hat{s}_x \hat{s}_z)$	1	σ	$\pm \sigma$

momentum index q (as can be verified by substituting $\hat{c}_{j\mu} = \frac{1}{\sqrt{L}} \sum_k e^{-iq \cdot j} \hat{c}_{q\mu}$), which is important to ensure that this drive addresses the same spin degrees of freedom as the spin Hamiltonians previously considered in Section 7.2. Second, each of $\tilde{\Omega}_0, \tilde{\Omega}_+, \tilde{\Omega}_-$ can be tuned independently by changing the amplitudes of the driving lasers; some particular Hamiltonians for specific values of these amplitudes are shown in Table 7.1. Third, due to the appearance of mutually commuting pairs of Hamiltonians in Table 7.1, specifically $-\hat{s}_\alpha^2$ and $\pm \hat{s}_\alpha + \hat{s}_\alpha^2$ for $\alpha \in \{z, x\}$, the three-laser drive admits pulse sequences that exactly implement arbitrary SU(2) (spatial) rotations of the form $e^{-i\chi \vec{n} \cdot \vec{s}}$, where χ is a rotation angle, \vec{n} is a rotation axis, and $\vec{s} \equiv (\hat{s}_x, \hat{s}_y, \hat{s}_z)$. The capability to perform arbitrary spatial rotations, together with the capability to measure the number of atoms with spin projection μ onto a fixed quantization axis, $\langle \hat{S}_{\mu\mu} \rangle$ (where $\hat{S}_{\mu\nu} = \sum_j \hat{s}_{\mu\nu j}$), implies the capability to reconstruct all components of the mean collective spin matrix $\langle \hat{\mathbf{S}} \rangle = \sum_{\mu\nu} \langle \hat{S}_{\mu\nu} \rangle |\mu\rangle\langle\nu|$ via spin qudit tomography [6, 246]. Moreover, we expect that advanced quantum control techniques (similar to those of Refs. [247, 248]) can be used to implement arbitrary SU(n) rotations by designing suitable time-dependent drive amplitudes.

If the excited-state manifold $|e\rangle$ has total spin $s \pm 1$, the effective ground-state Hamiltonians in Eq. (7.12) and Table 7.1 remain almost identical, but with some additional n -dependent factors that do not affect the general results and discussions above. These results still hold if (for example) all excited hyperfine manifolds of an electronic $^1S_0 \rightarrow ^3P_1$ transition (with total spins $s+1, s, s-1$) are addressed simultaneously. See Appendix 7.D for additional details.

Finally, we comment on the preparation of initial states. Initial states are nominally prepared in the “lab frame”, and must be transformed according to the gauge transformation $\hat{c}_{j\mu}^\dagger \rightarrow e^{i\phi_{\mu j}} \hat{c}_{j\mu}^\dagger$ prior to evolution under the three-laser drive \hat{H}_{3LD} in Eq. (7.11), which is expressed in the “gauge frame”. We assume the capability to prepare an initial state in which all spins are maximally polarized along the z axis, i.e. $|z\rangle^{\otimes N} = |s\rangle^{\otimes N}$, which is unaffected by the gauge transformation (up to a global phase). The three-laser then allows us to rotate this state into one that is polarized along any spatial axis (in the gauge frame). In addition, when $n > 2$ the three-laser drive allows us to prepare product states with nontrivial intra-spin correlations. For example, when n is even

we can prepare an N -fold product of the “kitten” state

$$e^{-i\frac{\pi}{2}(\hat{s}_y + \hat{s}_y^2)} |s\rangle \stackrel{n \text{ even}}{\propto} |s\rangle + |-s\rangle. \quad (7.14)$$

This state has a vanishing mean spin vector, $\langle \hat{s}_x \rangle = \langle \hat{s}_y \rangle = \langle \hat{s}_z \rangle = 0$, but variances $\langle \hat{s}_x^2 \rangle = \langle \hat{s}_y^2 \rangle = s/2$ and $\langle \hat{s}_z^2 \rangle = s^2$.

7.4 Spin-orbit coupling

We now consider the effect of spin-orbit coupling (SOC) induced by the control fields in Section 7.3. Before discussing SOC for n -level fermions, we briefly review the well-studied case of two-level SOC with a one-dimensional lattice [2, 25, 103, 104]. In this case, SOC is induced by an external driving field that imprints a phase $e^{-i\phi j}$ on lattice site j , or equivalently imparts a momentum kick $q \rightarrow q + \phi$, upon the absorption of a photon^b:

$$\hat{H}_{\text{drive}}^{(\phi)} = \frac{\Omega}{2} \sum_q \hat{c}_{q+\phi, \uparrow}^\dagger \hat{c}_{q, \downarrow} + \text{h.c.} \quad (7.15)$$

Identifying a numerical spin index $\mu = +\frac{1}{2}$ ($-\frac{1}{2}$) with the state \uparrow (\downarrow), this drive Hamiltonian can be diagonalized in its momentum index q by the gauge transformation $\hat{c}_{q\mu}^\dagger \rightarrow \hat{c}_{q-\mu\phi, \mu}^\dagger$ (equivalently $\hat{c}_{j\mu}^\dagger \rightarrow e^{i\phi\mu j} \hat{c}_{j\mu}^\dagger$), which takes

$$\hat{H}_{\text{drive}}^{(\phi)} \rightarrow \hat{H}_{\text{drive}} \equiv \Omega \hat{S}_x, \quad \hat{S}_x \equiv \sum_q \hat{s}_{x,q}, \quad (7.16)$$

where $\hat{s}_{x,q} = \frac{1}{2} \hat{c}_{q, \uparrow}^\dagger \hat{c}_{q, \downarrow} + \text{h.c.}$ for two-level spins.

The two-level SOC drive in Eq. (7.15) has been implemented with an external laser that couples the two electronic states of nuclear-spin-polarized atoms, with \downarrow (\uparrow) indexing the ground (excited) electronic state [2, 25, 26, 103, 104]. In contrast, the drive we considered in Section 7.3 addresses electronic excitations off-resonantly, inducing an effective Hamiltonian in the ground-state hyperfine manifold with spin projections $\mu \in \{s, s-1, \dots, -s\}$ (a similar scheme was used to

^b In order for the drive Hamiltonian $\hat{H}_{\text{drive}}^{(\phi)}$ to be well-defined, ϕ should be commensurate with the lattice, e.g. $\phi \in \mathbb{Z} \times 2\pi/L$ on a one-dimensional lattice of L sites.

study SOC in a subspace of the ground-state manifold in Ref. [123]). Nonetheless, both the two-level drive in Eq. (7.15) and the n -level drive in Eq. (7.11) become homogeneous (i.e. independent of the spatial mode index j or q) and independent of the SOC angle ϕ after the same spin-symmetric gauge transformation^c $\hat{c}_{j\mu}^\dagger \rightarrow e^{i\phi\mu j}\hat{c}_{j\mu}^\dagger$.

Of course, spin-orbit coupling cannot be “gauged away” entirely. Making a gauge transformation to simplify the drive comes at the cost of making the kinetic energy in Eq. (7.5) spin-dependent, taking

$$\hat{H}_{\text{kin}} \rightarrow \hat{H}_{\text{kin}}^{(\phi)} \equiv -2J \sum_q \cos(q + \mu\phi) \hat{s}_{\mu\mu q}, \quad (7.17)$$

as visualized in Figure 7.4. To better interpret this Hamiltonian, we can write it in the form

$$\hat{H}_{\text{kin}}^{(\phi)} = -2J \sum_q \left[\cos(q) \hat{w}_{+,q}^{(\phi)} - \sin(q) \hat{w}_{-,q}^{(\phi)} \right], \quad (7.18)$$

where

$$\hat{w}_{+,q}^{(\phi)} \equiv \sum_\mu \cos(\mu\phi) \hat{s}_{\mu\mu q}, \quad (7.19)$$

$$\hat{w}_{-,q}^{(\phi)} \equiv \sum_\mu \sin(\mu\phi) \hat{s}_{\mu\mu q}. \quad (7.20)$$

For two-level spins with $\mu = \pm\frac{1}{2}$, $\hat{w}_{+,q}^{(\phi)}$ is proportional to the identity operator and $\hat{w}_{-,q}^{(\phi)} = 2\sin(\phi/2) \hat{s}_{z,q}$, so the kinetic Hamiltonian in the gauge frame describes a (synthetic) inhomogeneous magnetic field:

$$\hat{H}_{\text{kin}}^{(\phi)} \Big|_{n=2} = 4J \sin(\phi/2) \sum_q \sin(q) \hat{s}_{z,q}. \quad (7.21)$$

When $n > 2$, an inhomogeneous magnetic field is likewise recovered in the weak SOC limit $s\phi \ll 1$, in which case

$$\hat{H}_{\text{kin}}^{(\phi)} \Big|_{s\phi \ll 1} = 2J\phi \sum_q \sin(q) \hat{s}_{z,q} + O\left((s\phi)^2\right). \quad (7.22)$$

For larger ϕ , this Hamiltonian acquires terms with higher powers of $\hat{s}_{z,q}$, up to $\hat{s}_{z,q}^{n-1}$.

^c The “asymmetric” gauge transformation $(\hat{c}_{j,\uparrow}^\dagger, \hat{c}_{j,\downarrow}^\dagger) \rightarrow (e^{i\phi j} \hat{c}_{j,\uparrow}^\dagger, \hat{c}_{j,\downarrow}^\dagger)$, sometimes performed in the two-state SOC literature, does not generalize as nicely to $n > 2$.

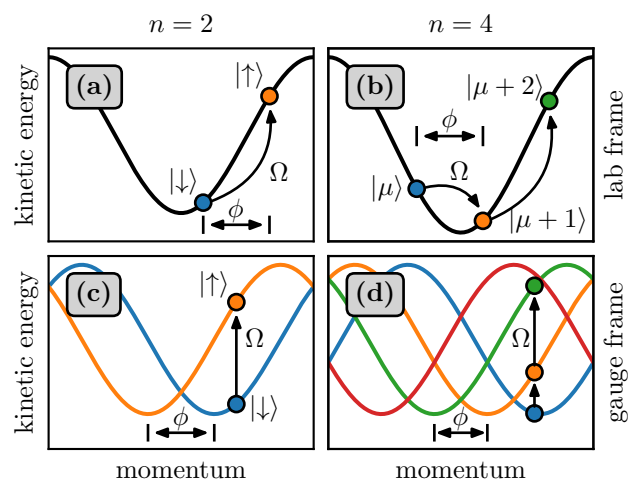


Figure 7.4: Spin-orbit coupling for 2-level (a,c) and 4-level (b,d) spins. Colors indicate different spin projections μ . In the “lab frame” (a,b), kinetic energy is insensitive to spin, but a spin transition $\mu \rightarrow \mu + 1$ is accompanied by a momentum kick $q \rightarrow q + \phi$ from the drive. Changing into the “gauge frame” (c,d), essentially by shifting the momentum label q for each spin state μ , makes the drive diagonal in the momentum index, but comes at the cost of making kinetic energy spin-dependent.

Finally, the gauge transformation $\hat{c}_{q\mu}^\dagger \rightarrow \hat{c}_{q-\mu\phi,\mu}^\dagger$ also transforms the interaction Hamiltonian. Applying this transformation to Eq. (7.4) and keeping only terms that respect coherences that can be imposed on initial states by the laser drive in Section 7.3 (applied to an initially spin-down-polarized state) again results in an effective spin model. For sufficiently weak SOC ($s\phi \rightarrow 0$) this spin model is still well-approximated by \hat{H}_{int} in Eqs. (7.6) and (7.9). The validity of this approximation has been previously benchmarked for SU(2)-symmetric interactions [2, 115], and we provide additional benchmarking for SU(4) and SU(6) in Appendix 7.A (which finds that the spin model works well even for *large* ϕ). To ensure that $\hat{H}_{\text{kin}}^{(\phi)}$ does not become trivial as $\phi \rightarrow 0$, we can keep $J\phi/u$ constant, either by increasing J/U or decreasing N/L . Altogether, the interacting spin Hamiltonian in the gauge frame becomes

$$\hat{H}_{\text{spin}} = -\frac{u}{2N} \hat{\mathbf{S}} \cdot \hat{\mathbf{S}} + 2J\phi \sum_q \sin(q) \hat{s}_{z,q}, \quad (7.23)$$

consisting of a spin-locking $\hat{\mathbf{S}} \cdot \hat{\mathbf{S}}$ term that energetically favors permutational symmetry, and an inhomogeneous magnetic field that causes inter-spin dephasing.

7.5 Mean-field theory and dynamical phases

We now study the dynamical behavior of the SOC spin Hamiltonian H_{spin} in Eq. (7.23), and henceforth work exclusively in the “gauge frame” of \hat{H}_{spin} and the three-laser drive \hat{H}_{3LD} in Eq. (7.11). We use a Ramsey-like setup wherein we prepare an initial state with the three-laser drive (using fast pulse sequences), then let the state evolve freely for some time under \hat{H}_{spin} , and finally apply again the three-laser drive to map observables of interest onto spin projection measurements (e.g. with spin qudit tomography [6, 246]). At the mean-field (MF) level, the undriven spin Hamiltonian (neglecting constant energy shifts) becomes

$$\hat{H}_{\text{MF}} = u \sum_q [-\langle \bar{\mathbf{s}} \rangle \cdot \hat{\mathbf{s}}_q + h \sin(q) \hat{s}_{z,q}]. \quad (7.24)$$

where $\bar{\mathbf{s}} \equiv \frac{1}{N} \sum_q \hat{\mathbf{s}}_q$ is the average spin matrix, and $h \equiv 2J\phi/u$ is a dimensionless strength of the inhomogeneous magnetic field. We assume that all momenta $q \in \mathbb{Z}_N \times 2\pi/N$ are occupied.

Fixing the atom number N , the spin Hamiltonian has one free parameter, h , which determines the relative strength of the single-particle and interaction terms. One should therefore expect distinct dynamical behaviors when $h \ll 1$, in which case strong spin-locking interactions should give rise to a long-range ordered phase, as opposed to $h \gg 1$, in which case long-range order should be destroyed by the strong inhomogeneous magnetic field [115].

To investigate these behaviors quantitatively, we examine time-averaged observables of the form

$$\langle\langle \hat{O} \rangle\rangle_{\text{MF}} = \lim_{T \rightarrow \infty} \frac{1}{T} \int_0^T dt \langle \hat{O}(t) \rangle_{\text{MF}}, \quad (7.25)$$

where $\langle \hat{O}(t) \rangle_{\text{MF}}$ is the mean-field value of observable \hat{O} at time t . Specifically, we consider the time-averaged magnetization

$$\sigma_{\text{MF}} \equiv |\langle\langle \vec{\sigma} \rangle\rangle_{\text{MF}}|, \quad \vec{\sigma} \equiv \frac{1}{N_s} \times \vec{S}, \quad (7.26)$$

where $\vec{S} \equiv (\hat{S}_x, \hat{S}_y, \hat{S}_z)$ with $\hat{S}_\alpha \equiv \sum_q \hat{s}_{\alpha,q}$, and the time-averaged (dimensionless) interaction energy

$$\langle\langle \bar{\mathbf{s}} \cdot \bar{\mathbf{s}} \rangle\rangle_{\text{MF}} = \frac{1}{N^2} \times \langle\langle \hat{\mathbf{S}} \cdot \hat{\mathbf{S}} \rangle\rangle_{\text{MF}}. \quad (7.27)$$

By design, these non-negative quantities are normalized to lie on the interval $[0, 1]$, independent of the system size N or spin dimension n . In the remainder of this section we will assume that n is even, both for the sake of experimental relevance (most relevant atomic nuclei are fermionic) and to avoid complications from parity effects.

Our numerical simulations of mean-field dynamics are performed with a Schwinger boson decomposition of spin operators: $\hat{s}_{\mu\nu q} = \hat{b}_{\mu q}^\dagger \hat{b}_{\nu q}$. This decomposition requires no approximations, and reduces the number of variables to keep track of by a factor of $\sim n$. See Appendices 7.E and 7.F for additional details about our numerical simulations and the Schwinger boson equations of motion.

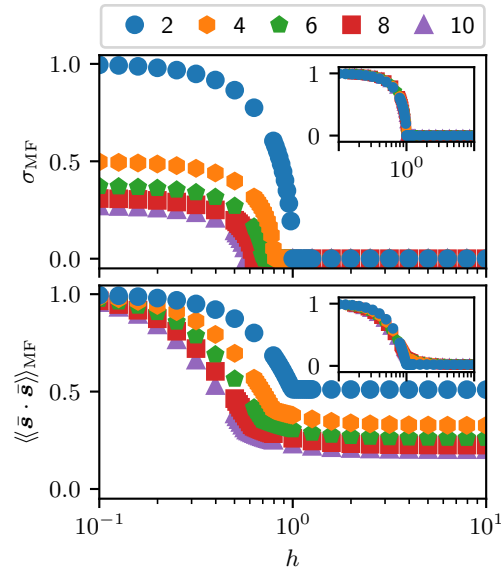


Figure 7.5: Time-averaged magnetization σ_{MF} and interaction energy $\langle\langle \bar{s} \cdot \bar{s} \rangle\rangle_{\text{MF}}$ for different spin dimensions n (indicated in the legend) as determined by mean-field simulations of $N = 100$ spins initially in the x-polarized state $|X\rangle$ for a time $T = 10^5/u$. Insets show same data after rescaling $h \rightarrow h \times (n/2)^{1/3}$, and transforming vertical axes according to Eq. (7.29).

7.5.1 Initial spin-polarized state

Figure 7.5 shows the time-averages of the magnetization σ_{MF} and interaction energy $\langle\langle \bar{\mathbf{s}} \cdot \bar{\mathbf{s}} \rangle\rangle_{\text{MF}}$ as computed by mean-field simulations of $N = 100$ spins initially in the x-polarized state $|X\rangle \equiv |\mathbf{x}\rangle^{\otimes N}$, where

$$|\mathbf{x}\rangle \equiv e^{-i\frac{\pi}{2}\hat{s}_y} |s\rangle = \frac{1}{2^s} \sum_{\mu} \binom{2s}{s+\mu}^{1/2} |\mu\rangle. \quad (7.28)$$

Here $\binom{m}{k}$ is a binomial coefficient. As expected, the spin model exhibits a mean-field dynamical phase transition between an ordered phase at small h and a disordered phase at large h . The ordered phase has a non-zero magnetization σ_{MF} and an interaction energy $\langle\langle \bar{\mathbf{s}} \cdot \bar{\mathbf{s}} \rangle\rangle_{\text{MF}}$ that asymptotically approach their maximal values as $h \rightarrow 0$. The disordered phase has no (time-averaged) magnetization, $\sigma_{\text{MF}} = 0$, but the interaction energy $\langle\langle \bar{\mathbf{s}} \cdot \bar{\mathbf{s}} \rangle\rangle_{\text{MF}}$ nonetheless indicates persistent non-trivial inter-spin correlations when $n > 2$. These nontrivial correlations vanish as $h \rightarrow \infty$, in which case $\langle\langle \bar{\mathbf{s}} \cdot \bar{\mathbf{s}} \rangle\rangle_{\text{MF}}$ approaches the minimal value allowed by conservation laws (clarified below). By minimizing the reduced field h for which $\sigma_{\text{MF}} = 0$, we numerically find that the transition between ordered and disordered phases occurs at a critical field $h_{\text{crit}} = (n/2)^{-\alpha}$ with $\alpha \approx 1/3$ (see Figure 7.6). When $n = 2$, this transition is consistent with the predictions of a Lax vector analysis [115, 249–252] that exploits integrability of \hat{H}_{spin} to determine long-time behavior. However, additional theoretical tools are necessary to understand this transition when $n > 2$. We elaborate on this point in Appendix 7.G.

As shown in insets of Figure 7.5, mean-field results for different spin dimensions n collapse onto each other when normalizing the field h to its critical value, $h \rightarrow h \times (n/2)^{1/3}$, and rescaling

$$\sigma_{\text{MF}} \rightarrow \frac{\sigma_{\text{MF}}}{\gamma(n/2)}, \quad \langle\langle \bar{\mathbf{s}} \cdot \bar{\mathbf{s}} \rangle\rangle_{\text{MF}} \rightarrow \frac{\langle\langle \bar{\mathbf{s}} \cdot \bar{\mathbf{s}} \rangle\rangle_{\text{MF}} - \gamma(n)}{1 - \gamma(n)}, \quad (7.29)$$

where

$$\gamma(k) \equiv \frac{\Gamma\left(k - \frac{1}{2}\right)}{\sqrt{\pi}\Gamma(k)} \stackrel{k \geq 2}{\approx} \frac{1}{\sqrt{\pi(k-1)}}. \quad (7.30)$$

The rescaling of magnetization and interaction energy can be understood by considering their limiting behavior as $h \rightarrow \infty$ or $h \rightarrow 0$.

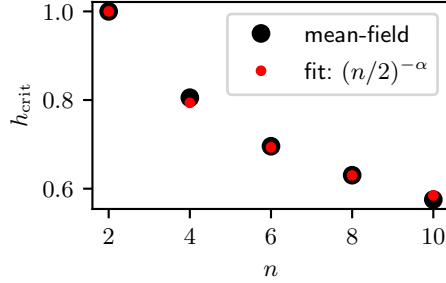


Figure 7.6: The critical value of h_{crit} as determined by mean-field simulations of $N = 100$ spins initially in the x-polarized state $|X\rangle$. A single-parameter fit to $h_{\text{crit}} = (n/2)^{-\alpha}$ finds $\alpha = 0.333(5)$, and $\alpha = 1/3$ is consistent with all mean-field results to within an uncertainty determined by the resolution of h in mean-field simulations.

In the strong-field limit $h \rightarrow \infty$, we can ignore interactions and treat spins as though they simply precess at different rates. The time-averaged transverse magnetization σ_{MF} then trivially vanishes as $h \rightarrow \infty$. The interaction energy $\langle \bar{\mathbf{s}} \cdot \bar{\mathbf{s}} \rangle_{\text{MF}} = \langle \bar{\mathbf{s}} \rangle_{\text{MF}} \cdot \langle \bar{\mathbf{s}} \rangle_{\text{MF}} + O(1/N)$, meanwhile, has contributions from: (i) the diagonal parts of the mean spin matrix $\langle \bar{\mathbf{s}} \rangle_{\text{MF}}$, which are conserved by inhomogeneous spin precession, and (ii) the off-diagonal parts of $\langle \bar{\mathbf{s}} \rangle_{\text{MF}}$, whose oscillations average to zero when evaluating the time average in $\langle \langle \bar{\mathbf{s}} \cdot \bar{\mathbf{s}} \rangle \rangle_{\text{MF}}$. Altogether, the interaction energy $\langle \langle \bar{\mathbf{s}} \cdot \bar{\mathbf{s}} \rangle \rangle_{\text{MF}}$ in the strong-field limit is determined by the time-independent diagonal part $\text{diag} \langle \bar{\mathbf{s}} \rangle_{\text{MF}} = \text{diag} |x\rangle\langle x|$, namely

$$\lim_{h \rightarrow \infty} \langle \langle \bar{\mathbf{s}} \cdot \bar{\mathbf{s}} \rangle \rangle_{\text{MF}} = \text{Tr} \left[(\text{diag} |x\rangle\langle x|)^2 \right] = \gamma(n). \quad (7.31)$$

The same result can be obtained by computing the time-averaged interaction energy of two spins precessing at different rates.

In the weak-field limit $h \rightarrow 0$, the spin-locking $\hat{\mathbf{S}} \cdot \hat{\mathbf{S}}$ interactions of the Hamiltonian \hat{H}_{spin} energetically restrict dynamics to the permutationally symmetric (PS) manifold. To first order in h , the effect of the inhomogeneous field can be acquired by projecting it onto the PS manifold, which takes $\hat{s}_{z,q} \rightarrow \frac{1}{N} \hat{S}_z$. The first order effect of the inhomogeneous field thus vanishes, as

$$\sum_q \sin(q) \hat{s}_{z,q} \rightarrow \sum_q \sin(q) \times \frac{1}{N} \hat{S}_z = 0. \quad (7.32)$$

At second order in h , the effective Hamiltonian within the PS manifold is related to the variance of the inhomogeneous field, rather than its (vanishing) average. On a high level, the second-order effect of the inhomogeneous field within the PS manifold thus consists of permutation-symmetrized products of two spin-z operators, $\hat{s}_{z,p}\hat{s}_{z,q}$ (with p, q possibly equal). Altogether, the effective spin Hamiltonian at second order in h is (see Appendix 7.B)

$$\hat{H}_{\text{spin}}^{\text{eff}} = \frac{h^2 u}{2(N-1)} \times \left[\hat{S}_z^2 - N \sum_q \hat{s}_{z,q}^2 \right], \quad (7.33)$$

which in the mean-field approximation becomes

$$\hat{H}_{\text{MF}}^{\text{eff}} = -\frac{1}{2} h^2 u \sum_q \hat{s}_{z,q}^2, \quad (7.34)$$

where we have used the fact that the axial magnetizations $\langle \hat{s}_{z,q} \rangle = \frac{1}{N} \langle \hat{S}_z \rangle$ within the PS manifold, and the initial value of $\langle \hat{S}_z \rangle = 0$ is conserved by \hat{H}_{spin} . The weak-field effective Hamiltonian preserves permutational symmetry, so $\langle \langle \bar{\mathbf{s}} \cdot \bar{\mathbf{s}} \rangle \rangle_{\text{MF}} \rightarrow 1$ as $h \rightarrow 0$. Moreover, the initial y-magnetization $\langle \hat{S}_y \rangle = 0$ is conserved by \hat{H}_{spin} , so the long-time-averaged magnetization σ_{MF} is determined by the time-average of \hat{s}_x for a single (any) spin:

$$\lim_{h \rightarrow 0} \sigma_{\text{MF}} = \frac{1}{s} \lim_{T \rightarrow \infty} \frac{1}{T} \int_0^T d\tau \langle \mathbf{x} | \hat{s}_x(\tau) | \mathbf{x} \rangle, \quad (7.35)$$

where

$$\hat{s}_x(\tau) = e^{i\tau \hat{s}_z^2} \hat{s}_x e^{-i\tau \hat{s}_z^2}. \quad (7.36)$$

We can adapt exact analytical results for the dynamics of an infinite-range Ising model [120]^d to find that

$$\langle \mathbf{x} | \hat{s}_x(\tau) | \mathbf{x} \rangle = s (\cos \tau)^{n-2}, \quad (7.37)$$

so for even n

$$\lim_{h \rightarrow 0} \sigma_{\text{MF}} = \frac{1}{2\pi} \int_0^{2\pi} d\tau (\cos \tau)^{n-2} = \gamma \left(\frac{n}{2} \right). \quad (7.38)$$

^d See Appendix K of Ref. [3] for a simpler adaptation of the analytics in Ref. [120] to the one-axis twisting model

$$\hat{H}_{\text{OAT}} = \chi \hat{s}_z^2.$$

When going beyond mean-field theory, inter-spin correlations generated by \hat{S}_z^2 in Eq. (7.33) will cause $\langle \hat{S}_x \rangle$ (and thereby the magnetization $\langle \vec{\sigma} \rangle$) to decay as $e^{-O(t^2/Ns)}$; the timescale of this decay diverges as $N \rightarrow \infty$. On a lattice of linear size L without periodic boundary conditions, additional corrections to the behavior predicted above will appear on $O(L/J)$ timescales.

7.5.2 Initial kitten states

We now consider the same setup as above, but with the initial “kitten” states $|XX\rangle \equiv |xx\rangle^{\otimes N}$ and $|XX_i\rangle \equiv |xx_i\rangle^{\otimes N}$, where

$$|xx\rangle \equiv \frac{|x\rangle + |-x\rangle}{\sqrt{2}}, \quad |xx_i\rangle \equiv \frac{|x\rangle + (-1)^s |-x\rangle}{\sqrt{2}}, \quad (7.39)$$

and $|-x\rangle$ is a state polarized along $-x$, defined similarly to $|x\rangle$ in Eq. (7.28):

$$|-x\rangle \equiv e^{-i\frac{\pi}{2}\hat{s}_y} |-s\rangle = \frac{1}{2^s} \sum_{\mu} (-1)^{s+\mu} \binom{2s}{s+\mu}^{1/2} |\mu\rangle. \quad (7.40)$$

Similarly to Figure 7.5, Figures 7.7 and 7.8 show the time-averaged magnetization σ_{MF} and interaction energy $\langle\langle \vec{s} \cdot \vec{s} \rangle\rangle_{\text{MF}}$ throughout mean-field dynamics of the initial states $|XX\rangle$ and $|XX_i\rangle$. These figures exclude the trivial case of spin dimension $n = 2$, for which $|xx\rangle = |-s\rangle$ is an eigenstate of \hat{H}_{spin} and $|xx_i\rangle = e^{-i\frac{\pi}{2}\hat{s}_z} |x\rangle \equiv |y\rangle$ is spin-polarized along the y axis. The first and perhaps most interesting observation to make about Figures 7.7 and 7.8 is that they are different, signifying the importance of intra-spin coherences for the dynamical behavior of multilevel spin models.

Unlike Figure 7.5 (for $|X\rangle$), Figure 7.7 (for $|XX\rangle$) exhibits no sharp transition between distinct dynamical phases: the time-averaged magnetization $\sigma_{\text{MF}} = 0$ for all values of the field h , and the interaction energy $\langle\langle \vec{s} \cdot \vec{s} \rangle\rangle_{\text{MF}}$ smoothly crosses over from a maximal value of 1 to a minimal value of $2\gamma(n)$. The minimal value of $\langle\langle \vec{s} \cdot \vec{s} \rangle\rangle_{\text{MF}}$ approached as $h \rightarrow \infty$ can be explained with arguments identical to those in the paragraph containing Eq. (7.31), which now imply that

$$\lim_{h \rightarrow \infty} \langle\langle \vec{s} \cdot \vec{s} \rangle\rangle_{\text{MF}} = \text{Tr} \left[(\text{diag } |xx\rangle\langle xx|)^2 \right] = 2\gamma(n). \quad (7.41)$$

The vanishing magnetization $\sigma_{\text{MF}} = 0$ in Figure 7.7 is protected by symmetries of \hat{H}_{spin} and $|XX\rangle$. For all initial states that we have considered, the value of $\langle \hat{S}_z \rangle = 0$ is conserved by the spin

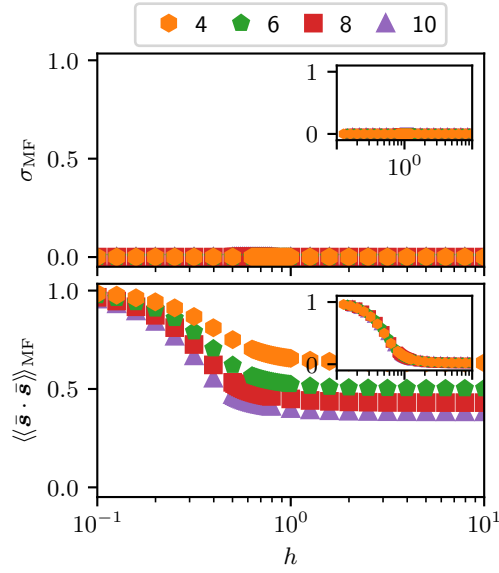


Figure 7.7: A corollary of Figure 7.5 for the initial state $|XX\rangle$. The inset for interaction energy $\langle\langle \bar{\mathbf{s}} \cdot \bar{\mathbf{s}} \rangle\rangle_{\text{MF}}$ in Figure 7.5 subtracts off the minimal value of $\langle\langle \bar{\mathbf{s}} \cdot \bar{\mathbf{s}} \rangle\rangle_{\text{MF}}$ and rescales to lie on the interval $[0, 1]$, as prescribed in Eq. (7.29). Here the subtracting and rescaling is identical, but with a minimal value of $2\gamma(n)$ rather than $\gamma(n)$.

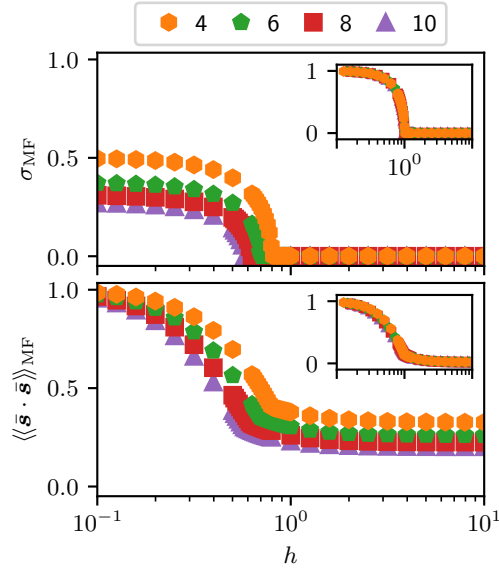


Figure 7.8: A corollary of Figure 7.5 for the initial state $|XX_1\rangle$. Insets show the same data shifted and rescaled identically to Figure 7.5.

Hamiltonian \hat{H}_{spin} . Moreover, both the spin Hamiltonian \hat{H}_{spin} and the state $|\text{XX}\rangle$ are invariant (up to global phase) under the action of \hat{R}_z^π , where $\hat{R}_z^\theta \equiv e^{-i\theta\hat{S}_z}$, which is to say that

$$\hat{R}_z^\pi \hat{H}_{\text{spin}} \hat{R}_z^{\pi\dagger} = \hat{H}_{\text{spin}} \quad \hat{R}_z^\pi |\text{XX}\rangle \simeq |\text{XX}\rangle, \quad (7.42)$$

where \simeq denotes equality up to an overall phase. This symmetry implies that

$$\langle \hat{S}_x \rangle = \langle \hat{R}_z^{\pi\dagger} \hat{S}_x \hat{R}_z^\pi \rangle = -\langle \hat{S}_x \rangle = 0, \quad (7.43)$$

$$\langle \hat{S}_y \rangle = \langle \hat{R}_z^{\pi\dagger} \hat{S}_y \hat{R}_z^\pi \rangle = -\langle \hat{S}_y \rangle = 0 \quad (7.44)$$

at all times, so altogether $\sigma_{\text{MF}} = 0$.

Turning now to mean-field results for the initial kitten state $|\text{XX}_i\rangle$ in Figure 7.8, we remark that the magnetization σ_{MF} and interaction energy $\langle\langle \bar{\mathbf{s}} \cdot \bar{\mathbf{s}} \rangle\rangle_{\text{MF}}$ behave identically to those for the initial spin-polarized state $|\text{X}\rangle$ in Figure 7.5. This finding can be understood through the fact that

$$|\text{XX}_i\rangle \simeq \hat{R}_z^{\pi/2} \hat{T}_z^{\pi/2} |\text{X}\rangle, \quad (7.45)$$

where $\hat{T}_z^\theta \equiv e^{-i\theta\hat{S}_z^2}$. The operators \hat{R}_z^θ and \hat{T}_z^θ are generated by axial fields that respect permutational symmetry, and therefore commute with the spin Hamiltonian \hat{H}_{spin} , so

$$e^{-it\hat{H}_{\text{spin}}} |\text{XX}_i\rangle \simeq e^{-it\hat{H}_{\text{spin}}} \hat{R}_z^{\pi/2} \hat{T}_z^{\pi/2} |\text{X}\rangle \quad (7.46)$$

$$\simeq \hat{R}_z^{\pi/2} \hat{T}_z^{\pi/2} e^{-it\hat{H}_{\text{spin}}} |\text{X}\rangle. \quad (7.47)$$

In turn, expanding $\bar{\mathbf{s}} \cdot \bar{\mathbf{s}}$ according to Eq. (7.8) shows that

$$\hat{T}_z^{\theta\dagger} \hat{R}_z^{\theta\dagger} \bar{\mathbf{s}} \cdot \bar{\mathbf{s}} \hat{R}_z^\theta \hat{T}_z^\theta = \bar{\mathbf{s}} \cdot \bar{\mathbf{s}}, \quad (7.48)$$

which implies that the interaction energy $\langle \bar{\mathbf{s}} \cdot \bar{\mathbf{s}} \rangle$ throughout dynamics of the initial kitten state $|\text{XX}_i\rangle$ is the same as that of the spin-polarized state $|\text{X}\rangle$.

To make sense of why the magnetization σ_{MF} is identical in Figure 7.8 for $|\text{XX}_i\rangle$ as in Figure 7.5 for $|\text{X}\rangle$, we follow a four-part argument:

- (i) The time-averaged magnetization vector $\langle\langle \vec{\sigma} \rangle\rangle_{\text{MF}}$ can be written as a function of the time-averaged spin matrix $\langle\langle \bar{\mathbf{s}} \rangle\rangle_{\text{MF}}$.

- (ii) The spin matrix $\langle\langle \bar{\mathbf{s}} \rangle\rangle_{\text{MF}}$ is only ever nonzero on its diagonal and anti-diagonal, regardless of the initial state. That is, nonzero components $\langle\langle \bar{s}_{\mu\nu} \rangle\rangle_{\text{MF}}$ of $\langle\langle \bar{\mathbf{s}} \rangle\rangle_{\text{MF}}$ always have $\mu = \pm\nu$ (see discussion below).
- (iii) The twist operator \hat{T}_z^θ acts trivially on the diagonal and anti-diagonal components of $\bar{\mathbf{s}}$, which together with point (ii) implies that $\langle\langle \hat{T}_z^{\theta\dagger} \bar{\mathbf{s}} \hat{T}_z^\theta \rangle\rangle_{\text{MF}} = \langle\langle \bar{\mathbf{s}} \rangle\rangle_{\text{MF}}$.
- (iv) The rotation operator \hat{R}_z^θ merely rotates the magnetization vector $\langle\langle \vec{\sigma} \rangle\rangle_{\text{MF}}$ without changing its magnitude.

Altogether, points (i)–(iv) imply that the magnetization

$$\sigma_{\text{MF}} = |\langle\langle \vec{\sigma} \rangle\rangle_{\text{MF}}| = |\langle\langle \hat{T}_z^{\theta\dagger} \hat{R}_z^\theta \vec{\sigma} \hat{R}_z^\theta \hat{T}_z^\theta \rangle\rangle_{\text{MF}}| \quad (7.49)$$

is the same for the initial state $|XX_i\rangle$ as for $|X\rangle$.

The only nontrivial step in the above argument is point (ii), which says that $\langle\langle \bar{s}_{\mu\nu} \rangle\rangle_{\text{MF}}$ is guaranteed to be zero unless $\mu = \pm\nu$. This observation, nominally a numerical result of mean-field simulations, can be understood as follows. The eigenstates $|m, w\rangle$ of \hat{H}_{spin} are uniquely identified by definite numbers $m = (m_s, m_{s-1}, \dots, m_{-s})$ of atoms occupying each internal spin state $\mu \in \{s, s-1, \dots, -s\}$, and an auxiliary index w that encodes how $|m, w\rangle$ transforms under permutations of all spins (see Appendix 7.B)^e. The operator $\bar{s}_{\mu\nu} = \frac{1}{N} \hat{S}_{\mu\nu}$ with $\mu \neq \nu$ couples the state $|m, w\rangle$ to states $|m', w'\rangle$ in which $(m'_\mu, m'_\nu) = (m_\mu + 1, m_\nu - 1)$. Generically, states $|m, w\rangle$ and $|m', w'\rangle$ with $m \neq m'$ will have different energies, so their coherence oscillates and averages to zero when evaluating time-averaged expectation values.

However, degeneracies yield stationary (time-independent) coherences that survive time-averaging. In the weak-field limit $h \rightarrow 0$, such a degeneracy occurs at the mean-field level between PS states differing only in the populations $m_\mu, m_{-\mu}$ (with a fixed value of $m_\mu + m_{-\mu}$), as the effective Hamiltonian becomes $\hat{H}_{\text{MF}}^{\text{eff}} \propto \sum_\mu \mu^2 m_\mu$. This symmetry is preserved at all orders in perturbation

^e Seen otherwise, since $\hat{S}_{\mu\mu}$ commutes with \hat{H}_{spin} , eigenvectors of \hat{H}_{spin} can be indexed by eigenvalues of $\hat{S}_{\mu\mu}$. The number m_μ is then the eigenvalue of $|m, w\rangle$ with respect to $\hat{S}_{\mu\mu}$, i.e. $\hat{S}_{\mu\mu} |m, w\rangle = m_\mu |m, w\rangle$, while w encodes all other information required to uniquely specify $|m, w\rangle$.

theory^f, so some coherence between such states is preserved as $h \rightarrow h_{\text{crit}}$, although this coherence decays as perturbative corrections to degenerate eigenstates cause them to leak out of the PS manifold (and thereby have a smaller overlap with the initial state $|X\rangle$). Note that beyond-mean-field effects break the symmetry protecting anti-diagonal components of $\langle\langle \hat{\mathbf{s}} \rangle\rangle_{\text{MF}}$, causing them to decay on time scales that should diverge as $N \rightarrow \infty$.

7.6 Conclusions and future directions

Starting with an $\text{SU}(n)$ Hubbard model describing ultracold fermionic alkaline-earth(-like) atoms on an optical lattice, we derived a momentum-space multilevel spin model with all-to-all $\text{SU}(n)$ -symmetric interactions. We then introduced external control fields, finding a simple three-laser drive that homogeneously addresses nuclear spins with a variety of spin Hamiltonians. Taking a closer look at the effect of the spin-orbit coupling (SOC) induced by the driving lasers, we found that maintaining the validity of the spin model requires weak SOC, which in turn gives rise to a (synthetic) inhomogeneous magnetic field. Finally, we examined dynamical behavior of the $\text{SU}(n)$ spin model at the mean-field level, finding that long-time observables obey simple scaling relations with n , and that when $n > 2$ dynamical behavior can be highly sensitive to intra-spin coherences.

Our work makes important progress in understanding the $\text{SU}(n)$ Fermi-Hubbard model in experimentally relevant parameter regimes, and we expect our findings to be readily testable in experiments with ultracold atoms. Given the possibility for long-range $\text{SU}(n)$ interactions, we hope our work stimulates further efforts into simulating SY and SYK-like models [230, 253] in cold atomic platforms. In follow-up work, it would be interesting to study the relationship between initial states and dynamical phases of our $\text{SU}(n)$ spin model more systematically, and to consider the effect of quantum corrections to mean-field behavior. There is also room to improve on the three-laser drive introduced in this work, for which it is natural to ask what additional techniques or ingredients are necessary to implement universal control of individual nuclear spins. Universal control would

^f Only even powers of the “perturbation” $\sum_q \sin(q) \hat{s}_{z,q}$ can be nonzero within the PS manifold, and even powers of this perturbation exhibit the same mean-field degeneracy between states differing only in the populations $m_\mu, m_{-\mu}$.

allow for an experimental study of n -dependence (including even/odd- n parity effects) in a single experimental platform, simply by controlling the occupation and coherence of internal spin states. Finally, one can also study the $SU(n)$ Hubbard model in the super-exchange regime that gives rise to a real-space (as opposed to momentum-space) spin model, where SOC gives rise to chiral multilevel spin interactions. Unlike our present work, the super-exchange regime does not require weak SOC, and therefore has a larger parameter space in which to explore dynamical behavior.

Acknowledgements

We thank Victor Gurarie, Emil Yuzbashyan, Asier P. Orioli, and Jeremy T. Young for helpful discussions on this work. This work was supported by the AFOSR grants FA9550-18-1-0319, FA9550-19-1-027, by the DARPA and ARO grant W911NF-16-1-0576, ARO W911NF-19-1-0210, DOE (QSA), NSF PHY1820885, NSF JILA-PFC PHY-1734006, NSF QLCI-2016244, and by NIST.

7.A Numerical benchmarking of the spin model

In this appendix we present numerical evidence to support the validity of the spin models derived in Sections 7.2 and 7.4. Figures 7.9 and 7.10 show a set of time-averaged observables computed with numerically exact simulations of a Fermi-Hubbard model and an effective spin model, respectively, with $n = 4$ (Figure 7.9) and $n = 6$ (Figure 7.10) internal levels per spin. Details for these simulations are provided in the caption of Figure 7.9. Our main conclusion from these figures is that the two models show remarkable agreement for the observables considered in our work. Note that these results are only intended to benchmark the approximation of a Fermi-Hubbard model by a spin model; these results are not expected to agree with the mean-field theory in Section 7.5 due to strong finite-size effects.

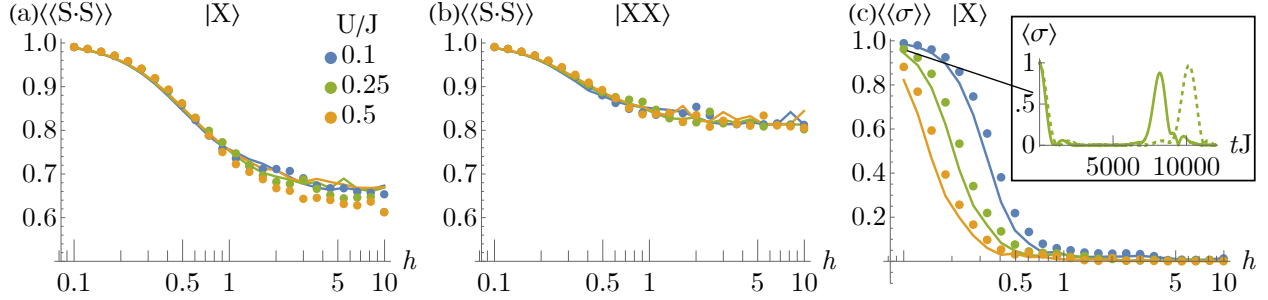


Figure 7.9: Numerical results (analogous to Figures 7.5, 7.7, and 7.8 of the main text) for the time-averaged interaction energy and magnetization (both normalized to a maximal value of 1) in a system of $L = 5$ lattice sites, for both a Fermi-Hubbard model (dots) and spin model (lines) with $n = 4$ internal states per spin. The corresponding initial state (defined in Section 7.5 of the main text) is indicated in each panel, and observables are averaged over a time $tJ = 200$. Color indicates the value of U/J , and the field h corresponds to $2J\phi/u$ in the case of the Fermi-Hubbard model. Simulations are performed in real-space, with spin-orbit coupling (SOC) implemented through a homogeneous drive (with no site or ϕ dependence) and nearest-neighbor tunneling terms that contain factors of $e^{\pm i\mu\phi}$. Results for the initial kitten state $|XX_i\rangle$ are excluded because they are identical to those of $|X\rangle$, and magnetization for the initial state $|XX\rangle$ is always 0. Note that while panels (a) and (b) are representative of infinite-time behavior, the inset in panel (c) shows that the Fermi-Hubbard and spin models exhibit different behaviors on very long time scales, although good agreement is restored by rescaling time in the spin model, indicating the likelihood of a need to renormalize spin model parameters. In any case, such time scales are inaccessible in current experiments and diverge as $N \rightarrow \infty$, so these corrections do not affect the main results of our work.

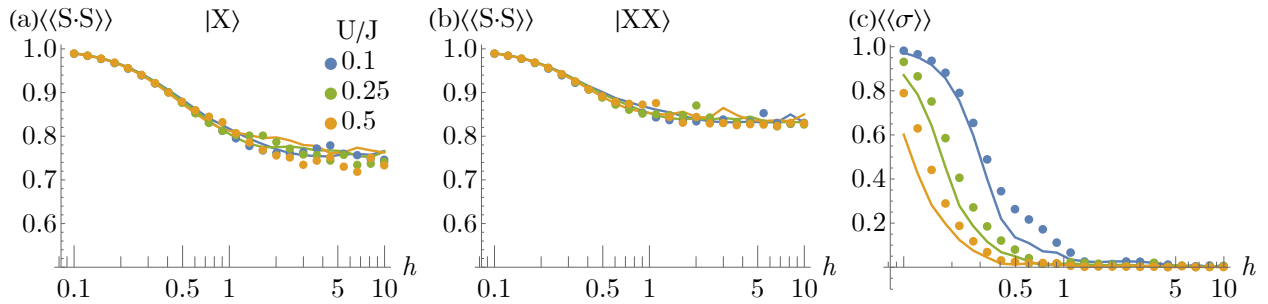


Figure 7.10: Numerical results identical to Figure 7.9, but with $L = 4$ lattice sites and $n = 6$ internal states per spin.

7.B Perturbation theory for $SU(n)$ ferromagnets

Here we work out a general perturbation theory for $SU(n)$ ferromagnets with a gapped permutationally symmetric (PS) manifold. We begin with an $SU(n)$ -symmetric interaction Hamiltonian

of the form

$$\hat{H}_0 = \sum_{i < j} g_{ij} \hat{\Pi}_{ij}, \quad \hat{\Pi}_{ij} \equiv \hat{\mathbf{s}}_i \cdot \hat{\mathbf{s}}_j = \sum_{\mu, \nu} \hat{s}_{\mu\nu i} \hat{s}_{\nu\mu j}, \quad (7.50)$$

where g_{ij} are (real) scalar coefficients for the permutation operators $\hat{\Pi}_{ij}$, and $\hat{s}_{\mu\nu i} \equiv \hat{c}_{\mu i}^\dagger \hat{c}_{\nu i}$ is a transition operator for spin i . We can then consider the addition of, for example, an inhomogeneous magnetic field or Ising couplings,

$$\hat{H}_{\text{field}} = \sum_i B_i \hat{s}_{z,i}, \quad \hat{H}_{\text{Ising}} = \sum_{i \neq j} J_{ij} \hat{s}_{z,i} \hat{s}_{z,j}, \quad (7.51)$$

or more generally an M -body operator^g

$$\hat{O}(w, \hat{X}) = \sum_{k \in \mathcal{D}_N(M)} w_k \hat{X}_k, \quad (7.52)$$

where w is a dimension- M (i.e. M -index) tensor of scalar coefficients $w_k \equiv w_{k_1 k_2 \dots k_M}$; X is an M -spin operator, e.g. $\hat{s}_z \otimes \hat{s}_z$ in the case of Ising interactions with $M = 2$; $k \equiv (k_1, k_2, \dots, k_M)$ is a list of the individual spins $k_i \in \mathbb{Z}_N \equiv \{1, 2, \dots, N\}$ that the operator $\hat{X}_k \equiv \hat{X}_{k_1 k_2 \dots k_M}$ acts on; and

$$\mathcal{D}_N(M) \equiv \left\{ k \in \mathbb{Z}_N^M : \text{all entries } k_i \text{ of } k \text{ are distinct} \right\}, \quad (7.53)$$

is the strictly “off-diagonal” part of \mathbb{Z}_N^M , which is necessary to identify for a consistent definition of \hat{X}_k as an M -body operator. In this notation, the magnetic field and Ising Hamiltonians in Eq. (7.51) respectively become $\hat{O}(B, \hat{s}_z)$ and $\hat{O}(J, \hat{s}_z \otimes \hat{s}_z)$.

If the addition $\hat{O}(w, \hat{X})$ to the $\text{SU}(n)$ -symmetric Hamiltonian \hat{H}_0 in Eq. (7.50) is sufficiently small, namely with operator norm $\|\cdot\|$ $\hat{O}(w, \hat{X})$ less than half the spectral gap Δ_{gap} of \hat{H}_0 , $\|\cdot\| \hat{O}(w, \hat{X}) < \Delta_{\text{gap}}/2$, then we can treat the effect of $\hat{O}(w, \hat{X})$ on the ground-state PS manifold \mathcal{E}_0 perturbatively. The effective Hamiltonians $\hat{H}_{\text{eff}}^{(1)}$ and $\hat{H}_{\text{eff}}^{(2)}$ induced by $\hat{O}(w, \hat{X})$ on the PS manifold \mathcal{E}_0 at leading orders in perturbation theory are [80]

$$\hat{H}_{\text{eff}}^{(1)} = \hat{\mathcal{P}}_0 \hat{O}(w, \hat{X}) \hat{\mathcal{P}}_0, \quad \hat{H}_{\text{eff}}^{(2)} = - \sum_{\Delta \neq 0} \frac{1}{\Delta} \hat{\mathcal{P}}_0 \hat{O}(w, \hat{X}) \hat{\mathcal{P}}_\Delta \hat{O}(w, \hat{X}) \hat{\mathcal{P}}_0, \quad (7.54)$$

^g At face value, an M -body operator with $M > 2$ does not typically appear in experiments. Nonetheless, considering $M > 2$ illuminates the structure of eigenstates (and eigenvalues) of \hat{H}_0 , and allows us to go to high orders in perturbation theory with single- and two-body perturbations.

where $\hat{\mathcal{P}}_\Delta$ is a projector onto the eigenspace \mathcal{E}_Δ of \hat{H}_0 with interaction energy Δ above that of the PS manifold. The first order effective Hamiltonian $\hat{H}_{\text{eff}}^{(1)}$ simply projects $\hat{\mathcal{O}}(w, \hat{X})$ onto the PS manifold \mathcal{E}_0 , and takes the form

$$\hat{H}_{\text{eff}}^{(1)} = \bar{w} \underline{X}, \quad (7.55)$$

where the coefficient \bar{w} is the average of all coefficients w_k ; and \underline{X} is a collective version of X :

$$\bar{w} \equiv \frac{1}{|\mathcal{D}_N(M)|} \sum_{k \in \mathcal{D}_N(M)} w_k, \quad \underline{X} \equiv \sum_{k \in \mathcal{D}_N(M)} \hat{X}_k, \quad (7.56)$$

with $|\mathcal{D}_N(M)| = \prod_{j=0}^{M-1} (N-j)$. In the case of a magnetic field \hat{s}_z or Ising interactions $\hat{s}_z \otimes \hat{s}_z$, for example,

$$\underline{\hat{s}}_z = \sum_i \hat{s}_z^{(i)} = \hat{S}_z, \quad \underline{\hat{s}}_z \otimes \underline{\hat{s}}_z = \sum_{i \neq j} \hat{s}_z^{(i)} \hat{s}_z^{(j)} = \hat{S}_z^2 - N \sum_i \hat{s}_{z,i}^2. \quad (7.57)$$

The second order effective Hamiltonian $\hat{H}_{\text{eff}}^{(2)}$ in Eq. (7.54) takes more work to simplify due to the presence of a projector $\hat{\mathcal{P}}_\Delta$ onto the manifold \mathcal{E}_Δ of states with excitation energy Δ . This projector essentially picks off the part of $\hat{\mathcal{O}}(w, \hat{X})$ that is strictly off-diagonal with respect to the ground- and excited-state manifolds \mathcal{E}_0 and \mathcal{E}_Δ . We therefore need to decompose $\hat{\mathcal{O}}(w, \hat{X})$ into components that generate states of definite excitation energy when acting on PS states $|\psi\rangle \in \mathcal{E}_0$. The $\text{SU}(n)$ symmetry of \hat{H}_0 enables such a decomposition to take the form

$$\hat{H}_0 \hat{\mathcal{O}}(w, \hat{X}) |\psi\rangle = \sum_{\Delta} (E_0 + \Delta) \hat{\mathcal{O}}(w^\Delta, \hat{X}) |\psi\rangle, \quad E_0 \equiv \sum_{i < j} g_{ij}, \quad (7.58)$$

where E_0 is the interaction energy of PS states, and thinking of the tensor w as a $|\mathcal{D}_N(M)|$ -component vector, the tensor w^Δ can be found by (i) using the coefficients g_{ij} to construct a matrix $g^{(M)}$ of dimensions $|\mathcal{D}_N(M)| \times |\mathcal{D}_N(M)| \sim N^M \times N^M$, and (ii) projecting w onto the eigenspace of $g^{(M)}$ with eigenvalue Δ . We construct $g^{(M)}$ for the single-body ($M=1$) case below (in Appendix 7.B.1), and provide explicit forms of $g^{(M)}$ with arbitrary M .

Equipped with the decomposition $\hat{\mathcal{O}}(w, \hat{X}) = \sum_{\Delta} \hat{\mathcal{O}}(w^\Delta, \hat{X})$ with terms $\hat{\mathcal{O}}(w^\Delta, \hat{X})$ that generate states of definite excitation energy Δ , we can expand

$$\hat{H}_{\text{eff}}^{(2)} = - \sum_{\Delta \neq 0} \frac{1}{\Delta} \hat{\mathcal{P}}_0 \hat{\mathcal{O}}(w^\Delta, \hat{X})^2 \hat{\mathcal{P}}_0. \quad (7.59)$$

If X is a single-body operator, then

$$\hat{H}_{\text{eff}}^{(2)} = \sum_{\Delta \neq 0} \frac{w^\Delta \cdot w^\Delta}{N(N-1)\Delta} \left(\underline{X^2} - N \underline{X^2} \right), \quad (7.60)$$

and if furthermore all $g_{ij} = -U/N$, as for \hat{H}_{int} in Eq. (7.9), then the only relevant excitation energy is $\Delta = U$ (see Section 7.B.2), and

$$w^U \cdot w^U = \sum_i (w_i - \bar{w})^2 = N\tilde{w}^2 \quad (7.61)$$

is simply N times the variance \tilde{w}^2 of w , so

$$\hat{H}_{\text{eff}}^{(2)} = \frac{\tilde{w}^2}{(N-1)U} \left(\underline{X^2} - N \underline{X^2} \right). \quad (7.62)$$

7.B.1 Generating excitation energy eigenstates

Here we construct the matrix $g^{(M)}$ that enables decomposing M -body operators $\hat{O}(w, \hat{X})$ into terms $\hat{O}(w^\Delta, \hat{X})$ that generate states of definite excitation energy Δ above the PS manifold, as in Eq. (7.58). We work through the calculation of $g^{(1)}$ explicitly, and provide the result for $g^{(M)}$ from a generalized version of the same calculation. To this end, we consider the action of a single-body operator $\hat{O}(w, \hat{X}) = \sum_i w_i \hat{X}_i$ on an arbitrary PS state $|\psi\rangle \in \mathcal{E}_0$ and expand

$$\hat{H}_0 \hat{O}(w, \hat{X}) |\psi\rangle = \frac{1}{2} \sum_{i \neq j} \sum_k g_{ij} w_k \hat{\Pi}_{ij} \hat{X}_k |\psi\rangle, \quad (7.63)$$

where strictly speaking g_{ij} has only been defined for $i < j$, so for completeness we define $g_{ji} = g_{ij}$ and $g_{ii} = 0$. The sum in Eq. (7.63) has terms with $k \in \{i, j\}$ and terms with $k \notin \{i, j\}$. In the case of $k \notin \{i, j\}$, the permutation operator $\hat{\Pi}_{ij}$ commutes with \hat{X}_k and annihilates on $|\psi\rangle$, and we can replace the sum

$$\sum_{k \notin \{i, j\}} \rightarrow \sum_k - \sum_{k \in \{i, j\}}, \quad (7.64)$$

allowing us to simplify

$$\frac{1}{2} \sum_{i \neq j} \sum_{k \notin \{i, j\}} g_{ij} w_k \hat{\Pi}_{ij} \hat{X}_k |\psi\rangle = E_0 \hat{O}(w, \hat{X}) |\psi\rangle - \frac{1}{2} \sum_{i \neq j} \sum_{k \in \{i, j\}} g_{ij} w_k \hat{X}_k |\psi\rangle, \quad (7.65)$$

where $E_0 = \frac{1}{2} \sum_{i \neq j} g_{ij}$ is the interaction energy the PS state $|\psi\rangle \in \mathcal{E}_0$. Switching the order of sums over $i \neq j$ and $k \in \{i, j\}$ as

$$\sum_{i \neq j} \sum_{k \in \{i, j\}} \rightarrow \sum_k \sum_{\substack{i \neq j \\ \{i, j\} \ni k}}, \quad (7.66)$$

we can simplify

$$\frac{1}{2} \sum_{\substack{i \neq j \\ \{i, j\} \ni k}} g_{ij} = \frac{1}{2} \sum_i g_{ik} + \frac{1}{2} \sum_j g_{kj} = g_k, \quad g_k \equiv \sum_i g_{ik}, \quad (7.67)$$

which implies that the terms in Eq. (7.63) with $k \notin \{i, j\}$ are

$$\frac{1}{2} \sum_{i \neq j} \sum_{k \notin \{i, j\}} g_{ij} w_k \hat{\Pi}_{ij} \hat{X}_k |\psi\rangle = E_0 \hat{\mathcal{O}}(w, \hat{X}) |\psi\rangle - \sum_k g_k w_k \hat{X}_k |\psi\rangle. \quad (7.68)$$

The terms in Eq. (7.63) with $k \in \{i, j\}$, meanwhile, are

$$\frac{1}{2} \sum_{\substack{i \neq j \\ k \in \{i, j\}}} g_{ij} w_k \hat{\Pi}_{ij} \hat{X}_k |\psi\rangle = \sum_{i, j} g_{ij} w_j \hat{X}_i |\psi\rangle. \quad (7.69)$$

so in total

$$\hat{H}_0 \hat{\mathcal{O}}(w, \hat{X}) |\psi\rangle = E_0 \hat{\mathcal{O}}(w, \hat{X}) |\psi\rangle + \sum_k \left[\sum_j g_{kj} w_j - g_k w_k \right] \hat{X}_k |\psi\rangle. \quad (7.70)$$

The action of the single-body perturbation $\hat{\mathcal{O}}(w, \hat{X})$ on a permutationally symmetric state therefore generates an eigenstate of \hat{H}_0 with interaction energy $E_0 + \Delta$ if the vector $w = \sum_k w_k |k\rangle$ satisfies the eigenvalue equation

$$g^{(1)} \cdot w = \Delta w, \quad g^{(1)} \equiv g - \text{diag } \vec{g}, \quad (7.71)$$

where $g \equiv \sum_{i, j} g_{ij} |i\rangle\langle j|$ is a matrix of all couplings g_{ij} ; the vector $\vec{g} \equiv \sum_{i, j} g_{ij} |i\rangle = \sum_i g_i |i\rangle$ is the sum of all columns of g ; and the matrix $\text{diag } \vec{g} \equiv \sum_i g_i |i\rangle\langle i|$ has \vec{g} on the diagonal and zeroes everywhere else.

A similar calculation as above with arbitrary M yields an eigenvalue equation of the form

$$g^{(M)} \cdot w = \Delta w, \quad (7.72)$$

where we treat w as an $|\mathcal{D}_N(M)|$ -component vector, and $g^{(M)}$ is a matrix with dimensions $|\mathcal{D}_N(M)| \times |\mathcal{D}_N(M)|$. In the case of $M = 2$, we have

$$g^{(2)} = \sum_{(k,\ell) \in \mathcal{D}_N(2)} |k\ell\rangle \left[\sum_{\substack{i \in \mathbb{Z}_N \\ i \notin \{k,\ell\}}} (g_{ik} \langle i\ell| + g_{i\ell} \langle ki|) + g_{k\ell} \langle \ell k| - (g_k + g_\ell - g_{k\ell}) \langle k\ell| \right], \quad (7.73)$$

and more generally

$$g^{(M)} = \sum_{k \in \mathcal{D}_N(M)} |k\rangle \left[\sum_{a \in \mathbb{Z}_M} \sum_{\substack{i \in \mathbb{Z}_N \\ i \notin k}} g_{ik_a} \langle k_{a:i}| + \sum_{\{a,b\} \in \mathcal{C}_M(2)} g_{k_a k_b} \langle k_{a \leftrightarrow b}| - \tilde{g}_k \langle k| \right], \quad (7.74)$$

where $k_a \in k = (k_1, k_2, \dots, k_M)$; $k_{a:i}$ a list that is equal to k except at the a -th position, where k_a replaced is by i , i.e. $k_{a:i} = (\dots, k_{a-1}, i, k_{a+1}, \dots)$; $\mathcal{C}_L(p)$ is the set of all subsets (“choices”) of p elements from \mathbb{Z}_L ; $k_{a \leftrightarrow b}$ is equal to k except at the a -th and b -th positions, at which k_a and k_b are switched; and

$$\tilde{g}_k \equiv \sum_{\substack{\{i,j\} \in \mathcal{C}_N(2) \\ i \in k \text{ or } j \in k}} g_{ij} = \sum_{i \in k} g_i - \sum_{\{a,b\} \in \mathcal{C}_M(2)} g_{k_a k_b}. \quad (7.75)$$

If the tensor w is permutationally symmetric, meaning that w_k is invariant under arbitrary permutations of k , then this symmetry is preserved by $g^{(M)}$. In this case, we can replace sums over $k \in \mathcal{D}_N(M)$ in Eqs. (7.73) and (7.74) by sums over $k \in \mathcal{C}_N(M)$, and replace vectors $|k_1, k_2, \dots, k_M\rangle \rightarrow |\{k_1, k_2, \dots, k_M\}\rangle$, such that e.g. $|k_{a \leftrightarrow b}\rangle = |k\rangle$. These replacements reduce the size of $g^{(M)}$ from $|\mathcal{D}_N(M)| \times |\mathcal{D}_N(M)|$ to $|\mathcal{C}_N(M)| \times |\mathcal{C}_N(M)|$, where $|\mathcal{D}_N(M)| = \prod_{j=0}^{M-1} (N-j) = M! \times \binom{N}{M}$ and $|\mathcal{C}_N(M)| = \binom{N}{M}$. Additional symmetries of g and w , such as translational invariance or lattice symmetries, can be used to further reduce the computational complexity of the eigenvalue problem in Eq. (7.72).

7.B.2 Recovering spin-wave theory

If the interaction Hamiltonian \hat{H}_0 is translationally invariant, then the single-body eigenvalue problem in Eq. (7.71) is solvable analytically. In this case, the couplings g_{ij} depend only on the

separation $|i - j|$, so eigenvectors of g are plane waves of the form

$$w_k \equiv \sum_{d \in \mathbb{Z}_L^D} e^{id \cdot k} |d\rangle, \quad (7.76)$$

where on a D -dimensional periodic lattice of $N = L^D$ spins, lattice sites are indexed by vectors $d \in \mathbb{Z}_L^D$, and wavenumbers take on values $k \in \mathbb{Z}_L^D \times 2\pi/L$. The eigenvalues of g can be determined by expanding

$$g \cdot w_k = \sum_{c, d \in \mathbb{Z}_L^D} g_{cd} e^{id \cdot k} |c\rangle = \sum_{c, d \in \mathbb{Z}_L^D} g_{c, c+d} e^{i(c+d) \cdot k} |c\rangle = \sum_{d \in \mathbb{Z}_L^D} g_{0, d} \cos(d \cdot k) w_k, \quad (7.77)$$

where the imaginary contributions vanish in the sum over d because $g_{0, d} = g_{0, -d}$. The remainder of Eq. (7.71) that we need to sort out is $\text{diag } \vec{g}$, where all $g_i = \sum_{i, j} g_{ij} = \sum_d g_{0, d}$ are equal, which implies that $\text{diag } \vec{g} = \sum_d g_{0, d}$ is a scalar. We thus find that

$$g^{(1)} \cdot w_k = \Delta_k w_k, \quad \Delta_k \equiv \sum_{d \in \mathbb{Z}_L^D} g_{0, d} [\cos(d \cdot k) - 1], \quad (7.78)$$

in agreement with standard spin-wave theory. Excitations generated by the action of $\hat{\mathcal{O}}(w_k, X)$ on PS states $|\psi\rangle \in \mathcal{E}_0$ are known as spin-waves. If $g_{ij} = -U/N$ is constant, then the spin-wave excitation energies are $\Delta_k = U$ independent of the wavenumber k .

7.C Restricting spin operators to the permutationally symmetric manifold

Here we provide the restriction of a general M -body spin operator $\hat{\mathcal{O}}$ to the permutationally symmetric (PS) manifold of N spins (each with n internal states). Denoting the projector onto the PS manifold by $\hat{\mathcal{P}}_0$, our task is essentially to find the coefficients of the expansion

$$\hat{\mathcal{P}}_0 \hat{\mathcal{O}}_M \hat{\mathcal{P}}_0 = \sum_{a, b \in \mathcal{A}_n(N)} \langle a | \hat{\mathcal{O}}_M | b \rangle |a\rangle \langle b|, \quad (7.79)$$

where $\mathcal{A}_n(N)$ is the set of all ways to assign N (identical) spins to n (distinct) states, such that for any $a \in \mathcal{A}_n(N)$ the state $|a\rangle = |a_1, a_2, \dots, a_n\rangle$ is labeled by the occupation number a_μ of state μ , with $\sum_\mu a_\mu = N$. Written out explicitly,

$$|a\rangle = \frac{1}{\sqrt{\mathcal{C}(a)}} \sum_{\substack{\text{distinct} \\ \text{permutations} \\ \hat{\Pi} \text{ of } \tilde{a}}} \hat{\Pi} |\tilde{a}\rangle, \quad |\tilde{a}\rangle \equiv \bigotimes_{\mu} |\mu\rangle^{\otimes a_\mu}, \quad \mathcal{C}(a) \equiv \frac{(\sum_\mu a_\mu)!}{\prod_\nu a_\nu!}. \quad (7.80)$$

Here $\mathcal{C}(a)$ is a multinomial coefficient that counts the number of distinct ways to permute the tensor factors of the “standard-ordered” state $|\tilde{a}\rangle$, enforcing $\langle a|a\rangle = 1$. Using these states, with some combinatorics we can expand

$$\langle a|\hat{\mathcal{O}}_M|b\rangle = \sum_{\substack{\alpha, \beta \in \mathcal{A}_n(M) \\ \alpha \leq a, \beta \leq b}} \delta_{a-\alpha, b-\beta} \sqrt{\frac{\mathcal{C}(\alpha)\mathcal{C}(a-\alpha)\mathcal{C}(\beta)\mathcal{C}(b-\beta)}{\mathcal{C}(a)\mathcal{C}(b)}}} \langle \alpha|\hat{\mathcal{O}}_M|\beta\rangle, \quad (7.81)$$

where the restriction $\alpha \leq a$ and the difference $a - \alpha$ are evaluated element-wise, i.e. $\alpha \leq a \implies \alpha_\mu \leq a_\mu$ and $(a - \alpha)_\mu = a_\mu - \alpha_\mu$ for all μ ; and $\delta_{cd} = 1$ if $c = d$ and zero otherwise. We sum over both α and β above merely to keep the expression symmetric with respect to transposition $(a, \alpha) \leftrightarrow (b, \beta)$; in practice, one can simply sum over $\alpha \in \mathcal{A}_n(M)$ and set $\beta = b - a + \alpha$, throwing out terms with any $\beta_\mu < 0$. Note that, by slight abuse of notation, the operator $\hat{\mathcal{O}}_M$ on the left of Eq. (7.81) acts on an arbitrary choice of M spins (out of N), whereas the operator $\hat{\mathcal{O}}_M$ on the right of Eq. (7.81) is simply an M -spin operator, with matrix elements $\langle \alpha|\hat{\mathcal{O}}_M|\beta\rangle$ evaluated with respect to the PS M -spin states $|\alpha\rangle, |\beta\rangle \in \mathcal{A}_n(M)$.

7.D Relaxing assumptions of the three-laser drive

In order to arrive at the drive Hamiltonian in Eq. (7.12) of the main text, we made two simplifying assumptions: (i) that the excited-state hyperfine manifold had the same total spin s as the ground-state manifold, and (ii) that all drive amplitudes are real (which enforces a phase-locking condition between the driving lasers). To derive an effective drive Hamiltonian for the general case in which the excited-state hyperfine manifold has total spin $s + r$ with $r \in \{+1, 0, -1\}$, we decompose all lasers into their right- and left-circular polarization components and write the full drive Hamiltonian in the form

$$\hat{H}_{\text{drive}}^{\text{full}} = \sum_{j, \mathbf{v}, \sigma} \Omega_{\mathbf{v}\sigma} \left(e^{-i\kappa \mathbf{v} \cdot \boldsymbol{\ell} j} \hat{s}_{\mathbf{v}\sigma j}^{(r)} \otimes |e\rangle\langle g|_j + \text{h.c.} \right) + \Delta \hat{N}_e, \quad (7.82)$$

where $\Omega_{\mathbf{v}\sigma}$ is the amplitude of σ -polarized light propagating along axis \mathbf{v} , with $\sigma = +1$ and -1 respectively for right and left circular polarizations; and $\hat{s}_{\mathbf{v}\sigma j}$ is a spin-raising/lowering operator

for atom j along axis \mathbf{v} , defined by appropriately rotating the single-atom spin operators

$$\hat{s}_{\pm}^{(r)} \equiv -\sqrt{\frac{n(n+1)(n-1)}{6}} \times \hat{T}_{\pm}^{(r)}, \quad \hat{T}_{\pm}^{(r)} \equiv \mp \sqrt{\frac{2(s+r)+1}{2\ell+1}} \sum_{\mu} \langle s\mu; 1, \pm 1 | s+r, \mu \pm 1 \rangle |\mu \pm 1\rangle \langle \mu|. \quad (7.83)$$

Here $\langle j_1 m_1; j_2 m_2 | j_3 m_3 \rangle$ is a Clebsch-Gordan coefficient, and we have normalized $\hat{T}_{\pm}^{(r)}$ such that $\text{tr} \left[\hat{T}_{\pm}^{(r)\dagger} \hat{T}_{\pm}^{(r)} \right] = 1$. Still assuming real drive amplitudes, the corresponding effective drive Hamiltonian that replaces Eq. (7.12) in the far-detuned limit $|\Delta| \gg |\Omega_{\nu\sigma}|$ is then

$$\hat{H}_{3\text{LD}}^{\text{single}} = f_r^{(1)} \left[\tilde{\Omega}_+ \tilde{\Omega}_- \hat{s}_z + \tilde{\Omega}_0 \tilde{\Omega}_- \hat{s}_x \right] + f_r^{(2)} \left[\tilde{\Omega}_0 \tilde{\Omega}_+ (\hat{s}_z \hat{s}_x + \hat{s}_x \hat{s}_z) - \left(\tilde{\Omega}_0^2 \hat{s}_z^2 + \tilde{\Omega}_+^2 \hat{s}_x^2 + \tilde{\Omega}_-^2 \hat{s}_y^2 \right) \right] - f_r^{(3)} \sum_m \tilde{\Omega}_m^2, \quad (7.84)$$

where $f_r^{(k)}$ are scalars that depend on the spin dimension n :

$$f_0^{(1)} = 1, \quad f_{+1}^{(1)} = -s, \quad f_{-1}^{(1)} = s+1, \quad (7.85)$$

$$f_0^{(2)} = 1, \quad f_{+1}^{(2)} = -\frac{s}{n+2}, \quad f_{-1}^{(2)} = -\frac{s+1}{n-2}, \quad (7.86)$$

$$f_0^{(3)} = 0, \quad f_{+1}^{(3)} = \frac{s(s+1)^2}{n+2}, \quad f_{-1}^{(3)} = \frac{s^2(s+1)}{n-2}. \quad (7.87)$$

If additionally the drive amplitudes are complex, $\Omega_m \rightarrow \Omega_m e^{-i\eta_m}$ (with real Ω_m, η_m), then

$$\begin{aligned} \hat{H}_{3\text{LD}}^{\text{single}} = f_r^{(1)} \tilde{\Omega}_+ \tilde{\Omega}_- \hat{s}_z + \tilde{\Omega}_0 \sum_{\sigma \in \{\pm 1\}} \frac{\tilde{\Omega}_+ + \sigma \tilde{\Omega}_-}{2} \left[f_r^{(1)} \sigma \hat{s}_{\tilde{\eta}_{\sigma,x}} + f_r^{(2)} (\hat{s}_z \hat{s}_{\tilde{\eta}_{\sigma,x}} + \hat{s}_{\tilde{\eta}_{\sigma,x}} \hat{s}_z) \right] \\ - f_r^{(2)} \left[\tilde{\Omega}_0^2 \hat{s}_z^2 + \tilde{\Omega}_+ \hat{s}_{\tilde{\eta}_{0,x}}^2 + \tilde{\Omega}_- \hat{s}_{\tilde{\eta}_{0,y}}^2 \right] - f_r^{(3)} \sum_m \tilde{\Omega}_m^2, \end{aligned} \quad (7.88)$$

where $\hat{s}_{\eta\alpha} \equiv e^{-i\eta\hat{s}_z} \hat{s}_{\alpha} e^{i\eta\hat{s}_z}$ is a rotated spin- α operator (e.g. $\hat{s}_{\pi/2,x} = \hat{s}_y$), and

$$\tilde{\eta}_{\pm} \equiv \pm(\eta_{\pm} - \eta_0), \quad \tilde{\eta}_0 \equiv \frac{\eta_+ - \eta_-}{2}, \quad (7.89)$$

are the relative phases of the drive amplitudes.

7.E Mean-field theory

Here we describe the mean-field theory used to simulate the spin Hamiltonian

$$\hat{H}_{\text{spin}} = -\frac{u}{2N} \hat{\mathbf{S}} \cdot \hat{\mathbf{S}} + 2J\phi \sum_q \sin(q) \hat{s}_{z,q} \quad (7.90)$$

in Eq. (7.23) of the main text. We begin by decomposing individual spin operators into Schwinger bosons as $\hat{s}_{\mu\nu q} = \hat{b}_{\mu q}^\dagger \hat{b}_{\nu q}$, such that the spin Hamiltonian becomes

$$\hat{H}_{\text{spin}} \rightarrow \hat{H}_{\text{boson}} = -\frac{u}{2N} \sum_{p,q,\mu,\nu} \hat{b}_{\mu p}^\dagger \hat{b}_{\nu p} \hat{b}_{\nu q}^\dagger \hat{b}_{\mu q} + 2J\phi \sum_{q,\mu} \sin(q) \mu \hat{b}_{\mu q}^\dagger \hat{b}_{\mu q}. \quad (7.91)$$

The Heisenberg equations of motion for the Schwinger boson operators are (see Appendix 7.F)

$$i\partial_t \hat{b}_{\mu q} = -\frac{u}{N} \sum_{\nu,p} \hat{b}_{\nu p}^\dagger \hat{b}_{\mu p} \hat{b}_{\nu q} + 2J\phi \sin(q) \mu \hat{b}_{\mu q}. \quad (7.92)$$

Our mean-field theory then treats all boson operators in these equations of motion as complex numbers, $\hat{b}_{\mu q} \rightarrow \langle \hat{b}_{\mu q} \rangle_{\text{MF}}$, with the initial value $\langle \hat{b}_{\mu q}(t=0) \rangle_{\text{MF}}$ equal to the initial amplitude of spin q in state μ . Specifically, for an N -fold product state of the form $|\psi\rangle = \bigotimes_q \sum_\mu \psi_{\mu q} |\mu\rangle$ we set $\langle \hat{b}_{\mu q}(t=0) \rangle_{\text{MF}} = \psi_{\mu q}$. For pure initial product states, this mean-field treatment of the boson operators $\hat{b}_{\mu q}$ is mathematically equivalent to a mean-field treatment of the spin operators $\hat{s}_{\mu\nu q}$, as in Eq. (7.24), but reduces the number of variables to keep track of by a factor of $\sim n$.

7.F Schwinger boson equations of motion for quadratic spin Hamiltonians

Here we decompose a quadratic spin Hamiltonian into Schwinger bosons, and derive the equations of motion for the resulting boson operators. We begin with a general spin Hamiltonian of the form

$$\hat{H} = \sum_{\substack{\mu,\nu,\rho,\sigma \\ j < k}} g_{\rho\sigma k}^{\mu\nu j} \hat{s}_{\mu\nu j} \hat{s}_{\rho\sigma k} + \sum_{\mu,\nu,j} \epsilon_{\mu\nu j} \hat{s}_{\mu\nu j}, \quad (7.93)$$

where μ, ν index orthogonal states of an n -level spin; j, k index one of N spins; $g_{\rho\sigma k}^{\mu\nu j}$ and $\epsilon_{\mu\nu j}$ are scalars; and $\hat{s}_{\mu\nu j} = |\mu\rangle\langle\nu|_j$ is a transition operator for spin j . Strictly speaking, Eq. (7.93) only defines the couplings $g_{\rho\sigma k}^{\mu\nu j}$ for $j < k$, so we enforce $g_{\rho\sigma j}^{\mu\nu k} = g_{\rho\sigma k}^{\mu\nu j}$ and $g_{\rho\sigma j}^{\mu\nu j} = 0$ for completion. Decomposing spin operators into Schwinger bosons as $\hat{s}_{\mu\nu j} = \hat{b}_{\mu j}^\dagger \hat{b}_{\nu j}$, where $\hat{b}_{\nu j}$ annihilates a boson of type ν on site j , we can write this Hamiltonian as

$$\hat{H} = \sum_{\substack{\mu,\nu,\rho,\sigma \\ j < k}} g_{\rho\sigma k}^{\mu\nu j} \hat{b}_{\mu j}^\dagger \hat{b}_{\nu j} \hat{b}_{\rho k}^\dagger \hat{b}_{\sigma k} + \sum_{\mu,\nu,j} \epsilon_{\mu\nu j} \hat{b}_{\mu j}^\dagger \hat{b}_{\nu j}. \quad (7.94)$$

The Heisenberg equations of motion for the boson operators are then

$$i\partial_t \hat{b}_{\alpha\ell} = [\hat{b}_{\alpha\ell}, \hat{H}] = \sum_{\substack{\mu,\nu,\rho,\sigma \\ j < k}} g_{\rho\sigma k}^{\mu\nu j} [\hat{b}_{\alpha\ell}, \hat{b}_{\mu j}^\dagger \hat{b}_{\nu j} \hat{b}_{\rho k}^\dagger \hat{b}_{\sigma k}] + \sum_{\mu,\nu,j} \epsilon_{\mu\nu j} [\hat{b}_{\alpha\ell}, \hat{b}_{\mu j}^\dagger \hat{b}_{\nu j}] \quad (7.95)$$

$$= \sum_{\mu,\nu,\rho,\sigma,k} g_{\rho\sigma k}^{\mu\nu\ell} [\hat{b}_{\alpha\ell}, \hat{b}_{\mu\ell}^\dagger \hat{b}_{\nu\ell}] \hat{b}_{\rho k}^\dagger \hat{b}_{\sigma k} + \sum_{\mu,\nu} \epsilon_{\mu\nu\ell} [\hat{b}_{\alpha\ell}, \hat{b}_{\mu\ell}^\dagger \hat{b}_{\nu\ell}] \quad (7.96)$$

$$= \sum_{\mu,\nu} \left(\sum_{\rho,\sigma,k} g_{\rho\sigma k}^{\mu\nu\ell} \hat{b}_{\rho k}^\dagger \hat{b}_{\sigma k} + \epsilon_{\mu\nu\ell} \right) [\hat{b}_{\alpha\ell}, \hat{b}_{\mu\ell}^\dagger \hat{b}_{\nu\ell}] \quad (7.97)$$

where

$$[\hat{b}_{\alpha\ell}, \hat{b}_{\mu\ell}^\dagger \hat{b}_{\nu\ell}] = \delta_{\alpha\mu} \delta_{\alpha\nu} \hat{b}_{\alpha\ell} + \delta_{\alpha\mu} (1 - \delta_{\alpha\nu}) \hat{b}_{\nu\ell} = \delta_{\alpha\mu} \hat{b}_{\nu\ell}, \quad (7.98)$$

so

$$i\partial_t \hat{b}_{\alpha\ell} = \sum_{\nu} \left(\sum_{\rho,\sigma,k} g_{\rho\sigma k}^{\alpha\nu\ell} \hat{b}_{\rho k}^\dagger \hat{b}_{\sigma k} + \epsilon_{\alpha\nu\ell} \right) \hat{b}_{\nu\ell}. \quad (7.99)$$

In the case of uniform $SU(n)$ -symmetric interactions of the form $\frac{g}{2} \hat{\mathbf{S}} \cdot \hat{\mathbf{S}}$ and a diagonal external field, we have

$$g_{\rho\sigma k}^{\alpha\nu\ell} = g \times \delta_{\alpha\sigma} \delta_{\nu\rho}, \quad \epsilon_{\alpha\nu\ell} = \epsilon_{\alpha\ell} \times \delta_{\alpha\nu} \quad (7.100)$$

so

$$i\partial_t \hat{b}_{\alpha\ell} = g \sum_{\nu,k} \hat{b}_{\nu k}^\dagger \hat{b}_{\alpha k} \hat{b}_{\nu\ell} + \epsilon_{\alpha\ell} \hat{b}_{\alpha\ell}. \quad (7.101)$$

7.G Lax vector analysis

We start with the spin Hamiltonian

$$\hat{H}_{\text{spin}} = -\frac{u}{2N} \sum_{\mu,\nu} \hat{S}_{\mu\nu} \hat{S}_{\nu\mu} + 2J\phi \sum_q \sin(q) \hat{s}_{z,q}, \quad (7.102)$$

where $\hat{S}_{\mu\nu} = \sum_q \hat{s}_{\mu\nu q}$. The single-body operators that appear in this Hamiltonian have squared norms

$$\text{tr} \left(\hat{s}_{\mu\nu q}^\dagger \hat{s}_{\mu\nu q} \right) = 1 \quad \text{and} \quad \text{tr} \left(\hat{s}_{z,q}^\dagger \hat{s}_{z,q} \right) = \sum_{\mu} \mu^2 = \frac{1}{12} (n+1)n(n-1) \equiv \xi^2. \quad (7.103)$$

The Lax formulation (following Refs. [115, 249–252]) requires all single-body operators involved to have the same normalization, so we substitute $\hat{s}_{\bar{z},q} \equiv \hat{s}_{z,q}/\xi$ to expand

$$\frac{\hat{H}_{\text{spin}}}{u} = -\frac{1}{2N} \sum_{\mu,\nu} \hat{S}_{\mu\nu} \hat{S}_{\nu\mu} + \xi h \sum_q \sin(q) \hat{s}_{\bar{z},q}, \quad \text{where} \quad h \equiv \frac{2J\phi}{u}. \quad (7.104)$$

The intensive, dimensionless, $(n^2 - 1)$ -component Lax vector $\vec{\ell}(z)$ associated with \hat{H}_{spin} , which is defined with an auxiliary complex parameter z , has components

$$\ell_\alpha(z) = \frac{1}{N} \sum_q \frac{\hat{s}_{\alpha,q}}{z - \sin q} + \delta_{\alpha,\bar{z}} \xi h, \quad (7.105)$$

where α indexes elements of a basis $\{\hat{s}_\alpha\}$ of self-adjoint generators of $\text{SU}(n)$, with normalization $\text{tr}(\hat{s}_\alpha^2) = 1$. The squared magnitude $\vec{\ell}(z)^2 = \sum_\alpha \ell_\alpha(z)^2$ is a constant of motion (for any z), and its residues provide N mutually commuting quantities whose weighted sum recovers \hat{H}_{spin} . When $n = 2$, conservation of these residues provides sufficient dynamical constraints to make the spin system fully integrable. In this case, dynamical behavior is governed by the roots of $\vec{\ell}(z)^2$, and the presence (or absence) of complex roots marks distinct dynamical phases of \hat{H}_{spin} . However, the size of Hilbert space grows with n , while the number of conserved quantities provided by the Lax analysis (namely, N) does not. When $n > 2$, there is therefore no guarantee that the roots of $\vec{\ell}(z)^2$ will similarly govern dynamical behavior. In fact, a straightforward generalization of the Lax analysis to $n > 2$ makes predictions that are inconsistent with the mean-field results in Figures 7.5–7.8 of the main text. We substantiate this claim with a direct calculation of the roots of $\vec{\ell}(z)^2$ below.

Within the permutationally symmetric manifold, we can replace $\hat{s}_{\alpha,q} \rightarrow \bar{s}_\alpha \equiv \frac{1}{N} \sum_q \hat{s}_{\alpha,q}$ at the cost of $O(1/N)$ errors that vanish as $N \rightarrow \infty$, so taking this limit we find

$$\ell_\alpha(z) = \mathcal{I}(z) \bar{s}_\alpha + \delta_{\alpha,\bar{z}} \xi h, \quad (7.106)$$

where

$$\mathcal{I}(z) \equiv \lim_{N \rightarrow \infty} \frac{1}{N} \sum_q \frac{1}{z - \sin(q)} = \frac{1}{2\pi} \int_0^{2\pi} \frac{dq}{z - \sin(q)} = \frac{1}{\sqrt{z^2 - 1}} \quad \text{for} \quad z \notin [-1, 1]. \quad (7.107)$$

The squared magnitude of the Lax vector is therefore

$$\vec{\ell}(z)^2 = \sum_{\alpha} \ell_{\alpha}(z)^2 = \mathcal{I}(z)^2 \sum_{\alpha \neq \bar{z}} \bar{s}_{\alpha}^2 + [\mathcal{I}(z) \bar{s}_{\bar{z}} + \xi h]^2, \quad (7.108)$$

where we can define the scalar $Q^2 \equiv \sum_{\alpha} \bar{s}_{\alpha}^2$ to simplify

$$\vec{\ell}(z)^2 = \mathcal{I}(z)^2 \left(Q^2 - \bar{s}_{\bar{z}}^2 \right) + [\mathcal{I}(z) \bar{s}_{\bar{z}} + \xi h]^2 = \mathcal{I}(z)^2 Q^2 + \xi^2 h^2 + 2\mathcal{I}(z) \xi h \bar{s}_{\bar{z}}. \quad (7.109)$$

For initial states with $\langle \bar{s}_z \rangle = 0$, we thus find that

$$\vec{\ell}(z)^2 = \frac{Q^2}{z^2 - 1} + \xi^2 h^2, \quad (7.110)$$

which is zero when^h

$$z = \pm \sqrt{1 - \left(\frac{Q}{\xi h} \right)^2}. \quad (7.111)$$

These roots change character when $z = 0$, suggesting that the critical field h_{crit} separating dynamical phases satisfies

$$h_{\text{crit}}^2 \stackrel{?}{=} \frac{Q^2}{\xi^2}, \quad (7.112)$$

where we use the relation $\stackrel{?}{=}$ to indicate that this “prediction” of the Lax analysis is not necessarily valid for all n . For a permutationally symmetric state, up to vanishing $O(1/N)$ corrections we can expand

$$Q^2 = \sum_{\alpha} \bar{s}_{\alpha}^2 = \sum_{\mu, \nu} \bar{s}_{\mu\nu} \bar{s}_{\nu\mu} - \frac{1}{n} = 1 - \frac{1}{n} = \frac{n-1}{n}, \quad (7.113)$$

which implies that

$$h_{\text{crit}}^2 \stackrel{?}{=} \frac{n-1}{n} \times \frac{12}{n(n+1)(n-1)} = \frac{12}{n^2(n+1)}. \quad (7.114)$$

This Lax analysis correctly predicts that $h_{\text{crit}} = 1$ when $n = 2$, but otherwise predicts $h_{\text{crit}} \sim n^{-3/2}$, which is inconsistent with the finding that $h_{\text{crit}} \sim n^{-1/3}$ in the mean-field results of the main text (see Figure 7.6). We emphasize that this inconsistency is not a failure of the Lax formalism, but rather an indication that new theoretical tools are necessary to understand multilevel spin models.

^h Strictly speaking, the zeros in Eq. (7.111) occur at values of z at which $\mathcal{I}(z)$ is undefined. We avoid this issue by analytically continuing $\mathcal{I}(z)^2$ to the interval $z \in (-1, 1)$.

Chapter 8

Spin qudit tomography and state reconstruction error

Prologue

In Chapter 7, we considered the dynamical behavior of a collective multilevel spin model. In order to make sense of numerical simulations, we had to make a judicious choice of order parameters to examine. Having to make such a choice naturally leads to the question: what order parameters are actually accessible experimentally, and how? Given that the spin model is encoded in nuclear spin degrees of freedom, we know that experiments should be able to measure the projection of spin onto a fixed quantization axis with relative ease. Moreover, in Section 7.3 we worked out how external controls can implement arbitrary spatial rotations of these nuclear spins, which expands the set of accessible observables to include spin projections onto arbitrary spatial axes. The remaining questions are then (i) whether these spin projection measurements are sufficient to reconstruct any collective spin observable, (ii) how should this reconstruction be performed, and (iii) how reliable are these reconstructions (i.e. what are the error bars on the estimates of observables)? These are the motivating questions of the work in this chapter. Reconstructing all collective single-body spin observables is equivalent to performing state tomography on the average single-spin density matrix; due to its numerous connections with existing literature we use the latter formulation of the problem in this chapter. The bulk of this chapter is taken from Ref. [6]. In addition to myself and Ana Maria Rey, this work featured major contributions from Diego Barberena.

Abstract

We consider the task of performing quantum state tomography on a d -level spin qudit, using only measurements of spin projection onto different quantization axes. After introducing a basis of operators closely related to the spherical harmonics, which obey the rotational symmetries of spin qudits, we map our quantum tomography task onto the classical problem of signal recovery on the sphere. We then provide algorithms with $O(rd^3)$ serial runtime, parallelizable down to $O(rd^2)$, for (i) computing a priori upper bounds on the expected error with which spin projection measurements along r given axes can reconstruct an unknown qudit state, and (ii) estimating a posteriori the statistical error in a reconstructed state. Our algorithms motivate a simple randomized tomography protocol, for which we find that using more measurement axes can yield substantial benefits that plateau after $r \approx 3d$.

8.1 Introduction

Quantum state tomography, the task of reconstructing a quantum state by collecting and processing measurement data, is an essential primitive for quantum sensing, quantum simulation, and quantum information processing. The central importance of quantum state tomography has led to the development of techniques based on least-squares inversion [254], linear regression [255], maximum likelihood estimation [256, 257], Bayesian inference [258–260], compressed sensing [261, 262], and neural networks [263], among others. These techniques are typically developed in a general, information-theoretic setting, and make minimal assumptions about the physical medium of a quantum state. As a consequence, even well-established techniques can be ill-suited for physical platforms with unique or limited capabilities.

Due to advancements in experimental capabilities to address nuclear spin states (i.e. hyperfine levels) in ultracold atomic systems [28, 45, 264–267], as well as developments in the control of ultracold molecular systems [203, 268–277], a particular setting of growing interest is the spin qudit, or a multilevel quantum angular momentum degree of freedom. Spin qudits can provide advantages

over their qubit counterparts for quantum sensing [278, 279], enable quantum simulations of $SU(d)$ magnetism [5, 7, 28, 51, 53, 65], and offer unique capabilities for quantum computation and error correction [280–282]. In all cases, quantum state tomography is necessary to take full advantage of a spin qudit^a.

The problem of qudit tomography is not new, with an extensive literature on a variety of techniques [246, 279, 283–292]. However, most existing protocols either rely on infinite-dimensional representations of a quantum spin [279, 285, 293], or require the capability to perform essentially arbitrary operations on a qudit [286–292], generally resulting in tomographic protocols that can be highly inefficient or unachievable in practice. The protocols based on infinite-dimensional representations of a quantum spin have the advantage of reconstructing its state from measurements of spin projection onto different spatial axes, which are generally accessible with any spin qudit. Nonetheless, these protocols obfuscate the minimal requirements for performing full state tomography, provide no straightforward error bounds or guarantees of accuracy, and (with the notable exception of Ref. [285]) generally extract only a small fraction of the information contained in measurement data.

In this work, we consider the task of performing spin qubit tomography using only measurements of spin projection onto different spatial axes. This sort of task was first considered in Ref. [246], as well as a few later works [283–285]. Specifically, Ref. [246] provided an explicit protocol for reconstructing a d -level spin qudit state from measurements of spin projection along $2d - 1$ axes, the minimum number necessary for full tomography of an arbitrary (possibly mixed) qudit state. However, the protocol in Ref. [246] involves a choice of a single (arbitrary) angle θ , and provides no means for comparing different choices of θ , which may result in wildly different statistical errors (i.e. precision) in a reconstructed state. Other works provide insightful discussions into the problem of spin qudit tomography, but either (i) require making assumptions about the qudit state in question [285] (making the tomographic protocol only valid for a restricted set of

^a Note that the measurement of collective observables for quantum sensing or simulation can be recast as a single-spin tomography task.

possible states), (ii) do not address the question of statistical error [283], or (iii) provide a measure of statistical error that is needlessly conservative and computationally demanding [284]. We address these shortcomings in this work, and identify remaining avenues for refining spin qudit tomography protocols.

In Section 8.2, we introduce a set of qudit operators that are closely related to the spherical harmonics, and which play a central role in our work. We then map the quantum problem of spin qudit tomography onto the classical problem of signal recovery on the sphere in Section 8.3, thereby providing an intuitive perspective on spin qudit tomography. In Section 8.4 we provide a priori upper bounds and a posteriori estimates of the statistical error in a qudit state reconstructed from measurements of spin projection along a given set of r measurement axes. The capability to determine upper bounds on reconstruction error a priori motivates a simple randomized tomography protocol that we outline in Section 8.5, and for which we numerically find that using more measurement axes yields substantial benefits that plateau after $r \approx 3d$. To facilitate the use of our protocols, we make all of our codes publicly available at Ref. [294], which also contains the best measurement axes we found for $d \leq 30$ and $r = 3d$.

8.2 Polarization operators

We begin by introducing a set of qudit operators that are closely related to the spherical harmonics (in a sense that will be clarified below), and which play a central role in our work. Consider a d -state spin qudit with total spin $s \equiv \frac{d-1}{2}$. The defining property of a spin qudit, distinguishing it from other qudits, is that it describes an angular momentum degree of freedom, which has specific implications for how a spin qudit should transform under the group $\text{SO}(3)$ of rotations in 3D space. Due to the central importance of these transformation rules for a spin qudit, we seek a basis of operators that transform nicely under 3D rotations^b. One such basis is that of

^b Technically speaking, we seek a basis of operators that transform as an irreducible representation of $\text{SO}(3)$.

the *polarization operators* [295, 296], defined by

$$T_{\ell m} \equiv \sqrt{\frac{2\ell+1}{2s+1}} \sum_{\mu, \nu=-s}^s \langle s\mu; \ell m | s\nu \rangle |\nu\rangle\langle\mu|, \quad (8.1)$$

where $|\mu\rangle$ is an eigenstate of the axial spin projection operator $S_z |\mu\rangle = \mu |\mu\rangle$; and $\langle s\mu; \ell m | s\nu \rangle$ is a Clebsh-Gordan coefficient that enforces $\ell \in \{0, 1, \dots, d-1\}$ and $m \in \{-\ell, -\ell+1, \dots, \ell\}$, such that there are d^2 polarization operators in total. For brevity, we will generally treat the value of d as constant but arbitrary throughout this work, and we will suppress any explicit dependence of quantities or operators such as $T_{\ell m}$ on d . The polarization operators are orthonormal with respect to the trace inner product, and transform nicely under conjugation:

$$(T_{\ell m} | T_{\ell' m'}) = \delta_{\ell\ell'} \delta_{mm'}, \quad T_{\ell m}^\dagger = (-1)^m T_{\ell, -m}, \quad (8.2)$$

where for any $d \times d$ matrix $X = \sum_{\mu, \nu} X_{\mu\nu} |\mu\rangle\langle\nu|$ we define the d^2 -component vector $|X\rangle \equiv \sum_{\mu, \nu} X_{\mu\nu} |\mu\nu\rangle$; $\langle X|$ is the conjugate transpose of $|X\rangle$, such that $\langle X|Y\rangle = \text{tr}(X^\dagger Y)$; and $\delta_{kk'} \equiv 1$ if $k = k'$ and 0 otherwise. These properties of the polarization operators allow us to expand any density operator ρ in the polarization operator basis as

$$\rho = \sum_{\ell=0}^{d-1} \sum_{m=-\ell}^{\ell} \rho_{\ell m} T_{\ell m}, \quad \rho_{\ell m} \equiv \langle T_{\ell m}^\dagger \rangle_\rho, \quad (8.3)$$

where $\langle X \rangle_\rho \equiv \text{tr}(\rho X) = (\rho | X)$, and $\rho^\dagger = \rho$ implies that $\rho_{\ell m}^* = (-1)^m \rho_{\ell, -m}$. The polarization operators can be interpreted in terms of an absorption process, whereby $T_{\ell m} |\psi\rangle$ is (up to normalization) the state obtained after a spin- s state $|\psi\rangle$ absorbs a particle with total spin ℓ and spin projection m onto a fixed quantization axis. Similarly to the complex spherical harmonics $Y_{\ell m}$, we will refer to ℓ as the *degree* and m as the *order* of $T_{\ell m}$.

The polarization operators are spherical tensor operators, whose degree is preserved under 3D rotations generated by the spin operators S_x, S_y, S_z . Moreover, the degree- ℓ polarization operators $T_{\ell m}$ transform similarly to spin- ℓ particles and spherical harmonics $Y_{\ell m}$ under 3D rotations (see Appendix 8.A). Specifically, for any triplet of angles $\boldsymbol{\omega} = (\alpha, \beta, \gamma)$, we can define the rotation operator

$$R(\boldsymbol{\omega}) \equiv e^{-i\alpha S_z} e^{-i\beta S_y} e^{-i\gamma S_z}, \quad (8.4)$$

and expand rotated polarization operators as

$$T_{\omega\ell m} \equiv R(\omega) T_{\ell m} R(\omega)^\dagger = \sum_{n=-\ell}^{\ell} D_{mn}^\ell(\bar{\omega})^* T_{\ell n}, \quad (8.5)$$

where $\bar{\omega} = (\gamma, \beta, \alpha)$ is the reversal of ω , and

$$D_{mn}^\ell(\bar{\omega}) \equiv \langle \ell m | R(\bar{\omega}) | \ell n \rangle \quad (8.6)$$

are (Wigner) rotation matrix elements. For reasons that will become clear shortly, throughout this work we will primarily consider rotations of the sphere that take the north pole to a point $\mathbf{v} = (\alpha, \beta)$ at azimuthal angle α and polar angle β . For ease of notation, we therefore define $R(\mathbf{v}) \equiv R(\alpha, \beta, 0)$, $T_{\mathbf{v}\ell m} \equiv T_{(\alpha, \beta, 0), \ell m}$, and $D_{mn}^\ell(\mathbf{v}) \equiv D_{mn}^\ell(0, \beta, \alpha)$.

The polarization operators $T_{\ell m}$ share a connection to the spherical harmonics $Y_{\ell m}$ that goes beyond the rules for their transformation under 3D rotations. In fact, the phase-space representation of $T_{\ell m}$ is proportional to $Y_{\ell m}$. The phase-space representation of a spin qudit operator X assigns, to each point \mathbf{v} on the sphere, the complex number

$$X^{\text{PS}}(\mathbf{v}) \equiv \langle s_{\mathbf{v}} | X | s_{\mathbf{v}} \rangle, \quad (8.7)$$

where $|s_{\mathbf{v}}\rangle \equiv R(\mathbf{v})|s\rangle$ is the state of a spin qudit polarized along \mathbf{v} . This representation is faithful in the sense that X is uniquely determined by the phase-space values $X^{\text{PS}}(\mathbf{v})$ at all points \mathbf{v} on the sphere. The transformation rules for polarization operators in Eq. (8.5), together with the fact that $\langle s | T_{\ell m} | s \rangle = 0$ unless $m = 0$, suffice to show that

$$T_{\ell m}^{\text{PS}}(\mathbf{v}) = c_\ell Y_{\ell m}(\mathbf{v}), \quad (8.8)$$

where the scalar c_ℓ simply enforces $\langle T_{\ell m} | T_{\ell m} \rangle = 1$ (see Appendix 8.A). The polarization operators $T_{\ell m}$ are thus a quantum analogue of the spherical harmonics $Y_{\ell m}$, and play an important role in phase-space formalisms for spin qudits [245].

As a special case, the phase-space representation ρ^{PS} of a spin qudit state ρ is commonly known as its Husimi distribution. Performing tomography on an unknown qudit state ρ is therefore equivalent to reconstructing the unknown distribution ρ^{PS} on the sphere. In principle, the

representation ρ^{PS} of a finite-dimensional qudit state ρ can be reconstructed from the values $\rho^{\text{PS}}(\mathbf{v}) = \langle s_{\mathbf{v}} | \rho | s_{\mathbf{v}} \rangle$ at a finite number of points \mathbf{v} . In practice, the value $\langle s_{\mathbf{v}} | \rho | s_{\mathbf{v}} \rangle$ is determined by measuring spin projection along \mathbf{v} , which also provides measurement data on all spin projections $\langle \mu_{\mathbf{v}} | \rho | \mu_{\mathbf{v}} \rangle$ with $\mu \in \{s, s-1, \dots, -s\}$ and $|\mu_{\mathbf{v}}\rangle \equiv R(\mathbf{v})|\mu\rangle$; one would like to make use of this additional data as well. We clarify the connection between the quantum problem of reconstructing ρ from spin projection measurements and the classical problem of reconstructing ρ^{PS} from its values $\rho^{\text{PS}}(\mathbf{v})$ in the following section.

8.3 Spin tomography as signal recovery on the sphere

Our goal is to reconstruct an arbitrary state ρ of a spin qudit from measurements of spin projection onto different quantization axes. We are thus nominally restricted to measuring projectors $\Pi_{\mathbf{v}\mu} \equiv |\mu_{\mathbf{v}}\rangle\langle\mu_{\mathbf{v}}|$, where $|\mu_{\mathbf{v}}\rangle \equiv R(\mathbf{v})|\mu\rangle$ is a state with spin projection μ onto the measurement axis \mathbf{v} . For any fixed axis \mathbf{v} , the sets $\{\Pi_{\mathbf{v}\mu}\}$ and $\{T_{\mathbf{v}\ell,0}\}$ (i.e. all $T_{\mathbf{v}\ell m}$ with $m=0$) are both complete bases for the space of operators that are diagonal in the basis $\{|\mu_{\mathbf{v}}\rangle\}$. Measuring the projectors $\{\Pi_{\mathbf{v}\mu}\}$ is therefore equivalent to measuring the polarization operators $\{T_{\mathbf{v}\ell,0}\}$, and provides data on the expectation values $\langle T_{\mathbf{v}\ell,0} \rangle_{\rho}$.

In order to reconstruct an arbitrary density operator ρ from the expectation values $\langle T_{\mathbf{v}\ell,0} \rangle_{\rho}$, we essentially need to find a set of coefficients $C_{\ell m k}(\mathbf{v})$ that would allow us to recover any matrix element $\rho_{\ell m}$ of ρ through

$$\rho_{\ell m}^* = \langle T_{\ell m} \rangle_{\rho} = \sum_{\mathbf{v}, k} C_{\ell m k}(\mathbf{v}) \langle T_{\mathbf{v}k,0} \rangle_{\rho}. \quad (8.9)$$

Expanding the rotated polarization operators $T_{\mathbf{v}k,0}$ into a sum of un-rotated polarization operators $T_{\ell n}$ according to Eq. (8.5), we find that the recovery condition in Eq. (8.9) is satisfied when

$$T_{\ell m} = \sum_{\mathbf{v}, k, n} C_{\ell m k}(\mathbf{v}) D_{0,n}^k(\mathbf{v})^* T_{kn}. \quad (8.10)$$

Orthogonality of the polarization operators then implies the decomposition $C_{\ell m k}(\mathbf{v}) = \delta_{\ell k} C_{\ell m}(\mathbf{v})$,

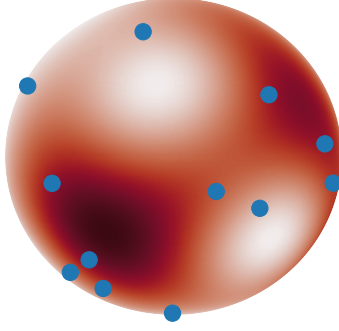


Figure 8.1: Signal recovery on the sphere is the problem of reconstructing an unknown function f (red distribution) from its values $f(\mathbf{v})$ at specific points $\mathbf{v} \in V$ (blue dots) on the sphere. For almost all choices of V , reconstruction of f is possible if there are at least as many points in V as there are degrees of freedom in f .

and in turn

$$\sum_{\mathbf{v}} C_{\ell m}(\mathbf{v}) D_{0,n}^{\ell}(\mathbf{v})^* = \delta_{mn} \quad (8.11)$$

for all ℓ .

In fact, the problem of finding suitable axes V and coefficients $C_{\ell m}(\mathbf{v})$ to satisfy Eq. (8.11) can be mapped onto the well-studied problem of signal recovery on the sphere (see Figure 8.1 [297–300]). The signal recovery problem can be stated as follows: given a square-integrable function f on the sphere, with the spherical harmonic expansion

$$f(\mathbf{v}) = \sum_{\ell,m} f_{\ell m} Y_{\ell m}(\mathbf{v}), \quad (8.12)$$

where $f_{\ell m}$ are complex coefficients, find a set of points $V = \{\mathbf{v}\}$ and associated coefficients $\tilde{C}_{\ell m}(\mathbf{v})$ with which we can reconstruct f , or equivalently its coefficients $f_{\ell m}$, from knowledge of the function's value $f(\mathbf{v})$ at all points $\mathbf{v} \in V$; that is

$$f_{\ell m} = \sum_{\mathbf{v}} \tilde{C}_{\ell m}(\mathbf{v}) f(\mathbf{v}) = \sum_{\mathbf{v},k,n} \tilde{C}_{\ell m}(\mathbf{v}) Y_{kn}(\mathbf{v}) f_{kn}. \quad (8.13)$$

Reconstruction of functions with arbitrary coefficients $f_{\ell m}$ implies that

$$\sum_{\mathbf{v}} \tilde{C}_{\ell m}(\mathbf{v}) Y_{kn}(\mathbf{v}) = \delta_{\ell k} \delta_{mn}, \quad (8.14)$$

which is a stronger version of the condition that we found for the spin qudit tomography problem in Eq. (8.11). We will refer to Eq. (8.14) as the *full recovery problem*, and Eq. (8.11) as the *reduced recovery problem*. Due to the fact that $D_{0,m}^\ell(\mathbf{v}) = \sqrt{\frac{4\pi}{2\ell+1}} Y_{\ell m}(\mathbf{v})$, any solution to the full recovery problem automatically solves the reduced recovery problem by setting $C_{\ell m}(\mathbf{v}) = \sqrt{\frac{2\ell+1}{4\pi}} \tilde{C}_{\ell m}(\mathbf{v})^*$. In principle, this mapping allows us to import a host of existing signal recovery algorithms [297–300] for the task of spin qudit tomography. In practice, spin qudits typically have only a modest dimension d , which allows for simpler and optimized tomography protocols that are practical despite worse scaling with d (see Section 8.5). A natural avenue to develop better spin qudit tomography protocols would therefore be to build on the existing classical signal recovery algorithms, tailoring them to solve the reduced recovery problem in Eq. (8.11) rather than the full recovery problem in Eq. (8.14). We leave these developments to future work.

If the function f is *band-limited* at degree L , which is to say that $f_{\ell m} = 0$ for all $\ell \geq L$, then the full recovery problem in Eq. (8.14) is provably solvable with a suitable choice of $|V| = L^2$ points on the sphere [301, 302]. The existence of these solutions to the full recovery problem in turn implies the existence of d^2 measurement axes that suffice to reconstruct arbitrary states of d -level spin qudit, whose possible states (or rather, phase-space representations) are band-limited at degree d . Moreover, for any fixed degree ℓ , finding solutions to the reduced recovery problem in Eq. (8.11) is equivalent to the recovery of a degree- ℓ function $f_\ell = \sum_m f_{\ell m} Y_{\ell m}$, which is provably possible with $|V| = 2\ell + 1$ samples [301]. In the case of spin qudit tomography, the degree ℓ takes a maximal value of $\ell_{\max} \equiv d - 1$, so state recovery requires as many measurement axes as there are polarization operators with degree ℓ_{\max} , namely $2\ell_{\max} + 1 = 2d - 1$.

8.4 State reconstruction error

For the practically minded, proving the existence of solutions to a problem is less interesting than the exposition of a particular solution. On a high level, a spin qudit tomography protocol consists of (i) selecting a set of measurement axes, (ii) collecting measurement data on spin projection onto these axes, and then (iii) processing the collected data to reconstruct the state of the

spin qudit. Whereas step (ii) can involve a host of platform-dependent technical challenges, in the following sections we discuss the steps to take before and after collecting measurement data.

To this end, we begin by asking a question: what is a “good” choice of measurement axes? Intuitively, a good choice of axes should minimize the error with which one can reconstruct an unknown quantum state from associated measurement data. If we can quantify this intuition, then we can optimize over different choices of measurement axes to find a set that (approximately) minimizes the error in reconstructed states.

A set of measurement axes $V = \{\mathbf{v}\}$ nominally induces a set of projectors $\{\Pi_{\mathbf{v}\mu}\}$ that will be measured in an experiment. By a simple change of basis, measuring these projectors is equivalent to measuring the polarization operators $\{T_{\mathbf{v}\ell,0}\}$. Flattening each $d \times d$ matrix $T_{\mathbf{v}\ell,0}$ into the d^2 -component column vector $|T_{\mathbf{v}\ell,0}\rangle$, we construct the *measurement matrix*

$$M_V \equiv \sum_{\mathbf{v},\ell} |\mathbf{v}\ell\rangle \langle T_{\mathbf{v}\ell,0}|. \quad (8.15)$$

Here \mathbf{v} and ℓ label a row of M_V , or equivalently label a standard (“one-hot”) basis vector $|\mathbf{v}\ell\rangle$ of a $(|V| \times d)$ -dimensional vector space, and $\langle T_{\mathbf{v}\ell,0}|$ is the conjugate transpose of $|T_{\mathbf{v}\ell,0}\rangle$. A necessary and sufficient condition for V to allow for full state tomography is that the measured polarization operators $T_{\mathbf{v}\ell,0}$, or equivalently the rows of M_V , span the entire (d^2 -dimensional) space of operators on a d -level spin qudit. In this case M_V must be full rank, with d^2 nonzero singular values. Indexing these singular values M_k^V and the corresponding (normalized) left singular vectors $\mathbf{x}_k^V \equiv \sum_j x_{kj}^V |j\rangle$ by an integer $k \in \{1, 2, \dots, d^2\}$, we can construct the orthonormal qudit operators

$$Q_k^V \equiv \sum_j \left(q_{kj}^V \right)^* T_j, \quad q_{kj}^V \equiv \frac{x_{kj}^V}{M_k^V}, \quad (8.16)$$

where for shorthand we use a combined index $j = (\mathbf{v}, \ell)$ to specify both a measurement axis \mathbf{v} and a degree ℓ , which identify the polarization operator $T_j \equiv T_{\mathbf{v}\ell,0}$. These operators allow us to expand any state ρ of a d -level spin qudit in the form

$$\rho = \sum_{k=1}^{d^2} \rho_k^V Q_k^V, \quad \rho_k^V \equiv \left\langle Q_k^{V\dagger} \right\rangle_\rho. \quad (8.17)$$

Given empirical estimates \tilde{T}_j of the expectation values $\langle T_j \rangle_\rho$, an empirical estimate $\tilde{\rho}_V$ of ρ is then

$$\tilde{\rho}_V \equiv \sum_k \tilde{\rho}_k^V Q_k^V, \quad (8.18)$$

where, using the fact that $T_j = T_j^\dagger$ (because they are diagonal polarization operators with degree $m = 0$),

$$\tilde{\rho}_k^V \equiv \sum_j q_{kj}^V \tilde{T}_j \approx \sum_j q_{kj}^V \langle T_j \rangle_\rho = \left\langle Q_k^{V\dagger} \right\rangle_\rho = \rho_k^V. \quad (8.19)$$

The measurement matrix M_V allows us to make concrete statements about the statistical error between the empirical estimate $\tilde{\rho}_V$ and the true state ρ . Assume, for example, that the estimates \tilde{T}_j are equal to $\langle T_j \rangle_\rho$ up to uncorrelated noise with variance no greater than ϵ^2 :

$$\tilde{T}_j = \langle T_j \rangle_\rho + \epsilon_j, \quad \langle\langle \epsilon_j \epsilon_{j'} \rangle\rangle \leq \epsilon^2 \delta_{jj'}. \quad (8.20)$$

Here $\{\epsilon_j\}$ are independent random variables, and we use the double brackets $\langle\langle \cdot \rangle\rangle$ to denote statistical averaging over experimental trials that estimate $\langle T_j \rangle_\rho$. In this case, the mean squared error with which $\tilde{\rho}_k^V$ approximates ρ_k^V is

$$\langle\langle |\tilde{\rho}_k^V - \rho_k^V|^2 \rangle\rangle = \langle\langle (\tilde{\rho}_k^V - \rho_k^V)^* (\tilde{\rho}_k^V - \rho_k^V) \rangle\rangle \quad (8.21)$$

$$= \sum_{j,j'} (q_{kj}^V)^* q_{kj'}^V \langle\langle \epsilon_j \epsilon_{j'} \rangle\rangle \quad (8.22)$$

$$\leq \sum_j |q_{kj}^V|^2 \epsilon^2 = \left(\frac{\epsilon}{M_k^V} \right)^2. \quad (8.23)$$

Using the fact that the operators Q_k^V are orthonormal, we can therefore bound the mean squared (Euclidean) distance between $\tilde{\rho}_V$ and ρ as

$$\mathcal{E}_V(\rho)^2 \equiv \langle\langle \|\tilde{\rho}_V - \rho\|^2 \rangle\rangle \leq \epsilon^2 \mathcal{S}_V^2, \quad (8.24)$$

where $\|X\|^2 \equiv (X|X) = \text{tr}(X^\dagger X)$ is the squared (Euclidean, Frobenius, or Hilbert-Schmidt) norm of X , and the *classical error scale* \mathcal{S}_V is defined by

$$\mathcal{S}_V^2 \equiv \sum_k (M_k^V)^{-2} = \|M_V^{-1}\|^2, \quad (8.25)$$

where M_V^{-1} is the left inverse of M_V , satisfying $M_V^{-1}M_V = 1$. We refer to the error scale \mathcal{S}_V as “classical” because the bound in Eq. (8.24) applies in the presence of classical sources of measurement error. Note that the classical error scale \mathcal{S}_V diverges if the measurement matrix M_V is singular, which indicates that measuring spin projections along all axes in V does not provide sufficient information to reconstruct arbitrary quantum states.

Computing the classical error scale \mathcal{S}_V and estimates $\tilde{\rho}_k^V \approx \rho_k^V$ requires building the measurement matrix M_V and computing its singular value decomposition. The complexity of this task can be greatly reduced by the fact that the degree ℓ of a polarization operator $T_{\ell m}$ is preserved under rotations, which implies that the unitary

$$U \equiv \sum_{\ell=0}^{d-1} \sum_{m=-\ell}^{\ell} |T_{\ell m}\rangle \langle \ell m|, \quad (8.26)$$

with vectors $|T_{\ell m}\rangle$ in a column indexed by integers (ℓ, m) , block-diagonalizes the measurement matrix into d blocks indexed by the degree ℓ :

$$M_V U = \sum_{\ell=0}^{d-1} |\ell\rangle\langle\ell| \otimes M_{V\ell}, \quad (8.27)$$

where the $|V| \times (2\ell + 1)$ -sized blocks are

$$M_{V\ell} \equiv \sum_{\mathbf{v}, m} |\mathbf{v}\rangle \langle T_{\mathbf{v}\ell, 0} | T_{\ell m}\rangle \langle m| = \sum_{\mathbf{v}, m} D_{0, m}^{\ell}(\mathbf{v}) |\mathbf{v}\rangle\langle m|. \quad (8.28)$$

Here $D_{0, m}^{\ell}(\mathbf{v})$ is a Wigner rotation matrix element, defined in Eq. (8.6). As the singular values of M_V are invariant under unitary transformations, it follows that

$$\mathcal{S}_V^2 = \sum_{\ell} \mathcal{S}_{V\ell}^2, \quad \mathcal{S}_{V\ell}^2 \equiv \left\| M_{V\ell}^{-1} \right\|^2, \quad (8.29)$$

where $M_{V\ell}^{-1}$ is the left inverse of $M_{V\ell}$. Constructing the block $M_{V\ell}$ and computing its singular value decomposition takes at most $O(|V|d^2)$ time. If we assume that $|V| \sim d$, then computing the classical error scale \mathcal{S}_V takes $O(d^4)$ serial or $O(d^3)$ parallel runtime (see Figure 8.2).

The assumption that observables can be estimated up to uncorrelated noise with maximal variance ϵ^2 , summarized by Eq. (8.20), is reasonable when measurement error is dominated by

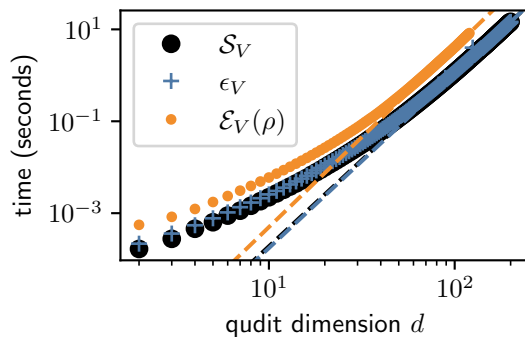


Figure 8.2: Serial runtime to compute \mathcal{S}_V , ϵ_V , or $\mathcal{E}_V(\rho)$ with $|V| = 2d - 1$ randomly chosen measurement axes and a randomly chosen qudit state ρ . Each point is an average over 10^3 calculations or 5 minutes of runtime, whichever comes first. These results do not count fixed runtimes to pre-compute quantities that can be recycled for every new choice of V and ρ . Dashed lines show fits to a runtime $t = cd^\alpha$ for the 20 largest values of d , finding $\alpha \approx 3.8 \pm 0.1$.

classical sources of experimental noise. However, this assumption breaks down when measurement error is limited by fundamental quantum shot noise (i.e. finite sampling error). We relax the assumption of Eq. (8.20) in Appendix 8.B, where we instead assume that $\tilde{\rho}_V$ is built from n independent measurements of spin projection along every axis $\mathbf{v} \in V$, with shot noise the dominant source of error. In this case, the constraints that $\text{tr}(\rho) = 1$ and $\langle \Pi_{\mathbf{v}\mu} \rangle_\rho \geq 0$ allow us to bound the mean squared distance between $\tilde{\rho}_V$ and ρ as

$$\mathcal{E}_V(\rho)^2 < \frac{\epsilon_V^2}{n}, \quad \epsilon_V^2 \equiv \sum_{\ell} \Gamma_{\ell}^2 \mathcal{S}_{V\ell}^2, \quad (8.30)$$

where the *quantum error scale* ϵ_V is defined in terms of the spectral range of $T_{\ell,0}$:

$$\Gamma_{\ell} \equiv \frac{\max_{\mu} t_{\ell\mu} - \min_{\mu} t_{\ell\mu}}{2}, \quad t_{\ell\mu} \equiv \langle \mu | T_{\ell,0} | \mu \rangle. \quad (8.31)$$

If d is even or ℓ is odd, then $\Gamma_{\ell} = \max_{\mu} t_{\ell\mu}$. For comparison with the “classical” error bound in Eq. (8.24), we note that $\epsilon_V^2 < \mathcal{S}_V^2/2$, so the previous bound still holds with the replacement $\epsilon^2 \rightarrow 1/2n$. The factors Γ_{ℓ}^2 are quick to compute and can be recycled for every new choice of axes V , so the complexity of computing ϵ_V is the same as that of \mathcal{S}_V (see Figure 8.2).

Though straightforward to compute, the bound in Eq. (8.30) is not tight, as it is acquired by bounding the statistical error $\epsilon_{\mathbf{v}\ell}$ in the empirical estimate $\tilde{T}_{\mathbf{v}\ell,0}$ of $\langle T_{\mathbf{v}\ell,0} \rangle_\rho$ by $\langle \langle \epsilon_{\mathbf{v}\ell}^2 \rangle \rangle \leq \Gamma_{\ell}^2$. The individual bounds on $\langle \langle \epsilon_{\mathbf{v}\ell}^2 \rangle \rangle$ for each axis \mathbf{v} and degree ℓ are tight, but these bounds cannot all be achieved simultaneously. There is therefore still room for improvement on the bound in Eq. (8.30) by maximizing \mathcal{E}_V over the set of all physical qudit states ρ . We discuss this maximization problem in Appendix 8.C, but leave its full solution to future work. We also note that the reconstruction error bound in Eq. (8.30) obeys the “standard quantum limit” of $\sim 1/n$ scaling in the number of measurements. In principle, this scaling can be improved to $\sim 1/n^2$ by preparing and measuring entangled copies of many qudits [31].

The error scales \mathcal{S}_V and ϵ_V provide pessimistic upper bounds on statistical error, which can be calculated without prior knowledge of the true qudit state ρ . The actual error in the reconstruction $\tilde{\rho}_V$ of a particular state ρ may be considerably smaller, and may depend on ρ itself. Written out

in full, the mean squared distance between $\tilde{\rho}_V$ and ρ is (see Appendix 8.B)

$$\mathcal{E}_V(\rho)^2 = \sum_{\mathbf{v}, \mathbf{w}, \ell} \left\langle \mathbf{v} \left| \left(M_{V\ell}^{-1} \right)^\dagger M_{V\ell}^{-1} \right| \mathbf{w} \right\rangle \langle\langle \epsilon_{\mathbf{v}\ell} \epsilon_{\mathbf{w}\ell} \rangle\rangle. \quad (8.32)$$

The covariances $\langle\langle \epsilon_{\mathbf{v}\ell} \epsilon_{\mathbf{w}\ell} \rangle\rangle$ are generally determined by the sources of measurement error in any given experiment, but will typically satisfy $\langle\langle \epsilon_{\mathbf{v}\ell} \epsilon_{\mathbf{w}\ell} \rangle\rangle = \delta_{\mathbf{v}\mathbf{w}} \langle\langle \epsilon_{\mathbf{v}\ell}^2 \rangle\rangle$ because measurements along \mathbf{v} are independent of measurements along \mathbf{w} . If measurement error is limited by shot noise, then (see Appendix 8.C)

$$\mathcal{E}_V(\rho)^2 \stackrel{\text{SNL}}{=} \frac{1}{n} \sum_{\ell} [\langle \chi_{V\ell} | \rho_{\ell} \rangle - \langle \rho_{\ell} | \mathcal{N}_{V\ell} | \rho_{\ell} \rangle], \quad (8.33)$$

where $\stackrel{\text{SNL}}{=}$ indicates equality in the ‘‘shot-noise-limited’’ regime; $|\rho_{\ell}\rangle \equiv \sum_m \rho_{\ell m} |m\rangle$ is a vector of the polarization operator components $\rho_{\ell m}$ of ρ , defined in Eq. (8.3); and the matrix $\mathcal{N}_{V\ell}$ and vector $|\chi_{V\ell}\rangle$ are defined below. While the true shot-noise-limited error in $\tilde{\rho}_V$ cannot be known exactly without knowing ρ , this error can be estimated a posteriori by $\mathcal{E}_V(\rho) \approx \mathcal{E}_V(\tilde{\rho}_V)$. After constructing an estimate $\tilde{\rho}_V$ of ρ , the complexity of computing the error $\mathcal{E}_V(\tilde{\rho}_V)$ from Eq. (8.33) is the same as that of computing \mathcal{S}_V or ϵ_V (see Figure 8.2).

We now define $\mathcal{N}_{V\ell}$ and $|\chi_{V\ell}\rangle$ for the sake of completion, but note that these definitions can be skipped without consequence for the remaining discussions in this paper. The matrix $\mathcal{N}_{V\ell}$ is

$$\mathcal{N}_{V\ell} \equiv M_{V\ell}^\dagger \text{diag} \left[\left(M_{V\ell}^{-1} \right)^\dagger M_{V\ell}^{-1} \right] M_{V\ell}, \quad (8.34)$$

where $\text{diag}[X]$ sets the off-diagonal parts of X to zero. The vector $|\chi_{V\ell}\rangle \equiv \sum_m \chi_{\ell m}^V |m\rangle$ is defined by

$$\chi_{LM}^V \equiv \sum_{\ell} (\mathcal{N}_{V\ell} | \mathcal{D}_M | \tilde{g}_{L\ell}), \quad (8.35)$$

$$\tilde{g}_{L\ell} \equiv \sum_{m, m'} (T_{L, m+m'} | T_{\ell m}^\dagger T_{\ell m'}) |m\rangle \langle m'|, \quad (8.36)$$

$$\mathcal{D}_M \equiv \sum_{m, m'} \delta_{M, m'-m} |mm'\rangle \langle mm'|. \quad (8.37)$$

Here $\tilde{g}_{L\ell}$ is essentially a matrix of structure constants for the polarization operator algebra (see Appendix 8.D), and \mathcal{D}_M simply picks off the M -th diagonal of the matrix it acts on.

8.5 Tomography protocol

The ability to certify a statistical error bound on the empirical estimate $\tilde{\rho}_V$ of an unknown quantum state ρ motivates the following protocol for spin qudit tomography:

- (i) Select a random set of measurement axes V by uniformly sampling points on the sphere^c, and use any standard minimization algorithm to optimize the $2|V|$ parameters in V (two angles for each point $\mathbf{v} \in V$) by minimizing the quantum error scale ϵ_V in Eq. (8.30). If $|V|$ is too large for such optimization, you can simply generate many sets of random measurement axes, and then choose the set with the smallest quantum error scale ϵ_V . Note that computing the error scale ϵ_V requires, for each $\ell \in \{0, 1, \dots, d-1\}$, constructing the measurement matrix $M_{V\ell}$ in Eq. (8.28) and computing its singular value decomposition. Save all measurement matrix data associated with the final measurement axes V for later use.
- (ii) For each axis $\mathbf{v} \in V$, make n measurements of spin projection, and set $\tilde{\Pi}_{\mathbf{v}\mu} \approx \langle \Pi_{\mathbf{v}\mu} \rangle_\rho$ to the fraction of times in which the measurement outcome was μ .
- (iii) Use the estimates $\tilde{\Pi}_{\mathbf{v}\mu}$ of $\langle \Pi_{\mathbf{v}\mu} \rangle_\rho$ to compute estimates of $\langle T_{\mathbf{v}\ell,0} \rangle_\rho$,

$$\tilde{T}_{\mathbf{v}\ell,0} \equiv \sum_{\mu} \langle \mu | T_{\ell,0} | \mu \rangle \tilde{\Pi}_{\mathbf{v}\mu}, \quad (8.38)$$

where the matrix elements of $T_{\ell,0}$ are provided in Eq. (8.1).

- (iv) Denoting the nonzero singular values of $M_{V\ell}$ by $M_{\ell k}^V$ and the corresponding left singular vectors by $\mathbf{x}_{\ell k}^V = \sum_{\mathbf{v}} x_{\ell k \mathbf{v}}^V |\mathbf{v}\rangle$, compute the operators and coefficients

$$Q_{\ell k} \equiv \frac{1}{M_{\ell k}^V} \sum_{\mathbf{v}} \left(x_{\ell k \mathbf{v}}^V \right)^* T_{\mathbf{v}\ell,0}, \quad (8.39)$$

$$\tilde{\rho}_{\ell k}^V \equiv \frac{1}{M_{\ell k}^V} \sum_{\mathbf{v}} x_{\ell k \mathbf{v}}^V \tilde{T}_{\mathbf{v}\ell,0}, \quad (8.40)$$

^c To sample a point (α, β) from the uniform distribution on the sphere (with azimuthal angle α and polar angle β), you can sample a point $(a, b) \in [0, 1] \times [0, 1]$ from the uniform distribution on the unit square, and then set $\alpha = 2\pi a$ and $\beta = \arccos(1 - 2b)$.

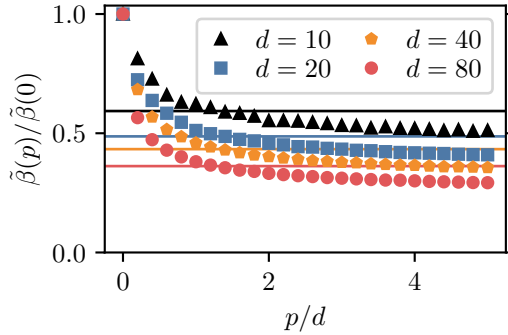


Figure 8.3: Empirical measurement-adjusted error scales $\tilde{\beta}(p)$ with p excess measurement axes, determined by minimizing over 10^3 choices of measurement axes V or 5 minutes of runtime (for each p), whichever comes first. Marker and color indicates the qudit dimension d . The rapid initial drop in $\tilde{\beta}(p)$ implies that using more measurement axes can substantially lower the upper bound on reconstruction error provided in Eq. (8.30), and that these benefits plateau after $p \approx d$. Horizontal reference lines mark the smallest measurement-adjusted error scales $\min_{\theta} \beta_{\theta}/\tilde{\beta}(0)$ achievable with the method in Ref. [246], which is parameterized by an arbitrarily chosen angle θ .

and combine them into the estimate

$$\tilde{\rho}_V = \sum_{\ell,k} \tilde{\rho}_{\ell k}^V Q_{\ell k} \approx \rho. \quad (8.41)$$

The expected reconstruction error in $\tilde{\rho}_V$, or its root-mean-square distance from ρ , is provided by Eq. (8.32). If measurement error is shot-noise-limited, then the error in $\tilde{\rho}_V$ is approximately $\mathcal{E}_V(\rho) \approx \mathcal{E}_V(\tilde{\rho}_V)$ and can be computed from Eq. (8.33). If $\tilde{\rho}_V$ has negative eigenvalues, its distance from ρ can be reduced with maximum-likelihood corrections [257], which will additionally guarantee that $\tilde{\rho}_V$ satisfies all requirements for being a physical state.

The tomography protocol outlined above leaves open the question of *how many* measurement axes to use. Though $2d - 1$ measurement axes may be sufficient to perform full state tomography, this is not necessarily the best choice of $|V|$. Increasing the number of measurement axes generally decreases the quantum error scale ϵ_V , but comes at the cost of having to estimate more observables. At a fixed total number of measurements, increasing $|V|$ reduces the number of measurements n devoted to each axis $v \in V$. This trade-off begs the question: how should one choose the number of measurement axes, $|V|$?

The reconstruction error bound in Eq. (8.30) nominally provides a straightforward answer: at a fixed total number of measurements, $N = n|V|$, the number of measurement axes should be chosen to minimize the (squared) reconstruction error $\mathcal{E}_V(\rho)^2 < \epsilon_V^2/n \propto \epsilon_V^2|V|$. We therefore consider the measurement-adjusted error scale $\beta(p)$ defined by

$$\beta(p)^2 \equiv \min_V \left\{ \epsilon_V^2 |V| : |V| = 2d - 1 + p \right\}, \quad (8.42)$$

where p is the number of “extra” measurement axes exceeding $2d - 1$. Though we cannot minimize over all suitable choices of measurement axes V to compute $\beta(p)$, we can compute an empirical upper bound $\tilde{\beta}(p) \geq \beta(p)$ by minimizing over a large number of randomly chosen V . Figure 8.3 shows the results of such empirical minimization, where we find that $\tilde{\beta}(p)$ drops substantially with p before plateauing at $p \approx d$, after which there are only minor benefits to using more measurement axes. In the interest of reducing experimental complexity as well as the runtime of our randomized tomography protocol, which grow linearly in $|V|$, we therefore conclude that this protocol should be performed with $|V| \approx 3d$ measurement axes. We provide the best measurement axes that we found for a randomized tomography protocol with $d \leq 30$ and $|V| = 3d$ in Ref. [294].

For reference, Figure 8.3 also shows the smallest measurement-adjusted error scales β_θ achievable with the method of Ref. [246], which is comparable to those achieved with our randomized protocol at $|V| \approx 3d$. The method of Ref. [246] requires choosing an angle θ , namely the polar angle of all measurement axes, and provides no prescription for making this choice. We therefore find the optimal choice of θ by minimizing the error scale β_θ over all θ (see Appendix 8.E), and show $\min \beta_\theta / \tilde{\beta}(0)$ in Figure 8.3. Empirically, we find that the optimal angle for the method of Ref. [246] is $\theta_{\text{opt}} \approx \frac{\pi}{2} \left(1 - \frac{1}{1.34d}\right)$ (see Appendix 8.E), which approaches $\pi/2$ as $d \rightarrow \infty$. However, the error scale $\beta_{\pi/2} = \infty$, reflecting the fact that full state tomography is impossible with measurement axes lying in a single plane. The method of Ref. [246] therefore requires extremely careful fine-tuning of measurement axis orientations for large spin dimensions. For this reason, we expect our randomized tomography protocol to be more robust to errors in axis orientation. We leave a detailed analysis of robustness to errors in axis orientation and the effect of these errors on state reconstruction to

future work.

As a final point, we note that any information about an unknown qudit state ρ , obtained from prior knowledge or preliminary measurement data, can be used to construct tailored or adaptive measurement protocols [258, 260, 303, 304] that are more efficient in terms of the number of measurements required to estimate ρ to a fixed precision. We leave the development of tailored and adaptive measurement protocols to future work as well.

Acknowledgements

We thank Anthony M. Polloreno and Jeremy T. Young for helpful feedback. This work is supported by the DARPA DRINQs grant, the ARO single investigator award W911NF-19-1-0210, AFOSR grant FA9550-19-1-0275, NSF grant PHY-1820885, NSF grant PHY-1734006 (JILA-PFC), and by NIST.

8.A Rotating polarization operators

Denoting the state of a spin- s particle spin projection μ onto a quantization axis by $|s\mu\rangle$, we define

$$S_z \equiv \sum_{\mu=-s}^s \mu |s\mu\rangle\langle s\mu|, \quad S_{\pm} \equiv \sum_{\mu=-s}^s \sqrt{s(s+1) - \mu(\mu \pm 1)} |s, \mu \pm 1\rangle\langle s\mu|, \quad (8.43)$$

as well as

$$S_x \equiv \frac{1}{2}(S_+ + S_-), \quad S_y \equiv -\frac{i}{2}(S_+ - S_-), \quad \mathbf{S} \equiv (S_x, S_y, S_z). \quad (8.44)$$

The spin vector \mathbf{S} generates rotations of a spin- s system in 3D space. Specifically, the operator $e^{-i\theta\mathbf{S}\cdot\hat{\mathbf{n}}}$ rotates a spin- s system by an angle θ about the unit vector $\hat{\mathbf{n}}$.

Observing that $S_z = T_{1,0}$ and $S_{\pm} \propto T_{1,\pm 1}$, we can use the operator product expansion of the polarization operators (see Appendix 8.D), the properties of Clebsch-Gordan coefficients, the properties of Wigner 6- j symbols, and a computer algebra system to simplify the commutators

$$[S_z, T_{\ell m}] = m T_{\ell m}, \quad [S_{\pm}, T_{\ell m}] = \sqrt{\ell(\ell+1) - m(m \pm 1)} T_{\ell, m \pm 1}, \quad (8.45)$$

which implies that $T_{\ell m}$ is a spherical tensor operator, whose degree ℓ is preserved under rotations generated by \mathbf{S} . Moreover, by comparing Eqs. (8.43) and (8.45) we see that the polarization operators $T_{\ell m}$ transform identically to spin- ℓ particles under the (adjoint) action of the spin operators S_z and S_{\pm} . For any triplet of angles $\boldsymbol{\omega} = (\alpha, \beta, \gamma)$, we can therefore define the rotation operator

$$R(\boldsymbol{\omega}) \equiv e^{-i\alpha S_z} e^{-i\beta S_y} e^{-i\gamma S_z}, \quad (8.46)$$

and expand rotated polarization operators as

$$T_{\boldsymbol{\omega}\ell m} \equiv R(\boldsymbol{\omega}) T_{\ell m} R(\boldsymbol{\omega})^\dagger = \sum_{n=-\ell}^{\ell} D_{mn}^{\ell}(\bar{\boldsymbol{\omega}})^* T_{\ell n}, \quad (8.47)$$

where $\bar{\boldsymbol{\omega}} = (\gamma, \beta, \alpha)$ is the reversal of $\boldsymbol{\omega}$, and

$$D_{mn}^{\ell}(\bar{\boldsymbol{\omega}}) \equiv \langle \ell m | R(\bar{\boldsymbol{\omega}}) | \ell n \rangle = (T_{\ell n} | R(\boldsymbol{\omega}) \otimes R(\boldsymbol{\omega})^* | T_{\ell m})^* = (T_{\ell m} | R(-\bar{\boldsymbol{\omega}}) \otimes R(-\bar{\boldsymbol{\omega}})^* | T_{\ell n}) \quad (8.48)$$

are matrix elements of the rotation operator $R(\boldsymbol{\omega})$ for spin- ℓ particles.

For any angle doublet $\mathbf{v} = (\alpha, \beta)$, we define $R(\mathbf{v}) \equiv R(\alpha, \beta, 0)$ and $D_{mn}^{\ell}(\mathbf{v}) = D_{mn}^{\ell}(0, \beta, \alpha)$ for shorthand. The transformation rules in Eq. (8.47) imply that we can expand the phase-space representation of $T_{\ell m}$ as

$$T_{\ell m}^{\text{PS}}(\mathbf{v}) \equiv \langle s_{\mathbf{v}} | T_{\ell m} | s_{\mathbf{v}} \rangle = \left\langle s \left| R(\mathbf{v})^\dagger T_{\ell m} R(\mathbf{v}) \right| s \right\rangle = D_{0,m}^{\ell}(\mathbf{v}) \langle s | T_{\ell,0} | s \rangle, \quad (8.49)$$

where

$$\langle s | T_{\ell,0} | s \rangle = \sqrt{\frac{2\ell+1}{2s+1}} \langle ss; \ell, 0 | ss \rangle = \sqrt{\frac{2\ell+1}{2s+\ell+1} \left(\frac{(2s)!}{(2s+\ell)!} \right) \left(\frac{(2s)!}{(2s-\ell)!} \right)}, \quad (8.50)$$

and the properties of the rotation matrix elements D_{mn}^{ℓ} imply that

$$D_{0,m}^{\ell}(\mathbf{v}) = \sqrt{\frac{4\pi}{2\ell+1}} Y_{\ell m}(\mathbf{v}), \quad (8.51)$$

so

$$T_{\ell m}^{\text{PS}}(\mathbf{v}) = \sqrt{\frac{4\pi}{2s+\ell+1} \left(\frac{(2s)!}{(2s+\ell)!} \right) \left(\frac{(2s)!}{(2s-\ell)!} \right)} Y_{\ell m}(\mathbf{v}). \quad (8.52)$$

In this way, the polarization operators are a quantum analogue of the spherical harmonics.

8.B An improved reconstruction error bound

In Section 8.4 of the main text, we provided a reconstruction error bound using the assumption of Eq. (8.20), namely that expectation values derived from spin projection measurements can be estimated up to uncorrelated errors with maximal variance ϵ^2 . This assumption is reasonable if measurement error is dominated by experimental sources of noise, and it yields a simple derivation of the reconstruction bound in Eq. (8.24). Nonetheless, there are two problems with the assumption of Eq. (8.20): (i) there is no a priori guarantee for the value of ϵ , which must be inferred from experimental outcomes, and (ii) the assumption that all measurement errors are uncorrelated is unjustified (and generally false). Here, we relax the assumption of Eq. (8.20) and derive an explicit error bound in terms of the qudit dimension d and the number of spin projection measurements made along every measurement axis.

To this end, we fix a particular set of measurement axes V , and consider performing n measurements of spin projection along every axis $\mathbf{v} \in V$, for a total of $N = |V| \times n$ measurements. Such a procedure is equivalent to making N local measurements of the N -fold product state $\rho^{\otimes N}$. For convenience, we index the tensor factors of $\rho^{\otimes N}$ by the integers (i, j) , with $i \in \{1, 2, \dots, |V|\}$ specifying a measurement axis $\mathbf{v}_i \in V$, and $j \in \{1, 2, \dots, n\}$ specifying the copy of ρ prepared for the j -th measurement spin projection along a particular axis. We then define the projectors $\Pi_{i\mu} \equiv |\mu_{\mathbf{v}_i}\rangle\langle\mu_{\mathbf{v}_i}|$ onto single-qudit states $|\mu_{\mathbf{v}_i}\rangle$ with definite spin projection μ along axis $\mathbf{v}_i \in V$, and define $\Pi_{i\mu}^j$ to be an N -qudit operator with $\Pi_{i\mu}$ on the (i, j) -th tensor factor and the identity elsewhere. We denote the experimental outcome of measuring $\Pi_{i\mu}$ in the (i, j) -th copy of ρ by $\tilde{\Pi}_{i\mu}^j \in \{0, 1\}$. In other words, $\tilde{\Pi}_{i\mu}^j$ is the “single-shot estimate” of $\Pi_{i\mu}$, with $\tilde{\Pi}_{i\mu}^j = 1$ if outcome μ was observed on the (i, j) -th experimental trial, and $\tilde{\Pi}_{i\mu}^j = 0$ otherwise. An empirical estimate of the expectation value $\langle \Pi_{i\mu} \rangle_\rho$ is provided by the fraction of times that outcome μ was observed when measuring spin projection along axis \mathbf{v}_i , that is

$$\tilde{\Pi}_{i\mu} \equiv \frac{1}{n} \sum_{j=1}^n \tilde{\Pi}_{i\mu}^j \approx \frac{1}{n} \sum_{j=1}^n \text{tr} \left(\rho^{\otimes N} \Pi_{i\mu}^j \right) = \text{tr} \left(\rho \Pi_{i\mu} \right). \quad (8.53)$$

For reasons that will be clarified shortly, it will be useful to think of $\tilde{\Pi}_{i\mu}$ as an empirical estimate

of $\langle \bar{\Pi}_{i\mu} \rangle_{\rho^{\otimes N}}$, where

$$\bar{\Pi}_{i\mu} \equiv \frac{1}{n} \sum_{j=1}^n \Pi_{i\mu}^j \quad (8.54)$$

is the average of $\Pi_{i\mu}$ applied to all copies of ρ for which spin projection is measured along the axis \mathbf{v}_i . Eq. (8.53) implies that

$$\tilde{\Pi}_{i\mu} \approx \langle \bar{\Pi}_{i\mu} \rangle_{\rho^{\otimes N}} = \langle \Pi_{i\mu} \rangle_{\rho}. \quad (8.55)$$

8.B.1 Errors in the spin-projection basis

Finite sampling error (i.e. shot noise) generally induces statistical error $\epsilon_{\mathcal{O}}$ into the empirical estimate $\tilde{\mathcal{O}}$ of an observable \mathcal{O} :

$$\epsilon_{\mathcal{O}} \equiv \tilde{\mathcal{O}} - \langle \mathcal{O} \rangle, \quad (8.56)$$

where the single brackets $\langle \cdot \rangle$ denote an expectation value with respect to the measured quantum state. On average, this statistical error will be zero, which is to say that

$$\langle \langle \epsilon_{\mathcal{O}} \rangle \rangle = \langle \langle \tilde{\mathcal{O}} - \langle \mathcal{O} \rangle \rangle \rangle = \langle \mathcal{O} - \langle \mathcal{O} \rangle \rangle = 0, \quad (8.57)$$

where the double brackets $\langle \langle \cdot \rangle \rangle$ to denote statistical averaging over experimental trials that estimate $\langle \mathcal{O} \rangle$. However, the covariance between statistical errors $\epsilon_{\mathcal{O}}$ and $\epsilon_{\mathcal{Q}}$ on the empirical estimates $\tilde{\mathcal{O}}$ and $\tilde{\mathcal{Q}}$ of observables \mathcal{O} and \mathcal{Q} is

$$\langle \langle \epsilon_{\mathcal{O}} \epsilon_{\mathcal{Q}} \rangle \rangle = \langle \langle (\tilde{\mathcal{O}} - \langle \mathcal{O} \rangle) (\tilde{\mathcal{Q}} - \langle \mathcal{Q} \rangle) \rangle \rangle = \langle (\mathcal{O} - \langle \mathcal{O} \rangle) (\mathcal{Q} - \langle \mathcal{Q} \rangle) \rangle = \langle \mathcal{O} \mathcal{Q} \rangle - \langle \mathcal{O} \rangle \langle \mathcal{Q} \rangle. \quad (8.58)$$

In the context of spin qudit tomography, we can therefore define the statistical error

$$\epsilon_{i\mu} \equiv \tilde{\Pi}_{i\mu} - \langle \Pi_{i\mu} \rangle_{\rho} = \tilde{\Pi}_{i\mu} - \langle \bar{\Pi}_{i\mu} \rangle_{\rho^{\otimes N}} \quad (8.59)$$

in the empirical estimate of $\langle \Pi_{i\mu} \rangle_{\rho}$, and use Eq. (8.54) to expand

$$\langle \langle \epsilon_{i\mu} \epsilon_{i'\mu'} \rangle \rangle = \langle \langle \bar{\Pi}_{i\mu} \bar{\Pi}_{i'\mu'} \rangle_{\rho^{\otimes N}} - \langle \bar{\Pi}_{i\mu} \rangle_{\rho^{\otimes N}} \langle \bar{\Pi}_{i'\mu'} \rangle_{\rho^{\otimes N}} \rangle \quad (8.60)$$

$$= \frac{1}{n^2} \sum_{j,j'=1}^n \left[\langle \Pi_{i\mu}^j \Pi_{i'\mu'}^{j'} \rangle_{\rho^{\otimes N}} - \langle \Pi_{i\mu}^j \rangle_{\rho^{\otimes N}} \langle \Pi_{i'\mu'}^{j'} \rangle_{\rho^{\otimes N}} \right]. \quad (8.61)$$

If $(i, j) \neq (i', j')$, then $\Pi_{i\mu}^j$ and $\Pi_{i'\mu'}^{j'}$ address different tensor factors of the product state $\rho^{\otimes N}$, so the expectation value of their product factorizes due to the fact that $\text{tr} \left[(A \otimes B) (A' \otimes B') \right] = \text{tr} (AA') \times \text{tr} (BB')$. This factorization can also be seen as a consequence of the fact that if $(i, j) \neq (i', j')$, then $\Pi_{i\mu}^j$ and $\Pi_{i'\mu'}^{j'}$ are “spatially separated” on $\rho^{\otimes N}$, which means that their expectation values cannot have quantum correlations. The terms in Eq. (8.61) with $(i, j) \neq (i', j')$ therefore vanish, so

$$\langle\langle \epsilon_{i\mu} \epsilon_{i'\mu'} \rangle\rangle = \delta_{ii'} \times \frac{1}{n^2} \sum_{j=1}^n \left[\langle \Pi_{i\mu}^j \Pi_{i'\mu'}^j \rangle_{\rho^{\otimes N}} - \langle \Pi_{i\mu}^j \rangle_{\rho^{\otimes N}} \langle \Pi_{i'\mu'}^j \rangle_{\rho^{\otimes N}} \right] \quad (8.62)$$

$$= \delta_{ii'} \times \frac{1}{n} \left[\langle \Pi_{i\mu} \Pi_{i'\mu'} \rangle_{\rho} - \langle \Pi_{i\mu} \rangle_{\rho} \langle \Pi_{i'\mu'} \rangle_{\rho} \right] \quad (8.63)$$

$$= \delta_{ii'} \times \frac{1}{n} \text{cov}_{\rho} (\Pi_{i\mu}, \Pi_{i'\mu'}), \quad (8.64)$$

where $\text{cov}_{\rho} (X, Y) \equiv \langle XY \rangle_{\rho} - \langle X \rangle_{\rho} \langle Y \rangle_{\rho}$.

8.B.2 Errors in the polarization operator basis

Rather than the statistical errors $\epsilon_{i\mu} \equiv \tilde{\Pi}_{i\mu} - \langle \Pi_{i\mu} \rangle_{\rho}$ in the estimates $\tilde{\Pi}_{i\mu}$ of the projectors $\Pi_{i\mu}$, we now consider the statistical errors $\epsilon_{i\ell} \equiv \tilde{T}_{i\ell} - \langle T_{i\ell} \rangle_{\rho}$ in the estimates $\tilde{T}_{i\ell}$ of the polarization operators $T_{i\ell} \equiv T_{v_i \ell, 0}$. We can expand the polarization operators $T_{i\ell}$ as a sum over projectors $\Pi_{i\mu}$ as

$$T_{i\ell} = \sum_{\mu} t_{\ell\mu} \Pi_{i\mu}, \quad t_{\ell\mu} \equiv \langle \mu | T_{\ell, 0} | \mu \rangle = \sqrt{\frac{2\ell + 1}{d}} \langle s\mu; \ell, 0 | s\mu \rangle, \quad (8.65)$$

and likewise $\tilde{T}_{i\ell} \equiv \sum_{\mu} t_{\ell\mu} \tilde{\Pi}_{i\mu}$. The covariance between errors in the polarization operator basis is then

$$\langle\langle \epsilon_{i\ell} \epsilon_{i'\ell'} \rangle\rangle = \sum_{\mu, \mu'} t_{\ell\mu} t_{\ell'\mu'} \langle\langle \epsilon_{i\mu} \epsilon_{i'\mu'} \rangle\rangle = \delta_{ii'} \times \frac{1}{n} \sum_{\mu, \mu'} t_{\ell\mu} t_{\ell'\mu'} \text{cov}_{\rho} (\Pi_{i\mu}, \Pi_{i'\mu'}) = \delta_{ii'} \times \frac{1}{n} \text{cov}_{\rho} (T_{i\ell}, T_{i'\ell'}), \quad (8.66)$$

where we used the fact that the covariance $\text{cov}_{\rho} (X, Y)$ is linear in both X and Y . Due to the appearance of $\delta_{ii'}$ above and the orthogonality of polarization operators $T_{i\ell}$ and $T_{i'\ell'}$ with degrees

$\ell \neq \ell'$, it turns out that only the variances $\langle\langle \epsilon_{i\ell}^2 \rangle\rangle$ will ultimately contribute to reconstruction error (see Appendix 8.B.3). We therefore seek to find an upper bound on $\langle\langle \epsilon_{i\ell}^2 \rangle\rangle$.

To this end, we define the probability $p_\mu^i \equiv \langle \Pi_{i\mu} \rangle_\rho$, collect these probabilities into the classical probability distribution $p^i = \sum_\mu p_\mu^i |\mu\rangle$, and define the vector $t_\ell \equiv \sum_\mu t_{\ell\mu} |\mu\rangle$. We then observe that

$$\langle\langle \epsilon_{i\ell}^2 \rangle\rangle = \frac{1}{n} \times \sigma_p^2(t_\ell), \quad \sigma_p^2(X) \equiv \sum_\mu p_\mu X_\mu^2 - \left(\sum_\mu p_\mu X_\mu \right)^2, \quad (8.67)$$

where $\sigma_p^2(X)$ is the weighted variance of X . This variance is maximal when p has equal weight on the largest and smallest values of X , which implies that

$$\sigma_p^2(t_\ell) \leq \Gamma_\ell^2, \quad \Gamma_\ell \equiv \frac{\max_\mu t_{\ell\mu} - \min_\mu t_{\ell\mu}}{2}, \quad \text{so} \quad \langle\langle \epsilon_{i\ell}^2 \rangle\rangle \leq \frac{1}{n} \times \Gamma_\ell^2. \quad (8.68)$$

Note that this bound on $\langle\langle \epsilon_{i\ell}^2 \rangle\rangle$ is tight, as equality is achieved by the state

$$\rho_i^* = \frac{1}{2} (\Pi_{i\mu_{\max}} + \Pi_{i\mu_{\min}}), \quad (8.69)$$

where μ_{\max} (μ_{\min}) is the index that maximizes (minimizes) $t_{\ell\mu}$.

To find an analytical bound on $\langle\langle \epsilon_{i\ell}^2 \rangle\rangle$ that is easier to interpret, we can use normalization of the polarization operators, $(T_{i\ell}|T_{i\ell}) = \sum_\mu t_{\ell\mu}^2 = 1$, and the fact that all probabilities $p_\mu \leq 1$ to bound

$$\sigma_p^2(t_\ell) \leq \sum_\mu p_\mu t_{\ell\mu}^2 \leq \sum_\mu t_{\ell\mu}^2 = 1, \quad \text{so} \quad \langle\langle \epsilon_{i\ell}^2 \rangle\rangle < \frac{1}{n}. \quad (8.70)$$

We can get a tighter bound by considering the fact that $t_{\ell\mu}^2 = t_{\ell,-\mu}^2$ due to the symmetries of the Clebsch-Gordan coefficients. It follows that if $\mu_{\max} \neq 0$ then

$$\sigma_p^2(t_\ell) \leq \sum_\mu p_\mu t_{\ell\mu}^2 \leq t_{\ell\mu_{\max}}^2 = \frac{1}{2} (t_{\ell\mu_{\max}}^2 + t_{\ell,-\mu_{\max}}^2) \stackrel{\mu_{\max} \neq 0}{\leq} \frac{1}{2} \sum_\mu t_{\ell\mu}^2 = \frac{1}{2}. \quad (8.71)$$

If $\mu_{\max} = 0$, then similarly

$$t_{\ell\mu_{\max}}^2 + 2t_{\ell\mu_{\min}}^2 = t_{\ell\mu_{\max}}^2 + t_{\ell\mu_{\min}}^2 + t_{\ell,-\mu_{\min}}^2 \stackrel{\mu_{\max}=0}{\leq} \sum_\mu t_{\ell\mu}^2 = 1, \quad \text{so} \quad |t_{\ell\mu_{\min}}| \stackrel{\mu_{\max}=0}{\leq} \sqrt{\frac{1 - t_{\ell\mu_{\max}}^2}{2}}, \quad (8.72)$$

which lets us bound

$$\Gamma_\ell = \frac{1}{2} (t_{\ell\mu_{\max}} - t_{\ell\mu_{\min}}) \leq \frac{1}{2} (t_{\ell\mu_{\max}} + |t_{\ell\mu_{\min}}|) \stackrel{\mu_{\max}=0}{\leq} \frac{1}{2} t_{\ell\mu_{\max}} + \frac{1}{2} \sqrt{\frac{1 - t_{\ell\mu_{\max}}^2}{2}} \equiv \lambda(t_{\ell\mu_{\max}}). \quad (8.73)$$

It is straightforward to show that $\lambda(x)$ is maximally $\lambda^* \equiv \max_x \lambda(x) = \sqrt{3/8}$, so

$$\Gamma_\ell^2 \stackrel{\mu_{\max}=0}{\leq} (\lambda^*)^2 = \frac{3}{8} < \frac{1}{2}. \quad (8.74)$$

Altogether, we thus find that in all cases

$$\sigma_p^2(t_\ell) \leq \frac{1}{2}, \quad \text{so} \quad \langle\langle \epsilon_{i\ell}^2 \rangle\rangle \leq \frac{1}{2n}. \quad (8.75)$$

8.B.3 Revisiting the reconstruction error bound

We now revisit the derivation of reconstruction error in Section 8.4 to make use of the bounds on variances $\langle\langle \epsilon_{i\ell}^2 \rangle\rangle$. To recap, for a set of measurement axes $V = \{\mathbf{v}\}$ and degrees $\ell \in \{0, 1, \dots, d-1\}$ we construct the measurement matrix

$$M_V \equiv \sum_{\mathbf{v}, \ell} |\mathbf{v}\ell\rangle \langle T_{\mathbf{v}\ell, 0}|, \quad (8.76)$$

which can be block diagonalized as

$$M_V U = \sum_\ell |\ell\rangle\langle\ell| \otimes M_{V\ell}, \quad U \equiv \sum_{\ell, m} |T_{\ell m}\rangle \langle \ell m|, \quad M_{V\ell} = \sum_{m, \mathbf{v}} D_{m, 0}^\ell(\mathbf{v}) |\mathbf{v}\rangle\langle m|, \quad (8.77)$$

where $D_{mn}^\ell(\mathbf{v}) \equiv \langle \ell m | R(\mathbf{v}) | \ell n \rangle$ is a (Wigner) rotation matrix element for a spin- ℓ particle. The block-diagonal structure of M_V allows us to index its singular values $M_{\ell m}^V$ and corresponding (normalized) left singular vectors $\mathbf{x}_{\ell m}^V = \sum_i x_{\ell m i}^V |\mathbf{v}_i\rangle$ by the indices (ℓ, m) , where the integer $|m| \leq \ell$. These singular vectors and values define the orthonormal operators

$$Q_{\ell m}^V \equiv \sum_i \left(q_{\ell m i}^V \right)^* T_{i\ell}, \quad q_{\ell m i}^V \equiv \frac{x_{\ell m i}^V}{M_{\ell m}^V}, \quad (8.78)$$

where $i \in \{1, 2, \dots, |V|\}$ indexes an axis $\mathbf{v}_i \in V$, with $T_{i\ell} \equiv T_{\mathbf{v}_i, \ell}$. The state ρ can be expanded in the basis of these operators as

$$\rho = \sum_{\ell, m} \left\langle Q_{\ell m}^V \right\rangle_\rho Q_{\ell m}^V, \quad (8.79)$$

and the estimates $\tilde{T}_{i\ell}$ of $\langle T_{i\ell} \rangle_\rho$ can be used to construct the following estimate $\tilde{\rho}_V$ of ρ :

$$\tilde{\rho}_V \equiv \sum_{\ell,m} \left[\sum_i q_{\ell mi}^V \tilde{T}_{i\ell} \right] Q_{\ell m}^V \approx \sum_{\ell,m} \left[\sum_i q_{\ell mi}^V \langle T_{i\ell} \rangle_\rho \right] Q_{\ell m}^V = \sum_{\ell,m} \langle Q_{\ell m}^V \rangle_\rho Q_{\ell m}^V = \rho. \quad (8.80)$$

Recalling that $\epsilon_{i\ell} \equiv \tilde{T}_{i\ell} - \langle T_{i\ell} \rangle_\rho$, we can use orthonormality of all $Q_{\ell m}^V$ to expand the mean squared distance between $\tilde{\rho}_V$ and ρ as

$$\mathcal{E}_V(\rho)^2 \equiv \left\langle \left\langle \|\tilde{\rho}_V - \rho\|^2 \right\rangle \right\rangle = \sum_{\ell,m,i,i'} \left(q_{\ell mi}^V \right)^* q_{\ell mi'}^V \langle \epsilon_{i\ell} \epsilon_{i'\ell} \rangle = \sum_{\ell,m,i} |q_{\ell mi}^V|^2 \langle \epsilon_{i\ell}^2 \rangle < \frac{1}{n} \sum_{\ell} \Gamma_{\ell}^2 \mathcal{S}_{V\ell}^2, \quad (8.81)$$

where we used the fact that $\langle \epsilon_{i\ell}^2 \rangle \leq \Gamma_{\ell}^2/n$, and

$$\sum_{m,i} |q_{\ell mi}^V|^2 = \sum_m \left(M_{\ell m}^V \right)^{-2} = \left\| M_{V\ell}^{-1} \right\|^2 = \mathcal{S}_{V\ell}^2. \quad (8.82)$$

Here $M_{V\ell}^{-1}$ is the left inverse of $M_{V\ell}$. The fact that $\langle \epsilon_{i\ell}^2 \rangle < 1/2n$ also implies that

$$\mathcal{E}_V(\rho)^2 < \frac{1}{2n} \sum_{\ell} \mathcal{S}_{V\ell}^2 = \frac{\mathcal{S}_V^2}{2n}. \quad (8.83)$$

Note that the bound in Eq. (8.81) is not tight, as the individual bounds on the variances $\langle \epsilon_{i\ell}^2 \rangle$ cannot all be achieved simultaneously. There is therefore still room for improvement on the bound in Eq. (8.30) by maximizing \mathcal{E}_V over the set of physically achievable qudit states ρ .

8.C Exact reconstruction error

Here we find exact expressions for reconstruction error, which can be used to estimate the error in a given reconstruction $\tilde{\rho}_V$ of an unknown state ρ after performing tomography. To this end, we start with Eq. (8.81) from Appendix 8.B.3 to write

$$\mathcal{E}_V(\rho)^2 = \sum_{\ell,m,i,i'} \left(q_{\ell mi}^V \right)^* q_{\ell mi'}^V \langle \epsilon_{i\ell} \epsilon_{i'\ell} \rangle = \frac{1}{n} \sum_{\ell,i} |\tilde{\mathbf{q}}_{\ell i}|^2 \text{cov}_\rho(T_{i\ell}, T_{i\ell}), \quad |\tilde{\mathbf{q}}_{\ell i}|^2 = \sum_m |q_{\ell mi}|^2, \quad (8.84)$$

where $\tilde{\mathbf{q}}_{\ell i} = \sum_m (q_{\ell mi})^* |m\rangle$, and we used the fact that $\langle \epsilon_{i\ell} \epsilon_{i'\ell} \rangle = \delta_{ii'} \times \text{cov}_\rho(T_{i\ell}, T_{i\ell})/n$. Identifying the singular value decomposition $M_{V\ell} = U_{V\ell} \Sigma_{V\ell}^{-1} U_{V\ell}^\dagger$, we then we observe that $\tilde{\mathbf{q}}_{\ell i} = \Sigma_{V\ell}^{-1} U_{V\ell}^\dagger |\mathbf{v}_i\rangle$, which allows us to simplify

$$|\tilde{\mathbf{q}}_{\ell i}|^2 = \left\langle \mathbf{v}_i \left| U_{V\ell} \Sigma_{V\ell}^{-2} U_{V\ell}^\dagger \right| \mathbf{v}_i \right\rangle = \left\langle \mathbf{v}_i \left| \left(M_{V\ell}^{-1} \right)^\dagger M_{V\ell}^{-1} \right| \mathbf{v}_i \right\rangle. \quad (8.85)$$

Using the fact that all $T_{i\ell} = T_{i\ell}^\dagger$, we can also expand

$$\text{cov}_\rho(T_{i\ell}, T_{i\ell}) = \text{cov}_\rho\left(T_{i\ell}^\dagger, T_{i\ell}\right) = \sum_{m,m'} D_{0,m}^\ell(\mathbf{v}_i) D_{0,m'}^\ell(\mathbf{v}_i)^* \text{cov}_\rho\left(T_{\ell m}^\dagger, T_{\ell m'}\right), \quad (8.86)$$

which implies that

$$\mathcal{E}_V(\rho)^2 = \frac{1}{n} \sum_{\ell,i,m,m'} D_{0,m'}^\ell(\mathbf{v}_i)^* |\tilde{\mathbf{q}}_{\ell i}|^2 D_{0,m}^\ell(\mathbf{v}_i) \text{cov}_\rho\left(T_{\ell m}^\dagger, T_{\ell m'}\right). \quad (8.87)$$

Altogether, this reconstruction error can be expressed more compactly by defining the *covariance matrix*

$$\mathcal{C}_\ell[\rho] \equiv \sum_{m,m'} \text{cov}_\rho\left(T_{\ell m}^\dagger, T_{\ell m'}\right) |m\rangle\langle m'|, \quad (8.88)$$

and the *noise matrix*

$$\mathcal{N}_{V\ell} \equiv M_{V\ell}^\dagger \text{diag}\left[\left(M_{V\ell}^{-1}\right)^\dagger M_{V\ell}^{-1}\right] M_{V\ell}, \quad (8.89)$$

where $\text{diag}[X]$ sets all off-diagonal entries of X to zero, in terms of which

$$\mathcal{E}_V(\rho)^2 = \frac{1}{n} \sum_\ell (\mathcal{N}_{V\ell} | \mathcal{C}_\ell[\rho]), \quad (8.90)$$

where $(X|Y) = \text{tr}(X^\dagger Y)$ is a trace inner product.

The result in Eq. (8.90) essentially expresses reconstruction error as a weighted sum of the covariances $\text{cov}_\rho(T_{\ell m}, T_{\ell m'})$, where the weights are given by the corresponding matrix elements of the noise matrix $\mathcal{N}_{V\ell}$. This expression is perhaps the most physically meaningful form of the reconstruction error $\mathcal{E}_V(\rho)$ that we will consider in this work, but in practice it turns out that Eq. (8.90) is inconvenient and inefficient to evaluate for any given state ρ . To find a more practical expression of reconstruction error, we use the fact that

$$\left\langle T_{\ell m}^\dagger \right\rangle_\rho = (\rho | T_{\ell m}^\dagger) = \text{tr}\left(\rho T_{\ell m}^\dagger\right) = \text{tr}\left(T_{\ell m}^\dagger \rho\right) = (T_{\ell m} | \rho), \quad (8.91)$$

to expand the covariance matrix as

$$\mathcal{C}_\ell[\rho] = \sum_{m,m'} |m\rangle\langle m'| \left[(\rho|T_{\ell m}^\dagger T_{\ell m'}) - (\rho|T_{\ell m}^\dagger)(\rho|T_{\ell m'}) \right] \quad (8.92)$$

$$= \sum_{m,m'} |m\rangle\langle m'| \left[(T_{\ell m'}^\dagger T_{\ell m}|\rho) - (T_{\ell m}|\rho)(T_{\ell m'}^\dagger|\rho) \right] \quad (8.93)$$

$$= \sum_{m,m'} |m\rangle\langle m'| \mathcal{I} \left[(T_{\ell m'} T_{\ell m}|\rho) - (T_{\ell m}|\rho)(T_{\ell m'}|\rho) \right] \quad (8.94)$$

where we define the inversion operator $\mathcal{I} \equiv \sum_m (-1)^m |-m\rangle\langle m|$. We then expand the product $T_{\ell m'} T_{\ell m}$ as

$$(T_{\ell m'} T_{\ell m}|\rho) = \sum_L g_{\ell m' m}^L (T_{L, m'+m}|\rho), \quad g_{\ell m' m}^L \equiv (T_{L, m'+m}|T_{\ell m'} T_{\ell m}) = f_{\ell m'; \ell m}^{L, m'+m}, \quad (8.95)$$

where the (real) factors $f_{\ell m'; \ell m}^{L, m'+m}$ are provided in Appendix 8.D. Substituting the covariance matrix back into Eq. (8.90) and replacing $(T_{\ell m}|\rho) \rightarrow \rho_{\ell m}$, we get

$$\mathcal{E}_V(\rho)^2 = \frac{1}{n} \left[\sum_{\ell, m} (\chi_{\ell m}^V)^* \rho_{\ell m} - \sum_{\ell, m, m'} \langle m' | \mathcal{I} \mathcal{N}_{V\ell} | m \rangle \rho_{\ell m} \rho_{\ell m'} \right], \quad (8.96)$$

where

$$\chi_{LM}^V \equiv \sum_{\ell, m, m'} \delta_{M, m'+m} \langle m' | \mathcal{I} \mathcal{N}_{V\ell} | m \rangle^* g_{\ell m' m}^L \quad (8.97)$$

$$= \sum_{\ell, m, m'} \delta_{M, -m'+m} \langle m | \mathcal{N}_{V\ell} | m' \rangle (-1)^{m'} g_{\ell, -m', m}^L \quad (8.98)$$

$$= \sum_{\ell} (\mathcal{N}_{V\ell} | \mathcal{D}_M | \mathcal{I} g_{L\ell}) \quad (8.99)$$

can be written in terms of the matrices

$$g_{L\ell} \equiv \sum_{m, m'} g_{\ell m' m}^L |m'\rangle\langle m|, \quad \mathcal{D}_M \equiv \sum_{m, m'} \delta_{M, -m'+m} |m' m\rangle\langle m' m|. \quad (8.100)$$

Here \mathcal{D}_M simply picks off the M -th diagonal of the matrix it acts on, such that $(\mathcal{N}_{V\ell} | \mathcal{D}_M | \mathcal{I} g_{L\ell})$ is an inner product of the M -th diagonal of $\mathcal{I} g_{L\ell}$ with the $(-M)$ -th diagonal of $\mathcal{N}_{V\ell}$. Defining the $(2\ell + 1)$ -component vectors

$$|\rho_\ell\rangle \equiv \sum_m \rho_{\ell m} |m\rangle, \quad |\chi_{V\ell}\rangle \equiv \sum_{\ell, m} \chi_{\ell m}^V |m\rangle, \quad (8.101)$$

we can write the expansion in Eq. (8.96) in the vectorized form

$$\mathcal{E}_V(\rho)^2 = \frac{1}{n} \sum_{\ell} [\langle \chi_{V\ell} | \rho_{\ell} \rangle - \langle \rho_{\ell} | \mathcal{N}_{V\ell} | \rho_{\ell} \rangle]. \quad (8.102)$$

8.C.1 Comments on a tight reconstruction error bound

In principle, maximizing the reconstruction error in Eq. (8.102) over all qudit states ρ would provide a tight upper bound on reconstruction error for any set of axes V . To simplify this task somewhat, we first maximize Eq. (8.102) over all ρ with $\text{tr}(\rho) = 1$: this maximum occurs at a “state” σ_V^* whose components are given by

$$|\sigma_{V\ell}^*\rangle \stackrel{\ell \neq 0}{\equiv} \frac{1}{2} \mathcal{N}_{V\ell}^{-1} |\chi_{V\ell}\rangle, \quad |\sigma_{V,0}^*\rangle \equiv \frac{1}{\sqrt{d}} |0\rangle. \quad (8.103)$$

The corresponding maximum of \mathcal{E}_V is given by

$$\mathcal{E}_V(\sigma_V^*)^2 = \frac{1}{n} \sum_{\ell > 0} \left[\frac{1}{4} \langle \chi_{V\ell} | \mathcal{N}_{V\ell}^{-1} | \chi_{V\ell} \rangle - \frac{1}{d} \text{tr}(\mathcal{N}_{V\ell}) \right], \quad (8.104)$$

where the $\text{tr}(\mathcal{N}_{V\ell})$ terms above come from simplifying the $\ell = 0$ terms of Eq. (8.102) with $\rho \rightarrow \sigma_V^*$. While $\mathcal{E}_V(\sigma_V^*)$ is a strict upper bound on $\mathcal{E}_V(\rho)$ over all ρ with $\text{tr}(\rho) = 1$, this bound turns out to be useless in practice, because σ_V^* will generally be a non-physical “state” with negative eigenvalues. To find tight bound on $\mathcal{E}_V(\rho)$ over the space of physical qudit states ρ , we also need to constrain ρ to have no negative eigenvalues. Equipped with σ_V^* and $\mathcal{E}_V(\sigma_V^*)$, we can expand

$$\mathcal{E}_V(\rho)^2 = \mathcal{E}_V(\sigma_V^*)^2 - \frac{1}{n} \|\rho - \sigma_V^*\|_V^2, \quad \|X\|_V^2 \equiv \sum_{\ell} \langle X_{\ell} | \mathcal{N}_{V\ell} | X_{\ell} \rangle, \quad (8.105)$$

where $X_{\ell} \equiv \sum_m (T_{\ell m} | X) | m \rangle$ is a vector of the degree- ℓ components of X in the polarization operator basis, and $\|X\|_V$ is a noise-weighted norm of X . Maximizing \mathcal{E}_V over all qudit states ρ thus amounts to finding the closest physical qudit state ρ to σ_V^* , with distance measured by the metric $D_V(X, Y) \equiv \|X - Y\|_V$. We leave this minimization problem to future work, and note that solving it will likely require making use of the positivity conditions derived in Ref. [295]. A loose lower bound on $\|\rho - \sigma_V^*\|_V$ can be found by minimization under the constraint $\|\rho\| \leq 1$, which may provide a tighter upper bound on $\mathcal{E}_V(\rho)$ than that in Eq. (8.30) of the main text.

8.D Polarization operator product expansion

The polarization operators on the d -dimensional Hilbert space of a spin- s system (with $s \equiv \frac{d-1}{2}$) are defined by

$$T_{\ell m} \equiv \sqrt{\frac{2\ell+1}{2s+1}} \sum_{\mu, \nu=-s}^s \langle s\mu; \ell m | s\nu \rangle |\nu\rangle\langle\mu|, \quad (8.106)$$

where $\langle s\mu; \ell m | s\nu \rangle$ is a Clebsch-Gordan coefficient that enforces $\ell \in \{0, 1, \dots, 2s\}$ and $m \in \{-\ell, -\ell+1, \dots, \ell\}$. We wish to compute the coefficients of the operator product expansion

$$T_{\ell_1 m_1} T_{\ell_2 m_2} = \sum_{L, M} f_{\ell_1 m_1; \ell_2 m_2}^{LM} T_{LM}, \quad f_{\ell_1 m_1; \ell_2 m_2}^{LM} \equiv (T_{LM} | T_{\ell_1 m_1} T_{\ell_2 m_2}), \quad (8.107)$$

which allow us to simplify the commutators in Eq. (8.45) of Appendix 8.A. Using the symmetry properties of Clebsch-Gordan coefficients, namely

$$\langle \ell_1 m_1; \ell_2 m_2 | LM \rangle = (-1)^{\ell_2+m_2} \sqrt{\frac{2L+1}{2\ell_1+1}} \langle L, -M; \ell_2 m_2 | \ell_1, -m_1 \rangle \quad (8.108)$$

$$\langle \ell_1 m_1; \ell_2 m_2 | LM \rangle = (-1)^{\ell_1+\ell_2-L} \langle \ell_1, -m_1; \ell_2, -m_2 | L, -M \rangle, \quad (8.109)$$

we can find that the polarization operators transform under conjugation as

$$T_{\ell m}^\dagger = \sqrt{\frac{2\ell+1}{2s+1}} \sum_{\mu, \nu} (-1)^m \langle s\nu; \ell, -m | s\mu \rangle |\mu\rangle\langle\nu| = (-1)^m T_{\ell, -m}, \quad (8.110)$$

which implies that

$$f_{\ell_1 m_1; \ell_2 m_2}^{LM} = (-1)^M \sqrt{\frac{(2L+1)(2\ell_1+1)(2\ell_2+1)}{(2s+1)(2s+1)(2s+1)}} \sum_{\mu, \nu, \rho} \langle s\nu; L, -M | s\mu \rangle \langle s\rho; \ell_1 m_1 | s\nu \rangle \langle s\mu; \ell_2 m_2 | s\rho \rangle. \quad (8.111)$$

Replacing Clebsch-Gordan coefficients by Wigner 3- j symbols with the identity

$$\langle \ell_1 m_1; \ell_2 m_2 | LM \rangle = (-1)^{2\ell_2} (-1)^{L-M} \sqrt{2L+1} \begin{pmatrix} L & \ell_2 & \ell_1 \\ -M & m_2 & m_1 \end{pmatrix}, \quad (8.112)$$

we can use the fact that $2\ell_2$ is always even (because ℓ_2 is always an integer) to expand

$$f_{\ell_1 m_1; \ell_2 m_2}^{LM} = (-1)^M \sqrt{(2L+1)(2\ell_1+1)(2\ell_2+1)} \times \sum_{\mu, \nu, \rho} (-1)^{3s-\mu-\nu-\rho} \begin{pmatrix} s & L & s \\ -\mu & -M & \nu \end{pmatrix} \begin{pmatrix} s & \ell_1 & s \\ -\nu & m_1 & \rho \end{pmatrix} \begin{pmatrix} s & \ell_2 & s \\ -\rho & m_2 & \mu \end{pmatrix}. \quad (8.113)$$

This sum can be simplified by the introduction of Wigner 6- j symbols, giving us

$$f_{\ell_1 m_1; \ell_2 m_2}^{LM} = (-1)^{2s+M} \sqrt{(2L+1)(2\ell_1+1)(2\ell_2+1)} \begin{pmatrix} L & \ell_1 & \ell_2 \\ M & -m_1 & -m_2 \end{pmatrix} \begin{Bmatrix} L & \ell_1 & \ell_2 \\ s & s & s \end{Bmatrix} \quad (8.114)$$

$$= (-1)^{2s+L} \sqrt{(2\ell_1+1)(2\ell_2+1)} \langle \ell_1 m_1; \ell_2 m_2 | LM \rangle \begin{Bmatrix} \ell_1 & \ell_2 & L \\ s & s & s \end{Bmatrix}. \quad (8.115)$$

8.E Optimizing the method of Newton and Young

Ref. [246] constructs an explicit protocol for spin qudit tomography, which involves measuring spin projection along $2d - 1$ axes equally spaced at a polar angle θ . However, this method does not provide any prescription for choosing θ . Here, we show the importance of making a good choice of θ , and empirically find the optimal value of θ_{opt} that minimizes the corresponding quantum error scale ϵ_θ , which controls state reconstruction error. To this end, Figure 8.4 shows the quantum error scale ϵ_θ as a function of the polar angle θ in the tomography method of Ref. [246] for a few qudit dimensions d . While a good choice of θ yields an error scale $\epsilon_\theta \approx d$ (for the dimensions shown), this error scale can increase by orders of magnitude for poor choices of θ . In turn, Figure 8.5 shows the optimal angle θ_{opt} as a function of the qudit dimension d , together with a fit to $\theta_{\text{opt}} = \frac{\pi}{2}(1 - \frac{1}{xd})$ finding $x \approx 1.34$.

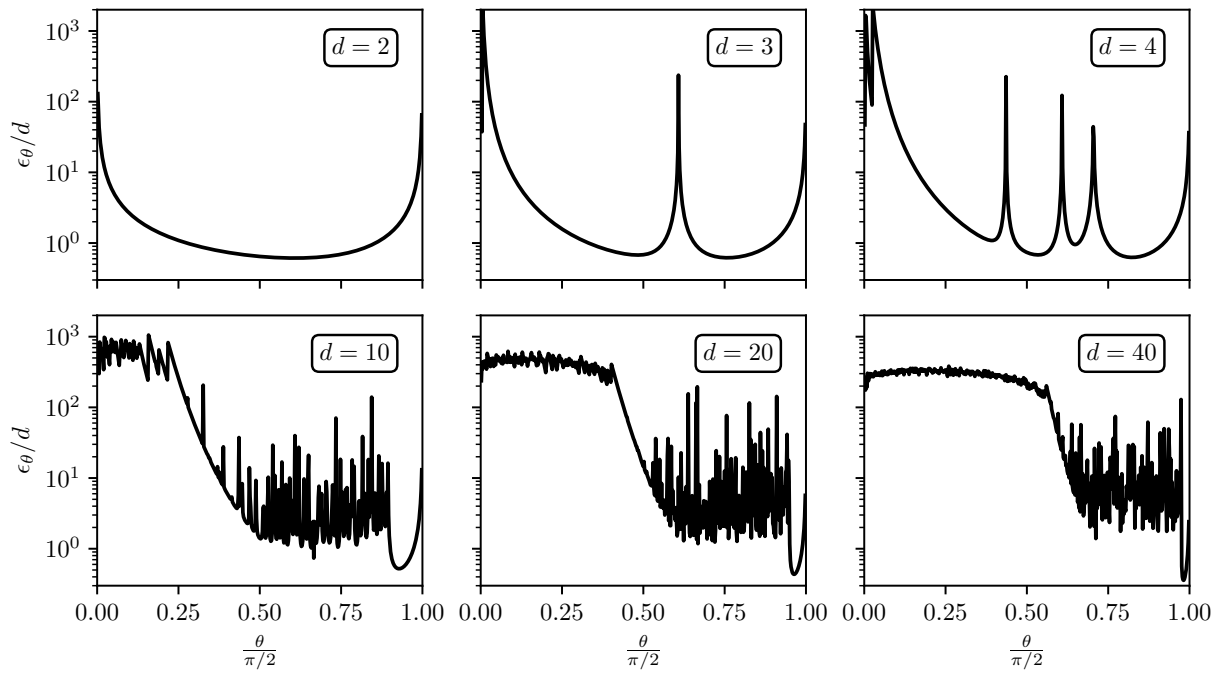


Figure 8.4: Quantum error scale ϵ_θ as a function of the polar angle θ in the tomography method of Ref. [246] for a few qudit dimensions d .

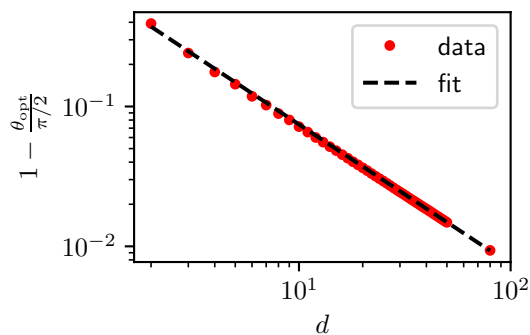


Figure 8.5: Optimum angle θ_{opt} as a function of qudit dimension d for the tomography method of Ref. [246], and a fit to $\theta_{\text{opt}} = \frac{\pi}{2}(1 - \frac{1}{xd})$ finding $x \approx 1.34$.

Chapter 9

Summary and conclusions

We examined some near- and mid-term prospects for quantum simulation and metrology with ultracold atomic systems. We began by introducing the essential players and recurring concepts in our work, including alkaline-earth(-like) atoms AEA and the properties that make them such a valuable tool for precision science. We discussed the basic physics of individual trapped atoms, the spin-orbit coupling induced by externally addressing atoms' internal states, and the $SU(n)$ -symmetric interactions that feature prominently in our later work to explore and exploit the many-body physics of AEAs. Considering the limit of frozen spatial degrees of freedom, we discussed the description of AEAs using both on-site and collective spin operators. Collective spin operators, in turn, are essential for describing the dynamics and properties of a permutationally symmetric spin system, which we used to introduce spin squeezing as the dominant strategy in this thesis for realizing a quantum advantage in state-of-the-art quantum sensors.

Equipped with this background, in Chapter 3 we took a deep dive into the emergence of multi-body interactions between AEAs. These multi-body interactions inherit the $SU(n)$ symmetry of atoms' two-body interactions, which simplifies the description of their multi-body excitation eigenstates. We then presented, in Chapter 4, a proposal to combine spin-orbit coupling and two-body interactions to prepare spin-squeezed states in an AEA-based optical lattice clock. Along the way, we developed (in Chapter 5) a new method to simulate the short-time dynamics of collective spin systems in strong-decoherence regimes that are inaccessible using other numerical methods. Borrowing some of the key ideas from Chapter 4, we considered the possibility of spin squeezing in a

broader class of spin models (called XXZ models) with interactions that decay as a power-law, which have been previously demonstrated in a variety of cold atomic, molecular, and optical platforms. We then combined elements of Chapters 3 and 4 to study a multilevel spin model with infinite-range interactions in Chapter 7. Finally, we considered the problem of precisely characterizing collective observables in the model of Chapter 7, under some realistic restrictions on experimental capabilities. We mapped this problem onto that of spin qudit tomography, which we studied closely in Chapter 8. Going forward, we hope that the techniques and theory in this thesis prove useful for the pursuit of scientific inquiry and development of quantum technologies in AEA-based platforms.

References

- [1] M. A. Perlin and A. M. Rey, “Effective multi-body $SU(N)$ -symmetric interactions of ultracold fermionic atoms on a 3D lattice”, *New Journal of Physics* **21** (2019).
- [2] P. He, M. A. Perlin, S. R. Muleady, R. J. Lewis-Swan, R. B. Hutson, J. Ye, and A. M. Rey, “Engineering spin squeezing in a 3D optical lattice with interacting spin-orbit-coupled fermions”, *Physical Review Research* **1** (2019).
- [3] M. A. Perlin and A. M. Rey, “Short-time expansion of Heisenberg operators in open collective quantum spin systems”, *Physical Review A* **101** (2020).
- [4] M. A. Perlin, C. Qu, and A. M. Rey, “Spin Squeezing with Short-Range Spin-Exchange Interactions”, *Physical Review Letters* **125** (2020).
- [5] M. A. Perlin, D. Barberena, M. Mamaev, B. Sundar, R. J. Lewis-Swan, and A. M. Rey, “Engineering infinite-range $SU(n)$ interactions with spin-orbit-coupled fermions in an optical lattice”, (2021), [arXiv:2109.11019 \[cond-mat\]](https://arxiv.org/abs/2109.11019).
- [6] M. A. Perlin, D. Barberena, and A. M. Rey, “Spin qudit tomography and state reconstruction error”, [arXiv \(2020\), arXiv:2012.06464 \[quant-ph\]](https://arxiv.org/abs/2012.06464).
- [7] A. Goban, R. B. Hutson, G. E. Marti, S. L. Campbell, M. A. Perlin, P. S. Julienne, J. P. D’Incao, A. M. Rey, and J. Ye, “Emergence of multi-body interactions in a fermionic lattice clock”, *Nature* **563** (2018).
- [8] M. Mamaev, I. Kimchi, M. A. Perlin, R. M. Nandkishore, and A. M. Rey, “Quantum Entropic Self-Localization with Ultracold Fermions”, *Physical Review Letters* **123** (2019).

- [9] M. A. Perlin, Z. H. Saleem, M. Suchara, and J. C. Osborn, “Quantum circuit cutting with maximum-likelihood tomography”, *npj Quantum Information* **7** (2021).
- [10] Z. H. Saleem, T. Tomesh, M. A. Perlin, P. Gokhale, and M. Suchara, “Quantum Divide and Conquer for Combinatorial Optimization and Distributed Computing”, (2021), [arXiv:2107.07532 \[quant-ph\]](#).
- [11] M. A. Perlin, Z.-Y. Wang, J. Casanova, and M. B. Plenio, “Noise-resilient architecture of a hybrid electron-nuclear quantum register in diamond”, *Quantum Science and Technology* **4** (2018).
- [12] J. K. Pommerenck, T. T. Simpson, M. A. Perlin, and D. Roundy, “Stochastic approximation Monte Carlo with a dynamic update factor”, *Physical Review E* **101** (2020).
- [13] A. Yambartsev, M. A. Perlin, Y. Kovchegov, N. Shulzhenko, K. L. Mine, X. Dong, and A. Morgun, “Unexpected links reflect the noise in networks”, *Biology Direct* **11** (2016).
- [14] M. M. Boyd, T. Zelevinsky, A. D. Ludlow, S. Blatt, T. Zanon-Willette, S. M. Foreman, and J. Ye, “Nuclear spin effects in optical lattice clocks”, *Physical Review A* **76** (2007).
- [15] J. A. Muniz, D. J. Young, J. R. K. Cline, and J. K. Thompson, “Cavity-QED determination of the natural linewidth of the ^{87}Sr millihertz clock transition with $30\mu\text{Hz}$ resolution”, *Physical Review Research* **3** (2021).
- [16] S. M. Brewer, J.-S. Chen, A. M. Hankin, E. R. Clements, C. W. Chou, D. J. Wineland, D. B. Hume, and D. R. Leibbrandt, “ $^{27}\text{Al}^+$ Quantum-logic clock with a systematic uncertainty below 10^{-18} ”, *Physical Review Letters* **123** (2019).
- [17] A. D. Ludlow, M. M. Boyd, J. Ye, E. Peik, and P. O. Schmidt, “Optical atomic clocks”, *Reviews of Modern Physics* **87** (2015).
- [18] M. S. Safronova, D. Budker, D. DeMille, D. F. J. Kimball, A. Derevianko, and C. W. Clark, “Search for new physics with atoms and molecules”, *Reviews of Modern Physics* **90** (2018).
- [19] A. M. Rey, “Ultracold bosonic atoms in optical lattices”, PhD thesis (Aug. 2004).

- [20] R. Coisson, G. Vernizzi, and X. Yang, “Mathieu functions and numerical solutions of the Mathieu equation”, in [2009 IEEE International Workshop on Open-source Software for Scientific Computation \(OSSC\)](#) (Sept. 2009).
- [21] H. Katori, M. Takamoto, V. G. Pal’chikov, and V. D. Ovsiannikov, “Ultrastable Optical Clock with Neutral Atoms in an Engineered Light Shift Trap”, [Physical Review Letters](#) **91** (2003).
- [22] J. Ye, H. J. Kimble, and H. Katori, “Quantum State Engineering and Precision Metrology Using State-Insensitive Light Traps”, [Science](#) **320** (2008).
- [23] R. B. Hutson, A. Goban, G. E. Marti, L. Sonderhouse, C. Sanner, and J. Ye, “Engineering Quantum States of Matter for Atomic Clocks in Shallow Optical Lattices”, [Physical Review Letters](#) **123** (2019).
- [24] A. M. Rey, G. Pupillo, C. W. Clark, and C. J. Williams, “Ultracold atoms confined in an optical lattice plus parabolic potential: A closed-form approach”, [Physical Review A](#) **72** (2005).
- [25] S. Kolkowitz, S. L. Bromley, T. Bothwell, M. L. Wall, G. E. Marti, A. P. Koller, X. Zhang, A. M. Rey, and J. Ye, “Spin-orbit-coupled fermions in an optical lattice clock”, [Nature](#) **542** (2016).
- [26] L. F. Livi, G. Cappellini, M. Diem, L. Franchi, C. Clivati, M. Frittelli, F. Levi, D. Calonico, J. Catani, M. Inguscio, and L. Fallani, “Synthetic Dimensions and Spin-Orbit Coupling with an Optical Clock Transition”, [Physical Review Letters](#) **117** (2016).
- [27] X. Zhou, J.-S. Pan, Z.-X. Liu, W. Zhang, W. Yi, G. Chen, and S. Jia, “Symmetry-Protected Topological States for Interacting Fermions in Alkaline-Earth-Like Atoms”, [Physical Review Letters](#) **119** (2017).
- [28] M. A. Cazalilla and A. M. Rey, “Ultracold fermi gases with emergent $SU(N)$ symmetry”, [Reports on Progress in Physics](#) **77** (2014).

- [29] A. V. Gorshkov, M. Hermele, V. Gurarie, C. Xu, P. S. Julienne, J. Ye, P. Zoller, E. Demler, M. D. Lukin, and A. M. Rey, “Two-orbital $SU(N)$ magnetism with ultracold alkaline-earth atoms”, *Nature Physics* **6** (2010).
- [30] R. H. Dicke, “Coherence in Spontaneous Radiation Processes”, *Physical Review* **93** (1954).
- [31] V. Giovannetti, S. Lloyd, and L. Maccone, “Quantum Metrology”, *Physical Review Letters* **96** (2006).
- [32] D. J. Wineland, J. J. Bollinger, W. M. Itano, F. L. Moore, and D. J. Heinzen, “Spin squeezing and reduced quantum noise in spectroscopy”, *Physical Review A* **46** (1992).
- [33] M. Kitagawa and M. Ueda, “Squeezed spin states”, *Physical Review A* **47** (1993).
- [34] D. J. Wineland, J. J. Bollinger, W. M. Itano, and D. J. Heinzen, “Squeezed atomic states and projection noise in spectroscopy”, *Physical Review A* **50** (1994).
- [35] J. Ma, X. Wang, C. P. Sun, and F. Nori, “Quantum spin squeezing”, *Physics Reports* **509** (2011).
- [36] A. Derevianko and H. Katori, “Colloquium: Physics of optical lattice clocks”, *Reviews of Modern Physics* **83** (2011).
- [37] H. Katori, “Optical lattice clocks and quantum metrology”, *Nature Photonics* **5** (2011).
- [38] S. G. Porsev and A. Derevianko, “Hyperfine quenching of the metastable $^3P_{0,2}$ states in divalent atoms”, *Physical Review A* **69** (2004).
- [39] R. Santra, K. V. Christ, and C. H. Greene, “Properties of metastable alkaline-earth-metal atoms calculated using an accurate effective core potential”, *Physical Review A* **69** (2004).
- [40] B. J. Bloom, T. L. Nicholson, J. R. Williams, S. L. Campbell, M. Bishof, X. Zhang, W. Zhang, S. L. Bromley, and J. Ye, “An optical lattice clock with accuracy and stability at the 10^{18} level”, *Nature* **506** (2014).

- [41] T. L. Nicholson, S. L. Campbell, R. B. Hutson, G. E. Marti, B. J. Bloom, R. L. McNally, W. Zhang, M. D. Barrett, M. S. Safronova, G. F. Strouse, W. L. Tew, and J. Ye, “Systematic evaluation of an atomic clock at 2×10^{-18} total uncertainty”, [Nature Communications](#) **6** (2015).
- [42] S. L. Campbell, R. B. Hutson, G. E. Marti, A. Goban, N. D. Oppong, R. L. McNally, L. Sonderhouse, J. M. Robinson, W. Zhang, B. J. Bloom, and J. Ye, “A Fermi-degenerate three-dimensional optical lattice clock”, [Science](#) **358** (2017).
- [43] A. J. Daley, M. M. Boyd, J. Ye, and P. Zoller, “Quantum Computing with Alkaline-Earth-Metal Atoms”, [Physical Review Letters](#) **101** (2008).
- [44] A. V. Gorshkov, A. M. Rey, A. J. Daley, M. M. Boyd, J. Ye, P. Zoller, and M. D. Lukin, “Alkaline-Earth-Metal Atoms as Few-Qubit Quantum Registers”, [Physical Review Letters](#) **102** (2009).
- [45] A. J. Daley, “Quantum Computing and Quantum Simulation with Group-II Atoms”, [Quantum Information Processing](#) **10** (2011).
- [46] A. J. Daley, J. Ye, and P. Zoller, “State-dependent lattices for quantum computing with alkaline-earth-metal atoms”, [The European Physical Journal D](#) **65** (2011).
- [47] M. D. Swallows, M. Bishof, Y. Lin, S. Blatt, M. J. Martin, A. M. Rey, and J. Ye, “Suppression of Collisional Shifts in a Strongly Interacting Lattice Clock”, [Science](#) **331** (2011).
- [48] N. D. Lemke, J. von Stecher, J. A. Sherman, A. M. Rey, C. W. Oates, and A. D. Ludlow, “ p -wave cold collisions in an optical lattice clock”, [Physical Review Letters](#) **107** (2011).
- [49] S. Taie, R. Yamazaki, S. Sugawa, and Y. Takahashi, “An SU(6) Mott insulator of an atomic Fermi gas realized by large-spin Pomeranchuk cooling”, [Nature Physics](#) **8** (2012).
- [50] M. J. Martin, M. Bishof, M. D. Swallows, X. Zhang, C. Benko, J. von-Stecher, A. V. Gorshkov, A. M. Rey, and J. Ye, “A Quantum Many-Body Spin System in an Optical Lattice Clock”, [Science](#) **341** (2013).

- [51] F. Scazza, C. Hofrichter, M. Höfer, P. C. D. Groot, I. Bloch, and S. Fölling, “Observation of two-orbital spin-exchange interactions with ultracold $SU(N)$ -symmetric fermions”, [Nature Physics](#) **10** (2014).
- [52] G. Cappellini, M. Mancini, G. Pagano, P. Lombardi, L. Livi, M. Siciliani de Cumis, P. Cancio, M. Pizzocaro, D. Calonico, F. Levi, C. Sias, J. Catani, M. Inguscio, and L. Fallani, “Direct Observation of Coherent Interorbital Spin-Exchange Dynamics”, [Physical Review Letters](#) **113** (2014).
- [53] X. Zhang, M. Bishof, S. L. Bromley, C. V. Kraus, M. S. Safronova, P. Zoller, A. M. Rey, and J. Ye, “Spectroscopic observation of $SU(N)$ -symmetric interactions in Sr orbital magnetism”, [Science](#) **345** (2014).
- [54] A. M. Rey, A. V. Gorshkov, C. V. Kraus, M. J. Martin, M. Bishof, M. D. Swallows, X. Zhang, C. Benko, J. Ye, N. D. Lemke, and A. D. Ludlow, “Probing many-body interactions in an optical lattice clock”, [Annals of Physics](#) **340** (2014).
- [55] M. A. Cazalilla, A. F. Ho, and M. Ueda, “Ultracold gases of ytterbium: ferromagnetism and Mott states in an $SU(6)$ Fermi system”, [New Journal of Physics](#) **11** (2009).
- [56] M. Hermele, V. Gurarie, and A. M. Rey, “Mott Insulators of Ultracold Fermionic Alkaline Earth Atoms: Underconstrained Magnetism and Chiral Spin Liquid”, [Physical Review Letters](#) **103** (2009).
- [57] M. Hermele and V. Gurarie, “Topological liquids and valence cluster states in two-dimensional $SU(N)$ magnets”, [Physical Review B](#) **84** (2011).
- [58] G. Chen, K. R. A. Hazzard, A. M. Rey, and M. Hermele, “Synthetic-gauge-field stabilization of the chiral-spin-liquid phase”, [Physical Review A](#) **93** (2016).
- [59] P. A. Lee, N. Nagaosa, and X.-G. Wen, “Doping a Mott insulator: Physics of high-temperature superconductivity”, [Reviews of Modern Physics](#) **78** (2006).

- [60] P. A. Lee, “From high temperature superconductivity to quantum spin liquid: progress in strong correlation physics”, [Reports on Progress in Physics](#) **71** (2008).
- [61] S.-S. Gong, W. Zhu, and D. N. Sheng, “Emergent Chiral Spin Liquid: Fractional Quantum Hall Effect in a Kagome Heisenberg Model”, [Scientific Reports](#) **4** (2014).
- [62] M. Freedman, C. Nayak, K. Shtengel, K. Walker, and Z. Wang, “A class of P,T-invariant topological phases of interacting electrons”, [Annals of Physics](#) **310** (2004).
- [63] Wiese U.-J., “Ultracold quantum gases and lattice systems: quantum simulation of lattice gauge theories”, [Annalen der Physik](#) **525** (2013).
- [64] E. Zohar, J. I. Cirac, and B. Reznik, “Quantum simulations of lattice gauge theories using ultracold atoms in optical lattices”, [Reports on Progress in Physics](#) **79** (2016).
- [65] D. Banerjee, M. Bögli, M. Dalmonte, E. Rico, P. Stebler, U.-J. Wiese, and P. Zoller, “Atomic quantum simulation of $U(N)$ and $SU(N)$ non-abelian lattice gauge theories”, [Physical Review Letters](#) **110** (2013).
- [66] E. Rico, M. Dalmonte, P. Zoller, D. Banerjee, M. Bögli, P. Stebler, and U.-J. Wiese, “SO(3) “Nuclear Physics” with ultracold Gases”, [Annals of Physics](#) **393** (2018).
- [67] C. Wu, J.-p. Hu, and S.-c. Zhang, “Exact SO(5) symmetry in the spin-3/2 fermionic system”, [Physical Review Letters](#) **91** (2003).
- [68] P. R. Johnson, D. Blume, X. Y. Yin, W. F. Flynn, and E. Tiesinga, “Effective renormalized multi-body interactions of harmonically confined ultracold neutral bosons”, [New Journal of Physics](#) **14** (2012).
- [69] X. Y. Yin, D. Blume, P. R. Johnson, and E. Tiesinga, “Universal and nonuniversal effective N -body interactions for ultracold harmonically trapped few-atom systems”, [Physical Review A](#) **90** (2014).
- [70] P. R. Johnson, E. Tiesinga, J. V. Porto, and C. J. Williams, “Effective three-body interactions of neutral bosons in optical lattices”, [New Journal of Physics](#) **11** (2009).

- [71] S. Will, T. Best, U. Schneider, L. Hackermüller, D.-S. Lühmann, and I. Bloch, “Time-resolved observation of coherent multi-body interactions in quantum phase revivals”, *Nature* **465** (2010).
- [72] M. J. Mark, E. Haller, K. Lauber, J. G. Danzl, A. J. Daley, and H.-C. Nägerl, “Precision Measurements on a Tunable Mott Insulator of Ultracold Atoms”, *Physical Review Letters* **107** (2011).
- [73] G. E. Marti, R. B. Hutson, A. Goban, S. L. Campbell, N. Poli, and J. Ye, “Imaging optical frequencies with 100 μHz precision and 1.1 μm resolution”, *Physical Review Letters* **120** (2018).
- [74] M. L. Wall and L. D. Carr, “Strongly interacting fermions in an optical lattice”, *Physical Review A* **87** (2013).
- [75] T. Busch, B.-G. Englert, K. Rzaewski, and M. Wilkens, “Two Cold Atoms in a Harmonic Trap”, *Foundations of Physics* **28** (1998).
- [76] S. Giorgini, L. P. Pitaevskii, and S. Stringari, “Theory of ultracold atomic Fermi gases”, *Reviews of Modern Physics* **80** (2008).
- [77] D. Blume and C. H. Greene, “Fermi pseudopotential approximation: Two particles under external confinement”, *Physical Review A* **65** (2002).
- [78] V. V. Flambaum, G. F. Gribakin, and C. Harabati, “Analytical calculation of cold-atom scattering”, *Physical Review A* **59** (1999).
- [79] W. Kohn, “Analytic Properties of Bloch Waves and Wannier Functions”, *Physical Review* **115** (1959).
- [80] S. Bravyi, D. P. DiVincenzo, and D. Loss, “SchriefferWolff transformation for quantum many-body systems”, *Annals of Physics* **326** (2011).
- [81] J. R. Schrieffer and P. A. Wolff, “Relation between the Anderson and Kondo Hamiltonians”, *Physical Review* **149** (1966).

- [82] C. Davis and W. M. Kahan, “Some new bounds on perturbation of subspaces”, *Bulletin of the American Mathematical Society* **75** (1969).
- [83] E. Brion, L. H. Pedersen, and K. Mølmer, “Adiabatic elimination in a lambda system”, *Journal of Physics A: Mathematical and Theoretical* **40** (2007).
- [84] D. F. James and J. Jerke, “Effective Hamiltonian theory and its applications in quantum information”, *Canadian Journal of Physics* **85** (2007).
- [85] F. Reiter and A. S. Sørensen, “Effective operator formalism for open quantum systems”, *Physical Review A* **85** (2012).
- [86] M. Sanz, E. Solano, and Í. L. Egusquiza, “Beyond Adiabatic elimination: Effective Hamiltonians and Singular Perturbation”, in **Applications + Practical Conceptualization + Mathematics = Fruitful Innovation**, Mathematics for Industry (Springer, Tokyo, 2016), pp. 127–142.
- [87] X.-P. Zang, M. Yang, F. Ozaydin, W. Song, and Z.-L. Cao, “Generating multi-atom entangled W states via light-matter interface based fusion mechanism”, *Scientific Reports* **5** (2015).
- [88] H. P. Büchler, “Microscopic Derivation of Hubbard Parameters for Cold Atomic Gases”, *Physical Review Letters* **104** (2010).
- [89] D. B. M. Dickerscheid, U. Al Khawaja, D. van Oosten, and H. T. C. Stoof, “Feshbach resonances in an optical lattice”, *Physical Review A* **71** (2005).
- [90] J. Eisert, M. Friesdorf, and C. Gogolin, “Quantum many-body systems out of equilibrium”, *Nature Physics* **11** (2015).
- [91] I. Bloch, J. Dalibard, and W. Zwerger, “Many-body physics with ultracold gases”, *Reviews of Modern Physics* **80** (2008).
- [92] C. Gross and I. Bloch, “Quantum simulations with ultracold atoms in optical lattices”, *Science* **357** (2017).

- [93] W. F. McGrew, X. Zhang, R. J. Fasano, S. A. Schäffer, K. Beloy, D. Nicolodi, R. C. Brown, N. Hinkley, G. Milani, M. Schioppo, T. H. Yoon, and A. D. Ludlow, “Atomic clock performance enabling geodesy below the centimetre level”, *Nature* **564** (2018).
- [94] M. Takamoto and H. Katori, “Spectroscopy of the 1S_0 - 3P_0 clock transition of ^{87}Sr in an optical lattice”, *Physical Review Letters* **91** (2003).
- [95] Z. W. Barber, C. W. Hoyt, C. W. Oates, L. Hollberg, A. V. Taichenachev, and V. I. Yudin, “Direct excitation of the forbidden clock transition in neutral ^{174}Yb atoms confined to an optical lattice”, *Physical Review Letters* **96** (2006).
- [96] T. Kessler, C. Hagemann, C. Grebing, T. Legero, U. Sterr, F. Riehle, M. J. Martin, L. Chen, and J. Ye, “A sub-40-mHz-linewidth laser based on a silicon single-crystal optical cavity”, *Nature Photonics* **6** (2012).
- [97] G. D. Cole, W. Zhang, M. J. Martin, J. Ye, and M. Aspelmeyer, “Tenfold reduction of Brownian noise in high-reflectivity optical coatings”, *Nature Photonics* **7** (2013).
- [98] D. G. Matei, T. Legero, S. Häfner, C. Grebing, R. Weyrich, W. Zhang, L. Sonderhouse, J. M. Robinson, J. Ye, F. Riehle, and U. Sterr, “1.5 μM lasers with sub-10 mhz linewidth”, *Physical Review Letters* **118** (2017).
- [99] W. M. Itano, J. C. Bergquist, J. J. Bollinger, J. M. Gilligan, D. J. Heinzen, F. L. Moore, M. G. Raizen, and D. J. Wineland, “Quantum projection noise: Population fluctuations in two-level systems”, *Physical Review A* **47** (1993).
- [100] C. L. Degen, F. Reinhard, and P. Cappellaro, “Quantum sensing”, *Reviews of Modern Physics* **89** (2017).
- [101] A. D. Ludlow, N. D. Lemke, J. A. Sherman, C. W. Oates, G. Quéméner, J. von Stecher, and A. M. Rey, “Cold-collision-shift cancellation and inelastic scattering in a Yb optical lattice clock”, *Physical Review A* **84** (2011).

- [102] G. K. Campbell, M. M. Boyd, J. W. Thomsen, M. J. Martin, S. Blatt, M. D. Swallows, T. L. Nicholson, T. Fortier, C. W. Oates, S. A. Diddams, N. D. Lemke, P. Naidon, P. Julienne, J. Ye, and A. D. Ludlow, “Probing Interactions Between Ultracold Fermions”, *Science* **324** (2009).
- [103] M. L. Wall, A. P. Koller, S. Li, X. Zhang, N. R. Cooper, J. Ye, and A. M. Rey, “Synthetic Spin-Orbit Coupling in an Optical Lattice Clock”, *Physical Review Letters* **116** (2016).
- [104] S. L. Bromley, S. Kolkowitz, T. Bothwell, D. Kedar, A. Safavi-Naini, M. L. Wall, C. Salomon, A. M. Rey, and J. Ye, “Dynamics of interacting fermions under spinorbit coupling in an optical lattice clock”, *Nature Physics* **14** (2018).
- [105] S. Dörscher, R. Schwarz, A. Al-Masoudi, S. Falke, U. Sterr, and C. Lisdat, “Lattice-induced photon scattering in an optical lattice clock”, *Physical Review A* **97** (2018).
- [106] E. Bauch, C. A. Hart, J. M. Schloss, M. J. Turner, J. F. Barry, P. Kehayias, S. Singh, and R. L. Walsworth, “Ultralong Dephasing Times in Solid-State Spin Ensembles via Quantum Control”, *Physical Review X* **8** (2018).
- [107] C. D. Aiello, M. Hirose, and P. Cappellaro, “Composite-pulse magnetometry with a solid-state quantum sensor”, *Nature Communications* **4** (2013).
- [108] S. C. Burd, R. Srinivas, J. J. Bollinger, A. C. Wilson, D. J. Wineland, D. Leibfried, D. H. Slichter, and D. T. C. Allcock, “Quantum amplification of mechanical oscillator motion”, *Science* **364** (2019).
- [109] L. Pezzè, A. Smerzi, M. K. Oberthaler, R. Schmied, and P. Treutlein, “Quantum metrology with nonclassical states of atomic ensembles”, *Reviews of Modern Physics* **90** (2018).
- [110] J. Aasi et al., “Enhanced sensitivity of the LIGO gravitational wave detector by using squeezed states of light”, *Nature Photonics* **7** (2013).
- [111] LIGO Scientific Collaboration and Virgo Collaboration, “GW150914: The Advanced LIGO Detectors in the Era of First Discoveries”, *Physical Review Letters* **116** (2016).

- [112] T. Esslinger, “Fermi-Hubbard Physics with Atoms in an Optical Lattice”, *Annual Review of Condensed Matter Physics* **1** (2010).
- [113] A. M. Rey, L. Jiang, M. Fleischhauer, E. Demler, and M. D. Lukin, “Many-body protected entanglement generation in interacting spin systems”, *Physical Review A* **77** (2008).
- [114] M. A. Norcia, R. J. Lewis-Swan, J. R. K. Cline, B. Zhu, A. M. Rey, and J. K. Thompson, “Cavity-mediated collective spin-exchange interactions in a strontium superradiant laser”, *Science* **361** (2018).
- [115] S. Smale, P. He, B. A. Olsen, K. G. Jackson, H. Sharum, S. Trotzky, J. Marino, A. M. Rey, and J. H. Thywissen, “Observation of a transition between dynamical phases in a quantum degenerate Fermi gas”, *Science Advances* **5** (2019).
- [116] P. T. Brown, D. Mitra, E. Guardado-Sanchez, P. SchauSS, S. S. Kondov, E. Khatami, T. Paiva, N. Trivedi, D. A. Huse, and W. S. Bakr, “Spin-imbalance in a 2D Fermi-Hubbard system”, *Science* **357** (2017).
- [117] G. Pupillo, A. M. Rey, C. J. Williams, and C. W. Clark, “Extended fermionization of 1D bosons in optical lattices”, *New Journal of Physics* **8** (2006).
- [118] Y. C. Liu, Z. F. Xu, G. R. Jin, and L. You, “Spin Squeezing: Transforming One-Axis Twisting into Two-Axis Twisting”, *Physical Review Letters* **107** (2011).
- [119] W. Huang, Y.-L. Zhang, C.-L. Zou, X.-B. Zou, and G.-C. Guo, “Two-axis spin squeezing of two-component Bose-Einstein condensates via continuous driving”, *Physical Review A* **91** (2015).
- [120] M. Foss-Feig, K. R. A. Hazzard, J. J. Bollinger, and A. M. Rey, “Nonequilibrium dynamics of arbitrary-range Ising models with decoherence: An exact analytic solution”, *Physical Review A* **87** (2013).

- [121] B. Braverman, A. Kawasaki, E. Pedrozo-Peñafiel, S. Colombo, C. Shu, Z. Li, E. Mendez, M. Yamoah, L. Salvi, D. Akamatsu, Y. Xiao, and V. Vuleti, “Near-Unitary Spin Squeezing in Yb 171”, *Physical Review Letters* **122** (2019).
- [122] M. Bishof, M. J. Martin, M. D. Swallows, C. Benko, Y. Lin, G. Quéméner, A. M. Rey, and J. Ye, “Inelastic collisions and density-dependent excitation suppression in a ^{87}Sr optical lattice clock”, *Physical Review A* **84** (2011).
- [123] M. Mancini, G. Pagano, G. Cappellini, L. Livi, M. Rider, J. Catani, C. Sias, P. Zoller, M. Inguscio, M. Dalmonte, and L. Fallani, “Observation of chiral edge states with neutral fermions in synthetic Hall ribbons”, *Science* **349** (2015).
- [124] H. Y. Carr and E. M. Purcell, “Effects of Diffusion on Free Precession in Nuclear Magnetic Resonance Experiments”, *Physical Review* **94** (1954).
- [125] S. Meiboom and D. Gill, “Modified Spin-Echo Method for Measuring Nuclear Relaxation Times”, *Review of Scientific Instruments* **29** (1958).
- [126] A. A. Maudsley, “Modified Carr-Purcell-Meiboom-Gill sequence for NMR fourier imaging applications”, *Journal of Magnetic Resonance* (1969) **69** (1986).
- [127] T. Gullion, D. B. Baker, and M. S. Conradi, “New, compensated Carr-Purcell sequences”, *Journal of Magnetic Resonance* (1969) **89** (1990).
- [128] A. Polkovnikov, “Phase space representation of quantum dynamics”, *Annals of Physics* **325** (2010).
- [129] J. Schachenmayer, A. Pikovski, and A. M. Rey, “Many-Body Quantum Spin Dynamics with Monte Carlo Trajectories on a Discrete Phase Space”, *Physical Review X* **5** (2015).
- [130] H. J. Lipkin, N. Meshkov, and A. J. Glick, “Validity of many-body approximation methods for a solvable model: (I). Exact solutions and perturbation theory”, *Nuclear Physics* **62** (1965).

- [131] N. Meshkov, A. J. Glick, and H. J. Lipkin, “Validity of many-body approximation methods for a solvable model: (II). Linearization procedures”, *Nuclear Physics* **62** (1965).
- [132] A. J. Glick, H. J. Lipkin, and N. Meshkov, “Validity of many-body approximation methods for a solvable model: (III). Diagram summations”, *Nuclear Physics* **62** (1965).
- [133] T. Takano, M. Fuyama, R. Namiki, and Y. Takahashi, “Spin Squeezing of a Cold Atomic Ensemble with the Nuclear Spin of One-Half”, *Physical Review Letters* **102** (2009).
- [134] J. Appel, P. J. Windpassinger, D. Oblak, U. B. Hoff, N. Kjærgaard, and E. S. Polzik, “Mesoscopic atomic entanglement for precision measurements beyond the standard quantum limit”, *Proceedings of the National Academy of Sciences* **106** (2009).
- [135] J. Klinder, H. Keßler, M. Wolke, L. Mathey, and A. Hemmerich, “Dynamical phase transition in the open Dicke model”, *Proceedings of the National Academy of Sciences* **112** (2015).
- [136] J. Estève, C. Gross, A. Weller, S. Giovanazzi, and M. K. Oberthaler, “Squeezing and entanglement in a BoseEinstein condensate”, *Nature* **455** (2008).
- [137] M. F. Riedel, P. Böhi, Y. Li, T. W. Hänsch, A. Sinatra, and P. Treutlein, “Atom-chip-based generation of entanglement for quantum metrology”, *Nature* **464** (2010).
- [138] C. Gross, T. Zibold, E. Nicklas, J. Estève, and M. K. Oberthaler, “Nonlinear atom interferometer surpasses classical precision limit”, *Nature* **464** (2010).
- [139] J. G. Bohnet, B. C. Sawyer, J. W. Britton, M. L. Wall, A. M. Rey, M. Foss-Feig, and J. J. Bollinger, “Quantum spin dynamics and entanglement generation with hundreds of trapped ions”, *Science* **352** (2016).
- [140] M. H. Schleier-Smith, I. D. Leroux, and V. Vuleti, “States of an Ensemble of Two-Level Atoms with Reduced Quantum Uncertainty”, *Physical Review Letters* **104** (2010).
- [141] Z. Chen, J. G. Bohnet, S. R. Sankar, J. Dai, and J. K. Thompson, “Conditional Spin Squeezing of a Large Ensemble via the Vacuum Rabi Splitting”, *Physical Review Letters* **106** (2011).

- [142] K. Baumann, C. Guerlin, F. Brennecke, and T. Esslinger, “Dicke quantum phase transition with a superfluid gas in an optical cavity”, *Nature* **464** (2010).
- [143] I. D. Leroux, M. H. Schleier-Smith, and V. Vuleti, “Implementation of Cavity Squeezing of a Collective Atomic Spin”, *Physical Review Letters* **104** (2010).
- [144] J. G. Bohnet, K. C. Cox, M. A. Norcia, J. M. Weiner, Z. Chen, and J. K. Thompson, “Reduced spin measurement back-action for a phase sensitivity ten times beyond the standard quantum limit”, *Nature Photonics* **8** (2014).
- [145] K. C. Cox, G. P. Greve, J. M. Weiner, and J. K. Thompson, “Deterministic Squeezed States with Collective Measurements and Feedback”, *Physical Review Letters* **116** (2016).
- [146] O. Hosten, N. J. Engelsen, R. Krishnakumar, and M. A. Kasevich, “Measurement noise 100 times lower than the quantum-projection limit using entangled atoms”, *Nature* **529** (2016).
- [147] O. Hosten, R. Krishnakumar, N. J. Engelsen, and M. A. Kasevich, “Quantum phase magnification”, *Science* **352** (2016).
- [148] H. Ritsch, P. Domokos, F. Brennecke, and T. Esslinger, “Cold atoms in cavity-generated dynamical optical potentials”, *Reviews of Modern Physics* **85** (2013).
- [149] J. I. Latorre, R. Orús, E. Rico, and J. Vidal, “Entanglement entropy in the Lipkin-Meshkov-Glick model”, *Physical Review A* **71** (2005).
- [150] M. A. Alcalde, A. L. L. de Lemos, and N. F. Svaiter, “Functional methods in the generalized Dicke model”, *Journal of Physics A: Mathematical and Theoretical* **40** (2007).
- [151] C. Wang, Y.-Y. Zhang, and Q.-H. Chen, “Quantum correlations in collective spin systems”, *Physical Review A* **85** (2012).
- [152] N. Majd, J. Payamara, and F. Daliri, “LMG model: Markovian evolution of classical and quantum correlations under decoherence”, *The European Physical Journal B* **87** (2014).

- [153] D. F. Walls, P. D. Drummond, S. S. Hassan, and H. J. Carmichael, “Non-Equilibrium Phase Transitions in Cooperative Atomic Systems”, *Progress of Theoretical Physics Supplement* **64** (1978).
- [154] S. Morrison and A. S. Parkins, “Dynamical Quantum Phase Transitions in the Dissipative Lipkin-Meshkov-Glick Model with Proposed Realization in Optical Cavity QED”, *Physical Review Letters* **100** (2008).
- [155] S. Morrison and A. S. Parkins, “Dissipation-driven quantum phase transitions in collective spin systems”, *Journal of Physics B: Atomic, Molecular and Optical Physics* **41** (2008).
- [156] S. Morrison and A. S. Parkins, “Collective spin systems in dispersive optical cavity QED: Quantum phase transitions and entanglement”, *Physical Review A* **77** (2008).
- [157] E. M. Kessler, G. Giedke, A. Imamoglu, S. F. Yelin, M. D. Lukin, and J. I. Cirac, “Dissipative phase transition in a central spin system”, *Physical Review A* **86** (2012).
- [158] A. B. Bhattacharjee, “Non-equilibrium dynamical phases of the two-atom Dicke model”, *Physics Letters A* **378** (2014).
- [159] Z. Zhiqiang, C. H. Lee, R. Kumar, K. J. Arnold, S. J. Masson, A. S. Parkins, and M. D. Barrett, “Nonequilibrium phase transition in a spin-1 Dicke model”, *Optica* **4** (2017).
- [160] J. Lang, B. Frank, and J. C. Halimeh, “Concurrence of dynamical phase transitions at finite temperature in the fully connected transverse-field Ising model”, *Physical Review B* **97** (2018).
- [161] Z.-R. Zhong, “A simplified scheme for realizing multi-atom NOON state”, *Optics Communications* **283** (2010).
- [162] M. H. Schleier-Smith, I. D. Leroux, and V. Vuleti, “Squeezing the collective spin of a dilute atomic ensemble by cavity feedback”, *Physical Review A* **81** (2010).
- [163] W. Muessel, H. Strobel, D. Linnemann, T. Zibold, B. Juliá-Díaz, and M. K. Oberthaler, “Twist-and-turn spin squeezing in Bose-Einstein condensates”, *Physical Review A* **92** (2015).

- [164] J. Huang, X. Qin, H. Zhong, Y. Ke, and C. Lee, “Quantum metrology with spin cat states under dissipation”, *Scientific Reports* **5** (2015).
- [165] J. Hu, W. Chen, Z. Vendeiro, A. Urvoy, B. Braverman, and V. Vuleti, “Vacuum spin squeezing”, *Physical Review A* **96** (2017).
- [166] S. S. Mirkhalaf, S. P. Nolan, and S. A. Haine, “Robustifying twist-and-turn entanglement with interaction-based readout”, *Physical Review A* **97** (2018).
- [167] R. J. Lewis-Swan, M. A. Norcia, J. R. K. Cline, J. K. Thompson, and A. M. Rey, “Robust Spin Squeezing via Photon-Mediated Interactions on an Optical Clock Transition”, *Physical Review Letters* **121** (2018).
- [168] G. S. Agarwal, R. R. Puri, and R. P. Singh, “Atomic Schrödinger cat states”, *Physical Review A* **56** (1997).
- [169] H. W. Lau, Z. Dutton, T. Wang, and C. Simon, “Proposal for the Creation and Optical Detection of Spin Cat States in Bose-Einstein Condensates”, *Physical Review Letters* **113** (2014).
- [170] M. Zwiernik, C. A. Pérez-Delgado, and P. Kok, “General Optimality of the Heisenberg Limit for Quantum Metrology”, *Physical Review Letters* **105** (2010).
- [171] J. Hu, W. Chen, Z. Vendeiro, H. Zhang, and V. Vuleti, “Entangled collective-spin states of atomic ensembles under nonuniform atom-light interaction”, *Physical Review A* **92** (2015).
- [172] S. Hartmann, “Generalized Dicke States”, *Quantum Information and Computation* **16** (2016).
- [173] M. Xu, D. A. Tieri, and M. J. Holland, “Simulating open quantum systems by applying SU(4) to quantum master equations”, *Physical Review A* **87** (2013).
- [174] M. B. Plenio and P. L. Knight, “The quantum-jump approach to dissipative dynamics in quantum optics”, *Reviews of Modern Physics* **70** (1998).
- [175] Y. Zhang, Y.-X. Zhang, and K. Mølmer, “Monte-Carlo simulations of superradiant lasing”, *New Journal of Physics* **20** (2018).

- [176] D. Meiser and M. J. Holland, “Steady-state superradiance with alkaline-earth-metal atoms”, *Physical Review A* **81** (2010).
- [177] H. Mori, “A Continued-Fraction Representation of the Time-Correlation Functions”, *Progress of Theoretical Physics* **34** (1965).
- [178] J. F. Annett, W. Matthew, C. Foulkes, and R. Haydock, “A recursive solution of Heisenberg’s equation and its interpretation”, *Journal of Physics: Condensed Matter* **6** (1994).
- [179] A. Micheli, D. Jaksch, J. I. Cirac, and P. Zoller, “Many-particle entanglement in two-component Bose-Einstein condensates”, *Physical Review A* **67** (2003).
- [180] G. Sorelli, M. Gessner, A. Smerzi, and L. Pezzè, “Fast and optimal generation of entanglement in bosonic Josephson junctions”, *Physical Review A* **99** (2019).
- [181] P. D. Blocher and K. Mølmer, “Quantum regression theorem for out-of-time-ordered correlation functions”, *Physical Review A* **99** (2019).
- [182] K. Tucker, B. Zhu, R. J. Lewis-Swan, J. Marino, F. Jimenez, J. G. Restrepo, and A. M. Rey, “Shattered time: can a dissipative time crystal survive many-body correlations?”, *New Journal of Physics* **20** (2018).
- [183] J. Maldacena, S. H. Shenker, and D. Stanford, “A bound on chaos”, *Journal of High Energy Physics* **2016** (2016).
- [184] B. Swingle, “Unscrambling the physics of out-of-time-order correlators”, *Nature Physics* **14** (2018).
- [185] I. García-Mata, M. Saraceno, R. A. Jalabert, A. J. Roncaglia, and D. A. Wisniacki, “Chaos Signatures in the Short and Long Time Behavior of the Out-of-Time Ordered Correlator”, *Physical Review Letters* **121** (2018).
- [186] A. Rivas and S. F. Huelga, “Time Evolution in Open Quantum Systems”, in **Open Quantum Systems: An Introduction**, edited by A. Rivas and S. F. Huelga, SpringerBriefs in Physics (Springer Berlin Heidelberg, Berlin, Heidelberg, 2012), pp. 19–31.

- [187] V. Giovannetti, S. Lloyd, and L. Maccone, “Advances in quantum metrology”, *Nature Photonics* **5** (2011).
- [188] G. Tóth and I. Apellaniz, “Quantum metrology from a quantum information science perspective”, *Journal of Physics A: Mathematical and Theoretical* **47** (2014).
- [189] M. Szczykulska, T. Baumgratz, and A. Datta, “Multi-parameter quantum metrology”, *Advances in Physics: X* **1** (2016).
- [190] T. Zibold, E. Nicklas, C. Gross, and M. K. Oberthaler, “Classical Bifurcation at the Transition from Rabi to Josephson Dynamics”, *Physical Review Letters* **105** (2010).
- [191] J. W. Britton, B. C. Sawyer, A. C. Keith, C.-C. J. Wang, J. K. Freericks, H. Uys, M. J. Biercuk, and J. J. Bollinger, “Engineered two-dimensional Ising interactions in a trapped-ion quantum simulator with hundreds of spins”, *Nature* **484** (2012).
- [192] M. Gabbrielli, L. Lepori, and L. Pezzè, “Multipartite-entanglement tomography of a quantum simulator”, *New Journal of Physics* **21** (2019).
- [193] R. M. Kroeze, Y. Guo, V. D. Vaidya, J. Keeling, and B. L. Lev, “Spinor Self-Ordering of a Quantum Gas in a Cavity”, *Physical Review Letters* **121** (2018).
- [194] E. J. Davis, G. Bentsen, L. Homeier, T. Li, and M. H. Schleier-Smith, “Photon-Mediated Spin-Exchange Dynamics of Spin-1 Atoms”, *Physical Review Letters* **122** (2019).
- [195] M. Foss-Feig, Z.-X. Gong, A. V. Gorshkov, and C. W. Clark, “Entanglement and spin-squeezing without infinite-range interactions”, (2016), [arXiv:1612.07805 \[cond-mat\]](https://arxiv.org/abs/1612.07805).
- [196] P. Cappellaro and M. D. Lukin, “Quantum correlation in disordered spin systems: Applications to magnetic sensing”, *Physical Review A* **80** (2009).
- [197] M. P. Kwasigroch and N. R. Cooper, “Bose-Einstein condensation and many-body localization of rotational excitations of polar molecules following a microwave pulse”, *Physical Review A* **90** (2014).

- [198] M. P. Kwasigroch and N. R. Cooper, “Synchronization transition in dipole-coupled two-level systems with positional disorder”, *Physical Review A* **96** (2017).
- [199] E. J. Davis, A. Periwal, E. S. Cooper, G. Bentsen, S. J. Evered, K. Van Kirk, and M. H. Schleier-Smith, “Protecting Spin Coherence in a Tunable Heisenberg Model”, *Physical Review Letters* **125** (2020).
- [200] I. Frérot, P. Naldesi, and T. Roscilde, “Entanglement and fluctuations in the XXZ model with power-law interactions”, *Physical Review B* **95** (2017).
- [201] C. S. Adams, J. D. Pritchard, and J. P. Shaffer, “Rydberg atom quantum technologies”, *Journal of Physics B: Atomic, Molecular and Optical Physics* **53** (2019).
- [202] A. Browaeys and T. Lahaye, “Many-body physics with individually controlled Rydberg atoms”, *Nature Physics* **16** (2020).
- [203] J. L. Bohn, A. M. Rey, and J. Ye, “Cold molecules: Progress in quantum engineering of chemistry and quantum matter”, *Science* **357** (2017).
- [204] S. A. Moses, J. P. Covey, M. T. Miecnikowski, D. S. Jin, and J. Ye, “New frontiers for quantum gases of polar molecules”, *Nature Physics* **13** (2017).
- [205] S. Lepoutre, J. Schachenmayer, L. Gabardos, B. Zhu, B. Naylor, E. Maréchal, O. Gorceix, A. M. Rey, L. Vernac, and B. Laburthe-Tolra, “Out-of-equilibrium quantum magnetism and thermalization in a spin-3 many-body dipolar lattice system”, *Nature Communications* **10** (2019).
- [206] A. Patscheider, B. Zhu, L. Chomaz, D. Petter, S. Baier, A.-M. Rey, F. Ferlaino, and M. J. Mark, “Controlling dipolar exchange interactions in a dense three-dimensional array of large-spin fermions”, *Physical Review Research* **2** (2020).
- [207] C. D. Bruzewicz, J. Chiaverini, R. McConnell, and J. M. Sage, “Trapped-ion quantum computing: Progress and challenges”, *Applied Physics Reviews* **6** (2019).

- [208] A. S. Sørensen and K. Mølmer, “Entanglement and Extreme Spin Squeezing”, *Physical Review Letters* **86** (2001).
- [209] M. van den Worm, B. C. Sawyer, J. J. Bollinger, and M. Kastner, “Relaxation timescales and decay of correlations in a long-range interacting quantum simulator”, *New Journal of Physics* **15** (2013).
- [210] J. Schachenmayer, A. Pikovski, and A. M. Rey, “Dynamics of correlations in two-dimensional quantum spin models with long-range interactions: a phase-space Monte-Carlo study”, *New Journal of Physics* **17** (2015).
- [211] L.-M. Duan, E. Demler, and M. D. Lukin, “Controlling Spin Exchange Interactions of Ultracold Atoms in Optical Lattices”, *Physical Review Letters* **91** (2003).
- [212] Y.-A. Chen, S. Nascimbène, M. Aidelsburger, M. Atala, S. Trotzky, and I. Bloch, “Controlling Correlated Tunneling and Superexchange Interactions with ac-Driven Optical Lattices”, *Physical Review Letters* **107** (2011).
- [213] A. Signoles, T. Franz, R. Ferracini Alves, M. Gärttner, S. Whitlock, G. Zürn, and M. Weidemüller, “Glassy Dynamics in a Disordered Heisenberg Quantum Spin System”, *Physical Review X* **11** (2021).
- [214] A. V. Gorshkov, S. R. Manmana, G. Chen, J. Ye, E. Demler, M. D. Lukin, and A. M. Rey, “Tunable Superfluidity and Quantum Magnetism with Ultracold Polar Molecules”, *Physical Review Letters* **107** (2011).
- [215] U. Schollwöck, J. Richter, D. J. J. Farnell, and R. F. Bishop, eds., **Quantum Magnetism**, Vol. 645, Lecture Notes in Physics (Springer Berlin Heidelberg, Berlin, Heidelberg, 2004).
- [216] P. Bruno, “Absence of Spontaneous Magnetic Order at Nonzero Temperature in One- and Two-Dimensional Heisenberg and XY Systems with Long-Range Interactions”, *Physical Review Letters* **87** (2001).

- [217] K. R. A. Hazzard, S. R. Manmana, M. Foss-Feig, and A. M. Rey, “Far-from-Equilibrium Quantum Magnetism with Ultracold Polar Molecules”, *Physical Review Letters* **110** (2013).
- [218] J. Choi, H. Zhou, H. S. Knowles, R. Landig, S. Choi, and M. D. Lukin, “Robust Dynamic Hamiltonian Engineering of Many-Body Spin Systems”, *Physical Review X* **10** (2020).
- [219] H. Zhou, J. Choi, S. Choi, R. Landig, A. M. Douglas, J. Isoya, F. Jelezko, S. Onoda, H. Sumiya, P. Cappellaro, H. S. Knowles, H. Park, and M. D. Lukin, “Quantum Metrology with Strongly Interacting Spin Systems”, *Physical Review X* **10** (2020).
- [220] S. R. Muleady, M. Yang, S. R. White, A. M. Rey, et al., **In preparation**, 2021.
- [221] J. Maldacena, “The Large- N Limit of Superconformal Field Theories and Supergravity”, *International Journal of Theoretical Physics* **38** (1999).
- [222] S. Ryu and T. Takayanagi, “Holographic Derivation of Entanglement Entropy from the anti-de Sitter Space/Conformal Field Theory Correspondence”, *Physical Review Letters* **96** (2006).
- [223] N. Read and S. Sachdev, “Valence-bond and spin-Peierls ground states of low-dimensional quantum antiferromagnets”, *Physical Review Letters* **62** (1989).
- [224] D. S. Rokhsar, “Quadratic quantum antiferromagnets in the fermionic large- N limit”, *Physical Review B* **42** (1990).
- [225] R. K. Kaul and A. W. Sandvik, “Lattice model for the $SU(N)$ Néel to valence-bond solid quantum phase transition at large N ”, *Physical Review Letters* **108** (2012).
- [226] P. Nataf, M. Lajkó, A. Wietek, K. Penc, F. Mila, and A. M. Läuchli, “Chiral spin liquids in triangular-lattice $SU(N)$ fermionic mott insulators with artificial gauge fields”, *Physical Review Letters* **117** (2016).
- [227] C. Nayak, S. H. Simon, A. Stern, M. Freedman, and S. Das Sarma, “Non-Abelian anyons and topological quantum computation”, *Reviews of Modern Physics* **80** (2008).

- [228] P. Nataf and F. Mila, “Exact diagonalization of heisenberg $SU(N)$ models”, *Physical Review Letters* **113** (2014).
- [229] P. Nataf and F. Mila, “Exact diagonalization of heisenberg $SU(N)$ chains in the fully symmetric and antisymmetric representations”, *Physical Review B* **93** (2016).
- [230] S. Sachdev and J. Ye, “Gapless spin-fluid ground state in a random quantum Heisenberg magnet”, *Physical Review Letters* **70** (1993).
- [231] K. R. A. Hazzard, V. Gurarie, M. Hermele, and A. M. Rey, “High-temperature properties of fermionic alkaline-earth-metal atoms in optical lattices”, *Physical Review A* **85** (2012).
- [232] L. Bonnes, K. R. A. Hazzard, S. R. Manmana, A. M. Rey, and S. Wessel, “Adiabatic loading of one-dimensional $SU(N)$ alkaline-earth-atom fermions in optical lattices”, *Physical Review Letters* **109** (2012).
- [233] S. Stellmer, F. Schreck, and T. C. Killian, “Degenerate quantum gases of strontium”, in *Annual Review of Cold Atoms and Molecules*, Vol. Volume 2, Annual Review of Cold Atoms and Molecules (WORLD SCIENTIFIC, Dec. 2013), pp. 1–80.
- [234] S.-K. Yip, B.-L. Huang, and J.-S. Kao, “Theory of $SU(N)$ fermi liquids”, *Physical Review A* **89** (2014).
- [235] G. Pagano, M. Mancini, G. Cappellini, P. Lombardi, F. Schäfer, H. Hu, X.-J. Liu, J. Catani, C. Sias, M. Inguscio, and L. Fallani, “A one-dimensional liquid of fermions with tunable spin”, *Nature Physics* **10** (2014).
- [236] S. Choudhury, K. R. Islam, Y. Hou, J. A. Aman, T. C. Killian, and K. R. A. Hazzard, “Collective modes of ultracold fermionic alkaline-earth-metal gases with $su(N)$ symmetry”, *Physical Review A* **101** (2020).
- [237] B. Song, Y. Yan, C. He, Z. Ren, Q. Zhou, and G.-B. Jo, “Evidence for bosonization in a three-dimensional gas of $SU(N)$ fermions”, *Physical Review X* **10** (2020).

- [238] L. Sonderhouse, C. Sanner, R. B. Hutson, A. Goban, T. Bilitewski, L. Yan, W. R. Milner, A. M. Rey, and J. Ye, “Thermodynamics of a deeply degenerate $SU(N)$ -symmetric fermi gas”, *Nature Physics* **16** (2020).
- [239] C. Hofrichter, L. Riegger, F. Scazza, M. Höfer, D. R. Fernandes, I. Bloch, and S. Fölling, “Direct probing of the Mott crossover in the $SU(N)$ Fermi-Hubbard model”, *Physical Review X* **6** (2016).
- [240] S. Taie, E. Ibarra-García-Padilla, N. Nishizawa, Y. Takasu, Y. Kuno, H.-T. Wei, R. T. Scalettar, K. R. A. Hazzard, and Y. Takahashi, “Observation of antiferromagnetic correlations in an ultracold $SU(N)$ Hubbard model”, (2020), [arXiv:2010.07730 \[quant-ph\]](https://arxiv.org/abs/2010.07730).
- [241] L. Messio and F. Mila, “Entropy dependence of correlations in one-dimensional $SU(N)$ antiferromagnets”, *Physical Review Letters* **109** (2012).
- [242] M. E. Beverland, G. Alagic, M. J. Martin, A. P. Koller, A. M. Rey, and A. V. Gorshkov, “Realizing exactly solvable $SU(N)$ magnets with thermal atoms”, *Physical Review A* **93** (2016).
- [243] R. J. Lewis-Swan, D. Barberena, J. R. K. Cline, D. J. Young, J. K. Thompson, and A. M. Rey, “Cavity-QED Quantum Simulator of Dynamical Phases of a Bardeen-Cooper-Schrieffer Superconductor”, *Physical Review Letters* **126** (2021).
- [244] J. P. Dowling, G. S. Agarwal, and W. P. Schleich, “Wigner distribution of a general angular-momentum state: Applications to a collection of two-level atoms”, *Physical Review A* **49** (1994).
- [245] F. Li, C. Braun, and A. Garg, “The Weyl-Wigner-Moyal formalism for spin”, *EPL (Europhysics Letters)* **102** (2013).
- [246] R. G. Newton and B.-l. Young, “Measurability of the spin density matrix”, *Annals of Physics* **49** (1968).

- [247] B. E. Anderson, H. Sosa-Martinez, C. A. Riofrío, I. H. Deutsch, and P. S. Jessen, “Accurate and Robust Unitary Transformations of a High-Dimensional Quantum System”, *Physical Review Letters* **114** (2015).
- [248] D. Lucarelli, “Quantum optimal control via gradient ascent in function space and the time-bandwidth quantum speed limit”, *Physical Review A* **97** (2018).
- [249] E. A. Yuzbashyan, B. L. Altshuler, V. B. Kuznetsov, and V. Z. Enolskii, “Nonequilibrium cooper pairing in the nonadiabatic regime”, *Physical Review B* **72** (2005).
- [250] E. A. Yuzbashyan and M. Dzero, “Dynamical Vanishing of the Order Parameter in a Fermionic Condensate”, *Physical Review Letters* **96** (2006).
- [251] E. A. Yuzbashyan, O. Tsypliyatyev, and B. L. Altshuler, “Relaxation and Persistent Oscillations of the Order Parameter in Fermionic Condensates”, *Physical Review Letters* **96** (2006).
- [252] E. A. Yuzbashyan, M. Dzero, V. Gurarie, and M. S. Foster, “Quantum quench phase diagrams of an *s*-wave BCS-BEC condensate”, *Physical Review A* **91** (2015).
- [253] G. Bentsen, I.-D. Potirniche, V. B. Bulchandani, T. Scaffidi, X. Cao, X.-L. Qi, M. Schleier-Smith, and E. Altman, “Integrable and Chaotic Dynamics of Spins Coupled to an Optical Cavity”, *Physical Review X* **9** (2019).
- [254] T. Opatrny, D.-G. Welsch, and W. Vogel, “Least-squares inversion for density-matrix reconstruction”, *Physical Review A* **56** (1997).
- [255] B. Qi, Z. Hou, L. Li, D. Dong, G. Xiang, and G. Guo, “Quantum State Tomography via Linear Regression Estimation”, *Scientific Reports* **3** (2013).
- [256] Y. S. Teo, H. Zhu, B.-G. Englert, J. cháek, and Z. Hradil, “Quantum-State Reconstruction by Maximizing Likelihood and Entropy”, *Physical Review Letters* **107** (2011).

- [257] J. A. Smolin, J. M. Gambetta, and G. Smith, “Efficient Method for Computing the Maximum-Likelihood Quantum State from Measurements with Additive Gaussian Noise”, *Physical Review Letters* **108** (2012).
- [258] F. Huszár and N. M. T. Houlby, “Adaptive Bayesian quantum tomography”, *Physical Review A* **85** (2012).
- [259] C. Ferrie, “Quantum model averaging”, *New Journal of Physics* **16** (2014).
- [260] C. Granade, J. Combes, and D. G. Cory, “Practical Bayesian tomography”, *New Journal of Physics* **18** (2016).
- [261] D. Gross, Y.-K. Liu, S. T. Flammia, S. Becker, and J. Eisert, “Quantum State Tomography via Compressed Sensing”, *Physical Review Letters* **105** (2010).
- [262] A. Kalev, R. L. Kosut, and I. H. Deutsch, “Quantum tomography protocols with positivity are compressed sensing protocols”, *npj Quantum Information* **1** (2015).
- [263] G. Torlai, G. Mazzola, J. Carrasquilla, M. Troyer, R. Melko, and G. Carleo, “Neural-network quantum state tomography”, *Nature Physics* **14** (2018).
- [264] M. Lu, N. Q. Burdick, S. H. Youn, and B. L. Lev, “Strongly Dipolar Bose-Einstein Condensate of Dysprosium”, *Physical Review Letters* **107** (2011).
- [265] B. E. Mischuck, S. T. Merkel, and I. H. Deutsch, “Control of inhomogeneous atomic ensembles of hyperfine qudits”, *Physical Review A* **85** (2012).
- [266] K. Aikawa, “Bose-Einstein Condensation of Erbium”, *Physical Review Letters* **108** (2012).
- [267] A. Smith, B. E. Anderson, H. Sosa-Martinez, C. A. Riofrío, I. H. Deutsch, and P. S. Jessen, “Quantum control in the cs $6S_{1/2}$ ground manifold using radio-frequency and microwave magnetic fields”, *Physical Review Letters* **111** (2013).
- [268] T. Takekoshi, L. Reichsöllner, A. Schindewolf, J. M. Hutson, C. R. Le Sueur, O. Dulieu, F. Ferlaino, R. Grimm, and H.-C. Nägerl, “Ultracold Dense Samples of Dipolar RbCs Molecules in the Rovibrational and Hyperfine Ground State”, *Physical Review Letters* **113** (2014).

- [269] M. Zeppenfeld, B. G. U. Englert, R. Glöckner, A. Prehn, M. Mielenz, C. Sommer, L. D. van Buuren, M. Motsch, and G. Rempe, “Sisyphus cooling of electrically trapped polyatomic molecules”, *Nature* **491** (2012).
- [270] I. Kozyryev, L. Baum, K. Matsuda, B. L. Augenbraun, L. Anderegg, A. P. Sedlack, and J. M. Doyle, “Sisyphus Laser Cooling of a Polyatomic Molecule”, *Physical Review Letters* **118** (2017).
- [271] P. Puri, M. Mills, C. Schneider, I. Simbotin, J. A. Montgomery, R. Côté, A. G. Suits, and E. R. Hudson, “Synthesis of mixed hypermetallic oxide BaOCa⁺ from laser-cooled reagents in an atom-ion hybrid trap”, *Science* **357** (2017).
- [272] X. Wu, T. Gantner, M. Koller, M. Zeppenfeld, S. Chervenkov, and G. Rempe, “A cryofuge for cold-collision experiments with slow polar molecules”, *Science* **358** (2017).
- [273] L. D. Marco, G. Valtolina, K. Matsuda, W. G. Tobias, J. P. Covey, and J. Ye, “A degenerate Fermi gas of polar molecules”, *Science* **363** (2019).
- [274] L. R. Liu, J. D. Hood, Y. Yu, J. T. Zhang, K. Wang, Y.-W. Lin, T. Rosenband, and K.-K. Ni, “Molecular Assembly of Ground-State Cooled Single Atoms”, *Physical Review X* **9** (2019).
- [275] L. Anderegg, L. W. Cheuk, Y. Bao, S. Burchesky, W. Ketterle, K.-K. Ni, and J. M. Doyle, “An optical tweezer array of ultracold molecules”, *Science* **365** (2019).
- [276] C. W. Chou, A. L. Collopy, C. Kurz, Y. Lin, M. E. Harding, P. N. Plessow, T. Fortier, S. Diddams, D. Leibfried, and D. R. Leibbrandt, “Frequency-comb spectroscopy on pure quantum states of a single molecular ion”, *Science* **367** (2020).
- [277] Y. Lin, D. R. Leibbrandt, D. Leibfried, and C.-w. Chou, “Quantum entanglement between an atom and a molecule”, *Nature* **581** (2020).
- [278] D. Hemmer, E. Montano, B. Q. Baragiola, L. M. Norris, E. Shojaei, I. H. Deutsch, and P. S. Jessen, “Squeezing the angular momentum of an ensemble of complex multi-level atoms”, (2018), [arXiv:1811.02519 \[quant-ph\]](https://arxiv.org/abs/1811.02519).

- [279] A. Evrard, “Enhanced Magnetic Sensitivity with Non-Gaussian Quantum Fluctuations”, *Physical Review Letters* **122** (2019).
- [280] V. V. Albert, J. P. Covey, and J. Preskill, “Robust Encoding of a Qubit in a Molecule”, *Physical Review X* **10** (2020).
- [281] J. A. Gross, “Designing Codes around Interactions: The Case of a Spin”, *Physical Review Letters* **127** (2021).
- [282] K. Barnes, P. Battaglini, B. J. Bloom, K. Cassella, R. Coxe, N. Crisosto, J. P. King, S. S. Kondov, K. Kotru, S. C. Larsen, J. Lauigan, B. J. Lester, M. McDonald, E. Megidish, S. Narayanaswami, C. Nishiguchi, R. Notermans, L. S. Peng, A. Ryou, T.-Y. Wu, and M. Yarwood, “Assembly and coherent control of a register of nuclear spin qubits”, (2021), [arXiv:2108.04790 \[quant-ph\]](https://arxiv.org/abs/2108.04790).
- [283] H. F. Hofmann and S. Takeuchi, “Quantum-state tomography for spin- l systems”, *Physical Review A* **69** (2004).
- [284] S. N. Filippov and V. I. Man’ko, “Inverse spin-s portrait and representation of qudit states by single probability vectors”, *Journal of Russian Laser Research* **31** (2010).
- [285] R. Schmied and P. Treutlein, “Tomographic reconstruction of the Wigner function on the Bloch sphere”, *New Journal of Physics* **13** (2011).
- [286] S. T. Flammia, A. Silberfarb, and C. M. Caves, “Minimal Informationally Complete Measurements for Pure States”, *Foundations of Physics* **35** (2005).
- [287] R. T. Thew, K. Nemoto, A. G. White, and W. J. Munro, “Qudit quantum-state tomography”, *Physical Review A* **66** (2002).
- [288] R. Salazar and A. Delgado, “Quantum tomography via unambiguous state discrimination”, *Physical Review A* **86** (2012).
- [289] H. Sosa-Martinez, “Quantum Control and Quantum Tomography on Neutral Atom Qudits”, (2017), [arXiv:1706.06536 \[quant-ph\]](https://arxiv.org/abs/1706.06536).

- [290] D. Ha and Y. Kwon, “A minimal set of measurements for qudit-state tomography based on unambiguous discrimination”, [Quantum Information Processing](#) **17** (2018).
- [291] Q. P. Stefano, L. Rebón, S. Ledesma, and C. Iemmi, “Set of $4d - 3$ observables to determine any pure qudit state”, [Optics Letters](#) **44** (2019).
- [292] A. M. Plici, T.-A. Isdrail, S. Ataman, and R. Ionicioiu, “OAM tomography with HeisenbergWeyl observables”, [Quantum Science and Technology](#) **5** (2020).
- [293] V. I. Man’ko and O. V. Man’ko, “Spin state tomography”, [Journal of Experimental and Theoretical Physics](#) **85** (1997).
- [294] **Spin Qudit Tomography**, https://github.com/perlinm/spin_qudit_tomography, 2021.
- [295] S. Kryszewski and M. Zachcia, “Positivity of the $N \times N$ density matrix expressed in terms of polarization operators”, [Journal of Physics A: Mathematical and General](#) **39** (2006).
- [296] R. A. Bertlmann and P. Krammer, “Bloch vectors for qudits”, [Journal of Physics A: Mathematical and Theoretical](#) **41** (2008).
- [297] J. D. McEwen and Y. Wiaux, “A Novel Sampling Theorem on the Sphere”, [IEEE Transactions on Signal Processing](#) **59** (2011).
- [298] H. Rauhut and R. Ward, “Sparse recovery for spherical harmonic expansions”, (2011), [arXiv:1102.4097 \[math\]](#).
- [299] Y. F. Alem, D. H. Chae, and R. A. Kennedy, “Sparse signal recovery on the sphere: Optimizing the sensing matrix through sampling”, in [2012 6th International Conference on Signal Processing and Communication Systems](#) (Dec. 2012), pp. 1–6.
- [300] Z. Khalid, R. A. Kennedy, and J. D. McEwen, “An Optimal-Dimensionality Sampling Scheme on the Sphere With Fast Spherical Harmonic Transforms”, [IEEE Transactions on Signal Processing](#) **62** (2014).

- [301] W. Freeden and M. Schreiner, **Spherical functions of mathematical geosciences** (Springer Science & Business Media, Dec. 2008).
- [302] W. Freeden, M. Z. Nashed, and M. Schreiner, **Spherical Sampling**, edited by W. Freeden, M. Z. Nashed, and M. Schreiner, Geosystems Mathematics (Springer International Publishing, 2018).
- [303] C. Ferrie, “Self-Guided Quantum Tomography”, *Physical Review Letters* **113** (2014).
- [304] L. Pereira, L. Zambrano, J. Cortés-Vega, S. Niklitschek, and A. Delgado, “Adaptive quantum tomography in high dimensions”, *Physical Review A* **98** (2018).

ProQuest Number: 28777628

INFORMATION TO ALL USERS

The quality and completeness of this reproduction is dependent on the quality and completeness of the copy made available to ProQuest.



Distributed by ProQuest LLC (2021).

Copyright of the Dissertation is held by the Author unless otherwise noted.

This work may be used in accordance with the terms of the Creative Commons license or other rights statement, as indicated in the copyright statement or in the metadata associated with this work. Unless otherwise specified in the copyright statement or the metadata, all rights are reserved by the copyright holder.

This work is protected against unauthorized copying under Title 17, United States Code and other applicable copyright laws.

Microform Edition where available © ProQuest LLC. No reproduction or digitization of the Microform Edition is authorized without permission of ProQuest LLC.

ProQuest LLC
789 East Eisenhower Parkway
P.O. Box 1346
Ann Arbor, MI 48106 - 1346 USA